

GEOTECHNICAL, GEOLOGICAL AND EARTHQUAKE ENGINEERING

EARTHQUAKE GEOTECHNICAL ENGINEERING

KYRIAZIS D. PITILAKIS
EDITOR

 Springer

CD-Rom
included

EARTHQUAKE GEOTECHNICAL ENGINEERING

GEOTECHNICAL, GEOLOGICAL AND EARTHQUAKE ENGINEERING

Volume 6

Series Editor

Atilla Ansal, *Kandilli Observatory and Earthquake Research Institute,
Boğaziçi University, Istanbul, Turkey*

Editorial Advisory Board

Julian Bommer, *Imperial College London, U.K.*
Jonathan D. Bray, *University of California, Berkeley, U.S.A.*
Kyriazis Pitilakis, *Aristotle University of Thessaloniki, Greece*
Susumu Yasuda, *Tokyo Denki University, Japan*

The titles published in this series are listed at the end of this volume

EARTHQUAKE GEOTECHNICAL ENGINEERING

4th International Conference on Earthquake
Geotechnical Engineering-Invited Lectures

edited by

KYRIAZIS D. PITILAKIS

*Department of Civil Engineering,
Aristotle University of Thessaloniki, Greece*



Springer

A C.I.P. Catalogue record for this book is available from the Library of Congress.

ISBN 978-1-4020-5892-9 (HB)

ISBN 978-1-4020-5893-6 (e-book)

Published by Springer,
P.O. Box 17, 3300 AA Dordrecht, The Netherlands.

www.springer.com

Printed on acid-free paper

All Rights Reserved

© 2007 Springer

No part of this work may be reproduced, stored in a retrieval system, or transmitted in any form or by any means, electronic, mechanical, photocopying, microfilming, recording or otherwise, without written permission from the Publisher, with the exception of any material supplied specifically for the purpose of being entered and executed on a computer system, for exclusive use by the purchaser of the work.

PREFACE

Geotechnical Earthquake Engineering and Soil Dynamics, as well as their interface with Engineering Seismology, Geophysics and Seismology, have all made important progress over the past 15 years, mainly due to the development of instrumented large scale experimental facilities, to the increase in the quantity and quality of recorded earthquake data, to the numerous well-documented case studies from recent strong earthquakes as well as enhanced computer capabilities. One of the major factors contributing to the aforementioned progress is the increasing social need for a safe urban environment, large infrastructures and essential facilities. The advances achieved are also confirmed by the increasing number of scientific journals and publications which are relevant to the field of Geotechnical Earthquake Engineering.

The successful International Conferences on Geotechnical Earthquake Engineering organized every 4 years by the Technical Committee of Earthquake Engineering of the International Society of Soil Mechanics and Geotechnical Engineering constitute irrefutable evidence as to the growing interest taken by the scientific and engineering community in Geotechnical Earthquake Engineering.

This book contains the full papers of the invited keynote and theme lectures, including the 2nd Ishihara lecture, given during the 4th International Conference on Geotechnical Earthquake Engineering (4ICEGE) held in June 2006 in Thessaloniki, Greece. It provides a thorough presentation of state-of-the-art topics related to Earthquake Geotechnical Engineering and Soil Dynamics and their interface with Engineering Seismology, Geophysics and Seismology. Interdisciplinary topics such as vulnerability assessment and seismic risk management of geotechnical structures and lifelines are also addressed and discussed. A comprehensive overview of the possibilities offered by the recent worldwide developments in large scale testing facilities and strong ground motion arrays is also illustrated.

The nineteen chapters of this book, prepared by distinguished scientists and experts, provide a panorama of recent achievements in Geotechnical Earthquake Engineering. Certain unresolved engineering issues are also highlighted and some speculations and ideas for the future are mentioned.

The main scope of the book is to provide the engineering society, including geotechnical and structural engineers, geologists and seismologists as well as risk managing scientists, with the most recent advances and developments in the study of soil dynamics, earthquake geotechnical engineering, seismology and risk assessment and management.

Kyriazis Pitilakis
Professor of Aristotle University, Chairman of 4ICEGE
Editor

TABLE OF CONTENTS

<i>Preface</i>	v
Chapter 1. SPT- and CPT-based relationships for the Residual Shear Strength of Liquefied Soils <i>I.M. Idriss and R.W. Boulanger</i>	
1. Introduction	1
2. Case history studies	3
3. SPT-based correlation for residual strength	7
3.1. Correlation of S_r with $(N_1)_{60cs-Sr}$	7
3.2. Correlation of S_r/σ'_{vo} with $(N_1)_{60cs-Sr}$	8
4. CPT-based correlation for residual strength	12
4.1. Converting the SPT Correlation	13
4.2. CPT Values for Case Histories	15
5. Concluding remarks	17
References	21
Chapter 2. Long Period Strong Ground Motion and its Use as Input to Displacement Based Design <i>E. Faccioli, C. Cauzzi, R. Paolucci, M. Vanini, M. Villani, and D. Finazzi</i>	
1. Introduction	23
2. Empirical prediction of displacement spectral response (DRS) over a broad period range	24
2.1. Data Selection	25
2.2. Prediction Equations for Displacement Spectral Response	28
2.3. Influence of Local Ground Conditions	31
2.4. Vertical Spectra	34
2.5. A Simplified Spectral Displacement Model	35
2.6. Other Aspects	36

3.	Response of alluvium filled valleys and basins	37
4.	Overdamped spectra	43
5.	Hazard representations in spectral displacements	44
	5.1. <i>Criteria for the Hazard Analysis</i>	44
	5.2. <i>Extent of the Long Period, Constant Displacement Range</i>	45
	5.3. <i>Overdamped, Uniform Hazard (UH) DRS</i>	45
	5.4. <i>Effects Related to Local Soil Amplification</i>	46
	5.5. <i>Spectral Displacement Maps</i>	47
	References	49

Chapter 3. Site Effects: From Observation and Modelling to Accounting for them in Building Codes

F.J. Chávez-García

1.	Introduction	53
2.	Estimation of site effects	55
3.	Modelling site effects. The importance of the model	61
4.	Accounting for site effects in building codes	67
5.	Concluding remarks	69
	References	70

Chapter 4. Source and Site Factors in Microzonation

A. Ansal and G. Tönük

1.	Introduction	73
2.	Input motion	74
	2.1. <i>Real Acceleration Records</i>	74
	2.2. <i>Simulated Acceleration Record</i>	76
3.	Site characterisation	78
4.	Microzonation	80
	4.1. <i>Microzonation with Respect to Ground Motion</i>	80
	4.2. <i>Microzonation with Respect to Liquefaction Susceptibility</i>	81
5.	Spectral accelerations for vulnerability assessments	86

6. Conclusions	89
References	90

Chapter 5. A Review of Large-Scale Testing Facilities in Geotechnical Earthquake Engineering

A. Elgamal, K. Pitilakis, R. Dimitrios, J. Garnier, SP. Gopal Madabhushi, A. Pinto, J. Steidl, H.E. Stewart, K.H. Stokoe, F. Taucer, K. Tokimatsu, and J.W. Wallace

1. Introduction	93
2. Instrumented test sites	95
2.1. Euroseis Project	95
2.1.1. Project objectives	96
2.1.2. General description of the test site	96
2.1.3. Instrumentation	99
2.1.4. Main scientific and engineering outcomes	101
2.2. Ucsb Nees Garner Valley and Wildlife Test Sites (Dr. Jamieson Steidl, PI)	102
2.2.1. Soil and seismic characteristics at Garner Valley	102
2.2.2. Geologic conditions	102
2.2.3. Garner Valley SFSI structure	103
2.2.4. Wildlife refuge liquefaction field site	104
3. Mobile laboratories	106
3.1. Nees Facilities at UCLA	106
3.1.1. Eccentric mass shakers	106
3.1.2. Linear shaker	107
3.1.3. Cone penetration testing truck	107
3.1.4. Satellite system	108
3.2. NEES Facilities at the University of Texas	109
3.2.1. Cruiser (instrumentation van)	109
3.2.2. Thumper	110
3.2.3. T-Rex (tri-axial vibrosies)	110

3.2.4. Liquidator (low frequency vibrosies)	110
3.2.5. Representative collaborative research project	111
4. Large-scale testing facilities	113
4.1. NEES Facilities at Cornell	113
4.2. UCSD Shake Table	115
4.3. Japan E-Defense Shake Table	116
4.3.1. Recent shaking table tests at E-Defense	116
4.3.2. Representative test results	118
5. Earthquake loading aboard geotechnical centrifuges	118
5.1. Dynamic Centrifuge Modelling	119
5.2. Shaking Facilities at Cambridge University	119
5.3. Pneumatic Shaker at CEA-CESTA, France	120
5.4. Earthquake Simulation at LCPC, France	120
5.5. Recent Advances in Earthquake Actuation Worldwide	121
6. International collaboration	123
6.1. Large Testing Facilities Worldwide	123
6.2. European Experience on Collaboration	123
6.3. The USA NEES Initiative	125
6.4. International Collaboration Challenges and Opportunities	126
6.4.1. Simulation	126
6.4.2. Cyberenvironments	127
6.4.3. Data infrastructure	127
7. Summary and conclusions	127
References	127

Chapter 6. Modelling of Dynamic Soil Problems

D.M. Wood

1. Introduction	131
2. Constitutive modelling framework	132
3. Fabric, soil stiffness and laboratory geophysics	133

4. NEMISREF mitigation of foundation response	137
5. Macroelement analysis	142
6. Conclusions	147
References	148

Chapter 7. Field Seismic Testing in Geotechnical Earthquake Engineering

K.H. Stokoe, II

1. Introduction	151
2. Deeper seismic profiling	152
3. In-situ parametric studies	154
4. Conclusions	156
References	157

Chapter 8. Liquefaction Strengths of Poorly-Graded and Well-Graded Granular Soils Investigated by Lab Tests

T. Kokusho

1. Introduction	159
2. Effect of grain size curve on S-wave velocity and <i>N</i> -value	163
2.1. <i>S-Wave Velocity</i>	164
2.2. <i>SPT N-Value</i>	167
3. Effect of grain size distribution on cyclic strength	169
3.1. <i>Soil Materials</i>	169
3.2. <i>Test Method</i>	170
3.3. <i>Effect of Particle Gradation for Clean Granular Soils</i>	172
3.4. <i>Effect of Fines Content</i>	174
4. Effect of particle gradation on post-liquefaction behavior	178
4.1. <i>Effect of Particle Gradation in Post-Liquefaction Shear Behavior</i>	178
4.2. <i>Effect of Fines Content in Post-Liquefaction Shear Behavior</i>	180
5. Conclusions	182
References	183

Chapter 9. Shallow and Deep Foundations Under Fault Rupture or Strong Seismic Shaking

G. Gazetas, I. Anastasopoulos, and M. Apostolou

1. Introduction	185
2. Fault-rupture propagation and its interaction with foundations	186
2.1. <i>Statement of the Problem</i>	186
2.2. <i>Numerical Analysis and Results: Shallow Foundations</i>	187
2.3. <i>Numerical Analysis and Results: Deep Foundations</i>	194
2.3.1. <i>Piles</i>	195
2.3.2. <i>Rigid caisson</i>	199
3. Nonlinear response of shallow foundations to strong seismic excitation	201
3.1. <i>Introduction</i>	201
3.2. <i>New Design Philosophy: “Plastic Hinging” in Shallow Foundations</i>	202
3.3. <i>Characteristic Results</i>	204
3.3.1. <i>Static nonlinear (“pushover”) analysis</i>	204
3.3.2. <i>Seismic response</i>	207
References	210

Chapter 10. Seismic Design and Performance of Surface Foundations

M. Pender

1. Introduction	217
2. Ultimate limit state design of shallow foundations in Eurocode 8	218
2.1. <i>Acceleration Induced Reduction in Vertical Foundation Strength</i>	221
2.2. <i>Undrained Response</i>	222
2.3. <i>Drained Response</i>	223
3. Serviceability limit state design of shallow foundations for earthquake loading	224
4. Spring models for shallow foundations on soil	228
4.1. <i>Shallow Foundations on a Continuous Elastic Soil</i>	229
4.2. <i>Nonlinear Soil Stress–Strain Behaviour</i>	232

5.	Integrated design of structure–foundation systems	235
5.1.	<i>Structure Description</i>	235
5.2.	<i>Ruaumoko Modelling of the Structure–Foundation System</i>	236
5.3.	<i>Elastic Structural Response with Fixed Column–Footing Connections</i> ...	237
5.4.	<i>Elastic Structural Response with Pinned Column–Footing Connections</i> ..	238
6.	Conclusions	241
	References	241

Chapter 11. Liquefaction Performance of Shallow Foundations in Presence of a Soil Crust

G. Bouckovalas and P. Dakoulas

1.	Introduction	245
2.	Existing background	246
2.1.	<i>Performance-Based Design Requirements</i>	246
2.2.	<i>Static Bearing Capacity Degradation</i>	248
2.3.	<i>Liquefaction-Induced Foundation Settlements</i>	250
3.	Numerical analysis of liquefaction performance	253
4.	Evaluation of degraded bearing capacity	256
5.	Evaluation of liquefaction settlements	260
6.	Performance-based design issues	266
7.	Concluding remarks	271
	References	273

Chapter 12. Seismic Design of Pile Foundations for Liquefaction Effects

*R.W. Boulanger, D. Chang, S.J. Brandenberg, R.J. Armstrong,
and B.L. Kutter*

1.	Introduction	277
2.	Pile groups in laterally spreading ground	278
2.1.	<i>General Approach</i>	278
2.2.	<i>Analysis of Piles for the Nonliquefaction Case</i>	278

2.2.1. Assemble a BNWF model	278
2.2.2. Estimate loads from the superstructure	279
2.2.3. Perform BNWF analysis	279
2.3. Evaluating the Potential for Liquefaction-Induced Ground Displacements	280
2.4. Analysis of Piles for the Liquefaction Case	281
2.4.1. Modify the BNWF model for the effects of liquefaction	281
2.4.2. Estimate loads from the superstructure	286
2.4.3. Perform the BNWF analysis	288
2.5. Additional Comments for Pile Groups in Lateral Spreads	291
3. Pinning effects for approach embankments	292
3.1. Definition and Background	292
3.2. Procedures for Estimating Pile Pinning Effects	294
3.2.1. Estimating embankment displacements for a range of restraining forces	294
3.2.2. Estimating pile/bridge restraining forces for a range of displacements	296
3.2.3. Compatibility of embankment and pile displacements	297
3.3. Evaluation Against Centrifuge Model Tests	297
4. Other issues and considerations	299
5. Summary remarks	300
References	301

Chapter 13. Seismic Analysis and Design of Geotechnical Structures

S. Iai and T. Tobita

1. Introduction	303
2. Assemblage of soil particles	304
3. Some findings on seismic analysis	310
3.1. Cyclic Deformation of Soil Under Initial Deviator Stress	310
3.2. Effect of Residual Strength of Soil on Seismic Settlements of Embankments	311

3.3. <i>Effect of Increase in Earth Pressures on Buried Structures</i>	315
3.4. <i>Effect of Initial Stress in the Backfill Soil on Retaining Walls</i>	316
4. Performance-based design	316
5. Emerging trends in design	320
5.1. <i>From Design-For-Construction to Design-for-Performance</i>	320
5.2. <i>From Standardized-Design to Site-Specific-Design</i>	320
5.3. <i>From Analysis-of-Structural/Foundation Parts to Analysis-of-Soil-Structure System</i>	320
5.4. <i>Further Emerging Trends: Producing Service</i>	320
6. Designing large urban areas against combined hazards	321
7. Conclusions	323
References	324

Chapter 14. Simplified Seismic Slope Displacement Procedures

J.D. Bray

1. Introduction	327
2. Seismic displacement analysis	328
2.1. <i>Critical Design Issues</i>	328
2.2. <i>Deviatoric-Induced Seismic Displacements</i>	328
3. Components of a seismic displacement analysis	329
3.1. <i>General</i>	329
3.2. <i>Earthquake Ground Motion</i>	329
3.3. <i>Dynamic Resistance</i>	330
3.4. <i>Dynamic Response</i>	332
4. Critique of some simplified seismic displacement methods	334
4.1. <i>General</i>	334
4.2. <i>Seed (1979) Pseudostatic Slope Stability Procedure</i>	334
4.3. <i>Makdisi and Seed (1978) Simplified Seismic Displacement Method</i>	335
4.4. <i>Bray et al. (1998) Simplified Seismic Displacement Approach</i>	337

5.	Bray and Travasarou (2007) simplified seismic displacement procedure	340
5.1.	<i>Earthquake Ground Motions</i>	340
5.2.	<i>Dynamic Resistance of the Earth/Waste Structure</i>	341
5.3.	<i>Dynamic Response of the Potential Sliding Mass</i>	341
5.4.	<i>Functional Forms of Model Equations</i>	342
5.5.	<i>Equations for Estimating Seismic Deviatoric Displacements</i>	343
5.6.	<i>Model Validation and Comparison</i>	346
5.7.	<i>Illustrative Seismic Evaluation Example</i>	348
6.	Conclusions	350
	References	351

Chapter 15. Developments of Soil Improvement Technologies for Mitigation of Liquefaction Risk

I. Towhata

1.	Introduction	355
2.	Sand densification	356
2.1.	<i>General Remarks</i>	356
2.2.	<i>Blasting</i>	356
2.3.	<i>Experimental Reproduction of Blasting Stress</i>	363
3.	Soil improvement by grouting	365
3.1.	<i>General Remarks</i>	365
3.2.	<i>Undrained Triaxial Tests on Sand Improved by Colloidal Silica</i>	370
4.	Dissipation of excess pore water pressure	376
5.	Conclusion	382
	References	382

Chapter 16. Remediation Methods Against Liquefaction Which Can be Applied to Existing Structures

S. Yasuda

1.	Introduction	385
2.	Remediation methods against liquefaction compiled in 1993 (partially quoted from Yasuda, 2005a)	386
3.	Restrictions to be considered in remediation techniques for existing structures	386

4.	Remediation methods for existing raft foundations	390
4.1.	<i>Principle of Remediation</i>	390
4.2.	<i>Example of Treated Structures</i>	390
4.2.1.	<i>A tank yard in Kawasaki (partially quoted from Ohmori, 1979; JGS, 1998)</i>	390
4.2.2.	<i>Fisherman's Wharf (partially quoted from TC4, 2001)</i>	391
4.2.3.	<i>The Yokohama Customs Building (partially quoted from Kaneko et al., 2003)</i>	391
4.2.4.	<i>An oil tank in Kawasaki (partially quoted from Nikkei Construction, 2005)</i>	392
4.2.5.	<i>An oil tank (partially quoted from Sawauchi et al., 1992)</i>	392
4.2.6.	<i>A timber house</i>	392
4.3.	<i>Other Related Studies</i>	392
5.	Remediation methods for existing pile foundations	393
5.1.	<i>Principle of Remediation</i>	393
5.2.	<i>Example of Treated Structures</i>	393
5.2.1.	<i>A bridge (partially quoted from JGS, 1998)</i>	393
5.2.2.	<i>A bridge (partially quoted from JGS, 2004)</i>	394
5.2.3.	<i>Elevated bridges in Kobe (partially quoted from Hanshin Express Way, 1997; TC4, 2001)</i>	394
6.	Remediation methods for existing embankments	394
6.1.	<i>Principle of Remediation</i>	394
6.2.	<i>Example of Treated Structures</i>	394
6.2.1.	<i>The Tokaido Shinkansen (partially quoted from Nasu, 1984; JGS, 1998)</i>	394
6.2.2.	<i>Yodogawa River dike (partially quoted from TC4, 2001)</i>	395
6.2.3.	<i>Arakawa River dike (partially quoted from JGS, 1998)</i>	395
6.2.4.	<i>Hachirogata Polder dike (partially quoted from Civil Eng. Dept. Akita Prefecture, 1990)</i>	396
6.2.5.	<i>Tokachi River dike (partially quoted from Hokkaido Development, 1994)</i>	396

7.	Remediation methods for existing sea walls	396
7.1.	<i>Principle of Remediation</i>	396
7.2.	<i>Example of Treated Structures</i>	396
7.2.1.	<i>Kushiro Port (partially quoted from TC4, 2001)</i>	396
7.2.2.	<i>Port of Oakland (partially quoted from TC4, 2001)</i>	397
7.2.3.	<i>Ishikari Port (partially quoted from Kawamura et al., 2001)</i>	397
7.2.4.	<i>Kobe Port (partially quoted from TC4, 2001)</i>	397
7.2.5.	<i>A quay wall in Tokyo (partially quoted from JGS, 1998)</i>	398
8.	Remediation methods for existing buried structures	398
8.1.	<i>Principle of Remediation</i>	398
8.2.	<i>Example of Treated Structures</i>	399
8.2.1.	<i>A multi-service tunnel (partially quoted from JGS, 1998)</i>	399
8.2.2.	<i>A subway station in Tokyo (partially quoted from Yokota et al., 2001)</i>	400
9.	Remediation methods for existing structures affected by ground flow	400
9.1.	<i>Principle of Remediation</i>	400
9.2.	<i>Example of Treated Structures</i>	400
9.2.1.	<i>Metropolitan Expressway in Tokyo (partially quoted from Yasuda and Ogasawara, 2004; Yasuda, 2005a)</i>	400
9.2.2.	<i>Hanshin Expressway (partially quoted from JGS, 2004; Yasuda, 2005b)</i>	404
10.	Concluding remarks	404
	References	405

Chapter 17. Lifeline Performance Under Extreme Loading During Earthquakes

T.D. O'Rourke and A.L. Bonneau

1.	Introduction	407
2.	Geotechnical earthquake loading	409
3.	Lifeline system response to earthquakes	411
4.	Large-scale tests of ground rupture effects on steel pipelines with elbows	416
5.	Lateral soil–structure interaction during ground failure	418

6. Large-scale tests of ground rupture effects on HDPE pipelines	425
7. Concluding remarks	429
References	431

Chapter 18. Seismic Risk Assessment of Underground Structures Under Transient Ground Deformations

R. Paolucci and K. Pitilakis

1. Introduction	433
2. Earthquake-induced transient ground strains	435
2.1. Experimentally Based PGS–PGV Relations from Dense Seismic Networks	435
2.2. Evaluation of PGS in the Presence of Strong Lateral Heterogeneities	440
3. Hazard maps and seismic risk assessment of underground pipeline systems ...	445
4. Application examples	447
5. Conclusions	456
References	457

Chapter 19. Issues in Seismic Risk Assessment of Transportation Networks

A.S. Kiremidjian, E. Stergiou, and R. Lee

1. Introduction	461
2. Overview of transportation risk assessment	463
2.1. Component Risk Analysis	463
2.2. Transportation Network Risk Assessment	465
2.3. Estimation of Total Risk	467
2.3.1. General formulation of point estimates of loss	467
2.3.2. Point estimates of the structural loss for multiple sites and single event	468
2.4. Ground Motion Correlation	469
2.5. Damage Correlation	469
2.5.1. Probability distributions of the structural loss for multiple sites and single event	470
2.6. Evaluation of the Network Functionality Loss	471

2.6.1.	<i>Expected value of network functionality loss</i>	471
2.6.2.	<i>Uncertainties in network functionality loss</i>	471
2.7.	<i>Transportation Network Risk Curve from Monte Carlo Simulation with Importance Sampling</i>	472
3.	Application to the San Francisco Bay Area Transportation Network	472
3.1.	<i>Hazard Assessment</i>	474
3.2.	<i>Damage Assessment</i>	474
3.3.	<i>Structural Loss</i>	474
3.4.	<i>Operational Loss</i>	475
3.5.	<i>Annual Seismic Risk Assessment</i>	476
3.6.	<i>Influence of Ground Motion and Damage Correlation on Loss Computations</i>	478
4.	Conclusions	479
	References	479
	Index	481

CHAPTER 1

SPT- AND CPT-BASED RELATIONSHIPS FOR THE RESIDUAL SHEAR STRENGTH OF LIQUEFIED SOILS

I.M. Idriss¹ and Ross W. Boulanger²

¹ *Department of Civil and Environmental Engineering, University of California at Davis, California, USA*

² *Department of Civil and Environmental Engineering, University of California at Davis, California, USA*

Abstract. An evaluation of post-earthquake stability of earth embankments or slopes that contain, or are founded on, soils that may liquefy requires estimating the liquefied soil's residual shear strength, S_r . Decisions regarding the need for expensive mitigation efforts, including ground improvement work, often hinge on the selected S_r values. This paper presents recommended SPT- and CPT-based relationships for estimating the residual shear strength ratio, S_r/σ'_{vo} , of liquefied nonplastic soils in the field based on a review of prior case history studies, laboratory testing studies, and recent findings regarding void redistribution mechanisms. The recommended relationships provide guidance regarding the unavoidable task in practice of having to extrapolate beyond the available case history data. Limitations in the state of knowledge are discussed.

1. Introduction

Procedures for estimating the residual shear strength, S_r , of liquefied cohesionless or non-plastic soils have evolved considerably over the past 25 years. Procedures that require laboratory testing of field samples have been developed that use samples obtained by frozen sampling techniques (e.g., Robertson et al., 2000) or samples obtained by high-quality tube sampling techniques coupled with procedures for “correcting” the shear strength for the estimated volume changes that occur during sampling and testing (e.g., Castro, 1975; Castro and Poulos, 1977; Poulos et al., 1985). Procedures based on using case histories for estimating the in-situ S_r of liquefied soils have been developed by back-analyses of liquefaction flow slides, as first presented by Seed (1987) and since modified by a number of investigators (e.g., Davis et al., 1988; Seed and Harder, 1990; Ishihara, 1993; Wride et al., 1999; Olson and Stark, 2002).

Whitman (1985) described situations where pore water seepage driven by earthquake-induced excess pore water pressure gradients could lead to the localized loosening of the liquefied soil, or “void redistribution”, that could result in S_r being much lower in the field than would be obtained from laboratory tests of samples at the pre-earthquake void ratio. These situations require the presence of a soil layer of significantly lower permeability overlying the liquefied soil layer, thereby impeding the outward seepage, as illustrated for an infinite slope in Figure 1.1. Physical and analytical modeling studies by Kokusho (2000), Kulasingam et al. (2004), and Malvick et al. (2004) have illustrated and evaluated

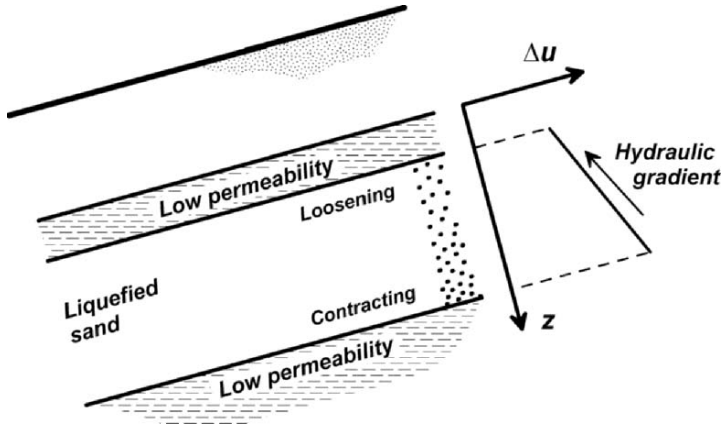


Fig. 1.1. Schematic of void redistribution in a confined sand layer due to upward seepage driven by earthquake-induced excess pore water pressure gradients (after Whitman, 1985)

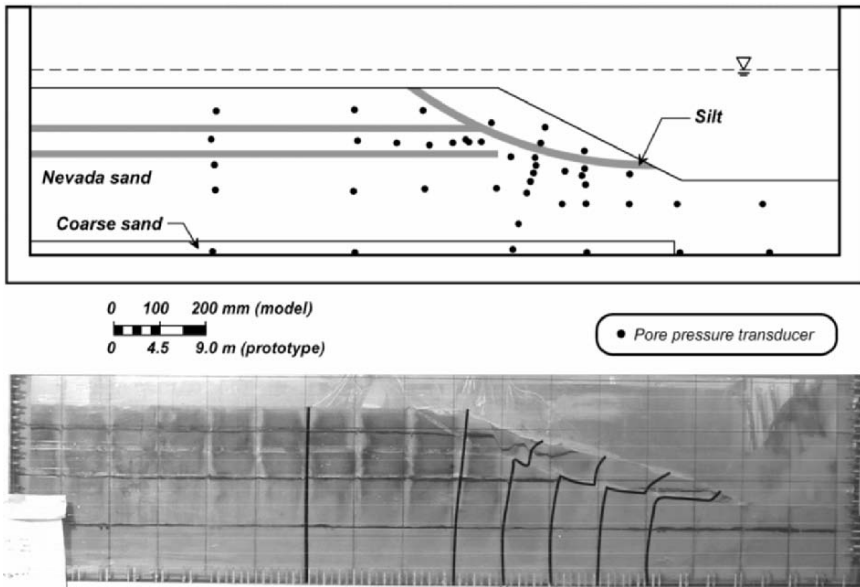


Fig. 1.2. Centrifuge model showing localized deformations beneath a silt layer in a saturated sand slope due to liquefaction-induced void redistribution (Malvick et al., 2004)

several factors that significantly affect the void redistribution phenomenon. For example, the photograph in Figure 1.2 shows slope deformations that developed in a centrifuge model of a saturated sand slope because of void redistribution-induced loosening and strength loss in the sand immediately beneath a low-permeability silt layer. Seed (1987)

noted that the case history based approach to estimating S_r may implicitly account for void redistribution effects, and is therefore preferred for practice over lab testing of field samples.

A number of definitions have been used in the literature for the shear strength of liquefied soils. The ultimate shear resistance, or critical state strength, that is measured in undrained laboratory element tests may be denoted as S_{CS} , whereas the quasi-steady state shear resistance, which corresponds to a local minimum in the stress–strain curve from an undrained laboratory element test, may be denoted as S_{QSS} . Residual shear strength, as used in this paper, refers to the shear resistance that a liquefied soil mobilizes in the field, which can be complicated by void redistribution and other field mechanisms that are not replicated in laboratory element tests. These three “strengths” are fundamentally different from a mechanics standpoint, and thus maintaining a distinction is essential.

This paper presents recommended SPT- and CPT-based relationships for estimating the ratio of residual shear strength to initial vertical effective stress, S_r/σ'_{vo} , for liquefied nonplastic soils in the field. Case history analyses by a number of investigators over the past 20 years are reviewed and utilized. The available case history data only constrain design relationships at low penetration resistances; therefore, the estimation of S_r/σ'_{vo} at higher penetration resistances requires extrapolation beyond the case history data. Consequently, development of the recommended design relationships was guided by laboratory testing studies and recent findings regarding void redistribution mechanisms. Development of the SPT-based relationship is presented first, followed by development of the CPT-based relationship. Limitations in the state of knowledge, including the uncertainties in the empirical data and the challenge of quantifying void redistribution processes, are considered.

2. Case history studies

The back-analysis of a case history involves performing a post-earthquake static stability analysis of the earth structure with each zone of nonliquefied soil assigned a best estimate of its shear strength, while the zone considered to have liquefied is assigned an unknown shear strength of S_r (with $\phi_u = 0$). This procedure is illustrated in Figure 1.3 for the Lower San Fernando Dam (Seed, 1987). An upper bound estimate for S_r is the value that gives a factor of safety against sliding equal to 1.0 for the undeformed geometry of the slope. Another estimate for S_r is similarly obtained for the final deformed geometry of the slope, if that deformed geometry is reasonably documented and if the final soil layering has not been seriously modified in the deformation process. Various procedures have then been used to interpolate between these two estimates of S_r by attempting to account for the role of sliding inertia, evolving geometry, strength losses due to intermixing with adjacent water bodies, and other factors. For example, Olson and Stark (2002) calculated, for the Lower San Fernando dam, S_r values of about 36 and 5 kPa for these two geometries, respectively, and an interpolated best estimate of about 19 kPa. This illustrates how the interpolation of strengths between deformed and undeformed geometries is a very

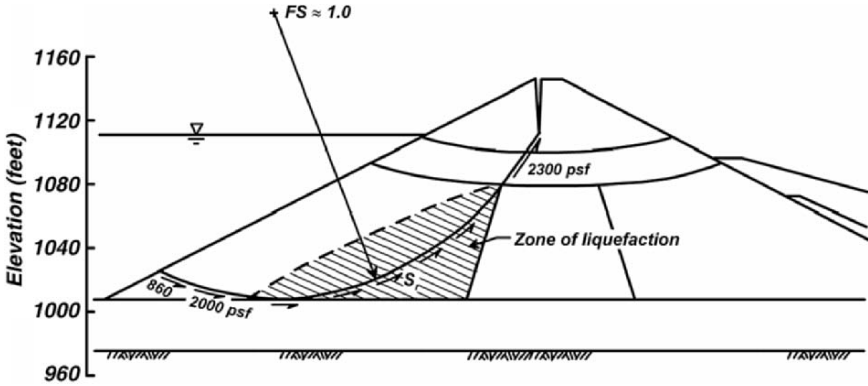


Fig. 1.3. Back-calculation of the residual shear strength for the liquefied shell materials of Lower San Fernando Dam using limit equilibrium analyses (from Seed, 1987)

significant and uncertain step in the interpretation of the case histories, which adds considerably to the already large uncertainty in estimated S_r values. It should also be kept in mind that what is needed for forward applications is the estimate of S_r during the early stages of instability rather than at some later stage (e.g., after significant intermixing has occurred).

Eighteen case histories are listed in Table 1.1 using the values published by Seed (1987), Seed and Harder (1990), and Olson and Stark (2002). Seed (1987) evaluated 12 case histories; ten of these are listed in Table 1.1, while two case histories of lateral spreading were omitted. Seed and Harder (1990) reevaluated the 12 cases originally investigated by Seed (1987) plus an additional five cases; 13 of their cases are listed in Table 1.1, while three cases of lateral spreading and one case of limited embankment slumping were omitted. Olson and Stark (2002) evaluated 33 case histories, which included 15 of the cases investigated by Seed and Harder. Olson and Stark (2002) utilized a number of procedures to back-calculate S_r . Among these procedures is the kinetic analysis, which they considered to provide the more accurate estimation of S_r . Only ten cases had enough subsurface and geometric information for them to complete the kinetic analysis. They note that the procedures they used for the other cases were likely to underestimate S_r . Accordingly, only their results based on kinetics are included in Table 1.1.

The 18 published case histories listed in Table 1.1 can be categorized into three groups as follows:

- **Group 1:** Case histories with an adequate amount of in-situ measurements (e.g., SPT, CPT) and reasonably complete geometric details. Seven case histories (Cases No. 1–7) fit this category.
- **Group 2:** Case histories with an adequate amount of in-situ measurements (e.g., SPT, CPT) but the geometric details are incomplete. Six case histories (Cases No. 8–13) fit this category.

Table 1.1. Published case histories of liquefaction flow failures

Number	Case history Structure	$(N_1)_{60cs-S_r}^*$ ①/②/③	FC**	Residual strength, S_r (kPa) published by			σ'_{vo} (kPa)***
				Seed (1987) ①	Seed and Harder (1990) ②	Olson and Stark (2002) ③	
1	Wachusett Dam – North Dike	–/–/7	5–10/5	–	–	16.0	151.2
2	Lower San Fernando Dam	15/13.5/13.5	5–90/25	35.9	19.2	18.7	166.7
3	Fort Peck Dam	11/10/12.5	55/50	28.7	16.8	27.3	351.5
4	Calaveras Dam	12/12/12.4	10–> 60/60	35.9	31.1	34.5	307.5
5	Hachiro-Gata Road Embankment	–/–/5.6	10–20/15	–	–	2.0	32.1
6	Lake Ackerman Highway Embankment †	–/–/3	0–5/0	–	–	3.9	51.5
7	Route 272 at Higashiarckinai	–/–/8.1	20/20	–	–	4.8	49.3
8	River Bank, Lake Merced	5/6/–	1–4/3	4.8	4.8	–	65.7
9	Kawagishi-cho	4/4/–	0–<5/3	5.7	5.7	–	70.6
10	Mochi-koshi Tailings Dam – Dike 2	6/5/–	> 60–85/85	12.0	12.0	–	52.2
11	La Marquesa Dam – U/S Slope ††	–/6/–	30/30	–	9.6	–	43.6
12	La Marquesa Dam – D/S Slope †††	–/11/–	20/20	–	19.2	–	47.9
13	La Palma Dam ††††	–/4/–	15/15	–	9.6	–	37.8
14	Uetsu Railway Embankment	3/3/3	0–2/2	1.7	1.9	1.7	61.3
15	Solfataro Canal Dike	5/4/–	<5–8/7	6.2	2.4	–	29.9
16	Koda Numa Railway Embankment	3/3/4	13/13	2.4	2.4	1.2	23.2
17	Shibecha-cho Embankment	–/–/7.6	12–35/25	–	–	5.6	64.7
18	Sheffield Dam	6/6/–	25–48/40	2.4	3.6	–	68.4

Cases 1–7 fit into Group 1, which consists of Case Histories with SPT and/or CPT measurements and reasonably complete geometric details.

Cases 8–13 fit into Group 2, which consists of Case Histories with SPT and/or CPT measurements, but geometric details are incomplete.

Cases 14–18 fit into Group 3, which consists of Case Histories with estimated SPT and/or CPT, but geometric details are reasonably complete.

*Values of $(N_1)_{60cs-S_r}$ from Seed (1987) and Seed and Harder (1990); for Olson and Stark, an adjustment for fines content was made to their $(N_1)_{60}$ values.

**Fines content (FC). Range of FC published by authors / FC value used herein to obtain $\Delta(N_1)_{60-S_r}$ from Table 2.

***Values of the average pre-failure vertical effective stress, σ'_{vo} , obtained from Olson and Stark (2002).

†This case history was published by Hryciw et al. (1990), who obtained a value of S_r ranging from 8 to 12 kPa and $(N_1)_{60cs-S_r} = 3$.

††This case history was published by de Alba et al. (1988), who obtained a value of S_r ranging from 3.6 to 16.2 kPa and $(N_1)_{60cs-S_r} = 6$.

†††This case history was published by de Alba et al. (1988), who obtained a value of S_r ranging from 12.7 to 27.7 kPa and $(N_1)_{60cs-S_r} = 11$.

††††This case history was published by de Alba et al. (1988), who obtained a value of S_r ranging from 5.7 to 14.3 kPa and $(N_1)_{60cs-S_r} = 4$.

- **Group 3:** Case histories with only estimated in-situ measurements (e.g., SPT, CPT) but the geometric details are reasonably complete. Five case histories (Cases No. 14–18) fit this category.

Of the 13 case histories in Table 1.1 with in-situ measurements (Groups 1 and 2), all had data on SPT blow counts while only four had data on CPT penetration resistances. For this reason, the correlation between residual strength and SPT blow counts is developed first, using the SPT blow counts that were reported or estimated by the researchers listed in Table 1.1.

Values of equivalent clean sand corrected SPT blow count, $(N_1)_{60cs-S_r}$, for each case history are listed in Table 1.1. The equivalent clean sand SPT corrected blow count, $(N_1)_{60cs-S_r}$, is obtained from the corrected SPT blow count, $(N_1)_{60}$, by the addition of $\Delta(N_1)_{60-S_r}$, which is a function of fines content, FC. Thus,

$$(N_1)_{60cs-S_r} = (N_1)_{60} + \Delta(N_1)_{60-S_r} \quad (1.1)$$

The values of $\Delta(N_1)_{60-S_r}$ initially proposed by Seed (1987) are listed in Table 1.2. Seed and Harder (1990) used these $\Delta(N_1)_{60-S_r}$ values, whereas Olson and Stark (2002) did not include any adjustments for FC in their studies. There are insufficient data to constrain any derivation of $\Delta(N_1)_{60-S_r}$, but the values recommended by Seed (1987) continue to appear reasonable. Consequently, the values of $(N_1)_{60cs-S_r}$ listed in Table 1.1 are those reported by the respective investigators, with the addition of $\Delta(N_1)_{60-S_r}$ for the values published by Olson and Stark (2002) as necessary.

Several other investigators have contributed to the analysis of case histories, including those referenced in the footnotes to Table 1.1. Wride et al. (1999) back-calculated values of S_r for most of the cases listed in Table 1.1, but chose to use the minimum value of $(N_1)_{60}$ for correlating to S_r . The choice of the minimum value of $(N_1)_{60}$ creates two difficulties, namely: (1) it is not certain that the data available for a given case history included the “minimum” value of $(N_1)_{60}$; and (2) an inordinate amount of drilling and sampling would be required in forward applications for a site to ensure that the minimum value of $(N_1)_{60}$ has been obtained. For these reasons, the results by Wride et al. are not included in Table 1.1. It is noted, however, that the values of S_r back-calculated by Wride et al. are not materially different from those listed in Table 1.1.

Table 1.2. Values of $\Delta(N_1)_{60-S_r}$ recommended by Seed (1987)

Fines content, FC (% passing No. 200 sieve)	$\Delta(N_1)_{60-S_r}$
10	1
25	2
50	4
75	5

3. SPT-based correlation for residual strength

3.1. CORRELATION OF S_r WITH $(N_1)_{60cs-Sr}$

Seed (1987) was the first to suggest back-calculating a residual strength, S_r , of liquefied soil from case histories of liquefaction failures and to correlate the S_r to equivalent clean sand SPT corrected blow counts, $(N_1)_{60cs-Sr}$. A direct correlation between S_r and $(N_1)_{60cs-Sr}$ was considered logical based on critical state concepts (e.g., steady state strength at large strains is a function of void ratio alone) and established correlations between the overburden corrected penetration resistance and relative density.

The values of S_r obtained by Seed (1987), Seed and Harder (1990), and Olson and Stark (2002), are listed in Table 1.1 and presented in Figure 1.4. A design relationship that has been widely used in practice over the past 10 years for estimating S_r based on median penetration resistance is also shown in this figure.

For stability analyses, it was recommended that the residual strength from this relationship be restricted to less than or equal to the soil's pre-earthquake drained shear strength. This restriction avoided the use of shear strengths that, usually at shallow depths, rely on negative pore water pressure.

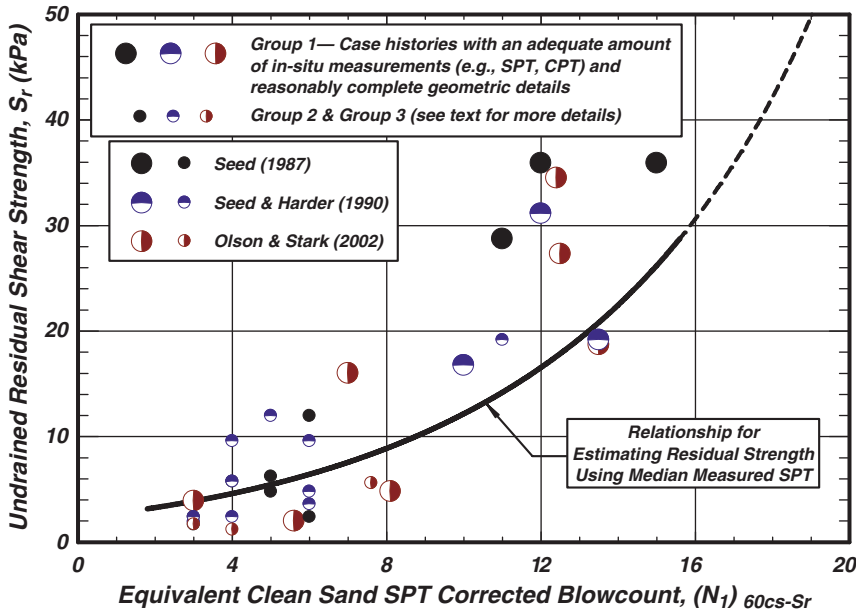


Fig. 1.4. Residual shear strength, S_r , of liquefied sand versus equivalent clean-sand, corrected SPT blow count based on case histories listed in Table 1.1

3.2. CORRELATION OF S_r/σ'_{vo} WITH $(N_1)_{60cs-Sr}$

Residual shear strengths from case histories have also been normalized with respect to the initial vertical effective stress, σ'_{vo} (e.g., Stark and Mesri, 1992; Ishihara, 1993; Wride et al., 1999; Olson and Stark, 2002). The use of a normalized shear resistance, S_r/σ'_{vo} , for sand was usually based on the observation that it provides a reasonable basis for describing the stress–strain behavior up to moderate strain levels in undrained laboratory element tests. In addition, recent studies suggest that the effects of void redistribution, while affected by numerous factors, may also be better represented by a correlation to S_r/σ'_{vo} than to S_r directly.

The values of S_r/σ'_{vo} for the case histories listed in Table 1.1 are plotted as a function of $(N_1)_{60cs-Sr}$ in Figure 1.5. Recommended design relationships for estimating S_r/σ'_{vo} based on median penetration resistances are presented in terms of two different curves: one curve for conditions where the effects of void redistribution are expected to be negligible, and the other curve for conditions where the effects of void redistribution could be significant. These two curves provide guidance for the unavoidable task of having to estimate the residual strengths of soils that have $(N_1)_{60cs-Sr}$ values greater than about 14, which is beyond the range of available case history data. The basis for the form of these recommended curves is discussed below.

The undrained stress–strain response of saturated sand for a range of initial relative densities (D_R) in direct simple shear loading is illustrated by the results in Figure 1.6 for Fraser

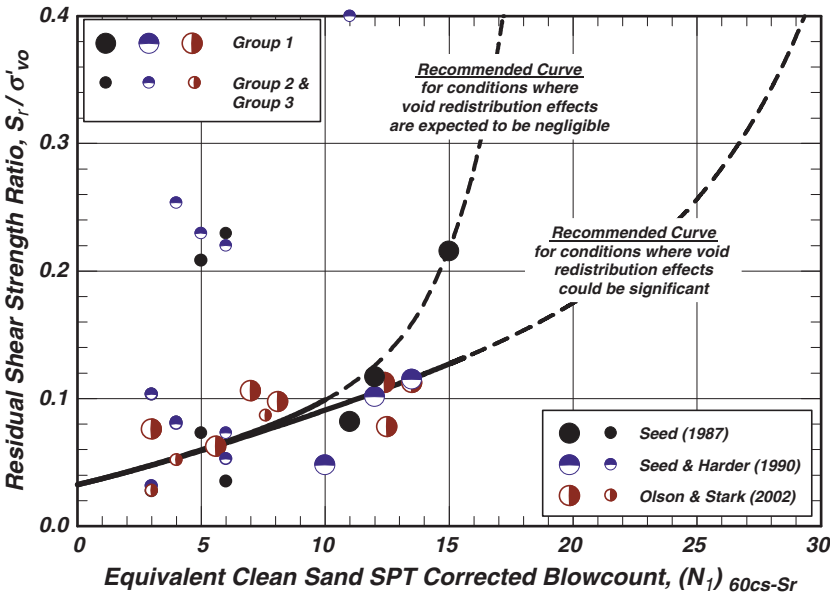


Fig. 1.5. Residual shear strength ratio, S_r/σ'_{vo} , of liquefied soil versus equivalent clean-sand, SPT corrected blow count for σ'_{vo} less than 400 kPa

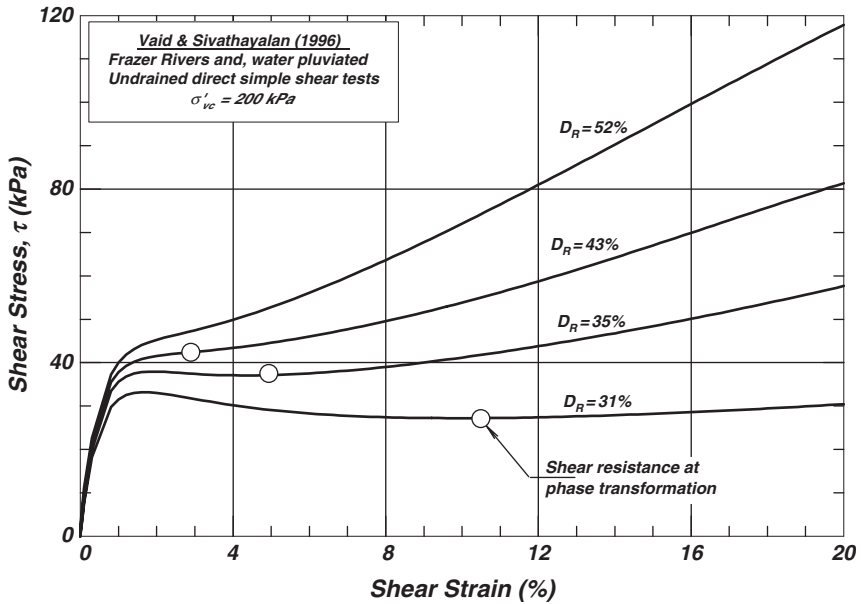


Fig. 1.6. Undrained direct simple shear tests on Fraser river sand at a range of relative densities by Vaid and Sivathayalan (1996)

river sand by Vaid and Sivathayalan (1996). The bullet symbols on this figure identify points of minimum shear resistance which correspond to the transition from an incrementally contractive to an incrementally dilative response in undrained shearing (i.e., phase transformation) and which have also been called a quasi-steady state condition (Ishihara, 1993). The monotonic shear resistance can increase significantly after phase transformation, with the rate of increase being greater for a higher initial D_R . The normalized shear resistance, τ/σ'_{vo} , for this sand at σ'_{vo} of 50 to 400 kPa are plotted versus D_R in Figure 1.7, showing that: (1) τ/σ'_{vo} at phase transformation is relatively independent of σ'_{vo} for σ'_{vo} ranging from 50 to 400 kPa, and (2) τ/σ'_{vo} increases with both increasing D_R and increasing shear strain beyond phase transformation.

The values of τ/σ'_{vo} mobilized at quasi-steady state or at shear strains of 5 to 20% increase rapidly as D_R exceeds about 40 to 50%. This is illustrated by the results in Figure 1.8 for undrained simple shear loading of saturated Toyoura sand at σ'_{vo} of 50 to 300 kPa by Yoshimine et al. (1999), as well as by the previously discussed results for Fraser river sand in Figure 1.7. The trends in Figures 1.7 and 1.8 suggest that the undrained shear strengths of these sands at σ'_{vo} less than 400 kPa would exceed their drained strengths (e.g., $\tau/\sigma'_{vo} = \tan \phi' \approx 0.6$) for D_R greater than 50 to 60%.

The potential for void redistribution to cause localized loosening and strength loss in the field depends on numerous factors, including the initial state and properties of the soil (e.g., cyclic strength, D_R , confining stress), the geometry and boundary conditions for

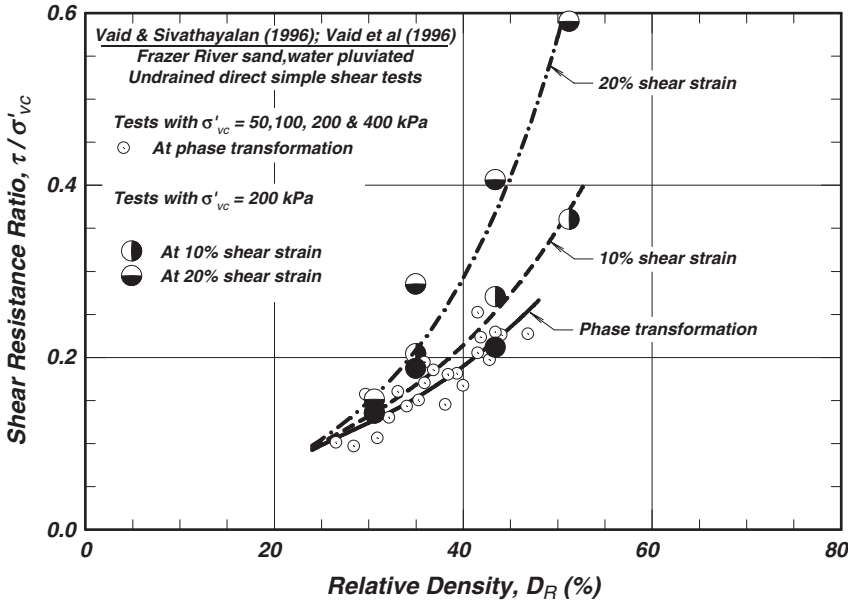


Fig. 1.7. Undrained shear resistance ratios mobilized in direct simple shear tests on Fraser river sand at different relative densities and shear strain levels (after Vaid and Sivathayalan, 1996; Vaid et al., 1996)

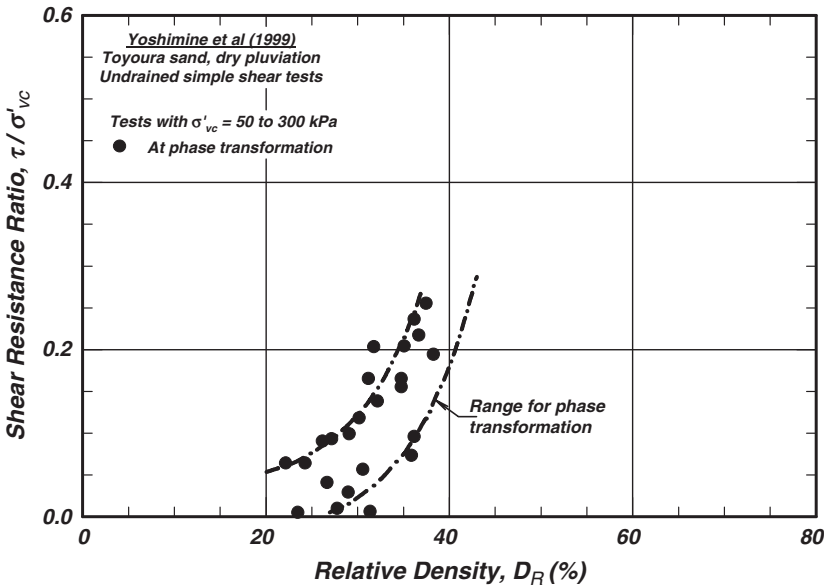


Fig. 1.8. Undrained shear resistance ratios mobilized in simple shear tests on Toyoura sand at phase transformation for different relative densities (after Yoshimine et al., 1999)

the slope (e.g., initial shear stress distribution; arrangement, thickness, and permeability of strata), and the characteristics of the ground motions (e.g., amplitude and duration of shaking). In adverse conditions, the process of void redistribution progressively reduces the shear resistance of a loosening zone until it is less than the shear resistance required for stability. The shear resistance in a loosening zone could be locally reduced to zero if a water film forms, but the average shear resistance over a large area is unlikely to be zero because water films can dissipate by piping into cracks that develop as the slope deforms and the geologic interfaces where loosening develops are likely to be irregular enough to preclude continuous films of water over large areas. The potential for void redistribution to cause significant slope deformations decreases quickly with increasing D_R because a greater D_R has the combined benefits of reducing the volume of water expelled by contracting zones and increasing the volume of water that can be absorbed by dilating zones. Simple analysis models (e.g., Malvick et al., 2006) and nonlinear coupled numerical analyses (e.g., Naesgaard et al., 2005) have illustrated the influence of various factors under very simple conditions. The reliable application of such analysis methods to the complex conditions encountered in the field, however, are less certain and yet to be adequately calibrated and fully evaluated.

The S_r/σ'_{vo} values in Figure 1.5 can also be interpreted as representing small fractions of the pre-earthquake drained strength. For example, assuming $\tan \phi' \approx 0.6$ for loose sands, the S_r/σ'_{vo} values of 0.03 to 0.1 at $(N_1)_{60cs-Sr}$ less than about 10 in Figure 1.5 are about 5 to 17% of the pre-earthquake drained strength (i.e., a strength loss of 83 to 95% due to liquefaction). For situations where void redistribution is significant, it seems reasonable to expect that the shear strength will drop to a small fraction of the pre-earthquake drained shear strength because the impeded pore water seepage allows the soil to shear at a sustained low value of σ'_v . Thus, these S_r/σ'_{vo} ratios are believed to provide a better representation of the potential effects of void redistribution than are provided by the direct S_r correlation in Figure 1.4, while recognizing that neither correlation fully accounts for the numerous factors that influence void redistribution processes.

It is also useful to compare the S_r/σ'_{vo} values in Figure 1.5 to the values expected for remolded, normally consolidated, slightly plastic silts that are at the transition between soils that should be analyzed as sands versus soils that should be analyzed using procedures appropriate for clays (Boulanger and Idriss, 2006). Such soils can be encountered as lenses and layers in hydraulic fills or tailings embankments and have low penetration resistances. The undrained shear strength ratio of young, normally consolidated, slightly plastic silts can be about $s_u/\sigma'_{vo} = 0.22$ (Ladd, 1991) and have sensitivities in the range of 2 to 4, such that the remolded shear strength ratio, S_{ur}/σ'_{vo} , can be about 0.05 to 0.11. Remolded strength ratios in this range of values have been reported for slightly plastic silts and sandy silts by Vasquez-Herrera et al. (1990), Castro and Troncoso (1989), and Finn et al. (1991). These S_{ur}/σ'_{vo} values are comparable to the S_r/σ'_{vo} values for the loose sands, silty sands, and nonplastic sandy silts represented in Figure 1.5.

The lower design relationship in Figure 1.5 corresponds to conditions where the effects of void redistribution could be significant. This would include sites with relatively thick layers of liquefiable soils that are overlain by lower-permeability soils that would impede

the post-earthquake dissipation of earthquake-induced excess pore water pressures, as discussed previously. This relationship can be represented by the following equation:

$$\frac{S_r}{\sigma'_{vo}} = \exp\left(\frac{(N_1)_{60cs-Sr}}{16} + \left(\frac{(N_1)_{60cs-Sr} - 16}{21.2}\right)^3 - 3.0\right) \leq \tan \phi' \quad (1.2)$$

The upper design relationship in Figure 1.5 corresponds to a condition where the effects of void redistribution can be confidently judged to be negligible. This could include sites where the stratigraphy would not impede post-earthquake dissipation of excess pore water pressures, such that the dissipation of excess pore pressures would be accompanied by densification of the soils at all depths. In this case, the available experimental data and correlations between relative density and $(N_1)_{60cs-Sr}$ indicate that the undrained shear resistance would increase rapidly as the $(N_1)_{60cs-Sr}$ approaches 16 or 17 (corresponding to a relative density of about 60%). This relationship can be represented by the following equation:

$$\begin{aligned} \frac{S_r}{\sigma'_{vo}} = \exp\left(\frac{(N_1)_{60cs-Sr}}{16} + \left(\frac{(N_1)_{60cs-Sr} - 16}{21.2}\right)^3 - 3.0\right) \\ \times \left(1 + \exp\left(\frac{(N_1)_{60cs-Sr}}{2.4} - 6.6\right)\right) \leq \tan \phi' \end{aligned} \quad (1.3)$$

The potential role of void redistribution or other strength loss mechanisms in the case histories is not fully clear at this time. Physical and analytical models indicate that void redistribution is potentially most severe for loose sands, and is likely to have played a role in many of the currently available case histories. This would suggest the two design relationships should be somewhat different at the lower penetration resistances, but the current state of knowledge does not provide a basis for incorporating any difference at this time.

The appropriate S_r/σ'_{vo} ratios for $\sigma'_{vo} > 400$ kPa are expected to be smaller than those recommended in Figure 1.5. For example, triaxial compression test results by Yoshimine et al. (1999) showed that S_r/σ'_{vo} ratios at a given D_R were relatively independent of σ'_{vo} up to σ'_{vo} of about 500 kPa, but decreased at higher values of σ'_{vo} . This effect may be approximately accounted for by using the state normalized penetration resistance, $(N_{1\xi})_{60cs-Sr}$ (Boulanger, 2003), in place of $(N_1)_{60cs-Sr}$ in equations (1.2) and (1.3).

4. CPT-based correlation for residual strength

The development of a CPT-based correlation for S_r/σ'_{vo} requires estimating CPT penetration resistances for 14 of the 18 case histories in Table 1.1, and therefore the procedures for estimating CPT penetration resistances are also discussed in this paper. Correlations between CPT and SPT penetration resistances that account for the effects of fines content and relative density are used to: (1) convert the previously derived $S_r/\sigma'_{vo}-(N_1)_{60cs-Sr}$

correlation to an $S_r/\sigma'_{vo}-q_{c1Ncs-Sr}$ correlation; (2) convert the SPT data in Table 1.1, measured or estimated, to corresponding values of CPT penetration resistance, as necessary; and (3) derive an adjustment for fines content for CPT penetration resistances that is consistent with the adjustment recommended by Seed (1987) for SPT blow counts. The resulting correlation and case history data points are then compared to ensure that consistency was maintained.

4.1. CONVERTING THE SPT CORRELATION

Correlations between D_R , $(N_1)_{60}$ and q_{c1N} in clean sands, as summarized below, were used to convert the $S_r/\sigma'_{vo}-(N_1)_{60cs-Sr}$ correlation in Figure 1.5 to a $S_r/\sigma'_{vo}-q_{c1Ncs-Sr}$ correlation. The D_R of clean sand has been expressed in terms of SPT $(N_1)_{60}$ using the following form:

$$D_R = \sqrt{\frac{(N_1)_{60}}{C_d}} \quad (1.4)$$

where D_R is expressed as a ratio, rather than a percentage. Meyerhof's (1957) original observations indicated a C_d value of about 41. Skempton (1986) suggested, based on a review of field and laboratory data, that the best average C_d values for normally consolidated natural sand deposits were about 55 for fine sands and 65 for coarse sands. Skempton further noted that C_d varied significantly with the age of a deposit, such that the typical C_d value for fine sands could range from 35 in laboratory tests, to 40 in recent fills, to 55 in natural deposits.

Cubrinovski and Ishihara (1999) showed that C_d is affected by the grain size characteristics and the type of soil under consideration. Cubrinovski and Ishihara included data for high quality undisturbed samples (obtained by in-situ freezing) for clean sand and for silty sand. The D_R , $(N_1)_{60}$, fines content (FC), and median grain size (D_{50}) values for the high quality undisturbed samples tabulated by Cubrinovski and Ishihara are summarized in Figure 1.9. Note that the N_1 values reported by Cubrinovski and Ishihara were most likely obtained with a delivered energy of about 78%, and were therefore multiplied by the ratio 78/60 to obtain equivalent values of $(N_1)_{60}$. The average values of C_d for the soils included in Figure 1.9 are about 51 for the clean sand samples, about 26 for the silty sand samples, and about 39 for all samples. It is interesting to note that the value of $C_d = 39$ for all samples is very close to the value of 41 originally obtained by Meyerhof (1957).

CPT tip resistances have also been correlated to D_R in various forms. Based on the work of Boulanger (2003) and the solutions by Salgado et al. (1997a, b) for clean sands, the following approximate relationships can be used to relate D_R to q_{c1N} :

$$q_{c1N} = C_1 \left(25.7 + 39.7D_R + 212.3D_R^2 \right) \left(\frac{K_o}{0.45} \right)^{m-0.077} \quad (1.5)$$

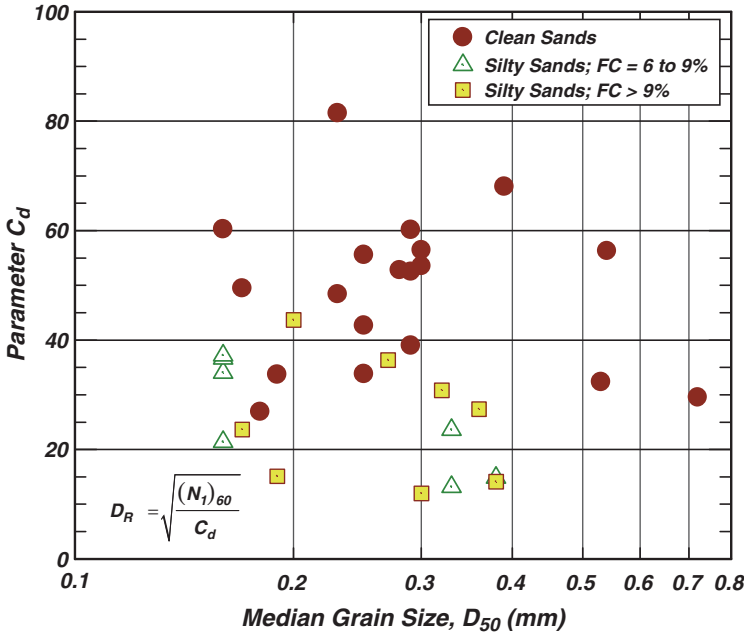


Fig. 1.9. Variations of the parameter C_d with D_R (values of relative density, N_1 , FC, and D_{50} are from Cubrinovski and Ishihara, 1999)

$$m = 0.7836 - 0.5208D_R \tag{1.6}$$

$$C_1 = 0.64 \text{ to } 1.55 \tag{1.7}$$

in which q_{c1} is the corrected (to $\sigma'_{vo} = 1$ atmosphere) CPT tip resistance and q_{c1N} is the normalized corrected CPT tip resistance ($q_{c1N} = q_{c1}/P_a$), K_0 is the lateral earth pressure coefficient at rest, and P_a is atmospheric pressure. The variation in the relationship between q_{c1N} and D_R described by the above equations is similar to the variation observed between $(N_1)_{60}$ and D_R , as illustrated in Figure 1.9.

The above q_{c1N} - D_R and $(N_1)_{60}$ - D_R correlations were used by Idriss and Boulanger (2003) to maintain consistency between SPT- and CPT-based liquefaction triggering correlations for clean sands. A value of $C_d = 46$ was used for the SPT relationship and values of $C_1 = 0.9$ with $K_0 = 0.45$ were used for the CPT relationship. These values, for example, indicate that a D_R of about 81% corresponds to $(N_1)_{60cs} = 30$ and $q_{c1N} = 175$. The resulting CPT expression was also shown to be closely approximated as

$$D_R = 0.478 (q_{c1N})^{0.264} - 1.063 \tag{1.8}$$

which simplifies the computation of D_R for a specified q_{c1N} .

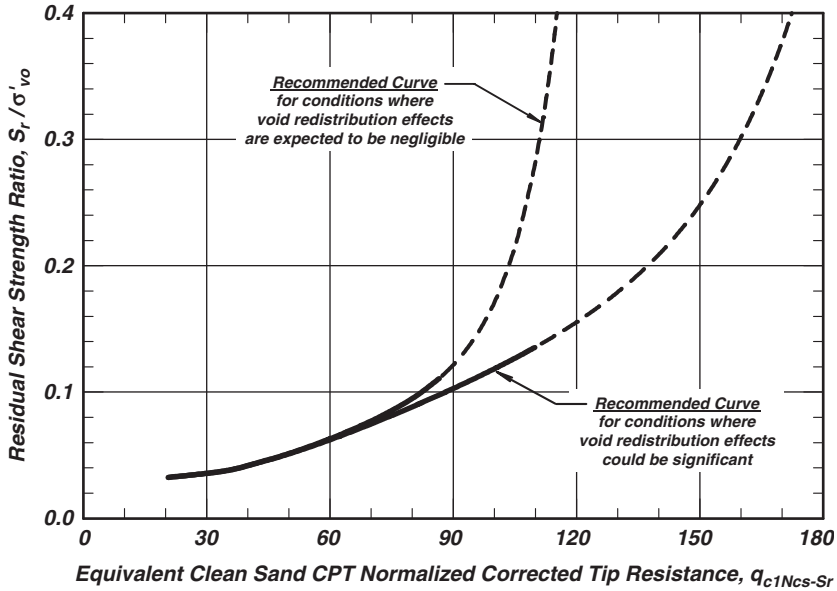


Fig. 1.10. Proposed curves for relating residual shear strength ratio, S_r / σ'_{vo} , of liquefied soil to median values of equivalent clean sand CPT normalized corrected tip resistance for σ'_{vo} less than 400 kPa

The above expressions were used to map the S_r / σ'_{vo} relationship in Figure 1.5 to the relationship in Figure 1.10 by converting the $(N_1)_{60cs-Sr}$ values to $q_{c1Ncs-Sr}$ values. The resulting relationships can be closely approximated as

$$\frac{S_r}{\sigma'_{vo}} = \exp\left(\frac{q_{c1Ncs-Sr}}{24.5} - \left(\frac{q_{c1Ncs-Sr}}{61.7}\right)^2 + \left(\frac{q_{c1Ncs-Sr}}{106}\right)^3 - 4.42\right) \leq \tan \phi' \quad (1.9)$$

for the case where void redistribution could be significant, and as

$$\frac{S_r}{\sigma'_{vo}} = \exp\left(\frac{q_{c1Ncs-Sr}}{24.5} - \left(\frac{q_{c1Ncs-Sr}}{61.7}\right)^2 + \left(\frac{q_{c1Ncs-Sr}}{106}\right)^3 - 4.42\right) \times \left(1 + \exp\left(\frac{q_{c1Ncs-Sr}}{11.1} - 9.82\right)\right) \leq \tan \phi' \quad (1.10)$$

for the case where void redistribution effects are expected to be negligible.

4.2. CPT VALUES FOR CASE HISTORIES

Estimates of CPT penetration resistances for each of the case histories in Table 1.1 were obtained using a modified form of the correlation between CPT and SPT penetration resistances presented by Suzuki et al. (1998). Suzuki et al. showed that the ratio q_c / N

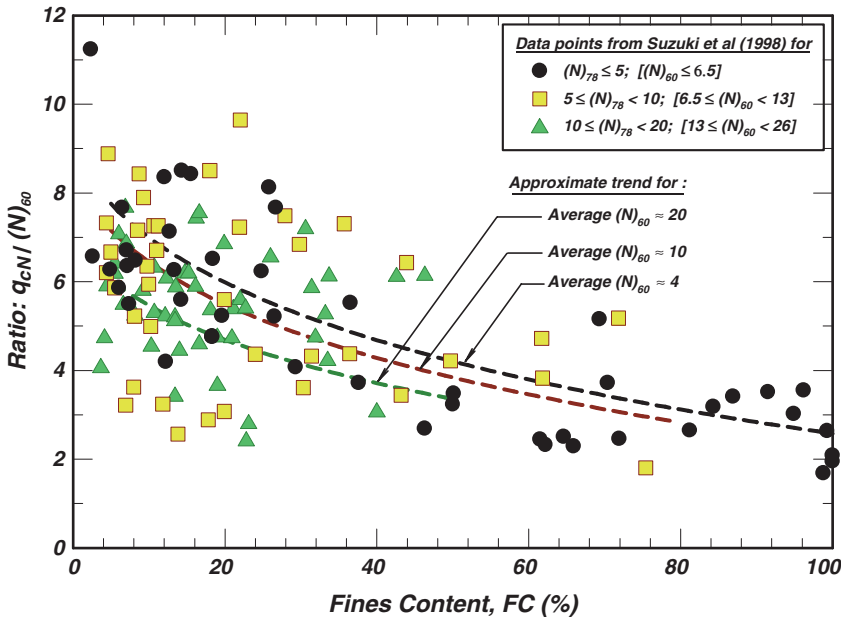


Fig. 1.11. Variations of the ratio $q_{cN}/(N)_{60}$ as a function of fines content (data points from Suzuki et al., 1998 adjusted by a factor of 78/60 to account for energy delivered to SPT sampler)

varied systematically with fines content and D_R (or N). This is illustrated in Figure 1.11 showing their data in terms of $q_{cN}/(N)_{60}$ versus fines content, FC, for three ranges of $(N)_{60}$ values. Their SPT blow count data most likely corresponded to an energy ratio of about 78%, and hence were adjusted to an equivalent energy ratio of 60% to obtain the $(N)_{60}$ values presented in Figure 1.11. The three sets of data points presented in Figure 1.11 are for $(N)_{60} < 6.5$ (average ≈ 4), for $(N)_{60}$ ranging from 6.5 to 13 (average ≈ 10), and for $(N)_{60}$ ranging from 13 to 26 (average ≈ 20).

The data points for $(N)_{60} < 6.5$ covered a sufficient range of fines contents to enable construction of a reasonable relationship between $q_{cN}/(N)_{60}$ and fines content for an average $(N)_{60}$ of 4. Also shown in Figure 1.11 are relationships that were derived for the other two ranges of $(N)_{60}$ and which follow the form derived for $(N)_{60} = 4$. These three relationships were used, with interpolation, to estimate $q_{cN}/(N)_{60}$ ratios for different values of $(N)_{60}$ and fines content.

Fines content adjustments, Δq_{c1N-Sr} , for CPT penetration resistances were derived to be consistent with those adopted for the SPT-based approach. The resulting values for Δq_{c1N-Sr} are listed in Table 1.3.

CPT penetration resistances were estimated for each of the case histories listed in Table 1.1 as follows. Values of q_{c1N} were estimated by multiplying the SPT $(N_1)_{60}$ values

Table 1.3. Recommended values of Δq_{c1N-Sr}

Fines content, FC (% passing No. 200 sieve)	Δq_{c1N-Sr}
10	10
25	25
50	45
75	55

from Table 1.1 with the appropriate $q_{cN}/(N)_{60}$ ratios developed from Figure 1.11. In some cases, Seed (1987) or Seed and Harder (1990) reported $(N_1)_{60cs-Sr}$ values and not $(N_1)_{60}$ values. In those cases, $(N_1)_{60}$ values were estimated by subtracting the fines content adjustment $\Delta(N_1)_{60}$ from their reported values of $(N_1)_{60cs-Sr}$. This process was applied separately to the data from each of the investigators listed in Table 1.1, with the resulting $(N_1)_{60}$ and q_{c1N} values summarized in Table 1.4. The exceptions were for Cases 2 and 5 by Olson and Stark (2002), for which the table lists their reported measured q_{c1N} values of 47 and 30, respectively. For comparison, applying the above procedure to the $(N_1)_{60}$ values by Olson and Stark produces estimated q_{c1N} values of 55.2 and 29.5 for these two cases, respectively.

Fines content adjustments based on Table 1.3 were then added to the values of q_{c1N} to arrive at the corresponding values of $q_{c1Ncs-Sr}$. These $q_{c1Ncs-Sr}$ values are listed in Table 1.5 along with the S_r/σ'_{vo} values computed for each case history and each investigator. These data are plotted in Figure 1.12 together with the $S_r/\sigma'_{vo-q_{c1Ncs-Sr}}$ curves represented by equations (1.9) and (1.10). Comparison of the CPT-based results presented in this figure with those shown in Figure 1.5 for the SPT-based results indicate a reasonably good consistency and correlation between the two approaches.

5. Concluding remarks

SPT- and CPT-based relationships for estimating the residual shear strength ratio, S_r/σ'_{vo} , of liquefied nonplastic soils in the field are recommended in this paper based on a review of prior case history studies, laboratory studies, and recent findings regarding void redistribution mechanisms. The recommended relationships are comparable with values recommended by other investigators for values of equivalent clean sand SPT corrected blow counts, $(N_1)_{60cs-Sr}$, less than about 13 or equivalent clean sand CPT normalized corrected penetration resistances, $q_{c1Ncs-Sr}$, less than about 75, which is where the majority of the available case history data are. The recommended relationships provide new guidance, however, regarding the unavoidable task of having to extrapolate beyond the available case history data in the process of estimating residual strengths of soils having $(N_1)_{60cs-Sr}$ values greater than about 14 or $q_{c1Ncs-Sr}$ values greater than about 80.

The development of the recommended design relationships, and particularly their extrapolation to penetrations resistances that are greater than represented by available case history data, has been guided by the results of undrained laboratory test studies and recent

Table 1.4. Values of q_{c1N} obtained for published case histories of liquefaction flow failures

Number	Case history Structure	FC(%)	Values for cases published by					
			Seed (1987)		Seed and Harder (1990)		Olson and Stark (2002)	
			$(N_1)_{60}$	q_{c1N}	$(N_1)_{60}$	q_{c1N}	$(N_1)_{60}$	q_{c1N}
1	Wachusett Dam – North Dike	5					7	51.8
2	Lower San Fernando Dam	25	13	60.5	11.5	55.2	11.5	47.0
3	Fort Peck Dam	50	7	25.6	6	22.5	8.5	30.2
4	Calaveras Dam	60	7.6	25.1	7.6	25.1	8	26.1
5	Hachiro-Gata Road Embankment	15					4.4	30.0
6	Lake Ackerman Highway Embankment	0					3	25.7
7	Route 272 at Higashiarckinai	20					6.3	38.4
8	River Bank, Lake Merced	3	5	40.5	6	48.0		
9	Kawagishi-cho	3	4	33.2	4	32.8		
10	Mochi-koshi Tailings Dam – Dike 2	85	1	2.9	0	0.0		
11	La Marquesa Dam – U/S Slope	30			4	22.0		
12	La Marquesa Dam – D/S Slope	20			9	53.1		
13	La Palma Dam	15			3	20.4		
14	Uetsu Railway Embankment	2	3	25.5	3	25.5	3	25.5
15	Solfataro Canal Dike	7	4.6	36.8	3.6	29.2		
16	Koda Numa Railway Embankment	13	1.8	13.3	1.8	13.3	3	21.9
17	Shibecha-cho Embankment	25					5.6	31.6
18	Sheffield Dam	40	2.8	13.6	2.8	13.6		

Notes:

- (1) Values of $(N_1)_{60}$ are either those published by author(s), or obtained from published $(N_1)_{60cs-Sr}$ and adjusted by subtracting applicable $\Delta(N_1)_{60}$.
- (2) Values of q_{c1N} are obtained by multiplying the values of $(N_1)_{60}$ by the ratio of $q_{c1N}/(N_1)_{60}$ for the applicable value of FC and $(N_1)_{60}$, except for Cases 2 and 5 by Olson and Stark. Olson and Stark list values of q_{c1N} of 47 and 30 for Cases 2 and 5, respectively, whereas applying the above procedure to their $(N_1)_{60}$ values produces q_{c1N} values of 55.2 and 29.5, respectively.

Table 1.5. Values of S_r/σ'_{vo} and $q_{c1Ncs-Sr}$ obtained for published case histories of liquefaction flow failures

Number	Case history Structure	FC(%)	Values for cases published by					
			Seed (1987)		Seed and Harder (1990)		Olson and Stark (2002)	
			$q_{c1Ncs-Sr}$	S_r/σ'_{vo}	$q_{c1Ncs-Sr}$	S_r/σ'_{vo}	$q_{c1Ncs-Sr}$	S_r/σ'_{vo}
1	Wachusett Dam – North Dike	5					51.8	0.106
2	Lower San Fernando Dam	25	85.5	0.215	80.2	0.115	72.0	0.112
3	Fort Peck Dam	50	70.6	0.082	67.5	0.048	75.2	0.078
4	Calaveras Dam	60	74.1	0.117	74.1	0.101	75.1	0.112
5	Hachiro-Gata Road Embankment	15					45.0	0.062
6	Lake Ackerman Highway Embankment	0					25.7	0.076
7	Route 272 at Higashiarckinai	20					58.4	0.097
8	River Bank, Lake Merced	3	40.5	0.073	48.0	0.073		
9	Kawagishi-cho	3	33.2	0.081	32.8	0.081		
10	Mochi-koshi Tailings Dam – Dike 2	85	57.9	0.229	55.0	0.229		
11	La Marquesa Dam – U/S Slope	30			51.0	0.220		
12	La Marquesa Dam – D/S Slope	20			73.1	0.400		
13	La Palma Dam	15			35.4	0.253		
14	Uetsu Railway Embankment	2	25.5	0.027	25.5	0.031	25.5	0.028
15	Solfatara Canal Dike	7	40.8	0.208	33.2	0.080		
16	Koda Numa Railway Embankment	13	26.3	0.103	26.3	0.103	34.9	0.052
17	Shibecha-cho Embankment	25					56.6	0.087
18	Sheffield Dam	40	50.6	0.035	50.6	0.053		

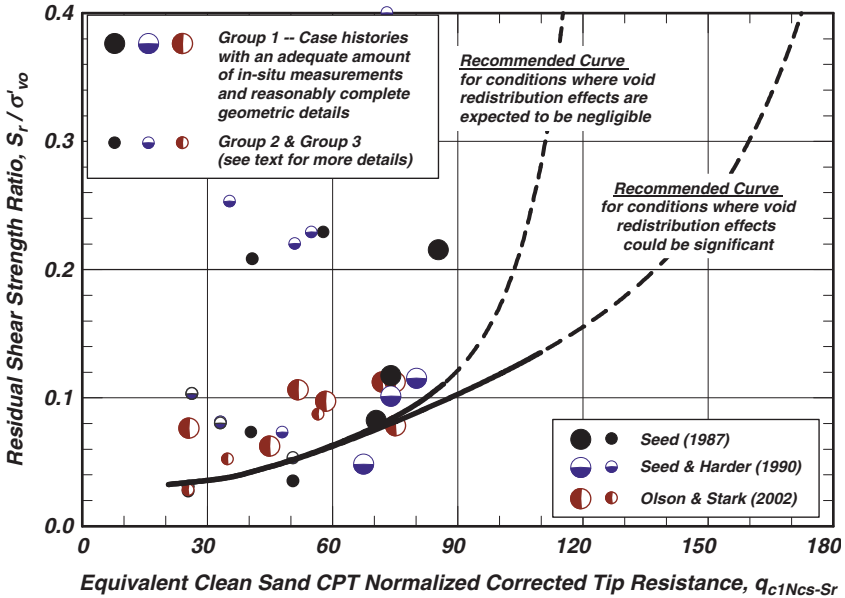


Fig. 1.12. S_r / σ'_{vo} versus $q_{c1Ncs-Sr}$ for case histories listed in Table 1.5 and curves proposed for relating residual shear strength ratio, S_r / σ'_{vo} , of liquefied soil to median values of equivalent clean-sand CPT normalized corrected tip resistance for σ'_{vo} less than 400 kPa

physical and analytical modeling studies of void redistribution mechanisms. A lower design relationship was provided for conditions where the effects of void redistribution could be significant, while an upper design relationship was provided for conditions where the effects of void redistribution can be confidently judged to be negligible. Making the distinction between these two cases for an earth embankment or slope will require appropriately detailed field and analytical studies.

It is hoped that the relationships included in this paper provide reasonable means for engineers to estimate the residual strength of liquefied soils in the field. It is also hoped that research in this area will continue using physical and analytical models to allow for greater understanding of the void redistribution phenomenon and its effects on residual strength.

Acknowledgments

The writers are grateful for the valuable review comments and thoughtful suggestions provided by Drs. Yoshi Moriwaki, Steve L. Kramer, Gonzalo Castro, and Robert Pyke on an earlier version of this manuscript that addressed SPT-based relationships.

REFERENCES

- Boulanger RW (2003) High overburden stress effects in liquefaction analyses. *Journal of Geotechnical and Geoenvironmental Engineering*, ASCE 129(12): 1071–1082
- Boulanger RW, Idriss IM (2006) Liquefaction susceptibility criteria for silts and clays. *Journal of Geotechnical and Geoenvironmental Engineering*, ASCE 132(11): 1413–1426
- Castro, G (1975) Liquefaction and cyclic mobility of saturated sands. *Journal of the Geotechnical Engineering Division*, ASCE 101(GT6): 551–569
- Castro G, Poulos SJ (1977) Factors affecting liquefaction and cyclic mobility. *Journal of Geotechnical Engineering Division*, ASCE 103(GT6): 501–506
- Castro G, Troncoso J (1989) Effects of 1989 Chilean earthquake on three tailings dams. In: *Proceedings, 5th Chilean Conference on Seismology and Earthquake Engineering*, Santiago
- Cubrinovski M, Ishihara K (1999) Empirical Correlation between SPT N-Value and Relative Density for Sandy Soils. *Soils and Foundations*, Japanese Geotechnical Society 39(5): 61–71
- Davis AP, Poulos SJ, Castro G (1988) Strengths back figured from liquefaction case histories. In: *Proceedings, 2nd International Conference on Case Histories in Geotechnical Engineering*, St. Louis, MO, pp 1693–1701
- de Alba P, Seed HB, Retamal E, Seed RB (1988) Analyses of dam failures in 1985 Chilean earthquake. *Journal of the Geotechnical Engineering Division*, ASCE 114(12): 1414–1434
- Finn WDL, Ledbetter RH, Fleming RL Jr, Templeton AE, Forrest TW, Stacy ST (1991) Dam on liquefiable foundation: Safety assessment and remediation. In: *Proceedings, 17th International Conference on Large Dams*, Vienna, pp 531–553
- Hryciw RD, Vitton S, Thomann TG (1990) Liquefaction and flow failure during seismic exploration. *Journal of the Geotechnical Engineering Division*, ASCE 116(12): 1881–1899
- Idriss IM, Boulanger RW (2003) Estimating K_α for use in evaluating cyclic resistance of sloping ground. In: Hamada, O'Rourke, Bardet (eds), *8th US–Japan Workshop on Earthquake Resistant Design of Lifeline Facilities and Countermeasures against Liquefaction*, Report MCEER-03-0003, MCEER, SUNY Buffalo, N.Y., pp 449–468
- Ishihara K (1993) Liquefaction and flow failure during earthquakes. *Geotechnique* 43(3): 351–415
- Kokusho T (2000) Mechanism for water film generation and lateral flow in liquefied sand layer. *Soils and Foundations* 40(5): 99–111
- Kulasingam R, Malvick EJ, Boulanger RW, Kutter BL (2004) Strength loss and localization at silt interlayers in slopes of liquefied sand. *Journal of Geotechnical and Geoenvironmental Engineering*, ASCE 130(11): 1192–1202
- Ladd CC (1991) Stability evaluation during staged construction. *Journal of the Geotechnical Engineering Division*, ASCE 117(4): 540–615
- Malvick EJ, Kutter BL, Boulanger RW, Feigenbaum HP (2004) Post-shaking failure of sand slope in centrifuge test. In: Doolin D et al. (eds), *11th International Conference on Soil Dynamics and Earthquake Engineering*, and *3rd International Conference on Earthquake Geotechnical Engineering*, Stallion Press, Vol. 2, pp 447–455
- Malvick EJ, Kutter BL, Boulanger RW, Kulasingam R (2006) Shear localization due to liquefaction-induced void redistribution in a layered infinite slope. *Journal of Geotechnical and Geoenvironmental Engineering*, ASCE 132(10): 1293–1303
- Meyerhof GG (1957) Discussion on Research on determining the density of sands by spoon penetration testing. In: *Proceedings, 4th International Conference on Soil Mechanics and Foundation Engineering*, London, Vol. 3, p 110

- Naesgaard E, Byrne PM, Seid-Karbasi SM (2005) Modeling flow liquefaction and pore water redistribution mechanisms. In: Proceedings, 8th US National Conference on Earthquake Engineering, San Francisco, CA, EERI, paper 1863
- Olson SM, Stark TD (2002) Liquefied strength ratio from liquefaction flow failure case histories. *Canadian Geotechnical Journal* 39: 629–647
- Poulos SJ, Castro G, France JW (1985) Liquefaction evaluation procedure. *Journal of the Geotechnical Engineering Division, ASCE*, 111(6): 772–791
- Robertson PK et al. (2000) The Canadian Liquefaction Experiment: An overview. *Canadian Geotechnical Journal* 37: 499–504
- Salgado R, Mitchell JK, Jamiolkowski M (1997a) Cavity expansion and penetration resistance in sand. *Journal of Geotechnical and Geoenvironmental Engineering, ASCE* 123(4): 344–354
- Salgado R, Boulanger RW, Mitchell JK (1997b) Lateral stress effects on CPT liquefaction resistance correlations. *Journal of Geotechnical and Geoenvironmental Engineering, ASCE* 123(4): 726–735
- Seed HB (1987) Design problems in soil liquefaction. *Journal of the Geotechnical Engineering Division, ASCE* 113(8): 827–845
- Seed RB Harder LF Jr (1990) SPT-based analysis of cyclic pore pressure generation and undrained residual strength. In: Duncan JM (ed), Proceedings, Seed Memorial Symposium, BiTech Publishers, Vancouver, B.C., pp 351–376
- Skempton AW (1986) Standard penetration test procedures and the effects in sands of overburden pressure, relative density, particle size, ageing and overconsolidation. *Geotechnique*, 36(3): 425–447
- Stark TD, Mesri G (1992) Undrained shear strength of sands for stability analysis. *Journal of the Geotechnical Engineering Division, ASCE* 118(11): 1727–1747
- Suzuki Y, Sanematsu T, Tokimatsu K (1998) Correlation between SPT and seismic CPT. In: Robertson PK, Mayne PW (eds), Proceedings, Conference on Geotechnical Site Characterization, Balkema, Rotterdam, pp 1375–1380
- Vaid YP, Sivathayalan S (1996) Static and cyclic liquefaction potential of Fraser Delta sand in simple shear and triaxial tests. *Canadian Geotechnical Journal* 33: 281–289
- Vaid YP, Sivathayalan S, Eliadorani A, Uthayakumar M (1996) Laboratory testing at UBC CANLEX Report, Department of Civil Engineering, University of British Columbia
- Vasquez-Herrera A, Dobry R, Baziar MH (1990) Re-evaluation of liquefaction triggering and flow sliding in the Lower San Fernando Dam during the 1971 earthquake. In: Proceedings, 4th U.S. National Conference on Earthquake Engineering, EERI 3: 783–792
- Whitman RV (1985) On liquefaction. In: Proceedings, 11th International Conference on Soil Mechanics and Foundation Engineering. San Francisco, CA. A.A. Balkema, pp 1923–1926
- Wride CE, McRoberts EC, Robertson PK (1999) Reconsideration of case histories for estimating undrained shear strength in sandy soils. *Canadian Geotechnical Journal* 36: 907–933
- Yoshimine M, Robertson PK, Wride CE (1999) Undrained shear strength of clean sands to trigger flow liquefaction. *Canadian Geotechnical Journal* 36: 891–906

CHAPTER 2

LONG PERIOD STRONG GROUND MOTION AND ITS USE AS INPUT TO DISPLACEMENT BASED DESIGN

E. Faccioli, C. Cauzzi, R. Paolucci, M. Vanini, M. Villani, and D. Finazzi

*Structural Engineering Department, Technical University (Politecnico) of Milan, Italy
faccioli@stru.polimi.it*

1. Introduction

Consistently with the use of seismic inertia forces for the verification of structural members, buildings have been traditionally designed for earthquake resistance by relying on ground acceleration from strong earthquakes to describe seismic loading; in most applications this is quantified by acceleration response spectra. However, structural design is increasingly becoming *performance based*, whereby displacements and deformations of structural and non-structural members, which directly control damage, are brought to the front stage to replace accelerations and inertia forces. Thus, the relative displacement of the structure caused by the imposed ground motion, quantified through the displacement response spectrum (*DRS*), becomes the primary descriptor of the seismic demand. Methods are available to replace the actual structure (a non-linear multi-degree-of-freedom system) with an equivalent linear 1 DOF system, in which energy dissipation due to the non-linear response is accounted for through a large viscous damping factor. A synthesis of the main steps involved in the (direct) displacement based approach is provided in Figure 2.1. Since the design involves the response of the damaged structure, which is “softer” than the undamaged one, the vibration period T at play is significantly larger than the elastic, or initial, period. Hence, depending on the structure, *DRS* will have to encompass a broad T range, e.g. up to 10 s, well beyond the typical 0–4 s range of current norms (CEN, 2004).

With this background, a national research project called S5 was initiated in Italy in mid-2005, aimed at providing: (a) a model of the seismic action in terms of arbitrarily damped *DRS*, extending to long periods and (b) national hazard map(s) depicting the *DRS* values needed for design. The project is sponsored (by the Department of Civil Defence) and carried out jointly with other projects, for which general consistency of inputs and outputs is a key requirement. Thus, common seismic source models for the country are adopted, and the hazard description to be provided by S5 in the 1–10 s range should be consistent with the short period (0–2 s) hazard mapping provided by another project.

Highlighted in this article are some salient parts and results of the work undertaken in S5 in the engineering seismology domain, including the empirical prediction of *DRS* at arbitrary damping for horizontal and vertical motion derived from a newly assembled set

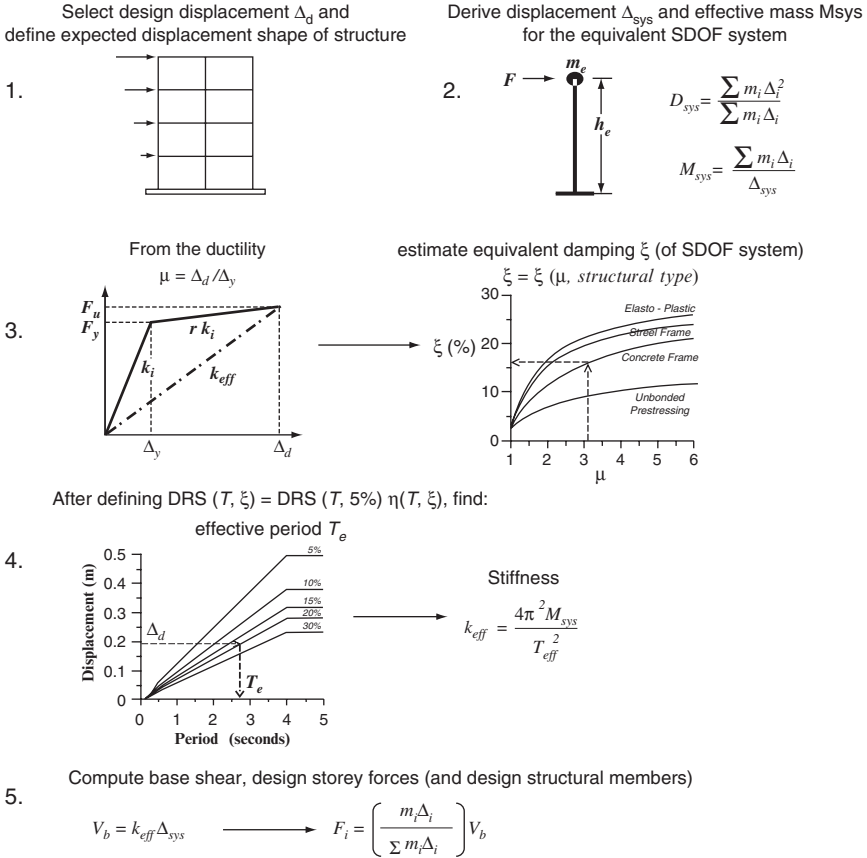


Fig. 2.1. Outline of main steps of the Direct Displacement Based Design (DDBD) method (courtesy of Prof. Rui Pinho)

of data, the amplification of spectral response on different ground profiles, and the special analysis devoted to alluvium filled valleys and basins. Finally, the type of hazard maps produced is illustrated both in terms of uniform hazard (UH) spectra and of a simplified bilinear *DRS* model.

2. Empirical prediction of displacement spectral response (*DRS*) over a broad period range

The experience gained from a previous study on *DRS* at long periods (Faccioli et al., 2004) indicated at an early stage that crucial for the entire work was a tool for making reliable empirical predictions of horizontal and vertical, arbitrarily damped *DRS*, at periods from <1 s to >10 s. Existing attenuation relations for spectral ordinates typically

used for European regions either do not cover the entire period range of interest (e.g. Ambraseys et al., 1996; Sabetta and Pugliese, 1996; Bommer et al., 2000; Fukushima et al., 2003; Ambraseys et al., 2005), or were found not to be sufficiently reliable at long periods (e.g. Berge-Thierry et al., 2003), presumably because of the high-pass filtering of the analog accelerograph recordings making up most of their calibration data sets.

Therefore, a new worldwide database was assembled consisting only of digitally recorded accelerograms of shallow crustal earthquakes, carefully selected as regards ground condition at the accelerograph station, minimal long period disturbances in the recording, and fullest possible coverage in the required magnitude and distance ranges.

The following subsections describe the data selection and the uniform processing applied, the features of the empirical predictions obtained for, the *DRS* of both vertical and horizontal motion, and the formulation of a simplified spectral model for design.

2.1. DATA SELECTION

As is well known, in selecting the calibration data for strong motion attenuation relations one should avoid to adopt both excessively loose criteria, because they lead to unreliable estimations, and the use of overly restrictive criteria that will result in lack of robustness of the predictions.

Strong motion data sources and format. By far the largest contributing source to the data set was the Japanese K-Net strong motion network (www.k-net.bosai.go.jp), while the rest of the data are from California, Europe, Iran, and Turkey. Additional data from Japan are those of the 1995 Hyogo-ken Nanbu earthquake, that were provided at the time of the Simultaneous Simulation Experiment of the Second International Symposium on ESG, in 1998 (ESG98 data distribution CD-ROM for the Kobe Simultaneous Simulation), and 10 records at rock sites, taken from the Kik-Net network database (www.kik.bosai.go.jp). The source of Iran data was the Iran Strong Motion Network, ISMN (www.bhrc.ac.ir/Bhrc/d-stgrmo/D-StGrMo.htm); for California we mainly used data available from the US National Strong-Motion Network, NSMN (nsmr.wr.usgs.gov) and, for the 1999 Hector Mine event, digital data from both the Engineering Strong Motion Data Center, CISN (www.quake.ca.gov/cisn-edc) and from the Southern California Seismic Network, SCSN (www.scsn.org). Concerning Europe and Turkey, most data come from the strong-motion data archive at the Imperial College of London (Ambraseys et al., 2002). A few (about 10) Italian records were provided by the National Accelerograph Network (RAN).

All data were acquired in the form of uncorrected acceleration histories, including nine records of the 1980 Irpinia (Italy) M 6.9 earthquake, which are the only analog recordings present in the database and were inserted in it only after a careful scrutiny of their long period characteristics.

Magnitude. Crustal earthquakes worldwide with independently determined moment magnitude were considered, in the $5.0 \leq M \leq 7.2$ range. The lower magnitude bound was

dictated by the results of probabilistic deaggregation analyses of seismic hazard at many sites in Italy, showing that contributions of the $M < 5$ events to spectral displacement hazard are negligible. On the other hand, the upper bound is close to the largest magnitude (7.41 ± 0.12 , possibly overestimated) in the historical earthquake catalogue in Italy (Gruppo di lavoro CPTI, 2004). M values of Japanese events, representing the majority of the dataset, come from the F-Net broadband network (www.fnet.bosai.go.jp/freesia/index-j.html), while most of those of the other events are from the global CMT catalogue (www.globalcmt.org/CMTsearch.html).

Magnitudes of the selected crustal earthquakes in Japan do not exceed 6.8, so that all the $M > 6.8$ events in the dataset are from Europe, the Middle East, and the United States. The upper magnitude bound adopted has led to rejecting extensively recorded events such as the 1999 (M 7.6) Chi Chi earthquake.

Distance, depth, and focal mechanism. The focal distance, R , was used, mainly for consistency with the current model of seismic source zones (SSZ) for Italy, which associates an “effective” focal depth to each source zone (zonismiche.mi.ingv.it/documenti/App2.pdf). The distance limit of 150 km was dictated by the mentioned deaggregation analyses. In addition to excluding all subduction zone events from the calibration dataset focal depths were restricted within about 22 km, since the largest “effective depth” class in the Italian SSZ model is 12–20 km. For what concerns Japanese earthquakes, the K-Net focal depths were chosen, after checking for a number of events that these are the same as those reported in the Hi-Net database (www.hinet.bosai.go.jp), while most of focal depths of the other events are taken from the global CMT catalogue. The smallest value of R in the dataset is about 6 km. Using a significant number of reverse and strike-slip fault events with well identified source geometry in the selected set, the following relationship was obtained between the focal distance R and the nearest distance R_f from the recording site to the ruptured fault:

$$R(\text{km}) = 10.70 + 0.99 R_f(\text{km}) (\sigma_R = 6.37 \text{ km}, r^2 = 0.97). \quad (2.1)$$

The distribution of the data used in terms of magnitude and focal distance is shown in Figure 2.2. Events with reverse, normal and strike-slip fault mechanisms are all represented in the database; at this stage of the study, no dependence was yet introduced on the type of focal mechanism.

Ground categories. For consistency with CEN (2004), the four basic ground categories A, B, C, and D defined therein mainly through the V_{s30} propagation velocity index, have been adopted for the classification of the recording sites. About 82% of the calibration dataset derives from the K-Net database, with a velocity profile at the recording sites known to a depth of 20 m at most. This created an evident practical difficulty in classifying the sites in terms of V_{s30} . Four different methods were proposed in Boore (2004) to estimate V_{s30} from velocity data not reaching 30 m depth. Three of them were applied here, and a further one was independently developed and adopted. The simplest method in Boore (2004) assumes that the lowermost measured velocity extends to 30 m, but this choice may lead to underestimating V_{s30} because V_s generally increases with

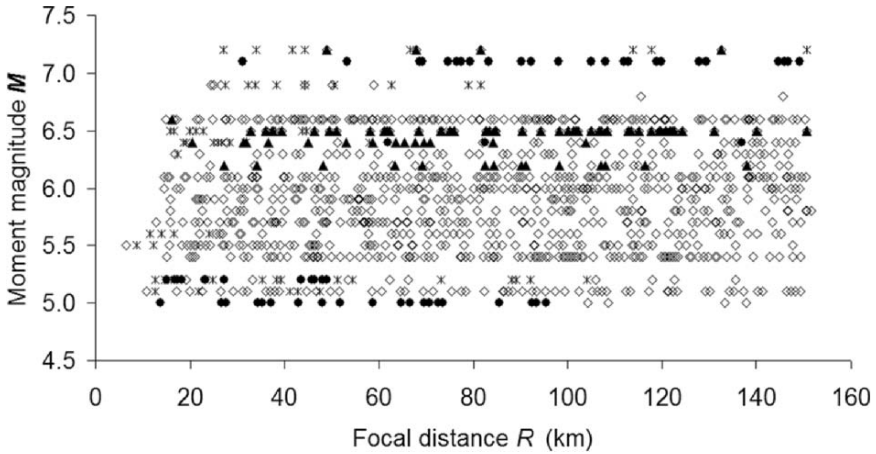


Fig. 2.2. Distribution of magnitude, distance and geographical origin for the acceleration records in the database. Diamonds are Japanese data. Data from California are represented by black circles. Black triangles are Iranian data, while asterisks refer to data from Europe and Turkey

depth in layered media. To overcome this problem we modified the criterion by assuming piece-wise uniform velocity profiles: specifically, the deepest measured velocity value is increased by 20% every 10 m. Two more options were borrowed from Boore (2004): the first is based on velocity statistics to determine site class, while the second one uses the correlation between V_{s30} and V_{sd} , where V_{sd} is the time-averaged velocity for a set of boreholes for which the actual depth d reaches or exceeds 30 m. The correlation between V_{s30} and V_{sd} was calibrated *ad hoc* for this study using about 100 velocity profiles from the Japanese Kik-Net network database (Figini, 2006). The actual classification of the K-Net stations was finally established by applying the four criteria just described, and the final decision taken on a simple majority rule.

For the recording sites from Europe and Turkey use was made of the information available in the European Strong-Motion database (Ambraseys et al., 2002), while ground conditions for the Iran data were identified, where possible, starting from the classification scheme proposed in Zare (2004).

Finally, for the Hector Mine earthquake, information on ground conditions is available for CISN network stations, while many NSMN stations can be classified using on-line data available from quake.wr.usgs.gov/~boore.

Data processing and representation. The basic processing applied uniformly to all records of the dataset is described in Paolucci et al. (2006); it has been shown that removal from the entire record of the baseline offset computed from the sole pre-event time window suffices to obtain reliable *DRS* ordinates at least up to 10 s period for the accelerogram components of the lower magnitude events, and to 15 s or more for the higher (>6.5) magnitudes. In addition, independent comparison of *DRS* from co-located

broad band velocity meters and SM accelerographs confirmed the reliability of the basic processing applied to acceleration records. The shortest period taken into account in deriving the attenuation relations is 0.1 s, thus making it unnecessary to apply a high-cut filter, commonly chosen to have a roll-off at 50 Hz and cut-off at 100 Hz, for digitally recorded data (Ambraseys et al., 2005). From the acceleration histories, baseline corrected as just described, the *DRS* ordinates were computed up to 20 s period for both horizontal and for the vertical component of each accelerogram. The horizontal ground motion is represented in this study by the geometric mean of the *DRS* ordinates of the two recorded horizontal components at a given period, and by the single ordinate of the vertical response spectrum. The spectral ordinates are expressed in cm.

2.2. PREDICTION EQUATIONS FOR DISPLACEMENT SPECTRAL RESPONSE

The empirical equations for the prediction of the *DRS*(T) ordinates were initially taken in the form (e.g. Ambraseys et al., 1996):

$$\log DRS(T) = a_1 + a_2 M + a_3 \log R + a_4 S_1 + a_5 S_2 + \varepsilon \quad (2.2)$$

where T (s) = vibration period, and $a_1 \dots a_5$ are numerical coefficients, ε denotes a random error term, assumed as normally distributed with zero mean and standard deviation $\sigma_{\log DRS}$. S_1 and S_2 are dummy variables accounting for the main local ground categories contemplated in both the Eurocode 8 and the Italian current norms (CEN, 2004; Ministero delle Infrastrutture e dei Trasporti, 2005), with the following values: $S_1 = S_2 = 0$ for type A (rocklike) ground, with $V_{s30} \geq 800 \text{ m s}^{-1}$; $S_1 = 1$ and $S_2 = 0$ for type B (stiff) ground, with $360 \text{ m s}^{-1} \leq V_{s30} \leq 800 \text{ m s}^{-1}$; $S_1 = 0$, $S_2 = 1$ for type C ground, with $180 \text{ m s}^{-1} \leq V_{s30} \leq 360 \text{ m s}^{-1}$, and $S_1 = S_2 = 1$ for type D (very soft) ground, with $V_{s30} < 180 \text{ m s}^{-1}$. Note that accounting for local ground conditions with two dummy variables only, as in (2.2), does not allow to discriminate between the amplification ratios D/B and C/A, both equal to $10^{a_5 S_2}$, and between B/A and D/C. To avoid such ambiguity, a third dummy variable S_3 should be introduced, so that the portion on the rhs of (2.2) accounting for ground conditions would become $a_4 S_1 + a_5 S_2 + a_6 S_3$. In such case, $S_1 = S_2 = S_3 = 0$ for ground A, while $S_i = 1$ ($i = 1, 2, 3$) and the other two dummy variables would be set equal to 0 for the other ground types. Table 2.1 shows the distribution of the calibration data in terms of M and ground type.

Table 2.1. Distribution of acceleration records in the database in terms of magnitude and ground types (CEN, 2004)

M	A	B	C	D	Unknown
5.0–5.4	17	95	97	13	34
5.5–5.9	11	141	131	38	0
6.0–6.3	8	127	135	21	16
6.4–6.6	23	96	59	15	49
6.7–7.2	9	13	11	0	22

A number of accelerograms (121) recorded at sites with unknown ground conditions was retained in the dataset; when regressing the data with (2.2), these sites were assumed to belong either to class B or to class C, the latter choice providing a lower prediction error.

Some tests on the spectral ordinate at 10 s period, denoted hereinafter as D_{10} , were performed to investigate whether the statistical significance of the prediction would be increased to adopt a functional form different from (2.2), e.g. by including a quadratic dependence on M , or a dissipative attenuation term, or a magnitude-dependent attenuation coefficient a_3 (see Joyner and Boore, 1981; Fukushima, 1996; Ambraseys et al., 2005). No significant improvement was obtained with respect to the results yielded by (2.2), that has the additional advantage of allowing an immediate comparison with the theoretical attenuation relation for the far field maximum ground displacement derived in Faccioli et al. (2004) from the Brune model, i.e.

$$\log d_{\max}(\text{cm}) = -4.46 + 0.33 \log \Delta\sigma (\text{MPa}) + M - \log R(\text{km}) \quad (2.3)$$

where d_{\max} is the maximum horizontal ground displacement and $\Delta\sigma$ the stress drop. The tests with a different functional form of the attenuation relation will be extended also to the shorter period DRS ordinates.

The coefficients a_i of (2.2) were calculated by the two-stage regression technique first introduced in Joyner and Boore (1981), allowing to decouple the magnitude and the distance dependence. The coefficients were determined in the range $0.10 \text{ s} \leq T \leq 20 \text{ s}$ for damping 0.05 (listed in Table 2.2), as well as for 0.10, 0.20, 0.30 damping.

Note from Table 2.2 that the magnitude and distance dependence of the DRS ordinates is consistent with the theoretical relationship (2.3) at periods between about 6 s and 10 s, confirming the soundness of the empirical prediction tool.

Table 2.2. Coefficients of Eq. (2.2) for the prediction of 5% damped $DRS(T)$

$T(\text{s})$	a_1	a_2	a_3	a_4	a_5	$\sigma_{\log DRS}$
0.10	-1.7769	0.4974	-1.7479	0.0465	0.042045	0.3935
0.15	-1.757	0.5153	-1.6367	0.0689	0.1379	0.3902
0.2	-1.8922	0.543	-1.5544	0.0844	0.2343	0.3902
0.25	-2.0734	0.5801	-1.5039	0.1004	0.2917	0.3836
0.5	-2.4256	0.6585	-1.416	0.2032	0.4611	0.3689
0.75	-2.6197	0.6964	-1.3616	0.2674	0.5368	0.370
1	-2.7652	0.7499	-1.3796	0.2482	0.5016	0.379
1.25	-2.8531	0.7772	-1.3624	0.2165	0.4463	0.3732
1.5	-2.945	0.8095	-1.3752	0.1856	0.4070	0.3651
1.75	-3.0231	0.8313	-1.3711	0.1643	0.3741	0.3571
2	-3.0489	0.8413	-1.3628	0.1504	0.3450	0.3477
4	-3.7533	0.9544	-1.213	0.1314	0.2578	0.3124
6	-4.3049	1.0321	-1.0915	0.0964	0.2136	0.2896
8	-4.5001	1.0389	-0.9864	0.1089	0.2170	0.2809
10	-4.5621	1.0391	-0.9584	0.1096	0.2157	0.2694

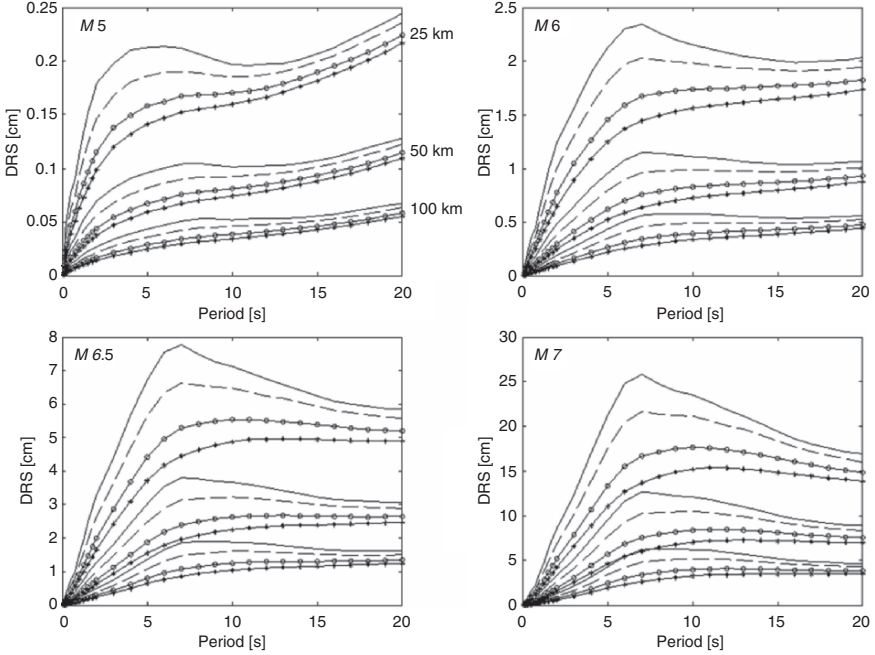


Fig. 2.3. $DRS(T)$ predicted on rock by Eq. (2.2) for different damping ratios: 5% (solid lines), 10% (dashed lines), 20% (lines with circle markers), 30% (lines with asterisk markers). The spectra are depicted for $M = 5, 6, 6.5, 7$ and three values of focal distance $R = 25, 50, 100$ km. Note the spurious long period trend at MS and 6, caused by lower S/N ratio

As shown in Figure 2.3 the median spectral shapes predicted by (2.2) on rock change smoothly with M and exhibit the same general behaviour, i.e. a strongly increasing initial branch up to a “corner” period varying from a few s to about 10 s (depending on magnitude and damping), followed by a branch that asymptotically approaches the maximum ground displacement with a nearly constant or moderately increasing/decreasing trend. Figure 2.3 clearly displays the effects of the long period errors that could not be removed in the data processing: for instance, for $5 \leq M \leq 6$, the final upward trend of the spectra that follows a minimum occurring for $10 \text{ s} < T < 16 \text{ s}$, is spurious. Hence, as observed earlier, it can safely be assumed that using (2.2) with the present dataset yields reliable $DRS(T)$ ordinates up to a maximum period that strongly increases with magnitude, i.e. from about 10 s for $M 5$ to about 20 s for $M 7$.

The possible dependence of the ground coefficients a_4 and a_5 on magnitude was separately investigated using the non-linear predictive relation

$$\log DRS(T) = b_1 + b_2 M + b_3 \log R + b_4 S_1 10^b S_5 M + b_6 S_2 10^b S_7 M. \quad (2.4)$$

The previous two-step approach was still used with (2.4), whereby b_5 and b_7 were determined within the first step through a Trust Region minimisation procedure. Among all possible solutions, that corresponding to the least standard error of the prediction was chosen. As initial conditions for the iterative minimisation procedure, the coefficients calculated for (2.2) were used, i.e. assuming $b_4 = a_4$, $b_6 = a_5$, $b_5 = b_7 = 0$ at the first iteration. The coefficients obtained for the non-linear form (2.4) are not given herein; the results (discussed in the following subsection) show that (2.4) leads to a negligible decrease in the standard error of the *DRS* predictions. Therefore only the linear form (2.2), or its variation containing three dummy variables for site conditions, was retained for applications of hazard mapping.

2.3. INFLUENCE OF LOCAL GROUND CONDITIONS

The influence of local ground conditions on the $DRS(T)$ ordinates is first illustrated through a version of the attenuation relations calibrated on a data sub-set consisting of the Japanese (K-Net Kik-Net) records only, restricted to $R < 75$ km. This subset of about 250 records contains ground motions of engineering significance, mostly in the 0.9 to 4.0 m s^{-2} maximum acceleration range. The appropriate parts of the terms $a_4 S_1 + a_5 S_2$ in (2.2) and $b_4 S_1 10^{b_5 M} + b_6 S_2 10^{b_7 M}$ in (2.4) are displayed first, since they depict directly the spectral amplification for a given ground class (B, C, or D) with respect to class A.

Class B ground. The B/A amplification ratio is simply given by $a_4(T)$ in (2.2) and is shown by the shaded band on the lhs graph in Figure 2.4, corresponding to the median value \pm the s.e. of estimate of the coefficient. The spectral amplifications from other attenuation relations (Sabetta and Pugliese, 1996; Ambraseys et al., 2005) and from CEN

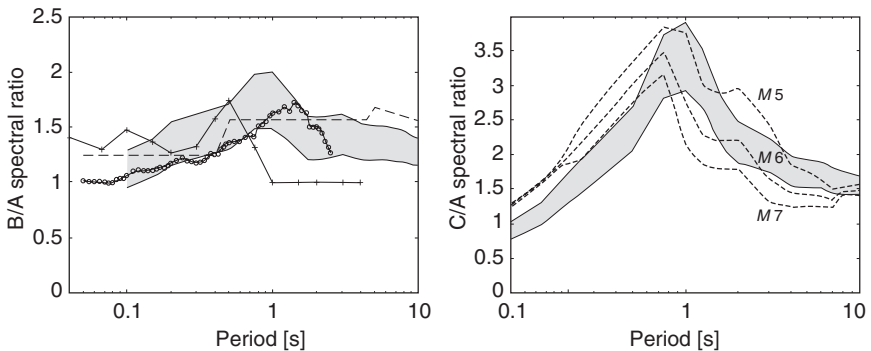


Fig. 2.4. (Left) The shaded band represents $B/A \pm 1$ s.e. spectral ratio obtained from Eq. (2.2) using two site dummy variables. Line with asterisks is derived from Sabetta and Pugliese (1996). Line with circles is computed from Ambraseys et al. (2005). The dashed line represents the Eurocode 8 spectral ratio (CEN, 2004). (Right) $C/A \pm 1$ s.e. spectral ratio obtained from Eq. (2.2) using two site dummy variables. Dashed lines represent C/A median ratio calculated through Eq. (2.4) for the indicated magnitudes

(2004) are also depicted, although the classification of ground categories adopted in the former do not coincide with the present one.

The ratio B/A yielded by (2.2) is constant and equal to about 1.2 for $T > 5.0$ s, while it exhibits significant broad-band amplification between 0.2 s and 5.0 s, reaching an (apparent) peak between 0.7 s and 0.8 s. Three main indications may be derived from Figure 2.4: (1) The difference between ground categories B and A is never negligible, since amplification ranges between 20% (at long period) and 75% (at $T < 1$ s). (2) Whichever the dataset used to calibrate the attenuation model, spectral ratios B/A tend to agree in terms of median amplification value, with some differences in the peak period. (3) Amplification factors obtained from CEN (2004) are too conservative for $T > 2$ s, and vice versa at lower periods.

Class C ground. The C/A spectral amplification is portrayed on the rhs graph of Figure 2.4, which contains results yielded by both (2.2) and (2.4); in the first case the factor shown as a function of period is a_5 while in the second it is $b_6 10^{b_7 M}$. A strong peak occurs at 1 s, with maximum amplification between about 2.7 and 4. For clarity, amplification curves from Sabetta and Pugliese (1996) and Ambraseys et al. (2005) are not shown in this case; the peak period of Sabetta and Pugliese (1996) for deep alluvium sites is about the same as in this study, but peak amplification does not exceed 1.7. The peak period from Ambraseys et al. (2005) is close to 2.0 s, with an ordinate of about 2.5. Median amplification curves yielded by (2.4), calibrated with the worldwide database, are shown in the same figure for three M values; they show, as expected on physical grounds, decreasing amplification when magnitude increases. The curves in question lie fairly close to or within the s.e. band of coefficient a_5 of (2.2), thus indicating that an attenuation model non-linear in the site coefficients, such as (2.4), results in a marginal improvement in statistical significance with respect to Eq. (2.2). Hence, the latter has been generally preferred in the applications.

H/V spectral ratios. An important source of uncertainty in predictions of the ground motion spectral amplitudes is likely to be due to errors in the attribution to ground categories based only on a geotechnical/geological site description or, ultimately, on V_{s30} values. Following Zhao et al. (2006) a preliminary investigation was made on the feasibility of subdividing the Japanese data subset into ground categories based on the H/V ratio of 5% damped horizontal to vertical spectra. Thus, the H/V ratios were computed for $0.05 \text{ s} \leq T \leq 2 \text{ s}$ for about 950 Japanese records, using for start the ground categories A, B, C, D, and picking from the ratio computed for each accelerogram the peak value and the corresponding period. Finally, for each ground class, the average and standard deviation of the peak value and the dominant period associated to it were derived. The evident aim was to detect correspondences between the geotechnical classification adopted and the peak periods of the H/V spectral ratios, in the hope of gaining insights as to the classification of stations with unknown soil conditions included in the worldwide database. Results, listed in Table 2.3, show that the uncertainty associated to the average dominant period and to average peak H/V value of each ground class is large, suggesting that a ground classification based on these two factors would bring no improvement.

Table 2.3. Mean peak period and corresponding peak amplification from H/V spectral ratios

Ground type	Peak period (s)	Peak amplification
B	0.44 ± 0.44	4.55 ± 2.38
C	0.72 ± 0.56	5.69 ± 2.90
D	0.80 ± 0.33	6.38 ± 2.58

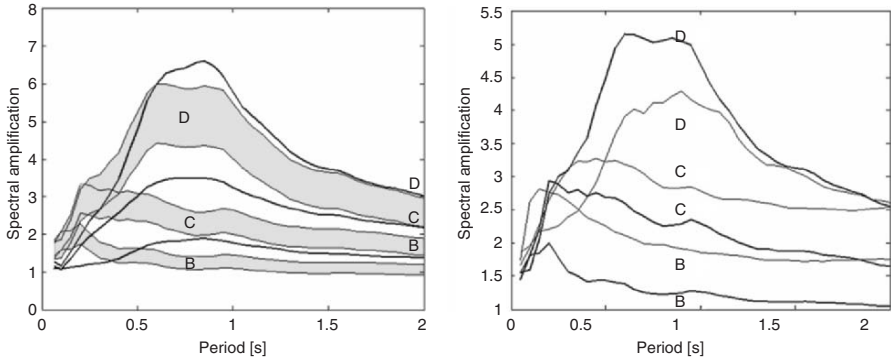


Fig. 2.5. (Left) Comparison of D/A, B/A, and C/A spectral amplification obtained using two dummy variables for site description (median values, thick black lines) or three dummy variables (shaded zones, median ± 1 s.e.) for Japanese data only. (Right) H/V spectral ratios (thin lines) vs median D/A, C/A, and B/A ratios obtained from (2.2) using three dummy variables

The mean H/V spectral ratios for different ground categories exhibit, however, a clear site-dependent shape, where physically meaningful dominant periods for each ground class can be identified (Figure 2.5, rhs). Starting from this observation, we recognised that modifying (2.2) by introducing three dummy variables was necessary to identify without ambiguity the influence of local ground conditions by means of the attenuation relation. The results of introducing such a modification into (2.2) are shown by the three shaded bands on the lhs of Figure 2.5, labelled as B, C, and D and representing the s.e. bands of the spectral ratios B/A, C/A, and D/A. The corresponding median spectral ratios resulting from the use of only two dummy variables are represented by the black solid curves. While the results are comparable in terms of maximum spectral amplification, the formulation with two dummy variables is clearly inadequate to segregate the dominant vibration periods for each ground class. The 95% confidence interval for the coefficient of S_3 always contains the D/A spectral ratio obtained with two dummy variables, while for the C and B ground classes the spectral ratio obtained by the two formulations are statistically equivalent only in the 0.3–0.6 s period range and for $T > 1.7$ s. This means that in the interval of periods where the peak amplification for ground B and C occurs, the difference in pattern obtained with three dummy variables is statistically significant and clearly preferable. For the same confidence level, the coefficient of S_1 is not statistically significant for $T > 0.7$ s.

2.4. VERTICAL SPECTRA

Using the same digital acceleration database, vertical components have been also analysed in terms of the median $V(T)/H(T)$ response spectral ratios. In this section, $V(T)$ is intended as the 5% damped *DRS* of the vertical component, while $H(T)$ is the geometric average of the response spectral ordinates of the horizontal components at period T .

A summary of results is plotted in Figure 2.6, for magnitude ranges from 5 to 6.6; the median V/H ranges typically from 0.4 to 0.7, with a variation with T weakly dependent on magnitude and distance, except for higher magnitudes and small distances, where the ratio tends to increase, but does not exceed 0.9.

Compared in Figure 2.7 are the present results for $6.0 \leq M \leq 6.3$ and $10 \text{ km} \leq R \leq 30 \text{ km}$, including the 16- and 84-percentile curves besides the median one, with the V/H ratios deduced from a few widely used attenuation relationships. Except for Ambraseys and Simpson (1996), exceeding the 84-percentile in a narrow range at short periods, the other ratios lie within the variability range of our data. Note, incidentally, that the vertical design spectra implemented in CEN (2004) are essentially based on the results of Ambraseys and Simpson (1996) that, based on this study, appear to be overconservative for $T < 0.2 \text{ s}$.

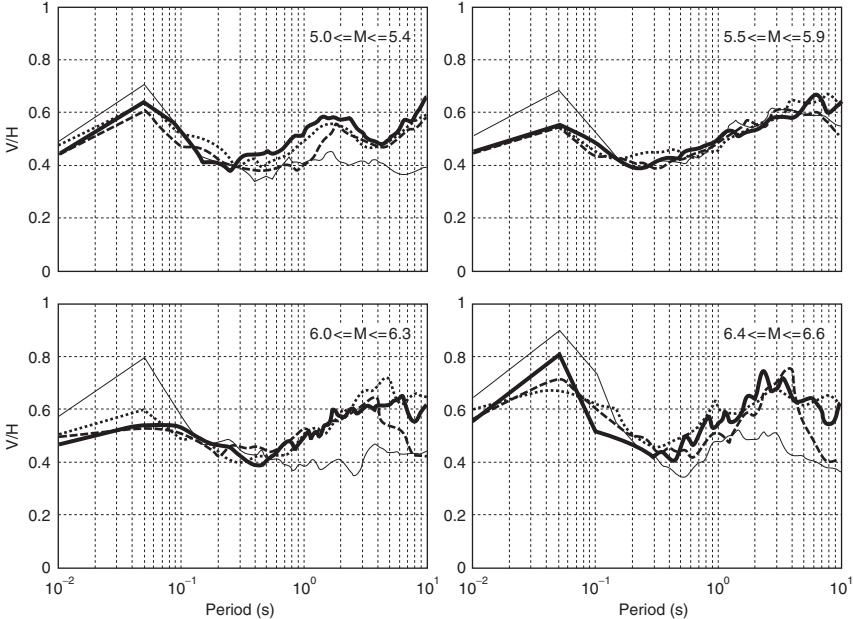


Fig. 2.6. Median response spectral ratios V/H for different magnitude and distance range: 10–30 km (thin solid lines), 30–50 km (dashed lines), 50–75 km (dotted lines), 75–100 km (thick solid lines)

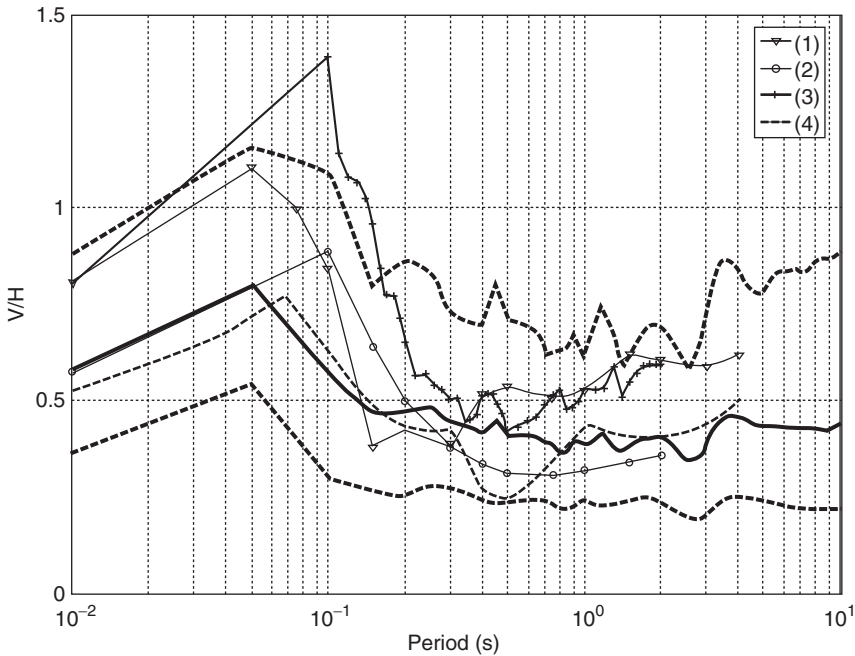


Fig. 2.7. Response spectral ratios V/H for $6.0 \leq M \leq 6.3$ and $10 \text{ km} \leq R \leq 30 \text{ km}$: 50-percentile (thick solid line), 16- and 84-percentile (thick dotted lines), compared with the values deduced from the attenuation relationships (1) Bozorgnia and Campbell (2004), (2) Ambraseys and Douglas (2003), (3) Ambraseys and Simpson (1996) and (4) Sabetta and Pugliese (1996), with $M = 6.15$ and $R = 15 \text{ km}$. Note that (2) is independent of magnitude and distance

Although not reported here for brevity, it was verified that the dependence of V/H on the site class is relatively modest with median values typically varying between 0.4 and 0.7 both for class B and for class C sites.

2.5. A SIMPLIFIED SPECTRAL DISPLACEMENT MODEL

In Figure 2.8 the median 5% damped displacement response spectra for different magnitude ranges, without distinction of ground type, are compared with the normalised spectrum obtained by multiplying the code (CEN, 2004) elastic acceleration spectrum for class A ground by $(T/2\pi)^2$. The observed median curves suggest that the design spectral shape of CEN (2004), consisting, for periods larger than 0.4–0.5 s, of a bi-linear curve with a constant plateau at long periods, provides a reasonable approximation, while the “bell-shaped” displacement spectrum defined in the Annex A of Eurocode 8 (CEN, 2004) for $T > 4 \text{ s}$ is not strongly supported by the observations. In the sequel, we will set the value of the long period plateau at D_{10} , already introduced in Section 2.2.

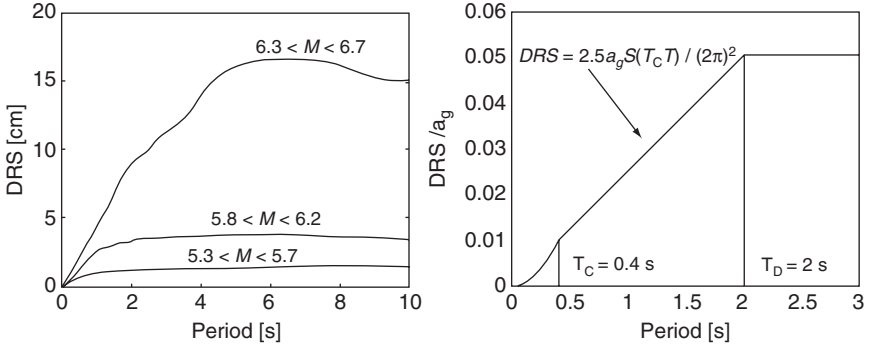


Fig. 2.8. (Left) Observed median DRS (without distinction of ground type, $10 < R < 30$ km) as a function of magnitude. (Right) Displacement spectral shape according to CEN (2004)

However, there are two major drawbacks to the bi-linear curve of CEN (2004). First, the constant plateau region is proportional to the peak ground acceleration a_g , that does not theoretically scale with magnitude as D_{10} , as shown by the observed median curves in Figure 2.8 and as it can be deduced by the dependence on period of the a_2 coefficient in Table 2.2. Second, a corner period $T_D = 2$ s is prescribed in CEN (2004) as the starting point of the constant displacement region, whatever the earthquake magnitude governing the seismic hazard of the region of interest. These points will be further discussed in Section 5, when displacement hazard representations will be introduced. At this stage, we only point out that it seems more rational to approximate the displacement spectral shape for design through the previous bi-linear curve with a constant level at $T > T_D$. However, instead of fixing the value of such plateau as a function of a_g and T_D and of arbitrarily setting $T_D = 2$ s, both D_{10} and a_g should be independently determined and T_D obtained as the intersection of the two lines, i.e.

$$T_D = \frac{(2\pi)^2 D_{10}}{2.5a_g S T_C} \quad (2.5)$$

The advantage of using (2.5) is that the dependence of T_D on magnitude is now implicit in D_{10} ; the drawback of this simplified spectral model is that it tends to be overconservative for intermediate periods, close to T_D , as it will become clearer in Section 5.

2.6. OTHER ASPECTS

We did not consider so far the treatment devoted to source and near-field effects in the S5 project. Briefly, there is only weak evidence of source directivity effects in the large database discussed in Section 2.1, and these were therefore neglected. On the other hand, remarkable radiation pattern effects for T values between few s and over 10 s were detected for strike-slip events in the M 6.5 to 7.0 range, notably the 2000 Tottori and 2005

Kyushu, Japan, earthquakes and the 2000 Iceland earthquake, all of them strong contributors to the calibration dataset. Systematic numerical simulations were also carried out using the D_{10} parameter.

The previous effects strongly depend on the fault-receiver configuration and their inclusion is hardly feasible in the frame of a nation-wide probabilistic hazard analysis, not to mention the uncertainties affecting the geometry and the slip rate of most active faults in Italy. Nevertheless, a modified form of the attenuation relation (2.2) was developed for D_{10} , that includes radiation pattern terms as a function of the fault-to-receiver angle of view. This should be apt for applications in scenario studies on a single site, with seismic hazard controlled by the activity of a single fault.

3. Response of alluvium filled valleys and basins

While the influence of alluvium filled basins on site response has been the subject of substantial research, the resulting modifications on the response spectra at the basins surface (especially for $T > 1-2$ s) has not been as thoroughly investigated (see e.g. Chavez Garcia and Faccioli, 2000) despite its importance in structural design.

Significant previous studies tried to estimate basin amplification effects through the analysis of strong-motion data and most of them quantified basin geometry only in terms of sediment depth (Trifunac and Lee, 1978), introducing such term in newly developed attenuation models. Other studies tried to relate basin effects also to the relative location of source and site position in the basin (Choi et al., 2005), or to the distance to the basin edge (Joyner, 2000).

Herein, in order to identify how alluvium filled valleys and basins affect the *DRS*, we consider both the wave field generated at the source and its propagation inside the basin sediments by applying a recently developed *Domain Reduction Method* (DRM), which allows to couple the separate analyses of source and basin response. This method, proposed in Bielak et al. (2003) on the basis of earlier work, was subsequently extended in a spectral element environment (Faccioli et al., 1997) and implemented in numerical codes suited for 2D/3D wave propagation analyses (Faccioli et al., 2005), to which we refer for details of implementation.

The main steps of the analyses are as follows. First a detailed numerical grid of the alluvium basin at study is prepared. Then the source mechanisms of interest are defined and the complete 3D displacement field in the zone occupied by the basin is computed using a horizontally layered local model of the Earth crust, through the efficient analytical method of Hisada and Bielak (2003). These displacements, properly manipulated, are used to calculate the effective forces to be applied at the boundary of the numerical model of the basin as an equivalent, effective dynamic excitation. Wave propagation inside the basin is then performed with the spectral code GeoELSE (Maggio et al., 2001; Stupazzini, 2004) and the damped *DRS* are finally calculated and analysed at the surface receivers of the basin.

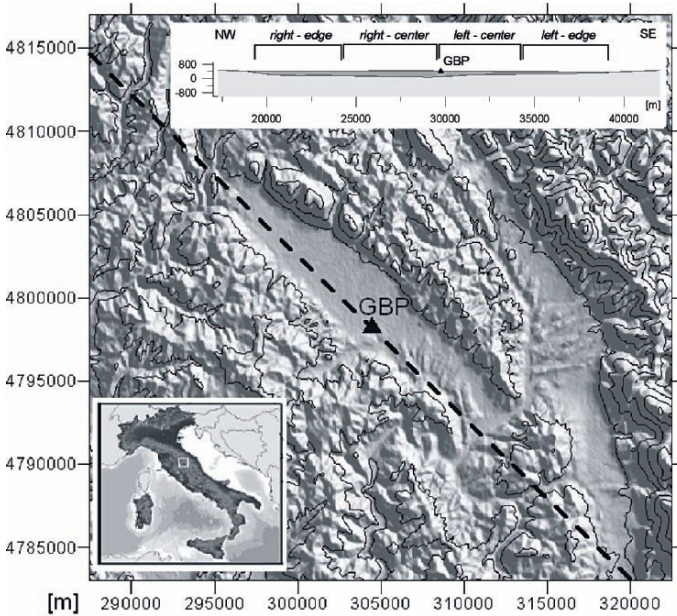


Fig. 2.9. Location of Gubbio Plain (Central Italy) and longitudinal cross-section used in numerical analysis. The position of the digital accelerometer station GBP is also displayed

A first application of the DRM approach was concerned with the 2D response analysis of the Gubbio sedimentary Plain (Figure 2.9) to the main shock of the damaging Umbria-Marche earthquake sequence of 1997 (26.09.97, 9.40 h, M 5.9), well recorded by a single digital accelerograph located in the middle of the Plain (station GBP) at 40 km epicentral distance. These analyses were intended to provide only preliminary quantitative insight into the problem, since the deep structure of the Gubbio Plain has not yet been clearly defined and is presently under study.

The source parameters and the slip distribution of the fault plane were taken from Hernandez et al. (2004). The crustal velocity model adopted combines the description given by the same authors, with that suggested in Mirabella et al. (2004); a smooth decrease in the rock properties with decreasing depth was also introduced to properly account for near-surface alteration (Cotton et al., 2006). For the valley sediments V_s values increasing from 500 m s^{-1} to 2000 m s^{-1} were derived from the inversion of Rayleigh wave dispersion curves and site response estimation from weak motions.

Shown in Figure 2.10 are the results of the numerical analysis of the longitudinal (NW-SE) cross-section of the valley. *DRS* were computed at closely spaced receivers at the surface and then averaged according to a subdivision of the cross-section into four zones (see Figure 2.9). The figure shows the average *DRS* for each zone, together with the Type I spectrum of CEN (2004, Annex A), ground category C (applicable to most valley

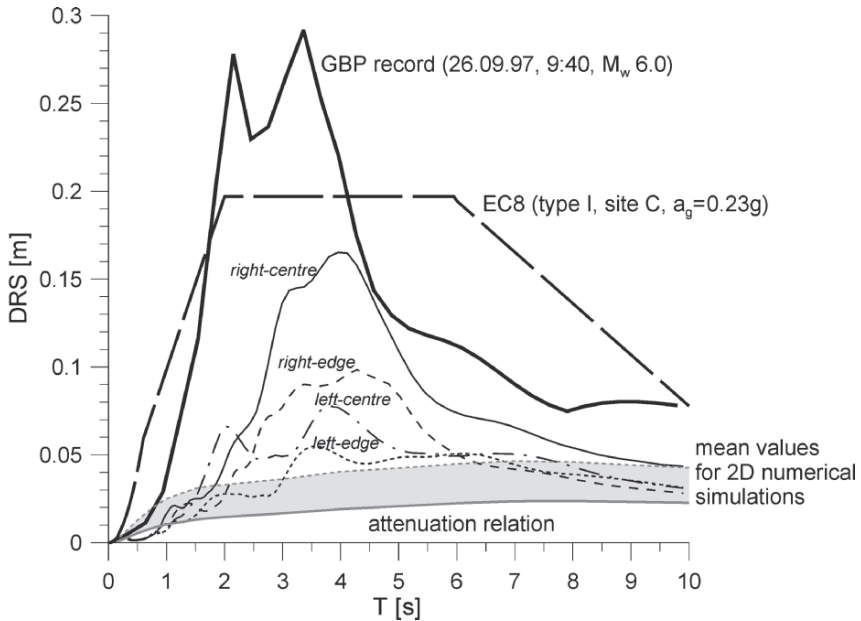


Fig. 2.10. Average 5% damped displacement response spectra (*DRS*) from 2D numerical simulations compared with the applicable Eurocode 8 (CEN, 2004) spectrum, median (+ s.e.) values from the form (2.4) of the attenuation relation (with shading) and corresponding strong motion record at GBP acceleration station (from simulated event 26.09.97, 9:40 h)

receivers), anchored at a 475 year peak acceleration $a_g = 0.23 g$ (yielded by regional probabilistic hazard analysis). The *DRS* from the horizontal strong motions recorded at GBP is also displayed (projected in the direction parallel to the cross-section). The mean +1 s.e. spectral band predicted by (2.4) is also included in the figure for comparison. The observed *DRS* has amplitudes that largely exceed the standard spectrum of the code from 1.5 s to 4.5 s period. These amplitudes, moreover, cannot be matched by either the numerical analysis or the attenuation relation. This casts proper light on the strong amplification effects affecting the response of alluvium valleys at long periods. Note that the fundamental 1D resonant period in the deepest portion of the valley is about 3 s.

The Gubbio observations (and similar ones in other parts of the world) prompted us to plan and perform a parametric analysis of alluvium filled valleys subjected to the radiation of different types of earthquake sources. A 2D model borrowed from the European Project Sismovalp (www-igut.obs.ujf-grenoble.fr/sismovalp) was chosen for valley shape, i.e. the so-called A0 model representative of the typical valley of the European Alps. The profile and mechanical properties of the layers inside the basin were defined as an average over a number of basins located in the Italian, French, and Swiss Alps. In Table 2.4 are given the velocity model of the basin and of the rock outside and beneath it. Ground category C identifies nearly all the sites at the surface of the basin.

Table 2.4. Adopted sediment and crustal velocity model for parametric analyses of 2D alluvium valleys

Valley sediments		Crustal model	
Thickness (m)	V_s (m s ⁻¹)	Thickness (m)	V_s (m s ⁻¹)
15	250	30	1200
15	350	70	2000
70	450	250	2400
250	600	2350	2800
100	800	2000	3300
–	–	–	3500
–	–	30	1200

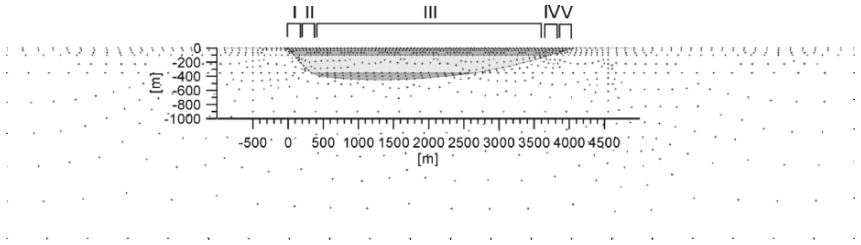


Fig. 2.11. Valley model with numerical grid (spectral nodes). Note zone subdivision (I, II, III, IV, V)

In Figure 2.11 the valley geometry with the spectral nodes of the 2D numerical grid is shown. Note the subdivision of the valley into four zones, aimed at capturing differences in the site response features. The boundary zones of the model are within a distance of respectively 200 m and 400 m from basin edges. The grid step allows to propagate frequencies up to about 3 Hz, with a sampling rate of 2.5 points per wavelength. The computational mesh contains 1126 spectral elements (with 5×5 integration points) and 1140 spectral nodes. Absorbing boundaries were introduced on all the vertical sides of the model and on its bottom face.

Source analysis, carried out with the Hisada and Bielak (2003) code, involved normal (here denoted as N), reverse (R) and strike slip (SS) focal mechanism. The dip angle of the fault was chosen to correspond to typical earthquake sources of Italy Alpine region: 60° for N, 20° for R and 85° for SS. A rectangular fault ($L = 2W$) with bilateral propagation (hypocenter at 10 km depth) was arbitrarily placed with strike 0° at the origin of the coordinate system. Rupture velocity on the fault was taken as $0.75 V_s$.

The first cycle of simulations regarded an M 5.2 event, the main source parameters of which are summarised in Table 2.5. From M , M_o and rupture area were estimated after Wells and Coppersmith (1994). From M_o and area, the slip was estimated, while the rise time was obtained from Geller (1976).

Table 2.5. Source parameters of simulated event in parametric analyses

M	M_o (Nm)	Fault area (km ²)	L (km)	W (km)	Rise time (s)	Slip (m)
5.2	$7.079 \cdot 10^{16}$	17.4582	5909.014	2954.51	0.49004	0.1141

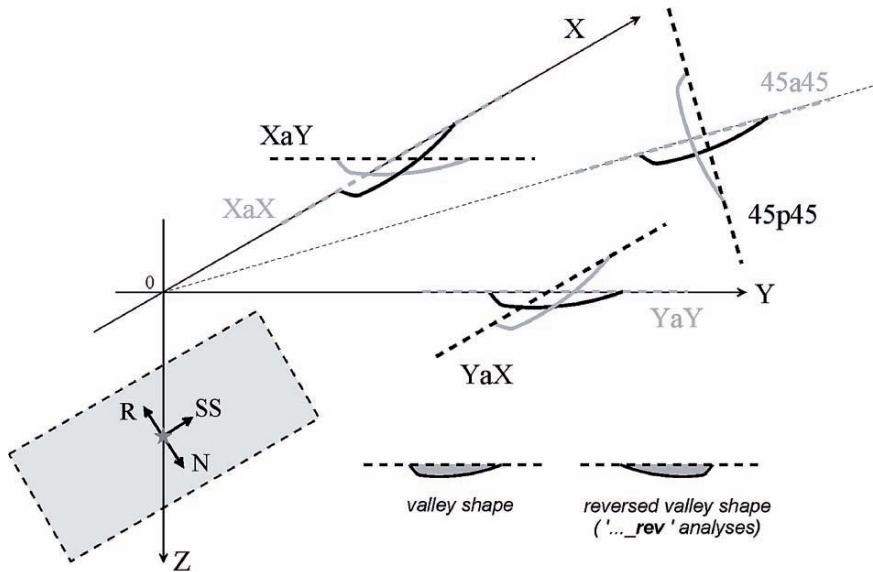


Fig. 2.12. Outline of valley-fault configurations used in source simulations

To investigate the influence of different types of radiation from the source onto the valley, a set of basin-fault configurations was chosen for the simulations. As shown in Figure 2.12, the valley longitudinal axis was placed along the X and Y axes and along the direction at 45°, either parallel or perpendicular to them. Since the cross-section considered is non-symmetrical, some analyses involved the valley with both a “normal” and a reversed shape. The hypocentral distance of the valley centre is about 20 km.

It is worth noting that the computational code adopted introduces an intrinsic high frequency cut-off at about 3 Hz. Simulated displacement histories were at the end band-pass filtered between 0.2 Hz and 5 Hz.

5% damped *DRS* were computed and then averaged over the valley zones defined in Figure 2.11. Figure 2.13 shows the results for every zone, for the different fault mechanisms and configurations, but only the worst case average *DRS* at the surface are shown. In each graph also the median \pm s.e. interval (shaded band) from the attenuation relation (2.2) is displayed, for ground type C, together with the median + s.e. band (unshaded) of the correction obtained from Choi et al. (2005) residuals, using model B2 for Southern California. The vertical lines indicate the fundamental (average) 1D period for the zone considered.

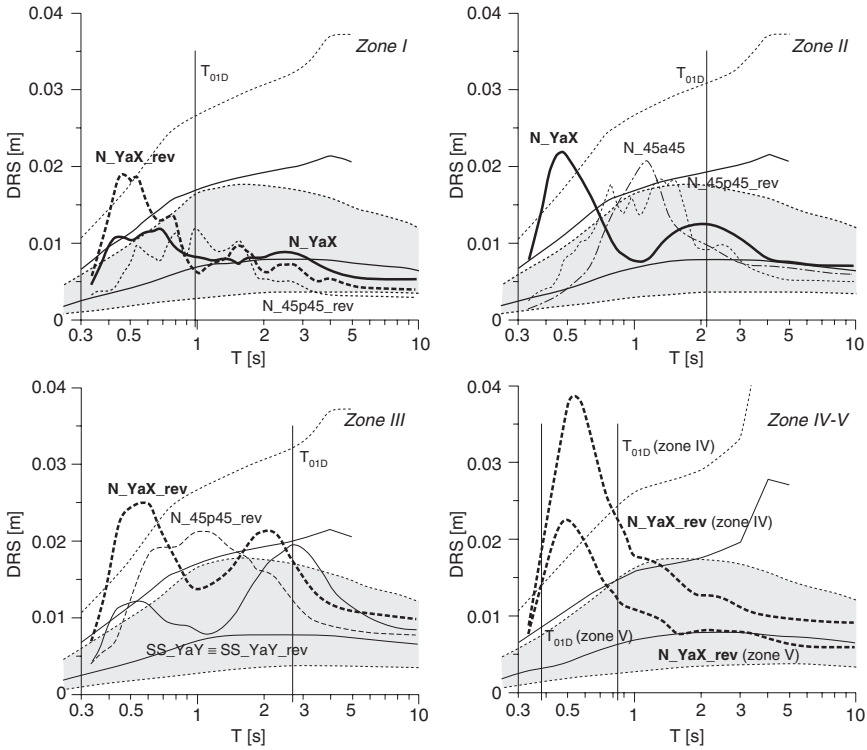


Fig. 2.13. 5% damped DRS from source simulations of valley-fault configurations. Only the worst case average DRS at the surface are shown for each valley zone, for different fault mechanisms and configurations as identified in Figure 2.12. Each graph also displays the median \pm s.e. interval (shaded band) from (2.2), ground type C; the two curves in grey enclose the median + s.e. band (unshaded) of the correction obtained from Choi et al. (2005) residuals (their model B2 for Southern California). Indicated with a vertical line is the fundamental (average) 1D period for the zone considered

No results are shown for valley positions along the X axis nor for reverse fault mechanisms. The mean DRS values in these cases are in fact comfortably enclosed within the dispersion band of the attenuation relation. The worst cases involve in particular the normal fault mechanism with the valley located along the Y axis, mainly in “reverse” mode, giving rise to relatively severe peaks at low periods, around 0.5 s. The position of the valley along the 45° direction results in high amplitudes only for the normal fault mechanism, with dominant periods of about 1 s. The strike-slip mechanism tends to emphasise mostly 1D basin response (see, e.g. zone III in the figure), while normal fault mechanisms generate high peaks probably related to 2D basin response, at lower periods. The use of a “reverse” valley exposes the less steep side of the valley to direct incident wave arrivals, featuring quite different (and unexpected) 2D effects probably related to the generation

and trapping of surface waves inside the basin. In any case, none of the results seems clearly predictable. The most severe peaks exhibited by the simulated *DRS* occur in all cases for $T < 1$ s and the attenuation relation (2.4), even when corrected with the residuals provided in Choi et al. (2005), cannot always account for their amplitude, in some cases quite high. This seems to confirm, albeit in a different range of periods, the previous case of the Gubbio Plain response, adding further support to the need of a separate, appropriate quantification of *DRS* on alluvium basins. Additional simulations for higher magnitudes are being carried out to reach more definitive conclusions.

4. Overdamped spectra

With reference to the illustration in Figure 2.1, the response spectra for viscous damping ratios (ζ) different from 5% are currently obtained by applying a damping correction factor (η) to the 5% damped spectrum, defined in the past in several ways (see e.g. Tolis and Faccioli, 1999; Bommer et al., 2000).

In CEN (2004) the spectral reduction factor has been taken from Bommer et al. (2000) at intermediate periods (between T_B and T_E) while at shorter and longer periods η increases linearly so as to reach the value 1 at $T = 0$ s and $T = T_F$ (T_B, T_E, T_F are defined in CEN, 2004 and depend on site conditions).

In order to define a reliable correction factor transforming the 5% damped *DRS* into the overdamped spectra, a comparison has been made between the available factors and those derived from UH spectra for different damping ratios (calculated as explained in Section 5 for about 50 locations equally distributed in Italy). The ratios of spectral ordinates for $T < 7$ s are constant, see Figure 2.14; in this interval the formulation of CEN (2004) provides the best agreement with the median ratios derived from the UH spectra. At $T > 7$ s the ratios linearly increase, as theory predicts, and tend to reach the value 1 at an approximate period of 25 s. This means that at such a period the relative displacement of the oscillator roughly equals the ground displacement. Hence, the expressions for the scaling factors proposed in this study are:

$$\eta_0 = \frac{SRS(\zeta)}{SRS(5\%)} = \sqrt{\frac{10}{5 + \zeta}} \quad T_B \leq T \leq 7 \text{ s} \quad (2.6)$$

$$\eta = \frac{1}{18} [(1 - \eta_0) T + 25\eta_0 - 7] \quad 7 \text{ s} \leq T \leq 25 \text{ s}$$

Figure 2.14 shows the comparison between the correction factors (2.6) and the UH median ratios. Although the fit of (2.6) to the data is not optimal for damping ratios of 0.20 and 0.30, the slight overestimation of the reduction factor leads to a conservative prediction of spectral ordinates, and hence it is deemed acceptable.

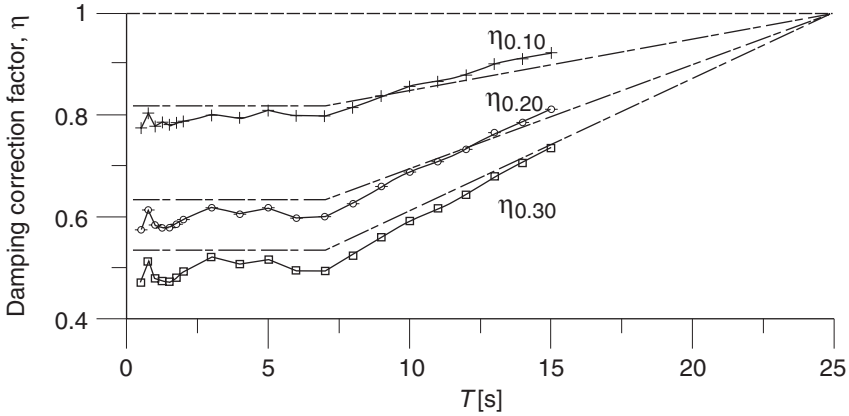


Fig. 2.14. Correction factors of spectral ordinates of overdamped spectra with respect to the 5% damped spectrum: solid lines with symbols represent median ratios derived from the UH spectra computed by using attenuation relations for different damping values, while dashed lines are the ratios yielded by (2.6)

5. Hazard representations in spectral displacements

5.1. CRITERIA FOR THE HAZARD ANALYSIS

In the engineering seismic hazard analyses, typically carried out by the classical method of Cornell (1968), seismic sources may be represented either as SSZs that, according to geological, seismological, and historical information, are regarded as homogenous in terms of seismic hazard, or as geological structures with their 3D geometry that can generate strong events (characteristic earthquakes). While the full treatment of uncertainties in PSHA would require a logic tree formulation, herein only some preliminary analyses are presented without introducing a logic tree. For consistency with other projects mentioned in the Introduction, a model of homogenous SSZs, named ZS9, has been adopted (essel.mi.ingv.it). This includes 36 SSZs for which the seismic parameters (Gutenberg–Richter parameters, average depth, maximum earthquake magnitudes, focal mechanism) were available. The attenuation relation (2.2) was used in the analysis, performed with the CRISIS2003 code (Ver. 3.0.1) (Ordaz et al., 1991). The code allows for different source-to-site distance definitions, including focal and fault distance. The fault equivalent radius is estimated by different relationships (e.g. Brune, 1970). By comparing the results obtained through the use of R (focal distance) and the fault distance derived from (2.1), no significant differences have been found in the results for a return period of 475 years.

5.2. EXTENT OF THE LONG PERIOD, CONSTANT DISPLACEMENT RANGE

Because, on one hand, DDBD is rather recent and, on the other hand, only few structures require accurate response spectra at long periods ($T > 4$ s) for design with the traditional approach, studies that provide regional maps of parameters controlling the response spectra at such periods are almost non-existent. In BSSC (2003) the long period spectral response is governed by a corner period (that represents the transition from constant spectral velocity to constant spectral displacement) named T_L . The meaning of this parameter is obviously akin to that of T_D in Subsection 2.5. T_L maps in BSSC (2003) were prepared following a two-step procedure; in the first step the following correlation was established between M and T_L :

$$\log T_L = -1.25 + 0.3M \quad (2.7)$$

This correlation was selected among several available formulas supported either by seismic source theory (Brune, 1970) or by the evaluation of T_L from response spectra of strong motion accelerograms with reliable long period content, recorded during moderate and large magnitude earthquakes. The second step made use of deaggregation analyses (for the 2% in 50-year exceedance level for *acceleration spectra*) aimed at constructing maps of modal magnitude. From (2.7) and the knowledge of the magnitude that most influences hazard at each site it was possible to construct a T_L map for the conterminous United States.

While BSSC (2003) provides important clues as to practical ways of defining spectra at long periods, only few records were used for calibrating (2.7) and, furthermore, the deaggregation analysis assumed that the modal magnitude–distance bin controlling the hazard at $T = 2$ s (in some cases even 1 s) would remain the same also at longer periods.

Using the Brune source model (Brune, 1970), with an average focal depth of 8 km, an average constant shear wave velocity of 3.0 km s^{-1} , and a stress drop of 10 MPa, the values of the corner period listed in the second column of Table 2.6 were obtained. In the third column, the values from (2.7) correlation are shown. These were compared, in the remaining columns of the same table, with those estimated in this study: (a) directly from (2.2) for ground types A and C; (b) from UH spectra (for ground types A and C) computed at many different locations uniformly distributed in Italy;¹ (c) using the bi-linear approximation discussed in Section 2.5.

The corner period estimated from UH spectra on hard ground appears to be insensitive to magnitude (see also Figure 2.16). As previously indicated, the bi-linear approximation underestimates the corner periods, thus providing a conservative approximation to the spectra at intermediate periods (see Section 5.4).

5.3. OVERDAMPED, UNIFORM HAZARD (UH) DRS

Overdamped UH spectra were calculated first directly through the attenuation relations derived for damping ratios 0.10, 0.20, and 0.30. Then, spectra for different locations have

Table 2.6. Comparison among values of *DRS* corner period obtained with different methods.

<i>M</i>	Brune (Brune, 1970)	NEHRP 2003 (BSSC, 2003)	From Eq. (2.2)		From UH spectra		Bi-linear approx.
			Ground A	Ground C	Ground A	Ground C	
5.0–5.5	1.4	2.1	4.0	1.5	6.0–8.0	1.0–2.5	0.2–1.0
5.5–6.0	2.5	3.0	5.0	4.0	6.0–8.0	2.0–5.0	0.2–1.1
6.0–6.5	4.4	4.2	6.0	6.0	6.0–8.0	4.0–6.0	1.0–2.0
6.5–7.0	7.8	6.0	6.3	6.3	6.0–8.0	6.0–8.0	1.0–2.0
7.0–7.5	13.8	8.4	6.5	6.5	6.0–8.0	6.0–8.0	1.0–2.0

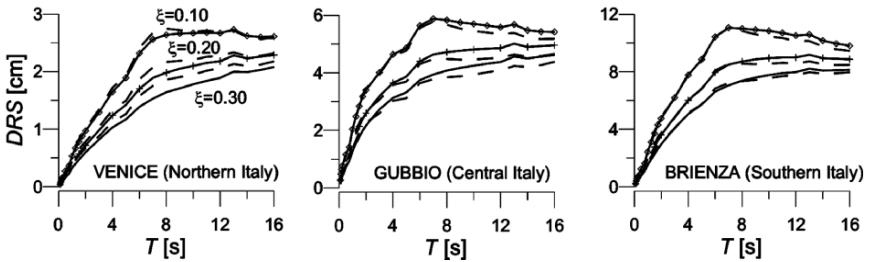


Fig. 2.15. UH *DRS* for three selected locations: solid curves denote spectra computed with attenuation relation for overdamped spectral ordinates, while dashed curves show the approximate spectra yielded by application of (2.6) to the 0.05 damped spectrum

been compared with those obtained by applying the reduction factor (2.6) to the 5% damped spectra. Figure 2.15 shows the comparison for three selected locations: Venice (low seismicity), Gubbio (intermediate seismicity), and Brienza (high seismicity).

At long periods the approximate spectra show some differences with respect to the UH spectra. Such differences are however small and can for practical purposes be neglected.

5.4. EFFECTS RELATED TO LOCAL SOIL AMPLIFICATION

The relationship (2.2) has been used in the hazard analyses to account for local soil amplification through the site variables S_1 and S_2 . Thus, UH spectra (solid curves in Figure 2.16) for ground types A and C at some locations in Italy were evaluated and compared with the bi-linear approximation (dashed straight lines in same figure). Note that the spectral shapes for the two ground conditions are not substantially different and, also, that the bi-linear spectra provide a good, mostly conservative approximation to the UH spectra. The conservatism at periods lower than T_D is a consequence of assuming a T^{-1} decay of spectral ordinates between the control periods T_C and T_D in the reference code (CEN, 2004) spectrum.

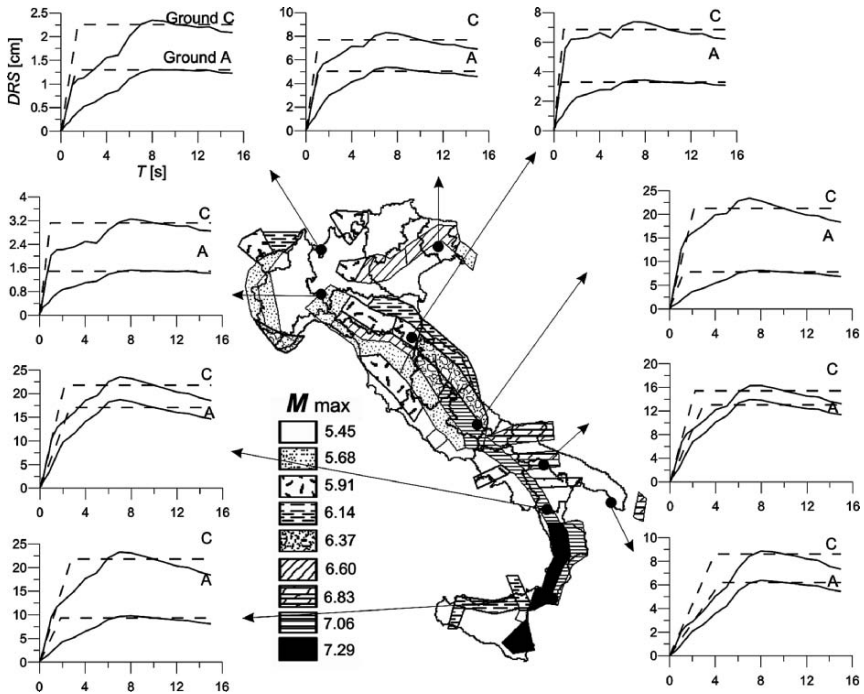


Fig. 2.16. Map of the maximum magnitudes in the ZS9 model of SSZs. UH spectra for ground types A and C are also shown at selected locations and compared with the bi-linear approximation proposed in this study (Section 2.5). The DRS ordinates are in cm, the periods on the abscissa in s

5.5. SPECTRAL DISPLACEMENT MAPS

Hazard maps in terms of spectral displacement have been produced with the previous criteria and computational tools. One example, shown in Figure 2.17, illustrates the D_{10} map for ground type A and for 475 years return period.

The comparison between the SSZs maximum magnitude map (Figure 2.16) and the D_{10} map (Figure 2.17) highlights the strong dependence of long period spectral displacement on magnitude. Figure 2.17 indicates, in fact, that D_{10} is less than 3 cm for the most part of Northern Italy, while in the Southern Apennines and Sicily it reaches 18 cm. Furthermore, according to the experts' opinion (Calvi, 2006), the value of 3 cm represents a threshold for structural analysis of current structures, i.e. the minimum response displacement for which any new structure ought to be designed.

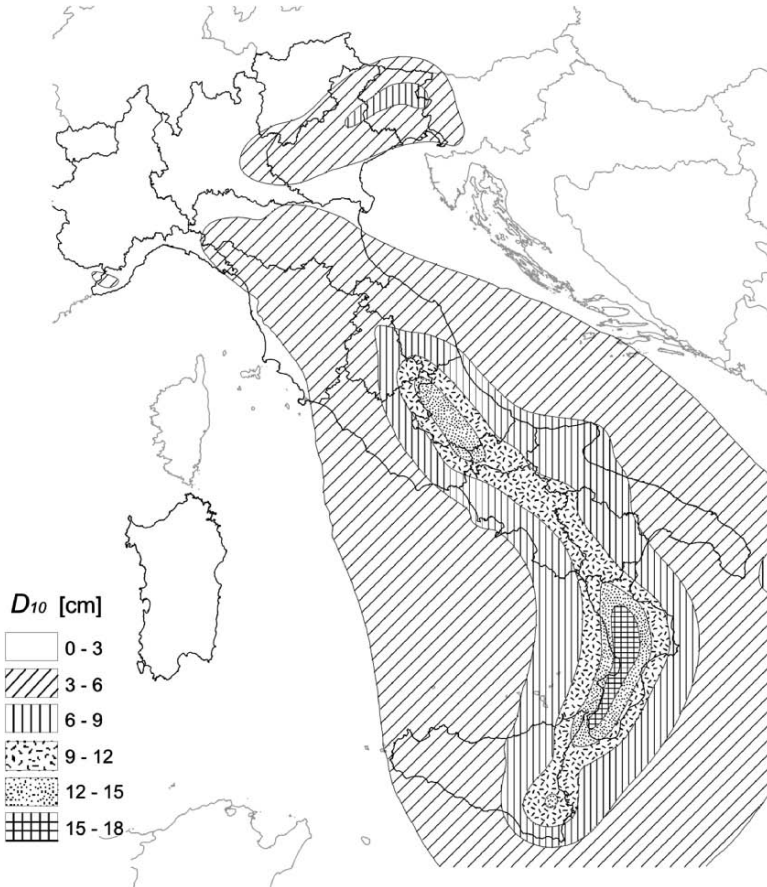


Fig. 2.17. Spectral displacement map for site type A and for a return period of 475 years at $T = 10$ s

Acknowledgements

The Civil Defence Department (Dipartimento della Protezione Civile) of Italy is financially supporting Project S5, while INGV (Istituto Nazionale di Geofisica e Vulcanologia) provides administrative coordination and support. Both are gratefully acknowledged.

Notes

¹To correlate each location with a magnitude interval a deaggregation analysis for DRS at 10 s was carried out and the modal magnitude was found.

REFERENCES

- Ambraseys NN, Simpson KA (1996) Prediction of vertical response spectra in Europe. *Earthquake Engineering and Structural Dynamics* 25: 401–412
- Ambraseys NN, Simpson KA, Bommer JJ (1996) Prediction of horizontal response spectra in Europe. *Earthquake Engineering and Structural Dynamics* 25: 371–400
- Ambraseys NN, Smit P, Sigbjornsson R, Suhadolc P, Margaris B (2002) Internet-Site for European Strong-Motion data. European Commission, Research-Directorate General, Environment and Climate Programme, www.isesd.cv.ic.ac.uk/ESD
- Ambraseys NN, Douglas J (2003) Near-field horizontal and vertical earthquake ground motions. *Soil Dynamics and Earthquake Engineering* 23: 1–18
- Ambraseys NN, Douglas J, Sarma SK, Smit PM (2005) Equations for the estimation of strong ground motions from shallow crustal earthquakes using data from Europe and the Middle East: horizontal peak ground acceleration and spectral acceleration. *Bulletin of Earthquake Engineering* 3: 1–53
- Berge-Thierry C, Cotton F, Scotti O, Griot-Pomniera DA, Fukushima Y (2003) New empirical spectral response attenuation laws for moderate European earthquakes. *Journal of Earthquake Engineering* 7(2): 193–222
- Bielak J, Loukakis K, Hisada Y, Yoshimura C (2003) Domain reduction method for three-dimensional earthquake modeling in localized regions. Part I: theory. *Bulletin of the Seismological Society of America* 93: 817–824
- Bommer JJ, Elnashai AS, Weir AG (2000) Compatible acceleration and displacement spectra for seismic design codes. *Proceedings of the Twelfth World Conference on Earthquake Engineering, Auckland, Paper No. 207*
- Boore DM (2004) Estimating $V_S(30)$ (or NEHRP Site Classes) from shallow velocity models (depths <30 m). *Bulletin of the Seismological Society of America* 94(2): 591–597
- Bozorgnia Y, Campbell KW (2004) The vertical to horizontal response spectral ratio and tentative procedures for developing simplified V/H and vertical design spectra. *Journal of Earthquake Engineering* 8(2): 175–207
- Brune JN (1970) Tectonic stress and the spectra of seismic shear waves. *Journal of Geophysical Research* 75: 4997–5009
- BSSC (2003) The 2003 NEHRP Recommended Provisions For New buildings And Other Structures. Part 1: provisions (FEMA 450), www.bssconline.org/NEHRP2003/provisions/
- Calvi GM (2006, September) Written personal communication to E. Faccioli
- CEN (2004) Eurocode 8: Design of structures for earthquake resistance – Part 1: general rules, seismic actions and rules for buildings. Bruxelles
- Chavez Garcia F, Faccioli E (2000) Complex site effects and building codes: making the leap. *Journal of Seismology* 4(1): 23–40
- Choi Y, Stewart JP, Graves RW (2005) Empirical model for basin effects accounts for basin depth and source location. *Bulletin of the Seismological Society of America* 95: 1412–1427
- Cornell CA (1968) Engineering seismic risk analysis. *Bulletin of the Seismological Society of America* 58: 1583–1600
- Cotton F, Scherbaum F, Bommer JJ, Bungum H (2006) Criteria for selecting and adjusting ground-motion models for specific target regions: application to central Europe and rock site. *Journal of Seismology*, online, May 9 2006
- ESG98 data distribution CD-ROM for the Kobe Simultaneous Simulation esse1.mi.ingv.it

- Faccioli E, Maggio F, Paolucci R, Quarteroni A (1997) 2D and 3D elastic wave propagation by a pseudo-spectral domain decomposition method. *Journal of Seismology* 1: 237–251
- Faccioli E, Paolucci R, Rey J (2004) Displacement spectra for long periods. *Earthquake Spectra* 20: 347–376
- Faccioli E, Vanini M, Paolucci R, Stupazzini M (2005) Comment on “Domain reduction method for three-dimensional earthquake modelling in localized regions, Part I: theory” by J. Bielak, K. Loukakis, Y. Hisada, C. Yoshimura, and “Part II: verification and applications”, by C. Yoshimura, J. Bielak, Y. Hisada, A. Fernández. *Bulletin of the Seismological Society of America* 95: 763–769
- Figini R (2006), *Analisi degli effetti di sito sui lunghi periodi degli spettri di risposta di spostamento* (Master’s Thesis). Politecnico di Milano
- Fukushima Y (1996) Scaling relations for strong round motion prediction models with M^2 terms. *Bulletin of the Seismological Society of America* 86(2): 329–336
- Fukushima Y, Berge-Thierry C, Volant P, Griot-Pommerehne DA, Cotton F (2003) Attenuation relation for West Eurasia determined with recent near-fault records from California, Japan and Turkey. *Journal of Earthquake Engineering* 7(3): 1–26
- Geller RJ (1976) Scaling relations for earthquake source parameters and magnitudes. *Bulletin of the Seismological Society of America* 66: 1501–1523
- Gruppo di lavoro CPTI (2004) *Catálogo Parametrico dei Terremoti Italiani, versione 2004 (CPTI04)*. Istituto Nazionale di Geofisica e Vulcanologia (INGV), Bologna, emidius.mi.ingv.it/CPTI
- Hernandez B, Cocco M, Cotton F, Stramondo S, Scotti O, Courboux F, Campillo M (2004) Rupture history of the 1997 Umbria-Marche (Central Italy) main shocks from the inversion of GPS, DInSAR and near field strong motion data. *Annals of Geophysics* 47: 1355–1376
- Hisada Y, Bielak J (2003) A theoretical method for computing near-fault ground motions in layered half-spaces considering static offset due to surface faulting, with a physical interpretation of fling step and rupture directivity. *Bulletin of the Seismological Society of America* 90: 1154–1168
- Joyner WB, Boore DM (1981) Peak horizontal acceleration and velocity from strong-motion records including records from the 1979 Imperial Valley, California, earthquake. *Bulletin of the Seismological Society of America* 71(6): 2011–2038
- Joyner WB (2000) Strong motion from surface waves in deep sedimentary basins. *Bulletin of the Seismological Society of America* 90: S95–S112
- Maggio F, Massida L, Sabadell J, Siddi G (2001) A parallel spectral element method for applications to computational mechanics. CRS4, Italy, Internal Report CRS4-TECH-REP-01/103
- Ministero delle Infrastrutture e dei Trasporti (2005) *Norme tecniche per le costruzioni – Parte I*. Roma
- Mirabella F, Ciaccio MG, Barchi MR, Merlini S (2004) The Gubbio normal fault (Central Italy): geometry, displacement distribution and tectonic evolution. *Journal of Structural Geology* 26: 2233–2249
- nsmg.wr.usgs.gov
- Ordaz M, Jara JM, Singh SK (1991) *Riesgo sísmico y espectros de diseño en el estado de Guerrero*. Technical Report, Instituto de Ingeniería, UNAM, Mexico City
- Paolucci R, Rovelli A, Faccioli E, Finazzi D, Di Alessandro C, Calderoni G (2006) Effect of different baseline correction procedures on the long period spectral ordinates of digital accelerograms. *Earthquake Engineering and Structural Dynamics* (submitted for publication)
- quake.wr.usgs.gov/~boore
- Sabetta F, Pugliese A (1996) Estimation of response spectra and simulation of nonstationary earthquake ground motions. *Bulletin of the Seismological Society of America* 86(2): 337–352

- Stupazzini M (2004) A spectral element approach for 3D dynamic soil–structure interaction problems (PhD Thesis). Politecnico di Milano
- Tolis SV, Faccioli E (1999) Displacement design spectra. *Journal of Earthquake Engineering* 3(1): 107–125
- Trifunac MD, Lee VW (1978) Dependence of the Fourier amplitude spectra of strong motion acceleration on the depth of sedimentary deposits. University of Southern California, Civil Engineering Department, Report No. CE 78–14
- Wells DL, Coppersmith J (1994) New empirical relationships among magnitude, rupture length, rupture width, rupture area, and surface displacement. *Bulletin of the Seismological Society of America* 84: 974–1002
- www.bhrc.ac.ir/Bhrc/d-stgrmo/D-StGrMo.htm
- www.fnet.bosai.go.jp/freesia/index-j.html
- www.globalcmt.org/CMTsearch.html
- www.hinet.bosai.go.jp
- www.k-net.bosai.go.jp
- www.kik.bosai.go.jp
- www.lgit.obs.ujf-grenoble.fr/sismovalp
- www.quake.ca.gov/cisn-edc
- www.scsn.org
- Zare M (2004) Long period Iranian strong motions recorded during 1994–2002, processing and analysis. Thirteenth World Conference on Earthquake Engineering, Vancouver, B.C., Canada, Paper No. 2002
- Zhao JX, Irikura K, Zhang J, Fukushima Y, Somerville PG, Asano A, Ohno Y, Oouchi T, Takahashi T, Ogawa H (2006) An empirical site-classification method for strong-motion stations in Japan using H/V response spectral ratio. *Bulletin of the Seismological Society of America* 96: 914–925
- zonesismiche.mi.ingv.it/documenti/App2.pdf

CHAPTER 3

SITE EFFECTS: FROM OBSERVATION AND MODELLING TO ACCOUNTING FOR THEM IN BUILDING CODES

Francisco J. Chávez-García

Coordinación de Ingeniería Sismológica, Instituto de Ingeniería, Universidad Nacional Autónoma de México

paco@pumas.ii.unam.mx

Abstract. Site effects are defined as the modifications that seismic motion undergoes when travelling through the topmost layers before hitting the ground surface or a structure built on it. The definition of topmost layers is frequency dependent. This paper compiles results regarding the estimation of site effects and their use to decrease seismic risk. Site effects may be estimated either by direct measurements or indirectly, meaning that subsoil mechanical properties and geometry are evaluated and from them an estimate of local amplification is computed. The first approach has the advantage of its directness. It has been shown that this approach is most effective when local amplification is significant and brought about by a simple configuration (e.g., one soft layer overlying a more rigid basement). However, this first approach lacks flexibility and when it fails the invested effort is practically lost. The second approach, although more tortuous, offers larger flexibility. It is very likely that efforts directed to the estimation of the subsoil structure, even if not completely successful, will allow to build some model and to estimate an order of magnitude of the amplification. Current methods used to estimate site effects based on earthquake or ambient noise data are discussed. In addition, the main techniques that are used to estimate the subsoil structure are reviewed, in particular, the new proposals regarding the use of the correlation of noise measurements to determine the properties of the subsoil layers. Finally, some comments are offered on the current approaches available to take into account site effects in the framework of building codes.

1. Introduction

Local amplification caused by surficial soft soils is a significant factor in destructive earthquake motion. It is frequent that site effects condition the occurrence of damages in moderate to large earthquakes. For this reason, site effects have received much attention during the last decades. Moreover, special theme conferences have been dedicated to this subject in its many facets (e.g., during August 2006, the ESG conference specialised on site effects was held at Grenoble, France). Obviously, a single article cannot do justice to such an ample subject, and this paper will deal only with some particular aspects.

The use of the term surficial soft soils is purposely vague. Very early it was recognised that what we name local must be frequency dependent. Moreover, its definition depends strongly on the medium. If the thickness of the soil layers is small, it is likely that their effects will appear at higher frequencies. Conversely, we observe amplification

at lower frequencies when the thicknesses involved are large. Site effects can be due to the heterogeneity of the subsoil materials (impedance contrasts) or to irregular geometry (amplification due to topography). Naturally, real cases involve a combination of these two. The major effect on ground motion due to local geology is the amplification of ground motion because of impedance contrasts underground. For example, in the case of Mexico City, this amplification attains a factor of 40 (in average, individual observations reach a factor of 80) at the resonant frequency on the soft clays that cover the lake bed zone of this valley. This amplification is in stark contrast with that due exclusively to geometry of an otherwise homogeneous medium, i.e., the topography effect, which does not exceed a factor of 2 even in the case of 3D topographies (e.g., Bouchon et al., 1996). Given that it is the impedance contrast that causes the largest amplifications, it is the geometrical irregularities of the interfaces between sediments and rock that are most relevant. In addition, soft soils are easily eroded and the free surface usually has not a pronounced topography. The recent years have seen many publications where the interaction between soft soils and an irregular subsoil structure combine to enhance the observed local amplification. Thus, we have observed a change from the 1D paradigm to the 2D and 3D models that commonly appear in the literature these days. With the increase in the number of dimensions (which entails a parallel increase in the number of details required to build the model), the loss of generality naturally follows. As the complexity of the models increases, the possibility of extrapolating the results of particular case studies to a general application decreases significantly. This is reflected in the current difficulties we experience to translate the knowledge we have gained on site effects into expressions that could be generally applicable in a building code, for example. For this reason, consideration of site effects in building codes is still generally based on the 1D paradigm.

This paper presents a compilation of results that reflects the current approaches to site effects, without any attempt to present a complete review of the field. A cursory search in internet using google finds almost half million references to site effects in seismology, evidence of the health of the research on this subject and of its importance in practical studies. The following section deals with the estimation of site effects, i.e., their direct measurement. The different techniques currently used are mentioned, and the advantages and disadvantages discussed. After that, the use of modelling is tackled. It is suggested that, currently, it is not so much the modelling method as the building of a model and its validation that are the hardest problems. A brief review of the different ways used to estimate mechanical properties of the subsoil and its geometry is presented. Then, the different approaches that have been proposed to include consideration of site effects in the reduction of seismic risk are presented. Their use depends very much in the case to case needs; either a building code, a microzonation map, or a reliable estimate for a significant structure on its own. Finally, some concluding remarks are offered.

Throughout we will not deal with non-linear behaviour. Non-linearity is, of course, a very important subject, but one that may be considered as a second stage in site effect studies. Indeed, a reliable estimate of the effects of non-linearity on ground motion requires a very dependable estimate of linear site effects at the site of interest. On top of this, the number

of parameters that need to be known for non-linear response evaluation imposes a heavy burden on the reconnaissance stage. In addition, the problem is again the lack of generality of the results; due to the in-depth details of the mechanical behaviour of the media that are required, non-linear studies can only be made for specific sites. The more specific the results are to a given site, the more unlikely is their generalisation. Finally, the author's experience comes mostly from working in a developing country, where the means to make a proper reconnaissance are lacking yet evaluations of site effects are needed badly. For these reasons, this paper deals only with linear site effects, even if recognising that it is not always straightforward to guess the modifications that non-linear behaviour will introduce in the ground motion for the large earthquakes, those that are our real concern in seismic risk.

2. Estimation of site effects

Site effects have been estimated using earthquake data and ambient noise records. Clearly, earthquake data are more reliable. However, in regions of moderate seismicity, installing a temporal network that would record enough events to compute a reliable estimate of local amplification may be too expensive. Recording ambient noise, in contrast, is easy, fast and very cheap anywhere. For this reason, methods based on ambient noise records have been very much used recently. In the following lines, we will review briefly the different techniques that have been used with those two kinds of data; earthquake and noise records.

The analysis of earthquake data to estimate site effects has made recourse to several techniques. It could be argued, for example, that attenuation relations that obtain independent regressions of PGA with distance and magnitude for rock and soft soil sites provide an estimate of local amplification. This approach has the advantage of its generality. However, the disadvantages are large; site classification is extremely imprecise, local amplification is evaluated using a single number, and a single estimate is obtained for all soft soil sites. In addition, PGA is a very poor measure of local amplification (see, e.g., Chávez-García and Faccioli, 2000).

Starting from the 1970s (Borcherdt, 1970), ratios of Fourier amplitude spectra of earthquakes recorded on soft soil relative to a reference station have been extensively used. The hypotheses on which this method is based can be clearly stated, which allows appraising the validity of its application. This is a significant advantage of this technique. Spectral ratios are a good estimate of local amplification provided that the reference site is effectively free of site effects and is located near to the soft soil site. The proximity of the reference station must, of course, be measured in terms of dominant wavelength. The choice of a reference station may pose large difficulties though (see, e.g., Steidl et al., 1996), and sometimes it is an unsolvable problem. A helpful analysis of the possible complications one may run into was presented by Steidl et al. (1996). Their conclusion is that surface rock sites are inevitably affected by amplification at frequencies as low as 4 to 5 Hz because of the thin weathered layer that is almost always present on rock

sites. They advocate the use of seismic stations at the bottom of deep boreholes. Steidl et al. (1996) show that deep borehole records, when corrected for the effect of downward propagating waves, are the more reliable records to use as reference. This conclusion is well substantiated but impractical in most places, especially in developing countries, because of its large cost. A cheaper alternative is to keep those limitations in mind and to restrict the analysis to frequencies not larger than 5 to 6 Hz. There are several justifications for this limit. First, it would avoid problems with the possible appearance of local amplification at the reference site alluded to above, whose consequence is the underestimation of amplification at the soft soil sites. In addition to this, as frequency increases, the distance between soil and reference sites also increases in terms of wavelength, and this could invalidate the assumptions behind spectral ratios. A further argument is that, as frequency increases anelastic attenuation in the sediments becomes more important, possibly eliminating the need to estimate ground motion at those frequencies. Anyhow, it is very likely, that for frequencies larger than 5 or 6 Hz, in most cases it will be very difficult to relate observed amplification to geological or geotechnical characteristics of the site of interest. If shear-wave velocity is about 150 m/s, wavelength will be 25 m at 6 Hz and 15 m at 10 Hz. It becomes very difficult, and probably not very useful, to detail the subsoil structure and its lateral changes at this scale.

An unorthodox approach to a reference site was taken by Hruby and Beresnev (2003). They proposed to use a synthetic record computed for the site of interest as the reference against which to measure amplification in an actual seismic record. The synthetic record was computed by those authors using the stochastic finite-fault modelling method (Beresnev and Atkinson, 1998). The idea is interesting and may be a way out of the dilemma posed by the impossibility of finding an acceptable reference site. Hruby and Beresnev (2003) validated this approach for the Los Angeles basin, for which nice results were obtained. However, this procedure cannot be generally applied at present because a model of the regional structure model for the site under study is necessary. Moreover, this model needs to have been validated. This requirement cannot be satisfied except for very few locations around the world. The limitations faced by the building of a model will be discussed in more depth in the following section.

Unfortunately, it is not infrequent that an adequate reference site is impossible to find. For this reason, two other techniques have been applied, which do not require a reference site. The first one is the inversion of a set of Fourier spectra for many stations and events (Boatwright et al., 1991; Field and Jacob, 1995; Raptakis et al., 2005). This technique, similarly to spectral ratios, has the advantage of having solid physical bases. Moreover, the results include estimates of the magnitude of the seismic events and of the regional Q factor that bests fits all the data. However, this method is really reliable only when the dataset is large; a significant number of events recorded simultaneously by several stations is necessary to obtain a reliable result.

The second technique that does not require a reference site uses spectral ratios of horizontal components relative to the vertical component motion recorded at the same site. This technique is a frequency domain application of the receiver functions proposed by

Langston (1979). It was applied to earthquake data by Lermo and Chávez-García (1993) and in many recent papers. H/V spectral ratios of earthquake records have a weaker theoretical basis than spectral ratios relative to a reference station. However, they have been successful to estimate site effects. The reasons are the same behind the success of receiver functions; the decrease of shear-wave velocity with decreasing depth brings the incoming rays closer to vertical. As a consequence, vertical motion includes mostly P waves (little affected by near-surface impedance contrasts) while horizontal components consist mostly of shear waves. The difference between horizontal and vertical motions, as measured by spectral ratios, would cancel common information related to source and regional path propagation and enhance the differences, mainly due to the near surface amplification of horizontal motion. This technique has been successful and has provided nice estimates of local amplification. It offers an alternative when there is no reference station, or when the reference station failed to record the same events as the soft soil stations. It works better when site effects are important, i.e., when large impedance contrasts significantly redress the incoming rays.

Very often, however, earthquake data are not available to estimate site amplification. For this reason, and following the work of Japanese seismologists, microtremors or ambient noise records have been used to characterise seismic response. The use of ambient noise records to estimate local amplification was proposed a long time ago (see Bard, 1999, for a thorough review). The analysis of Fourier spectra of microtremors and the computation of spectral ratios of microtremors relative to a reference site have both been used. However, in recent years, we have seen the thriving of the microtremors H/V spectral ratios (referred to simply as H/V in the following) on a very large scale. This paper will not go through a detailed review which can be consulted, for example, in Bard (1999) or in the many documents produced by the European project SESAME (<http://sesame-fp5.obs.ujf-grenoble.fr/index.htm>). Only a few experience based considerations will be discussed.

Most authors agree that H/V gives the dominant period of the soft soil layers. Of course the term dominant period may lose its meaning in many cases where site effects are still important. In those cases, H/V is not very useful. In addition to dominant period, the possibility of using H/V to estimate the level of amplification has been the subject of a large discussion. In the author's opinion, noise can be used to determine amplification level in some cases. Horike et al. (2001) have shown among others that amplification computed from H/V of noise is reliable when local amplification is caused by a marked impedance contrast at a single interface and the amplification level is important. This means that, if H/V ratios are large, the results are usually dependable. However, when their amplitude is small it could indicate either that amplification is not significant (and then we need not worry about site effects) or that amplification is significant but not due to a single impedance contrast but resulting from a complex situation (e.g., velocity gradient). This is a large problem and one that has no general solution at present.

Probably the more reliable results are those that compare different techniques among them. It is likely that real cases cannot depend on a single technique to estimate site

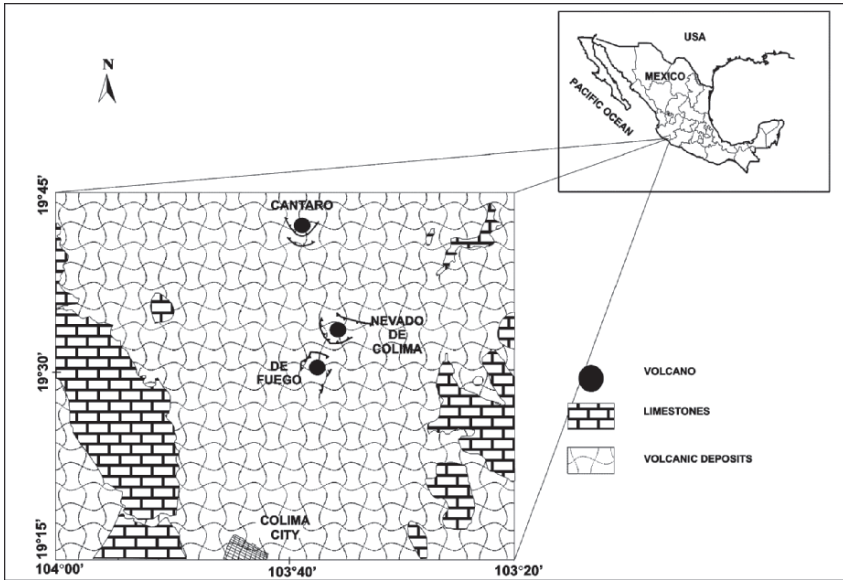


Fig. 3.1. Location of Colima city, Mexico, and its regional geology (After Chávez-García et al., 2007.)

effects. Whenever possible, the more adequate results are obtained through the comparison and complementation of different techniques (e.g., Lermo and Chávez-García, 1994; Chávez-García et al., 1999; Horike et al., 2001).

It is to be expected that this conference will show a few cases where H/V provided good results. For this reason, this paper would like to illustrate the opposite, the case where these measurements were not very useful, exemplified by the city of Colima in Western Mexico (Chávez-García et al., 2007). Large earthquakes occur in this region, the northern section of the Pacific coast subduction zone in Mexico (Figure 3.1) but the seismicity level is much smaller than further South along the subduction zone making it difficult to record earthquakes. Previous studies (Gutiérrez et al., 1996) had shown that local amplification (measured using earthquake spectral ratios) is significant in this city; about a factor 6 distributed in a wide frequency band. Colima is underlain by a column of volcanic sediments that attains 800 m thickness, filling a North–South valley surrounded by limestone. These volcanic sediments are characterised by their large irregularity, with a mixture of different kinds of avalanche, debris and lahar deposits. Figure 3.2 shows the surface geology in the city. Different volcanic formations have been identified by geologists, but it is far from evident that those differences are related to changes in the mechanical properties that condition seismic response. As mentioned already, previous studies indicated significant amplification, but were unable to analyse its distribution within the city.

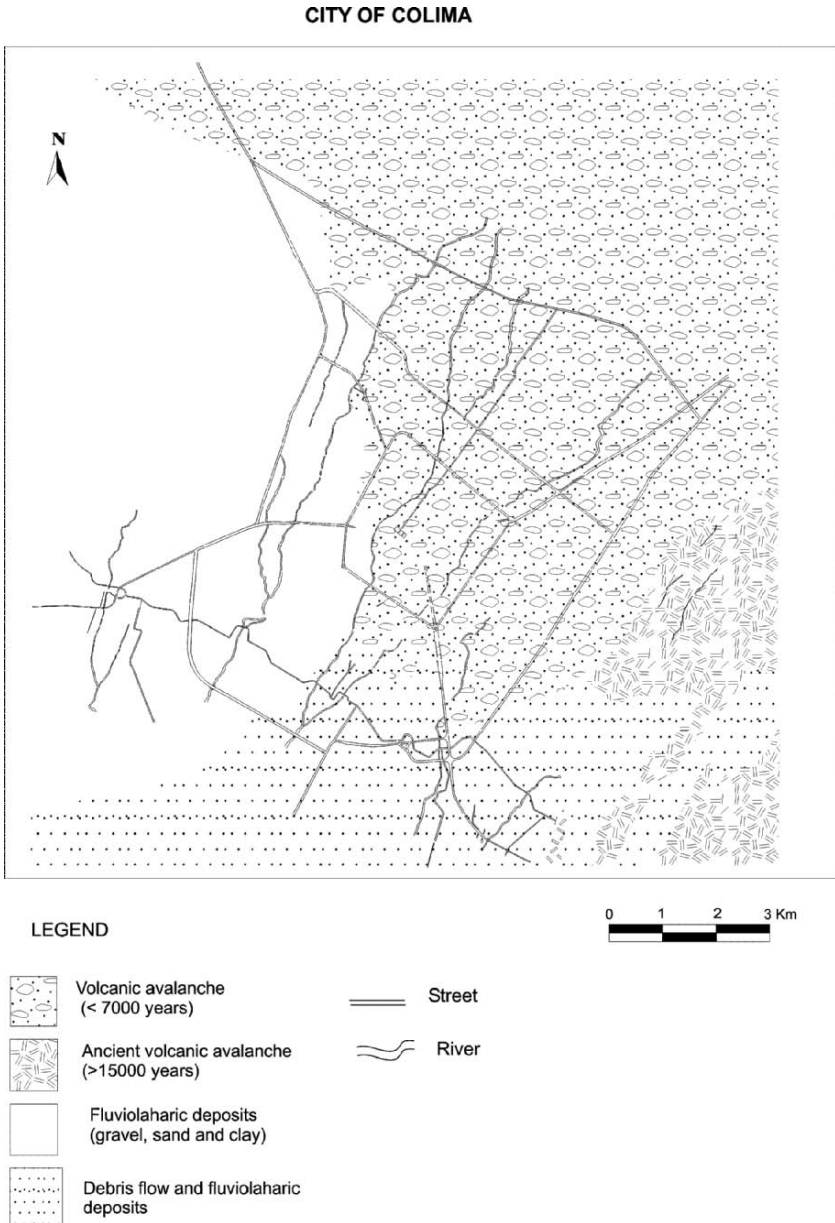


Fig. 3.2. Surface geology within Colima city. The main streets and rivers are shown with solid lines as reference. The urban zone is delimited by the rings formed by the main streets (After Chávez-García et al., 2007.)

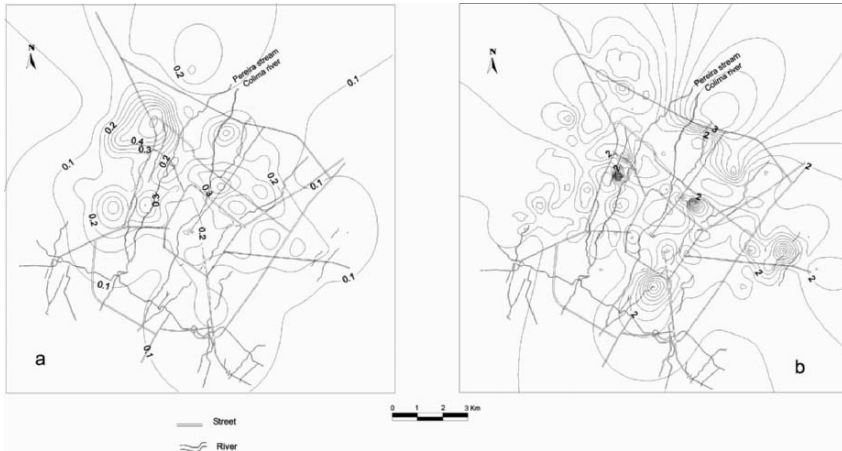


Fig. 3.3. Contour maps of (a) dominant period in sec and (b) relative amplification derived from 125 single station microtremor measurements, analysed using H/V, in Colima (After Chávez-García et al., 2007.)

A microtremor recording campaign was launched within the city of Colima. Although only one instrument could be used, plenty of student's time was available. Ambient noise was recorded at a total of 310 sites in an area roughly 10×10 km. H/V spectral ratios were computed. The results lead to the rejection of 185 sites; maximum amplitude of the H/V ratios was just too small, and no dominant period could be identified. The results for the 125 sites whose information was retained were used to draw dominant period and maximum amplification maps for Colima (Figure 3.3). These maps are not very useful. There is no correlation with surface geology, amplification is extremely small, and the results are uncorrelated with previous dominant period maps. These results indicate that, even when measurements are performed densely and carefully, if site effects are due to a complex structure, H/V of noise will not be very useful.

When we measure site effects, if we do it correctly, we are including both the effects of the media properties and the geometrical effects (the so-called site effects of structural origin). For example, spectral ratios relative to a reference site include all possible contributions to local amplification, were they to come from the resonance of soft layers or from any laterally propagating wave generated by lateral irregularities. The disadvantage is precisely the same. All possible factors are included, and we have no way to decompose the different contributions to the response brought about by different factors (i.e., impedance contrast and geometry). If we could, it would be possible to evaluate their relative importance. From this point of view, estimating site effects has little flexibility. This point is improved when we estimate the soil properties with the view of computing site response from the model built from them.

3. Modelling site effects. The importance of the model

If site effects cannot be estimated from measurements, it may still be possible to model them. In fact, many papers present both empirical estimates and numerical results. When the two coincide, their mutual validation strengthens the confidence with which the results can be used in seismic risk reduction. When empirical estimates are lacking, it might still be possible to evaluate local amplification by computing the seismic response of the local structure responsible for this amplification.

The first question to address when modelling site effects is the dimensionality of the model. We may choose among 1D, 2D, or even 3D models (recall that this paper passes over the controversy linear/non-linear), which refer to the possible irregularities that may be included. 1D models, those that consider heterogeneities only in the vertical direction, have been the preferred choice because of their simplicity, reliability (which is taken here to refer to the stability of the results and not necessarily to their trustworthiness), and the possibility of generalising the results. Cities are usually built on alluvial valleys, with more or less flat sediments overlying a rocky basement. If the boundaries of the valley are far from the site of interest relative to the depth of the sediments, intuition suggests that 1D models are appropriate. Moreover, as it has been already mentioned, local amplification is mostly due to impedance contrast between soil layers and their basement. When this is the governing phenomenon, 1D models provide an excellent estimate of site effects, and one that needs the least number of parameters. However, a word of caution is warranted. Intuition may be wrong here. For example, Euroseistest valley (Figure 3.4) looks as an ideal case where the 1D approximation would work well. It is 6 km wide and the sediments are only 200 m thick. Euroseistest has been extensively studied during the last decade and its seismic response is well known, much more than what is the usual case in Earthquake Engineering. For this reason, Euroseistest can be considered to be a benchmark to evaluate different ideas concerning site effects. Makra et al. (2004) used

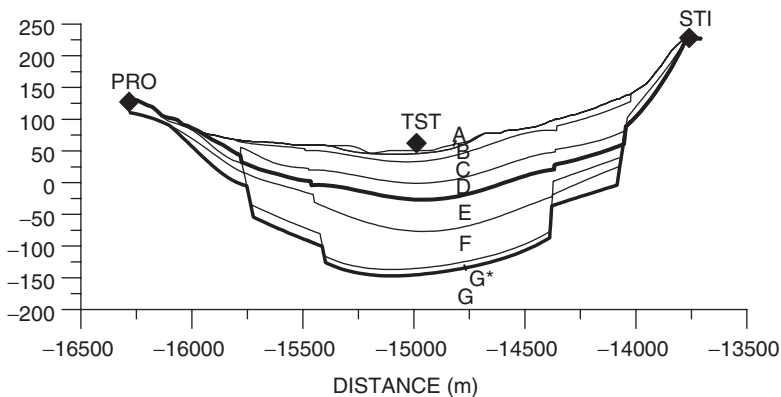


Fig. 3.4. 2D model built for a NW–SE cross-section of Euroseistest valley (After Raptakis et al., 2005.)

Euroseistest to evaluate how much detail was necessary in a model to predict the seismic ground response of this valley. They evaluated both 1D and 2D models at the centre of the valley. Their conclusion was that even a simplified 2D model was better than a very detailed 1D model to predict site response. These results are a warning that tells us that we must be careful when deciding where to concentrate the efforts. Clearly, for the end of understanding site response at the centre of the Euroseistest valley, a rough 2D model is better than detailed 1D analysis.

Two-dimensional models go one step further in that they allow variation of properties or geometry along one horizontal dimension. Three decades ago, a great many papers dealing with the simulation of ground motion in such irregular configurations were being published. Trifunac (1971) presented the analytical solution for the ground motion at the surface of a semi-circular, 2D alluvial valley subjected to plane SH incident waves. This solution was for many years the benchmark against which to show the reliability of solutions computed using numerical methods. In fact, when we revise the papers presenting results of numerical modelling of ground motion for irregular local conditions during the 1980s, all those papers included some sort of validation of the method used, either comparison with Trifunac's solution or with that computed using other numerical method. This is no longer the case. Papers that present results of numerical modelling these days need no longer need to validate the modelling method, as they have become very reliable. Modelling methods such as finite elements, finite differences, or boundary methods have been shown to be very reliable to compute the seismic response of complex configurations, and do not pose particular problems (although the huge amounts of computer power necessary to make the computations are still an issue in some cases). For this reason, the problem of modelling seismic response has shifted from the method and the computer to the building of the model; the properties to use, the geometry, and the reliability of all those parameters. These days, the problem of defining the properties of the subsoil to be used in a model is larger than that posed by the modelling method itself. A second obstacle is that there must be a way to evaluate the results of the modelling, when often there are no independent measures. This can be exemplified with the case of Parkway basin, modelled by Chávez-García (2003). There were not enough data to build a model for this basin. For this reason, the model used was very crude; only two different media were considered and the interface between sediments and basement was interpolated starting from the depth estimates obtained from observed values of dominant period measured at the surface. Surprisingly, the results were useful. In this case, validation of the model was made using previous estimates of site effects obtained from the analyses of earthquake data from a temporary seismograph network (Figure 3.5). Details of the observed transfer functions were well reproduced by the model, as were the preferred directions of propagation of diffracted surface waves. In addition, an estimate of the additional amplification brought about by the 3D configuration of the basin (in addition to the amplification due solely to impedance contrast) could be obtained. One of the conclusions of that paper is that even a crude model can be useful. The next paragraphs present some comments regarding the methods that have been used to obtain enough data to build a model from which to compute local response.

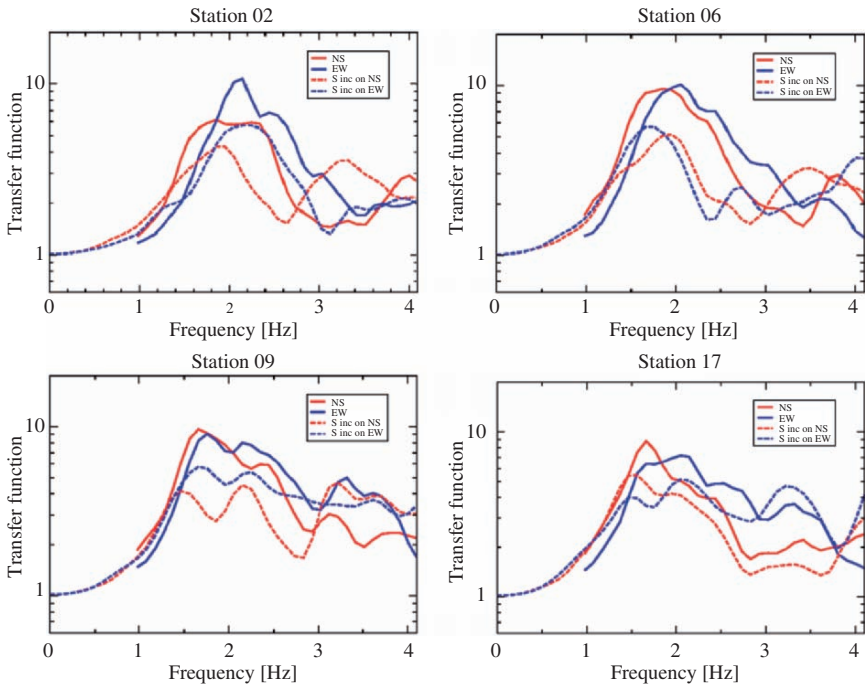


Fig. 3.5. Solid lines: observed transfer functions computed used spectral ratios relative to a reference site for soft soil stations in Parkway basin. Dashed lines: computed transfer functions using a very rough 3D model of the basin. Dominant period was used to constrain the model. However, in addition to the dominant peak, additional features of the observed transfer function are well reproduced by the 3D model (After Chávez-García, 2003.)

The more reliable method to determine the structure and the properties of the subsoil materials is seismic prospecting. However, it is seldom used in site effect studies. It may be too cumbersome to apply in a city, or straightaway impossible to use because of cultural noise in a city or its sheer size (e.g., Mexico City). It could be noted that, in some experiments, when first arrivals could not be used, advantage was taken of the surface waves (considered to be noise in seismic prospecting) generated by the source (e.g., Campos-Enríquez et al., 2004). Other seismic prospecting methods have been developed that explicitly exploit the surface waves such as SASW (e.g., Brown et al., 2002). However, the use of active sources is usually too expensive to be used generally in site effect studies.

Ambient noise is much cheaper. For this reason, we have seen many applications of microtremors to the determination of the subsoil structure. Horike (1985) showed a successful application of frequency–wavenumber analysis of ambient noise. This technique analyses the noise records obtained at an array of stations assuming they consist of surface

waves. A dispersion curve is determined, and from that a soil profile is derived. Another technique of analysis that relies in the surface waves composition of microtremors is the refraction microtremor (ReMi) introduced by Louie (2001). The advantage in this case is the use of an exploration seismograph, which is cheaper than 12 or 24 autonomous seismographs. The array in this case is linear and the result is again a phase velocity dispersion curve.

An additional method can be mentioned, based on the correlation of ambient noise records. The history of the use of noise correlation followed different paths according to the considered domain, either frequency or time. It is only recently that the publications are bringing together the two strands (Chávez-García and Luzón, 2005). The use of cross-correlation of noise records to determine the subsoil structure was proposed exactly 50 years ago by Aki (1957). He named it the SPAC (Spatial AutoCorrelation) method. If microtremors can be assumed to consist of plane dispersive waves propagating with equal power in all directions, Aki (1957) showed that the frequency domain cross-correlation between stations at a given distance, averaged azimuthally, took the form of a zero-order Bessel function, where the only unknown is the phase velocity of the waves. The details of the method have been presented several times. The method has been applied to the analysis of volcanic tremors (Ferrazzini et al., 1991; Chouet et al., 1998). Its application to site effects is straightforward and many papers that use it have been published (e.g., Apostolidis et al., 2005). Recently it has been shown (Ogori et al., 2002; Okada, 2003; Chávez-García et al., 2005) that it is possible to use of the SPAC method without the limitations imposed by the circular array. If the waves that form the microtremors propagate homogeneously in all directions, a single station pair samples all directions of propagation provided that temporal averaging is substituted for the azimuthal averaging.

If correlations in the frequency domain are useful, then because of Fourier transform, they should also be useful in the time domain. However, the development of correlations in time domain to explore the subsoil has a very different history. The first references are related to exploration seismology (e.g., Claerbout, 1968). It was rediscovered by helioseismologists (Duvall et al., 1993), before making its appearance in acoustics and seismology. In addition, time domain correlation of ambient noise has been the object of many theoretical studies that have been able to show its relation with the character of ambient noise and statistical properties of diffusive media. Weaver and Lobkis (2005) retrace briefly this history. This is a field where many publications are currently being published because development is possible in two domains, theoretical studies and practical applications.

It has been shown that the time derivative of the cross-correlation of seismic noise between two stations is proportional to the Green's function between them, under certain conditions. A review has been presented in Campillo (2006). Results have been published from very small inter-station distances (5 m in Chávez-García et al., 2006) to very large distances (thousands of km in Shapiro et al., 2005). Figure 3.6 shows, for example, a seismic section obtained from cross-correlations of ambient noise records computed for the vertical component recorded at different station pairs of a small linear array at

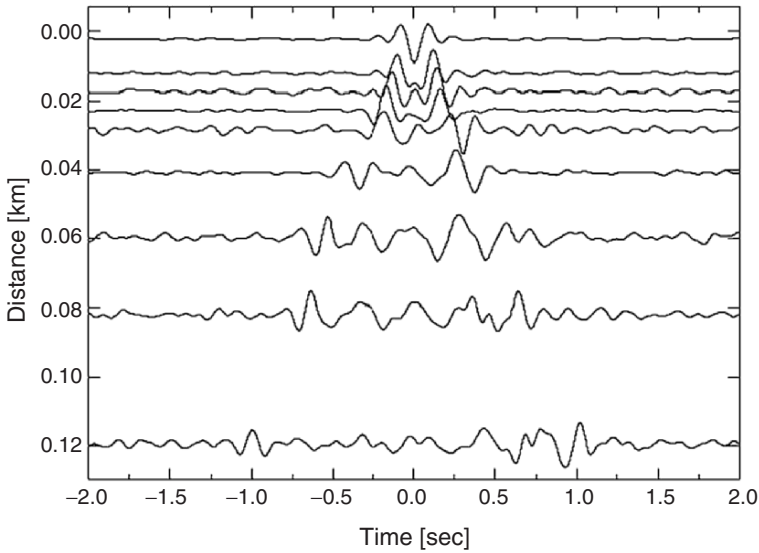


Fig. 3.6. Seismic section built from cross-correlation functions between the vertical component of pairs of stations. Each trace shows the average cross-correlation between two stations separated the corresponding distance. A clear pulse is observed. It corresponds to the fundamental mode of Rayleigh waves. Its phase velocity is about 270 m/s (After Chávez-García et al., 2006.)

Parkway basin, New Zealand. Each trace corresponds to a single station pair (Chávez-García et al., 2006). A clear pulse emerges, corresponding to the fundamental mode of Rayleigh waves. It is possible to measure phase velocity dispersion in this figure (it is about 270 m/s for the dominant frequency of the pulse, between 3 and 4 Hz).

Time domain cross-correlation of ambient noise between two sites should theoretically correspond to the complete Green's function between them. However, observations suggest that it is only the fundamental mode pulse of surface waves that is recovered. The frequency analysis of that pulse allows measuring phase (for inter-station distances small as compared to wavelength) or group (for very large inter-station distances as compared with wavelength) velocity dispersion. Inversion of dispersion curves allows recovering a shear-wave velocity profile.

We may note that all of these techniques give as a result a 1D profile. Indeed, all the techniques that are based on measuring and analysing surface wave dispersion assume, by definition, a 1D layered structure. If the structure being investigated has strong lateral variations, these techniques will fail. If the structure has smooth lateral variations, the repeated use of these techniques at different sites may be called for. Therefore, we have implicitly assumed that ambient noise consists essentially of surface waves. The fact that useful results have been obtained suggests strongly that ambient noise consists effectively of surface waves and that body waves, if present, have smaller amplitudes.

In addition, lateral variations of structure seem to be rather gentle at the many places where measurements have been carried out.

To end this section, we come back to the problem of Colima. H/V spectral ratios of ambient noise were not helpful to characterise site response in this city. For this reason, we reoriented our study to go through properties of the subsoil and modelling of seismic response. Ambient noise was recorded using linear arrays of stations. The recorded data were analysed using both ReMi and SPAC methods. We observed a very good agreement between the results obtained from these two methods (Figure 3.7). The resulting phase velocity dispersion curves were inverted, and 1D profiles derived for eight sites

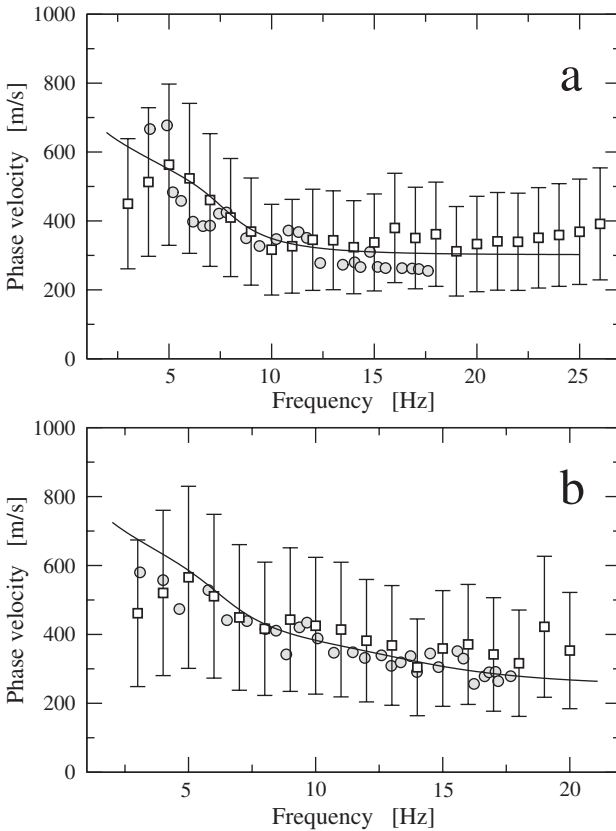


Fig. 3.7. Comparison between phase velocity dispersion curves from ReMi and SPAC methods at two sites in Colima. The grey circles show the phase velocity determined from the ReMi method. Open squares with error bars show the mean values and the standard errors determined from the SPAC measurements. The solid line shows the phase velocity dispersion curve computed from the S-wave velocity profile inverted from the SPAC measurements

throughout the city. These profiles could be validated at two sites, where shallow boreholes had been used to measure shear-wave velocities using a suspended logging tool. The amplification computed from the final 1D profiles was in good agreement with the previous estimates of local amplification by Gutiérrez et al. (1996). These results showed that a credible microzonation map was not a viable alternative for the city of Colima. Due to the large heterogeneity of the subsoil and the poor control on its properties the more reasonable option was to propose a homogeneous amplification of a factor 6 throughout the city in the frequency band 0.2 to 5 Hz. This conclusion offers no details on the seismic response, but has the merit of being consistent with all available data.

The case of Colima may be more representative of the usual problems faced to build a model of the subsoil than the Los Angeles basin, to take a very contrasting example. Los Angeles basin has been well instrumented for many years and has been the object of many different studies. The model that has been derived reflects a consensus among many capable people that have committed their efforts in this task. As a result, the model is very reliable. It has allowed the testing of many different hypotheses and the prediction of useful scenarios. This effort cannot be reproduced easily elsewhere. Most site effect studies must deal with very sketchy and incomplete information on the subsoil. Geotechnical borehole data are very useful, but they seldom constrain the properties of the basement. Thus, in site effect studies, rough 1D profiles are more the norm than detailed 3D models, especially in developing countries.

4. Accounting for site effects in building codes

As mentioned above, our ability to account for site effects in a general framework like that of a building code lags well behind our ability to compute site response at specific sites. Numerical simulation of ground motion can successfully tackle very complex models these days. However, the results are difficult to use for general application. In the first place, it is harder to verify the results of the model with the generality required by a building code. In the second place, the more complex the model is the less general will be the results computed for it, as by nature each specific model is valid for only one specific situation. When the most sophisticated models were 2D, it was easier to make parametric studies (Bard and Bouchon, 1980a, b). When we turn to 3D models, this possibility is lost because of the cost and the large number of parameters, in spite of interesting initiatives like Sismovalp (<http://www-lgit.obs.ujf-grenoble.fr/sismovalp/>).

A very effective approach, one that is useful, is the classification of the soil response using very simple parameters. The foremost example is the use of the average shear-wave velocity for the topmost 30 m, the V_{S30} value (e.g., Borchardt, 1994). The reason for its success is its simplicity. One may use the V_{S30} value to classify the site of interest. Expected amplification has been computed for each soil class. Lacking other information, if we are able to guess the average mechanical properties of the topmost 30 m, this approach is an honourable way out. There are, of course, some downsides. The largest, in the author's opinion, is that it assumes that the properties of the materials below 30 m

depth are the same everywhere. Amplification is caused by impedance contrast, where the properties of two media play an important role: those of the sediments and those of the bedrock. If we take into account only the properties of one medium disregarding the other, inevitably there will be sites where the actual amplification will be very different from that predicted.

When we are able to indicate in a map those zones where we expect rather homogeneous site effects, and characterise site effects for each one of them in simple terms, we can produce a microzonation map. Microzonation has also been the subject of specialised international conferences, and once again this paper cannot do justice to this subject. A microzonation map is a tool that can have an immediate impact in risk reduction and can be directly incorporated into building codes. Ideally, this map will evolve as more information becomes available. In the case of Mexico City, the first microzonation map was included in the building code of this city published in 1959. Since then, it has been revised several times. Currently, the code includes a “nanozonation” (a term introduced by M. Ordaz, *per. comm.*) of Mexico City, where the dominant period at any site within the city is given. The design spectrum imposed by the code at each site is constructed using five parameters, all of which are derived from the dominant period value. This has been possible thanks to two factors. The first is that local amplification is strongly governed by the very large impedance contrast between a soft surficial layer and its substratum we have already mentioned. A good estimate of this amplification can be obtained assuming a homogeneous flat layer (whose thickness is assumed to change with the location of the site of interest) overlying a rock basement. The second is the large number of strong motion stations that were installed after the disastrous 1985 earthquake. When the records are analysed using spectral ratios, and the resulting transfer functions interpreted in terms of a 1D model, it becomes possible to interpolate site effects and predict the response everywhere. This imposes, however, that we ignore the very large scatter observed in spectral ratios. The stability of the average that is obtained is very good, as long as we are interested in response spectra. The reason is the extremely large amplification due to a single subsoil interface, so large that it thwarts the significance of other factors. However, the 1D model has strong limitations, even at Mexico City, as shown by Chávez-García and Bard (1994). We are faced then by the paradox that a model that is not physically correct is very useful, while the more physically correct model (Chávez-García and Salazar, 2002) is not yet useful in practical applications.

Appealing as the “nanozonation” is, this approach is currently not feasible at most cities. In addition, this approach cannot be envisaged when more than one factor contributes significantly to site amplification. An extreme example is provided, once again, by the city of Colima. We mentioned this city with regard to the failure of ambient noise measurements to estimate site effects. In contrast, the analysis of dispersion using microtremor data allowed to build 1D models from which site amplification was computed, which was in good agreement with previous observations. The results, however, could not differentiate zones within the city with different site response characteristics. In the case of Colima, the conclusion was that it was not possible to draw a microzonation map for this city and that the better solution was to consider homogeneous amplification throughout

the city within a specified frequency band. Thus, the microzonation efforts for Colima resulted in the absence of any zonation at all.

Finally, with a clear bias, we will mention the tentative proposal by Chávez-García and Faccioli (2000) to formulate a way to include 2D site effects in the framework of building codes. The number of parameters involved with the response at each site in very long alluvial valleys makes this a daunting task. Indeed there does not seem to be an easy way to correctly include all the effects on seismic motion due to lateral heterogeneities in simple expressions. However, if one restricts oneself to response spectra, site to site variations become smaller. This made possible for Chávez-García and Faccioli (2000) to propose an “aggravation factor”. The hypothesis is that amplification is controlled by impedance contrast. Lateral irregularities increase this amplification by a variable amount. If impedance contrast is large, the lateral variations of that additional amplification can be neglected and a single factor can be used throughout the valley. This factor would affect (one would hope it would correct) 1D amplification by the effects of lateral irregularities. Those authors found this factor to be within 1.5 to 2 in terms of 5% damping response spectra. This factor was found to apply also to the case of Parkway valley (Chávez-García, 2003), notwithstanding the 3D character of its seismic response. This seems to be a viable alternative that could at least be investigated, while we wait for the development of better options to take 2D or 3D site effects into account in building codes. Of course, if ground motion duration is an issue, the “aggravation factor” is not useful.

5. Concluding remarks

We have discussed two possible paths to estimate site effects. The first one is direct measurement of the local amplification. This path is more direct but offers less flexibility. In addition, there may be cases where we run the risk of accepting an erroneous estimate of local amplification because of the difficulties involved in its verification. This risk is reduced when we are able to use more than one independent estimate. The second path is a very indirect one; determine subsoil structure and from there compute expected amplification. This second path compensates its shortcomings and tortuousness with its greater flexibility. Of course no single approach is appropriate for all circumstances. An important consideration is that, in many cases, developing countries face a large seismic risk. The scientific challenges related to site effect estimation are the same as anywhere else. However, the resources available with which to cope with them are much smaller. This is an important consideration to make when developing techniques.

In dealing with site effects, one must separate two different objectives. Although the two are related, each project may require the emphasis to be placed on one of them as both are necessary and one cannot substitute the other. The first objective is the prediction of local amplification at a given site, maybe to modify a regional estimate of expected ground motion. A microzonation map is a clear example. This objective is better served by an approach relying on direct estimates of the local transfer function or some proxy for it, such as regressions of intensity estimates or the use of the H/V spectral ratio using either earthquake or noise data.

The second objective is not so focused on an immediate application and could be stated as the understanding of the characteristics of ground motion. It is clear that this objective may be out of the question for many engineering projects, yet this is the more satisfying objective, at least from the scientific point of view. One could translate understanding a particular situation of site amplification as the ordering of the factors that contribute to the site response. Take for example Mexico City, a paradigmatic case for site amplification. Our current understanding of site effects there is that the first and most important factor in the observed response is the impedance contrast between a thin layer of extremely soft clay and its volcanic substratum. This factor alone allows reproducing the amplification of ground motion and its geographical distribution. However, this factor is insufficient to explain site response because it is incomplete. Models based on 1D approximation fail to reproduce the observed long duration of strong ground motion in this city. The reason for this failure is that the long duration is the result of a very long excitation wavefield, produced by the distance between Mexico City and the epicentral zone and the diffraction of the incident wavefield by the geological heterogeneities that plague the crustal structure in central Mexico. We note that, in the case of Mexico City, site effects are not to be understood if we do not consider the whole path between the subduction zone and the city (more than 300 km, see, e.g., Furumura and Kennett, 1998; Chávez-García and Salazar, 2002). This is a sobering reminder that site effects are not necessarily related exclusively to the site and that it is not always valid to separate source and path effects from them. The classification of the contributing factors in order of importance is fundamental here because at present we are not able to model every possible contributing factor. We must choose what to model and where to direct the available resources. Site effects continue to be a very exciting and useful field of research.

Acknowledgements

The comments by D. Raptakis greatly improved the manuscript. This research was supported by Consejo Nacional de Ciencia y Tecnología, Mexico, through the contract SEP-2003-C02-43880/A. Additional support was received from Coordinación de la Investigación Científica and Instituto de Ingeniería, Universidad Nacional Autónoma de México.

REFERENCES

- Aki K (1957) Space and time spectra of stationary stochastic waves, with special reference to microtremors. *Bull. Earthq. Res. Inst. Univ. Tokyo* 25: 415–457
- Apostolidis P, Raptakis D, Pandi K, Manakou M, Pitilakis K (2005) Definition of subsoil structure and preliminary ground response in Aigion city (Greece) using microtremors and earthquakes. *Soil Dyn. Earthq. Engng.* 26: 922–940
- Bard PY (1999) Microtremor measurements: a tool for site effect estimation? In: Irikura K, Kudo K, Okada H, Sasatani T (eds) *The effects of surface geology on seismic motion*. Balkema, Rotterdam, pp 1251–1279, 1999

- Bard PY, Bouchon M (1980a) The seismic response of sedimentfilled valleys, Part I. The case of incident SH waves. *Bull. Seism. Soc. Am.* 70: 1263–1286
- Bard PY, Bouchon M (1980b) The seismic response of sedimentfilled valleys, Part II. The case of incident P and SV waves. *Bull. Seism. Soc. Am.* 70: 1921–1941
- Beresnev IA, Atkinson GM (1998) FINSIM: a FORTRAN program for simulating stochastic acceleration time histories from finite faults. *Seism. Res. Lett.* 69: 27–32
- Boatwright J, Fletcher JB, Fumal TE (1991) A general inversion scheme for source, site, and propagation characteristics using multiply recorded sets of moderate-sized earthquakes. *Bull. Seism. Soc. Am.* 81: 1754–1782
- Borcherdt RD (1970) Effects of local geology on ground motion near San Francisco Bay. *Bull. Seism. Soc. Am.* 60: 29–61
- Borcherdt RD (1994) Estimates of site-dependent response spectra for design (methodology and justification). *Earthq. Spectra* 10: 617–653
- Bouchon M, Schultz CA, Toksöz NM (1996) Effect of three-dimensional topography on seismic motion. *J. Geophys. Res.* 101: 5835–5846
- Brown LT, Boore DM, Stokoe KH (2002) Comparison of shear-wave slowness profiles at 10 strong-motion sites from noninvasive SASW measurements and measurements made in boreholes. *Bull. Seism. Soc. Am.* 92: 3116–3133
- Campillo M (2006) Phase and correlation in ‘random’ seismic fields and the reconstruction of the Green function. *Pageoph* 163: 475–501
- Campos-Enríquez JO, Chávez-García FJ, Cruz H, Acosta-Chang JG, Matsui T, Arzate JA, Unsworth MJ, Ramos-López J (2004) Shallow crustal structure of Chicxulub impact crater imaged with seismic, gravity and magnetotelluric data: inferences about the central uplift. *Geophys. J. Int.* 157: 515–525
- Chávez-García FJ, Bard PY (1994) Site effects in Mexico City eight years after the September 1985 Michoacan earthquakes. *Soil Dyn. Earthq. Engng.* 13: 229–247
- Chávez-García FJ, Stephenson WR, Rodríguez M (1999) Lateral propagation effects observed at Parkway, New Zealand. A case history to compare 1D vs 2D site effects. *Bull. Seism. Soc. Am.* 89: 718–732
- Chávez-García FJ, Faccioli E (2000) Complex site effects and building codes: making the leap. *J. Seismol.* 4:34–40
- Chávez-García FJ, Salazar L (2002) Strong motion in central Mexico: a model based on data analysis and simple modeling. *Bull. Seism. Soc. Am.* 92: 3087–3101
- Chávez-García FJ (2003) Site effects in Parkway basin: comparison between observations and 3-D modeling. *Geophys. J. Int.* 154: 633–646
- Chávez-García FJ, Luzón F (2005) On the correlation of seismic microtremors. *J. Geophys. Res.* 110:B11313, doi:10.1029/2005JB003671
- Chávez-García FJ, Rodríguez M, Stephenson WR (2005) An alternative approach to the SPAC analysis of microtremors: exploiting stationarity of noise. *Bull. Seism. Soc. Am.* 95: 277–293
- Chávez-García FJ, Rodríguez M, Stephenson WR (2006) Subsoil structure using SPAC measurements along a line. *Bull. Seism. Soc. Am.* 96: 729–736
- Chávez-García FJ, Domínguez T, Rodríguez M, Pérez, F (2007) Site effects in a volcanic environment: a comparison between HVSr and array techniques at Colima, Mexico. *Bull. Seism. Soc. Am.* (in press)
- Chouet BC, DeLuca G, Milana P, Dawson M, Martin C, Scarpa R (1998) Shallow velocity structure of Stromboli volcano, Italy, derived from small-aperture array measurements of Strombolian tremor. *Bull. Seism. Soc. Am.* 88: 653–666

- Claerbout JF (1968) Synthesis of a layered medium from its acoustic transmission response. *Geophysics* 33: 264–269
- Duvall TL, Jefferies SM, Harvey JW, Pomerantz MA (1993) Time–distance helioseismology. *Nature* 362: 430–432
- Ferrazzini V, Aki K, Chouet B (1991) Characteristics of seismic waves composing Hawaiian volcanic tremor and gas-piston events observed by a near-source array. *J. Geophys. Res.* 96: 6199–6209
- Field EH, Jacob KH (1995) A comparison and test of various site response estimation techniques, including three that are not reference site dependent. *Bull. Seism. Soc. Am.* 85: 1127–1143
- Furumura T, Kennett BLN (1998) On the nature of regional seismic phases III. The influence of crustal heterogeneity on the wavefield for subduction earthquakes: the 1985 Michoacan and 1995 Copala, Guerrero, Mexico earthquakes. *Geophys. J. Int.* 135: 1060–1084
- Gutiérrez C, Masaki K, Lermo J, Cuenca J (1996) Microzonificación sísmica de la ciudad de Colima. Cuadernos de Investigación No. 33, México (in Spanish)
- Horike M (1985) Inversion of phase velocity of long-period microtremors to the S-wave-velocity structure down to the basement in urbanized areas. *J. Phys. Earth* 33: 59–96
- Horike M, Zhao B, Kawase H (2001) Comparison of site response characteristics inferred from microtremors and earthquake shear waves. *Bull. Seism. Soc. Am.* 91: 1526–1536
- Hruby CE, Beresnev IA (2003) Empirical corrections for basin effects in stochastic ground-motion prediction, based on the Los Angeles basin analysis. *Bull. Seism. Soc. Am.* 93: 1679–1690
- Langston CA (1979) Structure under Mount Rainier, Washington, inferred from teleseismic body waves. *J. Geophys. Res.* 84: 4749–4762
- Lermo J, Chávez-García FJ (1993) Site effect evaluation using spectral ratios with only one station. *Bull. Seism. Soc. Am.* 83: 1574–1594
- Lermo J, Chávez-García FJ (1994) Are microtremors useful in site effect evaluation? *Bull. Seism. Soc. Am.* 84: 1350–1364
- Louie JN (2001) Faster, better: shear-wave velocity to 100 meters depth from refraction microtremor arrays. *Bull. Seism. Soc. Am.* 91: 347–364
- Makra K, Chávez-García FJ, Raptakis D, Pitilakis K (2004) Parametric analysis of the seismic response of a 2D sedimentary valley: implications for code implementations of complex site effects. *Soil Dyn. Earthq. Engng.* 25: 303–315
- Ohoiri M, Nobata A, Wakamatsu K (2002) A comparison of ESAC and FK methods of estimating phase velocity using arbitrarily shaped microtremor arrays. *Bull. Seism. Soc. Am.* 92: 2323–2332
- Okada H (2003) The microtremor survey method. *Soc. of Expl. Geophys. of Japan*, translated by K. Suto, *Geophys. Monograph Series No. 12, Soc. of Expl. Geophys., Tulsa*
- Raptakis DG, Manakou MV, Chávez-García FJ, Makra KA, Pitilakis KD (2005) 3D configuration of Mygdonian basin and preliminary estimate of its seismic response. *Soil Dyn. Earthq. Engng.* 25: 871–887
- Shapiro NM, Campillo M, Stehly L, Ritzwoller M (2005) High resolution surface wave tomography from ambient seismic noise. *Science* 307: 1615–1618
- Steidl JH, Tumarkin AG, Archuleta RJ (1996) What is a reference site? *Bull. Seism. Soc. Am.* 86: 1733–1748
- Trifunac MD (1971) Surface motion of a semi-cylindrical alluvial valley for incident plane SH waves. *Bull. Seism. Soc. Am.* 61: 1755–1770
- Weaver RL, Lobkis OI (2005) Fluctuations in diffuse field–field correlations and the emergence of the Green’s function in open systems. *J. Acoust. Soc. Am.* 117: 3432–3439

CHAPTER 4

SOURCE AND SITE FACTORS IN MICROZONATION

Atila Ansal and Gökçe Tönük

Department of Earthquake Engineering, Kandilli Observatory and Earthquake Research Institute, Bogaziçi University, Istanbul, Turkey
ansal@boun.edu.tr

Abstract. The comprehensive calculation of site specific earthquake characteristics on the ground surface for microzonation requires input acceleration time histories compatible with the regional earthquake hazard representing source factors. Real and simulated acceleration records were used as input for site response analyses to evaluate the reliability and to observe the induced variability. The second component of site specific calculations is site characterisation and establishment of representative soil profiles down to engineering bedrock that represent the site factors. Grid systems with 250 m × 250 m cells were adopted to define the site conditions in terms of representative soil profiles for each cell. The third component of the site specific calculations is the analytical procedure used for site response analysis and the interpretation scheme of the calculated site specific parameters. Parametric studies were conducted for the probabilistic assessment of microzonation with respect to ground shaking intensity and liquefaction susceptibility as well as for vulnerability assessment based on acceleration response spectra, peak ground accelerations, and cyclic shear stress variation with depth, calculated by site response analyses for each cell.

1. Introduction

Site specific free field earthquake characteristics on the ground surface are the essential components for microzonation with respect to ground shaking intensity, liquefaction susceptibility, and for the assessment of the seismic vulnerability of the urban environment. The microzonation methodology can be considered as composed of three stages. In the first stage, regional seismic hazard analyses need to be conducted to estimate earthquake characteristics on rock outcrop for each cell. In the second stage, the representative site profiles should be modelled based on the available borings and in-situ tests. The third stage involves site response analyses for estimating the earthquake characteristics on the ground surface and the interpretation of the results for microzonation (Ansal et al., 2004a, b). In addition to the generation of base maps for urban planning, microzonation with respect to spectral accelerations, peak accelerations and velocity on the ground surface can be used to assess the vulnerability of the building stock (Ansal et al., 2005a, 2006b) and lifeline systems.

The regional earthquake hazard may be based on probabilistic or deterministic approach. In the case of microzonation for urban planning, it is preferable to adopt a probabilistic earthquake hazard assessment but in the case of earthquake scenarios for estimating

possible earthquake damage, depending on the seismicity of the investigated region, deterministic approach can be preferable (Erdik et al., 2004). Independent of the methodology adopted for the earthquake hazard evaluation, whether it is probabilistic or deterministic, realistic recorded (Bommer and Acevedo, 2004) or simulated acceleration time histories are needed to conduct site response analyses for the investigated area.

2. Input motion

One of the sources for the major uncertainty in ground response analysis arises from the variability of the input earthquake motion (Boore, 2004). Adopting a probabilistic approach, two hazard compatible alternatives, real and simulated acceleration time histories, were investigated. For both options earthquake hazard compatibility with respect to the expected fault type, fault distance, and magnitude was taken into account in the selection and in the generation of the acceleration time histories. The site response analyses were conducted using 1D equivalent linear model (Idriss and Sun, 1992) for the same area and for different site profiles to evaluate the reliability and variability of earthquake characteristics on the ground surface.

2.1. REAL ACCELERATION RECORDS

In using previously recorded real acceleration time histories, scaling scheme of the selected acceleration records becomes an important decision point. To evaluate the effects of different scaling options, the selected set of earthquake acceleration time histories were scaled with respect to peak ground acceleration (PGA), peak ground velocity (PGV), and Arias intensity (AI). Site response analyses for the same soil profiles are repeated and the variability of earthquake characteristics on the ground surface induced by scaling is evaluated. Scaling of input time histories was carried out in time-domain that involves only the amplitude of the time series (Ansal et al., 2006a; Durukal et al., 2005, 2006).

The selected site is located in Gölcük; a town in the epicentre area of the 1999 Kocaeli earthquake. Detailed site investigations were carried out in the town as a part of the post-earthquake studies (Ansal et al., 2000). The selected soil profile extending down to 45 m depth is analysed by Shake91 (Idriss and Sun, 1992). The regional earthquake hazard was estimated with earthquakes in the magnitude range of 7.0–7.5 that can be characterised by $PGA = 0.35 g$, $PGV = 30 \text{ cm/s}$ (Ambraseys, 1995; Joyner and Boore, 1988). AI is estimated as 2 m/s for the magnitude and distance range considered based on the empirical attenuation relationship proposed (Travasarou et al., 2003; Siyahi et al., 2001).

The ground motion sets were downloaded from PEER website (PEER, 2006). The criteria used in the selection were magnitude range of $M_w = 7.0-7.5$, strike slip earthquake mechanism, and site conditions with NEHRP (BSSC, 2001) site classification of B/C boundary. The site distance range of 0–40 km was considered with respect to four increments as; 0–10 km (11 records), 10–20 km (14 records), 20–30 km (10 records),

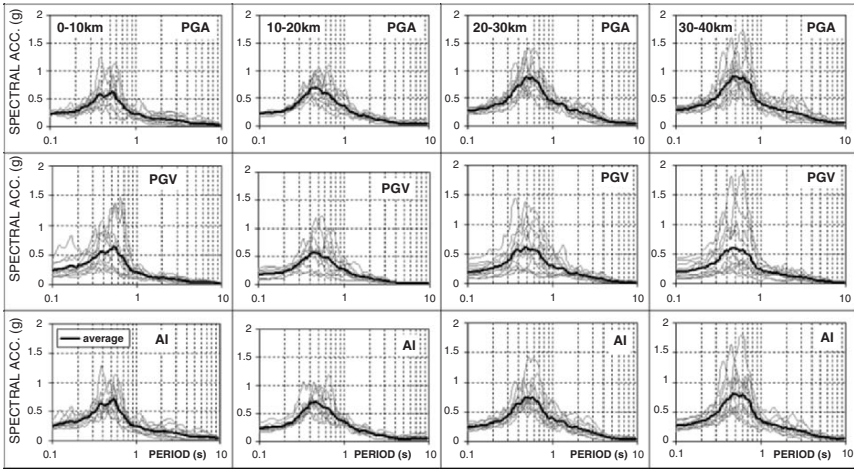


Fig. 4.1. Elastic acceleration spectra with respect to scaling scheme and fault distance

and 30–40 km (12 records) to evaluate the effect of distance as well as the scaling scheme. The elastic acceleration response spectra calculated on the ground surface by site response analysis for the same soil profile for four distance ranges are shown in Figure 4.1.

The results indicate that the scatter in the calculated amplitudes of elastic acceleration response spectra is increasing with distance for all scaling schemes. In addition, amplitudes of the average spectra for all three scaling schemes and for four distance ranges are also different. As can be observed in Figure 4.2, the amplitudes of the average elastic acceleration spectra are increasing with fault distance for PGA and AI scaled records but not for PGV scaled records. In general PGA scaling gave the most conservative elastic acceleration spectra almost in all cases.

When the results are compared with respect to average spectral accelerations calculated using different time histories recorded at different distances, there are differences in PGA scaled input motions, but there is almost no difference in PGV or AI scaled records. However, even though average spectra do not show any distance dependence for PGV and AI scaling, the scatter and the change in the range of the calculated acceleration spectrum shown in Figure 4.1, indicate the importance of the distance as one of the controlling parameters.

The scatter and range of elastic acceleration response spectra on the ground surface calculated by site response analyses increase with distance of the recorded time histories for all scaled input motions. This could lead to different spectral accelerations if the scatter is evaluated by statistical procedure based on a probabilistic approach. Therefore, it would be essential to select the real time histories for site response analysis at compatible distance range as determined by the site specific hazard study.

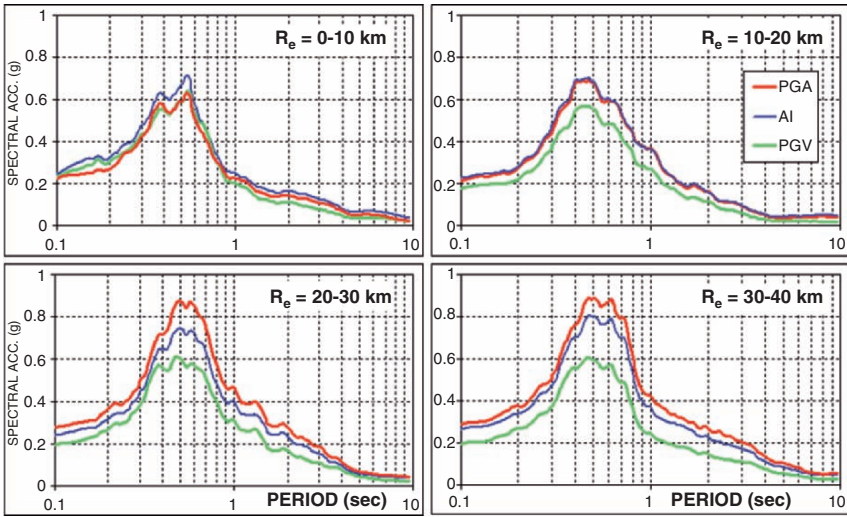


Fig. 4.2. Average elastic response spectra for different distance increments and scaling scheme

2.2. SIMULATED ACCELERATION RECORD

The second option is to use simulated acceleration time histories generated compatible with the estimated earthquake hazard spectra. The hazard spectrum compatible acceleration time histories generated for each cell based on the procedure suggested by Deodatis (1996) and Papageorgiou et al. (2000) were utilised for conducting site response analyses. Three simulated acceleration time histories were used for each cell for site response analyses. The average of the calculated acceleration response spectra was used for microzonation with respect to ground shaking intensity and for fitting the best NEHRP envelope spectra to calculate the spectral acceleration to be used in assessing the building stock vulnerability.

The microzonation maps with respect to spectral accelerations at short period range using one set of simulated (Kılıç et al., 2006) and two different sets of real acceleration time histories are shown in Figure 4.3. Even though there is a general agreement among all three options, there are also important differences. In this case, it would be difficult to justify the selection of one option to estimate the building stock vulnerability. As can be observed, using simulated acceleration time histories generally yielded higher amplitudes indicating more conservative solution. However, the degree of conservatism cannot be identified and the generated acceleration records may be considered unrealistically demanding as shown in Figure 4.4. Thus at this stage the use of regional earthquake hazard compatible previously recorded and PGA scaled real acceleration records appear more suitable for microzonation studies.

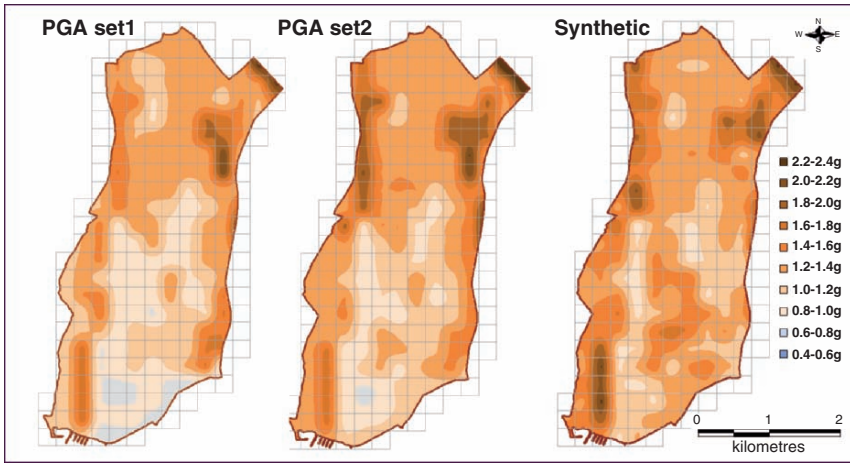


Fig. 4.3. Microzonation of Zeytinburnu with respect to short period ($T = 0.2$ s) spectral accelerations using two sets of PGA scaled real and one set of simulated acceleration input motion

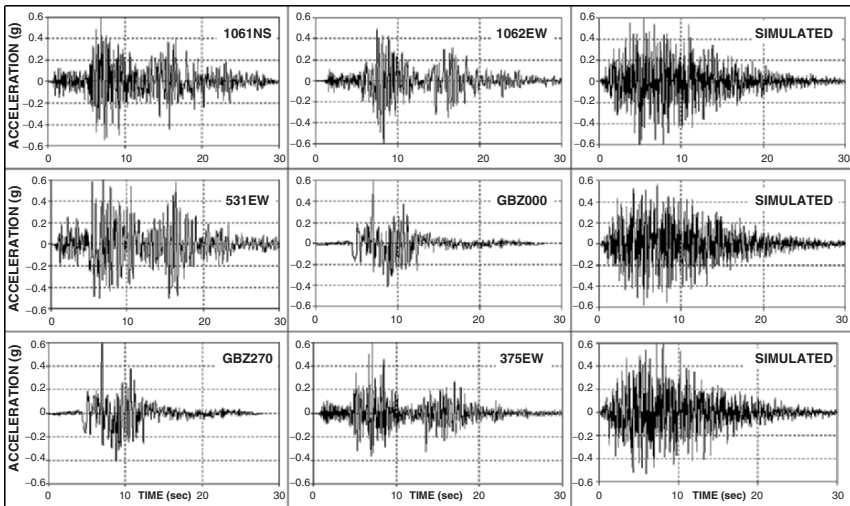


Fig. 4.4. Two sets of scaled real and one set of simulated acceleration records used for site response analyses for one cell

In the case of real acceleration records, it could be preferable to conduct site response analyses using large sets of data to eliminate the differences observed between different sets as shown in Figure 4.3. One alternative is to adopt a probabilistic interpretation for all elastic acceleration spectra with predefined exceedance probability to calculate the elastic acceleration spectra to be used for microzonation and for vulnerability assessment.

3. Site characterisation

The investigated regions may be divided into cells by a grid system and site characterisation may be performed for each cell based on the available borings and other relevant information by defining a representative soil profile. Shear wave velocity profiles need to be established down to the engineering bedrock with estimated shear wave velocity of 700–750 m/s.

The case study selected for evaluating the effects of site characterisation as well as scaling procedures adopted for site response is near the city of Izmir (Durukal et al., 2005). The site response analyses were conducted using Shake91 for the four soil profiles where in-hole shear wave velocity measurements were performed previously. These four borings are at the same site with spacing around 100 m, thus it is possible to assume that all of these four borings with measured shear wave velocity profiles could be in the same cell. The measured shear wave velocity profiles given in Figure 4.5 indicate the variability in the site conditions at one cell where for all practical purposes only one site specific elastic acceleration spectra is needed for microzonation and to evaluate the building stock vulnerability.

The effects of scaling for each soil profile were evaluated together to observe the effects of site variability in relation with the scaling of input motion. The scaled acceleration records were applied as rock outcrop motion where the engineering bedrock ($V_s = 750$ m/s) was taken at 45 m depth for four soil profiles.

The regional earthquake hazard analysis yielded an earthquake magnitude of 6.5–7.0 with an epicentre distance of 10–20 km. The hazard compatible input earthquake data were composed of 20 acceleration time histories recorded between 10 and 20 km fault distances. Site response analyses were conducted using scaling parameters determined

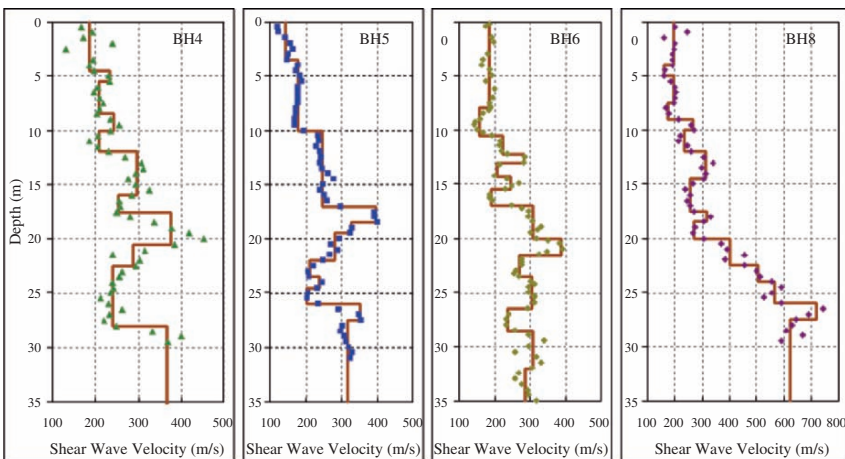


Fig. 4.5. Four soil profiles used in site response analyses for the case study

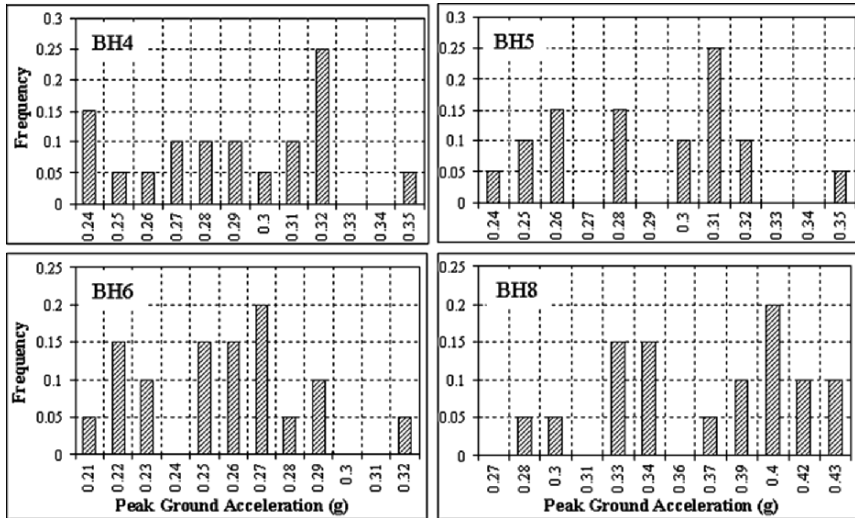


Fig. 4.6. PGA Histograms on the ground surface for PGA scaled acceleration records for four soil profiles

from related attenuation relationships as $PGA = 0.25$ g, $PGV = 30$ cm/s, and $AI = 55$ cm/s (Joyner and Boore, 1988; Ambraseys, 1995; Travararou et al., 2003).

The peak ground acceleration histograms calculated for four soil profiles shown separately in Figure 4.6, indicate the importance of the variations in the soil profiles. Thus one option to account for these differences in the soil profile at the site is to consider the site response results obtained for four soil profiles together and to determine the variation of peak ground acceleration with respect to different scaling procedures adopted as shown in Figure 4.7 for 80 site response analyses. The distribution of calculated PGA is assumed to fit normal distribution and PGA values corresponding to probability of exceedance level of 10% were calculated as shown in Figure 4.7.

The adopted procedure accounts for the statistical variability in the site conditions, therefore more consistent results would be obtained with respect to the initially selected hazard level. However, the limited number of soil borings and in-situ tests can be a problem for evaluating the statistical variability of the site conditions. In such cases, the site variability may be taken into account by assuming that this variability can be modelled by normal distribution with an assumed standard deviation. And thus the site response characteristics in terms of PGA or elastic acceleration response spectra can be calculated with respect to selected exceedance levels.

Based on the histograms for the calculated PGAs for all four borings and taking into consideration all three parameters calculated to determine the variability in each set (kurtosis and normalized standard deviation being minimum, and range being the smallest), among the three scaling options evaluated, the scaling with respect to peak ground accelerations yielded the most appropriate results for site response analyses and should be preferred for microzonation and vulnerability assessment of the building stock.

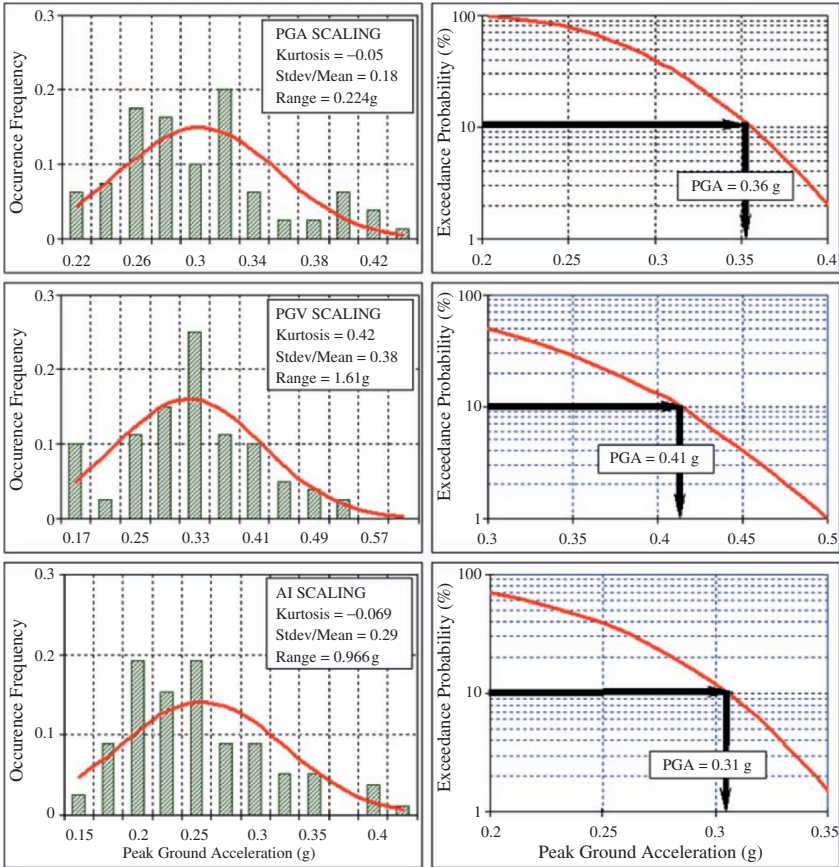


Fig. 4.7. PGA Histograms on the ground surface for PGA, PGV, and AI scaled records and PGAs corresponding to 10% exceedance probability

4. Microzonation

4.1. MICROZONATION WITH RESPECT TO GROUND MOTION

With the increase in the analytical, in-situ, and laboratory investigation capabilities, there has been significant increase in the accumulated databases concerning the regional geological formations, earthquake source mechanisms, seismic activity, and earthquake ground motion records. In the light of these scientific and technical advances, it became feasible to conduct seismic microzonation maps at urban level with sufficiently large scales. The main objective is to estimate earthquake characteristics on the ground surface based on more comprehensive analyses taking into account major controlling factors.

Microzonation studies were carried out for five municipalities located in different parts of the Marmara Region, Turkey. Depending on the availability of geological, geophysical, and geotechnical data the investigated areas were divided into total of 819 cells by a grid system composed of 500 m \times 500 m or 250 m \times 250 m (Erdik et al., 2005; Ansal et al., 2006b).

Three real acceleration time histories compatible with the earthquake hazard assessment in terms of probable magnitude, distance, and fault mechanism were selected as the input rock outcrop motion (Ansal et al., 2006b). The input acceleration time histories were scaled for each cell with respect to the peak accelerations obtained from earthquake hazard study (Erdik et al., 2005). The three scaled acceleration time histories for each cell were used as input motion for site response analyses using Shake91 (Idriss and Sun, 1992) and the average of the PGAs and acceleration response spectra at the ground surface were determined for each cell to obtain the necessary parameters for microzonation.

The ground shaking intensity map presents the estimated relative shaking intensity levels based on the combination of two parameters. The peak spectral accelerations (at 0.2 s) calculated from Borchardt (1994) using equivalent (average) shear wave velocities for the top 30 m were adopted as one of the microzonation parameters. The second parameter used was the average spectral accelerations calculated between the 0.1 s and 1 s periods using the average acceleration spectra determined from the results of the three site response analyses conducted for each cell. The microzonation with respect to ground shaking intensity was established with respect to these two parameters.

The approach adopted in the assessment of the calculated microzonation maps involves the division of the area into three zones as A, B, and C (Ansal et al., 2004a, b). Since the site characterisations, as well as all the analysis performed, require various approximations and some assumptions, it was preferred not to present the numerical values for any parameter. In all cases, the variations of the calculated parameters are considered for each study area separately and their frequency distributions were calculated. Thus the zone C shows the most unsuitable 33 percentile (e.g. high spectral accelerations or high spectral amplification), zone B the medium 34 percentile, and zone A shows the most favourable 33 percentile (e.g. low spectral accelerations or low spectral amplifications). Thus the final microzonation map is a relative map defined in terms of three zones independent of the absolute values of the ground shaking intensity as shown for Bandırma in Figure 4.8.

4.2. MICROZONATION WITH RESPECT TO LIQUEFACTION SUSCEPTIBILITY

Liquefaction of soil layers has been a major cause of damage to soil structures, lifeline facilities, and building foundations during the past earthquakes. The approach that has gained wide acceptance within the framework of urban planning is to establish microzonation maps with respect to liquefaction susceptibility to mitigate possible earthquake damage related to liquefaction (Kavazanjian et al., 1985; Todorovska, 1998; Ansal and Tönük, 2005).

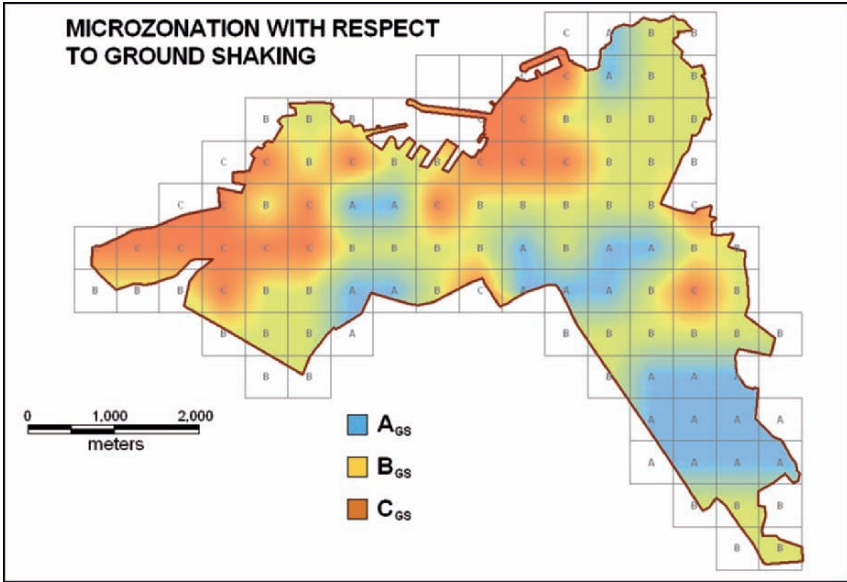


Fig. 4.8. Microzonation with respect to ground shaking intensity (Ansal et al., 2005a)

Liquefaction susceptibility microzonation maps were also produced for the five municipalities in the Marmara region (Erdik et al., 2005; Ansal et al., 2006b) to be used for urban planning. The local soil stratifications and soil characteristics were determined based on previously and recently conducted soil borings. The investigated regions were divided by grid systems with cell size of 250 m × 250 m or 500 m × 500 m depending on the available borings and other relevant information (Ansal et al., 2005b).

The liquefaction susceptibility is based on the calculation of the safety factors along the top 20 m depth for each soil profile for all liquefiable soil layers according to Youd et al. (2001) based on the available SPT-N blow counts and using the average peak ground accelerations calculated from site response analyses. The liquefaction potential (“liquefaction potential index”, PL) for each borehole was determined according to Iwasaki et al. (1982).

Two variables are required for the assessment of liquefaction susceptibility: (1) seismic demand on the soil layers, expressed in terms of cyclic stress ratio, CSR; and (2) capacity of the soil layers to resist liquefaction, expressed in terms of cyclic resistance ratio, CRR.

The oldest and still the most widely used approach as summarised by Youd et al. (2001) is the simplified procedure for assessing liquefaction susceptibility originally proposed by Seed and Idriss (1971) based on SPT-N values and cyclic stress ratio calculated using stress reduction factor. The cyclic stress ratio, CSR, is expressed as

$$CSR = \frac{\tau_{av}}{\sigma'_v} = 0.65 \frac{a_{max}}{g} \frac{\sigma_v}{\sigma'_v} \Gamma_d \quad (4.1)$$

where a_{\max} = peak horizontal ground surface acceleration; g = acceleration of gravity; σ_v = total vertical overburden stress; σ'_v = effective vertical overburden stress; r_d = stress reduction factor. The average value of r_d is calculated as given by Youd et al. (2001);

$$r_d = \frac{(1.00 - 0.4113z^{0.5} + 0.04052z + 0.001753z^{1.5})}{(1.00 - 0.4177z^{0.5} + 0.05729z - 0.006205z^{1.5} + 0.00121z^2)} \quad (4.2)$$

where z is the depth below ground surface in metres.

There have been various studies concerning the definition of stress reduction factor in the literature (Idriss and Boulanger, 2003; Cetin et al., 2004). In most of these studies, different formulations were proposed to calculate the variation of cyclic stress ratio that would be induced by the design earthquake and almost all of them are only dependent on the depth in the soil profile. In the recent formulation proposed by Cetin et al. (2004), the effect of other factors such as peak acceleration on the ground surface, magnitude of the design earthquake, and soil stiffness at the top 12 m in addition to the depth from the ground surface were considered as factors controlling the variation of stress reduction factor or in more general terms variation of maximum shear stresses with depth.

The more comprehensive alternative is to calculate average shear stress with depth using site response analyses. The comparison of the variation of CSR calculated using the simplified formulations proposed by Youd et al. (2001) and Cetin et al. (2004) and site response analyses given in Figure 4.9 indicates significant differences among the three approaches (Ansal and Tönük, 2006). The differences are not consistent and depend very much on the properties of the soil stratification, shear wave velocity profiles, and peak ground accelerations. The observed general trend indicates that the variation of CSR, calculated by site response analysis is higher compared to CSR calculated using the simplified stress reduction factor.

The CSR calculated by the procedure suggested by Youd et al. (2001) depends only on depth of the element and ground water level and incapable to account for the changes in the soil profile. Depending on the soil stratification and stiffness of the soil layers the variation of CSR obtained by site response analysis could be considered more reliable. Thus based on the results obtained in this study, the formulation suggested by Youd et al. (2001) in general yielded values on the unsafe side.

The approach adopted to perform microzonation maps in terms of liquefaction susceptibility was based on the method summarised by Youd et al. (2001) and Iwasaki et al. (1982). The safety factors were calculated along the whole 20 m depth of the borehole for all liquefiable soil layers using the available SPT-N blow counts based on (a) CSR using peak ground accelerations calculated from site response analysis and r_d procedure suggested by Youd et al. (2001) and (b) CSR calculated by site response analyses.

The liquefaction potential for each borehole was calculated according to the procedure proposed by Iwasaki et al. (1982) using the variation of the safety factors with depth.

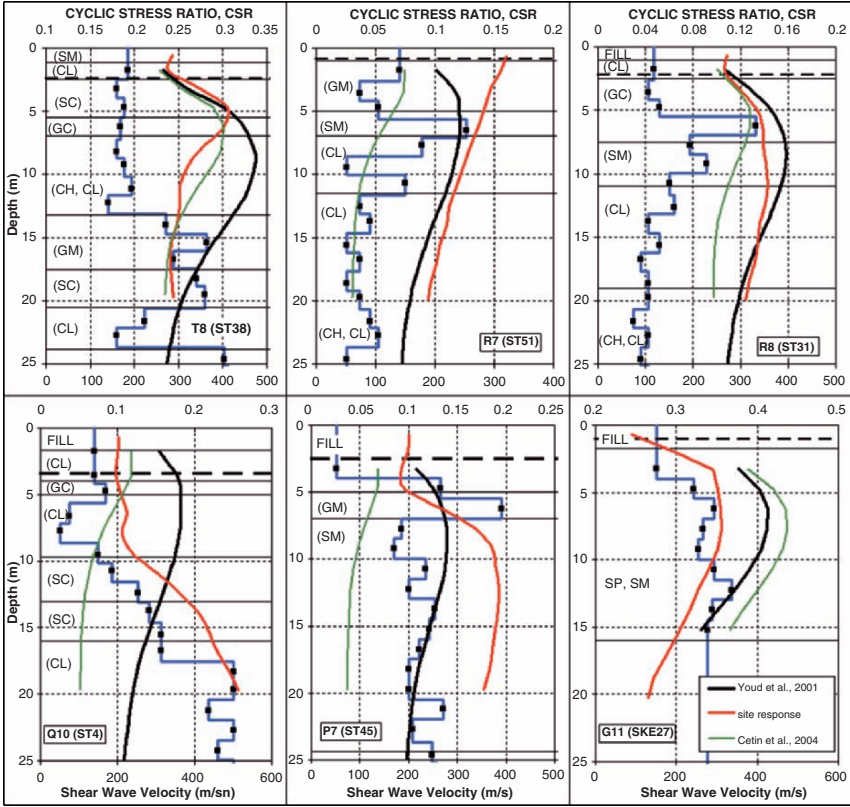


Fig. 4.9. Comparisons of CSR by site response analysis and r_d simplified procedure recommended by Youd et al. (2001) and Cetin et al. (2004)

The severity of possible liquefaction at any site was quantified by introducing a factor called the liquefaction potential index, PL, defined as

$$P_L = \int F(z)w(z)dz \tag{4.3}$$

where z is the depth below the ground water surface, measured in metres; $F(z)$ is a function of the liquefaction resistance factor, FL , where $F(z) = 1 - FL$ but if $FL > 1.0$, $F(z) = 0$; and $w(z) = 10 - 0.5z$. Eq. (4.3) gives values of PL ranging from 0 to 100.

Based on the results reported by Iwasaki et al. (1982), three zones (A, B, and C) were identified with respect to liquefaction potential index. Zone C is where the liquefaction potential index is $PL > 15$, zone B is the intermediate zone where the liquefaction potential index is $5 \leq PL \leq 15$, and zone A is the safest zone where liquefaction potential index is $PL < 5$.

The microzonation maps for liquefaction susceptibility determined by this approach using the safety factors computed by r_d simplified formulation and using the values obtained by site response analyses. There are differences between the two approaches and these may be considered significant with respect to urban planning as can be observed in Figure 4.10 for Gemlik city.

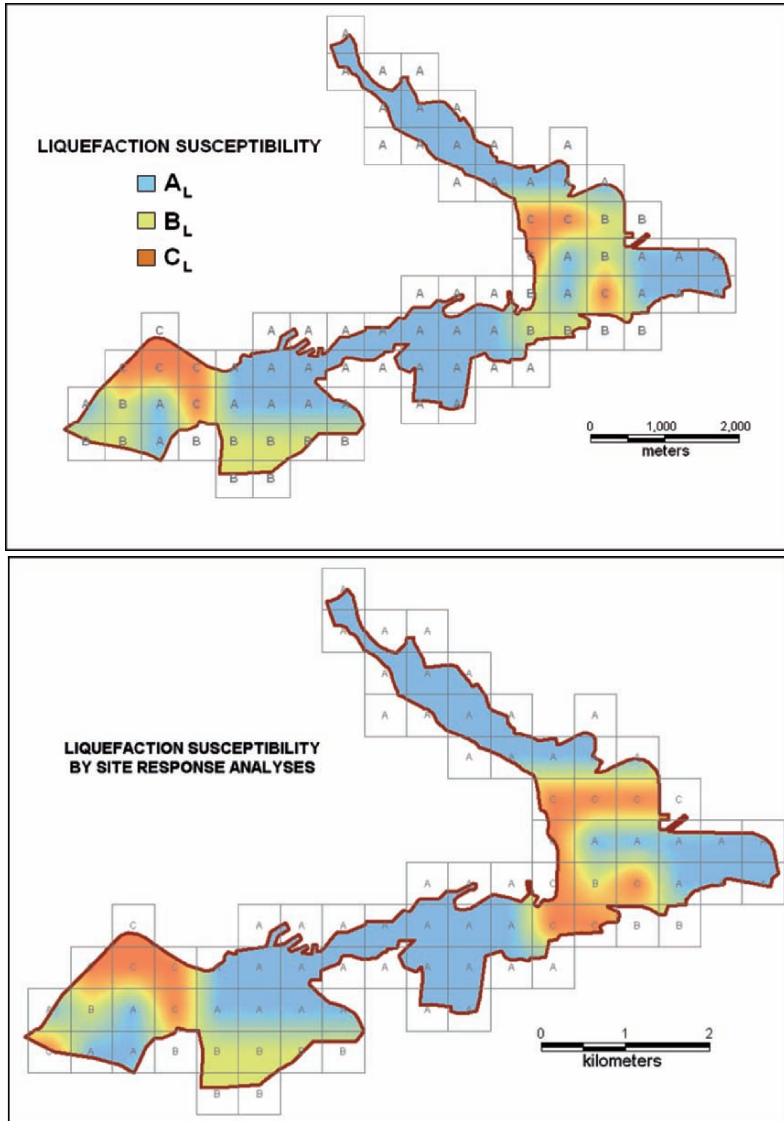


Fig. 4.10. Microzonation for Gemlik using stress reduction factor by Youd et al. (2001) and by site response analysis (Ansal and Tönük, 2006)

5. Spectral accelerations for vulnerability assessments

A parametric study was conducted to observe the effect of averaging and adopting a probabilistic approach (i.e. 10% exceedance probability) by assuming that the calculated elastic acceleration spectra can be modelled by normal distribution for all the period range considered. An example of the best fit NEHRP envelope obtained by this approach with respect to elastic acceleration response spectra with 10% exceedance probability is shown in Figure 4.11 in comparison with the average and all acceleration response spectra calculated for the selected (20) PGA scaled input acceleration time histories. The NEHRP design spectrum is preferred because of its flexibility in defining short period spectral accelerations and for vulnerability assessment of the building stock (Erdik and Fahjan, 2005).

However, the question of conservatism again becomes important as can be observed in Figure 4.12. One justification for using the probabilistic interpretation of the calculated elastic acceleration response spectra from all site response analyses using larger number of real input acceleration records is the capability of defining a hazard level in accordance with the purpose of the microzonation. The criteria adopted in this scheme was to use the same hazard level (10% exceedance probability) that was used to calculate the earthquake hazard on the rock outcrop used for site response analyses. The approach is still not completely probabilistic since the variability of the soil profile was not taken into account in a probabilistic manner.

The average acceleration response spectra obtained for each cell from site response analyses were evaluated for determining the spectral accelerations for the short period (S_s) corresponding to 0.2 s and for the long period (S_1) corresponding to 1 s. An approach was adopted to determine the best fit envelope to the calculated average acceleration response spectra (Ansal et al., 2005b). All the requirements of the NEHRP design spectra were applied in obtaining the short (S_s) and long (S_1) period spectral ordinates. The two independent variables in the developed optimization algorithm were S_s and S_1 .

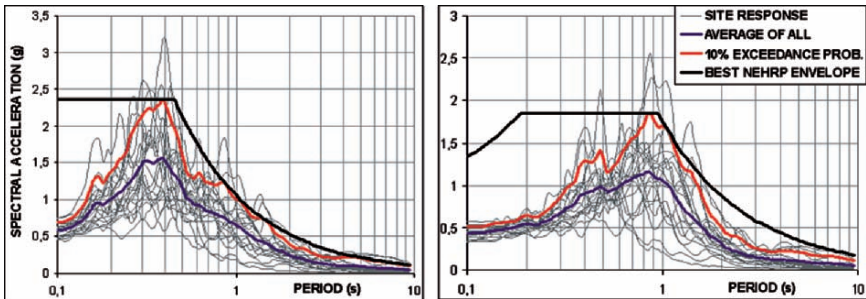


Fig. 4.11. Typical best envelope NEHRP spectra fitted to 10% probability of exceedance elastic acceleration response spectra, in comparison with the average and all acceleration response spectra calculated by site response analysis

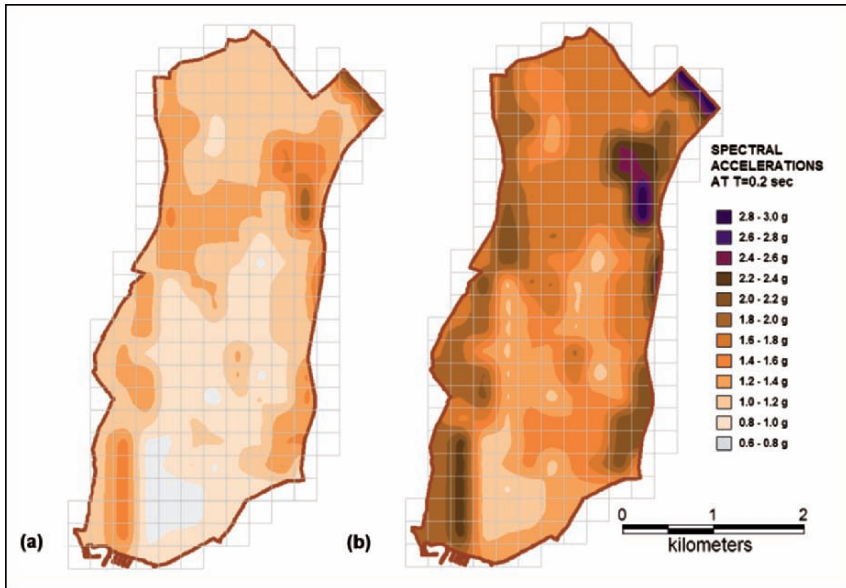


Fig. 4.12. Comparison of zonation with respect to spectral acceleration at $T = 0.2$ s calculated as (a) the average of all site response analyses and (b) corresponding to 10% exceedance probability

In order to determine the vulnerability of the building stock, the earthquake ground motion characteristics used in the assessment of the structural vulnerability may be calculated based on the conventional NEHRP procedure considering the microzonation map obtained in terms of NEHRP site classification as well as by site response analyses.

The comparison between the spectral accelerations obtained from site response analyses using the best envelope fitting procedure with the values obtained by the NEHRP formulation indicates as shown in Figure 4.13 that the values obtained by site response analyses shows much larger scatter. The difference in the data range is much more significant in the case of short period spectral accelerations. This may be the indication of more accurate determination of site effects. This is partly due to the fact that shear wave velocity ranges used in the NEHRP site classes are defined within relatively large ranges as shown in Table 4.1.

Most of the cells in the study areas were classified as NEHRP class C or D, as a result the spectral accelerations calculated on the ground surface based on the conventional formulation using NEHRP site related parameters F_a and F_v were same and the minor differences were due to the differences in the outcrop motion characteristics determined from the earthquake hazard study.

The variability of the calculated parameters to be used for the vulnerability assessment of the building stock is an important factor. Considering the variability taken into account by

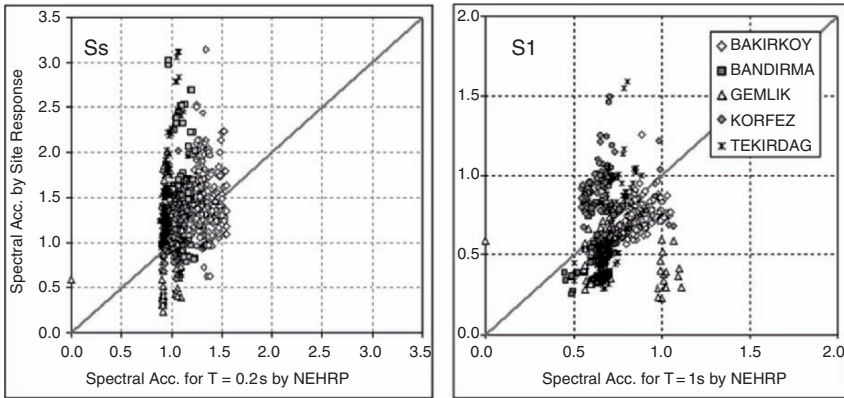


Fig. 4.13. Correlation between spectral accelerations at 0.2 and 1 s calculated by site response analyses and based on NEHRP formulation for all five cities

Table 4.1. NEHRP Site classification with respect to equivalent shear wave velocities

Site classification	Average shear wave velocity range
A	$V_{eq} > 1500 \text{ m/s}$
B	$1500 \text{ m/s} > V_{eq} > 760 \text{ m/s}$
C	$760 \text{ m/s} > V_{eq} > 360 \text{ m/s}$
D	$360 \text{ m/s} > V_{eq} > 180 \text{ m/s}$
E	$V_{eq} < 180 \text{ m/s}$

assigning different earthquake characteristics leading to different time history inputs for each cell and due to the differences in the soil profile, it appears logical to use the spectral acceleration values obtained from site response analysis for the vulnerability assessment. However, it is also possible to argue that the sophistication introduced during this process may not always give more correct or accurate results. In addition, the decision of using one of the spectral accelerations determined by best envelope approaches would play a very important role on the amplitude of the estimated vulnerability of the building stock.

At the present, one way to resolve these ambiguities is to rely on expert judgement and previously obtained damage data in similar earthquakes. However, the statistical evaluation of all the spectral accelerations obtained by both procedures may be useful in the decision process. One possible and positive interpretation of these results could be towards supporting the reliability of the site response analyses and thus one may conclude that it may be recommendable to conduct site response analyses to determine spectral accelerations and PGA on the ground surface to be utilised in assessing the vulnerability of the building stock rather than using the NEHRP procedure which appears to be rather limited.

6. Conclusions

Parametric studies were conducted to evaluate the significance of the induced variability arising from different types and sets of input acceleration records, differences in site characterisation, and due to the differences in the interpretation schemes adopted for microzonation with respect to different parameters.

The results obtained support the use of previously recorded real acceleration time histories as input motion for site response analysis. Among the scaling options studied, PGA scaling, in addition being on the conservative side, yielded more realistic ground motion characteristics. The fault distance of the acceleration records used in site response analysis is one of the parameters that affect the outcome both with respect to peak ground or spectral accelerations, thus acceleration records need to be selected compatible with the regional hazard in terms of fault type, magnitude, and fault distance.

The Zeytinburnu case study was used to compare microzonation maps with respect to PGA and spectral accelerations using real and simulated sets of input acceleration records. For each set, microzonation maps were different even though the differences may not be very significant. These results indicate the importance of the input motion selection scheme. One possibility is to use larger sets of input motion and adopt a probabilistic procedure assuming normally distributed PGA and spectral accelerations.

An interpretation scheme based on probabilistic evaluation of site response results with respect to set of input acceleration records and site conditions would reflect the uncertainty based on the selection of exceedance levels in accordance with the adopted initial probabilistic earthquake hazard level. Thus it may be more suitable for probabilistic microzonation studies.

Site response analyses and two empirical formulation suggested in the literature were used to calculate stress reduction factor for estimating liquefaction susceptibility with depth. There were significant differences among the results obtained by the three approaches. It was observed that in general the variation of CSR with depth, calculated by site response analysis is higher compared to CSR calculated using the simplified formulation for the stress reduction factor.

For the assessment of the vulnerability of the building stock, the average acceleration response spectra obtained for each cell from site response analyses were evaluated for determining the spectral accelerations for the short period corresponding to 0.2 s (S_s) and for the long period corresponding to 1 s (S_1). An approach was adopted to determine the best fitting envelope to the calculated average acceleration response spectra. The results obtained are compared in terms of short period (0.2 s) and long period (1 s) spectral accelerations obtained by NEHRP. The spectral accelerations determined by fitting NEHRP spectrum to response spectrum obtained by site response analyses vary in much broader range. In most cases spectral accelerations obtained by the NEHRP simplified procedure would yield values on the unsafe side compared to those determined by the site response analyses. Thus it would be more reliable to perform site response analyses

to determine the PGA and spectral accelerations on the ground surface to be used for the vulnerability studies.

Acknowledgements

The Authors would like to acknowledge the significant contributions of Prof. M. Erdik, E. Durukal, M. Demircioglu, and K. Sesetyan during all microzonation projects conducted at Kandilli Observatory and Earthquake Research Institute and of the ABS team who worked very hard to supply the necessary input data and technical support to the authors in finalising the microzonation studies within the context of the MEER project.

REFERENCES

- Ambraseys NN (1995) The prediction of earthquake peak acceleration in Europe. *Earthquake Eng. Structural Dynamics* 24: 467–490
- Ansal A, Togrol E, Kurtulus A, Iyisan R, Okur V (2000) Near fault site effects during 1999 Kocaeli Earthquake. Proc. 6th Int. Conf. Seismic Zonation, Cal., USA
- Ansal A, Laue J, Buchheister J, Erdik M, Springman SM, Studer J, Koksall D (2004a) Site Characterization and Site Amplification for a Seismic Microzonation Study in Turkey. Proc. 11th Int. Conf. Soil Dynamics and Earthquake Engineering and 3rd Earthquake Geotechnical Engineering, San Francisco, USA
- Ansal A, Erdik M, Studer J, Springman S, Laue J, Buchheister J, Giardini D, Faeh D, Koksall D (2004b) Seismic Microzonation for Earthquake Risk Mitigation in Turkey. Proc. 13th World Conf. Earthquake Eng., Vancouver, CD, Paper Number: 1428
- Ansal A, Tönük G (2005) Liquefaction Susceptibility and Microzonation. Proc. Int. Conf. Problematic Soils, Eastern Mediterranean University, Famagusta, N. Cyprus, 3: 935–948
- Ansal A, Özyayın K, Erdik M, Yıldırım M, Kılıç H, Adatepe S, Özener PT, Tonaroglu M, Sesetyan K, Demircioglu M (2005a) Seismic Microzonation for Urban Planning and Vulnerability Assessment. Proc. Int. Symposium of Earthquake Engineering (ISEE2005), Geotechnical Session, Awaji Island, Japan
- Ansal A, Tönük G, Bayraklı Y (2005b) Microzonation for Site Conditions for Bakirköy, Gemlik, Bandırma, Tekirdağ, Eskişehir and Körfez. WB MEER Project—A3 Component, Microzonation and Hazard Vulnerability Studies For Disaster Mitigation in Pilot Municipalities. Bogazici University, Kandilli Observatory and Earthquake Engineering Research Institute
- Ansal A, Tönük G (2006) Evaluation of Liquefaction Susceptibility for Microzonation and Urban Planning. Proc. Int. Conf. Geohazards—Technical, Economical and Social Risks, Lillehammer, Norway
- Ansal A, Durukal E, Tönük G (2006a) Selection and Scaling of Real Acceleration Time Histories for Site Response Analyses. Proc. ETC12 Workshop, Athens, Greece
- Ansal A, Tönük G, Demircioglu M, Bayraklı Y, Sesetyan K, Erdik M (2006b) Ground Motion Parameters for Vulnerability Assessment. Proceedings of the First European Conference on Earthquake Engineering and Seismology, Geneva, Switzerland, Paper Number: 1790
- Bommer JJ, Acevedo AB (2004) The use of real earthquake accelerograms as input to dynamic analysis. *J. Earthquake Eng.* 8(1): 43–91
- Boore DM (2004) Can site response be predicted? *J. Earthquake Eng.* 8(1): 1–42

- Borcherdt RD (1994) Estimates of Site Dependent Response Spectra for Design (Methodology and Justification). *Earthquake Spectra* 10(4): 617–654
- BSSC—Building Seismic Safety Council (2001) NEHRP (National Earthquake Hazards Reduction Program) Recommended Provisions for Seismic Regulations for New Buildings and other Structures, Part 1: Provisions (FEMA 368), Washington, D.C.
- Cetin KO, Seed RB, Der Kiureghian A, Tokimatsu K, Harder LF, Kayen RE, Moss RES (2004) Standard Penetration Test-Based Probabilistic and Deterministic Assessment of Seismic Soil Liquefaction Potential. *ASCE, JGGE* 130(12): 1314–1340
- Deodatis D (1996) Non-stationary Stochastic Vector Processes: Seismic Ground Motion Applications. *Probabilistic Eng. Mechanics* 11: 145–168
- Durukal E, Ansal A, Tönük G (2005) Effect of Ground Motion Scaling in Site Response Analyses. *Proc. Earthquake Geotechnical Engineering Satellite Conference, 16th ICSMGE, Osaka, Japan*
- Durukal E, Ansal A, Tönük G (2006) Effect of Ground Motion Scaling and Uncertainties in Site Characterisation on Site Response Analyses. *Proc. 100th Anniversary Earthquake Conference Commemorating the 1906 San Francisco Earthquake, San Francisco, USA*
- Erdik M, Demircioglu M, Sesetyan K, Durukal E, Siyahi B (2004) Earthquake Hazard in Marmara Region. *Soil Dynamics Earthquake Eng.* 24: 605–631
- Erdik M, Fahjan Y (2005) System Analysis and Risk. *Assessing and Managing Earthquake Risk Geo-scientific and Engineering Knowledge for Earthquake Risk Mitigation: Developments, Tools, Techniques, Part 3, Book Series: Geotechnical, Geological, and Earthquake Engineering, V2, Oliveira CS, Roca A, Goula X (eds)*
- Erdik M, Demircioglu M, Sesetyan K, Durukal E (2005) Assessment of earthquake hazard for Bakirköy, Gemlik, Bandırma, Tekirdağ and Körfez. *WB MEER Project—A3 Component, Microzonation and Hazard Vulnerability Studies for Disaster Mitigation in Pilot Municipalities, Bogazici University, Kandilli Observatory and Earthquake Engineering Research Institute*
- Idriss IM, Sun JI (1992) Shake91, A Computer Program for Conducting Equivalent Linear Seismic Response Analysis of Horizontally Layered Soil Deposits Modified based on the original SHAKE program Published in December 1972 by Schnabel, Lysmer and Seed
- Idriss IM, Boulanger RW (2003) Semi-Empirical Procedures for Evaluating Liquefaction Potential During Earthquakes. *Proc. 11th ICSDEE*, pp 32–56
- Iwasaki T, Tokida K, Tatsuoka F, Watanabe S, Yasuda S, Sato H (1982) Microzonation of Soil Liquefaction Potential Using Simplified Methods. *Proc. 3rd Int. Conf. Microzonation, Seattle* 3: 1319–1330
- Joyner WB, Boore DM (1988) Measurement, characterization, and prediction of strong ground motion. *Earthquake Engineering and Soil Dynamics II—Recent Advances in Ground Motion Evaluation, ASCE Geotech. Spl. Pub.* 20, pp 43–102
- Kavazanjian E Jr, Roth RA, Echezuria H (1985) Liquefaction potential mapping for San Francisco. *J. Geotech. Eng. ASCE* 111(1): 54–76
- Kilic H, Özener PT, Ansal A, Yıldırım M, Özaydın K, Adatepe S (2006) Microzonation of Zeytinburnu Region with Respect to Soil Amplification: A Case Study. *J. Eng. Geology* 86: 238–255
- Papageorgiou A, Halldorsson B, Dong G (2000) Target Acceleration Spectra Compatible Time Histories. *University of Buffalo, Dept. of Civil, Structural and Environmental Eng. NY*, <http://civil.eng.buffalo.edu/engseislab/>
- PEER (2006) Strong Motion Data Bank, <http://peer.berkeley.edu>.
- Seed HB, Idriss IM (1971) Simplified Procedure for Evaluating Soil Liquefaction Potential. *ASCE J. Soil Mechanics Foundations Div.* 97: 1249–1273

- Siyahi B, Durukal E, Altaç Z (2001) Evaluation of strong motion data from the Kocaeli and Düzce, Turkey Earthquakes in view of Arias intensity. Proc. 15ICSMGE Earthquake Geotechnical Engineering Satellite Conference on Lessons Learned from Recent Strong Earthquakes, Istanbul, pp 189–194
- Todorovska MI (1998) Quick reference liquefaction opportunity map for a metropolitan area. Proc. 3rd ASCE Speciality Conf. on Geotech. Earthquake Eng. Soil Dynamics, ASCE Spl. Pub. No., 75, 1: 116–127
- Travasarou T, Bray JD, Abrahamson NA (2003) Empirical attenuation relationship for arias intensity. Earthquake Eng. Structural Dynamics 32: 1133–1155
- Youd TL, Idriss IM, Andrus RD, Arango I, Castro G, Christian JT, Dobry R, Finn WDL, Harder LF Jr, Hynes ME, Ishihara K, Koester JP, Liao SSC, Marcuson WFIII, Martin GR, Mitchell JK, Moriwaki Y, Power MS, Robertson PK, Seed RB, Stokoe KHII (2001) Liquefaction Resistance of Soils: Summary Report from the 1996 NCEER and 1998 NCEER/NSF Workshops on Evaluation of Liquefaction Resistance of Soils. ASCE J. Geotech. Geoenvironmental Eng. 127(10): 817–833

CHAPTER 5

A REVIEW OF LARGE-SCALE TESTING FACILITIES IN GEOTECHNICAL EARTHQUAKE ENGINEERING

Ahmed Elgamal¹, Kyriazis Pitilakis², Dimitrios Raptakis³, Jacques Garnier⁴, SP Gopal Madabhushi⁵, Artur Pinto⁶, Jamieson Steidl⁷, Harry E Stewart⁸, Kenneth H Stokoe⁹, Fabio Taucer¹⁰, Kohji Tokimatsu¹¹, and John W Wallace¹²

¹ *Dept. of Structural Engineering, University of California, San Diego, USA*

² *Dept. of Civil Engineering, Aristotle U of Thessaloniki, Greece*

³ *Dept. of Civil Engineering, Aristotle U of Thessaloniki, Greece*

⁴ *Soil Mechanics and Site Survey Div., LCPC, Bouguenais, France*

⁵ *Reader in Geotech. Eng. & Asst. Director (Schofield Centre) Trumpington St, Cambridge, UK*

⁶ *ELSA Laboratory, IPSC, Joint Research Center, Ispra (VA), Italy*

⁷ *Associate Research Seismologist, University of California at Santa Barbara, Santa Barbara, USA*

⁸ *Civil and Environ. Eng., Cornell University, Ithaca, New York, USA*

⁹ *Civil, Architectural and Environmental Eng., U Texas at Austin, Austin, Texas, USA*

¹⁰ *ELSA Laboratory, IPSC, Joint Research Center, Ispra (VA), Italy*

¹¹ *Dept. of Architecture and Building Eng., Tokyo Institute of Tech., Japan*

¹² *Civil and Environ. Eng., University of California, Los Angeles, USA*

Abstract. In this new century, new large-scale testing facilities are being developed worldwide for earthquake engineering research. Concurrently, the advances in Information Technology (IT) are increasingly allowing unprecedented opportunities for: (i) remote access and tele-presence during extended remote off-site experimentation, (ii) hybrid simulation of entire structural systems through a multi-site experimentation and computational overall model, and (iii) near-real time data archival, processing and sharing. In this paper, a representative set of such state-of-the-art testing facilities is presented. Attention is focused on geotechnical earthquake engineering applications including instrumented test sites, mobile and large-scale testing laboratories, and centrifuge testing. Using such facilities, a number of collaborative research efforts are also included for illustration. The potential for further worldwide joint activities is finally highlighted.

1. Introduction

Over the last 50 years, earthquake engineers have relied on data from laboratory experiments and from post-earthquake reconnaissance efforts to gain knowledge and confidence

in our numerical analysis techniques and our design procedures. Recognizing the scarcity of reconnaissance data and the need for elucidating the response mechanisms associated with actual structures, full-scale and near full-scale experimentation is becoming an essential component of our research procedures. Such relatively expensive and time-consuming testing approaches, in turn motivate collaboration and the undertaking of research by expert teams covering experimentation, computational analysis/validation, and for the state of practice implications. With the aid of modern IT tools, geographically distributed experimental facilities and researchers are able to work together and capitalize on new and valuable data sets, of high relevance to full-scale seismic response scenarios.

In this paper, the elements and capabilities of a representative set of such world-class experimental facilities is presented. Examples of related collaborative research projects are included for illustration. The facilities are grouped into the categories:

1. Instrumented test sites to monitor ground response, structural response, and the associated soil–structure interaction (SSI) mechanisms. Of such sites, the elements and activities of the Euroseis project in Greece, and the University of California, Santa Barbara (UCSB) George E. Brown Network for Earthquake Engineering Simulation (NEES) sites (Garner Valley and Wildlife Refuge in the USA) are presented.
2. Mobile testing laboratories to exert dynamic excitation in-situ. Such facilities are transportable to any appropriate site and/or structure, where high levels of shaking may be imparted to document the response of full-scale and near full-scale soil, SSI, and structural behaviour. Of such facilities, the NEES shakers at the University of California, Los Angeles (UCLA), and the Vibroseis trucks at the University of Texas at Austin are discussed.
3. Large shake table facilities and large displacement containers provide the option to exert high levels of shaking on full-scale or near full-scale models of ground layers, and SSI scenarios. Foremost among such facilities today are the three-dimensional (3D) E-Defense laboratory in Japan, the NEES Large High Performance Outdoor Shake Table (LHPOST) at the University of California, San Diego (UCSD), and the NEES Large-displacement split container at Cornell University. Elements of these facilities are briefly presented and discussed.
4. Providing convenience and increasing the practical range of testing scenarios, the Centrifuge testing technique has been a resource to elucidate the mechanisms associated with seismic performance of soil and soil–structure systems. In this paper, the facilities at Cambridge in the UK, LCPC in France, and the NEES centrifuge testing seismic capabilities at the University of California, Davis (UCD), and Rensselaer Polytechnic Institute (RPI) are discussed.

A number of related collaborative research efforts will be also highlighted to demonstrate the strong potential of such large-scale research facilities. In this regard, international worldwide collaboration appears to be a critical element in harnessing the power of this new experimentation approach, and the related validation/verification efforts, and associated positive implications for the state of practice.

2. Instrumented test sites

2.1. EUROSEIS PROJECT

EUROSEIS is a large physical laboratory (Test Site), located at a distance of 30 km from Thessaloniki (at the epicentral area of the M6.5 1978 earthquake), in northern Greece (Figure 5.1). About 150 seismic events have been recorded. Of those, about five events are considered of moderate strength with peak acceleration of as much as 130 gals. The remainder are weak tremors with peak accelerations of about 50 gals. The EUROSEIS-RISK project encompasses integrated experimental and theoretical research studies in seismology, applied geophysics, engineering seismology, earthquake engineering, soil dynamics, and structural engineering. Specific topics include seismic hazard assessment, monitoring of seismicity (Table 5.1), design of two-dimensional (2D) and 3D soil models for site response evaluation, 2D/3D theoretical computations, site effects, soil–structure interaction (SSI) effects in the presence of yielding buildings or bridges, and validation of retrofitting techniques (<http://euroseis.civil.auth.gr>, Euroseistest 1993–1995, Euroseis-mod 1996–1998, and EUROSEISRISK Seismic 2002–2005).

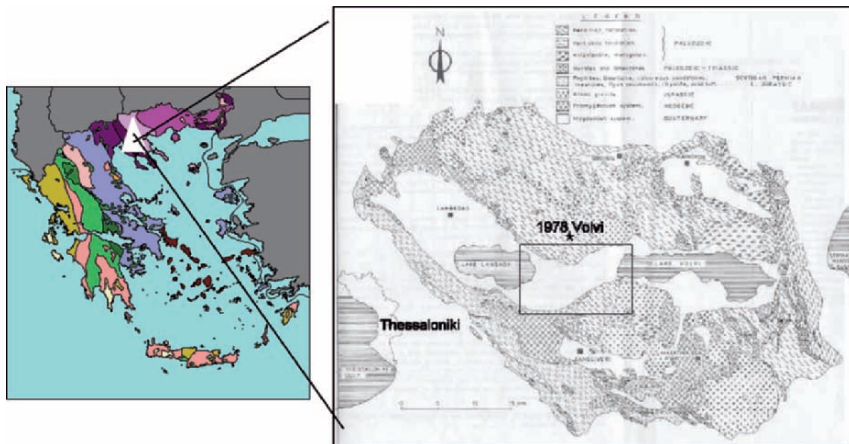


Fig. 5.1. Location of the test site in Greece, and Tectonic sketch of the Mygdonian basin together with the investigated area (box) and the epicentre of the 1978 $M_s = 6.5$ Volvi earthquake (shown by the star)

Table 5.1. Statistics on earthquakes in the vicinity of the test-site over the last 10 years

Magnitude	>7	6 to 7	5 to 6	4 to 5	3 to 4
Hypocentral distance					
<20 km				4	31
20 to 50 km				5	
50 to 100 km			1		
>100 km	2	5			

2.1.1. Project objectives

The main objectives during the time-period of the test-site operation have addressed the following issues:

- Definition of the geologic structure of the basin using geophysical and geotechnical studies in order to fully identify both dynamic properties and geometry of the main soil formations.
- Studies of seismicity, seismic hazard, and attenuation of strong ground motion using a large variety of approaches and techniques.
- Empirical and theoretical studies of site effects with emphasis on the development as well as the validation of existing and new numerical codes for the simulation of ground motion.
- Experimental and numerical dynamic behaviour analysis of soil–foundation–structure interaction for a six-storey model R/C building and a model bridge.
- Contribution to the ongoing elaboration of the new generation of Eurocode 8.
- Creation of a database of high quality and well constrained data easily accessible through Internet that may be used to better understand the complex phenomena, for the validation and improvement of existing codes in all aspects of earthquake engineering.

2.1.2. General description of the test site

Geometric configuration. The area of the basin is about 15 km × 8 km (= 120 km²) in size. The free surface is almost flat with exceptions at the northern and southern boundaries where a series of hills and mountains define the physical limits of the basin. Figure 5.2 shows a characteristic 2D cross-section at the centre of the basin and Figure 5.3 shows a map of the area of interest. In both figures, the location of sensor stations is depicted together with some details of the geologic structure (layering, geologic background, tectonic evidences, physical limits, etc.). The sediments-bedrock boundaries together with some important ruptures and seismic faults inside the basin form a rather complex but at the same time very common geologic structure.

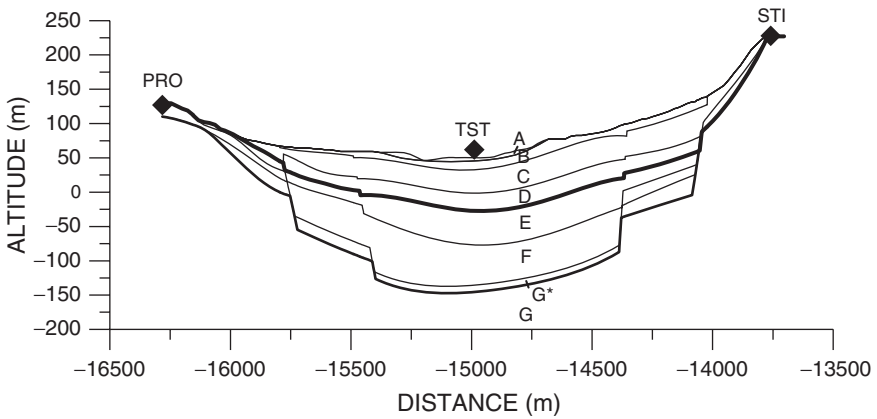


Fig. 5.2. 2D N-S cross-section at the centre of the valley. A to G represents different soil and rock (G) categories



Fig. 5.3. Map with the surface accelerographs (green rectangles) and the geologic background

Geological conditions. Numerous surveys on geology, geomorphology, tectonic, seismicity, water and aquifer level as well as geotechnical and geophysical surveys, GPS geodetic monitoring, etc., have been performed during the last 40 years. In the last 15 years (since the beginning of the project in 1993) a series of well oriented geotechnical and geophysical studies have contributed to the knowledge of the 3D complex structure of the basin.

The geology is composed of two main sedimentary geologic systems and the crystalline basement. The sedimentary units, Mygdonian and Promygdonian are differentiated by

their corresponding geological age. The first system was formed in the initial (older) Promygdonian basin during the Quaternary and consists of four successive formations such as conglomerates, sandstones, silt/sand sediments, and red clay beds. The second one was formed in the latter (younger) Mygdonian basin during the Neogene and consists mainly of mixtures of sands, silts, and clays. Bedrock depth inside the basin ranges from about 200 to 420 m. Bedrock is deeper in the western part of the basin rather than the eastern part (~200–300 m). At the northern and the east-southern boundaries of the basin, a rather fractured and weathered outcrop rock appears at the free surface giving the opportunity to use it as reference in site response studies. Water table ranges from 2 to 3 m (at the centre) down to 18 to 20 m (at the edges).

Geotechnical and geophysical conditions. Among the principal goals of Euroseistest project was the accurate assessment of thickness, stiffness, and attenuation of the soil materials (Pitilakis et al., 1999; Kudo et al., 2002). All in-situ (drillings, sampling, SPT and CPT) and laboratory (cyclic triaxial and resonant column tests, and other classical laboratory tests) geotechnical surveys together with geophysical (seismic prospecting, PS logging, electrical soundings and tomographies, aeromagnetic and gravimetric measurements) surveys were used. The entire area of the basin was covered to derive both dynamic properties and geometry of the main geologic formations, in terms of site response requirements. For this reason, an important campaign of field measurements was carried out mainly in two stages.

In the first stage, the geophysical campaign concerned the NS cross-section and was mainly conducted in the period 1993–1997 using seismic methods such as surface wave inversion (SWI), P and SH refraction (REF), crosshole and downhole (CH, DH) tests, in order to get both geometry and properties of a large volume of soil formations. Few electrical and magnetic soundings were also performed. In addition to the seismic prospecting, a detailed geotechnical survey was performed including drillings, sampling, ground water table measurements, SPT and CPT, and cyclic triaxial and resonant column (RC) tests. Additional boreholes were drilled for the installation of downhole 3D accelerometers, one pore-pressure sensor, and for special experiments using underground explosions.

In the second stage, during the period 2001–2004, additional CPT tests were performed at more than 20 sites along the EW direction together with long scale refraction measurements. These experiments covered a distance of about 20 km using forward and reverse long seismic profiles. Underground big explosions inside boreholes were used as seismic sources. The receivers were 3D accelerographs and seismographs installed at inter-distances between 60 and 130 m. At the borders of the basin, a large number of electrical tomographies of about 1.0 km each and soundings were also performed in order to get information about the shape of the edges. To get a systematic and complete image of the characteristics of the basin's structure, a large number (more than 30) of well distributed ambient noise measurements (SPAC method) were also performed in order to get vertical shear-wave velocity Vs profiles (down to the bedrock top surface). For all soil formations,

specific (shear modulus–shear strain–damping) G - γ - D curves have been also proposed describing the dynamic soil properties for linear elastic and nonlinear conditions.

The soil-layering from surface to bedrock presents a successive increase of the stiffness with V_s velocities from 90 to 450 m/s (mixtures of recent fills, loose sandy-sands, and soft clays with gravels at a thickness of some decades of metres) to 500 to 850 m/s (redbeds from stiff clays with gravels-stones, conglomerate and sandstones for a thickness larger than 100 m). The velocities and their variation with depth are not uniform in the whole area of the basin. This knowledge resulted from the synthesis of a great number of data (drillings, sampling, geophysical–geotechnical, passive (noise) and actual surveys, empirical transfer functions, parametric modelling, etc.). Finally, the 3D soil model of the Mygdonian sedimentary basin has a rather asymmetrical semi-cylindrical shape, which deepens at the open edges with different rates of deepening and without very strong immersions. Table 5.2 presents the classified basic soil formations met in the whole area of the basin together with the V_p and V_s velocities.

2.1.3. Instrumentation

At the broader area of the basin, a large permanent seismological network with more than 15 broadband stations operates continuously since 1981, providing useful information for the seismicity recorded in the whole Northern and Central Greece including the north Aegean Sea as well as the surrounding northern countries. This array operates under the responsibility of AUTH (GL). Additional national permanent seismological and accelerographic arrays with more than 80 instruments each (from National Observatory of Athens and ITSAK) provide full catalogues of weak and strong earthquakes in Greece.

Table 5.2. Geophysical parameters and soil description for the basic soil formations. Formations A, B, C, and D are included in the upper (Mygdonian) system and E, F, G*, and G in the lower one (Promygdonian). The characteristic V_s velocities of both main systems and the bedrock basement are also given as average velocities of the defined sub-layers from the top down to the bedrock

Layer	Description	V_s (m/s)	V_p (m/s)	V_{pw} (m/s)
A	Silty–clayey sand	95–150	220–450	
B	Silty sand and sandy clay	150–250	300–350	900–1650
C	Marly silt and silty sand	250–400	400–800	900–2200
D	Marly sandy clay and clayey silt	400–550		1650–1900
E	Clayey silt-sand and sandy clay	560–650		2200–2750
F	Clayey silt-sand and sandy clay	600–900		2200–2750
G*	Weathered Schist	1000–1700		3000–3500
G	Gneiss	2300–2600		4300–4900

Inside the sedimentary basin, a well designed 3D permanent strong motion array with an X shape and almost equidistant stations covers its central part. The array covers a surface of about $6 \text{ km} \times 8 \text{ km}$. At the intersection-point a dense downhole vertical array of six 3D accelerometers (at depths of 0, 21, 40, 72, 136, and 196 m) connected to the same 18 channel acquisition system, gives the third dimension of this array. At the outcrop rock site, operates a 2–3D sensor downhole vertical array. All the 20 instruments (surface and downhole) of the array (Figure 5.4) are digital accelerographs with A/D converters larger than 18 bits, supported by GPS, permanent remote monitoring and power supply.

In the middle of the basin, very close to the downhole array site, a system of well instrumented structural models (six-storey R/C model 1:3 building and a pier bridge) are constructed and instrumented operating on a permanent basis (Figure 5.5), providing data on the structural behaviour, the soil–structure interaction and the wave field generated around the structures. The permanent accelerograph array comprises Mt. Whitney, K2, Etna, Guralp CMG-5 instruments.

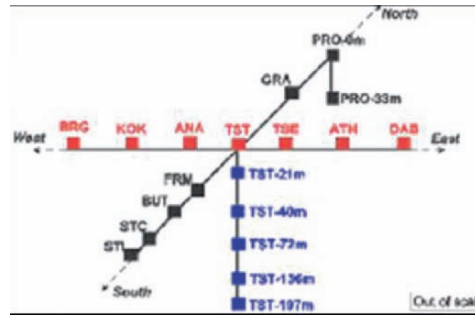


Fig. 5.4. 3D sketch of the permanent accelerograph network



Fig. 5.5. Experimental field facilities to study SSI effects and the behaviour of RC. structures (Instrumented five-storey RC building with masonry in fills and a pier bridge on surface foundation, models' scale 1:3)

2.1.4. Main scientific and engineering outcomes

The following items present a short summary of major scientific and engineering achievements for many topics in earthquake engineering, engineering seismology and seismology, taking advantage of a multidisciplinary field and laboratory experiment using the largest infrastructure in Europe (for further details, please see Raptakis et al., 1998, 2000, 2005; Chávez-García et al., 2000, 2002; Margaris and Hatzidimitriou, 2002; Moczo et al., 2002, 2004; Parolai and Bard, 2003; Guéguen and Bard, 2005; Makra et al., 2001, 2002, 2005; and Manos et al., 2005).

- Faulting patterns from stress-field analysis and neotectonic information.
- Optimization of algorithms for earthquake relocation.
- Deterministic and seismic probabilistic seismic hazard assessment for the broader EUROSEISTEST area and related scenarios of strong ground motion.
- Local attenuation relations and regional attenuation kappa-values determination.
- Source parameter estimation of events that triggered the strong motion array.
- Evaluation of liquefaction susceptibility at several sites based on CPT measurements.
- More than 150 Vs profiles defined from passive (noise) and active (explosives) techniques in the whole area of the basin.
- Synthesis of all past and new data sets to get a reliable 3D model.
- Definition of the 3D geological model of the Mygdonian basin.
- Determination of 3D velocity model of the broader Mygdonian area for site effects studies.
- Empirical evaluation—using all available techniques—of site effects based on noise and earthquake recordings for the whole basin.
- Theoretical analysis of site effects using different 1D, 2D, 3D soil models and modelling methods.
- Confrontation with empirical data and results in both time and frequency domains.
- Development of improved numerical codes for 2D and 3D simulation of ground motion.
- Validation of new and existing numerical models with recorded ground motion data.
- Creation of the seismic waveform database.
- Implications of the results of site effect analysis in complex media (valleys and basins) in seismic codes.
- Investigation of the SSI effects with experimental and numerical approaches.

- Evaluation of existing finite difference (FD), FE and boundary element (BE) codes for site and SSI effects.
- Investigation of the beneficial or detrimental role of SSI effects in presence of yielding of the superstructure lying over a very soft soil.
- Examination of the nature and the effect of the waves transmitted by the oscillation of the superstructure to the foundation level and the surrounding soil.
- Scrutinize the effect of foundation flexibility (i.e. footing/single cast-in-drilled-hole piles towards pile group) on the extent of dynamic SSI phenomena.
- Identification of possible code implications of soil–structure interaction phenomena.

2.2. UCSB NEES GARNER VALLEY AND WILDLIFE TEST SITES (DR. JAMIESON STEIDL, PI)

At the University of California, Santa Barbara (UCSB), the Garner Valley and the Wildlife refuge sites have been instrumented and are available for research (<http://nees.ucsb.edu/>). A brief description is included below (material below is extracted from the website <http://nees.ucsb.edu/>).

2.2.1. Soil and seismic characteristics at Garner Valley

The NEES field site in the Garner Valley (Figure 5.6) is very well suited to the study of soil–foundation–structure interaction and liquefaction. The area is located near several active faults on low density alluvial soil with a near surface water table. The site has been thoroughly characterized recently through borehole geotechnical tests and in other studies over the last 10 years.

Additionally, the valley bedrock is basin shaped and late arriving surface waves have been observed (likely Love waves), travelling from the edge of the basin. The torsions generated on foundations by Love waves are considered to be especially destructive. Thus, this field site provides a possibility to observe Love waves on a fully instrumented structure.

2.2.2. Geologic conditions

The upper 18–25 m consist of soil rich in organics and alluvium. Soil types present are silty sand, sand, clayey sand, and silty gravel. There is a gradual transition from alluvium



Fig. 5.6. Garner Valley SFSI field site and SFSI structure

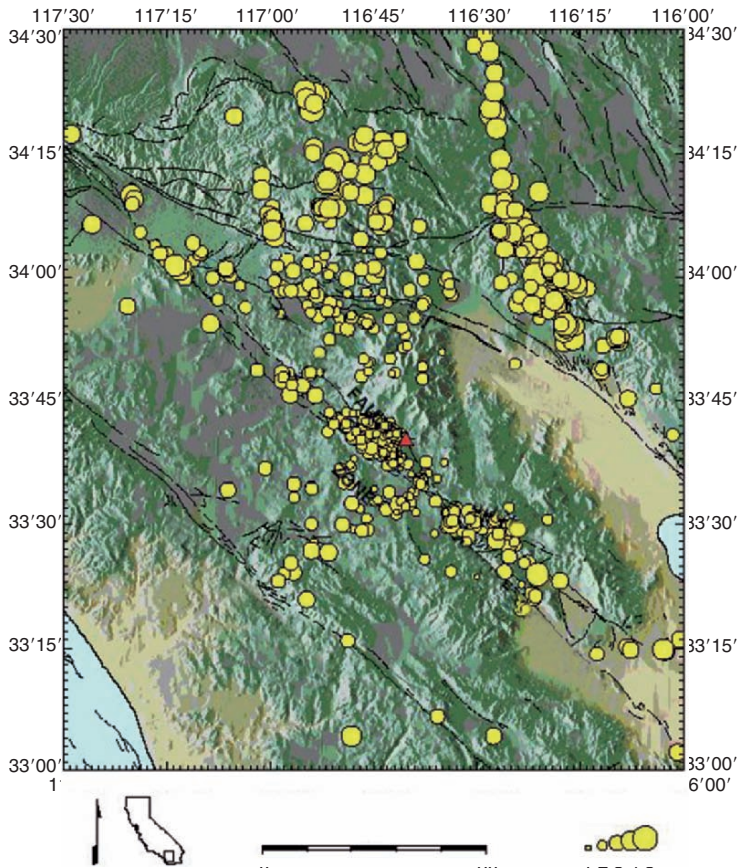


Fig. 5.7. Location of Garner Valley (red triangle), recorded seismicity (circles), shaded relief, and faults (black lines)

to decomposed granite from 18 to 25 m. Decomposed granite consisting of gravelly sand exists between 25 and 88 m. At 88 m the contact with hard competent bedrock is reached. The bedrock is granodiorite of the Southern California Peninsular Ranges batholith. The water table fluctuates at the Garner Valley site depending on the season and rainfall totals. In the wetter years the water table is at, or just below the surface in the winter and spring months. In the summer and fall months, or the entire dry years, the water table drops to 1 to 3 m below the surface.

2.2.3. Garner Valley SFSI structure

The Garner Valley Soil–Foundation–Structure Interaction (SFSI) test facility is composed of a medium-scale reconfigurable steel-frame structure founded on a rigid massive



Fig. 5.8. Garner Valley site during a UTexas collaborative study using T-Rex

concrete slab on grade. The superstructure is of a size appropriate for testing on one of the NEES shake tables. Shakers can be mounted on the roof for active experiments to complement passive earthquake monitoring. The SFSI facility was designed to study the passage of waves through the soil column below the structure, up through the foundation and into the structure. Often the observations of ground shaking recorded on the foundation of structures is not the same as that recorded on open ground due to the interaction between the soil and foundation. Understanding these interactions at a relatively simple site using a simple structure is a primary purpose of this facility. In addition, using a remotely operable shaker attached to the roof of the structure, temporal changes in the structures response can be monitored. Environmental factors like temperature and the level of saturation of the near-surface soil can have an effect on its response.

2.2.4. Wildlife refuge liquefaction field site

This liquefaction field site has been thoroughly characterized through geotechnical bore-hole samples, as was a nearby site that was previously studied by the USGS. Located in California's Imperial Valley the Wildlife Liquefaction Array (WLA) field site records numerous earthquakes daily in this seismically active area at the southernmost terminus of the San Andreas Fault system.

WLA is located on the west bank of the Alamo River 13 km due north of Brawley, California and 160 km due east of San Diego. This area has been frequently shaken by earthquakes with six events in the past 75 years generating liquefaction effects within 10 km of the WLA site.



Fig. 5.9. Wildlife refuge instrumented site

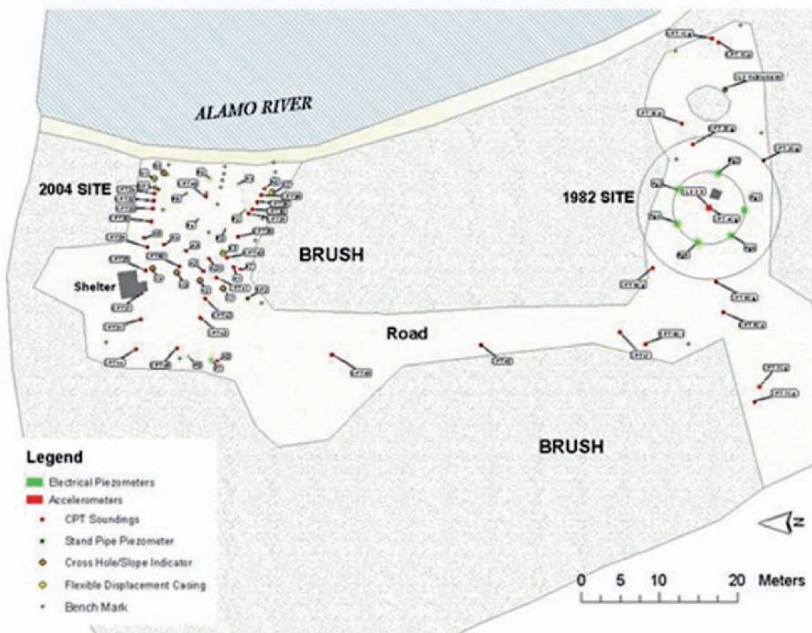


Fig. 5.10. The liquefaction field site thoroughly characterized through geotechnical borehole samples, and the nearby site previously studied by the USGS

Seismic records from the WLA site provide essential information about the liquefaction phenomenon. In particular, predicting the ground response, ground failure, and liquefaction effects from earthquakes using computer models requires such an instrumented site to validate the simulation methods against real observations.

Researchers are using earthquakes that occur on a daily basis near this site, as well as active testing using mobile shakers to try to better understand how the near-surface geologic conditions affect the ground shaking at this location.

3. Mobile laboratories

3.1. NEES FACILITIES AT UCLA (<http://nees.ucla.edu>, PROF. JOHN WALLACE, PI)

NEES at UCLA includes mobile dynamic excitation shakers and a fully mobile data acquisition laboratory. Capabilities include satellite Internet transmission as well (thus allowing for tele-participation). In addition, a CPT truck is available for estimation of soil properties in-situ (material below is extracted from the website <http://nees.ucls.edu>).

3.1.1. Eccentric mass shakers

Three eccentric mass shakers have been developed to enable forced vibration testing of full-scale buildings.

1. MK-14A: An omni-directional eccentric mass vibrator capable of low frequency, high amplitude harmonic loading. It has an operating frequency range of 0.1–4.2 Hz and maximum load of 20 kips.
2. MK-15: Two uni-directional eccentric mass vibrators (Figures 5.11 and 5.12) with a wide frequency range (0–25 Hz) and large force capability (100 kips).

For all three eccentric vibrators (MK-14A-5500 and MK-15's), a wireless control option was added to enable the operator (in the mobile command centre) to remotely control the shakers. Furthermore, synchronization between the MK-15 shakers is possible with the use of the new Vector motor drives. Two or more vibrators, spaced apart on a structure, can provide the tested structure with torsional as well as translational forcing, or



Fig. 5.11. MK-15 eccentric mass shaker during UCSD Elliot Field testing



Fig. 5.12. nees@UCLA team at the Four Seasons building in Sherman Oaks, CA



Fig. 5.13. UCLA NEES linear inertial shaker

enhance the response of one particular mode over another by force appropriation, which can be very helpful in distinguishing between closely spaced modes of vibration.

The three eccentric mass vibrators are useful for testing a wide range of structural systems, including moderate-scale destructive dynamic testing.

3.1.2. Linear shaker

The linear inertial shaker (Figure 5.13) capable of broadband excitation was developed jointly by Anco Engineers, dSPACE Inc., and Sysendes. The shaker controllers allow either force or displacement control. The nominal performance specifications for the linear shaker are a peak force amplitude of 15 kips, 30 inch stroke, and 90 gpm servovalve capacity.

3.1.3. Cone penetration testing truck

The UCLA NEES equipment portfolio includes a Hogentogler cone penetration testing truck (Figure 5.14), equipped with a seismic-piezcone to characterize soil consistency, pore water pressure, and shear-wave velocities. The rig has a 20-ton hydraulic push capacity. The rig weight is approximately 6 tons, and side augers provide additional reaction forces. The rig is equipped with 30 m of rod length. A fully automatic 5-channel ESFCS data acquisition system records measurements of cone tip resistance, sleeve friction, probe inclination, pore water pressure, and shear-wave velocities.



Fig. 5.14. Cone penetration testing truck

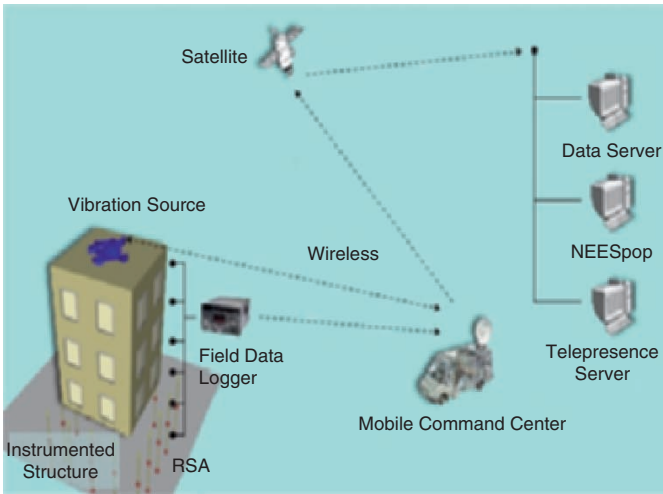


Fig. 5.15. UCLA NEES Satellite Transmission System

3.1.4. Satellite system

The satellite system service is provided by PSSI (Figures 5.15 and 5.16). It boasts a 1.8 m dish with GPS positioning and automatic satellite tracking for ease of deployment. Satellite modems, amplifiers, GPS navigation equipment, etc. are all housed in the equipment rack in the mobile command centre.

It provides for unlimited 128 Kbps bandwidth connectivity anywhere in the world with a view of the southwestern sky. Bandwidths of 512 Kbps, 768 Kbps, 1 Mbps, and



Fig. 5.16. Mobile command centre

1.544 Mbps (T1) are available on-demand at any time. The data that is consolidated in the mobile command centre is transmitted via satellite to a downlink hub in Las Vegas where it then travels over the commodity internet to the NEESpop server on the Campus-LAN.

3.2. NEES FACILITIES AT THE UNIVERSITY OF TEXAS (<http://nees.utexas.edu/>, PROF. KENNETH STOKOE II, PI)

NEES at the University Texas is an equipment site that specializes in dynamic field testing using large-scale shakers. The equipment includes three mobile shakers that have diverse force and frequency capabilities, an instrumentation van that houses state-of-the-art data acquisition systems, and a large collection of field instrumentation. The field equipment can be used in a variety of applications, including shear-wave velocity characterization, liquefaction testing, geophysical testing, and dynamic testing of structures. During experiments, the instrumentation van can connect to the NEESgrid via a satellite modem allowing offsite access to both live video and data (material below is extracted from the website <http://nees.utexas.edu>).

3.2.1. Cruiser (instrumentation van)

This instrumented van (Figure 5.17) was developed in house as a mobile command centre, designed to be able to get to and operate in remote locations for extended periods of time. It provides power, communication, video uplink, and data streaming capabilities at the experiment site.



Fig. 5.17. Ute van



Fig. 5.18. Ute Thumper

3.2.2. *Thumper*

Intended as both a high frequency source (Figure 5.18) with useful force up to 500 Hz and as an urban source built on top of a standard Ford 650 chassis. Total weight: is 22,000 lbs (9,990 kg) with vibration orientations possible in the vertical and horizontal directions. Peak force of about 6000 lbs becomes stroke and flow limited at 17 Hz and falls off above approximately 225 Hz due to valve limitations.

3.2.3. *T-Rex (tri-axial vibrosies)*

One of only a few large vibrosies (Figure 5.19) which provide axis transformation between vertical, inline, and cross-line at the push of a button (Buggy-mounted vibrator). Possible vibration orientations in the vertical, transverse, or longitudinal directions. Cone penetrometer functionality has been added to rear of vehicle. Peak force: of 60,000 lbs (267 kN) in the vertical direction, and 30,000 lbs (134 kN) in the horizontal direction. Peak force frequency range is 12 Hz–180 Hz (vertical) and 5 Hz–180 Hz (horizontal).

3.2.4. *Liquidator (low frequency vibrosies)*

The only large vibrosies (Figure 5.20) designed to provide useful force below 1 Hz which enables low frequency liquefaction studies (Buggy-mounted vibrator). Vibration can be imparted in the vertical or the horizontal directions. Cone penetrometer functionality has been added to rear of vehicle. Peak force: is 20,000 lbs (89 kN), with peak force at 1 Hz: of 10,000 lbs (45 kN).



Fig. 5.19. UTexas T-Rex (tri-axial) vibroseis



Fig. 5.20. Liquidator (low frequency) vibroseis

3.2.5. Representative collaborative research project

A collaborative project (Figure 5.21) led by Professor Sharon Wood (U. Texas) addressed the important topic of improved knowledge of soil–foundation–structure interaction (SFSI). It also provided an ideal opportunity for demonstrating and challenging the new NEES model for conducting research. The prototype structure selected for investigation is a continuous bridge structure. The dynamic response of this structure is influenced by the ground motion and the nonlinear characteristics of the soil, foundation, and superstructure. It is impossible to determine which will control the system response a priori. It is also impossible to test a single physical model of the prototype structure and reproduce all key aspects of the system. Therefore, a series of four complementary physical models are to be tested at four different sites: (1) centrifuge tests of individual bridge bents to evaluate the nonlinear response of the soil and foundation system (<http://nees.ucdavis.edu>), (2) dynamic field tests of individual bents using mobile shakers (Figure 5.22) to evaluate the response of the soil, foundation, and structure (<http://nees.utexas.edu>), (3) shaking table tests of a three-span model to evaluate the nonlinear response of the superstructure subjected to bi-directional, incoherent support motion (<http://nees.unr.edu>), and (4) laboratory tests of large-scale individual columns to evaluate strength degradation in flexure and shear (Purdue University).

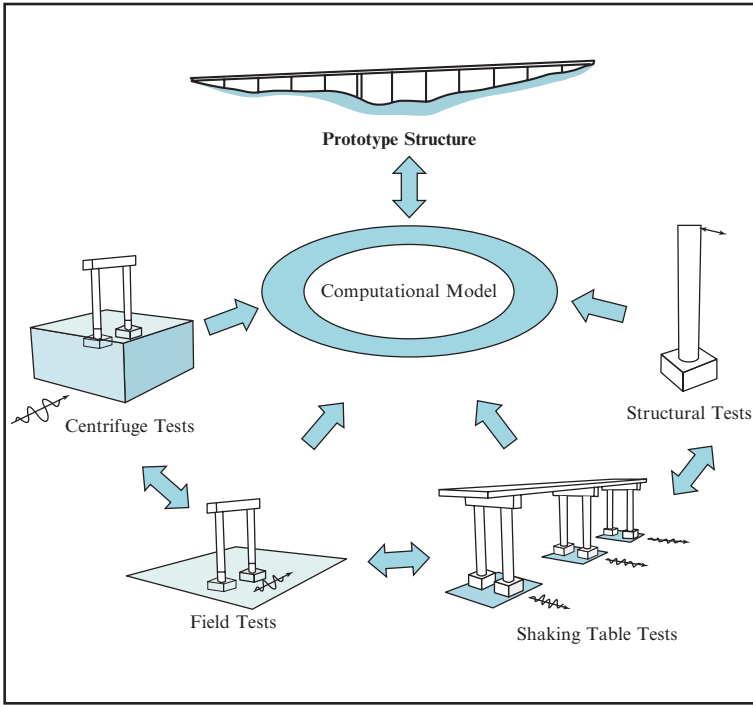


Fig. 5.21. Scope of research project



Fig. 5.22. Field test model construction and dynamic excitation (<http://nees.utexas.edu>)

Computational simulation also has a central role in the project for relating the individual component and system experiments. Simulation is needed to design and interpret the individual experimental tests. An important deliverable of the project is improved computational models for SFSI, calibrated from the experiments, in a form available for community use.

4. Large-scale testing facilities

4.1. NEES FACILITIES AT CORNELL (<http://nees.cornell.edu>, PROF. HARRY E. STEWART, PI)

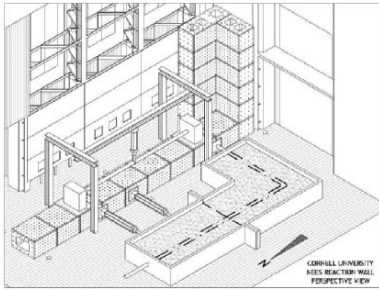
The Cornell Large-Displacement Facility is a unique, world-class resource for research, education, and outreach focused on underground lifeline response to large ground deformation and the seismic performance of highly ductile above-ground structures using advanced materials and construction (material below is extracted from the website <http://nees.cornell.edu>).

Figure 5.23a shows a 3-D perspective view of the Cornell facility to scale, showing a split test basin similar to one previously used for large-scale experiments. The split basin in the figure involves approximately 54 m^3 of soil, thus illustrating the size of test that can be run using the full capacity of soil stored in the facility soil storage bins (55 m^3). Large-displacement hydraulic actuators are used to move the test basins. Reaction for the actuators is provided by a modular reaction wall, which is heavily post-tensioned and anchored to bedrock with a system of rock bolts.

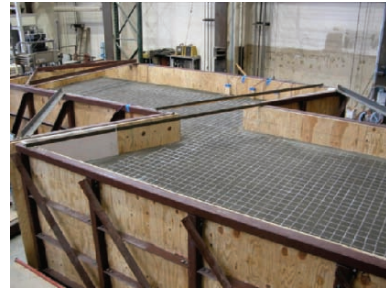
Figure 5.23b shows a new split test basin with a 65° fault crossing. One section of the basin is fixed to the low section of the modular reaction wall and the other movable. Buried in the test basin is a nominal 400-mm-diameter, IPS, HDPE pipe. The pipe section is approximately 11 m long and fixed at the test basin ends. There is roughly 1.2 m of soil cover above the pipe. The movable basin can be displaced 1.2 m along the 65° split, placing the pipe in tension and severe bending. This experiment engages over 100 tons of soil.

Figure 5.23c shows an overhead view of the test basing after movement. The deformed shape of the pipeline is sketched on the photo. In the figure the zones of active and passive soil movement can be seen close to the simulated fault. Figure 5.23d shows an alternate view of the test basing, showing the zones of soil movement. Experiments in the test basing also have been completed with a nominal 152-mm-diameter steel pipe and a nominal 254-mm-diameter HDPE pipe section.

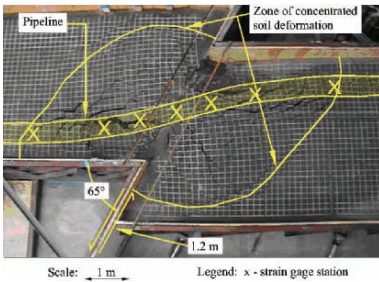
Large-scale experiments also were successfully completed to evaluate the effects of earthquake-induced ground rupture on welded steel pipelines with elbows. Figures 5.23e and 5.23f show two experimental basins with a total of 60-65 metric tons of soil that were displaced 1 m relative to each other to simulate the type of abrupt displacement generated by liquefaction-induced lateral spread, landslides, and surface faulting.



a) Perspective and Schematic Views of Large-Scale Test Facility



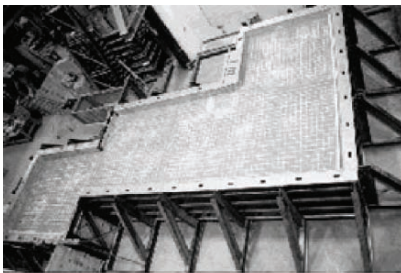
b) Overhead View of Simulated Fault Rupture and HDPE Pipeline Deformation (Image courtesy of N. Olson with photo taken at Cornell NEES Equipment Site)



c) Overhead View of Simulated Fault Rupture and HDPE Pipeline Deformation (Image courtesy of N. Olson with photo taken at Cornell NEES Equipment Site)

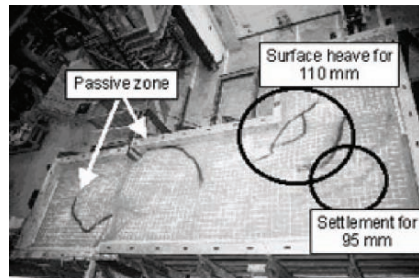


d) Active and passive soil zones following fault offset.



(a) Before experiment

e) Overhead view of test basin before the experiment (NOTE: Basin is over 10m long, max. 5m wide and 1.2m deep)



(b) After experiment

f) Overhead view of test basin after the experiment (NOTE: Basin is over 10m long, max. 5m wide and 1.2m deep)

Fig. 5.23. The NEES Cornell Testing Facility

4.2. UCSD SHAKE TABLE (<http://nees.ucsd.edu>, PROF. JOSE' RESTREPO, PI)

The University of California, San Diego (UCSD) Large High Performance Outdoor Shake Table (LHPOST) is being developed at the Englekirk Field Station, a site located 15 km away from the main UCSD campus. The shake table, acting in combination with equipment and facilities separately funded by the California Department of Transportation (Caltrans), which include a large laminar soil shear box (inside dimensions of the box are 6.71 m long by 2.90 m wide by as much as 5 m in height) and two refillable soil pits, represents a one-of-a-kind worldwide seismic testing facility (Figure 5.24).

This unique facility enables next generation seismic experiments to be conducted on very large structural and soil–foundation–structure interaction (SFSI) systems such as full-scale buildings, single and multiple column bridge bents in a laminar soil box, utility/lifeline structures such as electrical sub-stations, nuclear containment casks, and seismic isolation systems. Moreover, the proximity of a soil pit to the UCSD LHP Outdoor Shake Table will allow hybrid shake table-soil pit experiments to be conducted. UCSD is convinced that this innovative piece of NSF equipment in conjunction with the Caltrans SFSI facility will add unique testing capabilities to NEES and consolidate the leadership of the NEES collaboratory as a worldwide predominant earthquake testing consortium.



(a) Facility layout including shake table and adjacent large soil pit



(b) 7-Storey Shear building model on shake table



(c) Bridge abutment soil model construction on shake table



(d) Close-up of soil container on shake table during Model construction

Fig. 5.24. UCSD NEES Large High Performance Outdoor Shake Table (LHPOST)

The NEES/LHP Outdoor Shake Table is a 7.6 m wide by 12.2 m long single Degree-of-Freedom (DOF) system with the capability of upgrading to 6-DOF. The specifications for the first phase of the facility are a stroke of ± 0.75 m, a peak horizontal velocity of 1.8 m/s, a horizontal force capacity of 6.8 MN, an overturning moment capacity of 50 MN-m for a 400 ton specimen, and a vertical payload capacity of 20 MN. The testing frequency range will be 0–20 Hz. Although this table is not the largest of its kind in terms of size in the world, the velocity, frequency range, and stroke capabilities make it the largest table outside Japan and the world's first outdoor shake table. The facility will add a significant new dimension and capabilities to existing United States testing facilities with no overhead space and lifting constraints.

4.3. JAPAN E-DEFENSE SHAKE TABLE

The E-Defense, one of the largest shaking table facilities in the world (Figure 5.25), was opened in 2005, commemorating the tenth anniversary of the 1995 Kobe earthquake. The shaking table facility is located at the Hyogo Earthquake Engineering Research Center (E-Defense) of the National Research Institute for Earth Science and Disaster Prevention (NIED).

The E-Defense shaking table platform has a dimension of 15 m long and 20 m wide. It is supported on fourteen vertical hydraulic jacks and connected to ten horizontally hydraulic jacks, five each in both NS and EW directions, and can move in three directions. It has a payload capacity of 1200 tons with maximum accelerations, velocities, and displacements of 9 m/s^2 , 2 m/s, and 1 m in both horizontal directions and of 15 m/s^2 , 0.7 m/s, and 0.5 m in the vertical direction. About 900 channels of amplifiers and AD converters can be mounted under the shaking table platform for monitoring various outputs during shaking.

4.3.1. Recent shaking table tests at E-Defense

Large shaking table tests with a soil–pile–structure model were conducted to investigate the following:

1. Inertial and kinematic effects on pile stress and failure.
2. Earth pressure acting on embedded foundation.

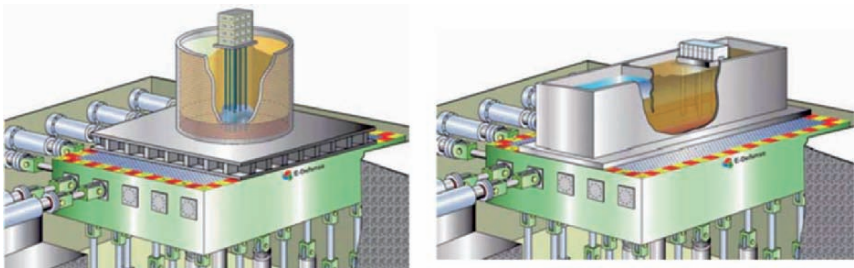


Fig. 5.25. E-Defense Shake Table schematic with planned liquefaction SFSI experiments in a 2D circular laminar container, and a waterfront pile-supported structure

3. Stress states in soil and its effect on sub-grade reaction development.
4. Deformation and failure mode of pile foundations under near prototype scale.

To investigate inertial and kinematic effects on failure and deformation mode of piles during three-dimensional shaking, physical model tests were conducted (Tabata and Sato, 2006). A 3×3 steel pile group (each pile had a diameter of 152.4 mm and a wall thickness of 2.0 mm) supporting a foundation with or without a superstructure was set in a dry sand deposit prepared in a cylindrical laminar box with a height of 6.5 m and a radius of 8.0 m (Figure 5.26). The piles were set up with a horizontal space of four-pile diameters centre to centre. Their tips were jointed to the laminar box base with pins and their heads were fixed to the foundation of a weight of 10 tons. Experimental variables included the natural period of the superstructure and the presence of foundation. Many strain gauges, accelerometers, velocity metre, earth pressure transducers displacement transducers, settlement metres and load cells, about 900 sensors in total, were placed in the deposit as well as on the pile-structure model. The tests were conducted under one-, two- or three-dimensional shaking with three types of ground motion having a peak acceleration adjusted from 0.3 m/s^2 to 8.0 m/s^2 .

Figure 5.26 shows a test model constructed in a cylindrical laminar box, 150 tons in total with a height of 6.5 m and a radius of 8.0 m, placed on the large shaking table. The cylindrical laminar box consists of 41 ring flanges, enabling shear deformation of the inside soil during two-dimensional horizontal shaking. The total weight of the test model excluding the cylindrical laminar box and its attachments was 750 tons. After setting the pile group in the laminar box, the sand was placed a relative density of about 70% to form a uniform deposit with a thickness of 6.3 m. A total of five test series were conducted, in which the presence of foundation embedment and superstructure, and the natural period of the superstructure, as well as the type of input motions, and their components and maximum acceleration were varied (Tokimatsu et al., 2007).

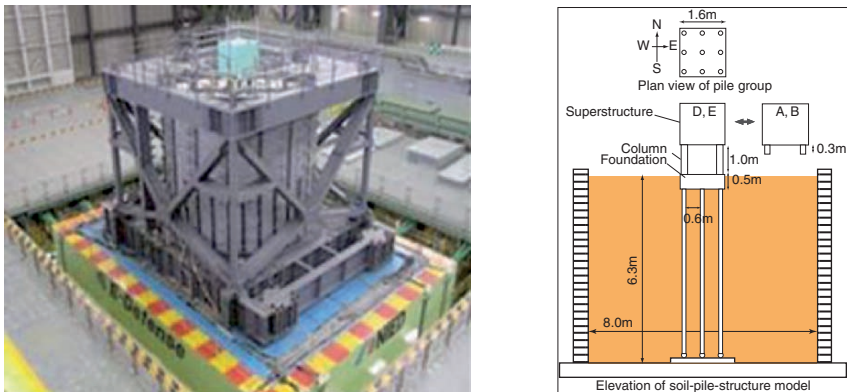


Fig. 5.26. Test layout in laminar container mounted on the E-Defense Shake table



Fig. 5.27. Superstructure before and after test

4.3.2. Representative test results

The superstructure became inclined after the final test (Figure 5.27). The piles yielded and buckled not only at their heads but also at depths from 0.7 m to 1.2 m during the final stage of shaking resulting in permanent deformation and inclination of the superstructure. The direction of pile deformation corresponds to those of the strong axes of ground displacement and acceleration, indicating that the ground displacement as well as inertial force had a significant effect on the failure of piles.

5. Earthquake loading aboard geotechnical centrifuges

Laboratory testing of small scale models is a particularly fruitful avenue in earthquake geotechnical engineering due to the paucity of data collected during real earthquake events which are both rare and often unpredictable. However, the particularly strong dependency of strength and stiffness of soil on the confining stress dictates that the models need to be tested under realistic stresses and strains. This could be readily achieved in a geotechnical centrifuge, provided suitable shaking tables that can impart strong earthquake loading to the models in-flight, can be mounted on to the centrifuge. This technique is generally termed as dynamic centrifuge modelling and has been widely used in USA, Europe, and Japan.

About 30 large geotechnical centrifuges (radius larger than 3 m) are in operation in the world carrying out many a kind of tests on footing, piles, tunnels, retaining walls, slopes. The payload capacity of many of the centrifuges is between 1 and 2 tons and models can be tested between 100 and 200 gravities.

Centrifuge model testing of the effect of earthquakes on geotechnical structures and of liquefaction of soils has been pursued actively worldwide. Of particular interest to many researchers are soil liquefaction and lateral spreading and their effects on a variety of geotechnical structures. Of the 32 geotechnical centrifuges listed in Japan by Kimura (2000), several of which were installed after the Kobe earthquake, 15 were equipped with shakers. The percentage of research papers devoted to earthquake modelling in the Centrifuge international conferences also attests to the increasing importance of this rather new field (Figure 5.28).

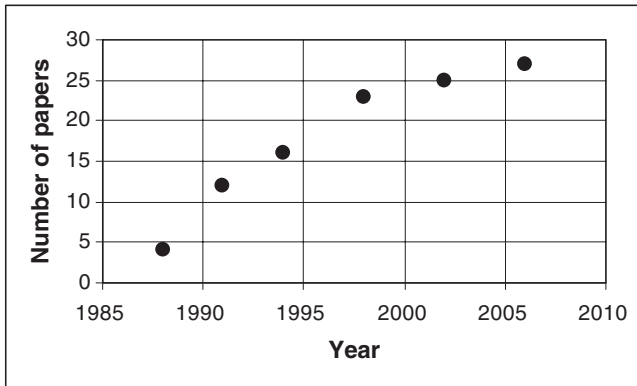


Fig. 5.28. Evolution of the number of papers presented at the Centrifuge conferences in the fields of earthquake simulation

5.1. DYNAMIC CENTRIFUGE MODELLING

In the early 1990s, significant progress in earthquake centrifuge modelling has been made within the framework of the North American programme “VELACS” (VERification of Liquefaction Analysis using Centrifuge Studies). Eight laboratories were associated to perform several series of very well-designed cross tests on soil liquefaction as well as to compare the data with numerical model predictions (Arulanandan et al., 1994). Based on this landmark series of tests, it became evident that repeatability of centrifuge tests on liquefaction is guaranteed only when the shakers are able to reproduce the repeatable earthquake loading. Preparation of the soil sample (including saturation) and of the model also exerts a strong effect on the quality of the experimental approach (Madabhushi et al., 2006). In Europe, only Cambridge University (UK), CEA-CESTA (France), and LCPC up to now have carried out dynamic centrifuge experiments, and with entirely original systems at Cambridge University and CEA-CESTA.

5.2. SHAKING FACILITIES AT CAMBRIDGE UNIVERSITY

Recently, the “Stored Angular Momentum” (SAM) actuator (Madabhushi et al., 1998; Coelho et al., 2006) is being employed. In the SAM actuator, high levels of energy are stored in a flywheel spinning at a high angular velocity. Thanks to a fast acting clutch, the stored energy is transferred to shake the model (Figure 5.29). The SAM actuator gives the user control of duration, frequency of the tone burst, and intensity of the earthquake loading. This system has proved quite successful and has to date produced about 10 PhDs and a significant number of publications. In general, mechanical shaking systems are inexpensive to build and can generate strong earthquakes. Their limits consist of the difficulty of mimicking a realistic earthquake input motion during testing and of the mechanical noise produced. Cambridge University is now starting the development of a 2-D servo-hydraulic shaker to provide the ability to model both horizontal shaking and vertical shaking on an independent basis.

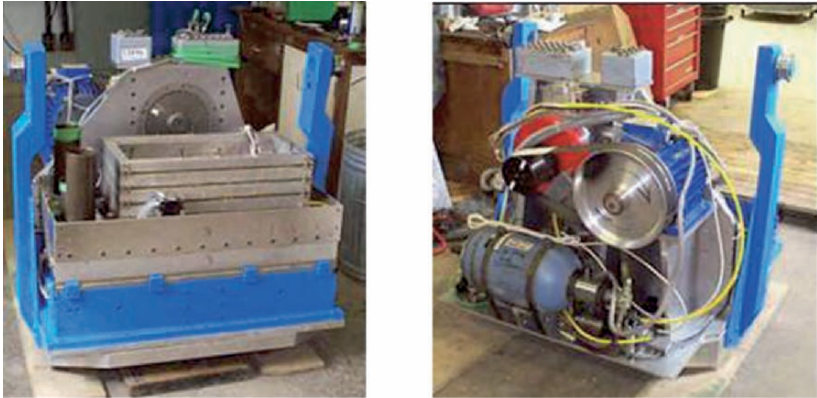


Fig. 5.29. ESB model container mounted on the shaking table on the SAM actuator, and the SAM actuator showing the 3-phase motor and flywheels

The Cambridge Philosophy has been to use single frequency tone bursts as input motions and investigate the soil response. For liquefaction problems, where the sole purpose of input motion is to generate excess pore water pressures that cause soil liquefaction, this type of input motion is considered satisfactory. On the other hand if the purpose of the dynamic centrifuge test is to investigate dynamic soil–structure interaction say in dry soils, then more realistic input motions may be required. Recently Madabhushi et al. (2006) have investigated the influence of type of input motion on the excess pore pressure generation in saturated sand beds.

5.3. PNEUMATIC SHAKER AT CEA-CESTA, FRANCE

Two decades ago, the CEA-CESTA used small explosions at the end of an air blast modification chamber. The resulting air blast would then be modified by resonating cavities and finally applied to the model through a membrane rubber (Zelikson and Leguay, 1985). A new pneumatic system (Figure 5.30) to generate vertical or horizontal shocks has also been designed (Sabourault et al., 1999).

5.4. EARTHQUAKE SIMULATION AT LCPC, FRANCE

An innovative shaker has recently been put in operation in the LCPC centrifuge. It was manufactured by Actidyn Systems and includes a dynamic balancing feature, both with respect to the mechanics and at the command-control level. This feature makes it possible to generate amplitude excitations, with direction and frequency being chosen in advance and controlled. The second advantage of this dynamic balancing feature is the reduction or elimination of vibrations currently being transmitted to the machine.

Figure 5.31 shows the LCPC shaker and the laminar box developed by LCPC. In Figure 5.31, an example of results of the commissioning tests recently carried out is

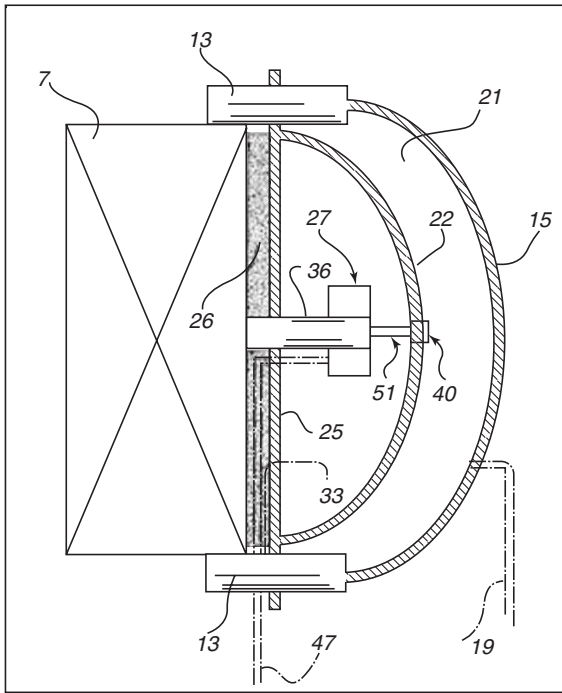


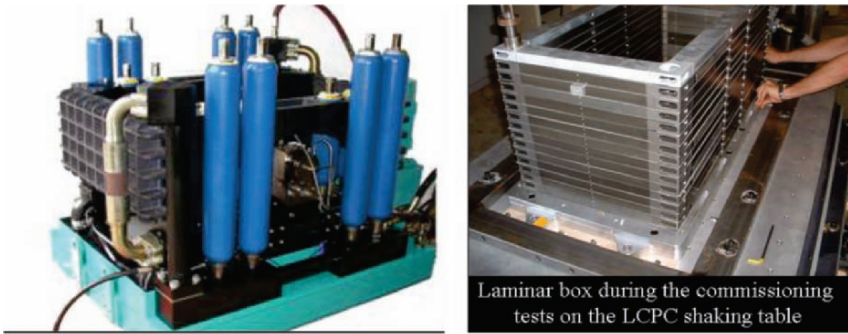
Fig. 5.30. CEA-CESTA pneumatic shock actuator

shown. A Mexico earthquake record was simulated at 50 g and a very good agreement is observed between the acceleration recorded on the table and the specified values.

5.5. RECENT ADVANCES IN EARTHQUAKE ACTUATION WORLDWIDE

The most widespread shakers installed on geotechnical centrifuges are indeed large 1D shaking tables using servo-hydraulic actuators. Some 2D shakers already exist (Figure 5.32) or are being developed in Honk-Kong, in USA (Davis and RPI), in Korea (Daejon), and in England (Cambridge). There is a definite need to understand the interplay of the vertical shaking effects along with the horizontal shaking. Europe needs to engage in this development and develop a 2D actuation facility. Currently, efforts are underway at Cambridge in this direction.

A great stride forward is being taken thanks to the North American project “NEES” (Network for Earthquake Engineering Simulation), launched in October 2000. More than US\$ 9 million of investment allowed upgrading the UC Davis (UCD) and RPI (New York) centrifuges. In the UCD facility, upgrades include the 2D (horizontal and vertical) shaker and a robot (Figure 5.33). Seismic and electrical tomography and 3D image processing will also be introduced. The data obtained during earthquake centrifuge tests are transmitted



Laminar box during the commissioning tests on the LCPC shaking table

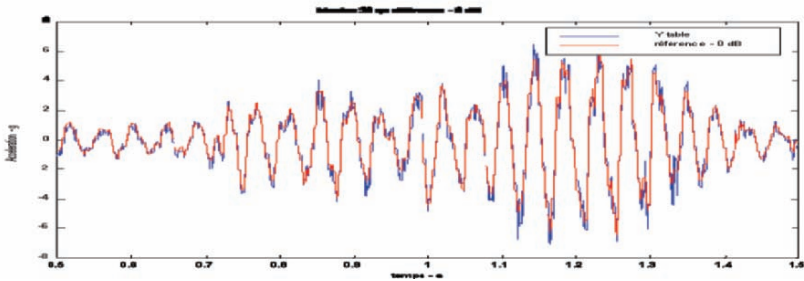


Fig. 5.31. The LCPC shaker, laminar box, and a Mexico earthquake record simulated at 50 g—Comparison between the recorded acceleration (in blue) and the specified values (in red)

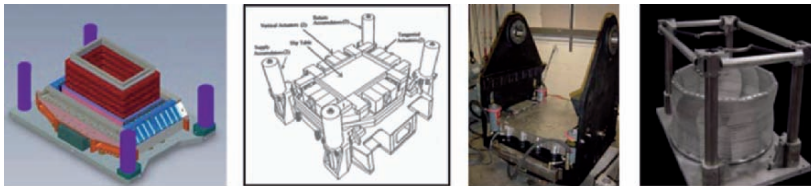


Fig. 5.32. Left to right: 2D shaker of UC Davis that can deliver horizontal and vertical shaking, 2D shaker of the University of Hong Kong (two horizontal directions) (Shen et al., 1998), and 2D shaker at RPI (two horizontal directions), and RPI 2D Laminar Container

in real time onto the NEES network (<http://nees.ucdavis.edu/>). A robot has also been installed on the RPI centrifuge (<http://nees.rpi.edu/>) along with the new 2D shaker (horizontal X- and Y-axis).

In Europe, there is a need to establish a network similar to USA-NEES. As a preliminary step in that direction, the centres within UK dealing with earthquake modelling, i.e. the shaking table facility at Bristol, the geotechnical centrifuge facility at Cambridge,

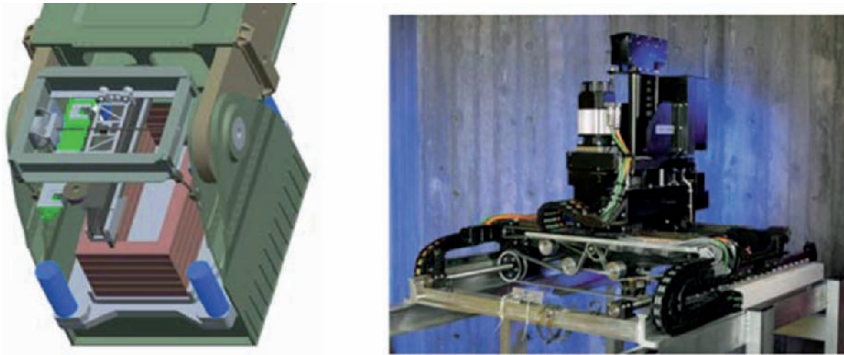


Fig. 5.33. UCD (left), and RPI (right) in-flight robots

and the sub-structure testing facility at Oxford are being linked under the UK-NEES programme funded by EPSRC to a tune of US\$ 1 million. The completion of this networking activity will enable distributed testing to happen between these centres in the UK. The UK-NEES will also be linked to USA-NEES which is expected to lead to strong collaboration with partners in the USA. Success of this UK-NEES may spawn an European-wide network between shaking table facilities at JRA in Italy and elsewhere, the geotechnical centrifuge facilities and the field monitoring sites at Thessalonica, Greece.

6. International collaboration

6.1. LARGE TESTING FACILITIES WORLDWIDE

As discussed by Pinto et al. (2006), in a recent report edited by Taucer and Franchioni (2005) a review of the existing testing facilities for earthquake research and qualification is provided. In another report, Taucer (2005) discusses enhancement of existing facilities in order to address new scientific topics in earthquake engineering. A summary of the worldwide Shake Table (ST) facilities is revisited herein for illustration (Figure 5.34). A quick look at Figure 5.34 shows that there is a quite balanced distribution of experimental facilities between American, Asiatic, and European continents, which would indicate that the research communities are backed by a suitable set of experimental facilities, which provide support to the progress on understanding and advancing earthquake resistant design and practice, training, and education worldwide. However, it is known that: (a) most of the infrastructures are essentially concentrated in a small number of countries, namely USA, Japan, and Italy and (b) a large part of the earthquake research community does not have access to those facilities.

6.2. EUROPEAN EXPERIENCE ON COLLABORATION

In Europe, the earthquake engineering laboratories initiated an enlarged collaboration at the beginning of the 1990s, as a direct consequence of financial support from the

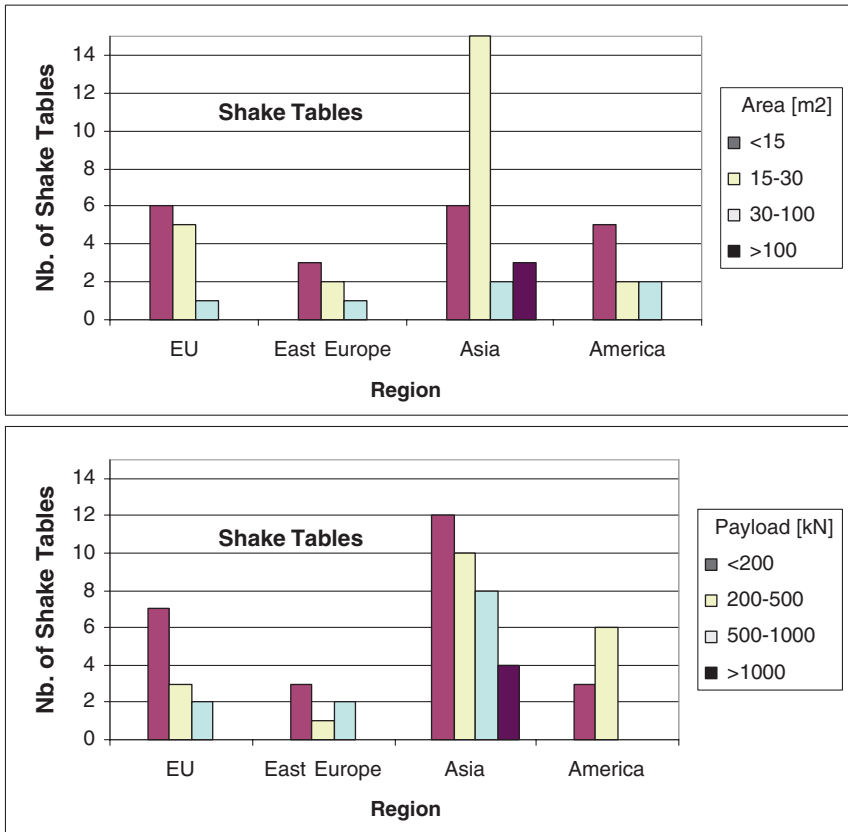


Fig. 5.34. Synopsis of large-scale earthquake Shake tables worldwide

European Commission. Five major shaking tables were involved, together with the ELSA reaction wall facility at JRC Ispra. As stated by Severn (2000), as a result of providing access to researchers from Member States, a major step forward was made in the fidelity and accuracy with which these six facilities could be used, leading to significantly enhanced performance. This major advance has put European earthquake engineering infrastructures at the international level and has opened up several new research areas for experimental study. Collaboration between the infrastructures group and three successive Research Networks has allowed significant progress to be made towards the validation of many aspects of Eurocode 8 and the mitigation of seismic risk.

It is noted that the first large-scale earthquake tests on structures for design with the Eurocodes (Eurocode 8) were performed in the framework of ECOEST with an enlarged research network of the earthquake engineering community (PREC8 Research Network, Coordinated by Prof. Calvi from the University of Pavia) acting as external user(s) of the facilities. The PREC8 network involved 18 European research groups working on the

following 4 broad themes, chosen because of their importance to the new European Seismic Design Code, namely: (1) Reinforced Concrete Highway Bridges (ISMES, Bristol, JRC Ispra), (2) Reinforced Concrete Frames (Athens), (3) Infilled Frames (Athens, ISMES, Bristol, LNEC); and (4) Geotechnical structures (Bristol).

Given the success of the co-operation and collaboration between research infrastructures, external researchers (Universities and Laboratories), and the outcome of the research activity and its relevance for European standards in process of development and approval by the European countries, the consortium was further financed to continue its activities, addressing now new topics, as part of the programme of the research network ICONS—Innovative Concepts for New and Existing Structures, with emphasis on: (1) Seismic Actions, (2) Assessment, strengthening and repair, (3) Innovative design concepts, (4) Composite structures, and (5) Shear-wall structures.

In the context of the 5th Programme of the Commission, the consortium was further expanded (ECOLEADER) and earthquake engineering research concentrated on the topics of the Network—Safety Assessment for Earthquake Risk Reduction—(SAFEER) research programme, namely: (1) characterization of seismic hazard, (2) assessment and design in low seismicity regions, (3) strategies/techniques for risk reduction, and (4) risk assessment systems. Details of the experimental research carried out at the European laboratories can be found in Severn (2000) and in the 27 Technical report series ECOEST-PREC8 (1996), ECOEST2-ICONS (2001), and CASCADE (2005). They were written and edited by several European researchers and published by the National Laboratory for Civil Engineering, Lisbon, constituting important milestones of the pioneering European cooperative research on earthquake engineering, involving experimental facilities, their users and the research community.

6.3. THE USA NEES INITIATIVE

As mentioned earlier, in the second half of the 1990s, the U.S. National Science Foundation (NSF) initiated a programme aimed at establishing the Network for Earthquake Engineering Simulation (NEES). As stated by Nelson et al. (2000) NEES is a project aiming at providing a national, networked collaboratory of geographically-distributed, shared-use next-generation experimental research equipment sites, with tele-observation and tele-operation capabilities, which will transform the environment for earthquake engineering research and education through collaborative and integrated experimentation, computation, theory, databases, and model-based simulation to improve the seismic design and performance of U.S. civil and mechanical infrastructure systems.

The NEES project developed by NSF through a series of competitive programme solicitations: (a) “System Integration” (SI) to develop the high performance system for the NEES collaboratory, (b) “Earthquake Engineering Research Equipment” NEES research equipment sites, and (c) a “Management Consortium” to operate the NEES collaboratory through 2014. In fact, all the three components have been developed in coordination, and today NEESinc, with headquarters located in Davis, California, acts as the

management consortium, integrating: (1) a system of 15 shared experimental facilities (NEES Research Sites), (2) a Cyberinfrastructure Center (NEESit) that operates and supports the extensive IT infrastructure used by NEES, and (3) a system of centralized repositories for storing shared documents, experimental data, simulation programmes, software tools, etc.

NEES is an outstanding initiative fostering collaboration in earthquake engineering research and is really pioneering in taking full advantage of the information and communication technologies as well as the most recent innovations and concepts in the IT sector. As stated in the NEESinc website, “NEES will revolutionize earthquake engineering research and education. NEES research will enable engineers to develop better and more cost-effective ways of mitigating earthquake damage through the innovative use of improved designs, materials, construction techniques, and monitoring tools. This research can also help prevent infrastructure damage from other natural disasters and from terrorism. Preparing for and protecting against these threats makes American communities more resilient and enhances their ability to meet the challenges posed by future disasters.”

6.4. INTERNATIONAL COLLABORATION CHALLENGES AND OPPORTUNITIES

Concerning co-operation for experimental facilities, there are several requirements but the most important seems to be the issue of “standardization” for data models and formats and communication protocols between countries and researchers, which will facilitate data exchange and interoperability. The international community is challenged to develop an international shared repository for earthquake engineering data, which could be used for research and education. A workshop on data standardization was organized during the 2004 World Conference on Earthquake Engineering held in Canada. Recently, NEES organized a dedicated world forum, which is addressed in the next section.

The NEES World Forum was organized by the NSF and hosted by NEES in San Francisco, March 2006 (Spencer et al., 2006). As stated by the organizers, the purpose of the World Forum is to engage a representative international group of researchers and research administrators to discuss and promote opportunities for collaboration with the NEES and similar programmes worldwide, as well as the linkages necessary to facilitate this collaboration. A brief overview of discussions during this world forum is included below.

6.4.1. *Simulation*

Simulation includes both computational and physical experimentation. Distributed and hybrid testing both fall within this class of techniques. Larger and faster simulation was identified as the immediate need within this cyberenvironment. To adequately study certain classes of systems, real-time simulation capabilities are required and should be pursued. The most significant strides will be made within the community by leveraging resources and sharing successes through the use of an open source, open architecture approach for the benefit of researchers worldwide.

6.4.2. *Cyberenvironments*

The challenge here is to explore how cyberenvironments can be leveraged to connect a geographically distributed set of international researchers for meaningful collaborative research. Focus was placed on: (1) identification of technological barriers that currently hinder international collaboration and (2) formulation of solutions that would assist in overcoming such barriers. It was argued that cyberenvironment software and hardware should be easier to use. To this end, some degree of standardization should be introduced to the earthquake engineering cyberenvironments to facilitate easier exchange of ideas and data across national boundaries. The cyberenvironment should also be designed to evolve with emerging information technologies to address additional demands from the research community.

6.4.3. *Data infrastructure*

It was envisioned that an international data repository would contain both experimental simulation data and analytical/numerical simulation data. Under consideration were basic policies, data models, metadata, procedures for documenting experiments and numerical simulations, and protocols for data curation, management, and maintenance.

7. Summary and conclusions

A class of large-scale testing facilities for earthquake engineering applications was presented. A wide variety of testing approaches and capabilities is currently available worldwide for documentation of seismic and dynamic moderate- and high-amplitude levels of structural response. The presented facilities include in-situ field testing sites, dynamic testing mobile laboratories, large-scale testing laboratories, and geotechnical centrifuges. Representative collaborative efforts using these facilities were discussed. Opportunities and challenges associated with worldwide collaboration were also highlighted.

It is envisioned that collaboration will increasingly become a common mode of conducting experimental research. Convenient availability of the experimentation data sets is an essential element, in view of the uniqueness and high expense associated with this type of large-scale testing. Definition of effective approaches towards such of worldwide collaboration is underway, in order to set the stage for a new paradigm in earthquake engineering research and education.

REFERENCES

- Arulananandan K, Manzari M, Zeng X et al. (1994) What VELACS project has revealed. Centrifuge 94, Singapore, Leung et al. (ed), Balkema, 25–32
- CASCADE Series Reports (2005) Published by LNEC, Lisbon
- Chávez-García FJ, Raptakis D, Makra K, Ptilakis K (2000) Site effects at Euroseistest—II. Results from 2D numerical modeling and comparison with observations, *Soil Dyn. Earthq. Engrg.* 19, 23–39

- Chávez-García FJ, Raptakis D, Makra K, Ptilakis K (2002) The importance of the reference station in modelling site effects up to larger frequencies. The case of "Euroseistest". Proc. 12th ECEE, Paper No. 589
- Coelho PALF, Haigh SK, Madabhushi G (2006) Effects of successive earthquakes on saturated deposit of sand. 6th ICPMG '06, Ng et al. (ed), Hong Kong, 4–6 August, Taylor & Francis, Vol. 1, 443–448
- ECOEST2-ICONS Series Reports (2001) Published by LNEC, Lisbon
- ECOEST-PREC8 Series Reports (1996) Published by LNEC, Lisbon
- Euroseismod Volvi-Thessaloniki: Development and Experimental Validation of Advanced Modeling Techniques in Engineering Seismology, Earthquake Engineering. Commission of the European Communities, 1996–1998
- EUROSEISRISK Seismic Hazard Assessment, Site Effects and Soil Structure Interaction Studies in an Instrumented Basin (EVG1-CT-2001-00040), 2002–2005
- Euroseistest Volvi-Thessaloniki: A European Test Site for Engineering, Seismology, Earthquake Engineering and Seismology. Commission of the European Communities, Project EV5V-CT93-0281 (DIR 12 SOLS), 1993–1995
- Guéguen P, Bard P-Y (2005) Soil–structure and soil–structure–soil interaction: Experimental evidence at the Volvi test site. *JEE* 9-4, pp 1–36
- Kimura T (2000) Development of geotechnical centrifuges in Japan. *Centrifuge 98*, Tokyo, Kimura et al. (ed), Balkema 2, 945–954
- Kudo K, Kanno T, Okada H, Sasatani T, Morikawa N, Apostolidis P, Ptilakis K, Raptakis D, Takahashi M, Ling S, Nagumo H, Irikura K, Higashi S, Yoshida K (2002) S-Wave Velocity Structure at EURO-SEISTEST, Volvi, Greece. Determined by the Spatial Auto-Correlation Method applied for Array Records of Microtremors. Proc 11th Japan Earthquake Engineering Symposium, Paper No. 62
- Madabhushi SPG, Schofield AN, Lesley S (1998). A new Stored Angular Momentum (SAM) based earthquake actuator. *Centrifuge 98*, Kimura et al. (ed), Balkema, 111–116
- Madabhushi SPG, Ghosh B, Kutter BL (2006) Role of input motion in excess pore pressure generation in dynamic centrifuge modeling. *International Journal of Physical Modelling in Geotechnics*, Japan, Vol. 6, No. 3.
- Makra K, Raptakis D, Chávez-García FJ, Ptilakis K (2001) Site effects and design provisions: the case of Euroseistest, *PAGEOPH* 158, 2349–2367
- Makra K, Raptakis D, Chávez-García FJ, and Ptilakis K (2002) How important is the detailed knowledge of a 2D soil structure for site response evaluation. Proc. 12th ECEE, Paper No. 682
- Makra K, Chávez-García FJ, Raptakis D, Ptilakis K (2005) Parametric analysis of the seismic response of a 2D sedimentary valley: Implications for code implementations of complex site effects. *Soil Dyn. Earthq. Engrg.* 25, 303–315
- Manos GC, Kourtidis V, Soulis V, Sextos AG, Renault P, Yasin B (2005) Numerical and experimental soil–structure–interaction of a bridge pier model at the Volvi-Greece European Test Site. *Proceedings: EURODDYN*, pp 1335–1340
- Margaris BN, Hatzidimitriou PM (2002) Source spectral scaling and stress release estimates using strong motion records in Greece. *BSSA* 92, 1040–1059
- Moczo P, Kristek J, Vavryčuk V, Archuleta RJ, Halada L (2002) 3D heterogeneous staggered-grid finite-difference modeling of seismic motion with volume harmonic and arithmetic averaging of elastic moduli and densities. *BSSA* 92, 3042–3066
- Moczo P, Kristek J, Gális M (2004) Simulation of the planar free surface with near-surface lateral discontinuities in the finite-difference modeling of seismic motion. *BSSA* 94, 760–768

- Nelson PP, Pauschke JM, Anderson TL, Goldstein SN (2000) Network for Earthquake Engineering Simulation (NEES). Proceedings of the workshop—Mitigation of the seismic risk: support to recently affected European countries, Belgirate 2000. Published by JRC, Ispra, Italy
- Parolai S, Bard P-Y (2003) Evaluation of amplification and frequency-dependent lengthening of duration of seismic ground motion due to local effects by means Joint Analysis of Sonogram and Standard Spectral Ratio. *Journal of Seismology* 7(4), 479–492
- Pinto A, Pegnon P, Taucer F (2006) Shaking Table Facilities and Testing for Advancement of Earthquake Engineering, International Cooperation, Experiences, Values, Chances. First European Conference on Earthquake Engineering and Seismology (a joint event of the 13th ECEE & 30th General Assembly of the ESC), Geneva, Switzerland, 3–8 September 2006, Paper No. 1538
- Pitilakis K, Raptakis D, Lontzetidis K, Tika-Vassilikou TH, Jongmans D (1999) Geotechnical and geophysical description of EURO-SEISTEST, using field, laboratory tests and moderate strong motion recordings. *J. Earthq. Engrg.* 3, 381–409
- Raptakis D, Theodulidis N, Pitilakis K (1998) Data analysis of the EURO-SEISTEST strong motion array in Volvi (Greece): Standard and horizontal to vertical spectral ratio techniques. *Earthq. Spectra* 14, 203–224
- Raptakis D, Chávez-García FJ, Makra K, Pitilakis K (2000) Site effects at Euroseistest—I. Determination of the valley structure and confrontation of observations with 1D analysis. *Soil Dyn. Earthq. Engrg.* 19, 1–22
- Raptakis D, Manakou M, Chávez-García FJ, Makra K, Pitilakis K (2005) 3D Configuration of Mygdonian basin and preliminary estimate of its site response. *Soil Dyn. Earthq. Engrg.* 25, pp 871–887
- Sabourault P, Defauchy J, Mariotti C, Siboni S (1999) *Simulateur de chocs*. INPI, Paris, 13 p
- Severn, RT (2000) Earthquake Engineering Research Infrastructures. Proceedings of the workshop—Mitigation of the seismic risk: support to recently affected European countries. Belgirate 2000. Published by JRC, Ispra, Italy
- Shen CK, Li XS, Ng CWW, Van Laak PA (1998) Development of a geotechnical centrifuge in Hong Kong. *Centrifuge 98*, Kimura et al. (ed), Balkema, 13–18
- Spencer B et al. (2006) World Forum on Collaborative Research in Earthquake Engineering: Summary, Conclusions and Recommendations. NEESinc, San Francisco, CA (USA), March 16–18
- Tabata K, Sato M (2006) Report of special project for earthquake disaster mitigation in urban areas, Ministry of Education, Culture, Sports Science and Technology, 489–554 (in Japanese)
- Taucer F (2005) Recent Advances and Future Needs in Experimental Earthquake Engineering. CASCADE Series Report No. 7, Published by LNEC, Lisbon (ISBN 972-49-1971-4)
- Taucer F, Franchioni G (2005) Directory of European Facilities for Seismic and Dynamic Tests in Support of Industry. CASCADE Series Report No. 6, Published by LNEC, Lisbon (ISBN 972-49-1970-6)
- Tokimatsu K, Suzuki H, Tabata K, Sato M (2007) Three Dimensional Shaking Table Tests on Soil-Pile-Structure Models Using E-Defense Facility, 4th International Conference on Earthquake Engineering, June 25–28, Thissaloniki, Greece
- Zelikson A, Leguay P (1985) Simulation sismique sur centrifugeuse. XI ICSMFE, San Francisco, Balkema, 955–958

CHAPTER 6

MODELLING OF DYNAMIC SOIL PROBLEMS

David Muir Wood

*Department of Civil Engineering, University of Bristol, Queen's Building,
University Walk, Bristol, UK
d.muir-wood@bristol.ac.uk*

Abstract. Some possibilities for the modelling of dynamic soil problems are described. Two basic features of constitutive models to be used in numerical analysis to simulate soil response under non-monotonic loading are: a description of the small strain elastic behaviour which will evolve and develop its own anisotropies as the stress or strain history unfolds; and provision for plasticity on reversal of stress or strain path. Laboratory geophysical techniques provide one possibility for tracking the evolution of stiffness anisotropy but have uncertainties of interpretation. Macroelement modelling is a form of numerical simulation using simple elemental systems which introduce important features from constitutive modelling. It lends itself to rapid parametric study of effects of geotechnical and seismic nonlinearity. Physical modelling can provide controlled data for validation of numerical modelling: the design of such models requires consideration of scaling laws. Results of some model tests on a single degree of freedom structure with a special isolating foundation are shown.

1. Introduction

Geotechnical modelling (Muir Wood, 2004) is undertaken to increase understanding of the mechanisms that occur in geotechnical systems in order to be able to predict the performance of those or other related systems. Prediction involves extrapolation from known behaviour towards an unknown region: the quality of the prediction will be as good as the quality of the models underpinning the understanding of the system.

The principal types of model used to predict performance of dynamic geotechnical problems are numerical and physical models. In general numerical models will be calibrated against observations made on physical models. However, contained within the numerical modelling and implicit in extrapolations made on the basis of physical modelling is some assumed constitutive model for the soil behaviour. Such constitutive models are themselves inspired by direct observation of material behaviour at the element level.

We begin by describing a rather elegant class of constitutive model for soils and then show how laboratory dynamic testing can feed into the selection of soil parameters. Physical modelling using an earthquake simulator has been used to support studies of mitigation of seismic response of existing foundations: some results will be shown as an example of data generation for calibration of numerical models. The nature of soil nonlinearity is

such that the constitutive models are subtle and the numerical analyses can be lengthy. Macroelement modelling can provide a shortcut for parametric study of system behaviour. The underlying principles of the constitutive models guide the choice of appropriate features for the macroelement models.

2. Constitutive modelling framework

Desirable features of a constitutive model appropriate for dynamic problems are shown in terms of the dependence of incremental soil stiffness on history (Figure 6.1). After any corner in the strain path, the incremental stiffness immediately increases by an amount dependent on the sharpness of the corner and then decays as deformation continues (Figure 6.1a, b). Seismic loading is quintessentially about strain paths with multiple irregular corners: in any seismic loading event with variable amplitude of cycles of loading the stiffness will vary constantly. Contrast this with the ability of an elastic-perfectly plastic model such as the widely used Mohr–Coulomb model (Figure 6.1c, d) which only has two values of incremental stiffness: the full elastic stiffness and zero.

Ingredients necessary for a successful model include: hardening plasticity to model the steady change in stiffness with strain; and kinematic yielding to imprint on the model some memory of recent history. Figure 6.2 illustrates the way in which kinematic yielding can function in an extended Mohr–Coulomb model in two views of effective stress space. Figure 6.2a shows mean effective stress p' and distortional stress q ; Figure 6.2b shows a deviatoric view of principal stress space. In each diagram there is a small region

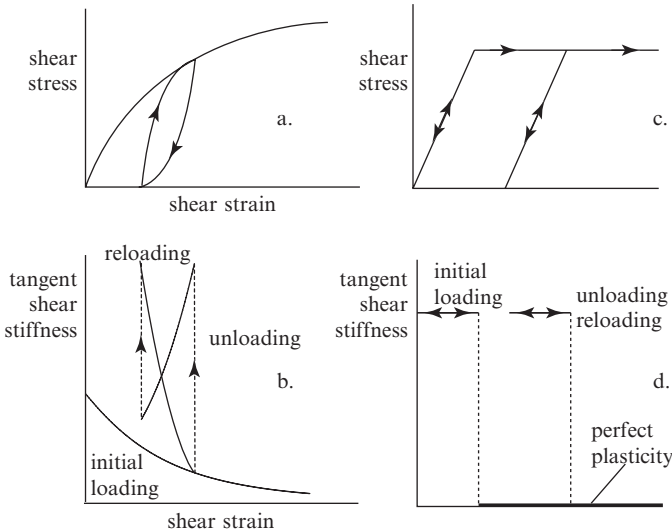


Fig. 6.1. (a) Typical irreversible stress–strain response and (b) typical variation of incremental stiffness for soil; (c) stress–strain response and (d) variation of incremental stiffness for elastic-perfectly plastic model

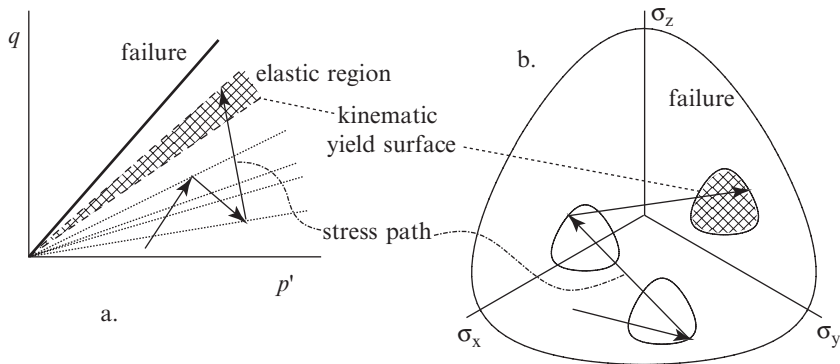


Fig. 6.2. Outline of kinematic hardening soil model in (a) $q : p'$ effective stress plane and (b) deviatoric stress plane

which travels around with the recent stress history, which represents the extent of the elastic region for the soil. In Figure 6.2a this elastic region is a 'wedge' representing a small range of values of mobilised friction; in Figure 6.2b it is a 'bubble' which floats around. The detailed implementation of kinematic hardening plasticity needs additional ingredients: for sands, the strength depends on density and mean stress level; a flow rule is required to define the way in which plastic strains develop when the stress state is engaging with the kinematic yield surface shown in Figure 6.2. Severn-Trent sand (Gajo and Muir Wood, 1999a,b) is a complete soil model which makes current strength a variable dependent on state parameter (Been and Jefferies, 1985) and describes softening of dense sands while retaining a simple monotonic distortional hardening relationship. In an undrained cyclic triaxial test it shows progressive pore pressure build-up and eventual liquefaction.

3. Fabric, soil stiffness and laboratory geophysics

The moving yield surface defines the current region of stress space which can be reached elastically as a result of the recent stress history. Once the stress path engages with this surface and starts to push it around, irrecoverable deformations will occur and the 'fabric' of the soil will change. The geometric fabric describes the orientation of contacts, and the kinetic fabric describes how these contacts are actually being used to carry forces through the soil. One geometric fabric can carry many different external loads: kinetic fabric can change much more rapidly than orientation fabric which requires significant relative movement of particles. The fabric of soils can only be seen incompletely—radiographic techniques reveal local variations in density (Muir Wood, 2002) and photographic techniques can monitor movement of individual particles (White et al., 2003). The way in which stress is carried through the soil by chains of particles can only be seen through numerical analysis. These force chains are anisotropic and the stiffness properties of the soil will also in general be anisotropic and evolve with stress history.

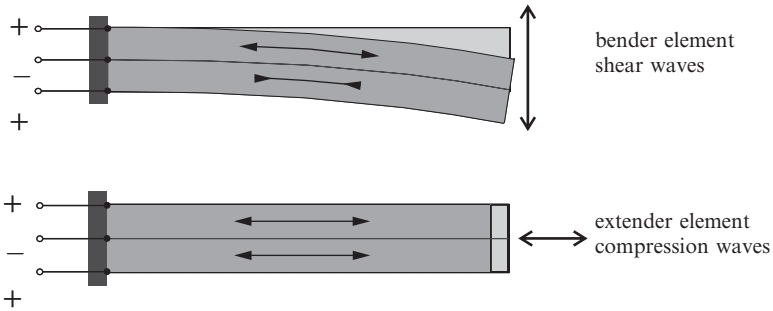


Fig. 6.3. Piezoelectric bender and extender elements for generation of shear waves and compression waves

Pluviated samples have a vertical axis of symmetry leading to cross-anisotropic stiffness which matches the symmetry of the conventional triaxial apparatus for vertical samples. Exploration of stiffness in such a way as to leave the fabric undisturbed requires very small perturbations: laboratory geophysical techniques are an obvious choice.

Bender elements (Figure 6.3) (Pennington et al., 1997; Lings and Greening, 2001) have become particularly popular as a laboratory geophysical technique for their ability to give a ‘zero strain’ or ‘constant fabric’ stiffness—we can probe the stiffness characteristics of the soil without disturbing the arrangement of the soil particles. A two-layer piece of piezoelectric material is electrically wired in such a way that, when a voltage pulse is applied, one layer wants to extend, the other to contract. The device is thus forced to bend. Embedded in the boundary of a soil sample, this pulsed bending generates a shear wave which passes through the soil sample to be received by a similar element at the other side of the sample. The velocity at which the wave travels across the sample can be directly interpreted in terms of shear stiffness. We have also developed a ‘bender-extender’ element (Figure 6.3) (Lings and Greening, 2001) which, when excited in such a way that both layers extend together, tends to generate more of a compression wave through the soil. This can be detected in essentially the same way as the shear wave. In dry soil, the compression wave can reveal relevant stiffness information. We have used bender elements in end-to-end measurements in triaxial apparatus and also for measurement across a diameter of the sample, installing them through the flexible membrane surrounding the sample.

The wave velocity is proportional to the square root of the appropriate elastic stiffness. The determination of the shear wave velocity requires the determination of the time it takes for the wave to travel from transmitter to receiver. There are many reasons why this is not straightforward. The dynamic motion is heavily damped as it passes through the soil so that the received signal has a much lower amplitude than the sent signal. The received signals never bear much resemblance to the sent signals because of reflections from the boundary and because of the dispersion of the wave through the soil—the dependence of the shear wave velocity on the frequency of the perturbation—and most input signals do not contain only one single frequency of excitation. The bender may try to excite

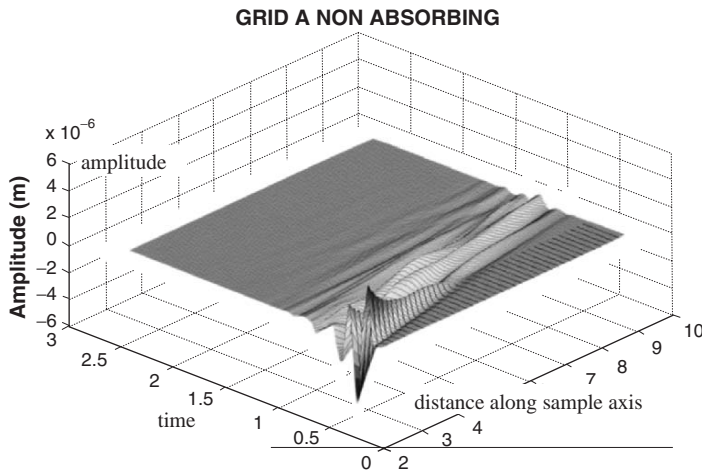


Fig. 6.4. Propagation of waves through cylindrical sample with non-absorbing boundary (Arroyo et al., 2006)

a pure shear mode of deformation in the soil but it will certainly generate other modes of deformation including compression waves which will travel at the compression wave velocity.

Numerical simulations of excitation of a bender element in the end of a cylindrical elastic soil sample have been performed using the three dimensional finite difference program FLAC-3D confirming the non-ideal nature of the wave (Arroyo et al., 2006). Figure 6.4 shows the time history of the wave (a single sinusoidal pulse at input) as it propagates along the axis of the cylinder with non-absorbing boundaries. Local effects, especially reflections from the lateral boundaries, turn the input trace into something more complex. As the distance along the axis increases the second peak actually becomes bigger than the first one.

The synthetic signals from the numerical simulation can be inspected in an attempt to discover an objective procedure for estimating the arrival time so that the shear wave velocity can be calculated (Figure 6.5). People have proposed various geometrical characteristics of the received wave that can be extracted more or less automatically (Figure 6.5): the most obvious one would be when the receiving bender element starts to move (T_0); but the moment of first significant reversal (T_1) or the first crossing of the time axis (T_2) or even the second peak (T_3) might provide more geometrical consistency. One of the difficulties of using the first point of movement (T_0) is that very often the received trace may well be preceded by a small movement associated with the arrival of the compression or p -wave—which is evident also in a typical experimental record (Figure 6.6). With these geometrical definitions (Figure 6.5), the received signal of the numerical calculations can be interpreted automatically to estimate the values of apparent shear wave velocity.

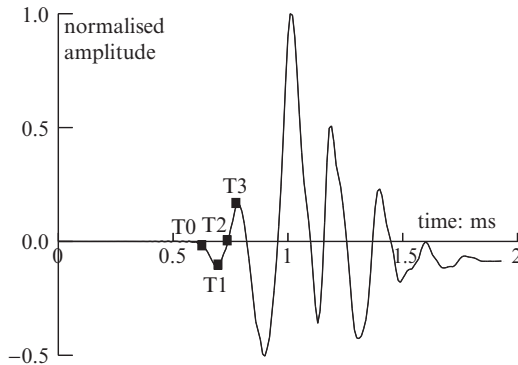


Fig. 6.5. Characteristic points on received signal for estimation of arrival time (Arroyo et al., 2006)

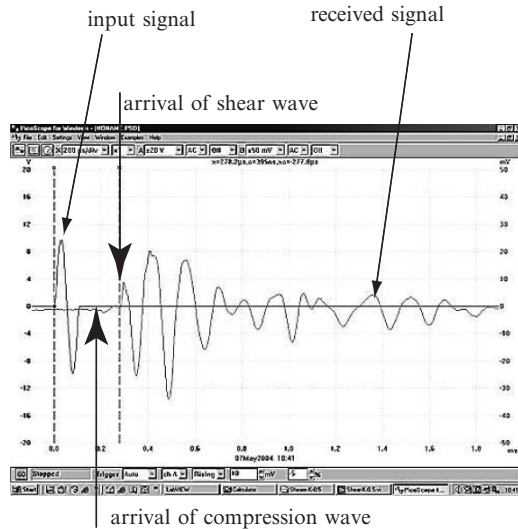


Fig. 6.6. Experimental observation of motion at bender element receiver for wave propagation through sand in cubical cell (Sadek, 2006)

The resulting velocities are shown in Figure 6.7 (normalised with the actual shear wave velocity) for different distances along the axis of the sample. (Velocity estimates made using a cross-correlation technique V_{cc} , which seeks the optimum match between the shapes of the input and received waveforms, and a frequency domain cross-spectrum technique V_{cs} which analyses the dependence of the phase of the received signal on frequency for a continuous harmonic input signal are also included.) The further the receiver from the source the closer all the velocity estimates approach the compression wave velocity $V_p/V_s = 1.5$.

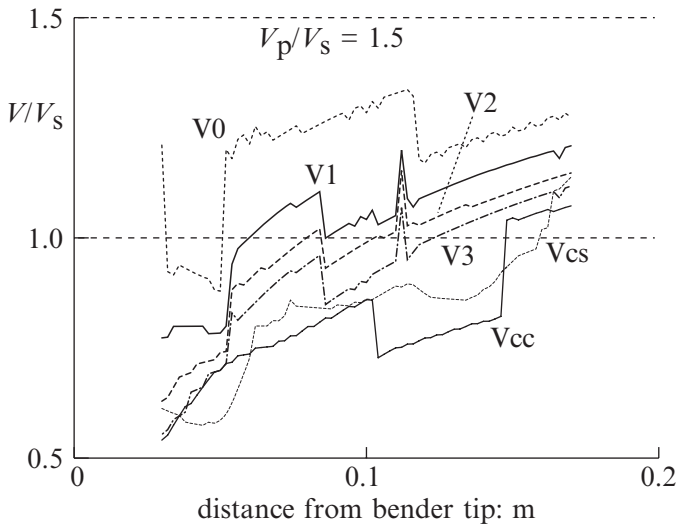


Fig. 6.7. Deduced shear wave velocities normalised with actual shear wave velocity ($V_p/V_s = 1.5$) (Arroyo et al., 2006)

Both simulation and experimental observation show very clearly the difference between the input and received waves: the output signal contains much richness which could in principle be decoded to reveal more information about the constitutive properties of the soil and the effectiveness of the boundaries.

4. NEMISREF mitigation of foundation response

A case history of physical modelling on the earthquake shaking table at Bristol University is provided by the NEMISREF project (New Methods of Mitigation of Seismic Risk on Existing Foundations), an EU funded project under the GROWTH programme involving academic and industrial partners from UK, France, Greece, Portugal and Romania. It addressed three themes: liquefaction of foundation soils, site effects (horizontal ground) and site effects (slopes). Here we show some of the results of modelling relating to the second theme.

Horizontal ground shaking is a major cause of damage during earthquake events. The design of new buildings can take advantage of many technologies to mitigate the hazard, but these mitigation techniques are quite costly, intrusive and damaging when used to retrofit an existing structure. Site effects result in neighbouring locations experiencing significantly different levels of shaking during earthquakes. The main motivation of the NEMISREF project was to investigate how an engineered modification of the characteristics of foundation soil could produce an artificial site effect which would significantly improve the effect of earthquake motion on the structure itself.

The EUROSEISTEST project (Pitilakis et al., 2005) provided a reference site and structure for the NEMISREF studies of site effects. The heavily instrumented test site of EUROSEISTEST is established in the epicentral area of the Thessaloniki 1978 earthquake ($M_s = 6.5$), 30 km northeast from Thessaloniki, an active graben with an annual extension rate of a few millimetres. The soft-loose soils at the surface have shear wave velocity $V_s < 160$ m/s.

The EUROSEISTEST research infrastructure includes two instrumented reinforced concrete model structures (scale 1:3), with surface foundations, in the centre of the valley: a five-storey reinforced concrete building with infill masonry walls and a pier bridge with deck. Forced vibration tests, short and long distance deep blast tests and pull-out tests have been performed, and a few records of small real earthquakes are also available.

The single degree of freedom sway frame model of the EUROSEISTEST structure used in the shaking table tests is shown in Figure 6.8. The model sits on the surface of a bed of Hostun sand in a shear stack (Crewe et al., 1995) with dimensions: 1.19 m long, 0.55 m wide and 0.81 m deep. The shear stack (or laminar box) is constructed from a series of rectangular aluminium box section rings. Each ring is separated from the rings above and below by neoprene blocks in such a way that the box has high flexibility when shaken in its long direction and can, as far as possible, permit the sand mass to deform as if it were an infinite free field. When empty the shear stack has a resonant frequency of about 7.7 Hz with 3% damping. When filled with dry sand, pluviated to a void ratio of about 0.76 (relative density about 70%) the resonant frequency is about 26.5 Hz with 8% damping.

The model on the shear stack was shaken on the Bristol 6-axis shaking table which has a 3×3 m working platform controlled by eight 50 kN actuators (Crewe, 1998). The tests described here were all controlled to generate purely unidirectional horizontal shaking along the long axis of the shear stack. Experience at Bristol has shown that the distribution of mass on the shaking table in almost any model means that there is a serious likelihood

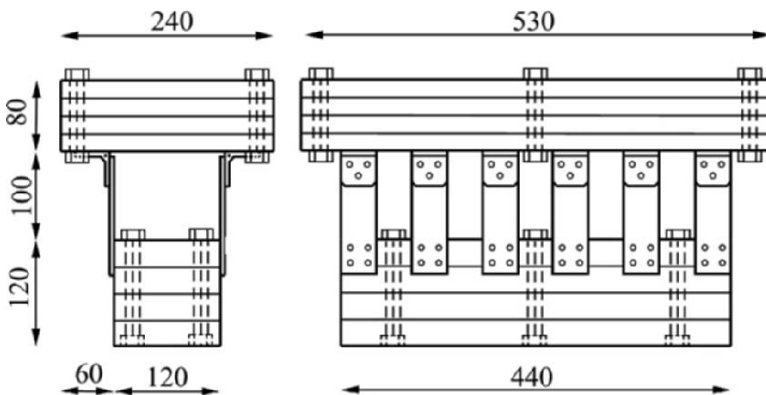


Fig. 6.8. Model single degree of freedom structure: dimensions in mm

of small but significant parasitic undesired motions including vertical and lateral motion, yawing and pitching which need to be actively controlled to be zero.

The linear scale factor for model design was driven by the need to permit the full development of a seismic bearing capacity failure mechanism on either side of the model when installed within the shear stack. A foundation width of 120 mm was chosen, giving a length scale factor of $n_\ell = 120/3500$. The width of the model foundation (440 mm) is close to the width of the shear stack (550 mm). No attempt has been made to apply scaling relations to the prototype foundation soil profile or to the footing load. If the footing loading were to be scaled together with the length scale, the load applied would be low and possibly insufficient to reveal the effect of any putative mitigation scheme. A model mass of 130 kg distributed over the model foundation reproduces the prototype 25 kPa bearing pressure and promotes soil–structure interaction effects in the shaking table model. To preserve the structure/foundation mass ratio of the prototype, 80 kg of the total mass are attributable to the ‘foundation’ and the remaining 50 kg to the ‘structure’. The height of the model structure above the model foundation is the scaled distance between the centre of mass of the prototype structure and the prototype foundation.

In the model structure (Figure 6.8) the foundation and structural mass are connected by a series of flexible steel columns, hinged to the structure. The natural resonant frequency of the model structure can be tuned between 4.4 Hz and 22.5 Hz by changing the number and thickness of these columns. The lowest value in this range reproduces the natural frequency (first mode) of the prototype; the highest is close to the scaled natural frequency of the prototype when modelled at 120/3500 scale (24 Hz).

Thus the design of the model represents a compromise. It is supposed that, because of the uncertainties of the stress level dependency of the soil behaviour, there is an advantage in working with stress levels around the foundation which are similar in model and prototype. It is not possible simultaneously to match the gravitational gradient of vertical stress. The increase in stress at a depth equal to the width of the foundation is of the order of 60 kPa in the prototype (more than twice the applied foundation loading) but is negligible in the model. However, the shaking table model is sufficiently large to provide a useful set of observations from which extrapolation to prototype scale can be made by means of numerical modelling—with an appropriate constitutive model. For scaling of frequency, the dominant effect is the length scale, and, in the region of interest around the foundation, the stress level and hence the soil stiffness are roughly the same in model and prototype. Frequency then scales with square root of the inverse of the linear scale: the resonant frequency and damping of the model measured by securing the model foundation to the shaking table (‘fixed-base’) are 22.5 Hz and 2.4% respectively, close to the fundamental frequency of the prototype (4.4 Hz) when scaled with the model/prototype length scale factor of 120/3500 (≈ 23.9 Hz).

The mitigation scheme studied in the NEMISREF project involved the construction of a ‘soft caisson’ around and beneath an existing foundation (Figure 6.9). By inserting a horizontal slip layer at some moderate depth (for example around 10 m), and also inserting soft trenches around the foundation, the foundation can be somewhat isolated from

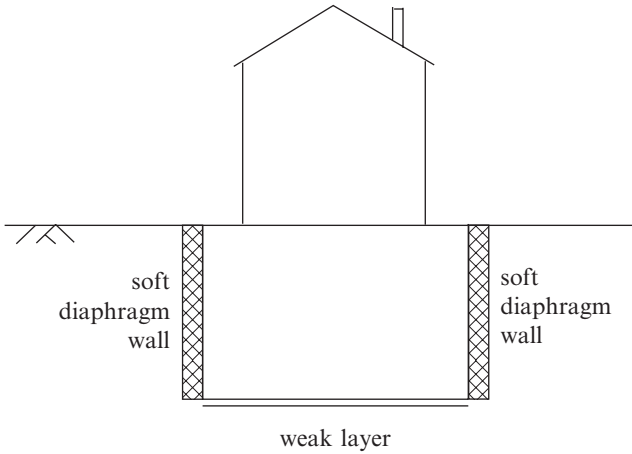


Fig. 6.9. Scheme for improvement of seismic performance of existing foundation by introduction of a soft caisson

upward propagating shear waves. In addition, the soft caisson adds the mass of the soil within the caisson to the mass of the structure and this modifies the dynamic performance by reducing the resonant frequencies. There are evidently potential practical problems with such a mitigation scheme, not least the need to ensure static stability particularly against rotation.

Modelling such a soft caisson provides its own challenges. The intention is that the weak layer should have a very low angle of friction. Assuming that the soft lateral walls (parallel to the direction of shaking) offer negligible shear stiffness, the resonant frequency for the mitigated system is around 0.9 Hz. With the scale factor for frequency, this gives a target model resonant frequency of around 5 Hz. The model soft caisson was contained within a plywood box resting on a base layer which was modelled by an array of roller bearings. These were found to permit sliding at a slope inclination of about 1.8° —close to the target value. The soft walls were modelled using cylinders of neoprene sponge sandwiched between the side walls of the plywood box and outer plywood sheets. The stiffness of the system could be tuned by altering the number and geometry of these cylinders: using four cylinders on each wall, with length 57 mm and diameter 60 mm gave a system resonant frequency of 7 Hz which was deemed to be near enough to the target frequency.

The shear stack was excited horizontally by two earthquake time histories (Figure 6.10): the Y–Y component of the Friuli-San-Rocco earthquake (15/9/76) and the N–S component of the Vrancea earthquake (4/4/1977). Similitude requires time to be scaled by a factor of 5.4 ($1/\sqrt{n_\ell}$): the 16.75 s Friuli-San-Rocco earthquake is replayed over 3.1 s; the 40 s Vrancea earthquake, over 7.4 s. The applied accelerations are shown in Figure 6.10 in both time and frequency domains. The Vrancea time history (Figure 6.10c, d) is charac-

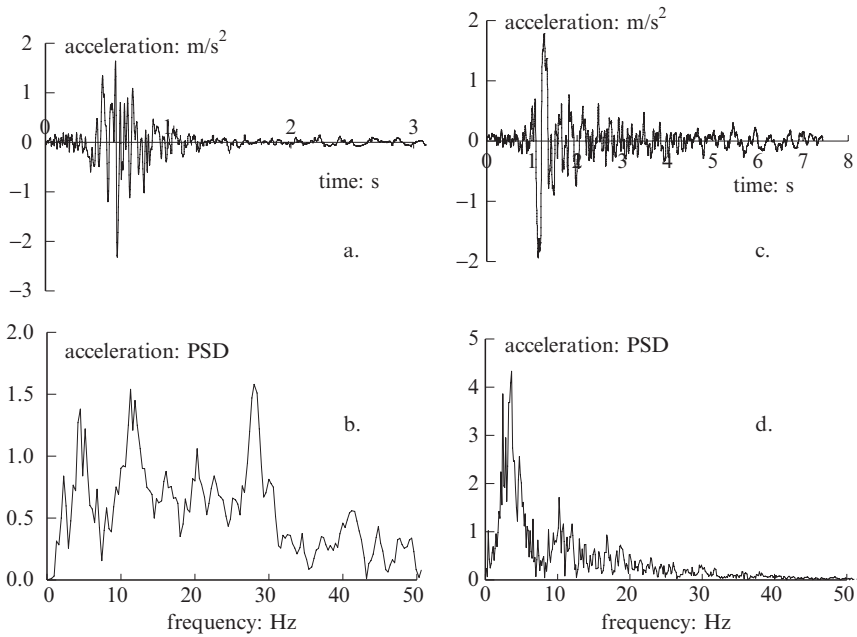


Fig. 6.10. (a), (b) Friuli-San-Rocco earthquake: (a) time history of acceleration and (b) spectral power density; (c), (d) Vrancea earthquake: (c) time history of acceleration and (d) spectral power density

terised by a single massive pulse at a frequency of about 3.5 Hz; the Friuli-San-Rocco history (Figure 6.10a, b) contains energy peaks at a number of frequencies.

The wider bandwidth of the Friuli-San-Rocco input motion induces a richer response in the unmitigated state. Accelerations are amplified by a deposit which undergoes appreciable shear strain. Excitation of the soil-structure interaction system results in rocking accelerations and settlements of the model structure at around 12 Hz. For this input motion, the mitigation scheme brings substantial improvements to the response (Figure 6.11). The amplification of acceleration within the soil deposit in the unmodified model disappears. Acceleration attenuation occurs at frequencies above 7 Hz, the resonant frequency of the model mitigation scheme. Rocking accelerations and inter-storey sways of the model structure are similarly improved.

However, with negligible energy at either the resonant frequency of the deposit (29 Hz) or the resonant frequency of the soil-structure interaction system (12 Hz), the Vrancea input motion produces small shear strains, settlements and structural rotations in the unmodified situation. The soft caisson has a resonance at 7 Hz and as a consequence has a major response to the Vrancea energy spike at 3.5 Hz. ‘Mitigation’ leads to increased accelerations in the foundation soil; there are beneficial effects of soil-structure

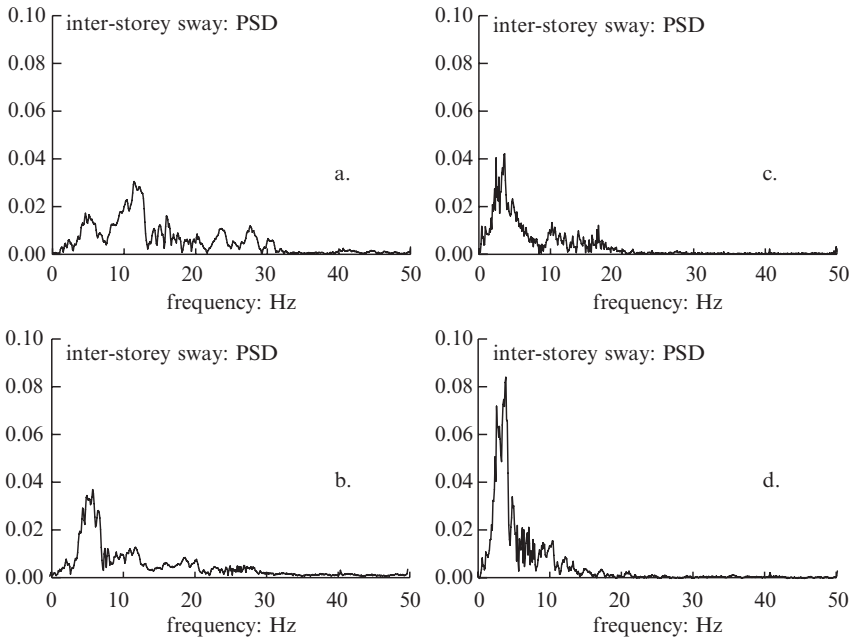


Fig. 6.11. Inter-storey sway power spectral density estimates:
 (a), (b) the Friuli-San-Rocco input motion; (c), (d) the Vrancea input motion;
 (a), (c) without soft caisson; (b), (d) with soft caisson

interaction but these do not outweigh the adverse effects of acceleration amplification: the frequency analysis of inter-storey sway is shown in Figure 6.11. For the Vrancea input motion, the mitigation scheme has an adverse effect.

It is not surprising that the mitigation scheme is successful when the frequency content of the input motion lies clearly above the resonant frequency of the mitigation scheme. Subject to satisfying conditions of static stability, reducing the stiffness of the soft caisson improves its benefit and widens its range of application. This sounds easier in theory than in practice where the frequency content of the earthquake motion is almost certain to be a surprise.

5. Macroelement analysis

The (apparent) randomness of natural earthquake motions means that any one motion may not be typical: a given system may respond in a completely different way to two different input histories (Figure 6.11). In addition, the degree of nonlinearity in any geotechnical system is such that the responses to apparently only slightly different inputs may be significantly different: the response is chaotic. One solution is to perform model tests using a very large number of different input motions, all of which are somehow related

in magnitude (probably all fitting a controlling frequency spectrum). If this is combined with other parametric studies then this implies a very large number of tests in order to ensure that attribution of consequences is secure.

In an extensive numerical study of the seismic response of a reinforced soil retaining wall, Hatami and Bathurst (2001) show that the response of the wall is influenced by, but not correlated with, many different characteristics of the input motion including: predominant frequency, peak ground velocity, earthquake intensity and duration of strong ground motion, and whether the input is a harmonic motion or a recorded earthquake accelerogram. A similar conclusion is reached by Simonelli and Viggiani (1995) from sliding block analyses (Newmark, 1965) of slope movement in earthquakes. Experimental studies of much simpler physical systems have shown clear evidence of chaotic response with non-monotonic relationships between, for example, amplitude of input motion and magnitude of permanent displacement response. This should also lead to caution in selecting and relying on particular input time histories.

Numerical modelling using a full finite element or finite difference analysis may be a heavy-handed way of seeking insight into some aspects of a problem of geotechnical behaviour. Macroelement modelling can be a helpful intermediate way of introducing some realistic geotechnical nonlinearity in order to compare different constitutive possibilities or to provide rapid ‘order-of-magnitude’ estimates of response against which the results of more extensive numerical—or physical—modelling can be compared. Such speedy modelling can be particularly beneficial where the concern is to study the dynamic response of a nonlinear geotechnical system, and, in particular, to study the way in which that response is influenced by the nature of the dynamic input motion. This has been the motivation behind the development of the macroelement model for a gravity retaining wall that is described here.

The system being considered is illustrated in Figure 6.12 (Muir Wood and Kalasin, 2004). This system contains enough detail to have a realistic geotechnical ‘feel’ about it while still retaining the simplicity associated with the macroelement approach. The wall interacts with the ground in two ways: the wall sits on a foundation described by a foundation macroelement or transfer function; the wall retains backfill soil and the interaction with the retained soil is described by the wall macroelement.

The foundation macroelement is subjected to simultaneous and interacting vertical, horizontal and moment loading. The macroelement model adopted here has emerged from several parallel experimental and theoretical studies of the response of footings (e.g., Nova and Montrasio, 1991; Cremer et al., 2001). The incentive for these investigations came from the demands of offshore foundations which are subjected to horizontal loads which are of magnitude comparable with the vertical load.

The response of the footing can be described by a macroelement model with exactly the same features as a constitutive model describing the behaviour of a single soil element—replacing work-conjugate groups of strain increment and stress variables with work-conjugate groups of displacement increments and force resultants. Constructing

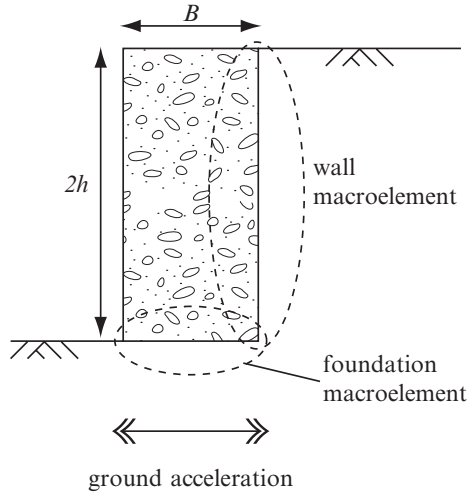


Fig. 6.12. Gravity retaining wall: macroelements

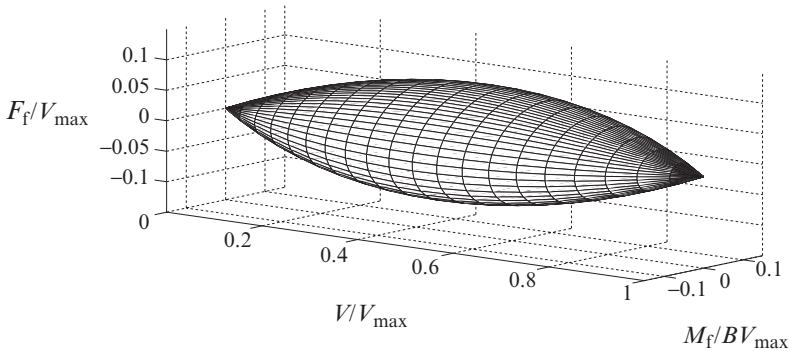


Fig. 6.13. Yield surface for footing under combined vertical, horizontal and moment load

this model within an elastic-plastic framework it is then necessary to make the usual statements about the ingredients of the model: elastic response; yield surface bounding elastically attainable states (Figure 6.13); plastic potential describing the mechanism of plastic deformation; and a hardening law.

For the interaction between the wall and the retained soil a rudimentary macroelement model can be devised by assuming that the earth pressure coefficient at any height in the soil is controlled by an elastic-perfectly plastic relationship (solid lines in Figure 6.14)—introducing a series of nonlinear independent Winkler springs. Analysing the different possible regimes of response—depending on the direction of translation and rotation of the wall and on whether the earth pressure at the top or bottom of the wall has reached the

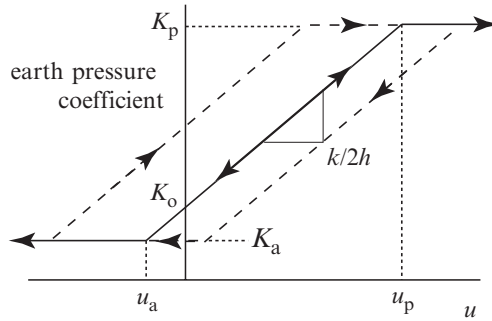


Fig. 6.14. Trilinear relationship between mobilised earth pressure coefficient and relative displacement of wall and soil

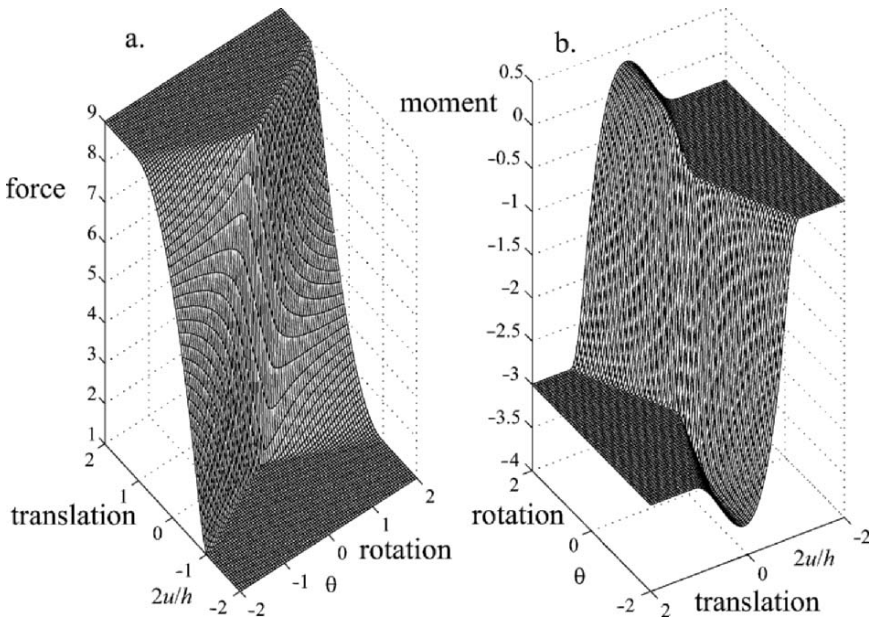


Fig. 6.15. Dependence of (a) wall force and (b) moment on relative displacement (translation) and rotation of wall

limiting Rankine active (*A*) or passive (*P*) value—interaction surfaces can be generated for the force and moment developed on the wall as a function of the two displacement components (Figure 6.15).

Our understanding of the response of soil elements under non-monotonic loading (Section 2) shows that at the element level any successful model will have to incorporate the possibility of kinematic hardening so that response (a) is influenced by recent history and (b) shows the occurrence of irrecoverable strains well before the bounding yield

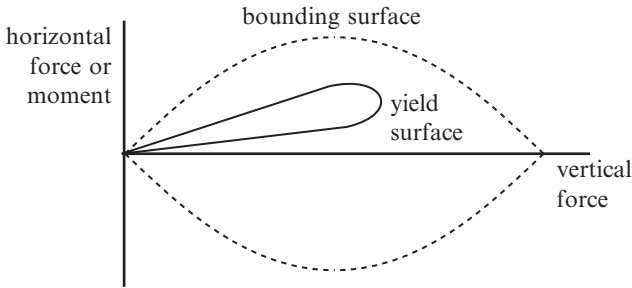


Fig. 6.16. Kinematic ‘ice-cream cone’ yield surface inside bounding surface of macroelement foundation model of DiPrisco et al. (2003)

surface is reached. Exactly the same arguments apply to the macroelement modelling. For the wall macroelement this can be achieved by modifying the Winkler springs to have the hysteretic characteristics of the dashed lines in Figure 6.14, so that whenever the direction of relative movement of wall and retained soil changes the local response is elastic. For the foundation macroelement DiPrisco et al. (2003) have added a kinematic yield surface inside the ‘bounding’ surface of Figure 6.13 (Figure 6.16). A macroelement that neglects the plasticity that occurs almost throughout the loading history will not be satisfactory.

Earthquake motion tends to be of quite short duration with a very few cycles of high acceleration and many cycles of much lower acceleration with a typical duration of 10–20 s depending on the location and nature of the earthquake. Once the motion becomes large enough to move into the regimes of nonlinear response of the wall interacting with the foundation and the retained soil, then the detail of the movement of the wall depends on the exact time within the earthquake that particular large pulses of ground acceleration occur. This can be illustrated by showing the dependence of the translation and rotation of the wall on the amplitude of the earthquake relative to the critical steady unidirectional acceleration required to generate active failure of the wall (Figure 6.17).

The system being analysed is extremely nonlinear. The input motion that is generated by an earthquake is extremely irregular. Put together, the overall system response is somewhat chaotic. There is no linear variation of displacement or rotation of the wall with this relative magnitude of the input motion (Figure 6.17). In fact, for some time histories of input motion there is not even a monotonic variation of movement with relative acceleration input magnitude.

The response of this simple macroelement system confirms rather clearly that, so far as *performance* of the system is concerned—the permanent displacement developed during the seismic event—the occurrence of high acceleration pulses of short duration is not necessarily devastating. The macroelement model also allows us to explore parametric variations of both the geotechnical features of the system and the input motion itself in

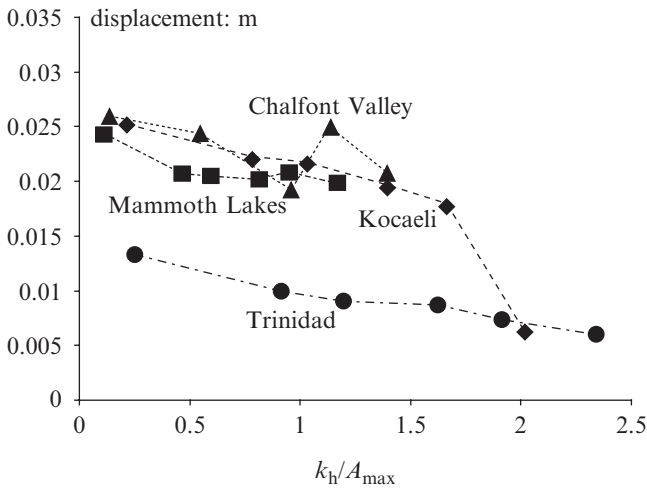


Fig. 6.17. Influence of relative earthquake acceleration on wall displacement (after Kalasin, 2004)

order to understand their interaction. The response is chaotic in the sense that the outcome is sensitive to the detail of the input motion and the time history.

6. Conclusions

Whatever the category of modelling that is undertaken, some detailed constitutive model is required: constitutive modelling plays a key role in defining characteristics of soil response to be simulated and in establishing the route to extrapolation from model or field observations. Key characteristics of the mechanical behaviour of soil *elements* under non-monotonic loading provide a strong hint as to the way in which macroelement models should be constructed to describe geotechnical *systems*. Even with these realistic features, macroelement models are considerably simpler numerically and more rapid to use than full finite element analyses from which there seems little prospect of escape for study of complex systems. Laboratory geophysics can provide a means of probing the evolving elastic anisotropy of the soil, but even in this controlled laboratory situation (or perhaps because of this) the dynamic signals are not easy to decode—they contain much richness of information about the detail of the passage of waves through the particulate soil which has not yet been greatly exploited. Nevertheless, the benefit of using such techniques for anchoring the elastic properties and for revealing information about evolving fabric is clear.

In the end any form of numerical modelling of static or dynamic geotechnical problems will need to be validated against observations from physical experiments at some scale. There is a role for all forms of modelling. Macroelement modelling—provided it can be calibrated for correct values of controlling parameters—provides a useful and effective

route for parametric study of both geotechnical and seismological variables. Provided the macroelement contains sufficient realism, it can aid understanding of the influence of nonlinearity and indicate clearly the potential for chaotic response.

Acknowledgements

Material for this paper has come from research projects for which substantial contributions were made by: Alessandro Gajo (constitutive modelling), Marcos Arroyo (interpretation of laboratory geophysical testing); Matthew Dietz (shaking table testing for NEMISREF project); and Thaveechai Kalasin (macroelement modelling).

REFERENCES

- Arroyo M, Muir Wood D, Greening PD, Medina L, Rio, J (2006) Effects of sample size on bender-based axial G_o measurements. *Géotechnique* 56(1): 39–52
- Been K, Jefferies MG (1985) A state parameter for sands. *Géotechnique* 35(2): 99–112
- Cremer C, Pecker A, Davenne L (2001) Cyclic macro-element for soil–structure interaction: material and geometrical nonlinearities. *International Journal for Numerical and Analytical Methods in Geomechanics* 25(13): 1257–1284
- Crewe AJ, Lings ML, Taylor CA, Yeung AK, Andrighetto R (1995) Development of a large flexible shear stack for testing dry sand and simple direct foundations on a shaking table. In: Elnashai A (ed) *European Seismic Design Practice*. Balkema, Rotterdam, pp 163–168
- Crewe AJ (1998) The characterisation and optimisation of earthquake shaking table performance. PhD thesis, University of Bristol
- DiPrisco C, Nova R, Sibilia A (2003) Shallow footing under cyclic loading: experimental behaviour and constitutive modelling. Chapter 4 in Maugeri M, Nova R (eds) *Geotechnical analysis of seismic vulnerability of monuments and historical sites*. Pàtron Editore, Bologna, pp 99–121
- Gajo A, Muir Wood D (1999a) A kinematic hardening constitutive model for sands: the multiaxial formulation. *International Journal for Numerical and Analytical Methods in Geomechanics* 23(5): 925–965
- Gajo A, Muir Wood D (1999b) Severn-Trent sand: a kinematic hardening constitutive model for sands: the $q-p$ formulation. *Géotechnique* 49(5): 595–614
- Hatami K, Bathurst RJ (2001) Investigation of seismic response of reinforced earth retaining walls. In: Prakash S (ed) *Proc. 4th Int. Conf. on Recent advances in geotechnical earthquake engineering*. Paper 7.18 University of Missouri-Rolla
- Kalasin T (2004) Dynamic macroelement model for gravity retaining walls. PhD thesis, University of Bristol
- Lings ML, Greening PD (2001) A novel bender/extender element for soil testing. *Géotechnique* 51(8): 713–717
- Muir Wood D (2002) Some observations of volumetric instabilities in soils. *International Journal of Solids and Structures* 39(13–14): 3429–3449
- Muir Wood D (2004) *Geotechnical modelling*. E & FN Spon (488pp) ISBN 0-419-23730-5
- Muir Wood D, Kalasin T (2004) Dynamic macroelement model for gravity retaining walls. In: Pande GN, Pietruszczak S (eds) *Numerical models in geomechanics NUMOG IX*, Taylor & Francis Group, London, pp 731–737

- Newmark NM (1965) Effects of earthquakes on dams and embankments (5th Rankine Lecture). *Géotechnique* 15(2): 139–160
- Nova R, Montrasio L (1991) Settlements of shallow foundations on sand. *Géotechnique* 41(2): 243–256
- Pennington DS, Nash DFT, Lings ML (1997) Anisotropy of G_o shear stiffness in Gault clay. *Géotechnique* 47(3): 391–398
- Pitilakis K, Manos G, Raptakis D, Makra K, Manakou M, Apostolidis P, Terzi V (2005) Theoretical and experimental studies in EUROSEISTEST. Proc 16th ICSMGE, Osaka 2005
- Sadek T (2006) Multiaxial testing of sands. PhD thesis, University of Bristol
- Simonelli AL, Viggiani C (1995) Effects of seismic motion characteristics on earth slope behaviour. In: Ishihara K (ed) *Earthquake geotechnical engineering (Proc 1st Int Conf, Tokyo)*. Rotterdam: Balkema, pp 1097–1102
- White, DJ, Take, WA, Bolton, MD (2003) Soil deformation measurement using particle image velocimetry (PIV) and photogrammetry. *Géotechnique* 53(7): 619–631

CHAPTER 7

FIELD SEISMIC TESTING IN GEOTECHNICAL EARTHQUAKE ENGINEERING

Kenneth H. Stokoe, II

Department of Civil, Architectural and Environmental Engineering,

The University of Texas at Austin, U.S.A.

k.stokoe@mail.utexas.edu

Abstract. Field seismic testing is an active and growing area in geotechnical earthquake engineering. The primary purpose of the field tests is to develop compression-wave velocity (V_p) and shear-wave velocity (V_s) profiles. These profiles are used to represent the stiffnesses of the geologic materials in the small-strain range. Many seismic methods are available for shallow investigations as discussed in the paper. Shallow investigations are defined as profiling to depths less than 75 m. Developments are occurring in profiling to intermediate (75 to 225 m) and deep (greater than 225 m) depths. The seismic methods used for deeper profiling are the downhole, suspension logging, and surface-wave methods. Examples of deeper profiling are presented. In addition, field seismic methods are being developed to perform parametric studies in situ. Examples are presented that show in-situ measurements of the effects of: (1) stress state on V_s and V_p , (2) nonlinear straining on shear modulus, and (3) cyclic loading leading to liquefaction.

1. Introduction

The starting point when evaluating the response to earthquake shaking of critical facilities founded on or embedded in the earth is small-strain stiffness profiles, expressed by the variation of compression-wave velocity (V_p) and shear-wave velocity (V_s) with depth (Kramer, 1996). Profiles of V_p and V_s are measured in the field using seismic methods. The seismic method or combination of seismic methods employed in field investigations depends upon: (1) the geologic profile, (2) the maximum profiling depth, (3) the size of the investigation area, and (4) the critical level assigned to the structure or facilities. In many instances, the field investigation is limited to the top 30 m at one to three locations. The purpose of the investigation is to evaluate the average V_s over the top 30 m (V_{s30}) for use in a code-based design. Both intrusive and nonintrusive seismic methods are used in these shallow investigations and only one field method is employed. Intrusive methods used in such investigations are the crosshole, downhole, seismic cone penetrometer (SCPT), seismic flat-plate dilatometer, and suspension logger (P-S logger). The nonintrusive methods are surface-wave methods and are based on measuring Rayleigh-type waves. The spectral-analysis-of-surface-waves (SASW) and multi-channel-analysis-of-surface-waves (MASW) methods are two active-source methods employed in shallow investigations.

The state of practice in shallow seismic investigations is good and improving. As noted above, a number of field seismic methods are readily available for use. Improvements in analysis methods, instrumentation and automation associated with the methods are occurring. The number of knowledgeable engineering practitioners is also increasing, and areas of application are growing. Surface-wave testing is the most rapidly growing area, due in large part to the efficiency and cost-effectiveness of nonintrusive testing. Developments are also occurring in two other aspects of field seismic testing. The first is profiling to deeper depths in all types of geologic settings. The second is performing parametric studies in situ. The effects of parameters such as stress state, strain amplitude, and cyclic loading leading to liquefaction are being evaluated in situ. Developments in both aspects are briefly discussed below and are covered in more detail in the presentation.

2. Deeper seismic profiling

In the past decade, considerably deeper investigations have been required at critical sites in the United States, with profiling depths in the range of 125 to 450 m. Intermediate and deep wave-velocity profiles have been measured with two or three seismic methods at several of these sites. Intermediate-depth profiles are defined as having maximum depths in the range of 75 to 225 m and deep profiles have depths exceeding 225 m. (Shallow profiles are defined as profiles less than 75 m deep.) The seismic methods used in deeper profiling have been downhole testing, surface-wave based tests and P-S suspension logging as discussed below.

Intermediate and deep profiles have been measured at several locations including: (1) Yucca Mountain, Nevada, (2) the northern Mississippi embayment, (3) the Salt Lake Valley, Utah, and (4) the Hanford Site near Richland, Washington. The spectral-analysis-of-surface-waves (SASW) method was used at each location, and measurements were performed over lateral extents ranging from 10 to 200 km. The large vibrator used as the SASW source is called “Liquidator”. Liquidator is shown in Figure 7.1a. It is a one-of-a-kind, low-frequency vibrator that is specially designed to give high-force output



Fig. 7.1. Large mobile vibrators used as controllable, high-energy seismic sources: (a) the low-frequency vibrator called Liquidator and (b) the tri-axial vibrator called T-Rex

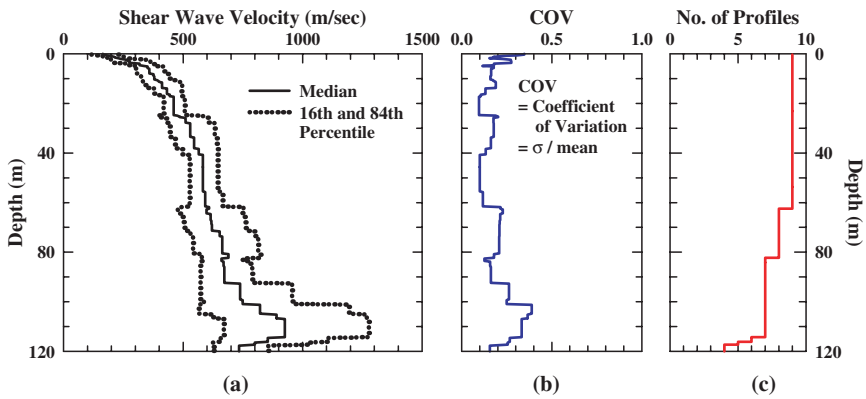


Fig. 7.2. Statistical analysis of intermediate-depth V_s profiles in an alluvial deposit from SASW testing: (a) median and \pm one standard deviation, (b) coefficient of variation, and (c) number of profiles (from Lin, 2007)

(a peak force of about 90 kN) in the low-frequency range (about 1 to 4 Hz). Liquidator is part of a shared-use equipment site that is operated by the University of Texas at Austin (nees@utexas) and funded by the U.S. National Science Foundation (NSF) as part of the George E. Brown, Jr. Network for Earthquake Engineering Simulation (NEES). Statistical analysis of nine, intermediate-depth V_s profiles of the alluvium at the Hanford Site is presented in Figure 7.2. The median V_s profile and the associated coefficient of variation (COV) are shown in Figure 7.2a and b, respectively. These results compare well with measurements from independent downhole tests, with the average median value of V_s from each test method within 4% over the same test depths. However, due to various constraints, downhole testing was only performed to an average depth of about 70 m.

Deep V_p and V_s profiles have also been measured by the downhole and P–S suspension logging methods at the Hanford Site. In this case, testing was performed in three boreholes spaced around the footprint of one set of buildings. Testing was conducted to a maximum depth of about 440 m. In the downhole test, generating measurable compression (P) and shear (S) waves at depths of 300 to 400 m was challenging due to the alternating layers of soil interbeds and basalt. Therefore, the triaxial vibrator, called “T-Rex”, was used as the seismic source. (Measurements with the P–S suspension logger were easier to perform at the deeper depths since the wireline tool containing the source and receivers is lower to the test depths.) T-Rex is another large vibrator operated by nees@utexas. T-Rex is capable of generating large dynamic forces in any of three directions (X, Y, or Z directions). The peak forces are about 270 kN in the vertical (Z) direction and about 135 kN in either horizontal direction. The vibration direction can be changed at the touch of a button. These capabilities, combined with the ability to prescribe the source signal, made T-Rex an excellent source for deep downhole profiling. The use of 20- to 50-Hz, fixed-sine input signals with 4 to 10 cycles worked well. Example travel-time records are presented in Figure 7.3. Sets of P- and S-wave records at depths of 137 and 290 m

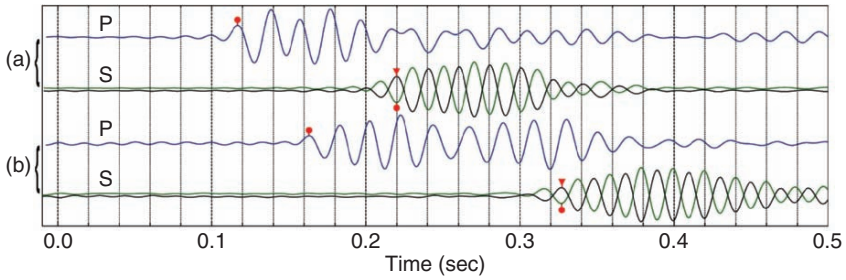


Fig. 7.3. Example compression (P) and shear (S) wave records using T-Rex as the downhole seismic source: (a) receiver at an intermediate depth of 137 m and (b) a deep depth of 290 m (from Li, 2007)

are shown in Figures 7.3a and b, respectively. Relative times of the direct P and S wave on each waveform are shown in the figure. These relative points were tracked throughout the complete depth range from which V_p and V_s profiles were determined.

3. In-situ parametric studies

Field seismic methods are also being developed to permit in-situ evaluation of various parameters that affect the dynamic response of soil during earthquakes. These parameters include: (1) state of stress, (2) strain amplitude in the nonlinear range, and (3) dynamic loading at strains creating pore pressure generation leading to liquefaction. The methods involve applying static and dynamic loads near the surface of the soil deposit and measuring the response of the soil mass beneath or around the loaded area using embedded instrumentation. In all cases, T-Rex (see Figure 7.1b) is an excellent source in applying both static and dynamic loads.

Two field approaches that are used to measure nonlinear shear moduli are shown in Figure 7.4. The first approach (Figure 7.4a) utilizes a surface footing that is dynamically loaded horizontally (Park, 2007). This approach is also used to evaluate the effect on V_s and V_p of in-situ changes in stress state as discussed below. The second approach (Figure 7.4b) utilizes a drilled shaft that is dynamically loaded vertically (Kurtulus, 2006). The third parametric study, involving controlled loading at strain levels that create pore pressures, is simply an adaptation of the surface-footing arrangement in Figure 7.4a. In this case, the embedded instruments are placed at larger depths below the surface, with the locations being within the upper portion of the potentially liquefiable soil layer (Cox, 2006). Brief examples of each parametric study are presented below.

Example 1 Log V_s –Log σ_o Relationship. This example, shown in Figure 7.5a, presents one set of measurements in which the log V_s –log σ_o relationship was determined (Stokoe et al., 2005). A 1.2-m diameter concrete footing was used as the loading platen. The soil beneath the footing was a poorly graded sand (SP) that was lightly cemented, overconsolidated, and unsaturated. Staged loading was performed with increasing static vertical

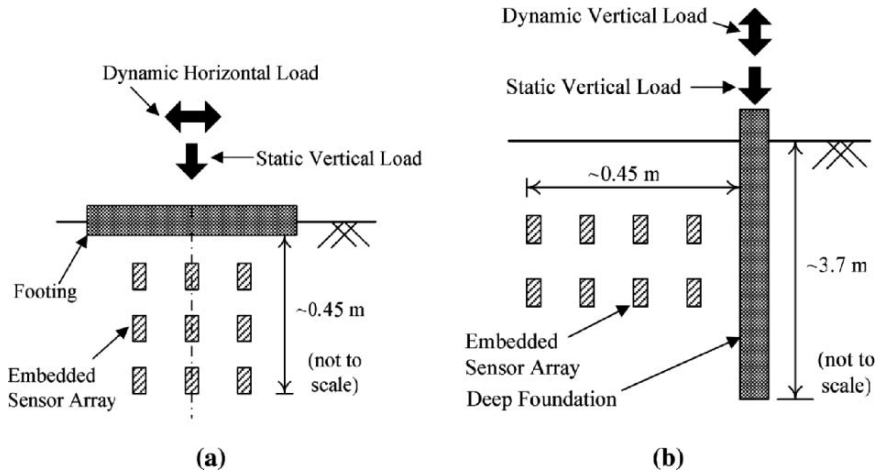


Fig. 7.4. Generalized testing arrangements to measure nonlinear shear-wave propagation in situ with a dynamically loaded foundation: (a) surface foundation and (b) drilled shaft (from Stokoe et al., 2006)

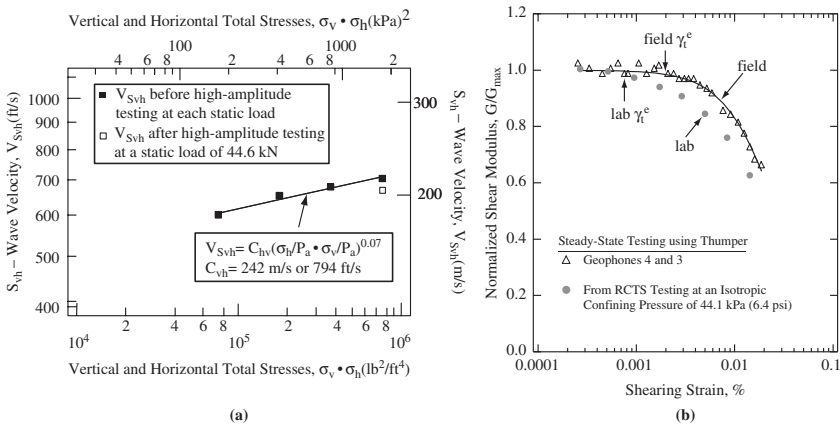


Fig. 7.5. In-situ evaluation of two parameters that affect the dynamic response of soil: (a) the variation of $V_{S_{vh}}$ with increasing stress (from Stokoe et al., 2005) and (b) comparison of the $G/G_{max}-\log \gamma$ relationships measured in the field and laboratory (from Park., 2007)

loads. At each static vertical load, small-strain, horizontal dynamic loads were generated which permitted vertically propagating and horizontally polarized shear waves (S_{vh}) to be measured. The stress state in the soil is expressed by the vertical and horizontal total stresses at each measurement depth, σ_v and σ_h , respectively, as discussed by Stokoe and Santamarina (2000). Clearly, the variation in V_s with stress state was measured. The $\log V_s-\log \sigma_v \cdot \sigma_h$ relationship reveals several important points that are discussed in the presentation (and in Stokoe et al., 2005, 2006).

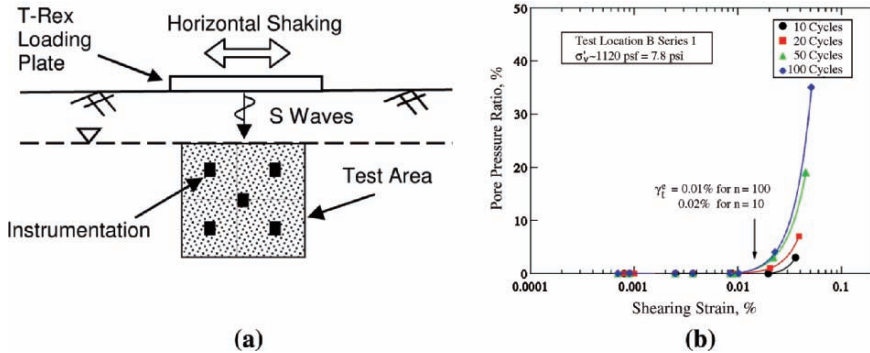


Fig. 7.6. In-situ evaluation of liquefaction resistance: (a) test area that is stage loaded and (b) in-situ pore pressure generation curves obtained from one test (from Cox., 2006)

Example 2 Nonlinear Shear Modulus Measurements Using a Surface Footing. The second example is presented in Figure 7.5b. In this example, a 0.9-m diameter surface footing was loaded with a constant vertical force. At this point, the footing was staged loaded with increasingly larger horizontal dynamic loads. Shear waves with increasing strains amplitude were measured from which the G - $\log \gamma$ and G/G_{\max} - $\log \gamma$ relationships were evaluated. The soil was a poorly graded sand and silty sand (SP-SM) that was lightly cemented. Results from an intermediate dynamic loading stage are shown in Figure 7.5b. Measurements of G in the linear range (hence, G_{\max}) and in the nonlinear range were clearly conducted. The maximum shearing strain was only 0.02% since this was an intermediate stage. The field G/G_{\max} - $\log \gamma$ relationship shows that the value of the elastic threshold strain (γ_t^e) in the field is around 0.002% at the imposed stress level. Comparison of the field relationship with laboratory results using an intact specimen is also shown in Figure 7.5b.

Example 3 In-Situ Dynamic Liquefaction Test. An in-situ dynamic liquefaction test is under development (Rathje et al., 2004; Cox., 2006). It is designed to measure pore water pressure generation under dynamic loading at field sites. T-Rex is used to provide the dynamic loading. The generalized test configuration is illustrated in Figure 7.6a. Shear waves dynamically load the test area. The level of shaking is controlled by specifying the number of cycles and their amplitudes. The shear waves induce cyclic shear strains which generate excess pore water pressure in the test area. One example of testing at the Wildlife Site in Imperial Valley, CA is shown in Figure 7.6b. This work is discussed in detail by Cox, (2006).

4. Conclusions

Field seismic testing to determine V_s and V_p profiles at depths less than 75 m is widely done in geotechnical earthquake engineering. This profiling is defined as shallow profiling herein, and many field methods are available. Deeper profiling is less often

performed but is required in the earthquake design of some critical facilities. The down-hole, suspension logging and surface-wave methods are applicable for profiling at the intermediate (75 to 225 m) and deep (greater than 225 m) depths associated with deeper profiling.

In-situ testing to study parameters that are important in geotechnical earthquake engineering is also progressing. Parameters such as stress state, strain amplitude, and liquefaction potential are being studied in situ with seismic tests.

Acknowledgments

Financial support for much of this work was provided through the National Science Foundation under grants CMS-0324326 and CMS-0421275 and through the U.S. Geological Survey (USGS) under awards 01HQR0036 and 06HQGR0050. Financial support for the development of the nees@utexas Equipment Site was provided by the George E. Brown, Jr. Network for Earthquake Engineering Simulation (NEES) under grant CMS-0086605. Support from the U.S. Department of Energy was provided for studies at the Yucca Mountain and Hanford Sites. Interactions with numerous colleagues are appreciated. Thanks also goes to graduate students and staff at the University of Texas at Austin who assisted in the field and laboratory work.

REFERENCES

- Cox BR (2006) Development of a direct test method for dynamically assessing the liquefaction resistance of soils in situ. Ph.D. Dissertation, The University of Texas at Austin, U.S.A.
- Kramer SL (1996) *Geotechnical earthquake engineering*. Prentice Hall, New York
- Kurtulus A (2006) Field measurement of the linear and nonlinear shear moduli of soils using drilled shafts as dynamic cylindrical sources. Ph.D. Dissertation, The University of Texas at Austin, U.S.A.
- Li S (2007) Procedures and analyses for deep downhole seismic testing. Ph.D. Dissertation, The University of Texas at Austin, U.S.A.
- Lin YC (2007) Characterizing V_s profiles by the SASW method and comparison with other seismic methods. Ph.D. Dissertation, The University of Texas at Austin, U.S.A.
- Park K (2007) Field measurements of the linear and nonlinear shear moduli of soils using dynamically loaded surface footings. Ph.D. Dissertation, The University of Texas at Austin, U.S.A.
- Rathje EM, Chang WJ, Stokoe II KH (2004) Development of an in situ dynamic liquefaction test. *ASTM Geotechnical Testing Journal* 28(1)
- Stokoe II, KH Santamarina CJ (2000) Seismic-wave-based testing in geotechnical engineering. International Conference on Geotechnical and Geological Engineering (GeoEng2000)
- Stokoe II, KH Axtell PJ, Rathje EM, Valle C (2005) In situ measurement of small-strain stiffnesses in soil beneath a footing with varying static loads. Proceedings of the Geo-Frontiers 2005 Congress, Austin, Texas, U.S.A.
- Stokoe II, KH Kurtulus A, Park K (2006) Development of field methods to evaluate the nonlinear shear and compression moduli of soil. Earthquake Geotechnical Engineering Workshop, University of Canterbury, Christchurch, New Zealand

CHAPTER 8

LIQUEFACTION STRENGTHS OF POORLY-GRADED AND WELL-GRADED GRANULAR SOILS INVESTIGATED BY LAB TESTS

Takaji Kokusho

*Civil Eng. Department, Faculty of Science & Engineering,
Chuo University, Tokyo Japan
kokusho@civil.chuo-u.ac.jp*

Abstract. In order to understand differences in liquefaction behavior of well-graded gravelly soils compared to poorly-graded sands, a series of lab tests was performed on granular soils with different particle gradations or fines content having different relative densities reconstituted in laboratory. Large soil container tests indicated that SPT N -value of well-graded gravels of relative density higher than 50% is considerably larger than that of sand of the same relative density, resulting in lower liquefaction strength of gravelly soils than that of poor-graded sand under the same corrected N -value, N_1 , for $N_1 > 25$ –30. Cyclic triaxial tests on reconstitutes specimens indicated that relative density can serve as a proper index to uniquely evaluate liquefaction strength corresponding to 5% DA strain for variety of granular soils having different gradations. In contrast, post-liquefaction undrained residual strength for larger strain is not uniquely determined by relative density but largely dependent on particle gradations. Also found was that the liquefaction strength clearly reduces with increasing fines content F_c both in well-graded and poorly-graded soils but the reduction occurs in a smaller range of F_c in accordance with smaller critical void ratio for well-graded soils than for poorly-graded sand. Increase in F_c also reduces post-liquefaction residual strength of granular soils particularly for higher relative density. Greater reduction occurs in smaller F_c range for well-graded soils than for poorly-graded sand because of the difference in the critical void ratio.

1. Introduction

So far, liquefaction research on granular soils has been focused on poorly-graded sandy soils. However, liquefaction of well-graded gravelly soils, though less frequent in past records than that of sands, has increasingly been witnessed during recent earthquakes. During the 1995 Hyogoken Nambu earthquake in Japan, reclaimed ground in Kobe filled with decomposed granite sandy soil called Masado containing large quantity of gravel and fines fraction liquefied extensively despite a widely accepted perception that gravelly soil was harder to liquefy than sand because of larger uniformity coefficient and larger dry density. The SPT N -value of the gravelly soil uncorrected by overburden stress was as low as 5 to 15. During the 1993 Hokkaido Nansei-Oki earthquake, rock debris avalanche soil containing large size rocks as well as sands and silts liquefied in Mori town in Hokkaido causing differential settlements of wooden houses. The SPT N -value was 8–16 and the S-wave velocity was unbelievably low as 60–90 m/s (Kokusho et al., 1995). During the 1983 Borah Peak earthquake in Idaho, USA, fluvial sandy gravel liquefied extensively

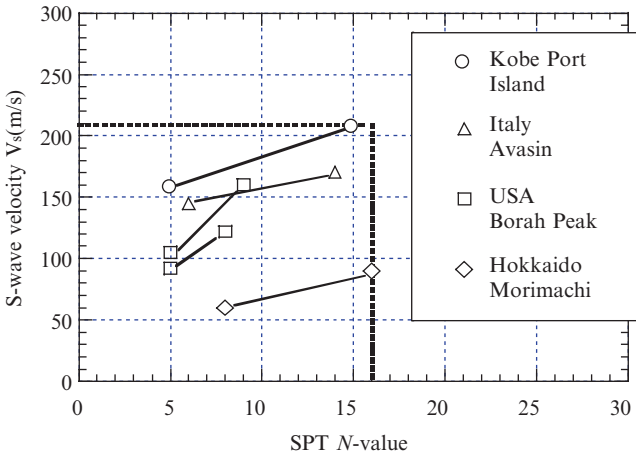


Fig. 8.1. Unadjusted SPT N -value versus S-wave velocity relationship for recently liquefied gravelly soils (Kokusho et al., 1995)

triggering lateral spread in gently sloping ground. The N -value of the loosely deposited gravel layers was 5–9 and the S-wave velocity 90–160 m/s (Andrus, 1994). Besides these cases, liquefaction of gravelly soils was also reported during several earthquakes, such as the 1948 Fukui earthquake in Japan, the 1964 Alaskan earthquake, Chinese earthquakes, etc. Figure 8.1 summarizes SPT N -values versus V_s relationships of liquefied gravelly deposits in recent years.

Figure 8.2 exemplifies typical grain size curves of the gravelly soils liquefied recently. They are actually the mixture of gravels, sands and sometimes even finer soils. In Figure 8.3, the mean grain size (D_{50}) is plotted versus the uniformity coefficient (C_u) for the same gravelly soils. So far, the upper limits for D_{50} and C_u are about 20 and 300 mm, respectively, but no limit may reasonably be justified, indicating that gravelly soils can liquefy if they are loose enough no matter how well graded and how coarse they may be. Dry densities of these gravelly soils are relatively high (1.7–2.0 t/m³ for reclaimed soil in Kobe and 2.0–2.1 t/m³ for debris avalanche soil in Hokkaido) due to large uniformity coefficients, actually much higher than typically liquefiable loose sands (e.g. 1.4–1.5 t/m³ for alluvial Niigata sand). Gravelly soils can be densely packed and are normally believed to be stiffer and seismically more stable than sands. However, gravelly soils as previously mentioned can sometimes have unexpectedly low N -value and S-wave velocity.

It should also be noted that permeability of well-graded gravelly soils cannot not be high enough to retard pore-pressure buildup, because sand particles filling the voids of gravels keep the permeability no higher than sandy soils. For example, permeability coefficients of the order of 10^{-2} – 10^{-4} cm/s are reported for gravelly layers in Japan; reclaimed DG fill of Port Island, Pleistocene gravel layer in Osaka and Holocene fluvial gravel near Tokyo (JGS Committee, 2001).

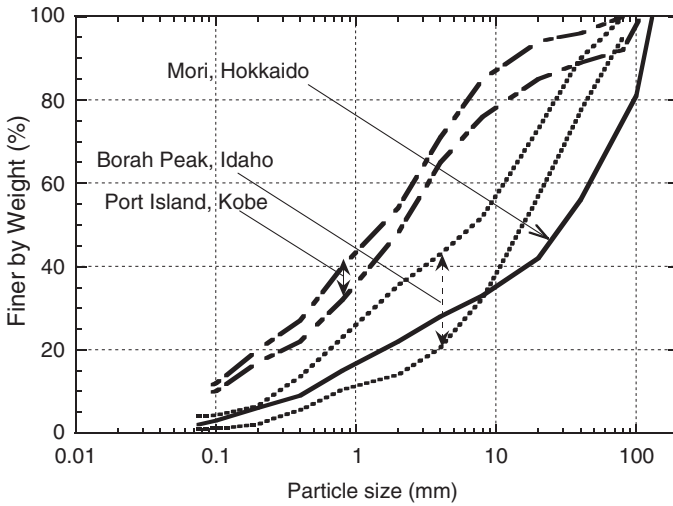


Fig. 8.2. Typical grain size curves of gravelly soils recently liquefied (Kokusho et al., 1995)

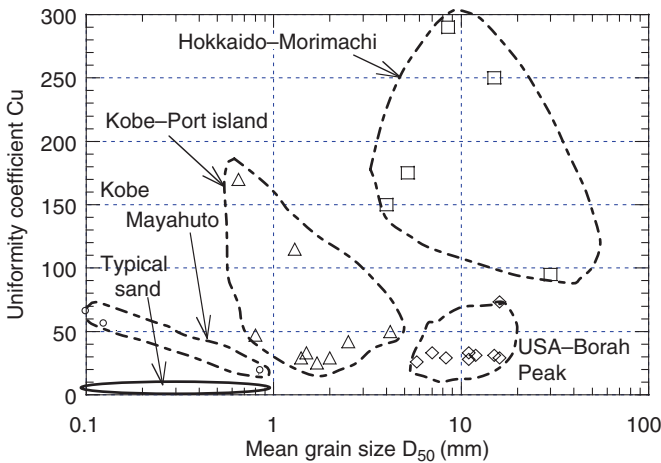


Fig. 8.3. Mean grain size versus uniformity coefficient relationship for recently liquefied gravelly soils (Kokusho et al., 1995)

Figure 8.4 summarizes undrained cyclic strengths of well-graded gravelly soils plotted versus SPT N_1 -values (N -values normalized for effective overburden stress of 98 kPa) based on previous researches (Tanaka et al., 1992; Andrus, 1994; Kokusho et al., 1995; Inagaki et al., 1996). Most of the undrained strengths (the stress ratio for 2%–2.5% double amplitude strain in 15–20 cycles) were obtained by cyclic triaxial tests on intact samples

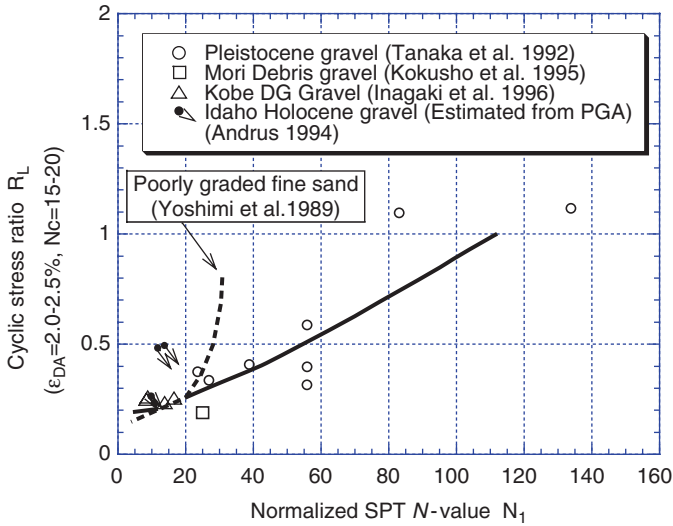


Fig. 8.4. Normalized SPT N_1 -value versus cyclic stress ratio of well-graded gravelly soils

recovered by in situ freezing sampling. For data points of Idaho gravel represented by solid circles with arrows in the chart, the stress ratio was evaluated from PGA (Peak Ground Acceleration) during the 1983 Borah Peak earthquake, indicating that the critical curve for the onset of liquefaction may be located somewhere below the points.

On the same chart, the similar relationship for poorly-graded clean sand with uniformity coefficient $C_u = 1.6$ on average proposed by Yoshimi et al. (1989) is drawn with a dashed curve. It is remarkable that the solid curve approximating well-graded gravelly soils have almost the same stress ratio as clean sand for N_1 smaller than 20–25. The solid curve in Figure 8.4, however, tends to largely deviate from the curve of sand as N_1 -value gets larger than around 25–30. It is also noted that all the gravelly soils actually liquefied during recent earthquakes have N_1 -value no larger than 25 and also contains measurable fines; fines content $F_c = 8\%–18\%$ for Kobe DG gravel, $F_c = 8.5\%$ for Mori debris gravel and $F_c = 3\%–18\%$ for Idaho fluvial gravel.

In order to understand differences in liquefaction behavior between poorly-graded and well-graded soils from the view point of particle gradation, results of a series of basic laboratory tests carried out by the present author and his colleagues are addressed here; (a) soil container tests for the effect of grain size distribution on N -value and V_s , (b) undrained triaxial tests for the effect of grain size distribution on liquefaction and post-liquefaction strength and (c) undrained triaxial tests for the effect of fines content on liquefaction and post-liquefaction strength.

2. Effect of grain size curve on S-wave velocity and N -value

Kokusho and Yoshida (1997) investigated the effect of particle gradations on N -values and S-wave velocities by large scale soil container tests for sands and gravels with varying C_u . Artificial soil layers were made in a large steel soil container, 2.0 m inside diameter and 1.5 m height, as shown in Figure 8.5. The soil layers were saturated and vertically loaded hydraulically with given overburden stresses by a rubber bag installed just beneath the container cap. The overburden was initially set as 50 kPa and then increased step by step either to the maximum of 200 kPa in the first series of test (named here as LC test) or to the maximum of 1 MPa in the second series called here as HC test. The stress condition in the soil layer was monitored vertically and horizontally by pressure cells installed at the bottom and side walls of the container. The soils were placed in the container with various initial density either by foot-tamping or by a mechanical tamper. Standard Penetration Test (SPT) was carried out through openings in the container cap into soils loaded with various overburden stresses under K_0 -condition. The K_0 -value, σ'_h/σ'_v , evaluated as a ratio of the measured horizontal effective pressure σ'_h versus the vertical pressure σ'_v was $K_0 = 1/2-1/4$ in most cases but $K_0 = 1/5$ for very dense soils. Velocity of SH-wave generated from a steel rod and vertically propagating upward was measured by using a set of sensors embedded in the soil layer as depicted in Figure 8.5.

Five soils with different particle gradations shown in Figure 8.6 were used in the test; two types of river sands (TS and TKS sands) and three types of gravels (G25, G50 and G75 gravels) with different mean grain size D_{50} and different uniformity coefficient C_u . The particle gradations were chosen to represent typical granular soils in nature covering poorly-graded sands to well-graded gravels. Gravel particles composing the materials were sub-round and hard in quality. The maximum and minimum densities of the soils were determined by using similar methods as will be explained later, but with a larger mold of 30 cm in diameter. In Table 8.1, physical properties of the soils are listed.

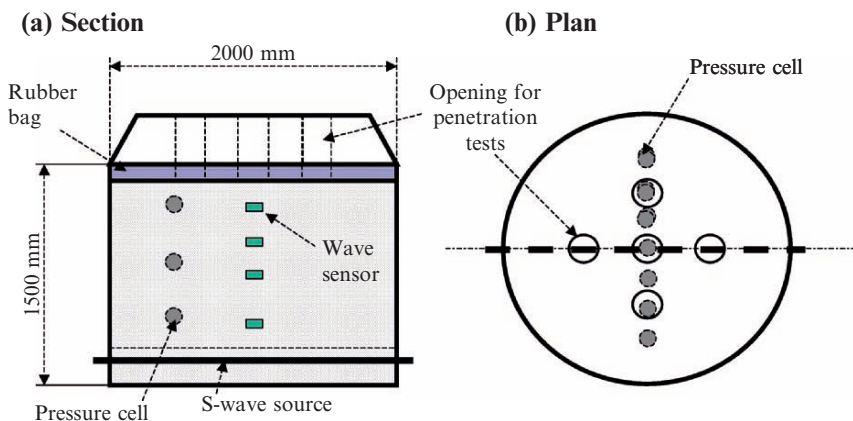


Fig. 8.5. Circular steel soil container with overburden pressure (Kokusho and Yoshida, 1997)

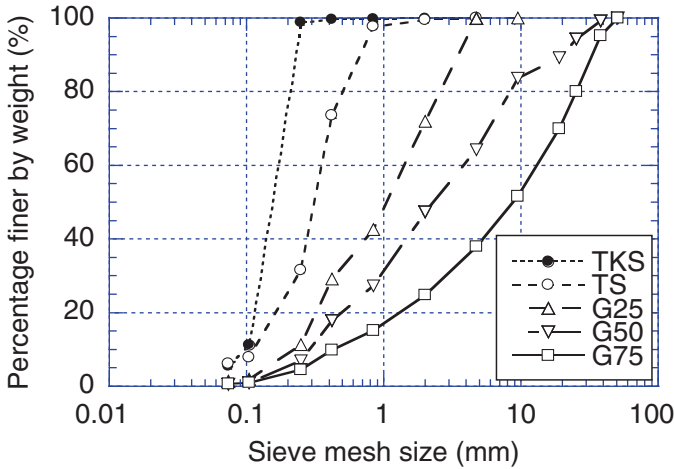


Fig. 8.6. Grain size distributions of five soils tested in soil container (Kokusho and Yoshida, 1997)

Table 8.1. Physical properties of tested soils

Soil	Mean grain size D_{50} (mm)	Uniformity coeff. C_u	Soil grain density ρ_s (g/cm^3)	Min. void ratio e_{min}	Max. void ratio e_{max}
TS sand	0.34	1.95	2.701	0.584	0.966
G25 gravel	1.13	5.67	2.674	0.334	0.567
G50 gravel	2.28	11.3	2.668	0.240	0.429
G75 gravel	7.30	31.1	2.653	0.161	0.308
TKS sand	0.15	1.88	2.660	0.595	1.023

2.1. S-WAVE VELOCITY

The S-wave velocity measured in the container tests for the five tested soils are first normalized by the vertical and horizontal stresses, σ'_v, σ'_h , as

$$V_{s0} = V_s / \{ (\sigma'_v / p_0) (\sigma'_h / p_0) \}^m \tag{8.1}$$

and the normalized S-wave velocity V_{s0} is plotted versus void ratio in Figure 8.7, where $p_0 = 98 \text{ kPa}$ is unit pressure. The power m in the Eq. (8.1) was evaluated by regression analysis on slopes of normalized V_s versus $\{ (\sigma'_v / p_0) (\sigma'_h / p_0) \}$ plots of individual test results. It is clearly seen that V_{s0} is almost linearly related to void ratio but the relationship is different from one soil to another. Similar relationships derived by Hardin and Richart (1963) for Ottawa sand and quartz sand are also superposed in Figure 8.7, indicating that their relationships are located near the sands tested here, but quite different from well-graded gravelly soils not only in void ratio but also in the range of S-wave velocity.

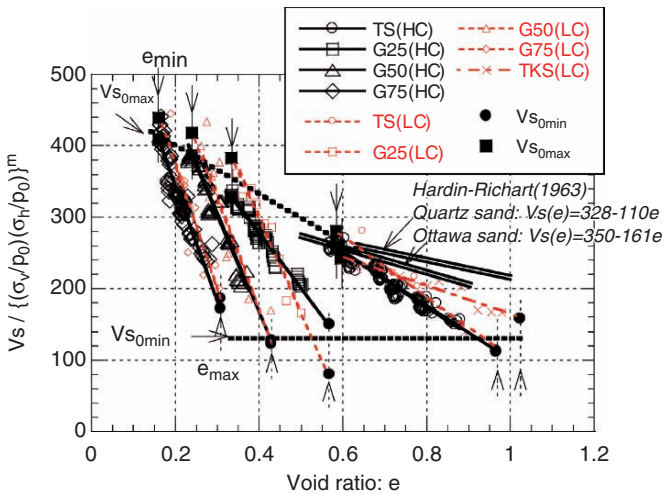


Fig. 8.7. Normalized S-wave velocity versus void ratio for five tested soils (modified from Kokusho and Yoshida, 1997)

Thus, it is obvious that the S-wave velocities of granular soils are not determined by a unique function of void ratio but highly variable with a difference in particle gradation.

In order to formulate the S-wave velocity of granular soils with widely different particle gradations, normalized S-wave velocities corresponding to e_{max} and e_{min} (see Table 8.1), denoted as V_{s0min} and V_{s0max} , respectively, were introduced. These values were determined at junctions of diagonal straight lines approximating the data points with vertical lines of e_{max} and e_{min} (indicated by the arrows) and plotted in Figure 8.7 with large solid symbols; circles for V_{s0min} and squares for V_{s0max} , respectively. It should be noted in Figure 8.7 that V_{s0min} , despite some scatters, tends to be almost stable, while V_{s0max} obviously increases as the uniformity coefficient Cu of soil increases from poorly-graded sands to well-graded gravels. In other words, the minimum S-wave velocity of well-graded gravels will remain at almost the same level as that of poorly-graded sands despite much lower void ratio than sands. This finding may help to explain why the S-wave velocity in the debris flow gravel in Mori could take as low as 60–90 m/s (Kokusho et al., 1995). In contrast, the maximum S-wave velocity of well-graded gravels tends to increase considerably with increasing Cu . The values of V_{s0min} and V_{s0max} are plotted against Cu in the semi-logarithmic plot in Figure 8.8. These plots can be approximated by simple equations indicated on the chart. The power m in Eq. (8.1) obtained by regression analysis can be assumed almost constant as $m = 0.125$ (Kokusho and Yoshida, 1997). Thus, S-wave velocity of granular soils including poorly-graded sands and well-graded gravels may be formulated by the next equation.

$$Vs = [136 + \{440Cu / (Cu + 1.4) - 136\}Dr] \{(\sigma'_v / p_0) (\sigma'_h / p_0)\}^{0.125} \quad (8.2)$$

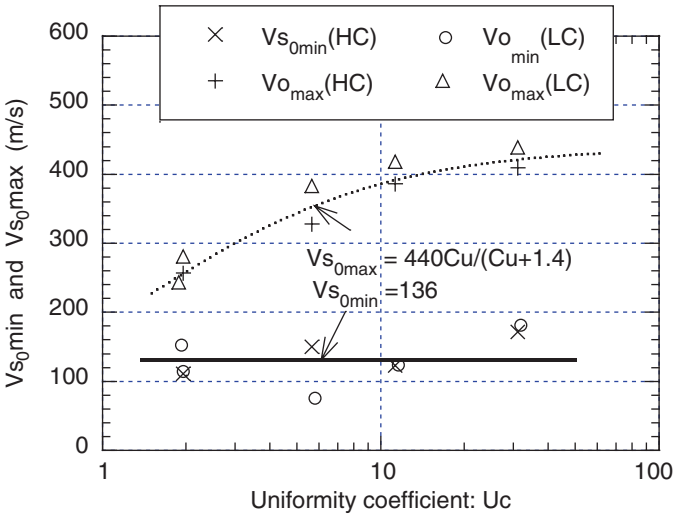


Fig. 8.8. Normalized max. and min. S-wave velocities versus uniformity coefficient for tested soils (modified from Kokusho and Yoshida, 1997)

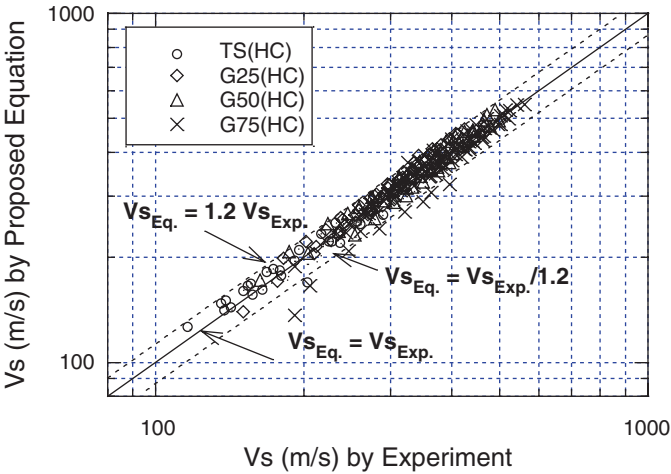


Fig. 8.9. Experimental S-wave velocities versus proposed equation for four soils (modified from Kokusho and Yoshida, 1997)

In Figure 8.9, the estimated V_s from Eq. (8.2) are compared with the values measured in the tests, indicating that the empirical equation evaluates most of the test results with a factor of 1.2 to 1/1.2.

2.2. SPT *N*-VALUE

Based on a number of the soil container tests for four different soils listed in Table 8.1 from poorly-graded sand to well-graded gravels, measured *N*-values are normalized as

$$N_0 = N / \{(\sigma' + 2\sigma'_h) / 3p_0\}^n \tag{8.3}$$

and plotted versus the void ratio in Figure 8.10. It was found that, on the full logarithmic chart, the data points may be approximated by parallel lines with different locations depending on different particle gradations.

The maximum and minimum *N*-values; N_{0max} and N_{0min} corresponding to e_{min} and e_{max} (see Table 8.1), defined as intersections of the straight lines for individual soils are marked with large solid circles and large solid squares, respectively, in Figure 8.10. N_{0max} tends to increase drastically for soils with higher uniformity coefficient, while the minimum N_{0min} stays almost constant. This implies that *N*-values of well-graded gravels can be as small as poorly-graded loose sand if they are loose enough despite tremendous differences in void ratio, whereas *N*-values can be considerably larger than that of dense sand if they are dense enough. In Figure 8.11, the normalized *N*-values N_0 are plotted versus the relative densities D_r , indicating that well-graded gravels can take a wider range of *N*-values than poorly-graded sand and the difference in *N*-values between soils of different particle gradations widens for D_r larger than around 50%.

In Figure 8.12, the values of N_{0max} and N_{0min} are plotted against uniformity coefficient C_u in the full logarithmic scale, which may be formulated by straight lines shown in the

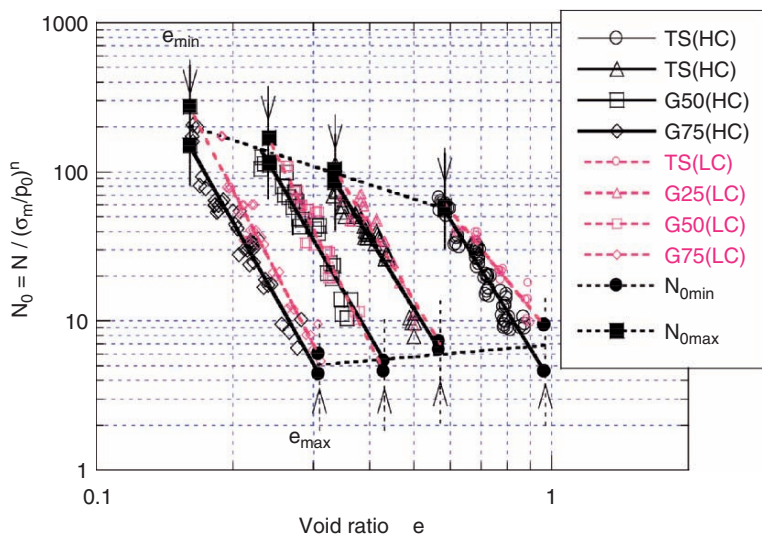


Fig. 8.10. Normalized SPT *N*-value versus void ratio for four tested soils (Kokusho and Yoshida, 1997)

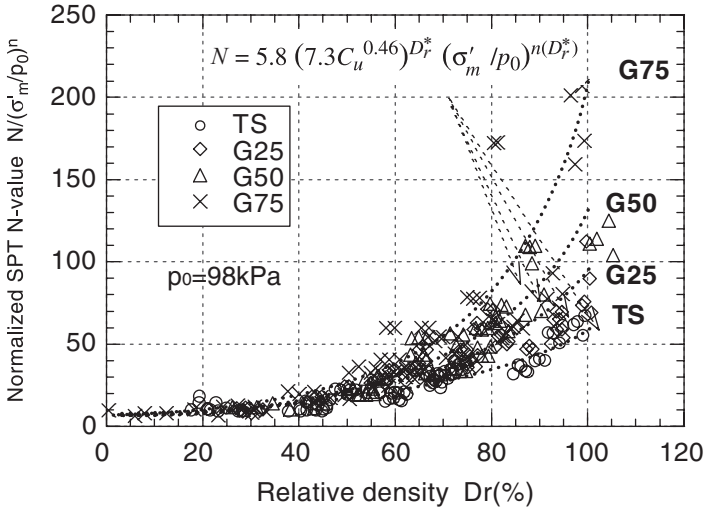


Fig. 8.11. Normalized SPT N -value versus relative density for four tested soils compared with the proposed equation (Kokusho and Yoshida, 1997)

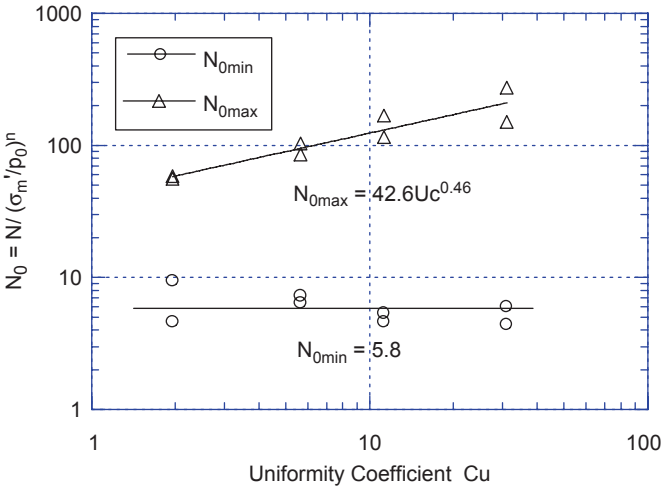


Fig. 8.12. Maximum and minimum normalized SPT N -value versus uniformity coefficient for four tested soils (Kokusho and Yoshida, 1997)

figure. Based on the linearity of the normalized N -value versus void ratio relationships observed in Figure 8.10, N -value may be formulated by the next equation

$$N = N_{0min} (N_{0max}/N_{0min})^{D_r^*} (\sigma'_m / p_0)^n \tag{8.4}$$

where D_r^* is logarithmic relative density defined here as

$$D_r^* = \log (e_{max}/e)/(e_{max}/e_{min}) \quad (8.5)$$

The values of power n is plotted against D_r^* and approximated by a simple function as $n(D_r^*) = 0.27(D_r^*)^{-0.4}$ (Kokusho and Yoshida, 1997). Thus N -value can be expressed by uniformity coefficient C_u , logarithmic relative density D_r^* and confining pressure σ'_m as

$$N = 5.8 \left(7.3 C_u^{0.46} \right)^{D_r^*} (\sigma'_m/p_0)^{n(D_r^*)} \quad (8.6)$$

This equation is superposed in Figure 8.11, indicating a fairly good coincidence with the test results.

Thus, the empirical formula have been determined from the large soil container tests. Needless to say, the soil conditions may not be exactly the same as natural soils and the constants presented in Eqs. (8.2) and (8.6) have to be revised if additional data from natural soil deposits becomes available. However, the basic trends presented in the empirical equations seem to hold in evaluating the effect of particle gradations on S-wave velocities and N -values for granular soils in general.

3. Effect of grain size distribution on cyclic strength

As demonstrated in Figure 8.2 and by other data (Kokusho and Tanaka, 1994), gravelly soils in nature are mostly well-graded with smooth grain size curves. Undrained cyclic strength of well-graded gravelly soils is not understood so well- as poorly-graded sands with regard to their density, particle gradations, etc., though they have significance in liquefaction potential evaluation for seismic design. Consequently, systematic cyclic undrained triaxial tests have been performed (Hara and Kokusho, 2000; Kokusho and Komiyama, 2001; Kokusho et al., 2004) for granular soils with different relative densities D_r , different C_u and different fines content F_c .

3.1. SOIL MATERIALS

Granular soils tested were three types, shown in Figure 8.13 and named here as RS1, RS2 and RS3, reconstituted from sands and gravels originated from a river, particle shapes of which are sub-rounded and hard to crush. Uniformity coefficients of RS1, RS2 and RS3 are $C_u = 1.44, 3.79$ and 13.1 respectively. In RS1 and RS3, fines (finer than $75 \mu\text{m}$) were mixed stepwise to reconstitute soils containing fines up to F_c (fines content) = 30% as shown in Figure 8.13. The fines were silty and clayey soils with low plasticity index of $I_p = 6$ sieved from decomposed granite in reclaimed ground of the Kobe city, Japan.

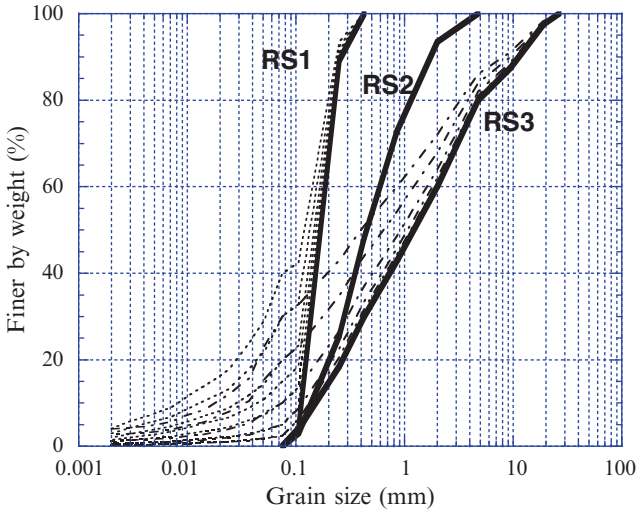


Fig. 8.13. Three kinds of particle gradation for river soils mixed with nonplastic fines

Relative density, D_r , is a pertinent parameter to evaluate mechanical properties of granular soils of different particle gradations and defined by soil dry density ρ based on maximum and minimum dry densities, ρ_{max} and ρ_{min} , respectively, as

$$D_r = \frac{1/\rho_{min} - 1/\rho}{1/\rho_{min} - 1/\rho_{max}} \times 100\% \quad (8.7)$$

Here, ρ_{max} and ρ_{min} were determined by a standardized test method of Japanese Geotechnical Society utilizing a soil mold of 195 mm inner diameter and 200 mm depth. For the maximum density ρ_{max} , soil was compacted in the mold by a vibrating disc in five layers. For the minimum density ρ_{min} , soil was gently placed into the mold through a metal funnel elevated slowly with zero drop height. Details of the test method are described in Hara and Kokusho (2004). Figure 8.14 shows relationships of maximum and minimum densities versus fines content obtained for the soil materials used in this research. If the data at $F_c = 0\%$ is concerned, both minimum and maximum densities tend to increase from RS1 to RS3 with increasing C_u .

3.2. TEST METHOD

In a triaxial apparatus used in this research, the specimen size was 100 mm in diameter and 200 mm in height. The diameter of 100 mm was about five times the maximum particle size of RS3. The soil specimen was loaded cyclically by a pneumatic actuator from above as a stress-control test as indicated in Figure 8.15. The soil specimens were prepared by wet tamping because other preparation methods such as air-pluviation or water-pluviation tend to intensify soil particle segregation for well-graded granular soils containing fines. The relative density of the specimen was approximately adjusted to

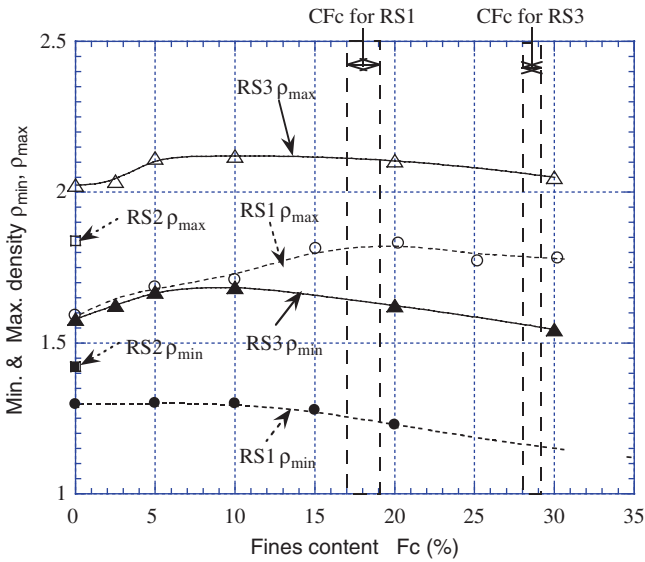


Fig. 8.14. Minimum and maximum density of three tested soils with different fines content

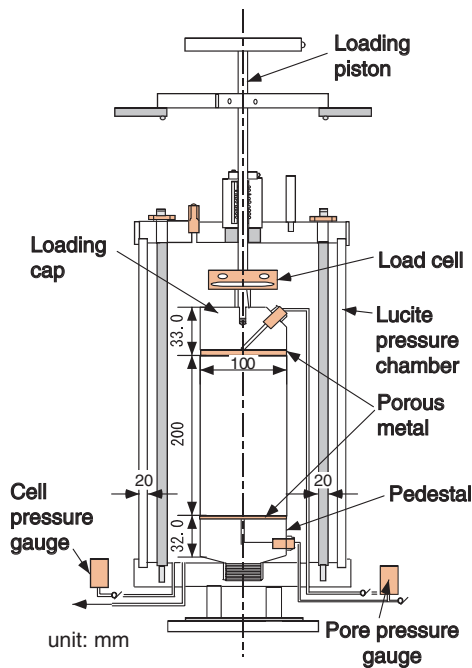


Fig. 8.15. Triaxial apparatus used in this research

target values $D_r = 30\%$, 50% and 70% by a tamping method. The specimen was isotropically consolidated by the effective stress of 98 kPa with the back-pressure of 294 kPa. The Skempton's B -value larger than 0.90 was measured in all tests indicating almost perfect saturation considering that well-graded soils with small void ratios have theoretically smaller B -values than poorly-graded soils even if they are fully saturated (Kokusho, 2000). The axial stress was cyclically controlled by sinusoidal waves with the frequency of 0.1 Hz. The membrane penetration effect on undrained cyclic strength was found generally small, less than 10% even for the coarsest RS3 material, because the specimen surface were actually smooth because of rich content of sand.

3.3. EFFECT OF PARTICLE GRADATION FOR CLEAN GRANULAR SOILS

Figure 8.16 exemplifies typical relationships between the cyclic stress ratio, $R_L (\sigma_d/2\sigma'_c; \sigma_d = \text{single axial stress amplitude, } \sigma'_c = \text{effective confining stress})$, for attaining 5% double amplitude (DA) strain versus the number of loading cycles N_L for the three soils for relative density $D_r \approx 50\%$. This stress ratio defined by 5% DA strain is almost identical with that defined by nearly 100% pore-pressure buildup at least for $D_r \approx 60\%$ or smaller (Hara and Kokusho, 2000). In Figure 8.17, the stress ratios for 5% DA strain corresponding to $N_L = 20, R_{L20}(\text{DA} = 5\%)$, which are often used as liquefaction strength in engineering practice in Japan, are plotted versus relative density D_r . The data points for soils RS1, RS2 and RS3 are located nearer to each other although some differences are visible at around $D_r = 50\%$ and 90% .

In order to see the effect of particle gradations on the strength more clearly, Figure 8.18 shows the relationship between R_{L20} and C_u for different D_r . Small differences in D_r

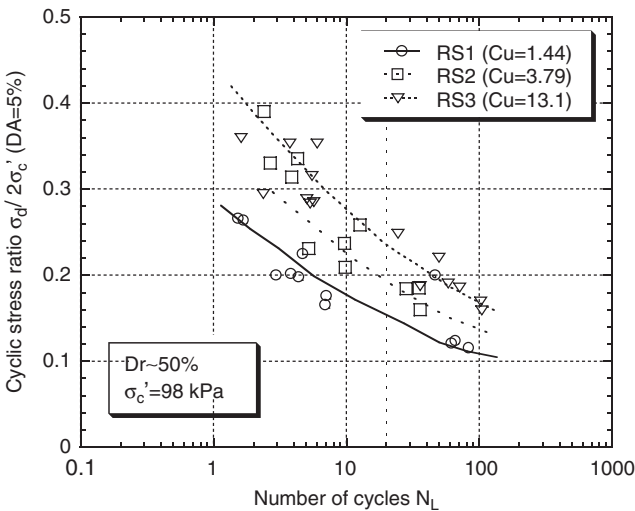


Fig. 8.16. Liquefaction strength (stress ratio) versus number of cycles compared among three soils of different particle gradation

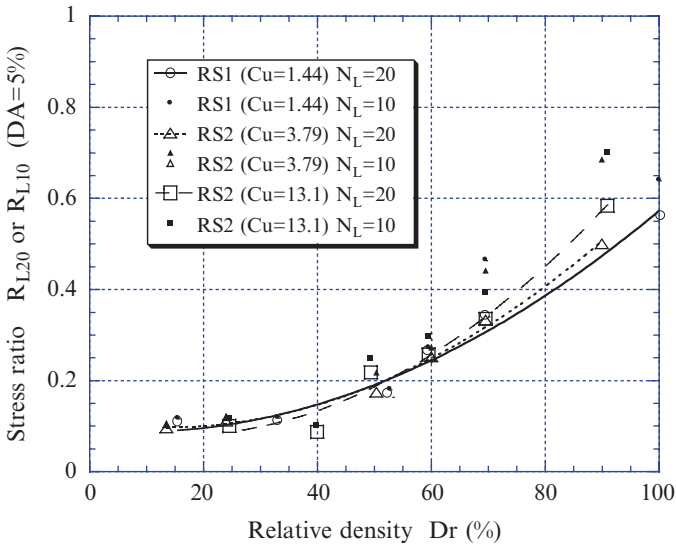


Fig. 8.17. Liquefaction strength (stress ratio) versus relative density plots compared among three soils of different particle gradation (Hara and Kokusho, 2000)

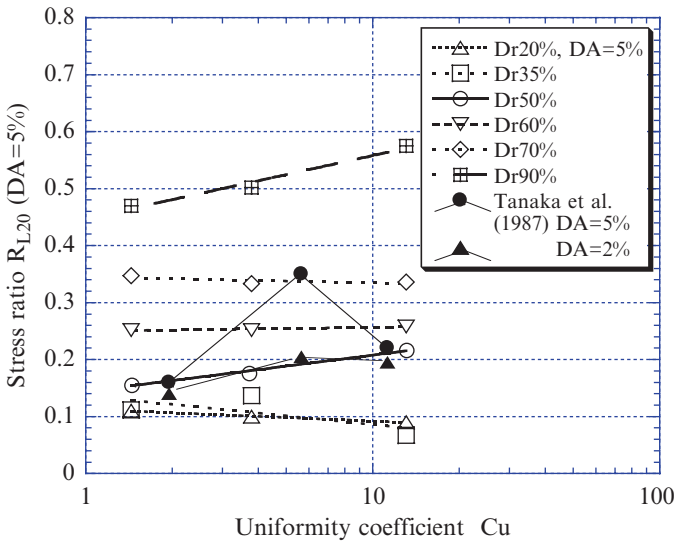


Fig. 8.18. Relationship between stress ratio R_{L20} and uniformity coefficient U_c for different relative density (Kokusho et al., 2004)

for individual plots on Figure 8.17 are adjusted based on the slopes of regression curves to evaluate R_{L20} at the target relative densities $D_r = 20\%–90\%$. The stress ratio R_{L20} increases with increasing Cu for $D_r = 50\%$ and 90% while it stays almost constant for other D_r . Hence, it may be said that the undrained cyclic strength is not so much dependent on Cu or soil particle gradation in contrast to its large dependency on D_r . Data points by Tanaka et al. (1987) in Figure 8.18 indicate that the trend is essentially the same although there exists one distinct separation. Thus, undrained cyclic strength defined by the stress ratio attaining 5% DA strain is strongly dependent on the relative density despite large difference in absolute density due to the difference in particle gradation. In other words, liquefaction strength (normally defined by 5% double amplitude strain or nearly 100% pore-pressure buildup) is not so much sensitive to the absolute density but more dependent on the relative density. Combining this finding with the fact that N -values of well-graded gravels are considerably larger than that of sands of the same D_r for $D_r > 50\%$ as shown in Figure 8.11, the reason can be explained why the relationship between liquefaction strength versus SPT N_1 -value of well-graded gravels largely deviates from that of poorly-graded sands for $N_1 > 25–30$.

3.4. EFFECT OF FINES CONTENT

As indicated from previous case histories, liquefied gravelly soils sometimes contained measurable fine soil particles smaller than 0.075 mm. It was demonstrated for poorly-graded sands by quite a few laboratory tests that liquefaction strength clearly decreases with increasing content of low plasticity fines under a constant relative density (e.g. Sato et al., 1997). In order to examine the effect of fines content on undrained cyclic strength of well-graded soils and compare it with poorly-graded sands, a series of tests have been conducted by mixing fines with RS1 and RS3 as depicted in Figure 8.13.

Figure 8.19 exemplifies typical relationships between the cyclic stress ratio, R_L for attaining 5% DA strain, and the number of loading cycles N_L for RS1 and RS3 of relative density $D_r \approx 50\%$ with fines content F_c changing stepwise from 0% to 30%. Though the data points show large scatters for smaller F_c for RS3 in particular, the strength obviously tends to decrease with increasing F_c . It can be pointed out that the slopes of R_L versus N_L curves are apparently steeper for well-graded RS3 than for poorly-graded RS1 with various fines content. Also noted is that the decrease in the strength is drastic for initial small increase of fines content from 0% to 10% particularly in RS3 while the change occurs more gradually in RS1.

In Figure 8.20, the stress ratios for 5% DA strain corresponding to $N_L = 20$, $R_{L20}(\text{DA} = 5\%)$, are plotted versus F_c for RS1 (smaller symbols) and RS3 (larger symbols) of relative densities $D_r \approx 30\%$, 50% and 70% . Solid symbols at $F_c = 0\%$ correspond to the data shown in Figure 8.17. Despite some data dispersions, liquefaction strength defined by $R_{L20}(\text{DA} = 5\%)$ obviously decreases with increasing F_c particularly for larger D_r not only for RS1 (poorly-graded sand) but also for RS3 (well-graded soil). The strength reduction may be somehow attributable to the role of fines as lubricators to decrease positive dilatancy, though the exact mechanism is not yet clarified.

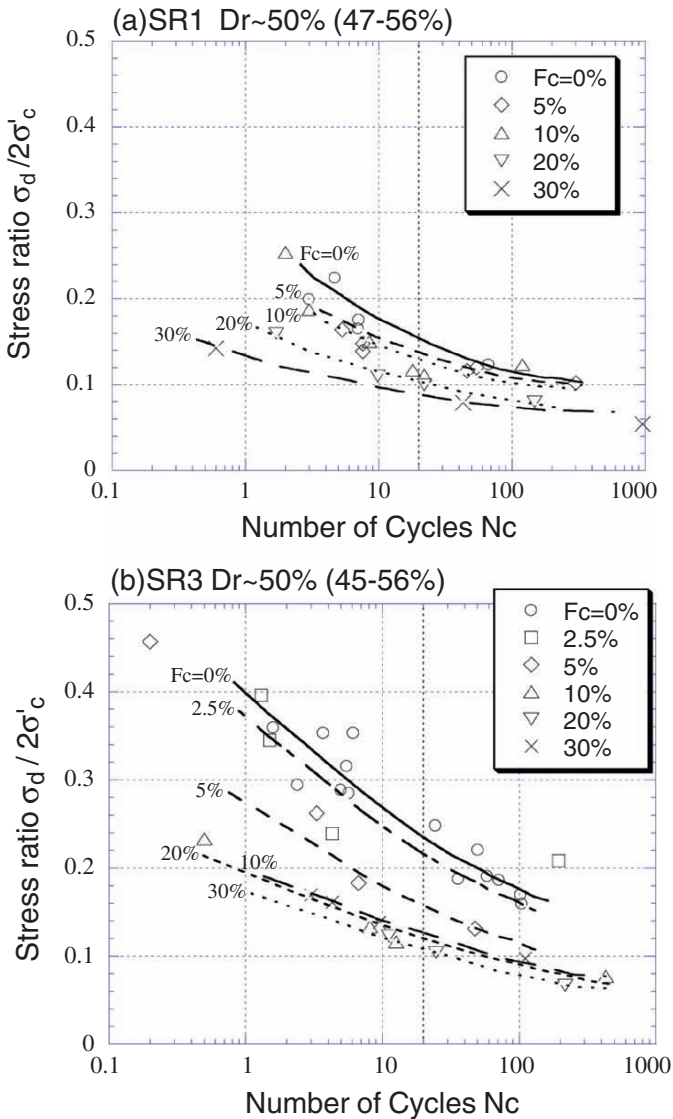


Fig. 8.19. Liquefaction strength (stress ratio) versus number of cycles for RS1 (a) and RS3 (b) with different fines content F_c

It is noted in Figure 8.20 that the decrease occurs in smaller F_c range for RS3 ($F_c < 10\%$) than for RS1 ($F_c < 30\%$) and the strength tends to recover slightly for larger F_c for RS3. In order to explain the difference between RS1 and RS3, let us look into the relationships between dry soil density and fines content shown in Figure 8.14, in which

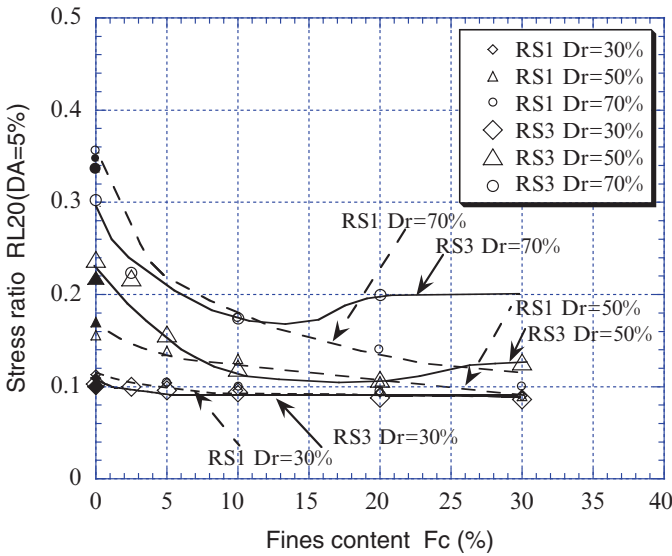


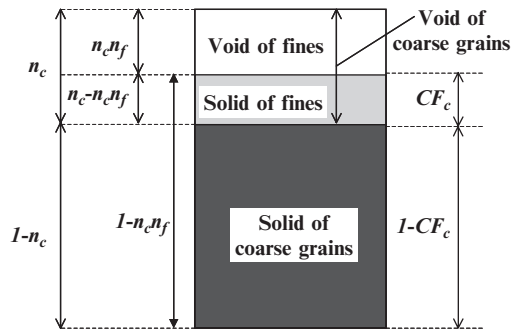
Fig. 8.20. Liquefaction strength (stress ratio) versus fines content F_c for RS1 and RS3 with different relative density D_r

the density tends to first increase and then decrease with increasing fines content, taking some peak values in between. If a soil is simplified as a combination of gap-graded coarse grains (sand or gravel grains) and fines, the fines fill the voids of the coarse grains up to some limit (critical fines content; CF_c) and then start to overflow the voids, leading complete change of soil structure from coarse grain supporting to matrix supporting. Correspondingly, the density increases in the interval $F_c = 0$ to CF_c because the void is filled with fines without increasing the total soil volume and then start to decrease because the total volume increases with increasing fines matrix of lighter density.

Figure 8.21 illustrates schematically how the voids of coarse grains are completely filled with fines at the critical fines content, where n_c and n_f are porosities for coarse grains and fines, respectively. If this ideal situation is postulated, then CF_c can be formulated as

$$CF_c = (n_c - n_c n_f) / (1 - n_c n_f) \tag{8.8}$$

Values of n_c and n_f are quantified from minimum and maximum densities, and hence critical CF_c can be calculated as listed in Table 8.2 for different relative densities D_r by assuming that both coarse grains and fines have the same D_r as the total relative density. Thus, under the simple assumption, CF_c is calculated as 28%–29% for RS1 and 17%–19% for RS3 for $D_r = 30\%$ – 70% . This difference in CF_c reflects largely different void ratio between RS1 and RS3. These CF_c values superposed in Figure 8.14 are somewhat

Fig. 8.21. Schematic diagram for critical fines content CF_c Table 8.2. Critical fines content calculated by simple model for RS1 and RS3 with different relative density D_r

Relative density D_r (%)	Porosity n_c		Porosity n_f	Criticle fines content CF_c (%)	
	RS1	RS3	Fines	RS1	RS2
0	0.519	0.406	0.642	27.9	19.6
30	0.491	0.363	0.595	28.1	18.8
50	0.471	0.332	0.557	28.3	18.0
70	0.449	0.298	0.510	28.5	17.2
100	0.412	0.238	0.419	28.9	15.4

larger than F_c corresponding to the peak values of the maximum density both for RS1 and RS3. It is probably because the actual particle gradations are not so distinctly gap-graded and the fines matrix starts to overflow before completely filling the voids of coarse soils. Nevertheless the value of F_c for the peak of the maximum density in Figure 8.14 is evidently smaller for well-graded RS3 than poorly-graded RS1 because CF_c for RS3 is smaller than RS1. Accordingly, most of the strength decrease tends to occur due to smaller increase of F_c in well-graded soils (RS3) than in poorly-graded sand (RS1).

Figure 8.20 clearly indicates that increasing fines tend to decrease liquefaction strength irrespective of particle gradation. In the current liquefaction potential evaluation, based on liquefaction case histories, higher liquefaction strength is given to a soil deposit containing more fines, if the penetration resistance is the same. If the same penetration resistance means the same relative density under the same overburden, the present test results seem quite contradictory to the current practice, implying that the penetration resistance will decrease with increasing fines content more drastically than the liquefaction strength. Further research for the effect of fines content on penetration resistance and liquefaction strength is needed (e.g., Kokusho et al., 2005).

4. Effect of particle gradation on post-liquefaction behavior

It is well known that liquefaction-induced damage sometimes takes place not directly by the seismic inertia force but by static shear stress caused by dead weights of structures due to the loss of effective stress after the onset of initial liquefaction. In order to investigate the effect of particle gradation and fines content on the post-liquefaction behavior of granular soils, undrained monotonic loading tests were carried out for the same soils previously used immediately after prior undrained cyclic loading.

4.1. EFFECT OF PARTICLE GRADATION IN POST-LIQUEFACTION SHEAR BEHAVIOR

Figure 8.22(a) exemplifies deviatoric stress or pore-pressure versus axial strain relationships obtained in undrained monotonic loading tests carried out without preceding water drainage just after cyclic loading for the three soils, RS1, RS2 and RS3 with relative densities of about 50%. In the cyclic loading tests, all specimens attained almost 100% pore-pressure buildup and about 10% DA axial strain and hence can be defined as being already liquefied in a normal engineering practice. In the initial response to monotonically increasing strain in Figure 8.22(a), deviatoric stress and pore-pressure change gradually up to some asymptotic values. It is remarkable that despite the same D_r -value, the induced stress is quite different for soils with different particle gradations.

In Figure 8.22(b), typical effective stress paths are shown on the mean effective stress (p') versus deviatoric stress (q) plane. All paths start near the origin after the full pore-pressure buildup and go up along straight failure lines to the right end marked with open circles, although in the soil RS2 the path is a little curved near the right end. From the slopes of the straight sections, internal friction angles for effective stress ϕ' are evaluated as 36.1° for RS1, 38.4° for RS2, 39.0° for RS3. This indicates that post-liquefaction dilatancy generating negative pore-pressure is more pronounced in well-graded soils despite

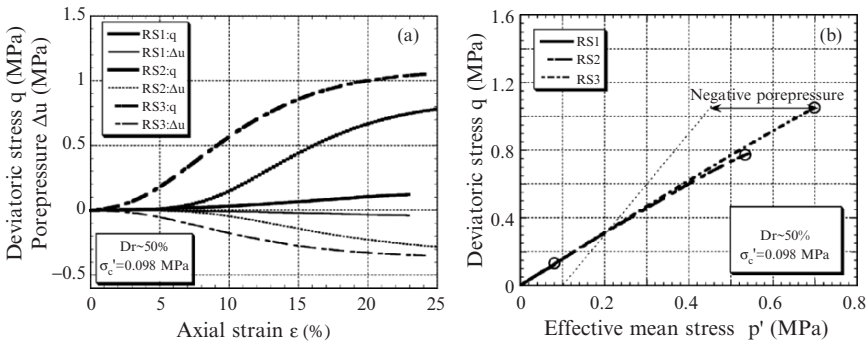


Fig. 8.22. Stress–strain curves (a) and pore water pressure–strain curves (b) obtained in post-liquefaction tests for three soils (Kokusho et al., 2004)

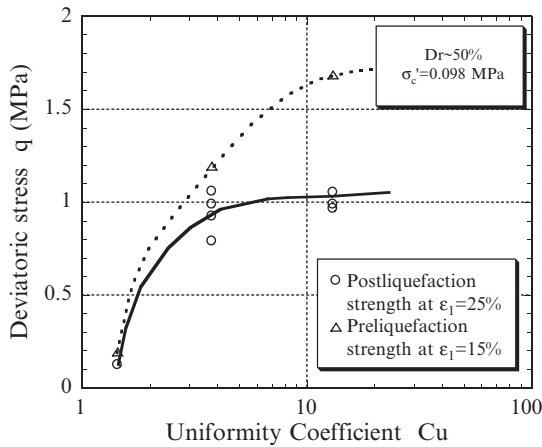


Fig. 8.23. Post-liquefaction or preliquefaction deviatoric strength by monotonic undrained tests (Kokusho et al., 2004)

the same relative density. In Figure 8.23, deviatoric stresses q at axial strain of 25% evaluated by all post-liquefaction tests are plotted versus C_u of tested soils with open circles. Data points for tests without cyclic loading (preliquefaction condition) defined at 15% strain are also plotted on the same chart with open triangles. Drastic increase in shear resistance for large strain with increasing C_u is evidently seen from the curves approximating the plots whether or not the soil is subjected to preceding undrained cyclic loading. The increase seems to occur mostly in the interval of C_u between 1.4 and 4.

Based on the findings mentioned before, it can be said in general that well-graded gravelly soils are prone to liquefaction corresponding to almost full pore-pressure buildup and 5% DA axial strain as much as poorly-graded sands, so long as their relative density is the same. However, if strength at larger strain is concerned, the relative density is no more a pertinent parameter. Instead, particle gradation represented here by the uniformity coefficient C_u makes a big difference even for soils of the same relative densities. This implies that well-graded clean gravelly soils are less prone to post-liquefaction failure accompanying large deformation. Considering that the uniformity coefficients of natural gravelly soils are normally larger than several tens as indicated in Figure 8.2, their post-liquefaction undrained strength corresponding to 25% axial strain may be judged at least eight times larger than poorly-graded sands according to Figure 8.23. This may be able to explain why liquefaction-induced damage in gravelly deposits was less witnessed in past earthquakes. Post-liquefaction large ground deformation such as cracks, differential settlements, etc. is harder to develop in well-graded soils than poorly-graded sands even after initial liquefaction with almost full pore-pressure buildup.

4.2. EFFECT OF FINES CONTENT IN POST-LIQUEFACTION SHEAR BEHAVIOR

Figure 8.24(a) and (b) shows deviatoric stress or pore-pressure versus axial strain relationships obtained in post-cyclic undrained monotonic loading tests for RS1 and RS3, respectively, of different fines content having relative density of about 50%. In prior cyclic loading history, all specimens attained almost 100% pore-pressure buildup and more than 10% DA axial strain. In the initial stage of monotonic loading, stress increases gradually with increasing strain reflecting softened shear stiffness due to preceding cyclic loading. The induced stress is much higher for RS3 than RS1 due to the difference in particle gradation as explained before. In both RS1 and RS3, however, increasing fines content tends to dramatically reduce the stress recovery after liquefaction. In Figure 8.25(a) and (b), post-liquefaction residual strengths defined as the deviatoric stresses at 20% axial strain are plotted versus fines content for RS1 and RS3, respectively, with $D_r = 30\%$, 50% and 70%. Although the absolute strength shown in the figures with solid symbols

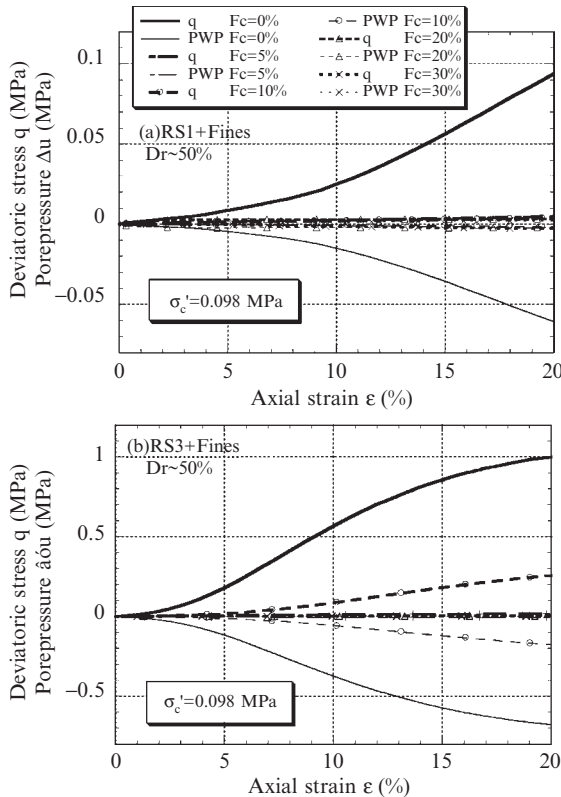


Fig. 8.24. Stress–strain curves in post-liquefaction tests for RS1 and RS3 with different fines content

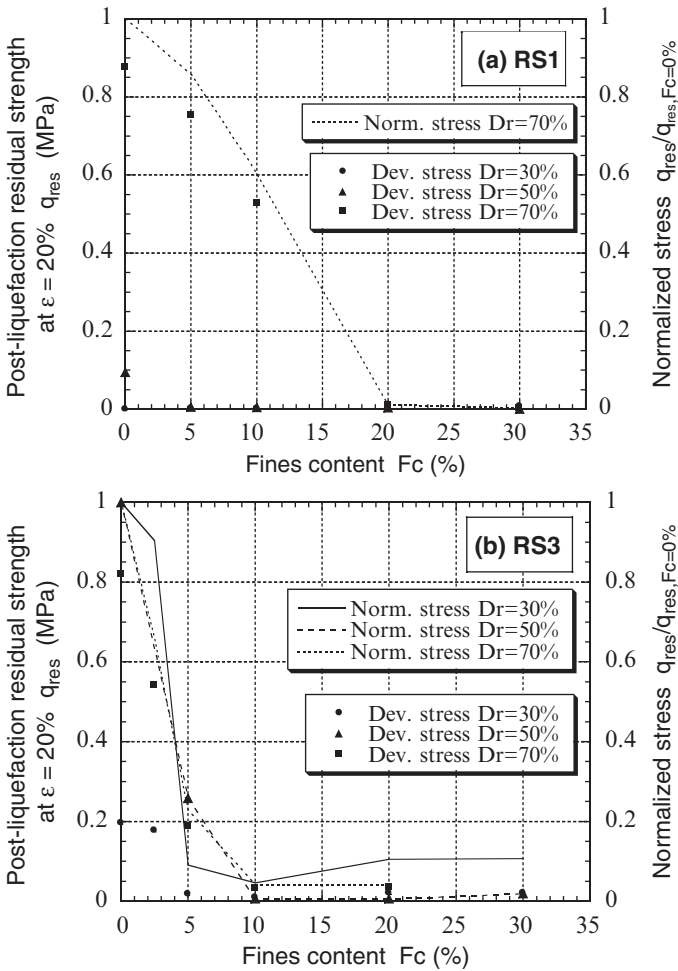


Fig. 8.25. Post-liquefaction deviatoric strength by monotonic undrained tests for two soils with different fines content

have some scatters, reflecting difficulties in controlling preceding cyclic straining history precisely as 10% DA strain, relative strength reduction normalized by the strength for $F_c = 0$ shown with thin curves in the figures may make the following observations possible. Both in RS1 and RS3, residual strength decreases more drastically in denser soils than looser soils. Although, the relative strength decreases eventually to less than 10% with increasing F_c for all the soils, it occurs by a smaller increase of F_c in RS3 than RS1.

The reason may again be explained by the difference in critical fines content CF_c or void ratio between RS1 and RS3 mentioned before. A soil structure change from coarse-grain supporting to matrix supporting occurs near the critical fines content which is much larger

for RS1 than for RS3. The residual strength reduction is much more considerable than the cyclic strength reduction indicated in Figure 8.20. Thus, fines content in liquefiable granular soils has more significant effect on post-liquefaction residual strength than liquefaction strength. Figure 8.25 also indicates that, for the same increment of fines content, the strength reduction occurs more drastically in well-graded soils than for poorly-graded soils particularly for higher density.

5. Conclusions

Recent case studies indicate that gravelly soils can liquefy if they are loose enough no matter how well graded and how coarse they may be. Gravelly soils liquefied during recent earthquakes have N_1 -value no larger than 25 and also contain relatively large quantity of fines. It is also indicated that liquefaction strength of well-graded gravelly soils largely deviates from that of poor-graded sand for N_1 -value higher than 25–30, although it shows almost the same stress ratio as poorly-graded loose sand for N_1 smaller than that. In order to understand the differences in liquefaction or post-liquefaction behavior of well-graded soils in contrast to poorly-graded sands, experimental results of soil container tests and undrained triaxial tests for soils with different particle gradations were examined, yielding the following major findings:

- (1) S-wave velocities of granular soils are not determined by a unique function of void ratio but highly dependent on particle gradation. Minimum S-wave velocity of well-graded gravels remains at almost the same value as that of poorly-graded sands despite much lower void ratio than sands. In contrast, maximum S-wave velocity of well-graded gravels tends to increase considerably with increasing C_u .
- (2) N -value of well-graded gravels can be as small as poorly-graded loose sands if their relative density D_r is low enough despite tremendous difference in void ratio, whereas it can be considerably larger than that of sands for $D_r > 50\%$. This may explain why the relationship between liquefaction strength versus SPT N_1 -value of well-graded soils deviates from that of poor-graded sands for $N_1 > 25$ –30.
- (3) Liquefaction strength of granular soils defined by R_{L20} (DA strain = 5%) may be uniquely evaluated by relative density, D_r , despite large difference in particle gradations.
- (4) Liquefaction strength defined by R_{L20} (DA strain = 5%) obviously decreases with increasing F_c particularly for larger D_r not only in poorly-graded sands but also in well-graded gravels. The decrease for well-graded soils occurs in smaller F_c range in accordance with smaller critical fines content or smaller void ratio than for poorly-graded sands.
- (5) Post-liquefaction strength for larger strain of 20%–25% is not uniquely determined by relative density but largely dependent on particle gradations. Namely, soils with larger C_u and larger absolute density tend to exhibit considerably larger residual strength.

- (6) Increasing F_c considerably reduces post-liquefaction residual strength of granular soils particularly for higher density. The effect is more pronounced by a smaller increase of F_c in well-graded gravels because of smaller critical fines content or smaller void ratio than in poorly-graded sands.

Acknowledgments

Experimental results used in this paper are from previous researches carried out in Central Research Institute of Electric Power Industry, Japan and in Graduate School of Chuo University. Mr. Yasuo Yoshida and Dr. Yukihiisa Tanaka of CRIEPI and a number of ex-graduate students of Chuo University, Tadashi Hara, Yoshiro Komiyama and Keita Murahata, in particular, are deeply acknowledged for their great contributions.

REFERENCES

- Andrus RD (1994) In-situ characterization of gravelly soils that liquefied in the 1983 Borah Peak earthquake. PhD. dissertation presented to the University of Texas, Austin
- Hara T, Kokusho T (2000) Effect of particle gradation on liquefaction and post-liquefaction strength by means of triaxial test. *Journal of Japan Society of Civil Engineers* (in Japanese) No. 645, No. III-50: 245–253
- Hara T, Kokusho T (2004) Experiments of influencing factors on minimum and maximum density for sandy-gravel. *Journal of Japan Society of Civil Engineers* (in Japanese) No. 778, No. III-69: 151–162
- Hardin BO, Richart FE (1963) Elastic wave velocities in granular soils. *Proc. ASCE*, Vol. 89, SM1, pp 33–65
- Inagaki H, Iai S, Sugano T, Yamazaki H, Inatomi T (1996) Performance of caisson type walls at Kobe Port. Special Issue, *Soils and Foundations*, Japanese Geotechnical Society, 119–136
- JGS Committee (2001) State-of-the-art report on mechanical properties of gravelly soil. *Proc. Symposium on Mechanical Properties of Gravelly Soils*, Japanese Geotechnical Society, pp 97–99 (in Japanese)
- Kokusho T, Tanaka Y (1994) Dynamic properties of gravel layers investigated by in-situ freezing sampling. *Proc., Ground Failure under Seismic Condition*, ASCE Convention in Atlanta, Geotechnical Special Publication No. 44, pp 121–140
- Kokusho T, Tanaka Y, Kawai T, Kudo K, Suzuki K, Tohda S, Abe S (1995) Case study of rock debris avalanche gravel liquefied during 1993 Hokkaido-Nansei-Oki Earthquake. *Soils and Foundations* 35(3): 83–95
- Kokusho T, Yoshida Y (1997) SPT N -value and S-wave velocity for gravelly soils with different grain size distribution. *Soils and Foundations*, 37(4): pp 105–113
- Kokusho T (2000) Correlation of pore-pressure B -value with P -wave velocity and Poisson's ratio for imperfectly saturated sand or gravel. *Soils and Foundations*, 40(4): 95–102
- Kokusho T, Komiyama Y (2001) Undrained shearing characteristics of gravelly soils containing non-plastic fines. *Proc. Symposium on Mechanical Properties of Gravelly Soils*, Japanese Geotechnical Society, pp 233–238 (in Japanese)
- Kokusho T, Hara T, Hiraoka R (2004) Undrained shear strength of granular soils with different particle gradations. *Journal of Geotechnical and Geoenvironmental Engineering*, ASCE130(6): 621–629

- Kokusho T, Hara T, Murahata K (2005) Liquefaction strength of fines-containing sands compared with cone-penetration resistance in triaxial specimens. Proc. Second Japan-U.S. Workshop on Geomechanics: Testing, Modeling and Simulation, Kyoto, ASCE Geo-Institute Geotechnical Publication No. 156, pp 356–373
- Sato M, Oda M, Kazama H, Ozeki K (1997) Fundamental study on the effect of fines on liquefaction characteristics of reclaimed ground. Journal of Japan Society for Civil Engineers, No. 561/III-38, 271–282 (in Japanese)
- Tanaka Y, Kudo K, Yoshida Y, Ikemi M (1987) A study on the mechanical properties of sandy gravel – Dynamic properties of reconstituted sample-”, CRIEPI Research Report No. U87019, Central Research Institute of Electric Power Industry (in Japanese)
- Tanaka T, Kudo K, Yoshida Y, Kokusho Y (1992) Undrained cyclic strength of gravelly soil and its evaluation by penetration resistance and shear modulus. Soils and Foundations 32(4): 128–142
- Yoshimi Y, Tokimatsu K, Hosaka Y (1989) Evaluation of liquefaction resistance of clean sands based on high-quality undisturbed samples. Soils and Foundations 29(1): 93–104

CHAPTER 9

SHALLOW AND DEEP FOUNDATIONS UNDER FAULT RUPTURE OR STRONG SEISMIC SHAKING

George Gazetas, Ioannis Anastasopoulos, and Marios Apostolou

Laboratory of Soil Mechanics

National Technical University of Athens, Greece

Abstract. Two topics of interest in soil–foundation–structure interaction are presented: the first refers to the consequences on shallow and deep foundations and their superstructures from a seismic fault rupture emerging directly underneath them; the second topic addresses the seismic response of tall structures resting on shallow foundations that experience uplifting and inducing large inelastic deformations in the soil. The numerical and analytical methodologies developed for each topic have been calibrated with centrifuge experiments. The outlined parametric results provide valuable insight to the respective soil–foundation interplay, and could explain qualitatively the observed behaviour in a number of case histories from recent earthquakes.

1. Introduction

Thirty years ago research and practice on dynamic soil–structure interaction (SSI) meant primarily the study of how soil compliance influences the dynamic response of superstructures (buildings, bridges, critical facilities). Determining the foundation stiffness and damping for various modes of vibration, foundation geometries, and soil profiles under essentially elastic conditions was a key intermediate step in such analyses.

In recent years the term has expanded to encompass studies related to all aspects of soil and foundation design against earthquakes, including the response of retaining systems and underground structures, the influence of liquefaction and lateral spreading, and the effects of ground deformation arising from a rupturing fault emerging under a foundation. There has been an evolutionary progress from idealised linear visco elastic soils and elastic structural system, to nonlinear inelastic response of soils and structures. This chapter highlights two such problems in which an interplay between the soil and structure takes place under conditions of large soil deformations and even failure.

A number of unresolved soil–foundation–structure interaction (SFSI) problems were the subject of investigation in a joint research project titled “Fault-Rupture and Strong Shaking Effects on the Safety of Composite Foundations and Pipelines” (acronym: QUAKER) that provided many of the findings reported in this paper. Conducted by research teams from the University of Dundee, Géodynamique et Structure, LCPC-Nantes, Studio Geotecnico Italiano, and National Technical University of Athens, the study of each topic was undertaken using an integrated approach, comprising

three interrelated steps: field studies, centrifugal experiments, and numerical/analytical modelling. Specifically:

- Field studies of documented case histories motivated our investigation and offered material for calibration of the theoretical methods and analyses.
- Carefully controlled centrifugal experiments helped in developing an improved understanding of mechanisms and in acquiring a reliable experimental data base for validating the theoretical simulations.
- Theoretical methods (analytical or numerical) calibrated against the above field and experimental data offered additional insight into the nature of the interaction, and were utilised in developing parametric results and design aids.

This paper summarises some of the key findings of these theoretical studies, which were later supplemented with further analyses by the authors pertaining to pile and caisson foundations. The emphasis of the paper is on elucidating the soil–foundation interaction in the presence of large soil deformation, and near failure conditions.

2. Fault-rupture propagation and its interaction with foundations

2.1. STATEMENT OF THE PROBLEM

It has long been recognised (Duncan and Lefebvre, 1973; Bray, 1990) that a “strong” structure founded on/in soil can resist successfully the loading induced by a rupturing seismic fault. In the Kocaeli, Düzce-Bolu, and Chi-Chi earthquakes of 1999 numerous structures (single-storey and multi-storey buildings, bankers, bridge piers, retaining structures, electricity pylons, dams, tunnels) were located directly above the propagation path of the rupturing (normal, strike-slip, reverse) faults. Some of these structures exhibited a remarkably good behaviour. This observation had a strong motivating influence for our research effort. For it became immediately clear that the strict prohibition: “Do not build in the immediate vicinity of active faults!”, which the prevailing seismic codes invariably imposed, was unduly restrictive (and in many cases meaningless).

Indeed, along the ground surface in the free–field, “ruptures are neither continuous, nor do they follow precisely the surface outcrop of pre-existing faults” (Ambraseys and Jackson, 1984).

In addition to several geologic factors that contribute to such behaviour, significant appears to be the role of a soil deposit that happens to overlie the rock base through which the rupture propagates. *If, where, and how large* will the dislocation emerge on the ground surface (i.e. the fault will outcrop) depends not only on the style and magnitude of the fault rupture, but also on the geometric and material characteristics of the overlying soils. Field observations and analytical and experimental research findings (Cole and Lade, 1984; Lade et al., 1984; Bray et al., 1994a, b; Lazarte and Bray, 1995) show that deep and loose soil deposits may even mask a small-size fault rupture which occurs at their base; whereas by contrast with a cohesive deposit of small thickness, a large offset

in the base rock will likely cause a distinct fault scarp of nearly the same displacement magnitude. One important finding of the above studies is that the rupture path in the soil is not a simple extension of the plane of the fault in the base rock: phenomena such as “diffraction” and “bifurcation” affect the direction of the rupture path, and make its outcropping location and offset magnitude difficult to predict.

Our interest here is not on the propagation of a rupture within the soil, but on how a structure sitting on top of the fault breakout behaves. It turns out that a fascinating interplay takes place between the propagating fault rupture, the deforming soil, the differentially displacing foundation, and the supported structure. Two different phenomena take place. First, the presence of the structure modifies the rupture path. Depending on the rigidity of the foundation and the weight of the structure, even complete diversion of the fault path before it outcrops may take place. Obviously, the damage to a given structure depends not only on its location with respect to the fault outcrop in the “free-field”, but also on whether and by how much such a diversion may occur. Second, the loads transmitted from the foundation on to the soil tend to compress the “asperities” and smoothen the “anomalies” of the ground surface that are produced around the fault breakout in the free-field, i.e. when the structure is not present. Thus, depending on the relative rigidity (bending and axial) of the foundation with respect to the soil, as well as on the magnitude of the structural load, the foundation and the structure will experience differential displacements and rotation different from those of the free-field ground surface.

This phenomenon, given the name “Fault-Rupture-Soil-Foundation-Structure Interaction” [FR-SFSI] by Anastasopoulos and Gazetas (2007), is briefly elucidated in the sequel for shallow and deep foundations.

2.2. NUMERICAL ANALYSIS AND RESULTS: SHALLOW FOUNDATIONS

The problem studied here is illustrated in Figure 9.1. We consider a uniform soil deposit of thickness H at the base of which a normal fault, dipping at an angle α (measured from the horizontal), produces downward displacement (“dislocation”, “offset”) of vertical amplitude h . The analysis is conducted in two steps. First, fault rupture propagation through soil is analysed in the free-field, ignoring the presence of the structure. Then, a strip foundation of width B carrying a uniformly distributed load q or a multistory frame-structure is placed on top of the free-field fault outcrop at a specified distance S (measured from its corner), and the analysis of deformation of the soil-structure system due to the same base “dislocation” h is performed. The analyses are conducted under 2D plane-strain conditions—evidently a simplification, in view of the finite dimensions of a real structure in the direction parallel to the fault. The relative location of outcropping is varied parametrically through the distance S . Comparing soil and ground-surface deformations in the two steps gives a first picture of the significance of SFSI.

Among several alternatives that were explored, the FE model shown in Figure 9.2 produced results in excellent accord with several centrifugal experiments conducted at the University of Dundee for both steps of the analysis (Anastasopoulos et al., 2007a, b).

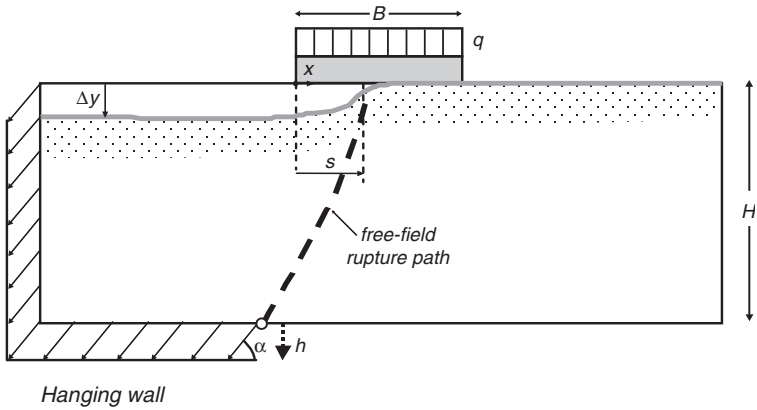


Fig. 9.1. Configuration of the soil–foundation system subjected to a normal fault dislocation at the base rock

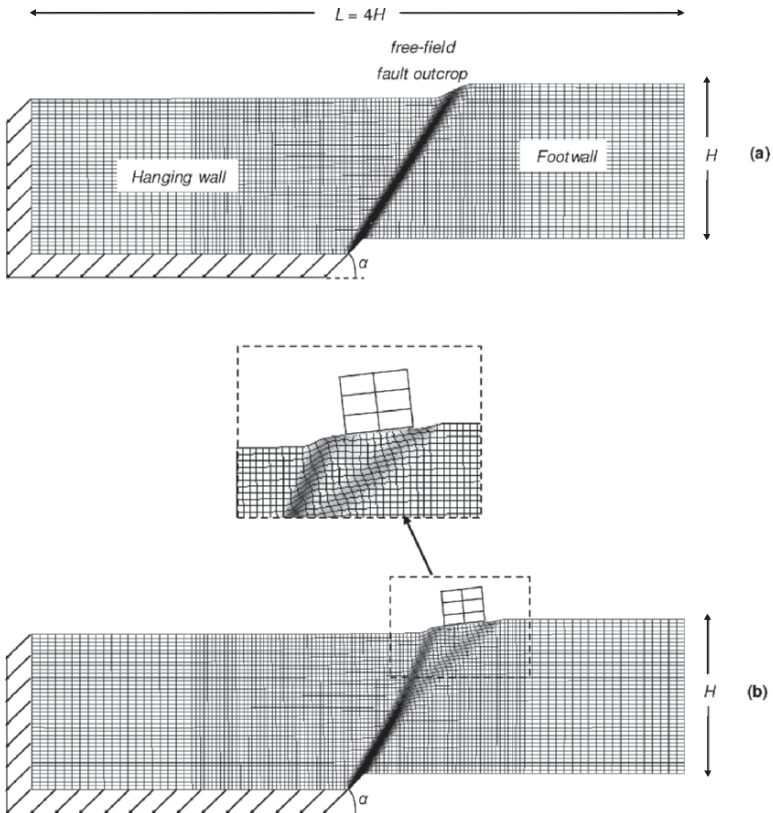


Fig. 9.2. Finite element discretisation and the two steps of the analysis: (a) fault rupture propagation in the free-field, and (b) interplay between the outcropping fault rupture and the structure (termed Fault Rupture–Soil–Foundation–Structure Interaction, FR-SFSI)

A parametric investigation revealed the need for a long ($B = 4H$) and very refined mesh (element size of 0.5–1.0 m) along with a suitable slip-line tracing algorithm in the region of soil rupture and foundation loading. An elastoplastic constitutive model with the Mohr–Coulomb failure criterion and isotropic strain softening was adopted and encoded in the ABAQUS finite element environment. Similar models have been successfully employed in modelling the failure of embankments and cut slopes (Potts et al., 1990). Modelling strain softening was shown to be necessary; it was introduced by suitably reducing the mobilised friction angle φ_{mob} and the mobilised dilation angle ψ_{mob} with increasing plastic octahedral shear strain. With all the above features, the FE formulation is capable of predicting realistically the effect of large deformations with the creation and propagation of shear bands.

The foundation, modelled with linear elastic beam elements, is positioned on top of the soil model and connected to it through special contact elements. The latter are rigid in compression but tensionless, allowing detachment of the foundation from the bearing soil (i.e. gap formation beneath the foundation). The interface shear properties follow Coulomb's friction law, allowing for slippage. Both detachment and slippage are important phenomena for a realistic foundation model.

A typical result elucidating the interplay between loose ($D_r = 45\%$) soil, rupture path, and a perfectly rigid foundation carrying a 4-storey structure is given in Figure 9.2. A base rock dislocation of 2 m (5% of the soil thickness) is imposed. The structure is placed symmetrically straddling the free-field fault breakout (i.e. the foundation is placed with its middle coinciding with the location where the fault would outcrop in the free-field). Yet, a distinct rupture path (with high concentration of plastic shearing deformation and a resulting conspicuous surface scarp) is observed only in the free-field. The presence of the structure with its rigid foundation causes the rupture path to bifurcate at about the middle of the soil layer. The resulting two branches outcrop outside the left and the right corner of the foundation, respectively. The soil deformations around these branches are far smaller and diffuse than in the free-field, and the respective surface scarps are much milder. Thanks to the substantial weight of the structure and the flexibility of the ground, the structure settles and rotates as a rigid-body. The foundation does not experience any loss of contact with the ground; apparently, the foundation pressure is large enough to eliminate any likely asperities of the ground surface.

As a result of such behaviour, the structure and its foundation do not experience any substantial distress, while their rotation and settlement could perhaps be acceptable.

The main factors influencing FR-SFSI are:

- the style of faulting (normal, thrust, strike-slip), the angle of dip and the offset (dislocation) at the basement rock,
- the total thickness (H) of the overlying soil deposit, and the stiffness (G), strength (φ , c) and kinematic (ψ) characteristics of the soil along the depth,

- the type of the foundation system (for example, isolated footings, mat foundation, box-type foundation, piles, caissons),
- the flexural and axial rigidity of the foundation system (thickness of mat foundation cross-section and length of tie beams, etc.),
- the load of the superstructure and the foundation,
- the stiffness of the superstructure (cross section of structural members, spacing of columns, presence or not of shear walls), and
- the location S from the foundation corner to the free-field outcrop.

However, a detailed investigation of the role of all the above parameters is beyond the scope of this chapter. Reference is made to Anastasopoulos (2005) and Anastasopoulos and Gazetas (2007b) for such a parameter study. Here we only outline a few characteristic results pertaining to a 20 m wide rigid mat foundation, supporting a 2-storey building frame. The soil layer is either loose ($D_r \approx 45\%$) or dense ($D_r \approx 80\%$) sand of total thickness $H = 40$ m. Three locations of the foundation with respect to the free-field outcrop are considered: $S = 4, 10, \text{ and } 16$ m, i.e. near the left edge, in the middle, and near the right edge of the foundation, respectively.

Figures 9.3–9.5 portray the response of the soil–foundation–structure system for each location S and each of the two soil densities, for a parametrically variable ratio of base dislocation over layer thickness: $h/H = 1\text{--}5\%$.

Shown in each figure are the deformed mesh, the distribution of plastic strains, the diversion of the rupture D , the vertical displacement profile Δ_y , the distortion angle β , and the contact pressures p_v along the soil–foundation interface. In all cases the results are compared with the corresponding free-field results to visualize the effects of FR-SFSI. The contact stresses are compared to their initial distribution (i.e. for $h/H = 0$, before the bedrock displacement is applied) to reveal which parts of the structure are losing contact with the bearing soil, and hence foundation uplifting takes place. The left part of the building that uplifts will be denoted as u_L , the right u_R , and u_C if the uplifting takes place around the centre. In similar fashion, the part of the foundation that maintains contact will be denoted as b_L , b_R and b_C , if it is located at the left side, the right side, or the middle, respectively.

The following trends are worthy of note:

- (1) For the fault emerging (without SFSI) near the left edge ($s = 4$ m, or $S/B = 0.20$), this lightly loaded foundation for a relative base dislocation $h/H = 5\%$ would cause only a minor diversion of the rupture path, easily noticeable only in the loose soil (about 2 m towards the hanging wall, to the left of the building). The differential settlement is higher on loose sand. The main difference between the two soils is in the uplifting of the foundation. In dense sand the building loses contact at both

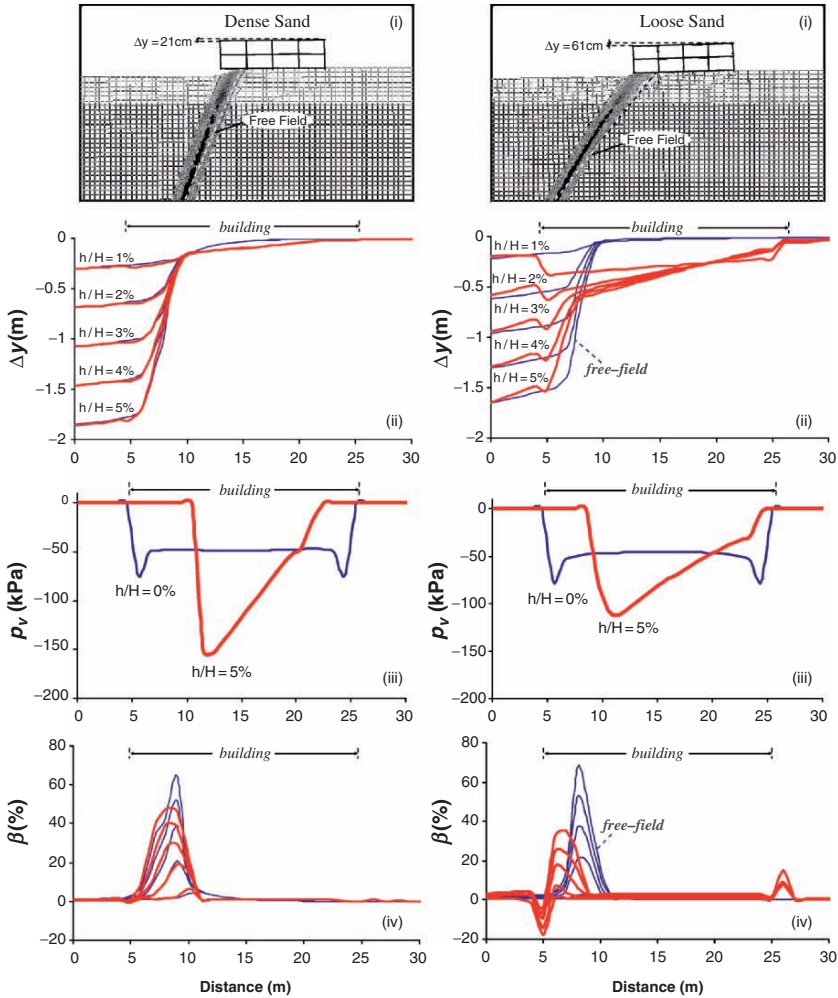


Fig. 9.3. FR-SFSI analysis of 2-storey, $B = 20$ m building, with a 1.3 m thick slab foundation. Fault rupture in the free-field emerging at $s = 4$ m: (i) deformed mesh and plastic strain, (ii) vertical displacement at the surface, (iii) contact pressure p , and (iv) distortion angle β . The results of the FR-SFSI analysis (red lines) are compared with the free-field results (blue lines) for $h/H = 1$ to 5%

sides, $u_L \approx 5$ m, $u_R \approx 3$ m; with only its central part maintaining contact over a width $b_C \approx 12$ m. On the other hand, in loose sand the building uplifts only at the left side, $u_L \approx 3$ m.

The foundation distress is about 50% higher in the dense sand, as a result of the creation of a wider cantilever, whereas in the loose sand the greater compression of the scarp is

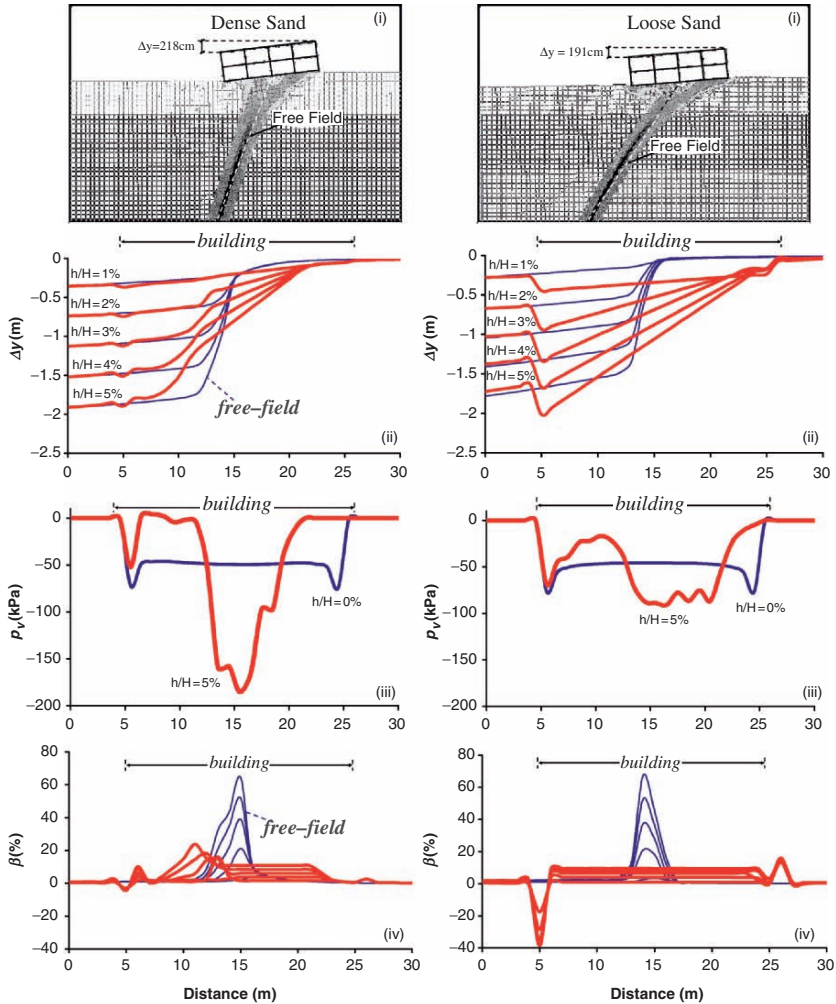


Fig. 9.4. FR-SFSI analysis of 2-storey, $B = 20$ m building, with a 1.3 m thick slab foundation. Fault rupture in the free-field at $s = 10$ m: (i) deformed mesh and plastic strain, (ii) vertical displacement at the surface, (iii) contact pressure p , and (iv) distortion angle β . The results of the FR-SFSI analysis (red lines) are compared with the free-field results (blue lines) for $h/H = 1$ to 5%.results

beneficial. However, the differential settlement and (rigid-body) rotation of the foundation is three-time higher on the loose sand.

- (2) For the fault emerging (without SFSI) in the middle of the foundation ($S = 10$ m, or $S/B = 0.50$) the rupture path is diverted, becomes very diffuse, and bifurcates for $h/H = 5\%$. The left branch (which is a secondary one) diverts by about 3 to 4 m

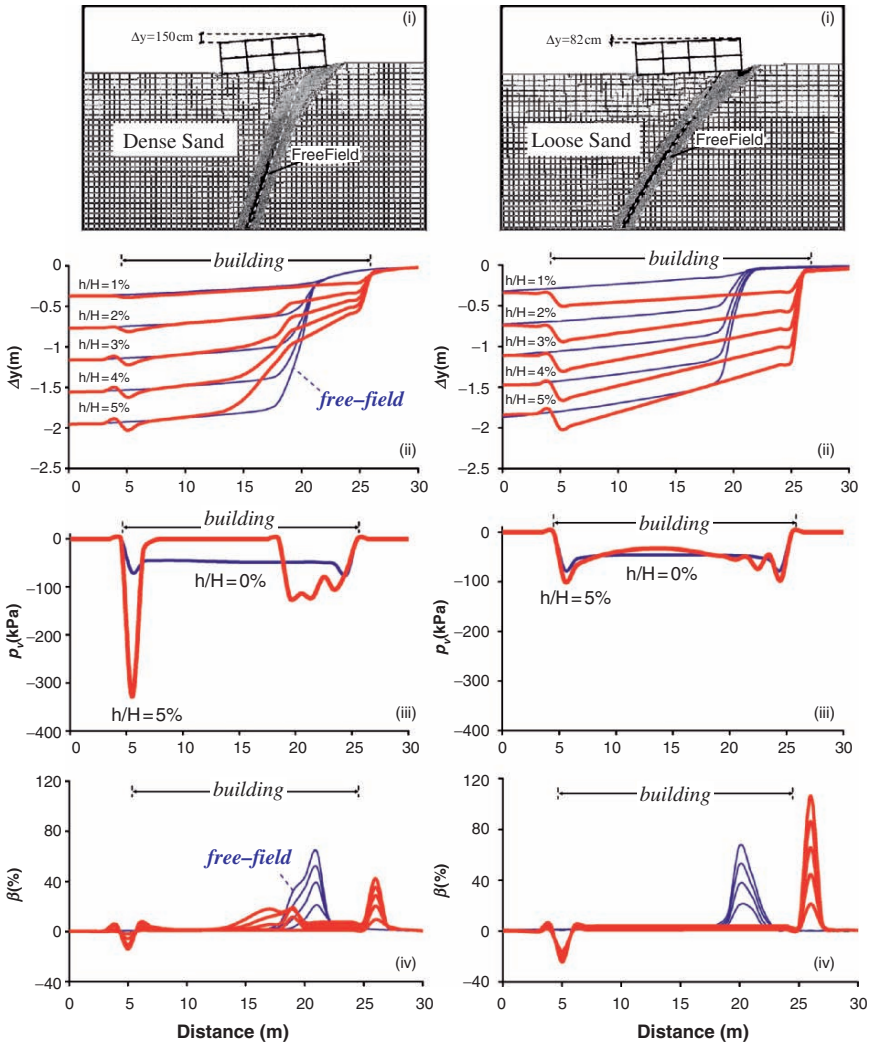


Fig. 9.5. FR-SFSI analysis of 2-storey, $B = 20$ m building with a 1.3 m thick slab foundation. Fault rupture at $s = 16$ m: (i) deformed mesh and plastic strain, (ii) vertical displacement at the surface, (iii) contact pressures p_v , and (iv) distortion angle β . The results of the FR-SFSI analysis (red lines) are compared with the free-field results (blue lines) for $h/H = 1$ to 5%

towards the hanging wall. In both cases of loose and dense sand a fault scarp develops beneath the building. The foundation maintains always contact at its left edge and at its middle part. In dense sand, moving from left to right, there is first a small part of the building $b_L \approx 2$ m that is in contact, followed by an uplifted portion, $u_L \approx 4$ m, then the middle part that remains in contact, $b_R \approx 10$ m,

and finally the far most right part of the foundation that uplifts $u_R \approx 4$ m. Although the situation is qualitatively similar with loose sand, uplifting is much less extensive ($u_R \approx 1$ m). The effective width of the foundation, i.e. in contact with the soil, is now: $b_L = b_C \approx 19$ m. And the differential settlement is about 2 m in both cases.

- (3) For the fault emerging (without SFSD) near the right edge of the foundation ($S = 16$ m, or $S/B = 0.80$), we see again diversion, diffusion, and a minor bifurcation of the rupture path for $h/H = 5\%$. The right branch (which is the most significant) diverts slightly towards the footwall by about 2–4 m, while the (barely noticeable) left branch is diverted towards the hanging wall (≈ 3 m). But a clear significant difference is noted between the loose and dense sand cases:
- The fault scarp that is formed near the right edge of the building is conspicuous only with loose sand.
 - On dense sand, the middle part of the building loses contact with the bearing soil, $u_C \approx 11$ m, while the left and right part of it remain in contact, $b_L \approx 2$ m and $b_R \approx 7$ m.
 - On loose sand, the response is quite favourable: not only is the dislocation diverted by more than 4 m and outcrops beyond the right edge of the structure, but full contact is maintained over the whole length of the soil–foundation interface.
 - The distress of the foundation is thus significantly less with loose than with dense sand. Also smaller on loose sand is the (rigid-body) rotation of the foundation.

Such a good response of a building on loose soil on the “hanging wall” is reminiscent of several success stories from the Kocaeli 1999 earthquake, especially of the building in Denizerler across the entrance from the Ford factory, near Gölcük (see Anastasopoulos and Gazetas, 2007).

- (4) Although not shown here, the effect of an increase in the number of stories from 2 to 5 is quite beneficial on loose sand, but almost negligible on dense sand. The most significant benefits are the decrease of foundation rotation (and of building tilting) and the elimination of a large part of uplifting. As a consequence, the survival of a “heavy” building on top of a major fault rupture in loose soil seems quite possible, in qualitative accord with numerous such success stories in several earthquakes.

2.3. NUMERICAL ANALYSIS AND RESULTS: DEEP FOUNDATIONS

Whereas piles are used for protecting structures by helping to keep total and differential settlements small, their role in supporting structures straddling seismic faults is far from clear. Scant (perhaps only circumstantial) evidence from recent earthquakes has implicated the piles in some structural damage—see for example the analysis of the damage of the pile-supported Attaturk Stadium in Denizerler during the Kocaeli Earthquake (Anastasopoulos and Gazetas, 2007a,b). Systems “tied” to the different blocks of the fault may indeed be vulnerable. An interesting analogy has been brought to our attention by Pro-

fessor J. Bray (2005): deep-rooted trees being torn apart by a fault rupturing directly underneath, apparently as a result of their roots being pulled in opposite directions.

Two typical foundation systems are examined here in order to highlight the interaction between a deep foundation and an emerging fault rupture:

- a 3×3 capped pile group and
- a square rigid embedded foundation (“caisson”).

A 3D finite element model was developed for each case, using eight-noded elements, and employing the same soil and interface constitutive models as described in the preceding section. Figure 9.6 presents a plane section of the complete model. In both cases the soil deposit consisted of dense sand, of total thickness $H = 20$ m. Needless to say, the choice of this limited depth was motivated solely by the desire for the smallest possible size of this 3D model.

2.3.1. Piles

The piles are of length $L_p = 15$ m, diameter $d_p = 1$ m and are spaced 4 m apart (from axis to axis). Their cap is $10 \text{ m} \times 10 \text{ m}$ in plan and 2.5 m thick, and carries a structural vertical load of 10 MN. A rigid connection is assumed between cap and piles (fixed-head piles). Only ideally elastic pile behaviour is considered at the present time, although the necessity for accounting for pile inelasticity will become apparent (if a realistic assessment of the response of the system to large fault offsets is needed).

Aiming at giving a first picture of the possible straining to be experienced by the piles, Figure 9.7 portrays the deformed finite-element mesh with the distribution of plastic shear strains. Four positions of the pile group with respect to the outcropping fault in the free-field are examined: $S = 1, 5, 9,$ and 13 m, where S is measured from the edge of the pile cap (which lies 1 m to the left of the nearby pile axis). Then Figure 9.8 presents detailed results (deformations and internal forces) for the case of $S = 5$ m, only. Several trends are worth noting in these figures:

- (1) For $S = 1$ m, when the fault emerges near the left edge of the pile group (and the group is therefore almost all in the footwall), a slight diversion of the rupture path to the left takes place. A very distinct scarp is formed immediately next to the piles. The scarp forms a slope of about the same angle α as that of the triggering basement rupture, and is appreciably larger than the imposed base offset, Δ . The pile group, however, remains almost intact: there is no displacement or rotation of the pile and only the piles in the front row experience some (rather minor) distress (bending moments of the order of 300 kNm).
- (2) For $S = 5$ m, the fault would have emerged at the centre of the foundation in the free-field. The presence of the axially loaded piles makes the rupture path: (i) to partly divert to the left and emerge just at the edge of the front of piles, and (ii) to become diffuse in the region between the piles. Substantial rotation and horizontal displacement of the pile cap take place. The front row of piles is being “pulled” outward and downward by the “dropping” hanging wall of the fault; as a result very

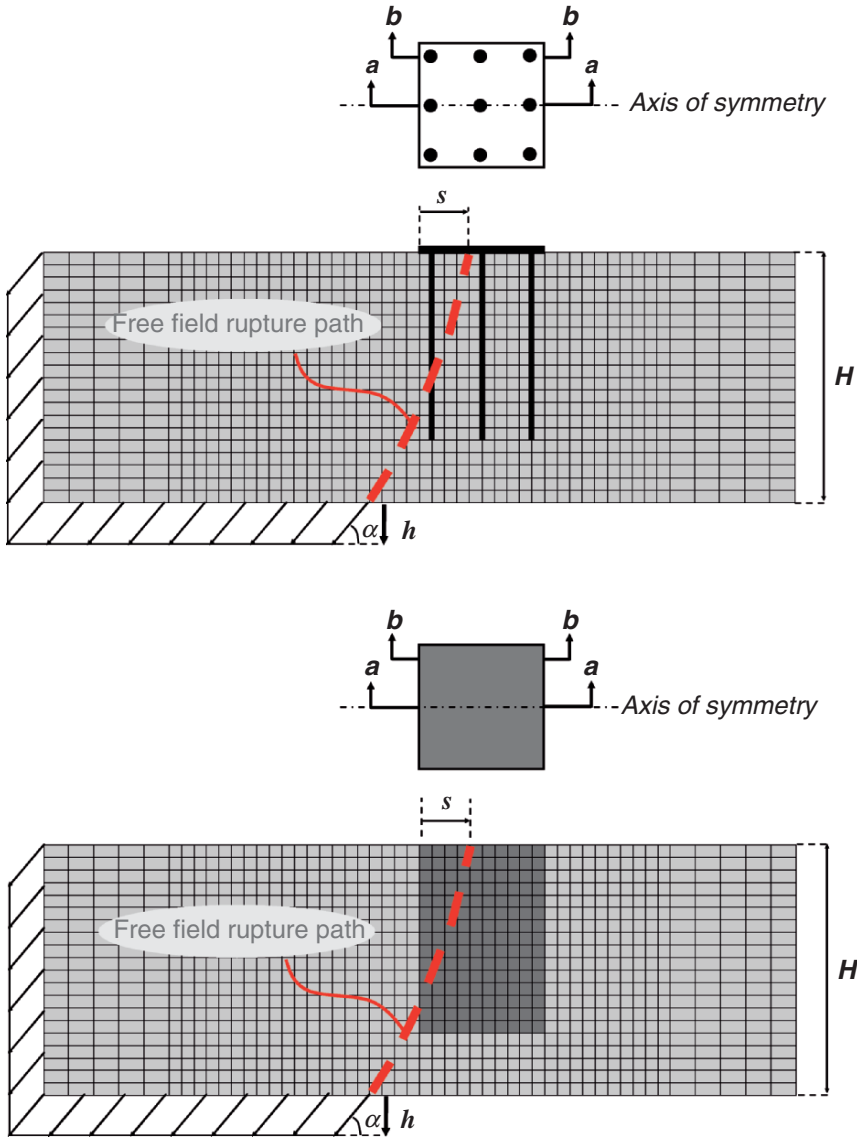


Fig. 9.6. Pile group and caisson foundations in the path of a rupturing fault.
Cross section aa of the 3D finite discretization

large bending moments would develop at the pilehead, in excess of 12 MNm for a dislocation of 2 m. The middle row of piles would experience much less distress, but the last row and especially the corner piles would develop substantial bending moments (almost 6 MNm for a dislocation of 2 m), as a result of being “pushed”

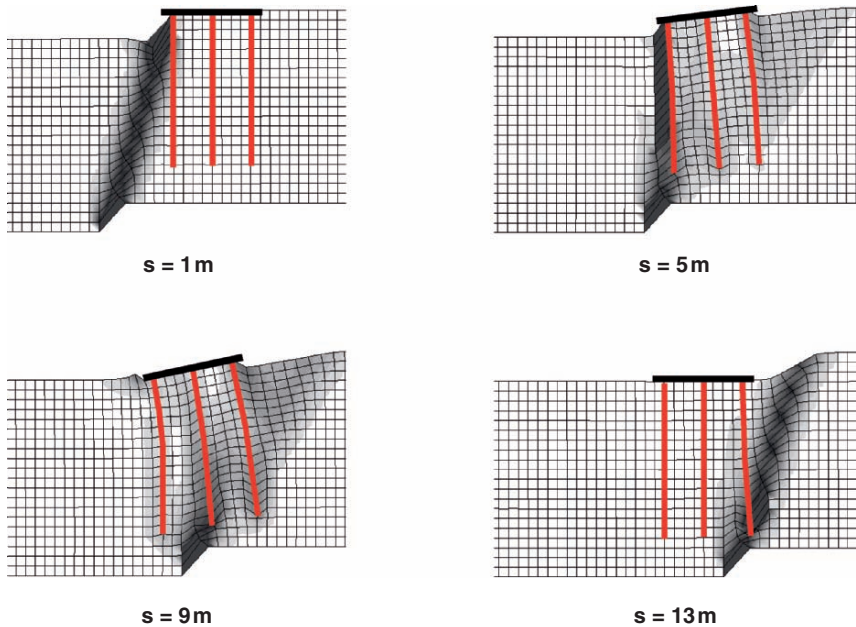


Fig. 9.7. Deformed mesh of the soil–pile–cap system with the concentration of plastic octahedral strains, for different positions ($s = 1\text{--}13\text{ m}$) of the emerging fault rupture

near their middle. Notice the completely different pattern of bending moments with depth between front-row and back-row piles in Figure 9.7: whereas for pile 1 (front row) the maximum is at the top, for pile 6 (corner pile) the maximum appears at 10 m depth. Evidently, such large bending moments, especially in the front row, exceed the maximum conceivable capacity of a well-reinforced 1 m diameter pile, implying structural failure at least of conventional-type piles.

- (3) For $S = 9\text{ m}$, the fault would have emerged near the right edge of the group in the free-field. The piles with their presence and transmitted loads diffuse the rupture, thereby suffering unequal settlements and nonuniform large displacements. As a result, the rotation and lateral displacement of the cap and the bending moments in the piles attain very large (unacceptable) values.
- (4) Finally, for $S = 13\text{ m}$ (free-field fault outcrop 3 m beyond the pile cap), there is a slight diversion of the rupture to the right with a simultaneous slight diffusion of the plastic shear strains. Only the last row of piles is stressed significantly (max $M \approx 4\text{ MNm}$ for $h = 2\text{ m}$). There is apparently no rotation of the pile cap, but a downward and outward displacement are unavoidable; such displacements might have a detrimental effect on a framed structure, one column of which is supported on the studied piled foundation.

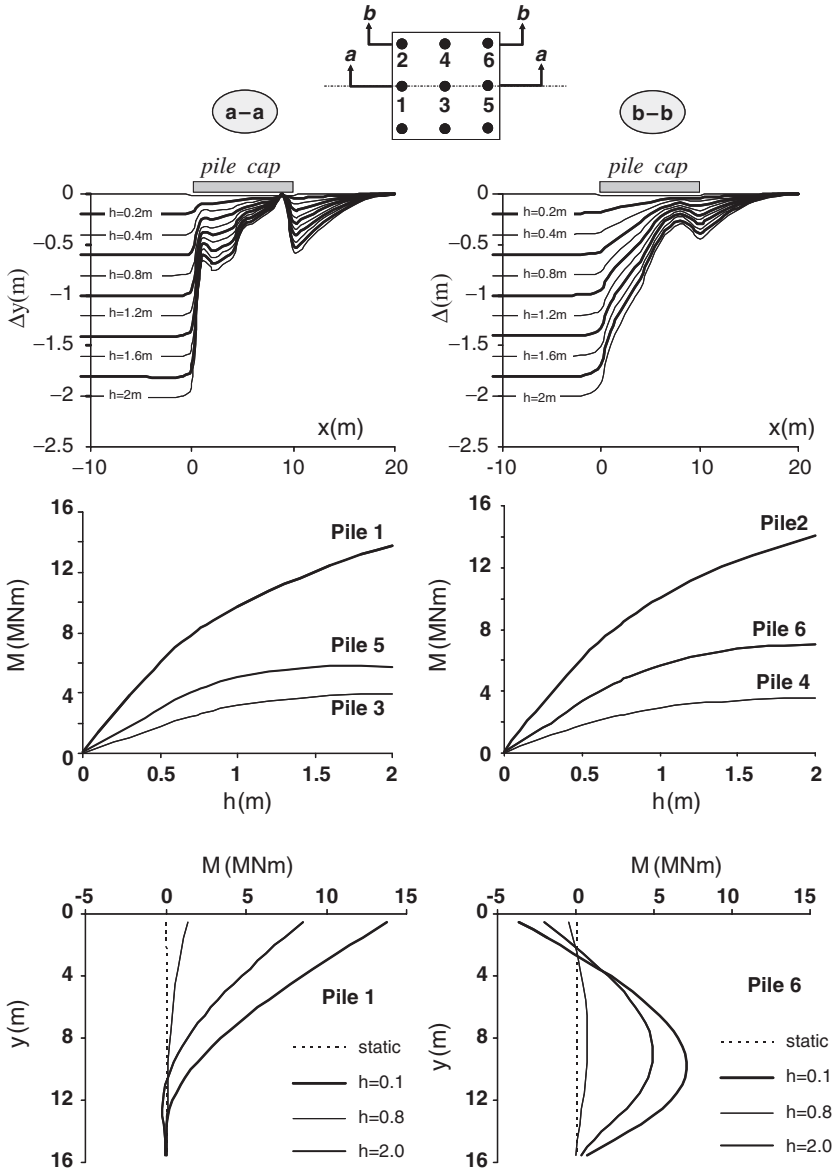


Fig. 9.8. Detailed results (vertical displacement Δy of the ground surface, largest bending moment in the piles, and distribution of bending moments in piles 1 and 6 for a 3 × 3 capped pile group, for a fault rupturing position $s = 5$ m. Pile: d_p 1 m, $L_p = 15$ m, pile cap: $B = L = 10$ m, $N = 10$ MN; soil dense sand

In conclusion, it appears that the response of piled foundations may be less favourable than that of rigid mat foundations. However, two significant limitations of the performed analyses on which these conclusions are partly based must be noted here:

- perfect (“bonded”) contact was assumed between piles and soil and
- the piles were modelled as a perfectly elastic material.

As a result of the first assumption, the forces upon the piles by the outward and downward moving “hanging wall” are exaggerated. Soil sliding around the piles would reduce the magnitude of such “drag” forces, thereby leading to smaller pile distress and smaller cap rotation/displacement. Regarding the second assumption, note that the large bending moments in the piles would not of course materialize in reality, since their ultimate structural capacity cannot be exceeded. Prediction of the consequences of the unavoidable redistribution of loads among the piles, and among piles and raft, cannot be made reliably with the results presented above for purely elastic piles.

2.3.2. Rigid caisson

The caisson is 10 m × 10 m in plan and also 15 m in depth. It carries 10 MN vertical load. Only fully bonded contact between the caisson and the soil is considered—an idealization that is likely to lead to a conservative assessment of the caisson displacement/rotation.

Dominant role in the response of a given caisson to fault rupturing underneath plays its position with respect to the free-field rupture outcropping. Again four such positions are considered: 1, 5, 9, and 13 m. Figures 9.8 and 9.9 portray the deformed mesh with the distribution of plastic octahedral shear strains for each value of S . Figure 9.8 gives the plane section α (along the axis) while Figure 9.9 depicts a 3D view (of half the model). The following conclusions are drawn:

- (1) For $S = 1$ m, the fault emerges to the left of the caisson, diverted slightly, and forms a distinct scarp similar to that in the case of the piled foundation. The caisson does not experience any measurable rotation or displacement.
- (2) More significant is the diversion of the rupture path in case of $S = 5$ m; the fault now emerges vertically along the side of the caisson. The latter hardly “feels” the rupture, experiencing a rotation of merely 1° for a vertical component of dislocation $h = 2$ m. By contrast, recall that the corresponding piled foundation had developed a rotation and horizontal displacement, while its front row of piles had been substantially distressed.

Notice also that a secondary rupture has begun to form, propagating at an angle of about 30° to the left of main rupture. It is about to reach the ground surface for $h = 2$ m, and the associated graben between the two normal ruptures is (barely) visible in the scale of the figure.

- (3) For $S = 9$ m, the rupture is diffused the caisson rotates substantially to the left (8° for $h = 2$ m), and an active state of stress develops on the back side of the caisson. Clearly this behaviour is not so favourable; for instance it would cause distress in a framed structure one column of which is supported on such a caisson.

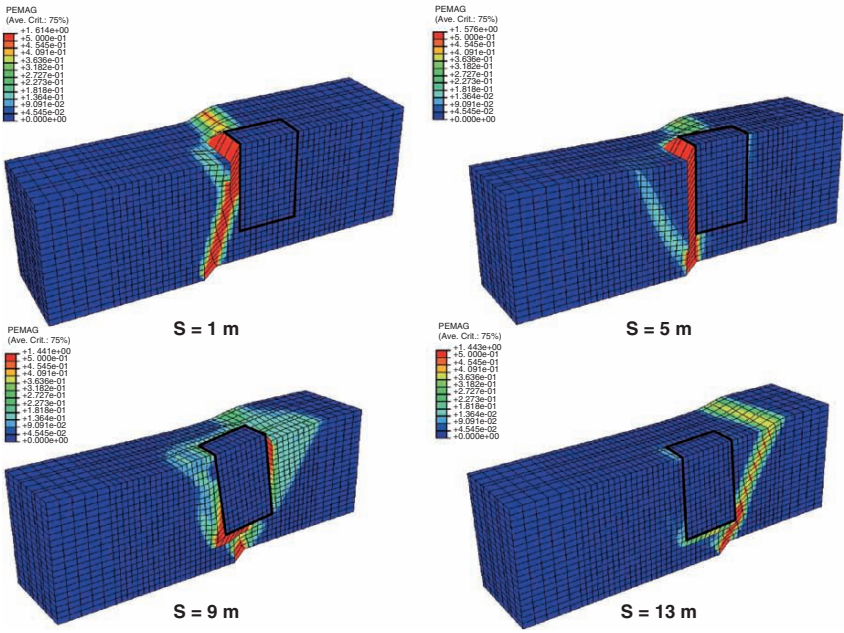
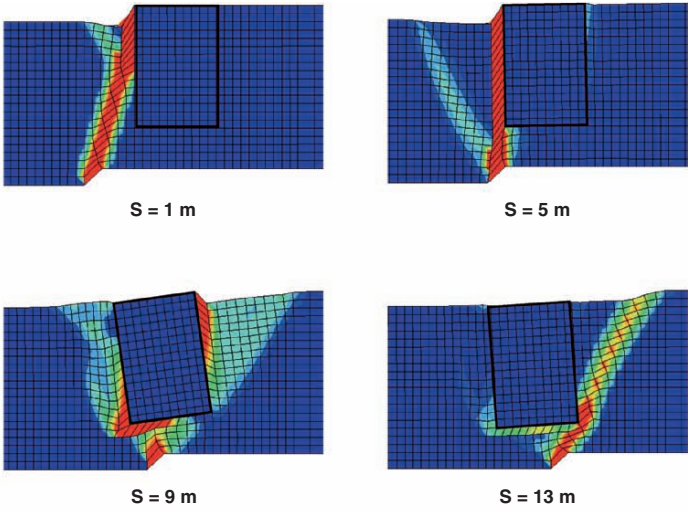


Fig. 9.9. Deformed mesh of the caisson–soil system with the concentration of plastic octahedral strains, for different positions ($s = 1\text{--}13$ m) of the emerging fault rupture: (a) Section aa; (b) 3D view

But by contrast to the piled foundation, the capability of the caisson to transmit the vertical load would be hardly affected.

- (4) For $S = 13$ m, the rupture path “hits” the base corner of the caisson and “defracts” to the right, emerging at the ground surface at a distance of $S = 18$ m, i.e. 5 m to the right of the free-field outcrop. The caisson essentially follows the movement of the “hanging wall”, thereby experiencing an appreciable rotation of about 3° for $h = 2$ m.

In conclusion, it appears that the response of deep embedded foundations (“caissons”) would in most cases be quite satisfactory, especially if structural provisions are taken to accommodate their unavoidable rotation at large fault offsets. Once again, one of the limitations in our modelling, namely the assumption of a perfectly-bonded interface, may have exaggerated the lateral displacement/rotation of the caisson.

3. Nonlinear response of shallow foundations to strong seismic excitation

3.1. INTRODUCTION

The conventional approach to foundation design introduces factors of safety against sliding and exceedance of ultimate capacity, in a way similar to the traditional static design. This approach involves two consecutive steps of structural and foundation analysis:

- (a) Dynamic analysis of the structure is performed in which the soil is modelled as an elastic medium, represented by suitable translational and rotational springs (and, sometimes, with the associated dashpots). The dynamic forces and moments transmitted onto the foundation are derived from the results of such analyses along with considerations for inelastic structural response (e.g. by reducing the moments in columns through the behaviour [“ductility”] factor q).
- (b) The foundations are then designed in such a way that these transmitted horizontal forces and overturning moments, increased by “overstrength” factors, would not induce sliding or bearing capacity failure.

The use of “overstrength” factors is necessitated by the so-called “capacity design” principle, under which plastic hinging is allowed only in the superstructural elements—not in the below-ground (and thus un-inspectable) foundation and soil. Therefore, structural yielding of the footing and mobilization of bearing capacity mechanisms is not allowed. Only a “limited” amount of sliding deformation and uplifting at the foundation–soil interface is allowed. However, there is a growing awareness in the profession of the need to consider soil–foundation inelasticity, in analysis and perhaps even in design (see Paolucci, 1997; Pecker, 1998; Martin and Lam, 2000; Allotey and Nagggar, 2003). This need has emerged from:

- The large (often huge) acceleration (and velocity) levels recorded in several earthquakes which are associated with even larger elastic spectral accelerations (of the

order of 2 g). Enormous ductility demands would be imposed to structures by such accelerations if soil and foundation “yielding” did not effectively take place to limit the transmitted accelerations.

- In seismically retrofitting a building or a bridge, allowing for soil and foundation yielding is the only rational alternative. Because increasing the structural capacity of some elements would imply that the forces transmitted onto the foundation be increased, to the point that it would not be technically or economically feasible to undertake them “elastically”. Thus, new retrofit design guidelines (FEMA 356) explicitly permit inelastic deformations in the foundation.

Even with new structures, it has been recognized that with improved analysis methods we need to better evaluate performance in terms of levels of damage. For the superstructure, “performance-based” design or equivalently “displacement-based” design have been used for a number of years, with inelastic “pushover” analyses becoming almost routine in seismic design practice. It is logical to extend the inelastic analysis to the supporting foundation and soil.

3.2. NEW DESIGN PHILOSOPHY: “PLASTIC HINGING” IN SHALLOW FOUNDATIONS

Excluding structural yielding in the isolated footing or the foundation beam, three types of nonlinearity can take place and modify the overall structure–foundation response:

- Sliding at the soil–foundation interface:* This would happen whenever the transmitted horizontal force exceeds the frictional resistance. As pointed out by Newmark (1965), thanks to the oscillatory nature of earthquake shaking, only short periods of exceedance usually exist in each one direction; hence, sliding is not associated with failure, but with permanent irreversible deformations. The designer must only ensure that the magnitude of such deformations would not be structurally or operationally detrimental. Although this philosophy has been applied to the design of earth dams and gravity retaining walls, its practical significance for foundations might be somewhat limited in view of the large values of the coefficient of friction at soil–footing interface and the passive–type resistance often enjoyed by embedded foundations.
- Separation and uplifting of the foundation from the soil:* This would happen when the seismic overturning moment tends to produce net tensile stresses at the edges of the foundation. The ensuing rocking oscillations in which uplifting takes place involve primarily geometric nonlinearities, if the soil is competent enough. There is no detriment to the vertical load carrying capacity and the consequences in terms of induced vertical settlements may be minor. Moreover, in many cases, footing uplifting is beneficial for the response of the superstructure, as it helps reduce the ductility demands on columns. Housner (1963), Pauley and Priestley (1992), and many others have reported that the satisfactory response of some slender structures in strong shaking can only be attributed to foundation rocking. Deliberately

designing a bridge foundation to uplift in rocking has been proposed as an effective seismic isolation method by Kawashima and Hosoiri (2005). Moreover, even with very slender and relatively rigid structures, uplifting would not lead to overturning except in rather extreme cases of little concern to the engineer (Makris and Roussos, 2000; Gerolymos et al., 2005).

In soft and moderately-soft soils much of what was said above is still valid, but inelastic action in the soil is now unavoidable under the supporting edge of the uplifting footing in rocking. At the extreme, inelastic deformations in the soil take the form of mobilization of failure mechanisms, as discussed below.

- (c) *Mobilisation of bearing capacity failure mechanisms in the supporting soil:* Such inelastic action under seismic loading would always be accompanied with uplifting of the foundation. In static geotechnical analysis large factors of safety are introduced to ensure that bearing capacity modes of failure are not even approached. In conventional seismic analysis, such as in the EC8 – Part 5 bearing capacity is avoided thanks to an “overstrength” factor of about 1.40. The oscillatory nature of seismic shaking, however, allows the mobilisation (for a short period of time!) of the maximum soil resistance along a continuous (“failure”) surface. No “collapse” or overturning failure occurs, as the applied (causative) moment “quickly” reverses, and a similar bearing-capacity “failure” mechanism may develop under the other edge of the foundation. The problem again reduces to computing the inelastic deformations, which in this case means *permanent rotation*. The designer must ensure that its consequences are not detrimental.

The concept of allowing mobilization of bearing capacity mechanisms in foundation design may represent a major change in foundation design philosophy (FEMA, 1997; Pecker, 1998). However, for analysis of the ultimate response of a structure–foundation system to extreme earthquake shaking, accounting for such a possibility is necessary. Martin and Lam (2000) illustrate with an example of a hypothetical structure containing a shear wall connected with a frame how dramatically different are the results of analyses in which inelastic action in the soil is considered or is ignored. With inelastic action (including uplifting) the shear wall “sheds” some of its load onto the columns of the frame, which must then be properly reinforced; the opposite is true when linear soil–foundation behaviour is assumed. Thus, computing the consequences of “plastic hinging” in shallow foundation analysis may be a necessity.

The interplay between uplifting and mobilization of bearing capacity mechanisms is governed *primarily* by the following factors:

- the vertical foundation load N in comparison with the ultimate vertical capacity N_{ult} , expressed through the ratio $\chi = N/N_{ult}$,
- the height, h , of the mass centre of gravity from the base compared with the foundation dimensions (width B , length L) and
- the intensity, frequency content and sequence of pulses of the seismic excitation.

3.3. CHARACTERISTIC RESULTS

3.3.1. Static nonlinear (“pushover”) analysis

Figure 9.10 sketches the problem considered here: a $B = 2b = 6$ m wide foundation on moderately soft soil layer, supporting a $2h = 12$ m high bridge pier (an effective aspect ratio $2h/b = 4$).

Two different models of soil–foundation interaction are implemented to determine the static response to progressively increasing lateral (inertial like) loading:

- an elastoplastic Winkler model and
- a finite-element inelastic model

Details of the models are described in Apostolou (2007), while an extensive calibration of these methods against centrifuge experiments have been presented in the 4th ICEGE Conference (Apostolou et al., 2007). The finite element mesh and some of its characteristics are shown in Figure 9.11.

A typical “pushover” moment–rotation relationship of the foundation under constant vertical load is sketched in Figure 9.12(a, b). In both figures uplifting of the foundation signals the end of the linear $M-\theta$ range, and in both there is a limited moment capacity, associated with a bearing capacity failure mechanism. The difference between the two figures stems from the consideration of $P-\delta$ effects in Figure 9.12(b), as the additional moment, $Nh\theta$, of the structure weight becomes significant at large values of rotation.

The elastic rotation is obtained through the rotational stiffness of the foundation in full contact with the soil. Analytical closed form expressions for a variety of foundation shapes, and idealised soil profiles has been presented by Gazetas (1991).

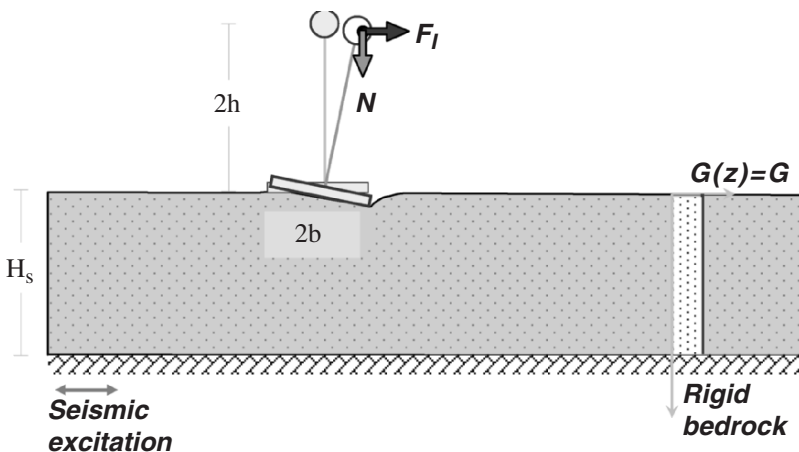


Fig. 9.10. Slender structure–foundation–soil system studied

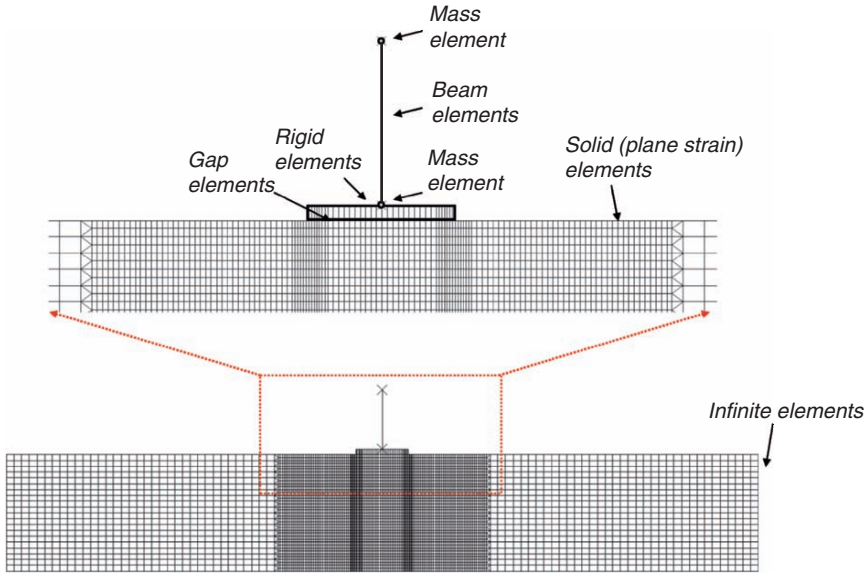


Fig. 9.11. Two-dimensional finite element discretisation and the types of elements applied

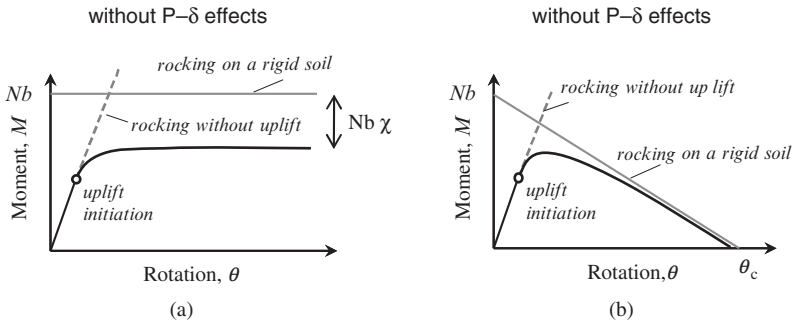


Fig. 9.12. Characteristic moment–rotation pushover curves of a shallow foundation (a) without and (b) with P– δ effects

The ultimate capacity of the soil–foundation system under combined of vertical load N , shear force Q , and moment M is best expressed in terms of the interaction surface in M – N – Q space. Several references can be cited for numerous examples on such a representation (e.g. Butterfield and Ticof, 1977; Pecker, 1998; Houlsby, 2003). For slender structures that are of interest here, most significant is the ultimate diagram in M – N space. An example of such a diagram, in dimensionless form, is given in Figure 9.13. It is based on an idealised elastoplastic Winkler model with the limiting pressures p_u , being equal to $(\pi + 2)S_u$, where S_u is the undrained shear strength of the “ $\varphi = 0$ ” soil. The figure

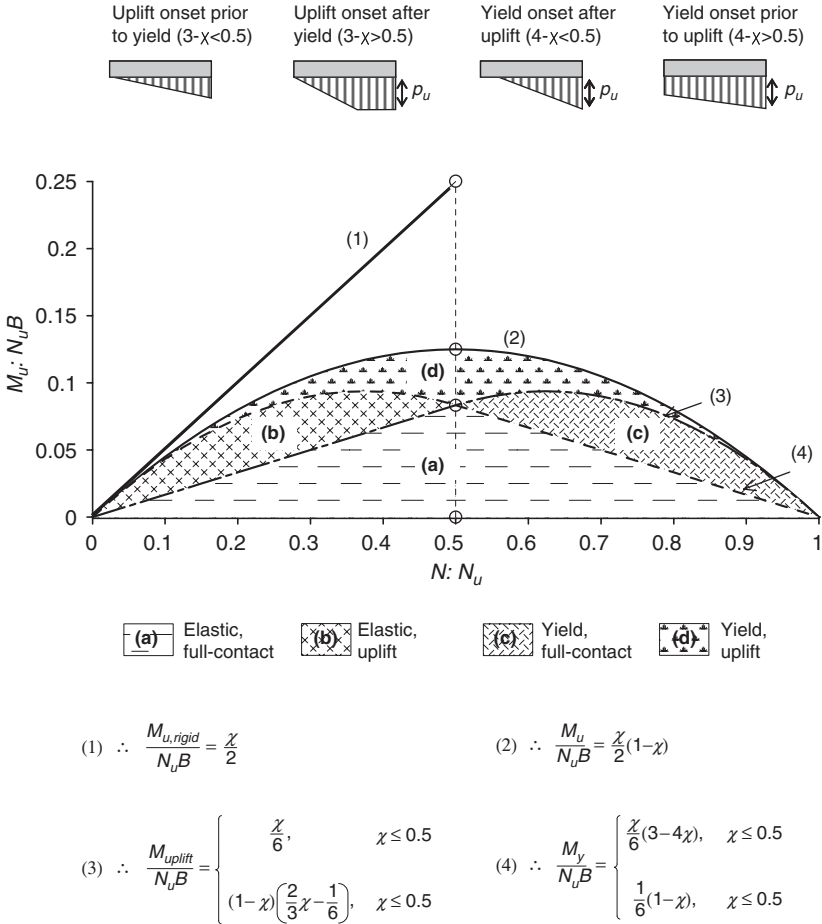


Fig. 9.13. Interaction curves in the normalised N–M plane for bearing capacity failure on rigid (1) or deformable (2) soil. Decomposition of uplifting and soil-yielding mechanisms

plots and gives the analytical expressions of the interaction ultimate curve, as well as its decomposition into *uplift only* and *soil-yield only* curves, in the form

$$M_u / N_u B = f(\chi)$$

in which $\chi = N/N_u$, and $B = 2b$ is the width of the rocking foundation. Notice the symmetric response about $\chi = 0.5$; for this value of χ the largest possible overturning moment,

$$\max(M_u) = 0.125N_u B = 1/4 N_u b$$

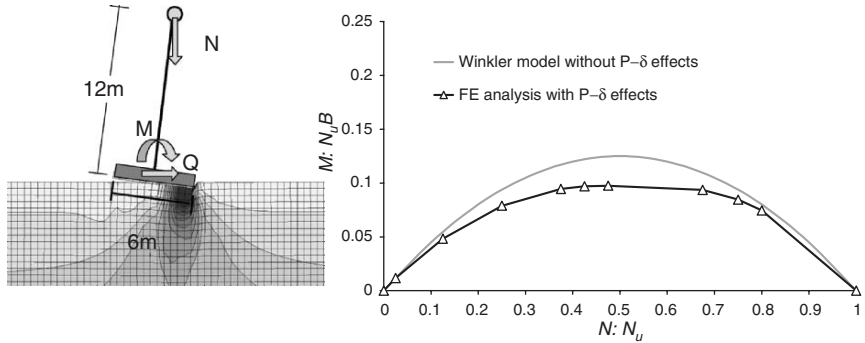


Fig. 9.14. Finite element obtained N – M failure curve for a slender structure on shallow foundation with P – δ effects

is achieved. Moreover, the passage to the inelastic soil domain also occurs at $\chi = 0$, when

$$\max(M_{\text{elast}}) = 0.0833N_u B = 1/6 N_u b$$

The above $(M_u : N_u)$ diagram is in excellent accord with the lower-bound solution of Hously and Purzin (1999). It refers however to loads applied at the foundation level, i.e. without P – δ effects. When the latter are taken into account, there is a slight drop in the ultimate capacity. For the aforesaid slender geometry of the bridge pier ($2h = 12$ m, $B = 2b = 6$ m) this drop, as seen in Figure 9.14, is about 25% so that now:

$$\max M_u \approx 0.10N_u B = 1/5 N_u b$$

More significant however seems to be the reduction in ductility capacity of the P – δ affected system, as seen in Figure 9.12.

For completeness, also sketched in Figure 9.14 is the plot on the FE mesh of the $\Delta\sigma_\gamma$ isostress contours, at $M \approx (2/3) \max M_u$.

3.3.2. Seismic response

The significance of uplifting and soil inelasticity on the seismic response of the slender structure of Figure 9.10 is explained in Figures 9.15 and 9.16. Seismic excitation in the form of a long-period Ricker pulse ($T_E = 2.2$ s, $\text{PGA} = 0.20$ g) is applied at the bedrock and is propagated through soil to produce a free-field “input motion” of a dominant period $T_E = 1.8$ s and $\text{PGA} = 0.34$ g. Such a Ricker-type excitation represents long-period pulses that are often attributed to near-source rupture-directivity effects.

The response is highlighted in terms of M – θ and M – w hysteresis loops (Figure 9.15), as well as time-histories of rotation θ , settlement w , and acceleration A_{cm} at the superstructure (Figure 9.16). Two cases are considered:

- a “light” weight structure: $N = (1/4)N_u = 1000$ kN, corresponding to $\chi = 0.25$
- a “heavy” weight structure: $N = (3/4)N_u = 3000$ kN, corresponding to $\chi = 0.75$

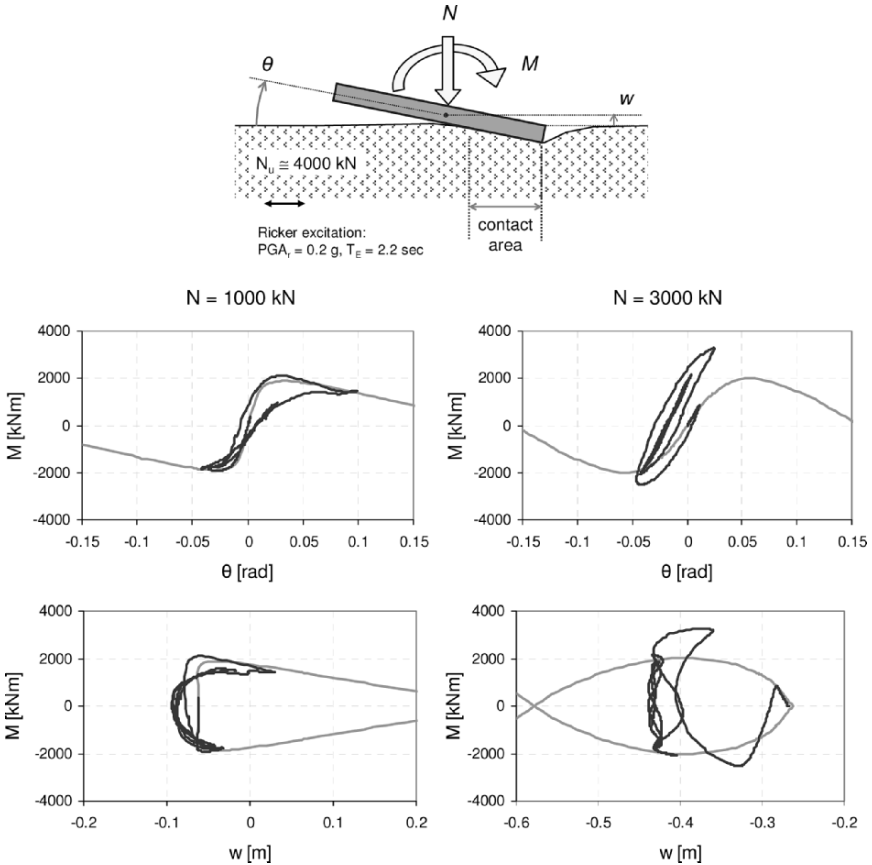


Fig. 9.15. Load–deformation curves (M – θ and M – w) in the two examined cases under earthquake loading. The outcropping excitation is a long duration Ricker pulse ($T_E = 2.2 \text{ s}$, $PGA = 0.20 \text{ g}$). The gray lines are the monotonic loading curves

Several conclusions may be drawn from Figures 9.15 and 9.16:

- For the light structure:* The initial loading cycle follows the monotonic pushover M – θ curve. Upon unloading after a small excursion in the descending branch of the monotonic curve, the path follows with small deviations the original monotonic curve. This is evidence of reversible behaviour—the result of *nonlinearly elastic* uplifting response. However, after a substantial excursion into the descending branch unloading departs slightly from the virgin curve, as soil inelasticity is “activated” due to the large concentration of the applied normal stress when uplifting reduces substantially the area of contact.
- For the heavy structure:* The departure of all branches of loading–unloading–reloading cycles from the monotonic curve is far more substantial—apparently the

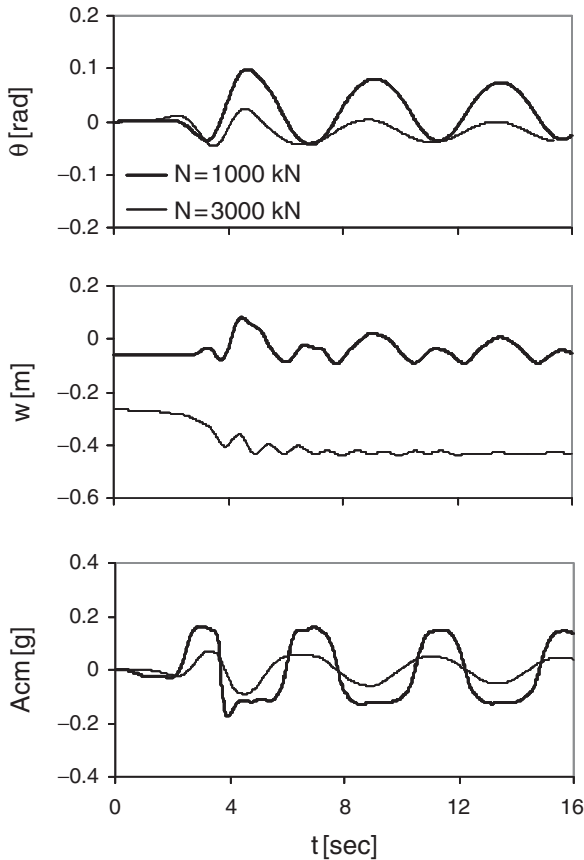


Fig. 9.16. Time-histories of the structure and foundation response under earthquake loading. The outcropping excitation is a long duration Ricker pulse ($T_E = 2.2$ s, $PGA = 0.20$ g)

result of strongly inelastic soil behaviour as the bearing capacity failure mechanisms (left and right) are fully “activated” in this case.

- The moment–settlement curves (M – w) reflect the above M – θ response, with the curve of the light-weight case showing the smallest deviation from the monotonic curve, and of the heavy weight the largest.
- From a design perspective, soil–foundation–structure interaction (SFSI) plays a beneficial role in reducing the acceleration A_{CM} at the centre of mass of the super-structure. This reduction is much greater in the heavy-load case, as result of significant soil inelasticity induced by the rocking foundation (“inertial” nonlinearities).

- The “penalty” of the heavily loaded foundation is to sustain substantial additional vertical settlements, Δw (of about 20 cm); by contrast the lightly loaded foundation ends-up with the same settlement as its original static settlement, $w \approx w_0 \approx 5$ cm.
- Particularly significant, although somewhat coincidental, is the very small residual rotation in both cases. This is due to the largely symmetric nature of the excitation, as a result of which the heavily loaded foundation develops “left” and “right” bearing-capacity failure mechanisms. The resulting two-sided inelastic deformations lead to a symmetric downward displacement (Δw) with only a minor residual rotation $\Delta \theta$.

Acknowledgements

This work formed part of the EU research project “QUAKER”, funded through the EU Fifth Framework Programme: Environment, Energy, and Sustainable Development, Research and Technological Development Activity of Generic Nature: the Fight against Natural and Technological Hazards (contract number: EVG1-CT-2002-00064). The research on pile and caisson foundations built on top of a rupturing normal fault was part of a project funded by the Greek Railway Organization—OSE.

REFERENCES

Part A: Foundations on Fault

- Ambraseys N, Jackson J (1984) Seismic movements. In: Attewell PB., Taylor RK (eds) *Ground Movements and their Effects on Structures*. Surrey University Press, pp 353–380
- Anastasopoulos I (2005) *Fault rupture–soil–foundation–structure interaction*. Ph.D. Dissertation, School of Civil Engineering, National Technical University, Athens, pp 570
- Anastasopoulos I, Gazetas G (2007a) Foundation–structure systems over a rupturing normal fault: part I. Observations after the Kocaeli 1999 earthquake. *Bulletin of Earthquake Engineering* 5(3)
- Anastasopoulos I, Gazetas G (2007b) Behaviour of structure–foundation systems over a rupturing normal fault: part II. Analysis of the Kocaeli Case Histories”. *Bulletin of Earthquake Engineering* 5(3)
- Anastasopoulos I, Gazetas G, Bransby MF, Davies MCR, El Nahas A (2007a) Fault rupture propagation through sand: Finite element analysis and validation through centrifuge experiments. *Journal of Geotechnical and Geoenvironmental Engineering*, ASCE, 133(6), in press
- Anastasopoulos I, Gazetas G, Bransby MF, Davies MCR, El Nahas A (2007b) Normal fault rupture interaction with strip foundations. *Journal of Geotechnical and Geoenvironmental Engineering*
- Barrientos SE, Ward SN, Gonzalez-Ruiz JR, Stein RS (1985) Inversion for moment as a function of depth from geodetic observations and long period body waves of the 1983 Borah Peak, Idaho earthquake, U.S. Geological Survey Open-file Report 85–290, pp 485–518
- Belousov VV (1961) Experimental geology. *Scientific American*, February, pp 96–06
- Berill JB (1983) Two-dimensional analysis of the effect of fault rupture on buildings with shallow foundations. *Soil Dynamics and Earthquake Engineering* 2(3): 156–160

- Bonilla MG (1970) Surface faulting and related effects. In: Wiegel RL (ed) *Earthquake engineering*. New Jersey: Prentice Hall, pp 47–74
- Bray JD (1990) The effects of tectonic movements on stresses and deformations in earth embankments. Ph.D. Dissertation, University of California, Berkeley
- Bray JD (2001) Developing mitigation measures for the hazards associated with earthquake surface fault rupture. In: *A Workshop on Seismic Fault-Induced Failures—Possible Remedies for Damage to Urban Facilities*, Japan Society for the Promotion of Science, University of Tokyo, Japan, January 11–12, pp 55–79
- Bray JD, Ashmawy A, Mukhopadhyay G, Gath EM (1993) Use of geosynthetics to mitigate earthquake fault rupture propagation through compacted fill. *Proceedings of the Geosynthetics'93 Conference* 1: 379–392
- Bray JD, Seed RB, Cluff LS, Seed HB (1994a) Earthquake fault rupture propagation through soil. *Journal of Geotechnical Engineering, ASCE* 120(3): 543–561
- Bray JD, Seed RB, Seed HB (1994b) Analysis of earthquake fault rupture propagation through cohesive soil. *Journal of Geotechnical Engineering, ASCE*, 120(3): 562–580
- Brune JN, Allen CR (1967) A low-stress-drop, low magnitude earthquake with surface faulting. The Imperial, California, Earthquake of March 4, 1966. *Bulletin of the Seismological Society of America* 57: 501–514
- Budhu M (1984) Non-uniformities imposed by simple shear apparatus. *Canadian Geotechnical Journal* 21(1): 125–137
- Buwalda JP, St. Amand P (1955) Geological Effects of the Arvin-Tehachapi Earthquake, California Division of Mines, Bulletin 171, pp 41–56
- Cole DA Jr., Lade PV (1984) Influence zones in alluvium over dip-slip faults. *Journal of Geotechnical Engineering, ASCE* 110(5): 599–615
- El Nahas A, Bransby MF, Davies MCR (2006) Centrifuge modelling of the interaction between normal fault rupture and rigid, strong raft foundations. *Proceedings of International Conference on Physical Modelling in Geotechnics*, Hong Kong, August, pp 337–342
- Erickson SG, Staryer LM, Suppe J (2001) Initiation and reactivation of faults during movement over a thrust-fault ramp: Numerical mechanical models. *Journal of Structural Geology* 23: 11–23
- Eurocode EC8 (1994) Structures in seismic regions. Part 5: Foundations, retaining structures, and geotechnical aspects. Brussels: Commission of the European Communities
- Friedman M, Handin J, Logan JM, Min KD, Stearns DW (1976) Experimental folding of rocks under confining pressure: Part III. Faulted drape folds in multilithologic layered specimens. *Bulletin of the Geological Society of America*, July, 87: 1049–1066
- Gaudin C (2002) Experimental and theoretical study of the behaviour of supporting walls: Validation of design methods. Ph.D. Dissertation, Laboratoire Central des Ponts et Chaussées, Nantes, France
- Gerolymos N, Apostolou M, Gazetas G (2005) Neural network analysis of overturning response under near-fault type excitation. *Earthquake Engineering and Engineering Vibration*, 4(2): 213–228
- Gerolymos N, Vardoulakis I, Gazetas G (2007) “A thermo-poro-viscoplastic shear band model for seismic triggering and evolution of catastrophic landslides”. *Soils and Foundations*, 47(1): 11–25
- Horsfield WT (1977) An experimental approach to basement-controlled faulting. *Geologie En Mijnbouw*, 56(4): 363–370
- Jewell RA, Roth CP (1987) Direct shear tests on reinforced sand. *Géotechnique*, 37(1): 53–68

- Johansson J, Konagai K (2004) Fault induced permanent ground deformations—Simulations and experimental verification. Proceedings of the 13th World Conference on Earthquake Engineering, August 1–6, Vancouver, Canada
- Kelson KI, Kang K-H, Page WD, Lee C-T, Cluff LS (2001) Representative styles of deformation along the Chelungpu Fault from the 1999 Chi-Chi (Taiwan) Earthquake: Geomorphic characteristics and responses of man-made structures. *Bulletin of the Seismological Society of America* 91(5): 930–952
- Lade PV, Cole DA, Jr., Cummings D (1984) Multiple failure surfaces over dip-slip faults. *Journal of Geotechnical Engineering, ASCE* 110(5): 616–627
- Lambe TW (1973) Predictions in soil engineering. *Géotechnique* 23(2): 149–202
- Lazarte CA, Bray JD (1995) Observed surface breakage due to strike-slip faulting. *Third International Conference on Recent Advances in Geotechnical Engineering and Soil Dynamics* 2: 635–640
- Loukidis D (1999) Active fault propagation through soil. Diploma Thesis, School of Civil Engineering, National Technical University, Athens
- Morgenstern NR, Tchalenko JS (1967) Microscopic structures in kaolin subjected to direct shear. *Geotechnique* 17(4): 309–328
- Muir Wood D (2002) Some observations of volumetric instabilities in soils. *International Journal of Solids and Structures* 39: 3429–3449
- Muir Wood D, Stone KJL (1994) Some observations of zones of localisation in model tests on dry sand. In: Chambon R., Desrues J., Vardoulakis I. (eds) *Localisation and Bifurcation Theory for Soils and Rocks*. A.A. Balkema, Rotterdam, pp 155–164
- Nakai T, Muir Wood D, Stone KJL (1995) Numerical calculations of soil response over a displacing basement. *Soils and Foundations* 35(2): 25–35
- Pietruszczak ST, Mroz Z (1981) Finite element analysis of deformation of strain softening materials. *International Journal for Numerical Methods in Engineering* 17: 327–334
- Potts DM, Dounias GT, Vaughan PR (1987) Finite element analysis of the direct shear box test. *Géotechnique* 37(1): 11–23
- Potts DM, Dounias GT, Vaughan PR (1990) Finite element analysis of progressive failure of Carsington Embankment. *Géotechnique* 40(1): 79–101
- Potts DM, Kovacevic N, Vaughan PR (1997) Delayed collapse of cut slopes in stiff clay. *Géotechnique* 47(5): 953–982
- Roth WH, Scott RF, Austin I (1981) Centrifuge modelling of fault propagation through alluvial soils. *Geophysical Research Letters* 8(6): 561–564
- Roth WH, Sweet J, Goodman RE (1982) Numerical and physical modelling of flexural Slip phenomena and potential for fault movement. *Rock Mechanics, Suppl.* 12, pp 27–46
- Saada AS, Townsend FC (1981) State of the art: laboratory strength testing of soils. *Laboratory shear strength of soil. ASTM Special Technical Publication* 740: 7–77
- Sanford AR (1959) Analytical and experimental study of simple geologic structures. *Bulletin of the Geological Society of America*, January, 70: 19–52
- Shibuya S, Mitachi T, Tamate S (1997) Interpretation of direct shear box testing of sands as quasi-simple shear. *Géotechnique* 47(4): 769–790
- Slemmons DB (1957) Geological effects of the Dixie Valley-Fairview Peak, Nevada, earthquakes of December 16, 1954. *Bulletin of the Seismological Society of America* 47(4): 353–375
- Stein RS, Barrientos SE (1985) The Borah Peak Idaho earthquake-Geodetic evidence for deep rupture on a planar fault, U.S. Geological Survey, Open-File Report 85-250, pp 181–234
- Stone KJL, Muir Wood D (1992) Effects of dilatancy and particle size observed in model tests on sand. *Soils and Foundations* 32(4): 43–57

- Take WA (2002) The influence of seasonal moisture cycles on clay slopes. Ph.D. Dissertation, University of Cambridge
- Taylor CL, Cline KMM, Page WD, Schwartz DP (1985) The Borah Peak, Idaho earthquake of October 28, 1983—surface faulting and other phenomena. *Earthquake Spectra* 2(1): 23–49
- Terzaghi K, Peck RB (1948) *Soil mechanics in engineering practice*. John Wiley, New York
- Walters JV, Thomas JN (1982) Shear zone development in granular materials. Proceedings of the 4th International Conference on Numerical Methods in Geomechanics, Edmonton, Canada, May 31–June 4, Vol. I, pp 263–274
- White RJ, Stone KJL, Jewel RJ (1994) Effect of particle size on localization development in model tests on sand. In: Leung, Lee, Tan (eds) *Centrifuge 94*. Balkema, Rotterdam, pp 817–822
- White DJ, Take WA, Bolton MD (2003) Soil deformation measurement using particle image velocimetry (PIV) and photogrammetry *Géotechnique* 53(7): 619–631
- Witkind IJ, Myers WB, Hadley JB, Hamilton W, Fraser GD (1962) Geologic features of the earthquake at Hebgen Lake, Montana, August 17, 1959. *Bulletin of the Seismological Society of America*, 52(2): 163–180
- Yerkes RF (1973) Effects of San Fernando earthquake as related to geology. In: Murphy LM (ed) *San Fernando, California, Earthquake of February, 1971*. Washington D.C.: U.S. Department of Commerce

Part B: Seismic Response of Foundation

- Allotey N, El Naggar H (2003) Analytical moment–rotation curves for rigid foundations based on a Winkler model. *J. Soil Dyn. Earth. Eng.* 23:367–381
- Apostolou M (2007) *Soil–Structure Interaction of shallow foundations under strong seismic moment: Material and Geometric Non-linearity*. PhD Disertation, National Technical University of Athens
- Apostolou M, Gazetas G, Garini E (2007) Seismic response of slender rigid structures with foundation uplifting. *Soil Dynamics and Earthquake Engineering*, 27(8): in press
- Bartlett P. (1976) *Foundation rocking on a clay soil*. M.E. Thesis, Report No. 154, School of Eng., Univ. of Auckland, 144 pp.
- Bolton M (1986) The strength and dilatancy of sands. *Géotechnique* 36(1): 65–78
- Butterfield R, Gottardi G (1994) A complete three-dimensional failure envelope for shallow footings on sand. *Géotechnique* 44(1): 181–184
- Butterfield R, Tiof J (1979) The use of physical models in design. Discussion. Proceedings of 7th European Conference on Soil Mechanics, Brighton 4:259–261
- Cremer C, Pecker A, Davenne L (2002) Modelling of nonlinear dynamic behaviour of a shallow strip foundation with macro-element. *J. Earth. Eng.* 6(2): 175–211
- Davis E, Booker J (1973) The effect of increasing strength with depth on the bearing capacity of clays. *Géotechnique* 23(4): 551–563
- Duncan JM, Lefebvre G (1973) Earth pressures on structures due to fault movement. *Journal of Soil Mechanics and Foundations Division, ASCE*, 99(12): 1153–1163
- FEMA (1997) *NEHRP Recommended Provisions for Seismic Regulations for New Buildings and other Structures*. Building Seismic Safety Council, Washington D.C.
- FEMA 356 (2000): *Prestandard and Commentary for the Seismic Rehabilitation of Buildings*
- Gajan S, Kutter B, Phalen J, Hutchinson T, Martin G (2005) Centrifuge modelling of load-deformation behaviour of rocking shallow foundations. *Soil Dynamics and Earthquake Engineering*, 25(12): 795–810

- Garnier J. Physical models in geotechnics: state-of-the-art and recent advances. 1st Coulomb Conference, Paris, 2001
- Gazetas G (1991) Foundation vibrations. Foundation engineering handbook, 2nd ed., Fang HY (ed), Van Nostrand Reinhold
- Gazetas G, Apostolou M (2004) Nonlinear soil–structure interaction: foundation uplift and soil yielding. In: Todorovska M, Celebi M. (eds) Proceedings of 3rd US–Japan Workshop on Soil–Structure Interaction, USGS, , Menlo Park, CA
- Gazetas G, Apostolou M, Anastasopoulos I (2003) Seismic uplifting of foundations on soft soil, with examples from Adapazari (Izmit 1999 earthquake). Proceedings of BGA International Conference on Foundations, Dundee 1:37–49
- Houlsby G, Purzin A (1999) The bearing capacity of strip footing on clay under combined loading. Proc. Roy. Soc. 455A:893–916
- Housner G (1963) The behavior of inverted pendulum structures during earthquakes. Bull. Seismological Soc. Am. 53(2): 404–417
- Kawashima K, Hosoiri K (2005) Rocking isolation of bridge columns on direct foundations. J Earthquake Eng. 6(2)
- Knappett J, Haigh S, Madabhushi S (2005) Mechanisms of failure for shallow foundations under earthquake loading. Soil Dynamics and Earthquake Engineering, 26(12): 91–102
- Makris N, Roussos YS (2000) Rocking response of rigid blocks under near-source ground motions. Geotechnique 50(3): 243–262
- Martin GR, Lam IP (2000) Earthquake Resistant Design of Foundations: Retrofit of Existing Foundations Proceedings, GeoEng 2000 Conference, Melbourne
- Newmark N (1965) Effect of earthquakes on dams and embankments. Geotechnique 15(2): 139–160
- Nova R, Montrasio L (1991) Settlements of shallow foundations on sand. Géotechnique 41(2): 243–256
- Paolucci R (1997) Simplified evaluation of earthquake induced permanent displacements of shallow foundations. J. Earthquake Eng. 1(3): 563–579
- Pauley T, Priestley MJN (1992) Seismic design of reinforced concrete and masonry buildings, Wiley Interscience
- Pecker A (1998) Capacity design principles for shallow foundations in seismic areas. In: Philippe Bisch, Pierre Labbe, Alain Pecker (eds) Proceedings of the Eleventh European Conference on Earthquake Engineering, Invited Lectures.
- Pecker A (2005) Design and construction of the foundations of the Rion-Antirion Bridge. Proceedings, 1st Greece Japan Workshop on Seismic Design, Observation and Retrofit of Foundations
- Poulos H, Carter J, Small J (2002) Foundation and retaining structures—Research and practice. Proceedings of 15th International Conference on Soil Mech. Found. Eng., Istanbul 1:1–80
- Priestley N, Seible F, Calvi GM (1996) Seismic design and retrofit of bridges. John Wiley and Sons, Inc., New York
- Quaker project website: www.dundee.ac.uk/civileng/quaker/index.htm.
- Rault G, Thorel L, Garnier J Non linearity of soil–footing interaction. Quaker program, Topic B2, Progress Report No. 1, 2005
- Salençon J, Pecker A (1995) Ultimate bearing capacity of shallow foundations under inclined and eccentric loads. Part II: Purely cohesive soil without tensile strength. Eur. J. Mech. A/Solids 14(3): 377–396
- Sidharthan R, Ara S, Norris G (1992) Simple rigid plastic model for seismic tilting of rigid walls. J. Struct. Eng. ASCE 118(2): 469–487

- Taiebat H (1999) Three-dimensional liquefaction analysis of offshore foundations. PhD thesis, University of Sydney, Australia
- Taiebat H, Carter J (2002) Bearing capacity of strip and circular foundations on undrained clay subjected to eccentric loads. *Géotechnique* 52(1): 61–64
- Terzaghi K (1943) *Theoretical soil mechanics*. John Wiley & Sons, Inc. New York, N.Y
- Thorel L, Rault G, Garnier J, Escoffier S, Boura C. Soil–footing interaction: building subjected to lateral cyclic loading, ICPMG06, 6p. (in press)
- Ticof J (1977) Surface footings on sand under general planar loads. PhD thesis, Southampton University
- TRISEE (1998) 3D site effects and soil–foundation interaction in earthquake and vibration risk evaluation. In: Facciolli E, Paolucci R, Vanini M (eds) EC: Directorate General XII for science, research and development
- Ukritchon B, Whittle A, Sloan S (1998) Undrained limit analyses for combined loading of strip footings on clay. *J. Geotech. Geoenv. Eng. ASCE* 124(3): 265–276
- Vesic A (1973) Analysis of ultimate loads of shallow foundations. *J. Soil Mech. Found. Div. ASCE* 99, No. SM1: 45–73

CHAPTER 10

SEISMIC DESIGN AND PERFORMANCE OF SURFACE FOUNDATIONS

Michael Pender

Department of Civil & Environmental Engineering, University of Auckland,

New Zealand

m.pender@auckland.ac.nz

Abstract. Within the context of shallow foundation design this paper considers the need for more effective interaction between geotechnical and structural design teams so that progress towards the integrated design of structure–foundation systems can be achieved. The paper considers four aspects: (i) the role of the shallow foundation bearing strength surface, (ii) the variability in soil properties relative to variations in structural properties, (iii) the observation that bed-of-spring models cannot represent correctly vertical and rotational stiffness of shallow foundation, and (iv) an example of the numerical prediction of seismic response of a low-rise structure founded on shallow foundations is presented which indicates that moment free connections between the foundations and building columns leads to a more economical design.

1. Introduction

Given the very powerful computer resources that are now available for civil engineering and infrastructure design, a pressing need is to improve interaction and communication between the structural and geotechnical communities. An obvious priority is for the two communities to work together in a more integrated fashion. The most direct way in which this can be achieved is by the two groups developing integrated numerical models of complete structure–foundation systems. Too often in the past the practice has been for consideration of the foundation and superstructure to be considered almost in isolation. Lapsing into anthropomorphism, we can say, that from the perspective of an incoming earthquake, the structure and the foundation system supporting it is seen as a single entity. If this is accepted then the design approach needs to be based on a single integrated model of the building–foundation system. Nowadays exceedingly capable software is used for analysis and design of structures. The full potential of this software will not be realised until a complete model of the structure–foundation system is used.

This point of view is certainly not based on the assumption that the future of engineering design lies in evermore sophisticated software in a manner that reduces human input and minimises opportunities for engineering judgement – certainly not. But what is intended is that the exercise of engineering design judgement will be enhanced, so enabling the designer to obtain a more realistic understanding of the how the design will perform, and yet this is not a big step forward for the capabilities of available software. What is needed

is simply that the human side of the process is organised to realise the best output from the numerical modelling.

The above sets a very broad scenario. This paper is concerned only with shallow foundations. A further limitation is that it will not be considering liquefaction effects on shallow foundations.

The paper starts with consideration of the bearing strength of shallow foundations under earthquake loading. The conventional wisdom is that the design of shallow foundations is controlled by considerations of settlement and differential settlement rather than bearing strength. This may be true enough for foundations subject only to static vertical load, but when cyclic moment loading is involved, such as in earthquake, wind and wave loading, then the stability is extremely sensitive to small increases in the applied moment. The designer needs to take account of this. Next the effect of soil variability relative to the variability of the properties of structural elements is discussed. Then the limitations of bed-of-spring models for shallow foundations is discussed. Finally, an example of the integrated design of three-story framed structure on shallow foundations is presented.

2. Ultimate limit state design of shallow foundations in Eurocode 8

Bearing strength theory gives us a way of estimating what combinations of vertical load, horizontal shear, and moment mobilise all the available shear strength of the soil underlying and surrounding a shallow foundation. The sum total of these combinations forms a bearing strength surface in a three-dimensional space.

A convenient way of presenting the surfaces is to use axes defined in terms of dimensionless parameters, one for vertical load, another for horizontal shear and a third for moment applied to the foundation. The suite of dimensionless parameters is defined as

$$\bar{V} = \frac{V}{V_{uo}}, \quad \bar{H} = \frac{H}{V_{uo}}, \quad \bar{M} = \frac{M}{V_{uo}B} \quad (10.1)$$

where:

B is the width of the foundation

V_{uo} is the ultimate vertical that may be applied to the foundation, in the absence of shear and moment loading, evaluated using conventional bearing capacity equations

V , H and M are a combination of actions that induce an ultimate limit state, i.e. the coordinates of a point on the bearing strength surface

\bar{V} , \bar{H} and \bar{M} are the normalised foundation actions.

To account for the effect of seismic inertia in the material beneath the foundation the following two additional dimensionless parameters are used.

$$\bar{F}_{\text{undrained}} = \frac{\rho a_g B}{s_u}, \bar{F}_{\text{drained}} = \frac{a_g}{g \tan \phi} \quad (10.2)$$

where:

$\bar{F}_{\text{undrained}}$ and \bar{F}_{drained} are the dimensionless parameters for undrained and drained loading respectively:

a_g is the horizontal acceleration in the soil beneath the foundation

ϕ is the angle of shearing resistance of the soil

ρ is the density of the soil

g is the gravitational acceleration

Several bearing strength surfaces appear in the literature dating from about the time of the paper by Butterfield and Gottardi (1994), Gottardi and Butterfield (2003). Bearing strength surface expressions for conventional bearing capacity equations are given by Pender (2006). Eurocode 8, Part 5 (CEN, 2003) has a bearing strength surface which allows for the effect of earthquake acceleration in the soil beneath a strip foundation. The surface specified in EC8 is

$$f8(\bar{V}, \bar{H}, \bar{M}, \bar{F}) = \frac{(1 - e\bar{F})^{c_T} (\beta |\bar{H}|)^{c_T}}{\bar{V}^a \left[(1 - m\bar{F}^k)^{k'} - \bar{V} \right]^b} + \frac{(1 - f\bar{F})^{c_{M'}} (\chi |\bar{M}|)^{c_M}}{\bar{V}^c \left[(1 - m\bar{F}^k)^{k'} - \bar{V} \right]^d} - 1 = 0 \quad (10.3)$$

where: the numerical values for the eight parameters in this equation, $a-d$, c_T , c_M , β and χ , are specified in Annexe F of EC8, Part 5. There are two sets of parameters, one for undrained conditions and the other for drained behaviour of the soil. Note that Equation (10.3) employs a slightly different notation from that used in EC8, Part 5.

The background to the derivation of this surface is given by Salençon and Pecker (1994a, b) and Pecker (1997). Design examples using this equation are given in Chapter 10 of Fardis et al. (2005).

Figures 10.1 and 10.2 show the surfaces for the short term undrained loading of saturated clay and drained loading of cohesionless soil. Both surfaces are limited to positive \bar{V} values simply because there must always be a compressive load on the foundation. The diagrams have positive and negative values for \bar{H} as the earthquake is a back and fourth motion. Similarly, the foundation moment \bar{M} can be positive and negative during the earthquake. Thus the surfaces in Figures 10.1 and 10.2 present the upper halves only of the complete surfaces. In Equation (10.3) this is handled by using only the magnitude of the normalised horizontal shear and moment.

The EC8 expressions are developed for a strip foundation. The document does not include shape factors that would allow the capacity to be increased to handle rectangular foundations, although Paulocci and Pecker (1997) have given expressions for these.

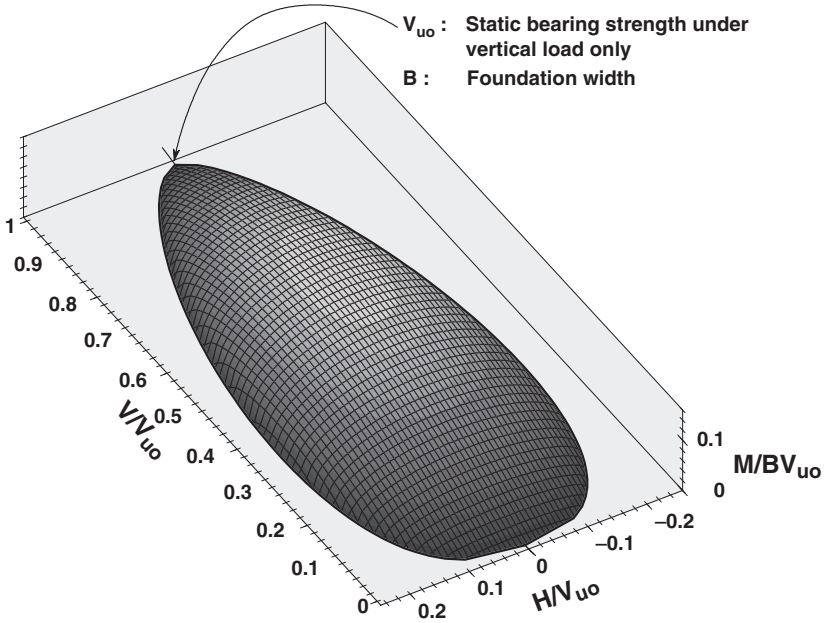


Fig. 10.1. EC8 undrained bearing strength surface for a surface strip foundation

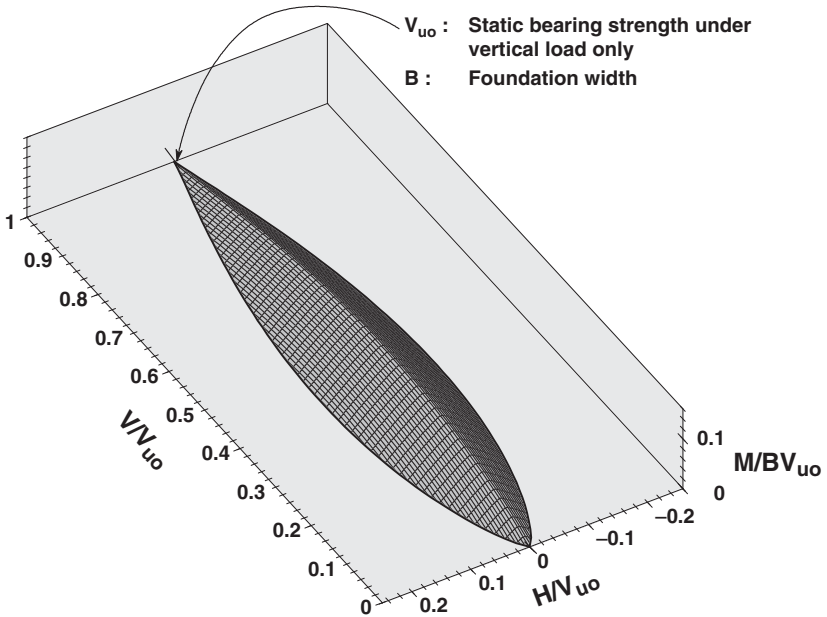


Fig. 10.2. EC8 drained bearing strength surface for a surface strip foundation

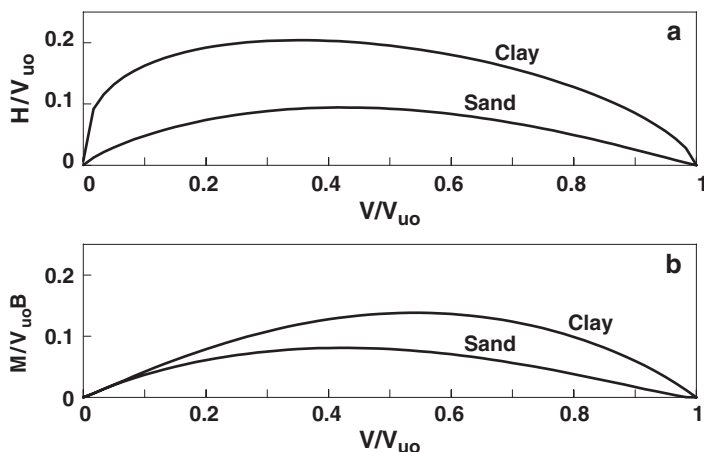


Fig. 10.3. Comparison of the undrained (a) and drained (b) $H-V$ and $M-V$ sections of the EC8 bearing strength surfaces for strip foundations at the ground surface

Figure 10.3 compares sections of the EC8 surfaces. The sections are a longitudinal section in the \bar{V} , \bar{M} boundary with the $\bar{H} = 0$ plane, the $\bar{V} - \bar{H}$ boundary in the $\bar{M} = 0$ plane. It is notable that, in terms of normalised parameters, the foundation on clay has a greater volume within the bearing strength surface.

2.1. ACCELERATION INDUCED REDUCTION IN VERTICAL FOUNDATION STRENGTH

The terms in the brackets on the bottom line of Equation (10.3) show how the vertical bearing strength, in the absence of shear and moment loading, is reduced by horizontal acceleration in the soil beneath the shallow foundation. The reduction of \bar{V} with increasing \bar{F} is plotted in Figure 10.4, the left hand side for the undrained case and the right hand side for the drained case. In the diagram V_{end} is the value to which \bar{V} , under zero shear and moment, is reduced by the horizontal acceleration in the ground beneath the foundation. This figure shows first that the range of values for $\bar{F}_{\text{undrained}}$ is quite different from those for \bar{F}_{drained} . The limiting condition when V_{end} becomes zero gives the maximum possible value for \bar{F} .

The maximum value for \bar{F}_{drained} is 1.04 and for $\bar{F}_{\text{undrained}}$ is 3.60. Figure 10.4 also shows that for the drained case there is a rapid decline in \bar{V} once \bar{F} is below about 0.9. This might be a manifestation of the “fluidisation” effect noted by Richards et al. (1993) when discussing the effect of horizontal acceleration on the bearing strength of shallow foundations in sand.

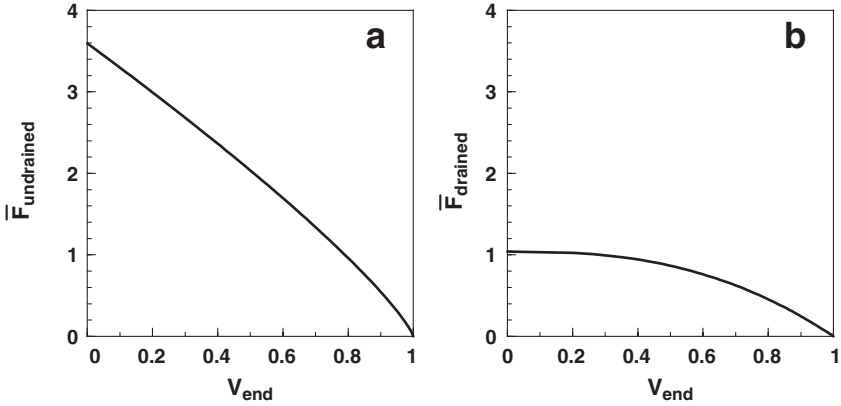


Fig. 10.4. Relationship between the seismic parameters $\bar{F}_{undrained}$ and $\bar{F}_{drained}$ and the dimension-less vertical load at the apex of bearing strength surface: (a) $\phi = 0$, (b) $\phi > 0$

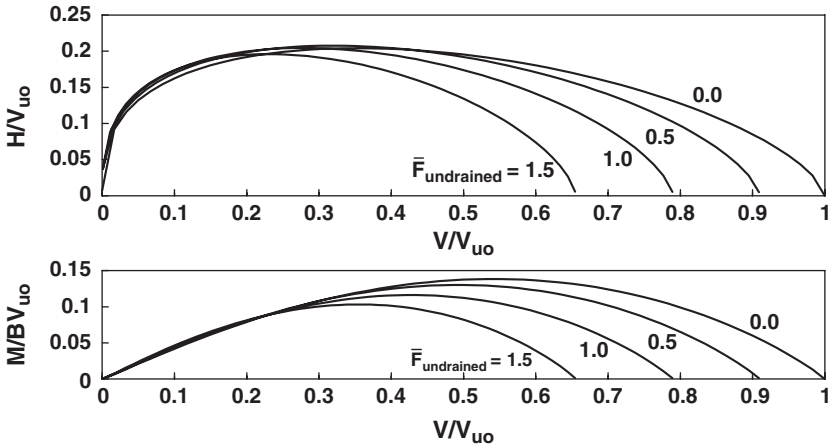


Fig. 10.5. Undrained sections of the EC8 bearing strength with increasing level of seismic acceleration

2.2. UNDRAINED RESPONSE

Figure 10.5 has plotted sections of the undrained bearing strength surface for a range of values of $\bar{F}_{undrained}$. The top part of the figure gives the $\bar{V} - \bar{H}$ boundary in the $\bar{M} = 0$ plane, whilst the bottom part of the figure gives $\bar{V} - \bar{M}$ boundaries in the $\bar{H} = 0$ plane through the surface. This figure shows that as long as $\bar{V} < 0.33$ then values of $\bar{F}_{undrained}$ up to about 1.5 have very little effect on the foundation bearing strength, so an assessment ignoring the effect of horizontal acceleration would be adequate. This is in line with the observation of Auvinet et al. (1986) that shallow foundations in clay, with appropriate static bearing strength factors of safety, perform well in earthquakes. Furthermore

it is known that the undrained shear strength of clay is increased at high strain rates (e.g. Ishihara, 1996; Ahmed-Zeki et al., 1999) and that, for insensitive clays, the post-cyclic loading undrained shear strength is not greatly diminished (Andersen et al., 1980; Ishihara, 1996). This observation indicates that the assessment of the bearing strength of shallow foundations on saturated clay can often ignore the effect of earthquake acceleration, as indicated in EC8 Part 5, and that traditional bearing strength approaches, which have greater scope for shape and embedment effects, can be used.

However, there is one important modifying factor that needs to be emphasised. The $\bar{F}_{\text{undrained}}$ dimensionless parameter indicates that there is a size effect on the undrained bearing strength of a shallow foundation associated with the inertia loading of the soil beneath the foundation. $\bar{F}_{\text{undrained}}$ is a function of the product of $a_g B$, so that an earthquake acceleration that is of negligible consequence for a foundation, say 2 m wide, might be of significance for one 20 m wide. This was also noted by Pender (1995) on the basis of a very simple analysis using a two block failure mechanism.

The undrained shear strength, s_u , in $\bar{F}_{\text{undrained}}$ suggests a clay soil. However, saturated sand also has an undrained shear strength (although it is rather more difficult to estimate than s_u for clay). Thus the comments in this section apply, in principle, to shallow foundations on saturated sand. Saturated sand presents problems as the behaviour is very much affected by cyclic loading. Leaving aside the question of liquefaction (as one would not consider a shallow foundation on a liquefiable deposit of sand) and considering dense sands one still observes that cyclic loading leads to a significant softening of the material (Ishihara, 1985) although not necessarily a loss in strength. Eurocode 8 suggests a way to handle this phenomenon. A model factor is introduced into the top line of the definition of the dimensionless parameters in Equation (10.3). This is intended to make some allowance for the uncertainty in the material and in particular to accommodate any differences between the actual material behaviour and that assumed in deriving the bearing strength surface specified in Equation (10.3). Values given in EC8 for this model parameter are given in Table 10.1. Clearly the main “target” in this table is loose saturated sand. It is well known that shallow foundations in these materials are likely to be subject to liquefaction, so that consideration of this case is unlikely.

2.3. DRAINED RESPONSE

Deposits of dry cohesionless soil will respond in a drained manner to earthquake loading. Figure 10.6 has plotted sections of the drained bearing strength surface for a range of values of \bar{F}_{drained} . The top part of the figure gives the $\bar{V} - \bar{H}$ boundary in the $\bar{M} = 0$

Table 10.1. Bearing strength model factors given in EC8

Medium-dense to dense sand	Loose dry sand	Loose saturated sand	Nonsensitive clay	Sensitive clay
1.00	1.15	1.50	1.00	1.15

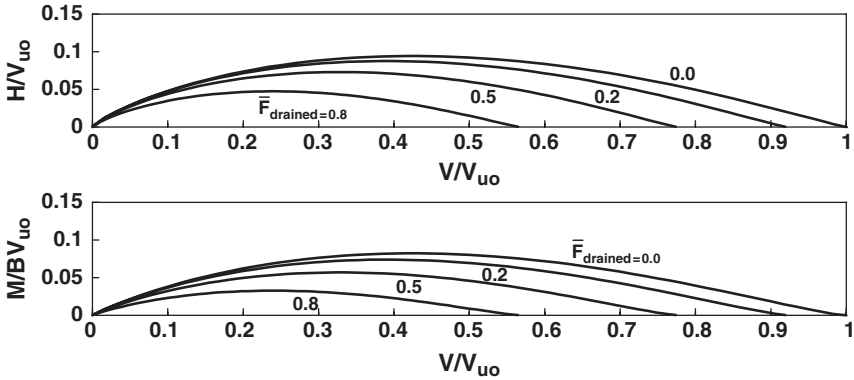


Fig. 10.6. Drained sections of the EC8 bearing strength with increasing level of seismic acceleration

plane, whilst the bottom part of the figure gives $\bar{V} - \bar{M}$ boundaries in the $\bar{H} = 0$ plane through the surface. Comparison of Figures 10.5 and 10.6 shows that the drained response is very much more sensitive to inertia loading than the undrained response. Note also that the definition of \bar{F}_{drained} is such that there is no suggestion of a size effect on drained response so the inertia effect will be important for shallow foundations of any size.

Figures 10.4, 10.5 and 10.6 are presented simply to clarify the workings of the EC8 bearing strength surface. They are not needed in making calculations of the response of shallow foundations to earthquake loading, that is taken care off by Equation (10.3), in which sense Equation (10.3) is operated as a “black-box”. Examples of the use of Equation (10.3) are given by Fardis et al. (2005).

An attractive feature of Equation (10.3) is that it does not focus on the vertical bearing strength of the shallow foundation in the manner of the more usual ultimate limit state methods, even when shear and moment loading are involved (Pender, 2006). Equation (10.3) simply checks that the state point does not lie beyond the bearing strength surface.

3. Serviceability limit state design of shallow foundations for earthquake loading

In evaluating shallow foundation deformations during earthquake excitation it is necessary consider the stiffness and damping properties of the soil and also the effect that the structure–foundation system has on the earthquake motions. This is usually divided into two steps – kinematic and inertial interaction, which is explained by Mylonakis et al. (2006). Dynamic stiffness and damping values for shallow foundations are given by Gazetas (1991) and Mylonakis et al. (2006).

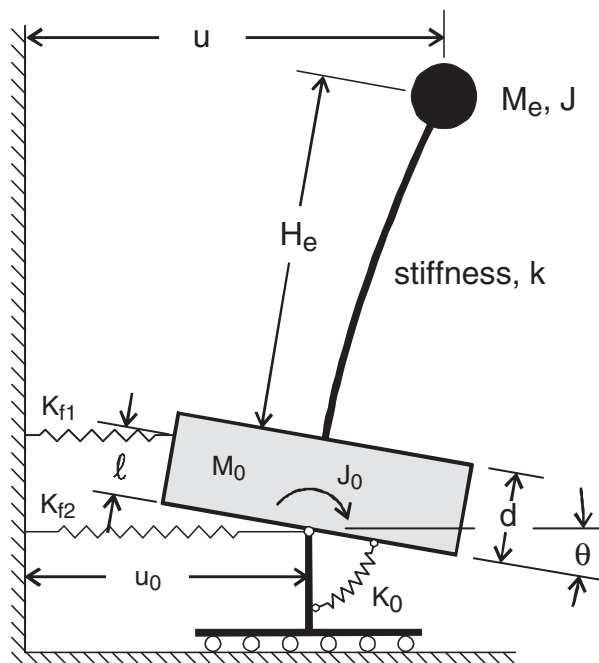


Fig. 10.7. Foundation–structure model for computation of system earthquake response

A method of representing the foundation and attached structure is shown in Figure 10.7. This reduces the attached structure to a single degree of freedom and models the foundation as a rigid block with three displacement degrees of freedom. Although the model in Figure 10.7 is a simplification of a real foundation–structure system there are still many parameters required to set up the model: two masses, two moments of inertia, the dimensions h , d , H_e , the stiffnesses k , K_{f1} , K_{f2} , K_θ as well as the damping values associated with each stiffness. The outputs from the model are the displacements u , u_0 , and θ , as well as the actions in the various springs. Shallow foundation stiffness and damping values are frequency dependent. Usually the values associated with the first mode period of the system are used. Mylonakis et al. (2006) show how combining stiffness and damping within a complex impedance leads to efficiencies in the calculation of the system response.

The above paragraphs refer to elastic soil behaviour. It is well known that soil is not elastic for other than very small shear strains. Fully nonlinear dynamic numerical analyses are possible, but they are hardly design tools. One approach uses an approximate equivalent linear calculation in which the stiffness of the soil is decreased and the damping increased as the level of earthquake excitation increases, but the calculations are still performed assuming elastic behaviour. Suggestions along these lines are given in the EC8 Part 5 and FEMA 273 (FEMA, 1997). Those from EC8 are repeated here in Table 10.2 and those in FEMA 273 in Table 10.3.

Table 10.2. Degradation of soil stiffness according to ground acceleration from EC8 Part 5

Ground acceleration ratio, αS	Damping ratio	V_s/V_{smax}	G/G_{max}
0.10	0.03	0.90 (± 0.07)	0.80 (± 0.10)
0.20	0.06	0.70 (± 0.15)	0.50 (± 0.20)
0.30	0.10	0.60 (± 0.15)	0.36 (± 0.20)

Table 10.3. Degradation of soil stiffness according to ground acceleration effective shear modulus and shear wave velocity from FEMA 273

Effective PGA (g) (at 5% damping)	0.10	0.70
Ratio of effective to initial shear modulus (G/G_0)	0.50	0.20
Ratio of effective to initial shear wave velocity	0.71	0.45

The paragraph immediately following this table in FEMA 273 recommends that the equivalent modulus is calculated according to the above, then response calculations done by taking an upper and lower bound – twice the equivalent modulus and half the equivalent modulus.

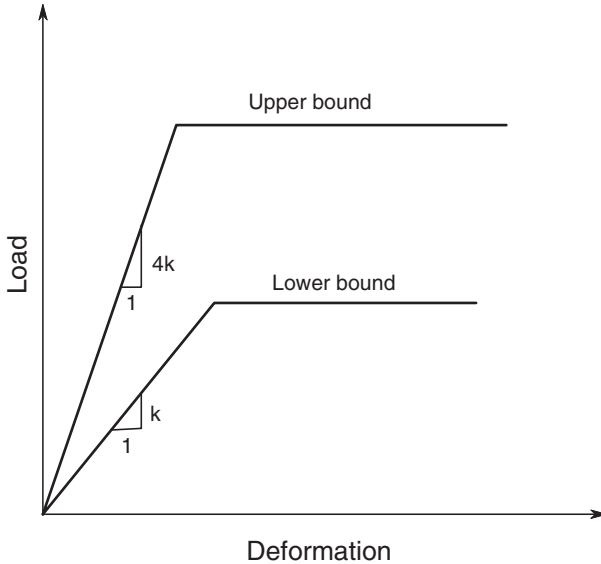


Fig. 10.8. Suggested upper and lower bounds on soil stiffness given in the FEMA 273 document (cf Table 10.3)

Tables 10.2 and 10.3 allow for natural variability of the soil and uncertainties in site investigation by giving bounds on the effect of the earthquake excitation on degradation of the soil modulus. The FEMA 273 document is quite specific as shown in Figure 10.8. With respect to damping EC8 gives single values, in contrast to the bounds on stiffness, whereas FEMA 273 makes no mention of soil damping. The damping values in the EC8 table represent hysteretic dissipation in the soil, radiation damping, if appropriate, is additional.

The response of the structure–foundation system is what the designer needs to predict. If a response spectrum approach is being used, one aspect of this is to evaluate the way the stiffness of the structure and foundation contribute to the first mode period of the system. Similarly the soil damping, both radiation and hysteretic, need to be combined with the structural damping.

These two factors, variability of the soil properties relative to those of the structure, and combination of damping values, need structural engineering and geotechnical engineering teamwork to arrive at the appropriate design model. It is of note that the FEMA 273 document makes this point in the Chapter 4 dealing with foundations.

Figures 10.1 and 10.2 deal with the ultimate bearing strength of the foundation. In this section we are considering dynamic response of the foundation under the assumption that the soil contribution can be modelled by assuming that the soil behaves “elastically”. In other words what is envisaged here is a two stage process. First check to see that the foundation actions do not violate the bearing strength surface. Then evaluate the deformations of the foundation assuming “elastic” behaviour. The two-step nature of this process may be perceived as a disadvantage and so one wonders if there might be an alternative. Given the magnificent computing resources available today a fully nonlinear dynamic analysis of the structure–foundation system could be suggested. However, as stated above, this is not a design approach. What is attractive is the concept of a macro-element to represent the elastic and nonlinear behaviour of the foundation block shown in Figure 10.7 in one computational entity. This has the elastic vertical, lateral and rocking stiffnesses of the foundation to represent the response of the foundation at low levels of excitation. In addition the bearing strength surface acts as yield boundary and so a plastic method is used to estimate permanent deformations of the foundation. The criterion for satisfactory foundation response is then based on the residual permanent displacements and rotations. Macro-elements have been developed by Paolucci (1997), Cremer et al. (2001) and Gajan et al. (2005a). Centrifuge model testing also provides information about the likely earthquake response of shallow foundations on idealised soil profiles. Data obtained by Gajan et al. (2005b) indicates that the limiting factor on the performance of shallow foundations might be the residual deformation at the end of the earthquake.

Further insight into foundation–structure interaction during earthquakes can be obtained by analyzing data from the recorded response of structures during earthquake shaking, particularly where data from several instruments located at different positions in the structure and the surrounding ground are available. A comprehensive study of this type has been reported by Stewart et al. (2001). Some of the results are presented in Figure 10.9 in which the period lengthening attributed to soil–structure interaction is plotted against a dimensionless parameter involving the shear wave velocity of the soil and the first mode period and height of the structure. The results indicate that soil–structure induced period lengthening is usually less than 20% of the first mode period (that is $\tilde{T}/T < 1.2$) although there may be some cases where the lengthening is considerably greater. From this one concludes that, from the perspective of foundation design, the effects modelled by the foundation block in Figure 10.7 are generally modest. Possibly more significant

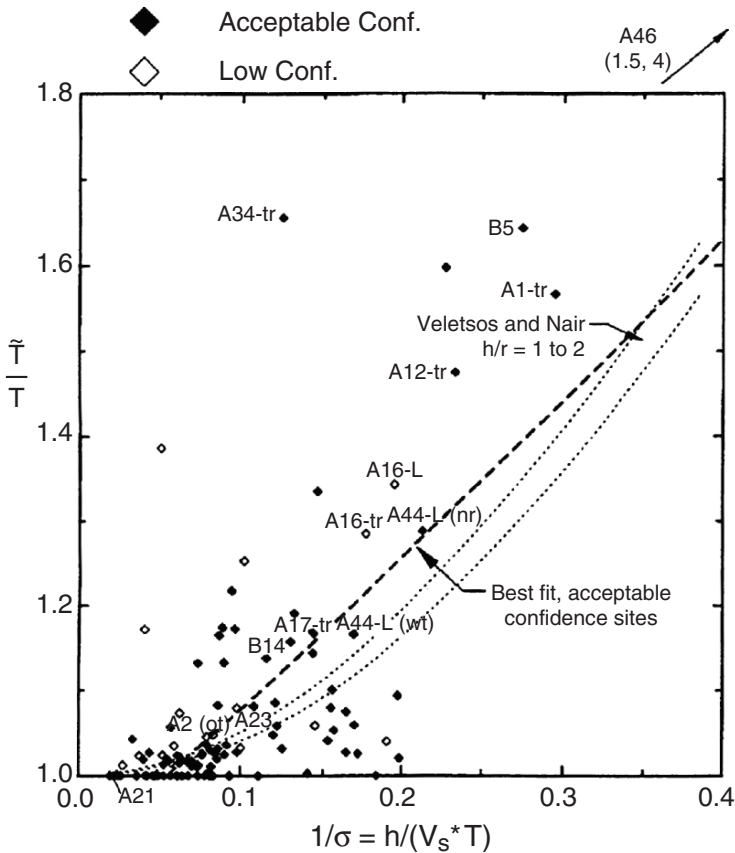


Fig. 10.9. Soil–structure interaction period lengthening ratio from recorded earthquake response of buildings (after Stewart et al., 2001). (The factor plotted on the horizontal axis is the height of the structure divided by the shear wave velocity of the soil times the first mode period of the structure.)

for design are the jumps between the different seismic hazard coefficient curves specified in EC8 for various ground types. Not surprisingly, this places a premium on good quality site investigation before design proceeds too far.

4. Spring models for shallow foundations on soil

A popular method for modelling soil–structure interaction is to represent the soil as a bed of independent springs. It is well established that this provides valid modelling for structural elements that are flexible in comparison to the medium which supports them. One the other hand the model does not give valid soil–structure interaction modelling

for rigid structural elements. The basis for these comparative comments is, of course, response of a continuous elastic medium.

The main thrust of this section of the paper is concerned with the vertical and rotational stiffness of shallow foundations. The stiffnesses obtained using the two models are compared. The main conclusion is that, for given dimensions of a rigid rectangular foundation resting on the ground surface, the rotational stiffness of a bed of springs is less than that of the same foundation on a continuous elastic material. Furthermore, when the soil is modelled as a nonlinear material the ratio of rotational to vertical stiffness gradually decreases as bearing failure is approached.

4.1. SHALLOW FOUNDATIONS ON A CONTINUOUS ELASTIC SOIL

Gazetas (1991) presents a set of expressions, developed by him and his co-workers, giving vertical and rotational stiffness of rigid shallow foundations of arbitrary shape and embedment condition. At this point we consider only foundations on the ground surface.

The vertical stiffness of a rectangular foundation on a bed of springs is given by

$$K_{V_springs} = A_b k_s \quad (10.4)$$

where: $K_{V_springs}$ is the vertical stiffness of the foundation on a bed of springs and k_s is the spring stiffness per unit area of the foundation and A_b is the contact area of the foundation.

The rotational stiffness of the rectangular foundation on a bed of springs is given by

$$K_{\theta_springs} = \frac{1}{2} A_{f_s} k_s s^2 \sum_{j=1}^{N_{L_springs}/2} (2j - 1)^2 \quad (10.5)$$

where:

k_s is the vertical stiffness of the bed of springs per unit area of the foundation,

s is the spring spacing (assumed to be the same in the length and breadth directions),

j is a counter,

$N_{L_springs}$ is the number of rows of springs (assumed to be even) in the longitudinal direction of the footing ($= L/s$),

and A_{f_s} is the area of the foundation associated with each row of springs ($= B \times s$).

In Figure 10.10 the ratio of the rotational stiffness to the vertical stiffness of square foundations resting on the ground surface is plotted for both the elastic soil and the bed of springs. These calculations were done by setting the spring stiffness for the bed of springs so that, for a given foundation dimension, the vertical stiffness was the same for both models. Figure 10.10 makes very clear that the rotational stiffness of a shallow

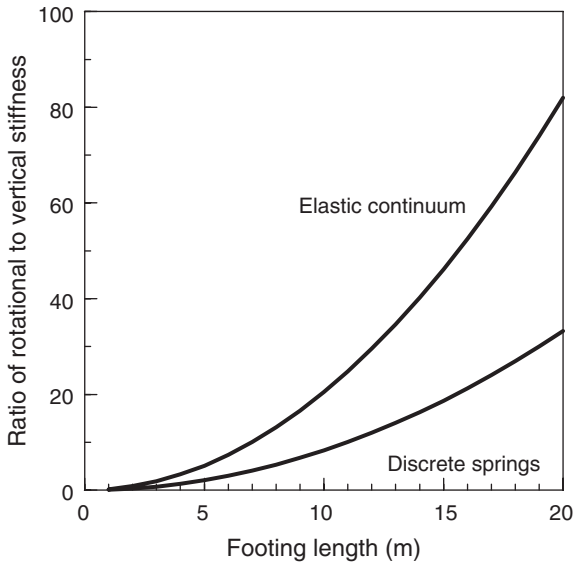


Fig. 10.10. Ratio of the rotational to vertical stiffness of square rigid shallow footings, for a uniform elastic foundation material and the foundation represented as a bed of discrete springs

foundation on a bed of springs is considerably less than that when the foundation is on a continuous elastic material.

The explanation of this difference is apparent if one considers the reaction pressure distribution beneath these foundations. For the bed of springs at every point the reaction pressure depends only on the displacement at that point. So for uniform vertical displacement of a rigid foundation there will be a uniform reaction pressure. Similarly for a rotational displacement of a foundation on the bed of springs the reaction pressure distribution will be linear following the spring displacements. However for a rigid foundation on a continuous elastic material the reaction pressure distribution is not uniform for a uniform settlement. The pressure tends to be very large at the edges. The reason for this is that the strains imposed on the soil are very large at the edges of a rigid foundation. Furthermore the pressure at any point beneath the foundation influences the pressure at every other point beneath the foundation. The calculated pressure distribution for uniform vertical displacement of a rigid square footing and is plotted in Figure 10.11a. The vertical load applied to the foundation resting on saturated clay with an undrained shear strength of 100 kPa is such that $V/V_{uo} = 0.33$. The calculation was done using the well-known solution for the vertical displacement of the surface of an elastic half-space when a pressure loading is applied over a rectangular area (cf, for example, Poulos and Davis, 1974). In a similar manner the pressure distribution when the foundation is subject to moment can be calculated. The distribution when the foundation is subject to moment superimposed on the vertical loading is plotted in Figure 10.11b. The magnitude of the

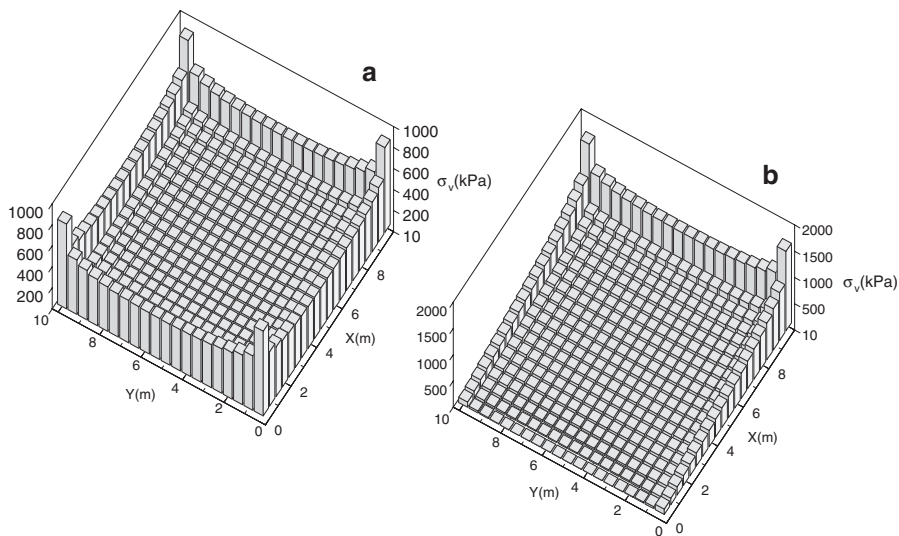


Fig. 10.11. (a) Pressure distribution beneath a vertically loaded rigid square shallow foundation. (b) With moment superimposed on the vertical load

moment in this case is such that one edge of the foundation is at the point of generating negative contact pressure, that is the edge of the foundation is about to start pulling on the soil below, clearly this is not possible, and the underside will start to detach from the soil.

Thus for both vertical and moment loading of rigid shallow square foundations on a continuous elastic soil the reaction pressure distribution is far from constant, or linear, and is concentrated towards the edges. It is the concentration of the reaction towards the edge of the foundation that is the explanation for the rotational stiffness of the foundation on the continuous elastic soil being so much larger than the rotational stiffness of the same sized foundation on a bed of springs, the stiffness of which is adjusted so that the vertical stiffness of the foundations is the same. The underlying reason is that for the spring foundation there is no interaction between the springs so that what happens at one point has no communication with what happens at the other points. In the FEMA 273 document an attempt is made to address this problem by recommending that the springs at the edge of the foundation stiffer than those under the centre part of the foundation.

If one is concerned only with elastic modelling this incompatibility between the two models can be remedied by adding an additional rotational spring beneath the footing, or alternatively adding additional width to the footing and adjusting the spring stiffnesses so that the vertical and rotational stiffnesses of the footing from the spring model are the same as those for a continuous elastic medium. Both of these approaches were explored by Wotherspoon et al. (2004) and Pender et al. (2006). However, one can ask why go to all this trouble? Surely the correct foundation stiffness can be obtained by using separate

discrete springs for the rotational and vertical stiffness of the footing, as is catered for in the majority of software packages for the analysis of structures. The attraction of the bed of springs is simply that it allows modelling of the progressive uplift of the shallow foundation under moment loading. The quest to achieve a correct ratio of vertical to rotational stiffness is to ensure that any progressive uplift from the edges of the footing is modelled realistically.

4.2. NONLINEAR SOIL STRESS–STRAIN BEHAVIOUR

What we have touched upon only briefly so far is the fact that the reaction pressure beneath our footing is limited by the ultimate bearing pressure of the soil beneath. We are then presented with the possibility that the elastic calculations discussed above might be totally misleading and that nonlinear soil behaviour will eliminate the peaks in the pressure distribution at the edges of the foundation. If this was the case then the linear pressure distribution of the bed of springs might be found to be a more realistic pressure distribution not only because of computational convenience but also because it represents more adequately the actual behaviour of the soil–structure interaction. Presented below are some results along these lines, but at this stage for strip foundations rather than the square footings discussed above.

The basis of this work is an implementation in **FLAC (Fast Lagrangian Analysis of Continua, Itasca, 2005)** of a simplified nonlinear stress–strain model for soil (Pender, 1999). The average bearing pressure–settlement curve calculated for a rigid strip foundation subject to gradually increasing vertical load on a saturated clay (undrained shear strength of 50 kPa) produced by this model is shown in Figure 10.12a. The numerical result approaches the theoretical ultimate bearing pressure ($q_u = 5.14s_u = 257$ kPa).

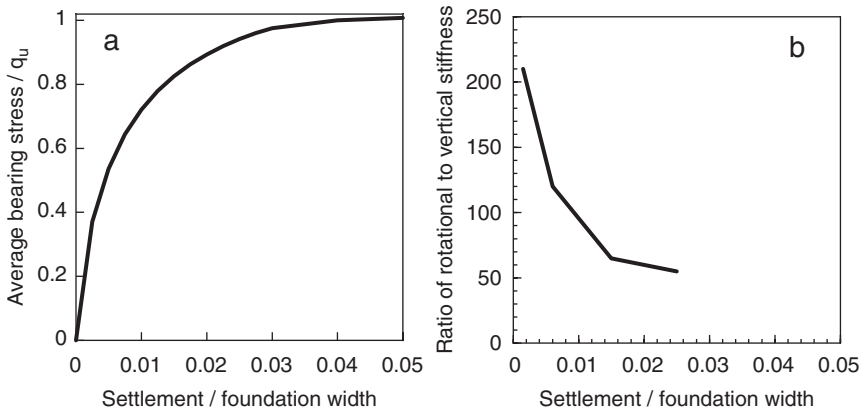


Fig. 10.12. (a) Average bearing pressure–settlement curve for a rigid strip foundation on a nonlinear soil. (b) Decreasing ratio of rotational to vertical stiffness as bearing failure is approached

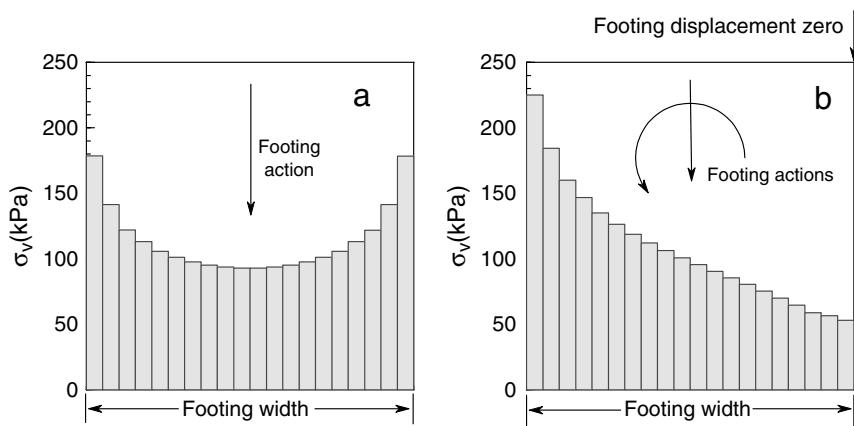


Fig. 10.13. Bearing pressure distribution beneath a shallow rigid strip foundation on a nonlinear soil. (a) Pressure distribution under a vertical load corresponding to $V/V_{uo} = 0.33$. (b) Bearing pressure distribution under the vertical load in (a) with moment superimposed (the magnitude of the moment is such that the vertical displacement of the right hand edge of the footing just reaches zero)

In Figure 10.13a the distribution of vertical pressure beneath the footing is plotted at a vertical load at which $V/V_{uo} = 0.33$. Comparing Figures 10.11a and 10.13a (and making due allowance for the fact that Figure 10.9 is for a square footing whilst Figure 10.11 is for a strip foundation, and that the undrained shear strength of the soil in Figure 10.11 is 100 kPa and that of Figure 10.13 is 50 kPa) it is apparent that the nonlinear stress–strain behaviour of the soil means that although the concentration of vertical stress at the edge of the footing is still apparent it is not as sharp as in the elastic case.

The next step in the FLAC modelling is to apply some moment loading. First the footing is taken to the “working” vertical load and then, while keeping the vertical load constant, some moment is applied to the footing. The easiest way to apply these loads is by imposing displacements at the nodal points and evaluating the applied actions from the nodal forces. For the vertical loading of the rigid footing uniform vertical displacements are imposed, whilst for the subsequent moment loading an additional displacement profile is applied which has a linear downward displacement on one side of the footing and an upward displacement on the other, but zero vertical movement at the centre.

The pressure distribution beneath the foundation on a nonlinear soil is shown in Figure 10.13b. It is of note that at this point the vertical displacement of the footing edge is zero (that is the upward rotational displacement is equal to the downward vertical displacement at the commencement of the moment loading). This is an interesting demonstration of how the simple spring model does not represent what is occurring beneath the footing – if the spring model was used then the reaction pressure at the edge of the foundation at that moment would be zero.

We are now in a position to compare the rotational and vertical stiffness of the foundation on the nonlinear soil. Because of the nonlinearity this is not as simple as the ratio plotted in Figure 10.10, now it depends on the vertical load applied to the foundation. Presented in Figure 10.12b is the ratio of rotational to vertical stiffness at various points around the average bearing pressure–settlement curve (Figure 10.12a), from initial points with “elastic” behaviour to points approaching bearing failure. That is we evaluate, for values of the vertical load on the footing, the rotational stiffness for the initial application of moment with the vertical load held constant and the vertical stiffness for an additional vertical load increment with no moment. This ratio is found to decrease as the load on the footing increases, or in other words as nonlinear soil behaviour becomes more significant. Therefore as the footing load increases the stiffnesses of the footing decrease but the decrease in the rotational stiffness is more rapid than the decrease in vertical stiffness.

It was commented earlier that the distribution of bearing pressure shown in Figure 10.13b is not linear, but the peak at the edge is not as severe as that for the continuous elastic model. The decreasing stiffness ratio plotted in Figure 10.12b indicates that as bearing failure of the footing is approached it is possible that the bed of springs model represents the rotational stiffness of the footing more effectively.

The above discussion shows that when considering foundation stiffness the simple representation of the soil beneath a shallow foundation as a bed of springs is unlikely to be fully satisfactory. When the soil behaves as an “elastic” material (a common representation when the loads on the foundation are considerably less than the bearing strength) the bed of springs, calibrated so that the vertical stiffness is correct, under predicts the rotational stiffness of the foundation. We found that when nonlinear soil behaviour occurs the nonlinearity has a more significant effect on the rotational than on the vertical stiffness. Consequently, nonlinear soil behaviour appears to lead to an improvement as the stiffness ratio decreases with increasing nonlinearity, Figure 10.12b. However, even then the simple spring approach, with nonlinear springs, is not fully satisfactory as the pressure at the footing edge is still not zero when the displacement is zero, Figure 10.13b.

Despite these difficulties it may be possible to get the approximately correct stiffness behaviour for the footing if a bed of nonlinear springs is coupled with a nonlinear rotational spring at the centre of the footing. This means that the correct stiffness ratio could be achieved in the “elastic” region. Like the linear springs this spring would need to be nonlinear with a decreasing rotational stiffness as the rotation increases. In this way it might be possible to develop a suitable nonlinear spring configuration that represents the foundation stiffness. However, even if this is achieved the model would not give the correct bending moment and shear force distribution in the footing. So obtaining a valid stiffness model for a shallow foundation is fraught with difficulties, but certainly more than a simple bed of springs is needed.

5. Integrated design of structure–foundation systems

In recent years there has been a rising demand for superior performance under earthquake loading of both existing and new infrastructure. Assessing accurately the existing state of foundation systems is particularly demanding. By considering the structure and foundation as an integrated system, new opportunities may arise for achieving superior performance; an example of this is the purpose of this part of the paper which extends initial work in this area (Wotherspoon et al., 2004a, b).

Computer modelling was undertaken using Ruaumoko (Carr, 2004), a nonlinear dynamic structural analysis program. Yielding of beams and columns in the structure can be included. Both yielding of the foundations and uplift can be modelled. Various foundation and structural characteristics were investigated to demonstrate effects on the behaviour of the whole system. The purpose of using a software package such as Ruaumoko, which is intended for structural analysis, is to investigate what can be achieved with existing facilities and also to develop an environment to enhance communication between structural and geotechnical specialists. Discussion is confined to low-rise framed structures on shallow foundations where foundation uplift is the main challenge for the numerical model.

Existing Ruaumoko elements allow uplift when the vertical load on the foundation becomes zero, but do not allow detachment of the shear and moment springs at the instant of uplift. A detaching foundation element that uplifts when the vertical load on the foundation is zero and also detaches shear and moment springs at the same time has now been developed for Ruaumoko.

5.1. STRUCTURE DESCRIPTION

The design of a three-storey framed structure with shallow foundations is considered, with the details of the structure illustrated in Figure 10.14. As can be seen, the structure is five bays long and three bays wide, each bay is 7.5 m by 9.0 m and the storey heights are 3.65 m with the exception of the first storey which is 4.50 m. The shallow foundations were located in a layer of clay with an undrained shear strength of 100 kPa.

The seismic load on each floor was equivalent to 8.65 kPa, the roof seismic weight was comprised of a 6.75 kPa distributed load and 1000 kN of plant. The basis of these loads was the imposed load required by current New Zealand structural design actions standard, NZS 1170.1 (Standards New Zealand, 2002), and the permanent load resulting from reinforced concrete frames supporting prestressed precast concrete floor slabs with 65 mm of site poured concrete topping.

Following NZS 1170.5 (Standards New Zealand, 2004) and NZS 3101 (Standards New Zealand, 1995), structural models were designed such that all members contributed to the seismic resistance of the structure and each frame parallel to earthquake propagation had an identical member configuration. Both nominally elastic and limited ductility

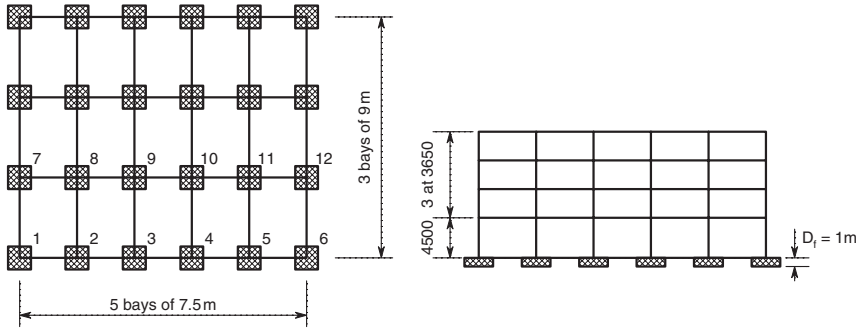


Fig. 10.14. Three-storey structure elevation, plan and footing numbering

(ductility 3) structural models were designed using the loads and dimensions described above. The fixed base period of the structure detailed in Figure 10.14 is close to 0.9 s.

Footings 3.1 m square, with the underside 1 m beneath the ground surface, were adopted for all 24 column foundations (the reason for this constant footing size will become apparent later). Using the load factors given in NZS 1170.5 (1.2 for permanent load and 1.5 for imposed load), bearing capacity calculations revealed that these foundations had adequate to generous bearing strength for the applied static vertical loads.

5.2. RUAUMOKO MODELLING OF THE STRUCTURE–FOUNDATION SYSTEM

Ruaumoko models of the three-dimensional three-storey reinforced concrete moment resisting frame structures were developed to undertake detailed nonlinear modelling. The numerical models could be run with an elastic or a ductile structure on fixed base or compliant foundations.

For ductile behaviour under seismic loading a sway mechanism develops with column hinging at foundation level and beam hinging within 1.5 beam depths from the column faces. All of the calculations in this paper were for an elastic structure. Columns were modelled using concrete beam–column frame members, and beams were modelled using Giberson beam frame members. The Giberson frame members consisted of an elastic central section with potential plastic spring hinges located at the ends. The concrete beam–column members were of similar form, but the central section was defined by a beam column yield surface.

Each floor was modelled as a lumped mass and a rigid diaphragm which restrained the floor such that all points moved the same distance horizontally. All the footings were connected with tie-beams. These were assumed to act under axial load but provide no moment restraint where connected to the footings. For the Ruaumoko modelling Rayleigh tangential stiffness viscous damping was applied to give 5% damping to the fundamental mode and at least 3% damping to every other mode.

The specially developed foundation element used in the Ruaumoko calculations has vertical, horizontal and rotational stiffness, all of which are coupled so at uplift all three are detached from the underlying soil. In addition all three springs can exhibit nonlinear behaviour.

Initially the stiffness of the springs was elastic and gave the settlement under gravity load. To estimate the foundation stiffnesses formulae for the vertical, horizontal and rotational stiffness of rigid rectangular foundations on an elastic soil from Gazetas (1991) were used.

A single earthquake record was used in the analysis and was applied parallel to the longest plan dimension of the structure. This record was from the La Union event, N85W Michoacan, Mexico 1985. The earthquake spectrum was scaled using the method in NZS 1170.5 to the spectrum representing an earthquake in the Wellington region of New Zealand for a 1 in 500 year return period event. The resulting earthquake time history had a peak ground acceleration of 3.46 m/s^2 . The response spectrum with 5% damping gives a spectral acceleration at the natural period of the structure of 5.6 m/s^2 .

Initially three methods were used to size the shallow foundations: (i) all footings with adequate bearing strength from static LFRD ultimate limit state considerations, (ii) all footings to have equal static settlement, and (iii) all footings to have equal vertical stiffness with the most heavily loaded footings having adequate static LFRD bearing strength. However, as the bearing capacity of shallow footings decreases rapidly with the application of moment this was found to be the critical design consideration. Whether the structure remains elastic or is designed as ductile, moments are generated at the base of the ground floor columns, and these moments are transferred to the foundation. It was found that only the equal stiffness footings were of sufficient size to accommodate these moments. This appears to give the exterior footings sizes which are extravagant, but although these footings carry the smallest gravity loads they have the largest cyclic vertical loads during the earthquake as well as cyclic shear and moment. During the unloading part of the cycle things become critical as it is then that the moment has the most adverse affect on the bearing strength of the footing. Results below were taken from the equal stiffness footing design method.

5.3. ELASTIC STRUCTURAL RESPONSE WITH FIXED COLUMN-FOOTING CONNECTIONS

Figure 10.15 shows the time history of the vertical load and vertical displacement of the corner footing, footing number 1 in Figure 10.14, during the earthquake. As the corner footings carry the smallest gravity load it is these that are most affected by the earthquake. It is seen that there are five brief instances of uplift during the earthquake. These are indicated by zero vertical load on the footing and positive vertical displacement. The upper part of Figure 10.15 shows that the gravity load on the footing is about 680 kN and the static settlement is about 2 mm (the sign convention being negative for compressive

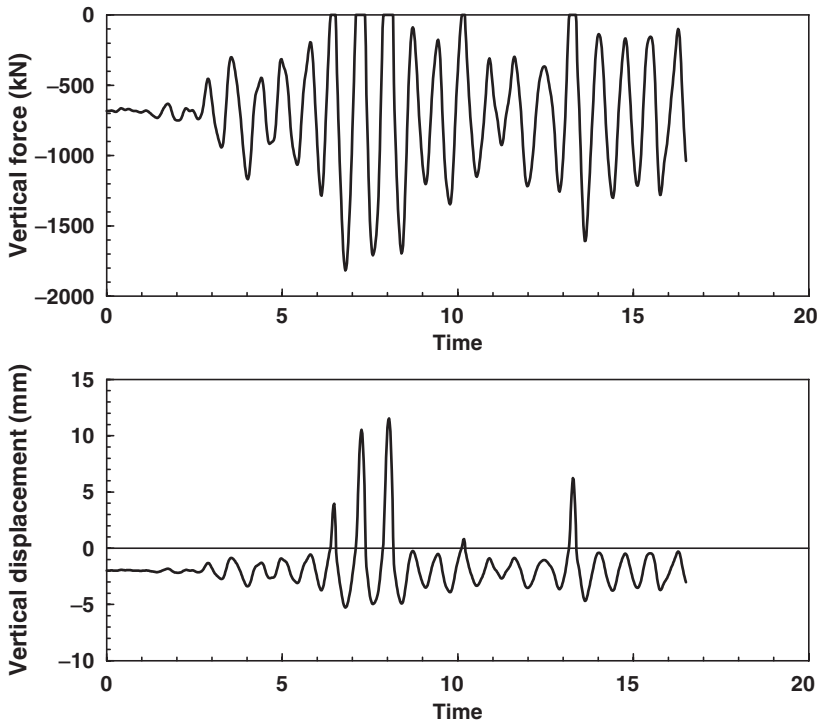


Fig. 10.15. Vertical force and displacement of footing 1

forces and downward displacements). Figure 10.16 plots the vertical, shear and moments applied to footing 1. This shows that when uplift occurs the horizontal shear and moment are also set to zero. The lower part of the figure has at an expanded scale to show more clearly the actions during the five uplift events.

The response of footing 6 is similar. However, footings 7 and 12 had reductions in vertical force and consequent upward movement of the footing but no uplift. Even so there were some brief periods for footings 1, 2 and 3 during which the bearing strength and moment demand exceeded the capacity. A most interesting outcome from the Ruamoko modelling was the vertical force history at the internal footings, 2 to 5 and 8 to 11, exhibit very nearly constant vertical force during the earthquake motion.

5.4. ELASTIC STRUCTURAL RESPONSE WITH PINNED COLUMN–FOOTING CONNECTIONS

Modelling of the uplift mechanism is clearly important for the outer footings of this framed structure. In Figure 10.17 the state paths for footing 1 are plotted with respect to the bearing strength surface. It is apparent the portions of the state path lie outside

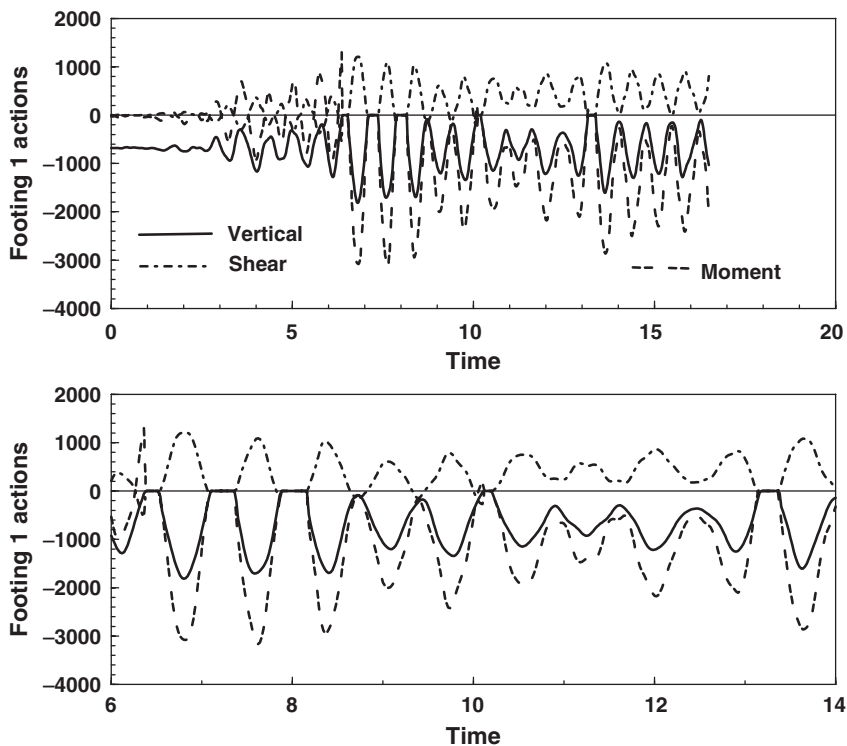


Fig. 10.16. Vertical load, horizontal shear and moment calculated for footing 1

State paths outside bearing strength surface

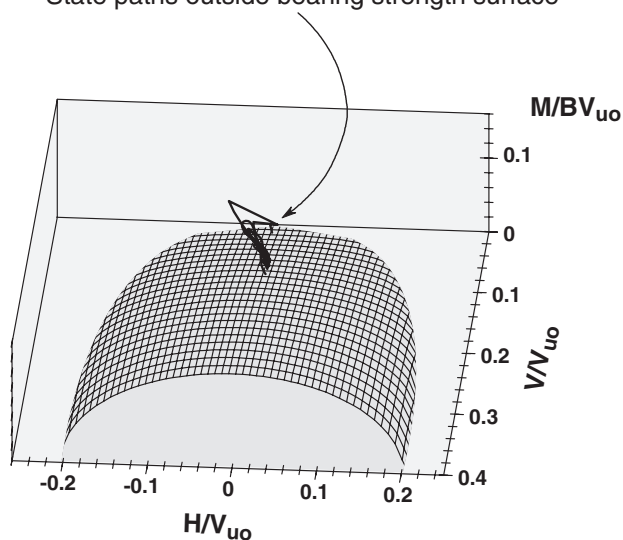


Fig. 10.17. Bearing strength surface and state paths beyond the surface for footing 1 during the earthquake loading

the bearing strength surface, so more than correct modelling of uplift is required for a satisfactory shallow foundation model. A macro-element like that developed by Cremer et al. (2001) or Paolucci (1997) is clearly what is required.

However, another approach was adopted in one set of Ruaumoko calculations and the column base-footing connections were modelled as pinned. Since then there was no moment applied to the shallow foundations during the earthquake no demand was made on the footing bearing strength which exceeded the available capacity. The state paths for footing 1 are shown in Figure 10.18. Now that there is no moment applied to the shallow

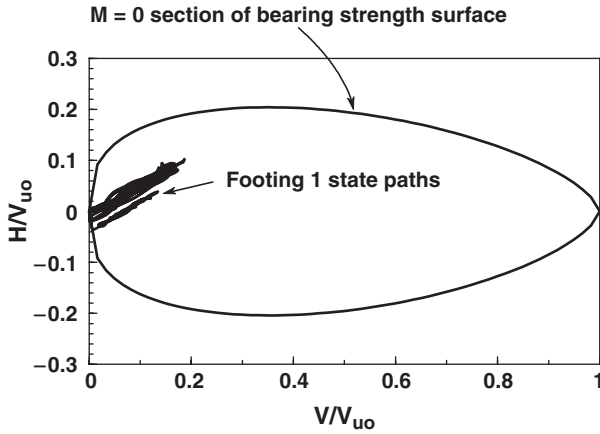


Fig. 10.18. State paths within the bearing strength surface for footing 1 when there is a moment free connection between the footing and column

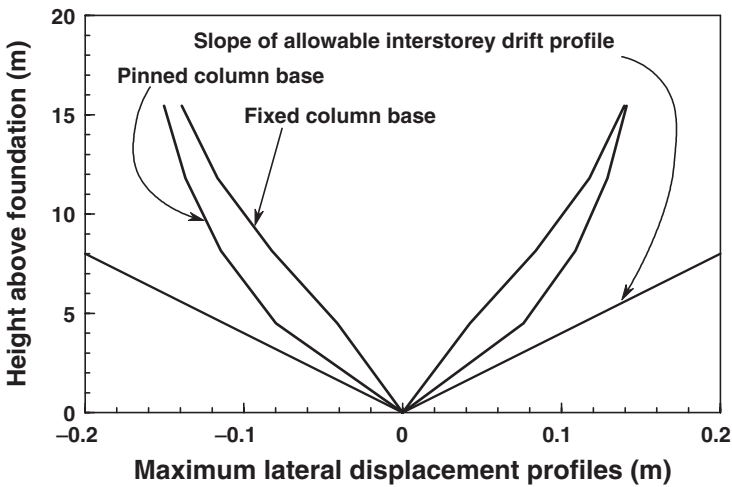


Fig. 10.19. Peak structural horizontal displacement envelopes for the three-storey structure shown in Figure 10.14

foundation the state paths lie within the bearing strength surface. With the reduced moment demand on the footings it is also possible to use smaller footings.

One question that comes to mind when the column–footing connections are pinned is the deformation of the structure during the earthquake shaking. Figure 10.19 gives the peak horizontal displacement envelopes for the two cases. It is clear that the profiles are well within the drift limits specified in NZS 1170.5.

6. Conclusions

In this paper we have discussed four aspects of the design of shallow foundations to resist earthquakes and as a sub-theme have indicated that the way ahead is to develop the integrated design of structure–foundation systems which will require tight interaction between the structural and geotechnical communities.

Firstly the shallow foundation bearing strength surface shows that the combinations of vertical load, horizontal shear and moment that lead to bearing failure are quite complex. To assess footing behaviour under earthquake loading requires more than a conventional bearing strength calculation. However the Ruaumoko calculations at the end of the paper show that there is useful insight to be gained by looking at the response of a complete model of the structure–foundation system.

Variability of the soil properties is much greater than the variability of structural member properties. This means that careful checking is necessary to ensure that the design considers the most critical case.

Figures 10.10 and 10.13 indicate that, although a simple representation of shallow foundation behaviour, the bed-of-springs model is of limited value in situations where both the vertical load and moment are changing during the course of the earthquake.

Finally, as a demonstration of the potential of integrated design of structure–foundation systems, an example of a low-rise structure on shallow foundations indicated that moment-free column–footing connections give more economical footing design, even so, the structure–foundation system still achieves satisfactory lateral displacement behaviour of the structure during earthquake loading.

Clearly there is much scope for future development of the integrated design of structure–foundation systems.

REFERENCES

- Ahmed-Zeki AS, Pender MJ, Fitch NR (1999) Strain-rate effects on the undrained shear strength of Waitemata residual clay. Proc. of 8th Australia–NZ Conference on Geomechanics, Hobart, Vol. 2, pp 791–796
- Andersen KH, Pool JH, Brown SF, Rosenbrand WF (1980) Cyclic static and laboratory tests on Drammen clay. Journal of Geotechnical Engineering, 106(GT5): 499–529

- Auvinet G, Pecker A, Salencon J (1986) Seismic bearing capacity of shallow foundations in Mexico City during the 1985 Michoacan earthquake. Proc. of 11th World Conference on Earthquake Engineering, Acapulco, Paper No. 1966
- Butterfield R, Gottardi G (1994) A complete three-dimensional failure envelope for shallow footings on sand. *Geotechnique* 44(1): 181–184
- Carr AJ (2004) 3D RUAUMOKO: inelastic three-dimensional dynamic analysis program, University of Canterbury – Department of Civil Engineering, Christchurch, NZ
- Comité Européen de Normalisation Eurocode 8. Part 1: Geotechnical Design, General Rules, Draft 6, January 2003
- Cremer C, Pecker A, Davenne L (2001) Cyclic macro-element for soil structure interaction: material and geometrical nonlinearities. *International Journal of Analytical and Numerical Methods in Geomechanics* 25(13): 1257–1284
- Fardis MN, Carvalho E, Alnashi A, Faccioli E, Pinto P, Plumier A (2005) Eurocode 8: design provisions for earthquake resistant structures. Thomas Telford, London
- Federal Emergency Management Agency NEHRP (1997) Guidelines for the Seismic Rehabilitation of Buildings. FEMA 273
- Gajan S, Kutter BL, Thomas JM (2005a) Physical and numerical modelling of cyclic moment – rotation behaviour of shallow foundations. Proc. of 16th International Conference on Soil Mechanics and Geotechnical Engineering, Osaka, Vol. 1, pp 795–798
- Gajan S, Kutter BL, Phalan JD, Hutchinson TC, Martin GR (2005b) Centrifuge modeling of load–deformation behaviour of rocking shallow foundations. *Soil Dynamics and Earthquake Engineering* 25: 773–783
- Gazetas G (1991) Foundation Vibrations. In: Fang HY (ed) Foundation engineering handbook. Van Nostrand, pp 553–593
- Gottardi G, Butterfield R (2003) On the bearing capacity of footings on sand under general plane loads. *Soils and Foundations* 33(3): 68–79
- Ishihara K (1985) Stability of natural deposits during earthquakes. Proc. of 11th ICSMFE, San Francisco, Vol. 1, pp 321–376
- Ishihara K (1996) Soil behaviour in earthquake geotechnics, Oxford
- Itasca Consulting Group (2005) Fast Lagrangian Analysis of Continua Version 5.0, Minneapolis
- Mylonakis G, Nikolaou S, Gazetas G (2006) Footings under seismic loading: Analysis and design issues with emphasis on bridge foundation. *Soil Dynamics and Earthquake Engineering* 26(9): 824–853
- NZS 1170.5 Structural design actions. Part 5: Earthquake Design Actions – New Zealand. Standards New Zealand, Wellington, 2004
- Paolucci R (1997) Simplified evaluation of earthquake-induced permanent displacements of shallow foundations. *Journal of Earthquake Engineering* 1(3): 563–579
- Paolucci R, Pecker A (1997) Soil inertia effects on the bearing capacity of rectangular foundations on cohesive soils. *Engineering Structures* 19(8): 637–643
- Pecker A (1997) Analytical formulae for seismic bearing capacity of shallow strip foundations. In *Seismic behaviour of ground and geotechnical structures*, P. Seco e Pinto (ed), Balkema, pp 261–268
- Pender MJ (1995) Design of foundations to resist earthquake loading. Keynote Address Pacific Conference on Earthquake Engineering, Melbourne, Vol. 2, pp 1–21
- Pender MJ (1999) Implementing a soil stress strain model with hysteretic damping in FLAC. Proc. of the Symposium: FLAC and Numerical Modelling in Geomechanics, Minneapolis, Balkema, pp 475–482

- Pender MJ (2006) Integrated design of structure foundation systems: role of shallow foundation bearing strength surfaces. Proc. of New Zealand Workshop on Geotechnical Earthquake Engineering, 2006, pp 168–204
- Pender MJ, Wotherspoon LM, Ingham JM, Carr AJ (2006) Approach to design of shallow foundations for low-rise framed structures. Proc. of 100th Anniversary Earthquake Conference Commemorating the 1906 San Francisco Earthquake, EERI
- Poulos HG, Davis EH (1974) Elastic solutions for soil and rock mechanics, Wiley, New York
- Richards R, Elms DG, Buhdu M (1993) Seismic bearing strength and settlement of shallow foundations. *Journal of Geotechnical Engineering* 9(5): 477–500
- Salençon J, Pecker A (1994a) Ultimate capacity strength of shallow foundations under inclined and eccentric loads. Part I: purely cohesive soil. *European Journal of Mechanics A/Solids* 14(3): 349–375
- Salençon J, Pecker A (1994b) Ultimate bearing capacity of shallow foundations under inclined and eccentric loads. Part II: purely cohesive soil without tensile strength. *European Journal of Mechanics A/Solids* 14(3): 377–396
- Standards New Zealand, The Design of Concrete Structures, NZS 3101:1995
- Standards New Zealand, Structural Design Actions AS/NZS 1170.1: 2002
- Standards New Zealand, Structural Design Actions NZS 1170.5: 2004
- Stewart JP, Seed RB, Fenves GL (2001) Seismic soil–structure interaction in buildings. II: empirical findings. *Journal Geotechnical and Geoenvironmental Engineering* 125(1): 38–48
- Wotherspoon LM, Pender MJ, Ingham JM (2004a) Effects of foundation model on the earthquake response of building systems. Proc. of 3rd ICEGE and 11th ICSDEE, Berkeley, CA, pp 766–773
- Wotherspoon LM, Pender MJ, Ingham JM (2004b) Combined modelling of structural and foundation systems. Proc. of 13th World Conference on EQ Engineering, Vancouver, Paper 411, 15 pages

CHAPTER 11

LIQUEFACTION PERFORMANCE OF SHALLOW FOUNDATIONS IN PRESENCE OF A SOIL CRUST

George Bouckovalas¹ and Panos Dakoulas²

¹ *Geotechnical Engineering, National Technical University of Athens, Greece*
gbouck@central.ntua.gr (www.georgebouckovalas.com)

² *Department of Civil Engineering, University of Thessaly, Volos, Greece*
dakoulas@uth.gr

Abstract. Liquefiable soils are currently categorized by all seismic codes as extreme ground conditions where, following a positive identification of this hazard, the construction of surface foundations is essentially allowed only after proper treatment soil. This article examines to what extent this situation may change in presence of a non-liquefiable soil crust, between the foundation and the liquefiable soil. Means are provided for analytical evaluation of the degraded bearing capacity and the associated seismic settlements for the specific case of strip foundations on a cohesive (clay) crust. Furthermore, the conditions are explored which ensure a viable performance-based design, and the issue of a critical soil crust thickness, beyond which liquefaction effects are minimal, is addressed.

1. Introduction

Building a well engineered surface foundation directly upon the surface of a liquefiable soil layer, without prior improvement or reinforcement, is clearly out of the question, since settlements will be excessive and uneven, leading to structural, as well as operational failure. The foundation failures shown in Figure 11.1 are merely some typical examples from the ensuing hazard. However, it is possible that such a solution becomes feasible in the presence of a sufficiently thick and shear resistant non-liquefiable soil crust (e.g. clay, dense or dry sand and gravel, improved soil) between the foundation and the liquefiable subsoil. The reason is simple: as the thickness of the non-liquefiable soil crust increases gradually, beyond the maximum depth of a Prandtl type failure mechanism, failure is likely to develop exclusively into that layer and consequently any liquefaction of the subsoil will have a minor effect on the post-shaking failure load and the associated settlements.

Thus, the question is not whether there is a beneficial effect of the non-liquefiable soil crust, but what this effect is and whether it is of engineering interest. In providing a satisfactory overall answer to these questions, one must first resolve the following design issues:

- (a) What is the bearing capacity of surface foundations on a liquefied subsoil, in the presence of a non-liquefied soil crust?
- (b) What are the liquefaction-induced settlements of the footing in the above case?

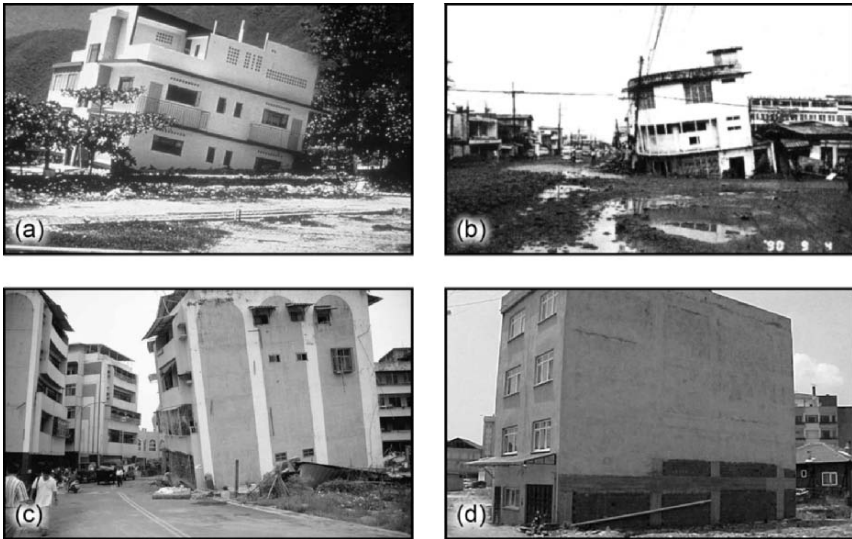


Fig. 11.1. Liquefaction induced failures of shallow foundations. (a) Caracas Venezuela, 1967, $M = 6.5$, (b) Dagupan, Philippines, 1990, $M = 7.8$, (c) Chi-Chi Taiwan, 1999, $M = 7.3$, and (d) Adapazari, Turkey, 1999, $M = 7.4$

- (c) Is it meaningful to seek an acceptable (in terms of bearing capacity and seismic settlements) allowable bearing pressure, or the range of the corresponding soil and foundation conditions is too narrow for any practical application, so that soil treatment is always inevitable?

This article deals with the above issues, based on published evidence, as well as on non-published research which is currently underway at the Geotechnical Division of N.T.U.A. To remain focused, and also to respect the length limits of the presentation, the article will address only the case of strip foundations resting upon the free surface of a liquefiable soil profile with a cohesive (clay) crust. However, many of the concepts, methods and data presented herein have more general applicability, and can be independently used to extend the findings of the article to other foundation and soil profile types.

2. Existing background

2.1. PERFORMANCE-BASED DESIGN REQUIREMENTS

Figure 11.2 presents results from a typical numerical analysis, similar to the ones which will be presented later in this article, which simulates the static and the seismic loading of a rigid foundation on liquefiable soil. It may be observed that:

- (a) During shaking (part *bc* of the load–settlement curve), the footing settles without any change of the static load Q . Seismic settlements may become considerably

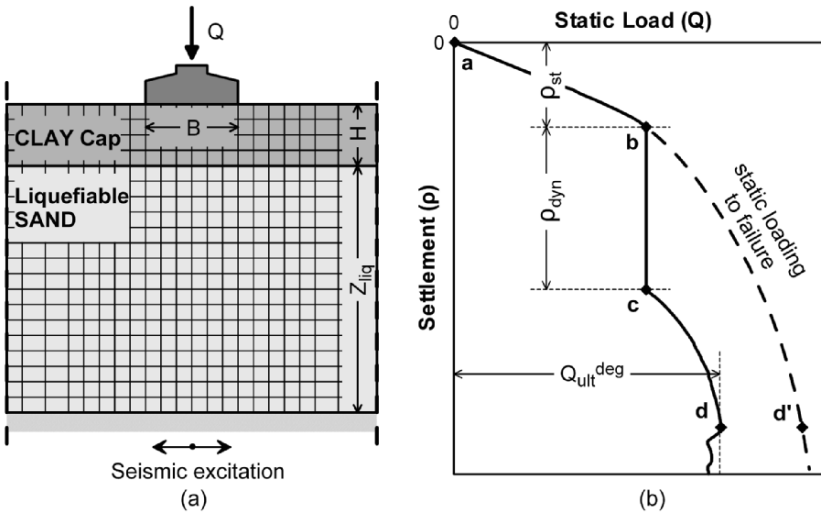


Fig. 11.2. Seismic load–settlement response of shallow foundations on liquefiable soil

larger than the initial ones, due to static loading (part *ab* of the load–settlement curve), and take place mostly (at a percentage of 80–90%) during shaking.

- (b) Static loading to failure, following the end of shaking (part *cd* of the load–settlement curve), shows that the bearing capacity of the footing has been degraded compared to the initial bearing capacity (branch *bd'* of the curve), as the subsoil is still under liquefaction and its shearing resistance has nearly diminished.

Thus, for a performance-based design of the foundation, the degraded post-shaking factor of safety against bearing capacity failure, but also the total settlement of the foundation have to satisfy certain requirements, i.e.

$$FS_{deg} = \frac{Q_{ult}^{deg}}{Q} > FS_o \tag{11.1}$$

and

$$\rho_{tot} = \rho_{st} + \rho_{dyn} < \rho_{all} \tag{11.2}$$

The design values of FS_o may be defined in relation with the severity of shaking and the importance of the structure. Nevertheless, as it refers to a rather short-living threat, which will no longer exist when earthquake-induced excess pore pressures have dissipated, its value must be well below the conventional values for static loads, and close to unity (i.e. $FS_o = 1.00–1.50$). On the other hand, the allowable settlement ρ_{all} is a function of safety but also operation requirements, and consequently it is specified by owners or code provisions, depending upon the type of structure and the return period of the design seismic actions.

2.2. STATIC BEARING CAPACITY DEGRADATION

A simple failure mechanism which can be used to compute the degraded bearing capacity of surface foundations at the end of shaking, while the soil below the soil crust is still in a liquefied state, is shown in Figure 11.3: the footing punches through the crust forcing the development of a wedge-type failure mechanism within the liquefied subsoil. Based on this mechanism, for the simplified case of vertical slip surfaces within a clay crust, Naesgaard et al. (1997) proposed the following expression for the degraded factor of safety of strip footings:

$$FS_{deg} = \frac{2HC_u + 5.14\tau_{RES}B}{Q} \quad (11.3)$$

where H and C_u are the thickness and the undrained shear strength of the clay crust, while τ_{RES} is the residual shear strength of the liquefied sand (e.g. Seed and Harder, 1990; Stark and Mesri, 1992; Olson and Stark, 2002) and Q is the static load carried by the footing.

Working along a parallel track, Cascone and Bouckovalas (1998) use also the failure mechanism of Figure 11.3 but assume that the shear strength of the liquefied subsoil is expressed in terms of a degraded friction angle φ computed as

$$\tan \varphi = (1 - U) \tan \varphi_o \quad (11.4)$$

where φ_o is the actual friction angle of the sand and $U = \Delta u / \sigma'_{vo}$ is the excess pore pressure ratio induced by seismic shaking, taken as uniform over the entire liquefied layer. Consequently the degraded bearing capacity is computed as

$$Q_{ult}^{deg} = \min \left\{ \begin{array}{l} 5.14C_u B \\ (2C_u H - \gamma' H B) + \left(\frac{1}{2} \gamma' B N_\gamma + \gamma' H N_q \right) B \end{array} \right\} \quad (11.5)$$

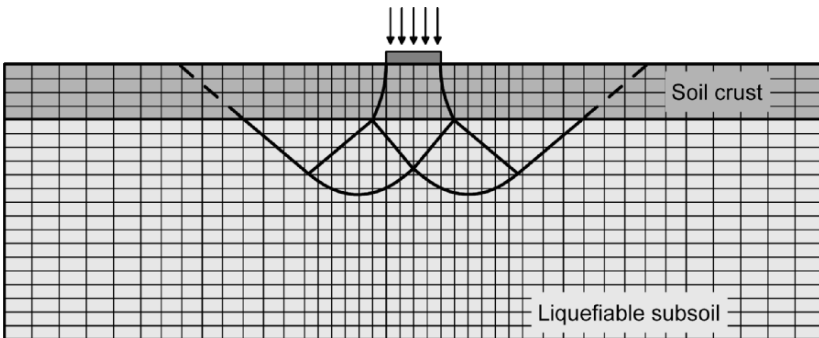


Fig. 11.3. Composite mechanism for end-of-shaking failure of shallow foundations resting on a soil crust over liquefied subsoil

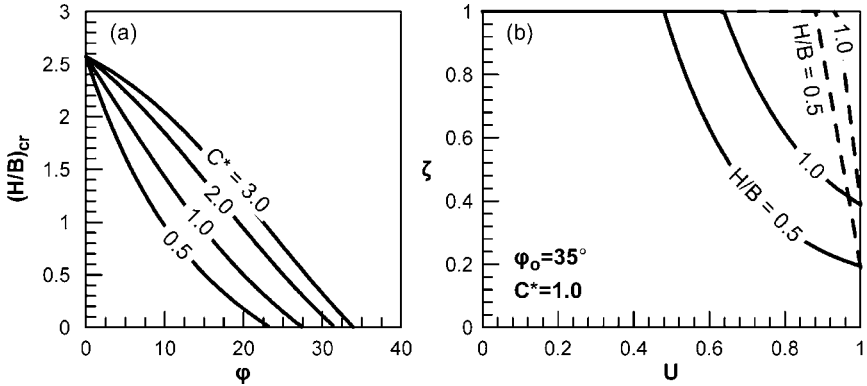


Fig. 11.4. Analytical prediction of liquefaction response of strip foundations resting on a clay crust (after Cascone and Bouckovalas, 1998). (a) Critical thickness of clay crust, and (b) bearing capacity degradation factor

where γ' is the buoyant unit weight of the subsoil and N_γ, N_q are the bearing capacity factors corresponding to ϕ .

Based on the above approach, the authors end up with two basic design parameters. The first is the critical thickness of the soil crust H_{cr} beyond which failure occurs totally within the clay crust, and consequently any partial or complete liquefaction of the sand does not have any significant effect on the bearing capacity. For strip foundations, H_{cr} is computed from the following analytical expression (Figure 11.4a):

$$\left(\frac{H}{B}\right)_{cr} = \frac{10.28C^* - N_\gamma}{2 / (N_q - 1 + 2C^*)} \tag{11.6}$$

with $C^* = C_u / (\gamma' B)$.

The second design parameter is the bearing capacity degradation factor $\zeta = Q_{ult}^{deg} / (5.14C_u B)$ which is expressed in terms of the above non-dimensional parameters and the normalized thickness of the crust H/B , as

$$\zeta = \min \left\{ \left. \begin{aligned} &1.00 \\ &\left(\frac{1}{10.28C^*}\right) \left[N_\gamma + 2 \left(\frac{H}{B}\right) (N_q - 1 + 2C^*) \right] \end{aligned} \right\} \tag{11.7}$$

The variation of ζ versus the excess pore pressure ratio U and the normalized thickness of the clay crust H/B are shown in Figure 11.4b, for typical values of the soil parameters C^* and ϕ_o . Bouckovalas et al. (2005) tried to refine the above solution, considering the possibility of inclined slip planes within the clay crust, as well as a non-zero residual shear strength for the liquefied sand. Furthermore, they recasted the solution assuming a reduced buoyant unit weight of the soil $\gamma'^* = \gamma'(1 - U)$, instead of a degraded

friction angle (ϕ in Eq. 11.4). The effect of the first two refinements proved of secondary importance. On the contrary, the use of a reduced buoyant unit weight led to much higher values of ζ , shown with dotted lines in Figure 11.4b, leaving essentially open the question of how to model the degraded shearing resistance of sand upon partial or complete liquefaction.

It is noteworthy that none of the solutions for bearing capacity degradation reviewed above has been thoroughly documented against experimental and numerical evidence.

2.3. LIQUEFACTION-INDUCED FOUNDATION SETTLEMENTS

The literature on liquefaction settlements is richer compared to that on degraded bearing capacity. However, before proceeding to a brief review of relevant methodologies, it is important to clarify that seismic settlements of footings cannot be predicted using empirical methodologies developed for free field conditions (e.g. Tokimatsu and Seed, 1987; Ishihara and Yoshimine, 1992) as the controlling mechanisms for the two events are different. Namely, free field settlements are due to volume densification, and consequently they take place during the dissipation of earthquake-induced excess pore pressures, mostly after the end of shaking. On the contrary, footing settlements are associated with failure in the foundation soil, caused by the combined action of static and inertia foundation loads, shear strength degradation of the liquefiable soil and earthquake-induced shear stresses in the soil. Thus, the latter are significantly larger than the former, and they take place mostly during (not after) shaking. A number of experimental studies (Liu and Dobry, 1997; Adalier et al., 2003; Coehlo et al., 2004, 2005, etc.) and field observations (Cetin et al., 2002; Seed et al., 2003; Bird et al., 2006) bear witness on the above differences.

Based on field evidence, Figure 11.5 shows a widely known empirical relationship for the beneficial effect of the normalized footing width B/Z_{liq} on the respective seismic foundation settlements S/Z_{liq} , where Z_{liq} is the thickness of the liquefied soil. This chart includes data regarding building settlements in Niigata City, Japan, after the 1964 earthquake (Yoshimi and Tokimatsu, 1977), and Dagupan City, Philippines, after the 1990 Luzon earthquake (Adachi et al., 1992), as well as tank settlements during the 1983 Nihonkai-chubu, Japan, earthquake (Yasuda and Berrill, 2000). The important effect of a soil crust over the liquefied subsoil is addressed by Ishihara et al. (1993), who use observations from Dagupan City in order to define the minimum soil crust required to prevent surface evidence of liquefaction in terms of the corresponding thickness of liquefied soil. Later on, Acacio et al. (2001) extended the above relation in order to define safety limits against excessive foundation settlements and tilting, using also field evidence from the Dagupan event.

Alternative means for the evaluation of liquefaction-induced settlements of light structures based on a clay crust are provided by Naesgaard et al. (1997), based on a considerable number of static and dynamic numerical analyses. These analyses were performed in terms of total stresses, assuming an elastic-perfectly plastic shear stress (τ)–strain (γ) relationship for the liquefied soil, fitted to the response of liquefied sands (Byrne, 1991;

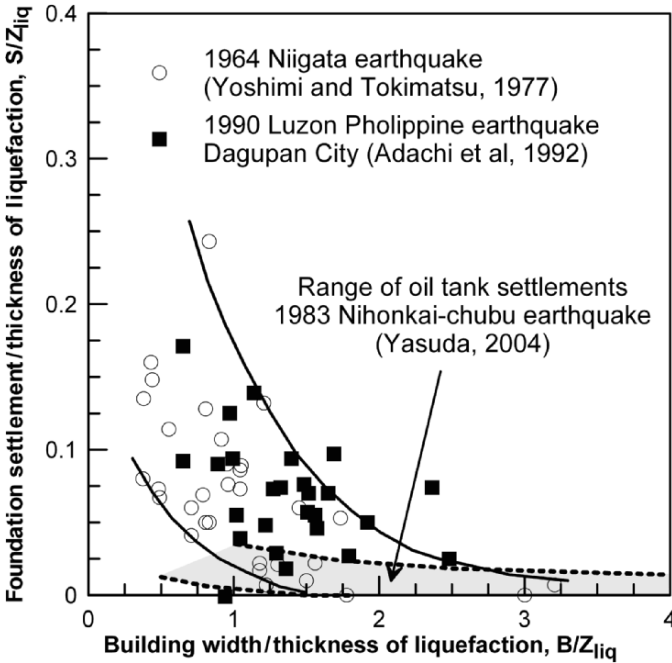


Fig. 11.5. Effect of footing width on liquefaction induced subsidence of shallow foundations (based on Liu and Dobry, 1997, and Yasuda and Berrill, 2000)

Jitno, 1995). In all cases, a specific velocity time history, for a magnitude 7.0 seismic event, scaled to various peak values, was applied at the base of the liquefiable soil, while the foundation consisted of a number of equally sized strip footings interconnected by an irregular two-storey structural skeleton. Furthermore, liquefaction was triggered artificially at an intermediate stage of the analysis, by setting the stress state in the liquefiable soil to that of a heavy fluid (equal horizontal normal stresses combined to zero shear stresses).

In that way, it was finally concluded that liquefaction-induced settlements could be directly related to the degraded factor of safety $F_S (= F_{S_{deg}}$ from Eq. 11.3) or, for larger accuracy, to the following factor:

$$X_S = \frac{F_S}{Z_{liq}^{1/3} \gamma_{lim}^{1/2} Q^{1/4}} \tag{11.8}$$

which takes also into account the thickness of the liquefied sand (Z_{liq} in m) and the corresponding maximum shear strain amplitude (γ_{lim} in %). Both these correlations are reproduced in Figure 11.6. Comparison with field evidence, recalled by the authors, suggests that minor or no building damage due to foundation settlements correspond to $F_S > 3.00$ or $X_S > 1.00$.

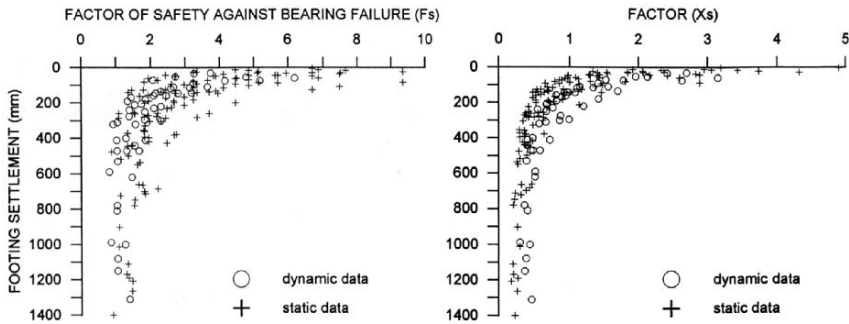


Fig. 11.6. Liquefaction settlement of light structures resting on top of a clay crust in terms of (a) the degraded factor of safety F_s , and (b) the degraded bearing capacity index X_s (after Naesgaard et al., 1997)

A different approach for the computation of liquefaction-induced displacements has been proposed by Yasuda et al. (1999) under the abbreviated name ALID (analysis for liquefaction-induced displacements). This methodology is proposed in connection with the numerical analysis of various geotechnical structures and foundations, but its basic principle can be readily extended to analytical computations as well, based on code provided simplified methods for static settlement computation. For the case of surface foundations,

- Settlements are first computed for the static loads applied to the foundation, using the initial (prior to liquefaction) shear moduli of the subsoil layers.
- The shear moduli are consequently reduced, in order to account for the effects of liquefaction, on the basis of the empirical charts shown in Figure 11.7.
- The static analyses are repeated, using the reduced shear moduli, and liquefaction-induced settlements are finally computed after subtracting the static settlements of the first step.

ALID has been successfully used in a number of case studies (Yasuda et al., 2001; Yasuda, 2004, 2005) and proved to be well suited for case specific practical applications. Nevertheless, it does not provide immediate insight to all factors which control the liquefaction performance of footings and consequently it cannot be easily used to establish more general design criteria.

Acknowledging the uncertainties associated with the very soft and simultaneously extremely non-linear shear stress–strain response of liquefied sands (e.g. Figure 11.7), as well as the objective difficulties encountered in applying the finite element method under such conditions, Acacio et al. (2001) propose an analytical prediction method for liquefaction-induced subsidence, where the liquefied soil was modeled as a viscous fluid. Although application of this method is also computer aided, it does not presume the use of any non-linear numerical (finite element or finite difference) algorithm. Comparison with observed settlements of buildings in Dagupan City after the 1990 Luzon earthquake

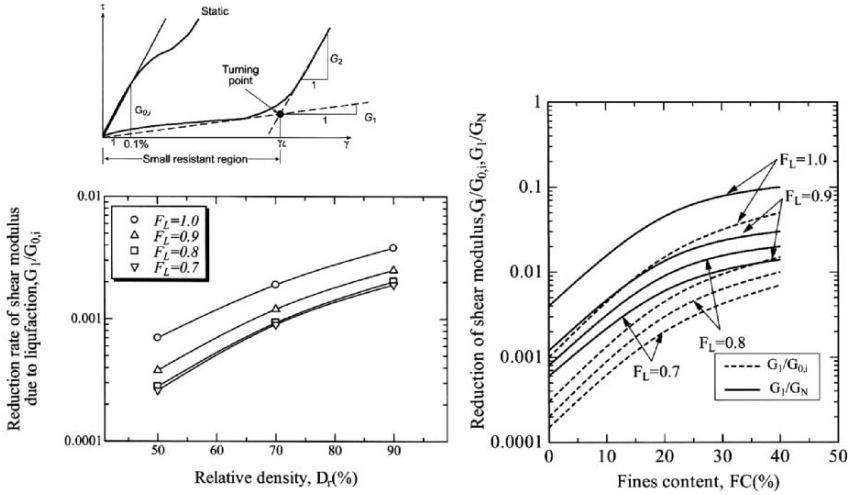


Fig. 11.7. Basic elements and definitions for the ALID approach. (a) Initial and post-liquefaction shear stress–strain relationship, (b) effect of relative density and liquefaction factor of safety on degraded shear modulus, and (c) effect of fines and liquefaction factor of safety on degraded shear modulus (after Yasuda, 2004)

shows reasonable consistency for large settlement values (>0.60 m) and a clear tendency for underprediction for smaller ones.

3. Numerical analysis of liquefaction performance

In the sequel, the aforementioned approaches of Naesgaard et al. (1997) and Cascone and Bouckovalas (1998) are followed up, under the light of new, mostly numerical evidence, obtained from dynamic fully coupled effective stress analyses calibrated against the results of centrifuge tests. Details on this algorithm, that incorporates a modified version of the bounding surface critical state model of Papadimitriou and Bouckovalas (2002) and its experimental verification are presented in another paper of this conference (Andrianopoulos et al., 2007), and elsewhere (Andrianopoulos et al., 2005, 2006; Bouckovalas et al., 2005), and consequently they will not be repeated here in any extent. It is only briefly mentioned that the reliability of the analyses was checked against three different series of centrifuge tests, namely VELACS models 1, 2 and 12 (Arulmoli et al., 1992; Carnevale and Elgamal, 1993; Farrell and Kutter, 1993; Krstelj and Prevost, 1993) which model seismic liquefaction under level or slightly sloping ground conditions, as well as the seismic response of a rigid foundation over liquefied soil.

The configuration for VELACS Model 12 experiment, which is directly related to the topic of this article, is shown in Figure 11.8. Furthermore, Figure 11.9 shows typical comparisons between numerical predictions and experimental measurements of excess

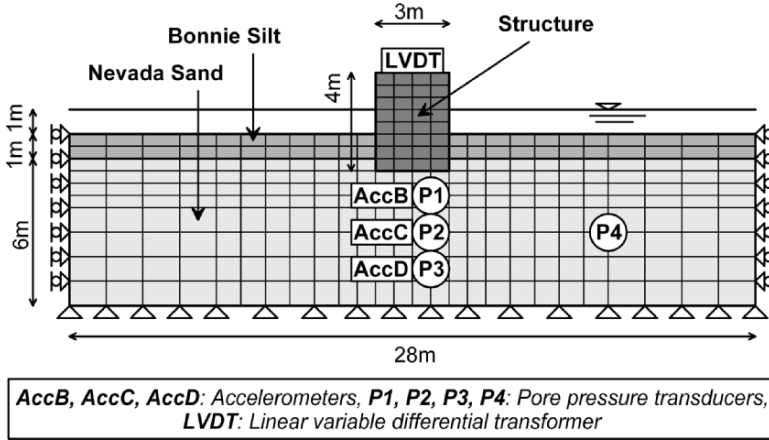


Fig. 11.8. Configuration used for the numerical (finite difference) simulation of VELACS Model 12 centrifuge tests (prototype scale)

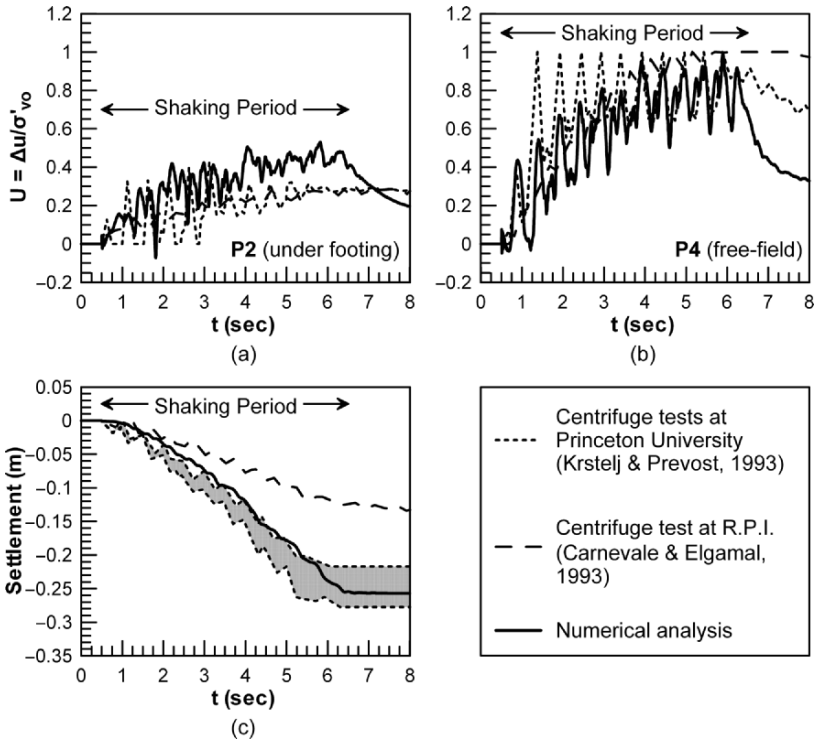


Fig. 11.9. Numerical predictions and experimental measurements from VELACS Model 12 centrifuge tests. (a) Excess pore pressure ratio below the foundation, (b) excess pore pressure ratio in the free field, and (c) foundation settlements

pore pressures and settlements, which are indicative of the level of accuracy that should be expected from the numerical analyses.

Using the above mentioned numerical algorithm, we went on with a number of parametric analyses (i.e. “numerical experiments”) of the response of strip footings resting on the surface of a liquefiable layer, consisting of fine Nevada sand at various densities, with a clay crust. In all, 73 such analyses were performed, each one including three steps:

- initial static loading, performed under drained conditions,
- dynamic loading due to horizontal seismic shaking applied at the base of the model, performed under partially drained conditions, and
- post-seismic static loading to failure, performed under undrained conditions.

The basic geometry of the model, the static and seismic loads, the basic soil characteristics, as well as the assumed discretization and boundary conditions are shown in Figure 11.10. In addition to the information given in this figure, note that the footing was rigid and massless, while the average reported values of initial static loads correspond to static factors of safety $FS_o = 1.50-5.00$. Furthermore, to simulate free field conditions at the side boundaries of the model, the corresponding opposite nodes were tied rigidly to each other so that they were forced to exhibit the same horizontal displacements during shaking.

A detailed presentation of the parametric analyses is not within the scope of this article. Still, it is worth presenting a set of typical excess pore pressure and settlement time histories predicted from the parametric analyses (Figure 11.11a and b). A closer look at these results reveals some basic internal mechanisms of foundation–soil interaction during liquefaction, which have been also identified in a number of centrifuge experiments (e.g.

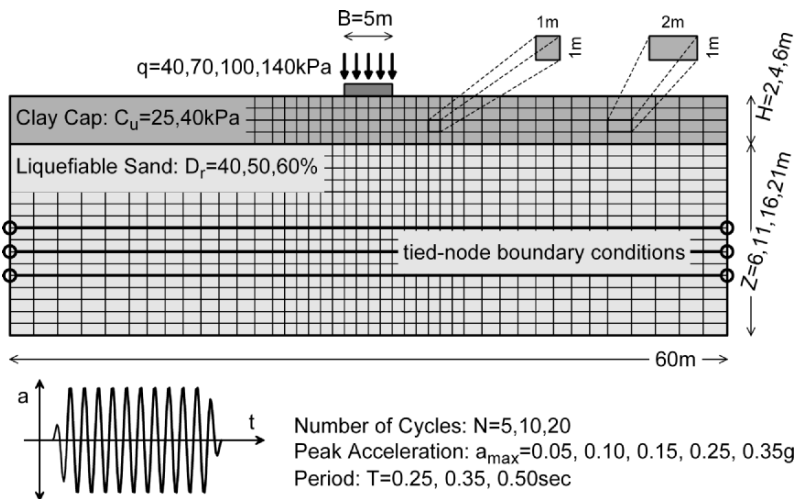


Fig. 11.10. Numerical model used for the parametric analysis of the liquefaction performance of strip foundations, and range of basic input parameters

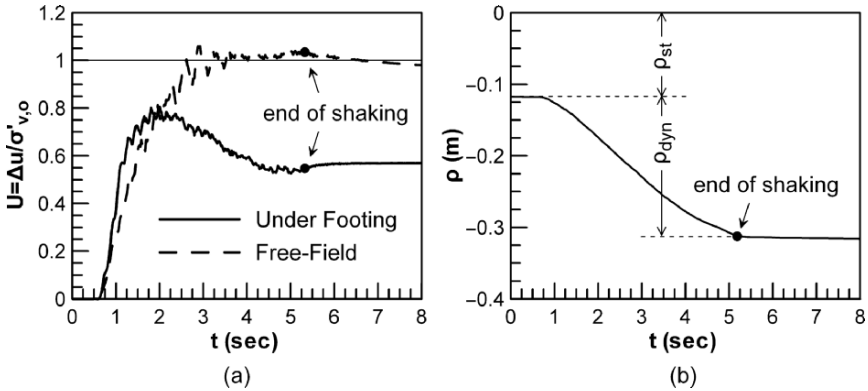


Fig. 11.11. Typical results of parametric numerical analyses. (a) Time history of excess pore pressure ratio, and (b) time history of liquefaction induced settlements

Liu and Dobry, 1997; Adalier et al., 2003; Coehlo et al., 2004, 2005; Fujiwara et al., 2005) and field case studies (Cetin et al., 2002; Seed et al., 2003; Bird et al., 2006) and will prove essential for the analysis of the liquefaction performance of foundations. For instance, observe that:

- (a) The excess pore pressure ratio in the free field approaches 1.0, a clear indication of liquefaction, while it does not exceed about 0.60 under the footing.
- (b) Excess pore pressures under the footing reach a peak value and consequently decrease while shaking is still in progress. Note that the same trend is observed under undrained conditions as well (not shown here), indicating that this is not only the result of excess pore pressure mitigation, from the high overburden area under the footing towards the free field, as it was originally believed, but it is due to dilation associated with the intense shearing which is induced by foundation settlement.
- (c) The accumulation of foundation settlement is essentially linear with time and practically stops short after the end of shaking, while the dissipation of earthquake-induced excess pore pressures is far from complete. This observation indicates that observed settlements are not due to densification of the liquefiable soil layer but due to dynamic shear failure, such as the one predicted by the sliding block method of Newmark (1965). Note that Richards et al. (1993) made the same assumption in an attempt to explain and predict analytically seismic settlements of surface foundations on dry sand.

4. Evaluation of degraded bearing capacity

In the present study, the degraded bearing capacity at the end of shaking, before any significant dissipation of earthquake-induced excess pore pressures takes place, will be evaluated analytically based on an extension of the method proposed by Cascone and

Bouckovalas (1998). It is reminded that, in its present status, this method requires systematic verification with respect to one basic assumption which may distort analytical predictions significantly: the simplified modeling of the liquefaction-induced shearing resistance degradation in terms of an equivalent degraded friction angle $\varphi = \tan^{-1} [(1 - U) \tan \varphi_0]$ or an equivalent reduced effective unit weight $\gamma'^* = (1 - U)\gamma'$. Furthermore, an analytical computation of the excess pore pressure ratio U , which will take into account the existence of the structure, needs to be established.

So far, our effort to obtain experimental evidence for a quantitative evaluation of the above methodology was not successful. The main reason is that, with a few exceptions (e.g. Yasuda, 2004), all centrifuge and shaking table experiments retrieved from the literature did not proceed beyond the evaluation of earthquake-induced settlements and excess pore pressures in the foundation soil. In other words, it was not possible to find well documented experiments where the footing was driven to a static bearing capacity failure, immediately after the end of shaking, while the subsoil was still at a liquefied state.

Hence, we relied on the numerical evaluation of the post-shaking bearing capacity, using the fully coupled, effective stress, solution algorithm presented in the previous chapter. More specifically, Figures 11.12 and 11.13 compare the analytically and numerically predicted variation of degradation factor ζ against the excess pore pressure ratio U . The first figure refers to problem parameters (N , a_{max} , T , q , Z_{liq}) which should have only an indirect effect on the $\zeta-U$ relation, through the excess pore pressure ratio U , while the second figure refers to the remaining parameters (H/B , C_u and D_r) which are analytically

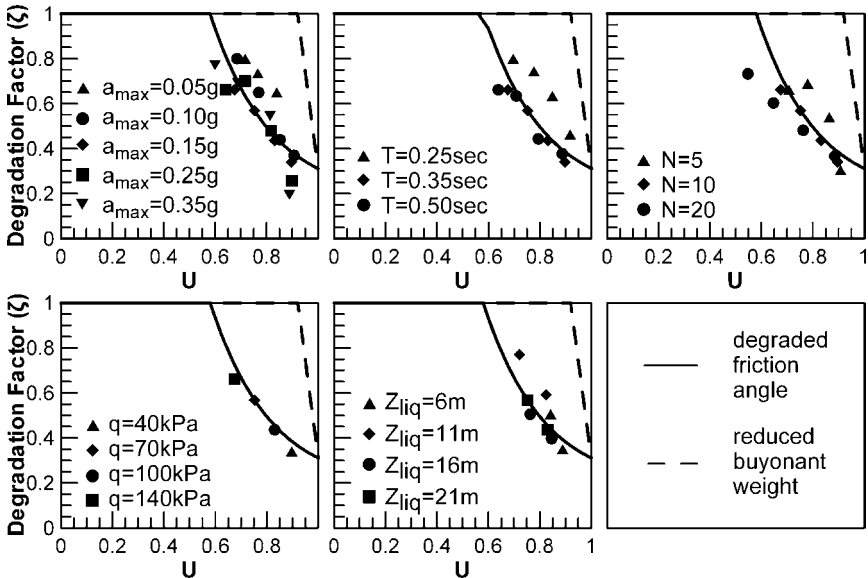


Fig. 11.12. Comparison between numerical and analytical predictions of the bearing capacity factor ζ for various combinations of seismic motion characteristics (a_{max} , T , N), foundation loads (q) and thickness of liquefied subsoil (Z_{liq})

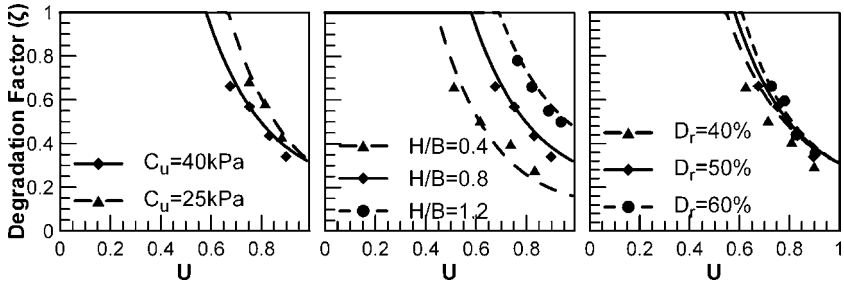


Fig. 11.13. Comparison between numerical and analytical predictions of the bearing capacity factor ζ for various combinations of soil crust characteristics (C_u , H/B), and liquefiable soil density (D_r)

identified as having a direct effect. In Figure 11.12, analytical predictions obtained for a degraded friction angle are distinguished from those obtained for a reduced effective unit weight. The first thing to observe is that the numerical predictions are in close agreement with the analytical $\zeta-U$ relationships obtained with the more conservative assumption of a degraded friction angle for the liquefied subsoil. Furthermore, it may be observed that the numerical analyses predict reasonably well the relative effect of the afore mentioned independent problem parameters H/B , C_u and D_r .

A key issue for the successful comparisons shown in Figures 11.12 and 11.13 is the correct choice of an “equivalent uniform” value of the excess pore pressure ratio U which is used to relate with the numerically predicted values of ζ . This is because, the analytical solution assumes that U is uniform all over the liquefiable foundation soil, unlike the numerical analyses which show clearly that the presence of the footing leads to a considerably non-uniform distribution of U in the horizontal direction, as well as with depth. Following a trial-and-error examination of various alternatives, it was finally found that a best fit to the analytical predictions was obtained when U was computed as the mean between the free field value U_{ff} and the average value below the footing U_{foot} , computed over an $1.2B \times 1.2B$ area of liquefiable soil, i.e. at the core of the failure wedge.

Among these two components, U_{ff} is easy to compute as in most cases of practical interest the degradation of bearing capacity becomes a design issue only upon complete liquefaction in the free field. Thus, it can be safely assumed that $U_{ff} \approx 1.00$. The computation of U_{foot} is more tedious as it presumes that the 2-D distribution of U under the footing, at the end of shaking, is known. For the sake of simplicity, it was first examined whether U_{foot} could be related to the U value of a single “characteristic” point on the axis of the footing. Among the various points which were considered (Figure 11.14), it was finally found that this role could be attributed to a point at depth between $z_c = 0.60B$ and $0.80B$ below the crust.

The next step was to devise a simplified procedure for the computation of U at the characteristic point, taking also into account the stress concentration caused by the foundation

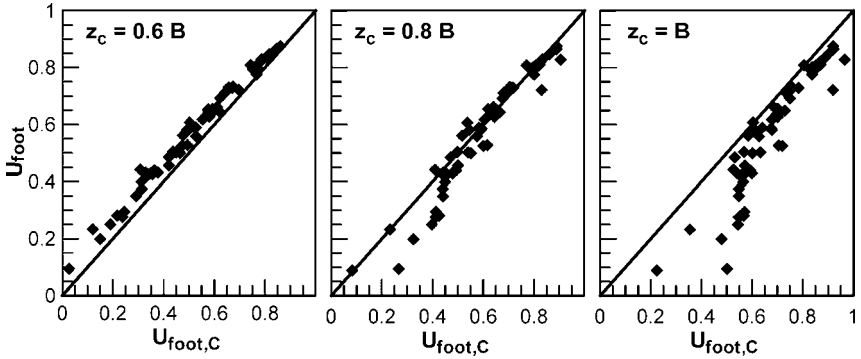


Fig. 11.14. Comparison between the average excess pore pressure ratio below the foundation and that of different “characteristic” points on the foundation axis

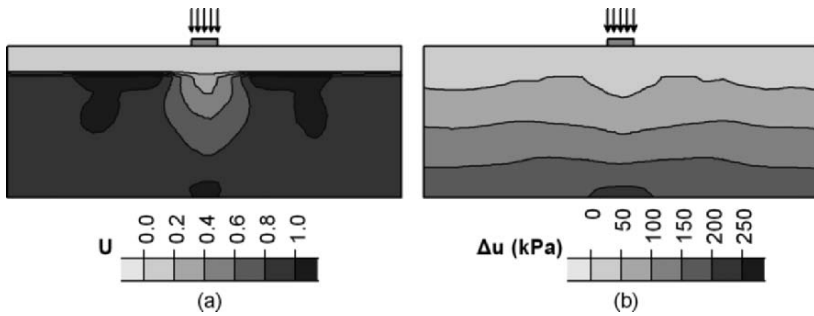


Fig. 11.15. Typical distribution within the liquefiable soil of end of shaking (a) Excess pore pressure ratios $U = \Delta u / \sigma'_{vo}$, and (b) excess pore pressures Δu

loads. In an approximate way, this can be achieved if one focuses upon the distribution within the foundation soil of the excess pore pressures themselves (Δu) instead of the corresponding excess pore pressure ratios U . The reason is explained with the aid of Figures 11.15a and 11.15b, which show the variation of U and Δu respectively at the end of shaking, obtained from a typical numerical analysis. It becomes evident that, although the spatial variation of U is considerably non-uniform, the respective variation of Δu varies mostly with depth and is considerably more uniform in the horizontal direction. Based on this observation, excess pore pressures in the free field (Δu_{ff}) and under the footing (Δu_{foot}) may be interrelated as

$$\Delta u_{foot} = a \Delta u_{ff} \tag{11.9}$$

Furthermore, assuming that the free field soil is at a liquefied state, Δu_{ff} is approximately equal to the geostatic vertical effective stress at the level of the characteristic point ($\sigma'_{vo,C}$) and consequently the excess pore pressure ratio of the characteristic point may be finally computed as

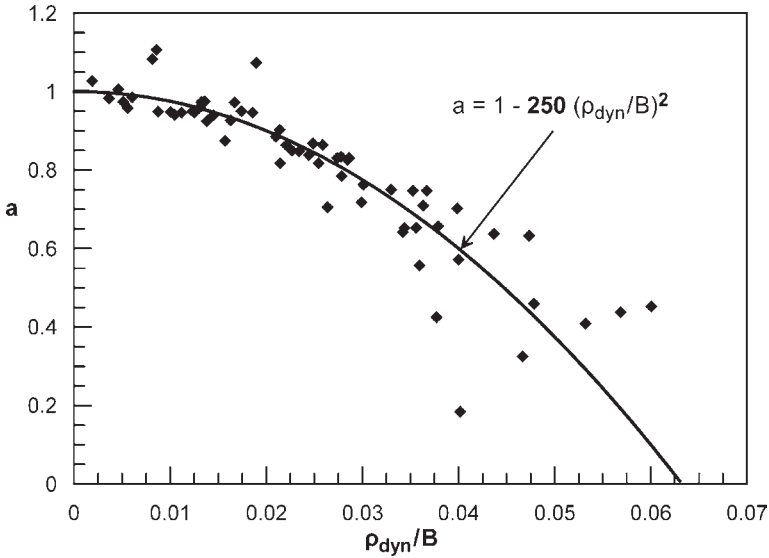


Fig. 11.16. Effect of liquefaction induced settlements ρ_{dyn}/B on excess pore pressure parameter a (Eq. 11.11)

$$U_{foot,C} = \alpha \left(\frac{\sigma'_{vo}}{\sigma'_{vo} + \Delta\sigma_v} \right) \quad (11.10)$$

where $\Delta\sigma_v$ is the additional vertical stress caused by the foundation load at the characteristic point. Consistently with the view expressed earlier with regard to the settlement induced dilation of the liquefiable subsoil, and its effect on the excess pore pressures below the foundation, it was found (Figure 11.16) that the pore pressure parameter a in Eq. 11.10 can be reasonably well correlated to normalized seismic settlements, as

$$a = 1 - 250 \left(\frac{\rho_{dyn}}{B} \right)^2 \quad (11.11)$$

5. Evaluation of liquefaction settlements

Computation of liquefaction-induced settlements is the second step for the completion of the performance-based design process, as these settlements may become excessive even for values of the degraded factor of safety larger than 1.0. Unlike the problem of degraded bearing capacity, that of settlement accumulation has not been yet modeled analytically in a simple and robust way. Thus, for a first approximate solution of this problem we relied on a step-by-step statistical analysis of results obtained from the parametric numerical analyses which were described in previous sections.

The numerical predictions, as well as a number of relevant experimental studies (e.g. Liu and Dobry, 1997; Adalier et al., 2003), lean towards a linear $\rho_{dyn}-N$ relationship. Thus, the statistical analyses focused on the remaining problem parameters, i.e.:

- peak input acceleration, at the base of the liquefiable sand layer, a_{max} (= 0.15 g)
- excitation period T (= 0.35 s)
- average contact pressure q (= 100 kPa)
- relative density D_r (= 50%)
- undrained shear strength of the clay crust C_u (= 40 kPa)
- normalized thickness of the clay crust H/B (= 0.80)
- thickness of the liquefied (in the free field) sand layer Z_{liq} (= 16 m)

Namely, the effect of these parameters on settlements after ten uniform loading cycles ($\rho_{dyn,10}$) is shown in Figure 11.17(a) to (g). The effect of each parameter is examined separately, while all others are given the reference values provided in parentheses above. Using the same format, these figures are also used to show the effect of the above parameters on the static loading ratio $Q/Q_{ult}^{deg} = 1/FS_{deg}$. This parallel evaluation is driven by the perception that the overall effects of liquefaction on ρ_{dyn} and $1/FS_{deg}$ are similar in qualitative terms. In that case, these two quantities could be inter-related, leading to a simpler expression for the computation of settlements. In addition, the target value of FS_{deg} could be related to the project (and owner) dependent value of acceptable displacements ρ_{all} .

Figure 11.17(a) to (g) show that the effect of four problem parameters (q , D_r , C_u and H/B) is indeed qualitatively the same for $\rho_{dyn,10}$ and $1/FS_{deg}$. The three remaining parameters (a_{max} , T and Z_{liq}) affect strongly $\rho_{dyn,10}$, but have a minor effect on $1/FS_{deg}$ that can be readily overlooked. In view of the above observations, ρ_{dyn} was finally related to $1/FS_{deg}$, a_{max} , T , N and Z_{liq} by means of the following approximate relation (Figure 11.18):

$$\rho_{dyn} = 0.016 \cdot \left[a_{max} T^2 Z_{liq} \right]^{0.50} \cdot N \cdot \left[\frac{1}{FS_{deg}} \right]^{2.50} \quad (11.12)$$

The accuracy of Eq. 11.12 is evaluated against the results of the numerical analyses in Figure 11.19. Observe that the agreement between approximate and numerical predictions is fairly consistent, with an average expected error less than $\pm 30\%$.

A similar verification against experimental and field evidence faces objective difficulties due to the general scarcity of fully documented published data. Still, it was possible to collect seismic settlement measurements from five centrifuge testing programs (Arulmoli et al., 1992; Carnevale and Elgamal, 1993; Farrell and Kutter, 1993; Krstelj and Prevost, 1993; Liu and Dobry, 1997; Coehlo et al., 2004), as well as from one case study: the settlement of buildings in the city of Dagupan, Philippines, during the Luzon 1990 ($M = 7.8$) earthquake (Ishihara et al., 1993; Tokimatsu et al., 1994; Acacio, 1997).

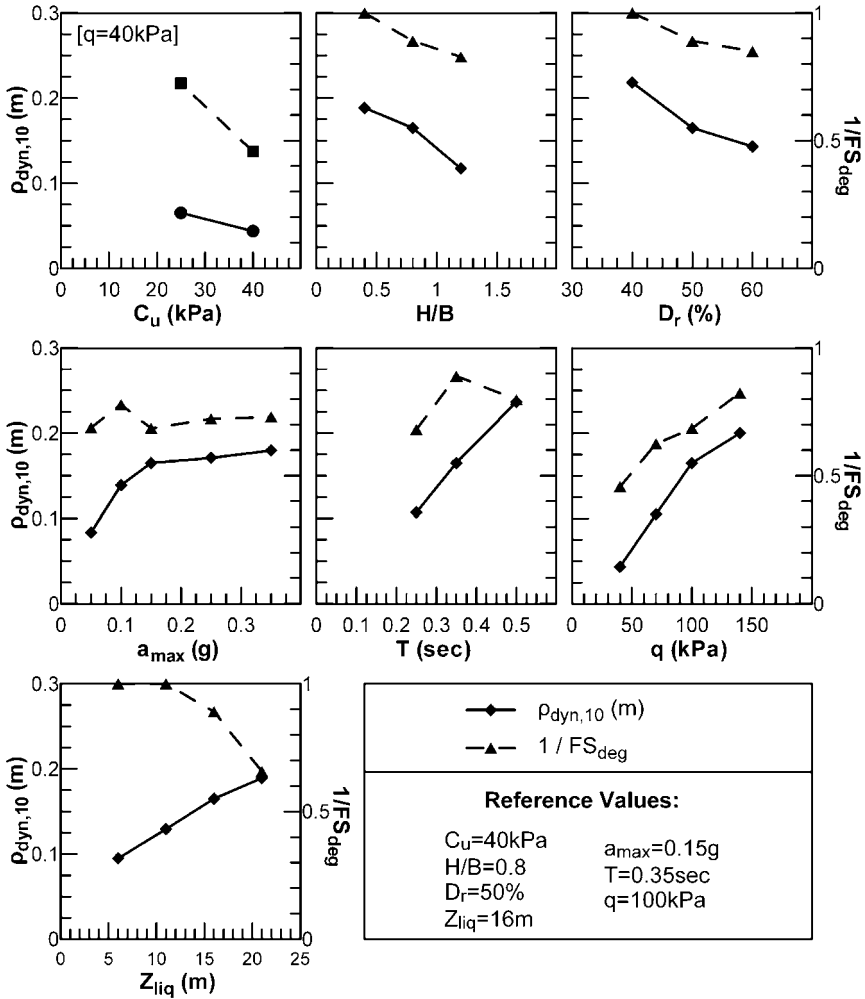


Fig. 11.17. Effect of basic soil, excitation and foundation parameters on liquefaction induced settlements and degraded static factors of safety (inversed)

The seismic settlements, as well as the basic input parameters which were used to obtain the analytical predictions are summarized in Table 11.1. Note that:

- (a) Centrifuge tests are much better defined in terms of the input data parameters, as opposed to the field case study where many input data were actually missing and had to be indirectly evaluated. For that reason, the analytical predictions for Dagupan City were performed parametrically, for the possible range of input data retrieved from the literature, and the range of analytical predictions was compared to that of the field observation, in the form of the S/Z_{liq} versus B/Z_{liq} diagram shown previously in Figure 11.5.

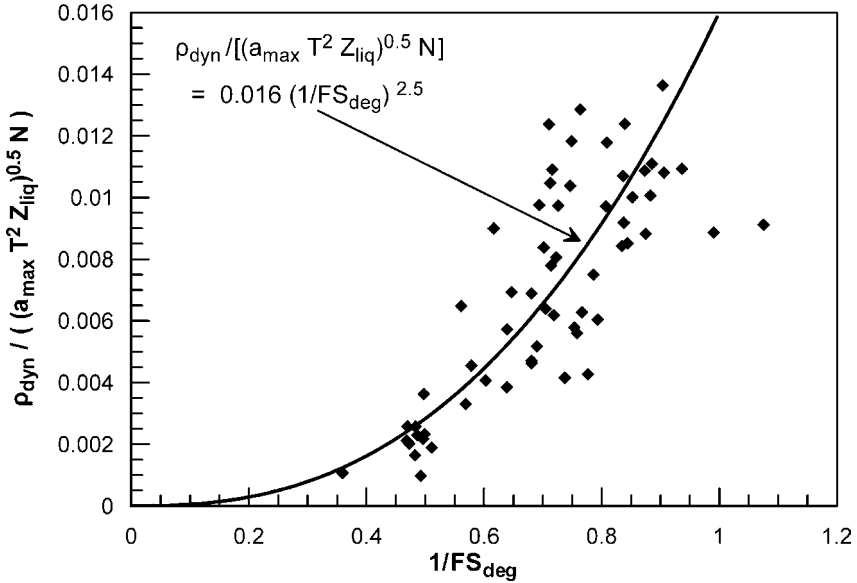


Fig. 11.18. Correlation between normalized liquefaction settlements and (inversed) degraded static factor of safety

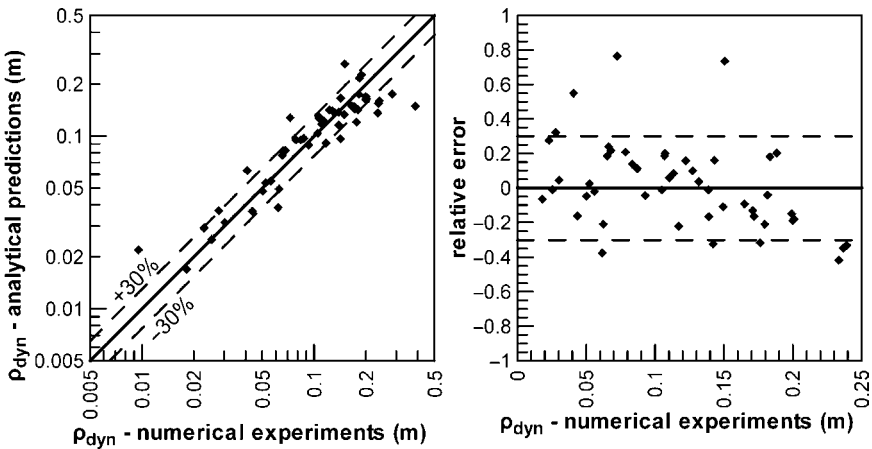


Fig. 11.19. Comparison between analytical and numerical predictions of liquefaction induced settlements

- (b) In the majority of centrifuge tests and in the Dagupan case study the foundation was rectangular, with a width over length ratio $B/L = 1/2$ which is different from the strip foundation geometry which is associated with Eq. 11.11. In all these cases, the average bearing pressure of the rectangular footing was artificially reduced so

Table 11.1. Summary of centrifuge testing conditions and recorded foundation settlements used in the comparison of Figure 11.21

Name	B (m)	H (m)	Z_{liq} (m)	q (kPa)	C_u (kPa)	φ_o (deg)	a_{max} (g)	T (s)	N	ρ (m)
Krstelj and Prevost (1993)	3	0	5.5	95	0	37	0.27	0.50	10	0.270
	3	0	5.5	95	0	37	0.35	0.50	10	0.470
	3	0	5.5	95	0	37	0.20	0.50	10	0.220
	3	0	5.5	95	0	37	0.20	0.50	10	0.210
Farrell and Kutter (1993)	3	0	5.5	95	0	35	0.36	0.50	10	0.180
Carnevale and Elgamal (1993)	3	0	5.5	95	0	35	0.21	0.50	10	0.130
Coehlo et al. (2004)	4	0	18.0	75	0	37	0.19	1.00	10	0.500
Liu and Dobry (1997)	4	0	12.5	60	0	36	0.20	0.67	10	0.558

that analytically computed static elastic settlements for the actual footing and for an equivalent strip of the same width B became equal.

- (c) In the majority of centrifuge tests, the foundation rested directly upon the surface of the liquefied sand, i.e. without interference of any soil crust. This situation is of little practical interest, as it usually leads to foundation failure, and consequently it has not been part of the numerical analyses program. Hence, the use of Eq. 11.12 to predict the corresponding settlements is at the limits of its application range.

The comparison between predicted and observed liquefaction settlements is shown in Figure 11.20 for the centrifuge tests and in Figure 11.21 for the Dagupan case study. Despite the above limitations, both comparisons reveal a consistent agreement, although the average error has now increased as compared to that for the prediction of the numerical results.

In concluding with the prediction of seismic settlements, it is worth to note that the general form of Eq. 11.12 is typical of systems with elasto-plastic (stick-slip) response during seismic loading, which are commonly modeled on the basis of Newmark's sliding block approach. For instance, it is easy to show that the downslope displacement of such a block when subjected to N uniform cycles of sinusoidal motion is expressed as

$$d = 0.159 \cdot [a_{max} T^2] \cdot N \cdot \left[\frac{a_{max}}{a_{cr}} \right]^\lambda \quad (11.13)$$

where $a_{cr} (< a_{max})$ is the horizontal acceleration required to trigger downwards slip and exponent $\lambda = 2-4$.

In addition, dealing with another "sliding block" problem, i.e. that of liquefaction-induced lateral spreading, Hamada (1999) proposed the following empirical relationship for the computation of maximum lateral ground displacement:

$$d = 0.0125 \cdot [a_{max} T^2 Z_{liq}]^{0.50} \cdot N \cdot \left[\frac{\theta}{N_{SPT}^{0.88}} \right] \quad (11.14)$$

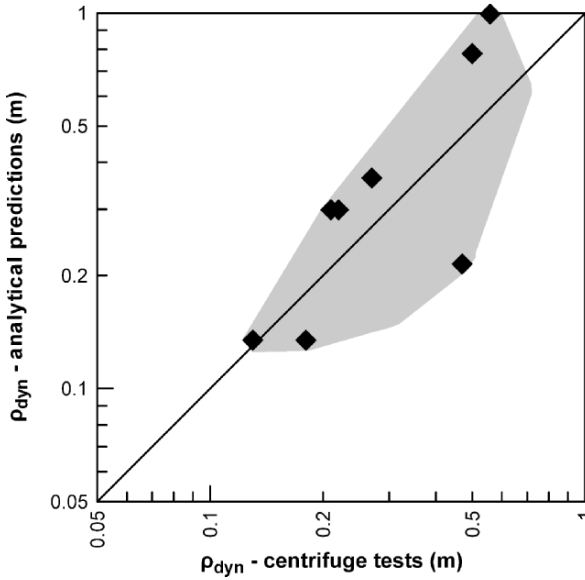


Fig. 11.20. Evaluation of analytical settlement predictions against experimental results from centrifuge tests

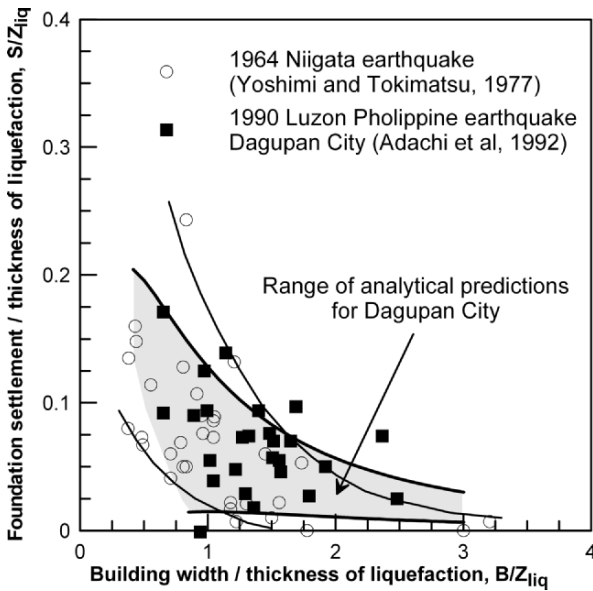


Fig. 11.21. Evaluation of analytical settlement predictions against field observations of foundation settlements in Dagupan City, Philippines, following the Luzon 1990 earthquake (analytical predictions for $H = 1-2$ m, $Z_{liq} = 6-10$ m, $q = 70-100$ kPa, $C_u = 10-50$ kPa, $\phi_o = 30-38^\circ$, $\alpha_{max} = 0.10-0.15$ g, $T = 0.35-0.50$ s, $N = 10-15$)

where θ (%) is the ground surface inclination and \bar{N}_{SPT} is the average *SPT* blow count within the liquefiable soil layer.

Observe that, although they refer to three (at least seemingly) different engineering problems, Eqs. 11.12, 11.13 and 11.14 have an apparent similarity, especially if one recognizes that the terms $[a_{max}/a_{cr}]^\lambda$ and $[\theta/\bar{N}_{SPT}^{0.88}]$ appearing in Eqs. 11.13 and 11.14 are directly or indirectly related to the (degraded) factor of safety against an earthquake-induced failure, i.e. the term $[1/FS_{deg}]^{2.50}$ of Eq. 11.12.

6. Performance-based design issues

The findings of the two previous sections can be combined with a value of the allowable seismic settlement ρ_{all} and be used for the preliminary analytical evaluation of the liquefaction performance of strip foundations. For the readers' convenience, Table 11.2 summarizes the equations and the sequence of computations needed for that purpose. Note that the dependence of excess pore pressures under the footing on the final settlements (e.g. Eq. 11.11) makes the solution algorithm non-linear. However, this should cause minor concern as 3 to 4 iterations are usually sufficient for convergence and the associated computations are simple.

In addition, Figures 11.22 and 11.23 present charts for quick computations of seismic settlements ρ_{dyn} , normalized against the width of the footing B , in terms of the following non-dimensional problem parameters:

- the average bearing pressure $q/\gamma' B$,
- the thickness of the clay crust H/B ,
- the undrained shear strength of the clay crust $C_u/\gamma' H$, and
- the intensity of seismic motion and the extent of liquefaction expressed as

$$\frac{\rho_o}{B} = 0.016 \cdot \frac{\sqrt{a_{max} T^2 Z_{liq} \cdot N}}{B} \quad (11.15)$$

The friction angle of the sand ϕ is also a problem parameter. Nevertheless, for the anticipated range of values for liquefiable sands (e.g. $\phi_o = 32^\circ - 38^\circ$) its effect is relatively minor, and consequently the charts were drawn for an average value $\phi_o = 35^\circ$. Note in addition that, due to practical drawing difficulties, only two distinct values of the seismic intensity parameter are considered in the charts, $\rho_o/B = 0.01$ and 0.06 . For common strip foundations, the lower value corresponds to weak seismic motions and the larger to strong ones. For instance, when $B = 3.0$ m,

- $\rho_o/B = 0.01$ may represent a seismic motion with $a_{max} = 0.10$ g, $T = 0.30$ s, $N = 3$ cycles and $Z_{liq} = 5$ m, while
- $\rho_o/B = 0.06$ may represent a seismic motion with $a_{max} = 0.30$ g, $T = 0.40$ s, $N = 7$ cycles and $Z_{liq} = 5$ m.

Table 11.2. Computation algorithm for the degraded bearing capacity and the seismic settlements of strip foundations resting on the surface of a clay crust over liquefiable subsoil

Design Requirements

$$FS_{deg} \geq FS_o (= 1.0-1.5)$$

$$\rho = \rho_{st} + \rho_{dyn} \leq \rho_{all}$$

Degraded (end of shaking) Static Factor of Safety

$$FS_{deg} = \min \left\{ \begin{array}{l} 5.14 C_u / q \\ FS_{deg}^{c-s} \end{array} \right\}$$

$$FS_{deg}^{c-s} = \frac{(2C_u H - \gamma' H B) + \left(\frac{1}{2} \gamma' B N_\gamma + \gamma' H N_q \right) B}{q B}$$

$$\phi = \tan^{-1} [(1 - U) \tan \phi_o]$$

$$U = 0.50 \left[1 + a \frac{\sigma'_{vo}}{\sigma'_{vo} + \Delta \sigma_v} \right]$$

$$a = 1 - 250 \left(\frac{\rho_{dyn}}{B} \right)^{2.0}$$

Seismic Settlements

$$\rho_{dyn} = \rho_o \cdot \left[\frac{1}{FS_{deg}^{c-s}} \right]^{2.50}$$

$$\rho_o = 0.016 \cdot \sqrt{a_{max} T^2 Z_{liq} \cdot N}$$

Symbols

q = average contact pressure of footing

ρ_{st} = static settlement corresponding to q

B = width of footing

H = thickness of soil crust

γ' = buoyant unit weight of subsoil (soil crust and liquefiable soil)

ϕ_o = friction angle of liquefiable soil (before shaking)

N_γ, N_q = static bearing capacity factors for the liquefied soil (for the degraded friction angle ϕ)

a_{max} = (effective) seismic ground acceleration, at the base of the liquefiable soil layer

T = predominant excitation period

N = number of cycles corresponding to a_{max}

Z_{liq} = thickness of liquefied subsoil

σ'_{vo} = vertical effective geostatic stress at depth equal to B below the soil crust

$\Delta \sigma_v$ = additional vertical stress caused by static loading (e.g. q) at the same depth, on the footing axis

To provide insight to the beneficial effect of the clay crust, Figure 11.24 shows the variation of seismic settlements and degraded factors of safety against the non-dimensional thickness of the clay crust H/B , for a typical strip foundation with $B = 3.0$ m, undrained shear strength of the clay $C_u = 40$ kPa and the two different

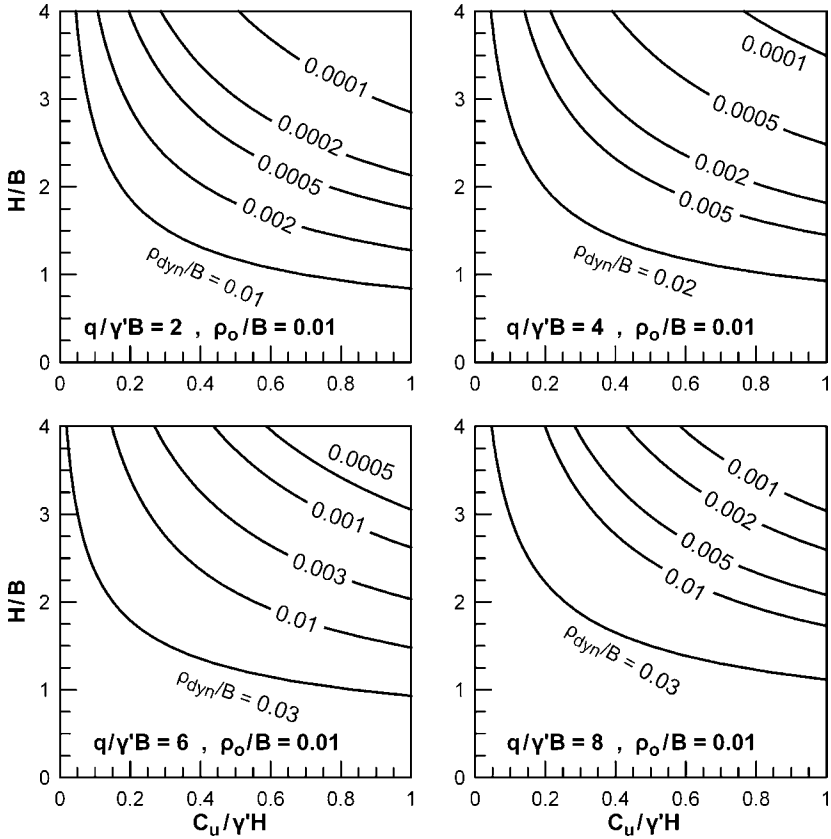


Fig. 11.22. Charts for the evaluation of liquefaction settlements of strip foundations resting on a cohesive (clay) crust – “weak” seismic excitations ($\rho_o/B = 0.01$)

seismic scenarios (“weak” and “strong” motion) defined previously. The average contact pressure was kept constant at $q = 100$ kPa, bearing in mind that lower values would probably guide the designer to alternative means of foundation, involving ground improvement or the use of pile foundation.

This figure makes clear that, when the thickness and the shearing resistance of the clay crust increase, seismic settlements ρ_{dyn} are drastically reduced and degraded factors of safety FS_{deg} increase. Moreover, an acceptable foundation performance is possible for undrained shear strength values and thicknesses of the clay crust which are commonly met in practice. For instance, for a reinforced concrete building where the allowable settlement is of the order of 0.05 m, the average bearing pressure would be safely sustained by a clay crust with $C_u = 40$ kPa and the following values of normalized thickness:

- $H/B = 0.80$ [$FS_{deg} = 1.00$, $\rho_{dyn} = 3.0$ cm < 5.00 cm], for “weak” seismic shaking, and

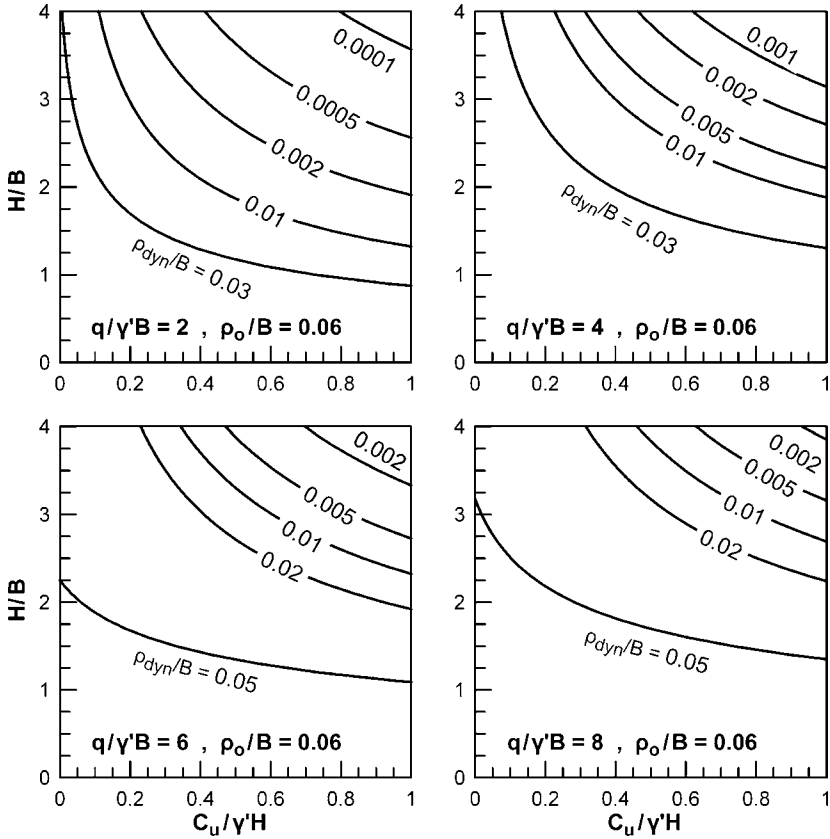


Fig. 11.23. Charts for the evaluation of liquefaction settlements of strip foundations resting on a cohesive (clay) crust – “strong” seismic excitations ($\rho_o/B = 0.06$)

- $H/B = 1.70$ [$FS_{deg} = 1.50 > 1.00$, $\rho_{dyn} = 5.0$ cm], for “strong” seismic shaking. When the allowable settlement is increased to 15 cm (e.g. in the case of a similar steel structure), the above H/B values are further reduced to:
- $H/B = 0.80$ [$FS_{deg} = 1.00$, $\rho_{dyn} = 3.0$ cm < 15.0 cm] for “weak” seismic shaking,
- $H/B = 0.70$ [$FS_{deg} \approx 1.30$, $\rho_{dyn} = 15.0$ cm] for “strong” seismic shaking

Getting back to the variation of FS_{deg} versus H/B in Figure 11.24, it may be also observed that there is indeed a critical value of the thickness ratio, denoted as $(H/B)_C$ thereafter, beyond which the degraded factor of safety maintains a constant value:

$$FS_{deg}^{max} = \frac{5.14C_u}{q} \tag{11.16}$$

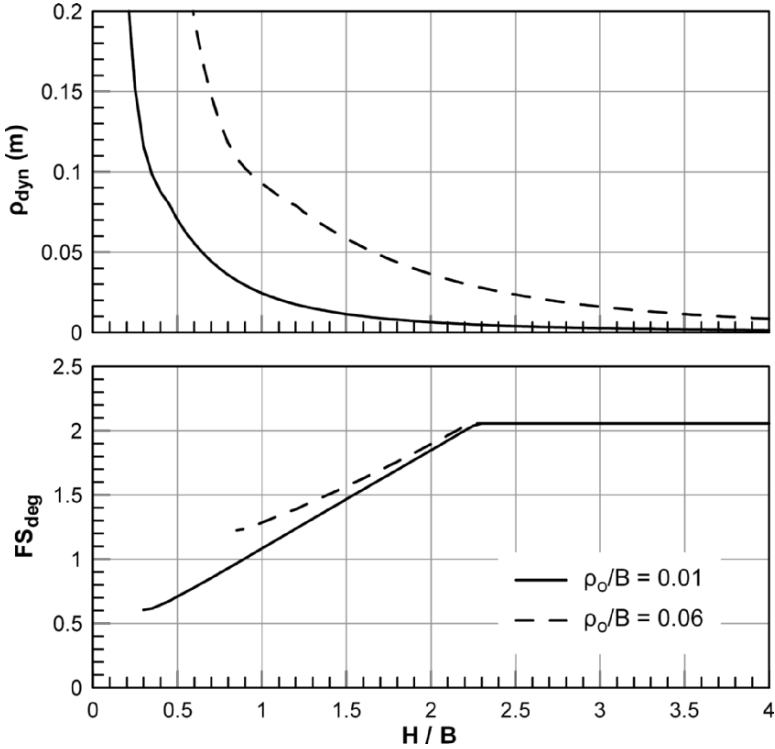


Fig. 11.24. Effect of soil crust thickness and shear strength on (a) liquefaction settlements, and (b) degraded static factors of safety

while the corresponding seismic settlements become lower than a critical value, i.e.

$$\rho_{dyn} < \rho_{dyn,c} = 0.016 \cdot \sqrt{a_{max} T^2 Z_{liq}} \cdot N \cdot \left(\frac{q}{5.14 C_u} \right)^{2.50} \tag{11.17}$$

The value of $(H/B)_{cr}$ corresponds to that clay crust thickness where the bearing capacity obtained by the composite failure mechanism shown in Figure 11.3 becomes equal to that for a wedge-type failure mechanism developing exclusively within the clay crust. Thus, it may be readily computed from Eq. 11.6 in connection with the analytical methodology outlined in Table 11.2. For quick reference, Figure 11.25 shows the variation of $(H/B)_{cr}$ and $\rho_{dyn,c}/B$ versus $1/FS_{deg}^{max} = q/(5.14 C_u)$, $C_u/\gamma' H$ and ρ_o/B . In this case also, the friction angle of the sand has a relatively minor effect and was kept constant ($\varphi_o = 35^\circ$).

In practical applications, this chart may be used for a preliminary evaluation of the allowable average bearing pressure $q = q_{all}$ in terms of the specific soil profile characteristics (H/B and C_u) and the severity of shaking expressed through ρ_o/B . Nevertheless, in case that the corresponding critical seismic settlement $\rho_{dyn,c}$, obtained from the same figure

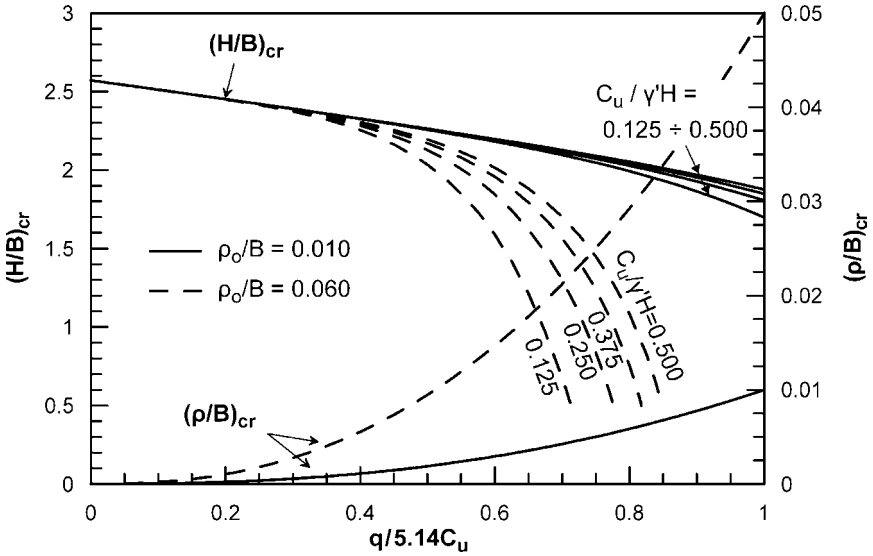


Fig. 11.25. Charts for the evaluation of (a) the “critical thickness” of a soil crust required for minimization of the static bearing capacity degradation, and (b) the associated liquefaction settlements

or from Eq. 11.17, is higher than the allowable settlement, the average bearing pressure q should be reduced following the detailed computational procedure outlined in Table 11.2.

7. Concluding remarks

This article has been devoted to analytical and simple numerical methods which can be applied in practice for the evaluation of end-of-shaking degraded bearing capacity and settlement of strip foundations resting on the surface of liquefiable sand covered by a clay crust. Following a brief literature review, an integrated analytical procedure has been presented which was built upon the results of numerical (fully coupled dynamic) parametric analyses and calibrated against centrifuge test measurements and field observations from Dagupan City, Philippines, after the 1990 Luzon $M = 7.8$ earthquake. In closure, it is felt that attention should be drawn to the following main points:

- (a) Liquefaction-induced bearing capacity degradation and settlement accumulation are two rather complex engineering problems, affected by a considerable number of soil, foundation and seismic excitation parameters (e.g. H/B , $C_u/\gamma'H$, $q/\gamma'B$, $\rho_o = 0.016 \cdot \sqrt{a_{max} T^2 Z_{liq} \cdot N}$ and ϕ_o). Thus, empirical or other simplified methodologies which necessarily rely only upon a limited number of these parameters should be used with caution and a strong spirit of conservatism.

- (b) Liquefaction settlements of footings take place during shaking, being associated with plastic failure of the subsoil. Thus, they are much higher than free field settlements, which are merely due to soil densification, and consequently they cannot be predicted with the same empirical methodologies. Furthermore, they may exceed the allowable limits even though the degraded (at the end of shaking) static factor of safety FS_{deg} is higher than 1.0.
- (c) Seismic settlements and degraded factors of safety are inter-related. Thus, it is indeed possible to check the seismic performance of a shallow foundation using a conventional static factor of safety, only that its value should be defined in terms of the allowable settlements, the seismic motion characteristics and the anticipated thickness of liquefied soil.
- (d) The presence of a soil crust may drastically reduce seismic settlements and of static bearing capacity degradation, so that the use of a shallow foundation may be found adequate, without prior soil improvement. For instance, typical examples presented herein have shown that 2–5 m of clay crust with $C_u = 40$ kPa can bear a strip footing, of 3 m width and 100 kPa average contact pressure, with reasonably low settlements. Based on preliminary findings for rectangular footings, not presented herein, it appears that the above minimum requirements are further reduced as the length of the footing decreases below $4B$.
- (e) There is indeed a critical thickness of the clay crust beyond which the bearing capacity is not affected by liquefaction anymore. The exact value of $(H/B)_{cr}$ depends on the shearing resistance of the crust, the average bearing pressure and the intensity of the shaking. However, the value of $(H/B)_{cr}$ does not become higher than about 2.6. Furthermore, note that the above limiting value of $(H/B)_{cr}$ decreases for rectangular footings, and becomes approximately equal to 1.3 in the case of square footings.
- (f) The seismic settlements corresponding to $(H/B)_{cr}$ are relatively low and may satisfy design criteria for weak or moderate seismic motions and high ductility structures. However, for strong seismic motions and low ductility structures somewhat larger H/B values may be necessary for an acceptable performance-based design.
- (g) Although the results of this study are strictly relevant to a purely cohesive crust, they may prove useful for a gross qualitative assessment of the effects of other types of liquefaction resistant soil crust as well, such as dense sand and gravel mixtures. Furthermore they may be extended in order to guide the selection of the optimal depth of application of various liquefaction mitigation measures.

It is finally noted that our studies so far have not considered a number of engineering factors (soil–structure interaction, seismic excitation time history, cohesionless soil crust, footing shape and embedment, etc.), which may have a potentially important effect. Thus,

the methodology and the associated design charts of this article may need to be refined in the future in order to provide improved accuracy and a wider range of application. For this reason, a possible application of the proposed methodology in practice should conform to the soil, foundation and seismic shaking conditions of the parametric numerical analyses which were used herein.

Acknowledgments

The authors wish to express sincere appreciation to Dimitris Karamitros for the unre-served donation of not published results from his ongoing Doctoral Dissertation studies, as well as to Dr. Achilleas Papadimitriou for contributing valuable comments on the contents of this article, and to Ioannis Chaloulos for managing the parametric numerical analyses. The first author wishes also to acknowledge the financial support provided by the General Secretariat for Research and Technology (GSRT) of Greece (Contract No. ΔΠ23 of Dec. 1. 2003).

REFERENCES

- Acacio AA (1997) Risk assessment of structures with shallow foundations resting on liquefiable deposits. PhD Thesis, University of Tokyo, October
- Acacio AA, Kobayashi Y, Towhata I, Bautista RT, Ishihara K (2001) Subsidence of building foundations resting upon liquefied subsoil: Case studies and assessment. *Soils and Foundations* 41(6): 111–128
- Adachi T, Iwai S, Yasui M, Sato Y (1992) Settlement and inclination of reinforced concrete buildings in Dagupan City due to liquefaction during 1990 Philippine Earthquake. *Proceedings of 10th World Conference on Earthquake Engineering*, Vol. 2, A.A. Balkema, Rotterdam, The Netherlands, pp 147–152
- Adalier K, Elgamal A, Meneses J, Baez JI (2003) Stone columns as liquefaction countermeasure in non-plastic silty soils. *Soil Dynamics and Earthquake Engineering* 23: 571–584
- Andrianopoulos KI, Bouckovalas GD, Karamitros DK (2005) Effective stress analysis for the seismic response of shallow foundations on liquefiable sand. *Proceeding of 1st Greece–Japan Workshop: Seismic Design, Observation, and Retrofit*, NTUA, Athens, 11–12 October 2005
- Andrianopoulos KI, Bouckovalas GD, Karamitros DK, Papadimitriou AG (2006) Effective stress analysis for the seismic response of shallow foundations on liquefiable sand. *Proceedings of 6th European Conference on Numerical Methods in Geotechnical Engineering*, 6–8 September 2006, Graz, Austria
- Andrianopoulos KI, Papadimitriou AG, Bouckovalas GD (2007) Use of a new bounding surface model for the analysis of earthquake-induced liquefaction phenomena. *Proceedings of 4th International Conference on Earthquake Geotechnical Engineering*, Thessaloniki, Greece, 25–28 June 2007
- Arumoli K, Muraleetharan KK, Hossain MM, Fruth LS (1992) VELACS: verification of liquefaction analyses by centrifuge studies; Laboratory Testing Program – Soil Data Report. Research Report, The Earth. Technology Corporation

- Bird JF, Bommer JJ, Crowley H, Pinho R (2006) Modelling liquefaction-induced building damage in earthquake loss estimation. *Soil Dynamics and Earthquake Engineering*, 26(1): 15–30
- Bouckovalas GD, Valsamis AI, Andrianopoulos KI (2005) Pseudo static vs. performance based seismic bearing capacity of footings on liquefiable soil. Proceedings of Geotechnical Earthquake Engineering Satellite Conference, Osaka, Japan, 10 September 2005 (in CD-Rom)
- Byrne PM (1991) A model for predicting liquefaction induced displacements. 2nd International Conference on Recent Advances in Geotechnical Earthquake Engineering and Soil Dynamics, St. Louis, MO, Paper 7.14
- Carnevale RA, Elgamal A (1993) Experimental results of RPI centrifuge Model No 12. Verifications of Numerical Procedures for the Analysis of Soil Liquefaction Problems, Arulanandan and Scott (eds), 1993 Balkema, Rotterdam, ISBN 90 5410 360 4
- Cascone E, Bouckovalas G (1998) Seismic bearing capacity of footings on saturated sand with a clay cap. Proceedings of 11th European Conference in Earthquake Engineering, Paris, September (in CD-Rom)
- Cetin KO, Youd TL, Seed RB, Bray JD, Sancio R, Lettis W, Yilmaz MT, Durgunoglu HT (2002) Liquefaction induced ground deformations at Hotel Sapanca during Kocaeli (Izmit), Turkey earthquake. *Soil Dynamics and Earthquake Engineering*, 22(9–12): 1083–1092
- Coehlo PALF, Haigh SK, Madabhushi SPG (2004) Centrifuge Modelling of the effects of earthquake-induced liquefaction on bridge foundations. The 11th International Conference on Soil Dynamics and Earthquake Engineering, The 3rd International Conference on Earthquake Geotechnical Engineering, 7–9 January 2004, University of California, Berkeley, United States of America
- Coehlo PALF, Haigh SK, Madabhushi SPG (2005) Development, effects and mitigation of earthquake induced liquefaction: A comprehensive study based on dynamic centrifuge modeling. Proceedings of the 16th International Conference on Soil Mechanics and Geotechnical Engineering, Ozaka 2005
- Elgamal A, Lu J, Yang Z (2005) Liquefaction-induced settlement of shallow foundations and remediation: 3D numerical simulation. *Journal of Earthquake Engineering* 9 (Special Issue 1): 17–45
- Farrell TM, Kutter BL (1993) Experimental results of Model No 12. Verifications of Numerical Procedures for the Analysis of Soil Liquefaction Problems, Arulanandan and Scott (eds), 1993 Balkema, Rotterdam, ISBN 90 5410 360 4
- Fujiwara T, Horikoshi K, Sakai K (2005) Development of a sampler designed for laminar box and its application to dynamic centrifuge modeling of footing settlement due to liquefaction. Proceedings of the 16th International Conference on Soil Mechanics and Geotechnical Engineering, Ozaka 2005
- Hamada M (1999) Similitude law for liquefied ground flow. Proceedings of the 7th US–Japan Workshop on Earthquake Resistant Design of Lifeline Facilities and Countermeasures against Soil Liquefaction, pp 191–205
- Iai S, Kameoka T, Matsunaga Y (1993) Numerical (Class A) prediction of Model No 12. Verifications of Numerical Procedures for the Analysis of Soil Liquefaction Problems, Arulanandan and Scott (eds), Balkema, Rotterdam
- Ishihara K, Yoshimine M (1992) Evaluation of Settlements in Sand Deposits following liquefaction during earthquakes. *Soils and Foundations* 32(1): 177–188
- Ishihara K, Acacio A, Towhata I (1993) Liquefaction-induced ground damage in Dagupan in the July 16, 1990 Luzon earthquake. *Soils and Foundations* 33(1): 133–154
- Jitno H (1995) Liquefaction induced deformation of earth structures. PhD Thesis, Department of Civil Engineering, University of British Columbia, Van. B.C.

- Kawasaki K, Sakai T, Yasuda S, Satoh M (1998) Earthquake induced settlement of an isolated footing for power transmission tower. Centrifuge 98, Kimura, Kusakabe and Takemura (eds), 1998 Balkema, Rotterdam, ISBN 90 54 10 986 6
- Krstelj I, Prevost JH (1993) Experimental results of Model No 12. Verifications of Numerical Procedures for the Analysis of Soil Liquefaction Problems, Arulanandan and Scott (eds), 1993 Balkema, Rotterdam, ISBN 90 5410 360 4
- Law H, Pak R, Ko H, Yashima A (1993) Numerical prediction of Model No 12. Verification of Numerical Procedures for the Analysis of Soil Liquefaction Problems, Arulanandan and Scott (eds), Balkema, Rotterdam
- Liu L, Dobry R (1997) Seismic Response of Shallow Foundation on Liquefiable Sand. *Journal of Geotechnical and Geoenvironmental Engineering*, ASCE 123(6)
- Meyerhof GG, Hanna AM (1978) Ultimate Bearing Capacity of Foundations on Sand Layer Overlying Clay. *Canadian Geotechnical Journal*, 15(4): 565–572
- Naesgaard E, Byrne PM, Ven Huizen G (1997) Behaviour of light structures founded on soil 'crust' over liquefied ground. *Proceedings, Geotechnical Engineering and Soil Dynamics III*
- Newmark NM (1965) Effects of earthquakes on dams and embankments. *Fifth Rankine Lecture, Geotechnique*, 15, pp 139–159
- Olson S, Stark T (2002) Liquefied strength ratio from liquefaction flow failure case histories, *Canadian Geotechnical Journal* 39: 629–647
- Papadimitriou AG, Bouckovalas GD (2002) Plasticity model for sand under small and large strains: A multiaxial formulation. *Soil Dynamics and Earthquake Engineering* 22:191–204,
- Richards Jr. R, Elms DG, Budhu M (1993) Seismic bearing capacity and settlements of foundations. *Journal of Geotechnical Engineering – ASCE* 119(4): 662–674
- Seed RB, Harder LF (1990) SPT-based analysis of cyclic pore pressure generation and undrained residual strength. In: Duncan JM (ed) *Proceedings, H. Bolton Seed Memorial Symposium*, University of California, Berkeley, Vol. 2, pp 351–376
- Seed RB, Cetin KO, Moss RES, Kammerer AM, Wu J, Pestana JM (2003) Recent advances in soil liquefaction engineering: A unified and consistent framework. 26th annual ASCE Los Angeles Geotechnical Spring Seminar, Long Beach, California, Keynote presentation
- Shiomi T, Shigeno Y, Zienkiewicz OC (1993) Numerical prediction for Model No 12. *Verification of Numerical Procedures for the Analysis of Soil Liquefaction Problems*, Arulanandan and Scott (eds), Balkema, Rotterdam
- Stark TD, Mesri G (1992) Undrained shear strength of liquefied sands for stability analysis. *Journal of Geotechnical Engineering ASCE* 118(11)
- Tokimatsu K, Seed BH, (1987) Evaluation of settlement in sands due to earthquake shaking. *Journal of Geotechnical Engineering* 113(8): 861–878
- Tokimatsu K, Kojima H, Kuwayama S, Abe A, Midorikawa S (1994) Liquefaction-induced damage to buildings in 1990 Luzon earthquake. *Journal of Geotechnical Engineering*, 120(2):290–307
- Yasuda S, Yoshida N, Adachi K, Kiku H, Gose S, Masuda T (1999) Simplified practical method for evaluating liquefaction-induced flow. *Journal of geotechnical engineering*, Japanese Society of Civil Engineer, No. 638/III-49, pp 71–89, 1999 (in Japanese)
- Yasuda S, Berrill J (2000) Observation of the response of foundations in soil profiles containing saturated sands. 1st International Conference on Geotechnical and Geological Engineering, Geo-Eng 2000, Issue Lecture, pp 1141–1470.
- Yasuda S, Yoshida N, Kiku H, Abo H, Uda M (2001) Analyses of liquefaction-induced deformation of grounds and structures by a simple method. *Proceedings of 4th International Conference on Recent Advances in Geotechnical Earthquake Engineering and Soil Dynamics*, Paper No. 4.34

- Yasuda S (2004) Evaluation of liquefaction-induced deformation of structures. A. Ansal (ed) *Recent Advances in Earthquake Geotechnical Engineering and Microzonation*, pp 199–230, Kluwer Academic Publishers. Printed in the Netherlands
- Yasuda S (2005) Recent several studies and codes on performance-based design for liquefaction in Japan. *Proceedings of Geotechnical Earthquake Engineering Satellite Conference*, Osaka, Japan, 10 September 2005
- Yoshimi Y, Tokimatsu K (1977) Settlement of buildings on saturated sand during earthquakes. *Soils and Foundations* 17(1): 23–38

CHAPTER 12

SEISMIC DESIGN OF PILE FOUNDATIONS FOR LIQUEFACTION EFFECTS

Ross W. Boulanger¹, Dongdong Chang¹, Scott J Brandenburg², Richard J Armstrong¹, and Bruce L. Kutter¹

1. Department of Civil and Environmental Engineering, University of California at Davis, California, USA

2. Department of Civil and Environmental Engineering, University of California at Los Angeles, California, USA

Abstract. Procedures for the seismic design of pile foundations for liquefaction effects are presented with emphasis on the conditions relevant to bridges. Two local subsystems for a bridge are discussed in detail: (1) pile groups in laterally spreading ground away from the abutments and (2) pile groups at the abutments where the restraining or “pinning” effects of the piles and bridge superstructure can be advantageous. The recommended design procedures involve equivalent static analyses using beam on nonlinear Winkler foundation models. Guidance for these design procedures was derived from a combination of dynamic centrifuge model tests and associated nonlinear dynamic finite element studies. The design procedures, their basis, and other issues for design of bridges for liquefaction effects are discussed.

1. Introduction

The seismic performance and design of pile foundations in areas of liquefaction and lateral spreading have been studied extensively in recent years, leading to an improved understanding of fundamental mechanisms and associated advances in analysis and design methodologies (e.g., Boulanger and Tokimatsu, 2006). Design procedures for liquefaction conditions using a variety of beam on soil spring models have been proposed with a range of recommendations regarding parameter selections and loading details (e.g., Tokimatsu and Asaka, 1998; Martin et al., 2002; Boulanger et al., 2003; Dobry et al., 2003; Tokimatsu, 2003; Liyanapathirana and Poulos, 2005; Rollins et al., 2005; Cubrinovski and Ishihara, 2006; Brandenburg et al., 2007a). Some of the differences in recommended parameter relationships and loading conditions are important to practice and warrant further study to resolve.

This paper presents guidance on the seismic design of pile foundations for liquefaction effects, with a specific focus on conditions relevant to bridges. Two situations, as illustrated in Figure 12.1, are described: (1) pile groups in laterally spreading ground where the out-of-plane thickness of the spreading ground is sufficiently large that free-field soil displacements are relatively unaffected by the presence of the pile groups and (2) pile groups at approach embankments where the restraining or “pinning” effects of the piles and bridge superstructure can reduce the lateral spreading demands imposed by the finite-width embankment. Guidance for both situations is limited to equivalent static analyses

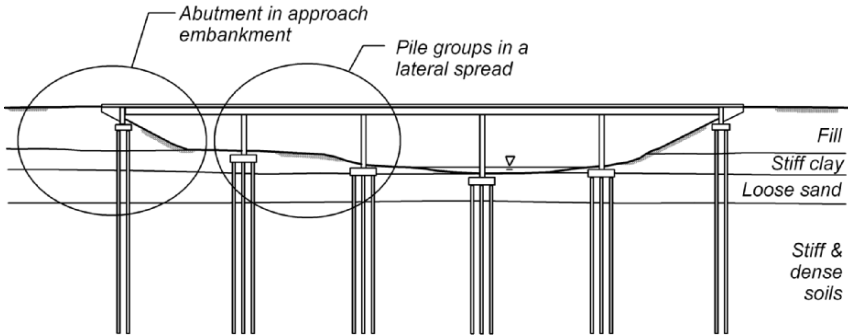


Fig. 12.1. Schematic of bridge showing two local subsystems for analysis

using beam on nonlinear Winkler foundation (BNWF) analysis methods, with recognition that nonlinear dynamic analyses may be warranted for important bridges. Details of the BNWF method and supporting design correlations are only briefly referenced, as these are well established in the literature. Emphasis is instead given to a few issues where guidance was derived from the results of recent dynamic centrifuge model tests and nonlinear dynamic finite element analyses. These issues include the specification of inertia and lateral spreading combinations and the inclusion of pile pinning effects for bridge abutments. Other issues and considerations for design of bridges for liquefaction effects are briefly discussed.

2. Pile groups in laterally spreading ground

2.1. GENERAL APPROACH

This section considers the design analysis of a pile group for an individual bridge bent that is located within an area of lateral spreading away from the abutments, as illustrated in Figure 12.1. The design of local systems, such as individual bents or abutments, is generally followed by an evaluation of the global bridge system except in certain cases (e.g., Caltrans, 2006). The specification of seismic hazard levels and bridge performance objectives are important steps, but are not discussed herein.

The design steps for a pile group of an individual bent include: (1) analyzing the piles for the inertia loading that would occur in the absence of liquefaction, (2) evaluating the potential for liquefaction-induced ground displacements, and (3) analyzing the piles for the inertia and lateral spreading loads that would occur if liquefaction is triggered. These steps are discussed in the following sections.

2.2. ANALYSIS OF PILES FOR THE NONLIQUEFACTION CASE

2.2.1. Assemble a BNWF model

Assembly of a BNWF model requires selection of lateral (p - y), axial (t - z), and tip bearing (q - z) spring parameters for the piles and pile cap. The determination of the stiffness,

capacity, and nonlinear shape of these spring elements may be made from estimates of the soil strength and stiffness parameters, from correlations to in situ test results (e.g., SPT or CPT), from analysis of dynamic monitoring records (e.g., CAPWAP analyses), or from results of pile load tests. These estimates may require further adjustments for pile group effects and pile set-up with time. The uncertainty in the estimated spring parameters depends on the approach taken. For seismic design, it is important that this step identify best estimates and some measure of uncertainty for these different spring parameters (e.g., upper and lower design values) because it is not always evident whether a conservative design will correspond to underestimating or overestimating the spring parameters.

Some existing expressions for p - y curves in sand (e.g., API, 1993) overestimate the p - y stiffness at depths greater than several pile diameters, which is not a concern for inertia loading cases but can be significant for the lateral spreading cases. The initial stiffness parameter in the API relationship for sand was modified to be proportional to the square root of effective overburden stress to compensate for this effect (Boulanger et al., 2003).

2.2.2. Estimate loads from the superstructure

Seismic displacement and associated internal force demands on the global bridge structure or its local subsystems may be estimated in different ways, often starting with an estimate of the “elastic” response from the design linear-elastic acceleration response spectra (ARS) for the site or from a dynamic elastic analysis of the structure (e.g., Caltrans, 2006). Displacement capacities and their associated internal forces within the bridge structure may then be determined from inelastic static pushover analyses. Thus, the lateral loads and overturning moments imposed on the foundation by the superstructure may be limited by the lateral strength (with allowance for over-strength) of the supporting columns or piers. The analysis of the pile foundation may be directly coupled to, or separated from, the analysis of the superstructure.

2.2.3. Perform BNWF analysis

The pile foundation is then analyzed for the lateral loads and overturning moments that are produced by the superstructure’s dynamic response, both transversely and longitudinally. Kinematic loading from ground deformation is generally not included in this analysis; special analyses are required in cases where ground deformations may be significant (e.g., in soft clays or liquefiable soils). An estimate of the pile foundation stiffness may have been needed for estimating the superstructure’s dynamic response, such that a round of iteration may be required between these two steps. It is often preferable to have the piles remain elastic because subsurface damage is difficult to assess or repair, but there are cases where allowing a limited amount of yielding in the piles can provide significant economy. Piles are also checked for their maximum uplift and compressive axial loads. Uplift or plunging of the outer piles under the imposed overturning moments can contribute to the cyclic accumulation of permanent displacements and rotations at the pile cap, which should be evaluated.

2.3. EVALUATING THE POTENTIAL FOR LIQUEFACTION-INDUCED GROUND DISPLACEMENTS

Estimates of free-field soil displacements are used to represent lateral spreading demands. The term “free-field” refers to the soil displacements that would occur if the pile group was not there, or to the soil displacements that would occur outside the zone of influence of the pile group with all other conditions being the same. Free-field lateral spreading displacements may be estimated in a number of ways, including: (1) the integration of shear strain profiles that are estimated in conjunction with SPT and CPT based liquefaction analyses, (2) empirical relationships based on case history data and broad site characteristics, (3) Newmark sliding block analyses, and (4) nonlinear dynamic numerical analyses. There is considerable uncertainty in the estimates of lateral spreading displacement obtained from any of these methods, with the overall uncertainty including contributions from the uncertainties in ground motion, site characterization, spatial heterogeneities, soil property estimation, and approximations inherent to each analysis methods. Estimating ground displacements using more than one of these methods is often advisable, after which judgment can be used in selecting a best estimate and a design value that accommodates epistemic and aleatory uncertainties to an extent that is appropriate for the specific bridge or structure.

The distribution of lateral spreading displacements versus depth must also be estimated. Numerical and physical models have shown that shear strains may be larger at the top or bottom of a liquefying soil layer depending on various factors, such as the initial relative density distribution in the layer and details of the pore water pressure diffusion process (e.g., presence of lower-permeability strata over a liquefied layer). For cases where the piles are laterally stiff and strong enough to provide satisfactory performance, the pile head displacement and maximum bending moment are often relatively insensitive to the assumed soil displacement profile shape, such that a simplified profile with linear variations across layers can be assumed for design. For more flexible pile foundations, the bending moment and curvature demands versus depth can be controlled by the assumed shape of the free-field soil displacement profile, such that a range of soil displacement profile shapes may need to be considered.

Timing of the lateral spreading displacements relative to the interval of strong ground shaking is difficult to assess. Case histories, physical models, and numerical analyses have shown that there are cases where the lateral spreading displacements will develop primarily during shaking and cases where the lateral spreading displacements will continue to increase significantly after the end of strong shaking. For example, delayed lateral movements can develop as a consequence of loosening associated with the trapping of upwardly seeping pore water beneath a clay layer and the formation of a localized dilating shear zone at the sand/clay interface (e.g., Malvick et al., 2006). This phenomenon was observed in a series of centrifuge models with cross-sections similar to the one shown in Figure 12.2, wherein a clay crust layer spread laterally downslope when the underlying saturated loose sand liquefied during shaking. The crust displacements were often observed to progressively increase after the end of shaking, as illustrated by the

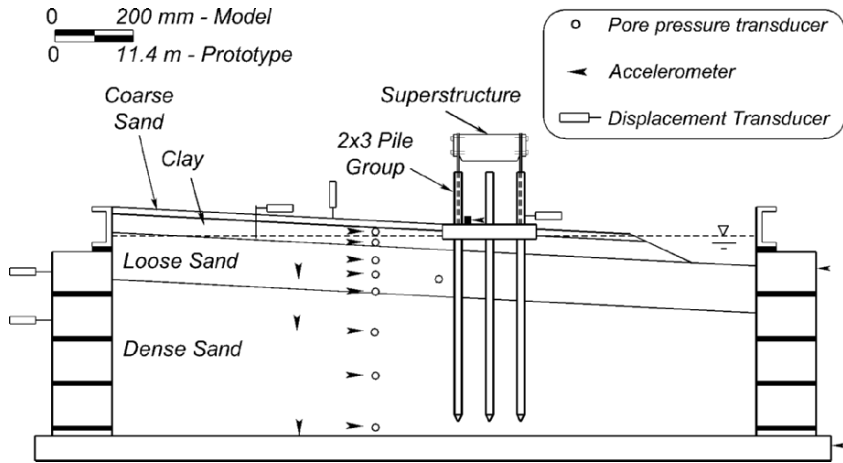


Fig. 12.2. Centrifuge model with a superstructure supported by a pile group embedded in profile that develops lateral spreading during shaking (most sensors omitted for clarity)

typical set of recording data shown in Figure 12.3, with much of the movement developing in a localized shear zone at the interface between the liquefied sand and the overlying clay. Thus, the timing of lateral spreading displacements can be affected by the numerous factors that affect the diffusion of earthquake-induced excess pore water pressures. For design purposes, it is prudent to assume that a significant portion of the final lateral spreading displacements occur during strong shaking, such that the lateral spreading and inertia demands can be additive.

The transient lurching of liquefied ground during strong shaking can produce significant kinematic loading in the direction transverse to the primary direction of lateral spreading and at level sites that are far from a free face and not prone to lateral spreading. The lateral displacements during ground lurching are generally smaller than the permanent displacements associated with lateral spreading, but they can still be large enough to impose substantial demands on pile foundations. Tokimatsu and Asaka (1998) suggest that the amplitudes of cyclic ground displacements can be estimated by integrating potential cyclic shear strain profiles, in a way that is similar to that used for estimating lateral spreading displacements. They present relationships that suggest the cyclic shear strains during ground lurching may be estimated as about 10%–20% of the maximum potential shear strains used for estimating permanent lateral spreading displacements.

2.4. ANALYSIS OF PILES FOR THE LIQUEFACTION CASE

2.4.1. Modify the BNWF model for the effects of liquefaction

The BNWF analysis for the liquefaction case requires the application of soil displacements to the free-field ends of the p–y springs in addition to the application of inertia loads as illustrated in Figure 12.4(a).

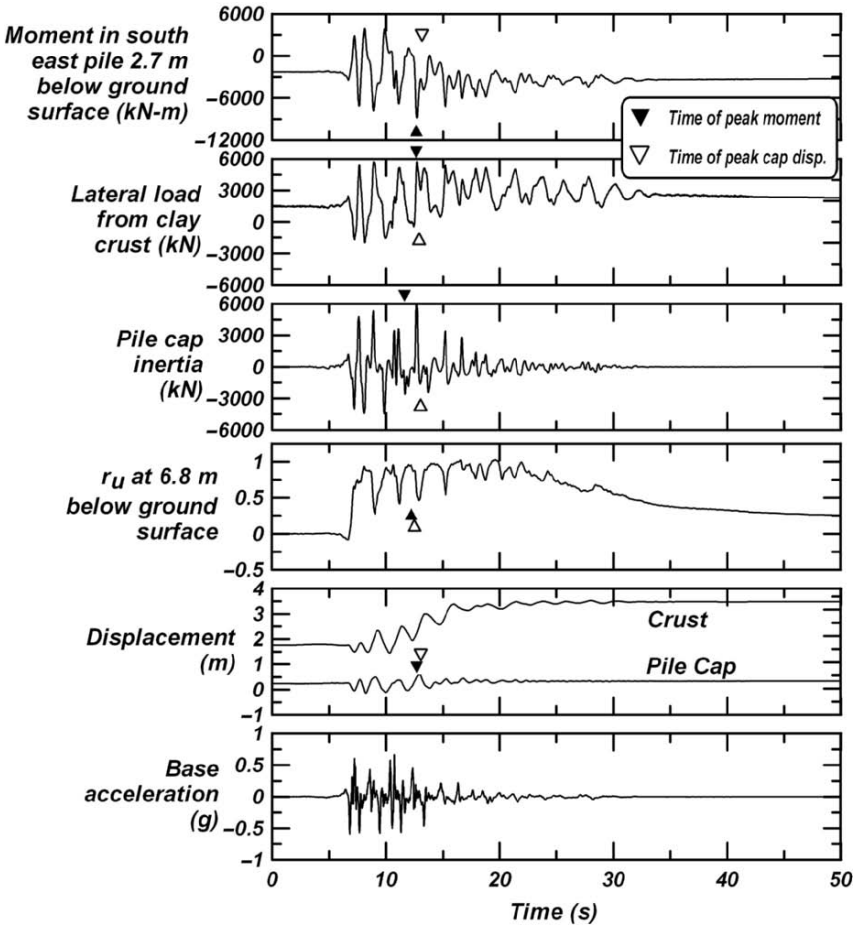


Fig. 12.3. Responses from a centrifuge model of a pile group in laterally spreading ground showing that peak pile-cap displacements and peak pile bending moments occurred during shaking while the lateral spreading displacements continued to increase after the end of shaking. Note that some records have nonzero starting values because the model had been shaken by a previous event

The influence of liquefaction on BNWF springs for sand can be approximately accounted for by applying scaling factors, or p -multipliers (m_p), to the p - y resistances. The scaling factors shown in Figure 12.5, for example, only account for the first order effects of relative density (D_R). For cases where the free-field excess pore water pressure ratio (r_u) is expected to be less than 100%, a value for m_p may be linearly interpolated between the values that are estimated for free-field r_u values of 0% and 100% (e.g., Dobry et al., 1995). The actual p - y behavior during liquefaction and lateral spreading is much more complex, as illustrated by the subgrade reactions that have been back-calculated from experimental

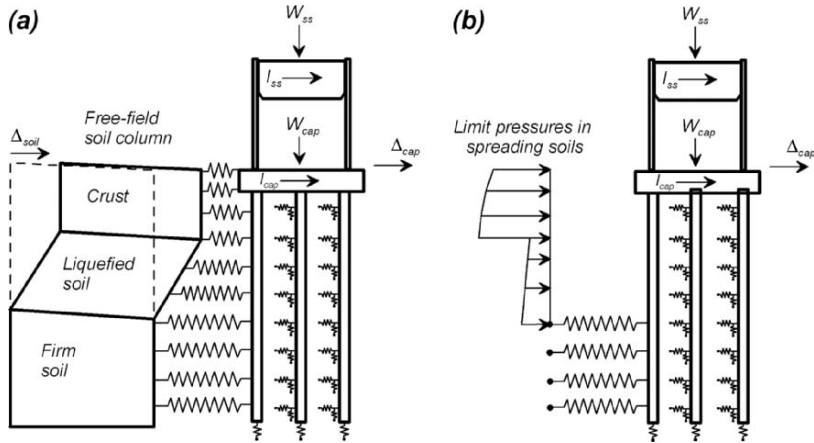


Fig. 12.4. Static BNWF analysis methods: (a) BNWF_SD with imposed soil displacements and (b) BNWF_LP with imposed limit pressures

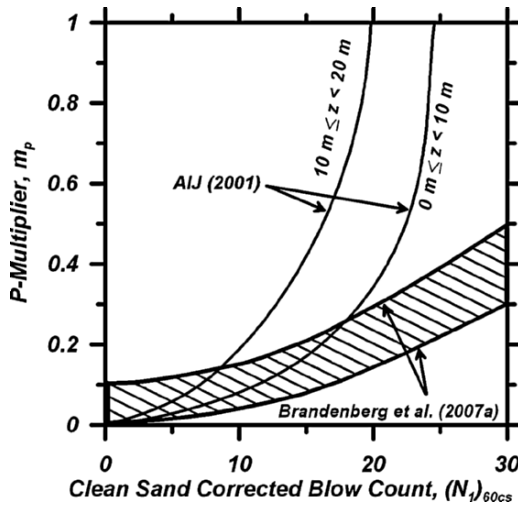


Fig. 12.5. p-Multipliers for liquefied ground

measurements (e.g., Wilson et al., 2000; Rollins et al., 2005; Tokimatsu et al., 2005). Subgrade reactions have been observed to depend on the same factors that affect the cyclic loading response of liquefying soils (e.g., D_R , strain, and strain history) plus the factors that affect the local variations of stress and strain around the piles (e.g., pile foundation flexibility, ground motions, lateral spreading displacements) and the diffusion of pore water pressures between the far-field and near-field (e.g., permeability, pile diameter, relative velocities). Similar data or guidance regarding $t-z$ and $q-z$ behavior is generally

not available, so for simplicity, the p-multipliers may be assumed to characterize the effects of liquefaction on t-z and q-z behavior as well.

Procedures for estimating the ultimate lateral loads imposed by a clay crust against a pile cap were evaluated using dynamic centrifuge model data (e.g., Figure 12.2). Conventional earth pressure theories were capable of reasonably estimating the peak crust loads, provided that the frictional resistance along the pile-cap sides and along a portion of the pile-cap base were included (Brandenberg et al., 2005, 2007b).

Load transfer between the nonliquefied crust and the pile cap is affected by the occurrence of liquefaction. Brandenberg et al. (2005) developed backbone relationships for the load transfer between pile groups and free-field nonliquefied crusts using the virgin peaks in the dynamic loads observed during centrifuge tests, as shown in Figure 12.6. The backbone relationships were about an order of magnitude softer than the relationships that have been obtained from static load tests in nonliquefied ground. The softer load transfer behavior is attributed to: (1) liquefaction of the underlying sand layer which caused the interaction stresses between the crust and pile cap to be distributed throughout a larger zone of influence in the crust, thereby requiring the development of larger relative displacements to reach a given load level and (2) the combined effects of cyclic degradation and cracking in the nonliquefied crust. A simple analytical model for the former mechanism is illustrated in Figure 12.7, while more complete models are presented in Brandenberg et al. (2007b).

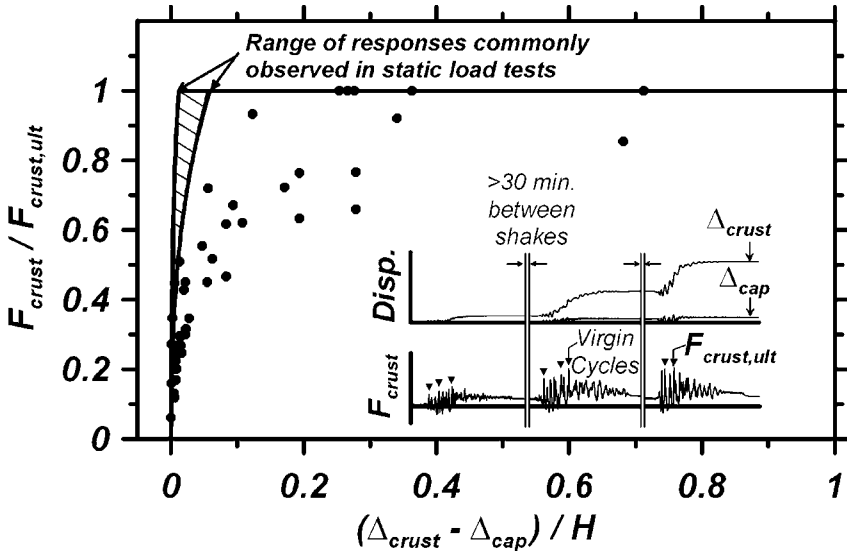


Fig. 12.6. Backbone load transfer relationships between a laterally spreading clay crust and a pile cap from five centrifuge tests

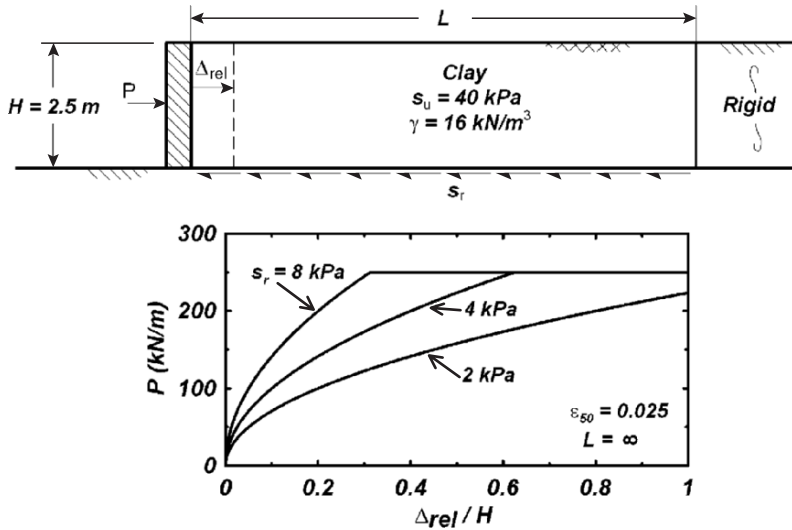


Fig. 12.7. Effect of liquefaction on the load transfer in an overlying layer of elastic-plastic clay: (a) two-dimensional geometry, (b) load transfer if the clay layer is infinitely long and the underlying liquefied sand has various residual strengths

Lateral load transfer between the nonliquefied crust and individual piles may also be affected by liquefaction in the underlying sands. A closely-spaced group of piles has the potential to effectively act as a wall for the nonliquefied crust if the total lateral load capacity against the piles is greater than the total lateral load capacity that would develop if the piles act as a wall. If they act as a wall, then the lateral load transfer would be softened in the same way as described for the pile cap. If the piles act individually, the effect of liquefaction on their combined load transfer behavior is less certain and more likely depends on the specific problem geometry. In either case, the presence of the liquefied layer will reduce the ultimate lateral loads that can develop against the pile in the overlying or underlying nonliquefied layers to a distance of a few pile diameters from their contact with the liquefied layer (as illustrated by 3D finite element analyses for layered soils by Yang and Jeremic, 2002).

The ultimate p - y capacities for single piles subject to large numbers of loading cycles at the pile head are often reduced from their static capacities by cyclic loading factors (e.g., Matlock 1970, API 1993). For seismic loading, piles may experience only a few strong cycles of inertia loading from the superstructure, and the lateral loading from a spreading crust will have a monotonic bias in the direction of spreading. Results of centrifuge model tests and analyses of single piles in a profile similar to that in Figure 12.2 showed that the loading imposed by a laterally spreading clay crust was comparable to the monotonic lateral loading capacity of the p - y springs, and that the use of cyclic loading factors would have been unconservative (Boulanger et al., 2003).

2.4.2. Estimate loads from the superstructure

The effects of liquefaction on the inertia loads from the superstructure and pile cap have been evaluated by parametric studies using nonlinear dynamic finite element analyses that were calibrated against the results of dynamic centrifuge model tests (Chang et al., 2005, 2006; Chang, 2007). For example, the deformed finite element mesh shown in Figure 12.8 is for the centrifuge model shown in Figure 12.2. The finite element platform OpenSees with the constitutive models developed by Yang et al. (2003) was used. The parametric FE analyses considered a range of ground motions, pile foundation stiffness, superstructure elastic period, superstructure mass, crust strength, and other variables. Each case was analyzed once with liquefaction being possible and once with pore water pressure generation eliminated. The inertia loads computed with and without liquefaction were compared as

$$I_{cc,liq} = C_{cc}C_{liq}I_{max_nonliq} \quad (12.1)$$

where I_{max_nonliq} = the maximum or peak inertial load in the absence of liquefaction, C_{liq} = the ratio of maximum inertial load with liquefaction versus without liquefaction, and C_{cc} = the fraction of the maximum inertial load with liquefaction that occurs at the critical loading cycle (i.e., when the maximum pile bending moments and shear forces occur). Values of C_{liq} for the superstructure depended on the frequency content of the input motion, as represented by the spectral shapes in Figure 12.9 and summarized by the parametric results in Figure 12.10. Values of C_{cc} varied less significantly.

For design, the values of C_{liq} and C_{cc} in Table 12.1 were subsequently proposed. The I_{max_nonliq} value for the superstructure can be estimated using the procedures discussed in previous sections, while the I_{max_nonliq} value for the pile cap can be estimated as equal to the peak ground surface acceleration. The lateral loads and overturning moments imposed on the foundation by the superstructure may be limited by the lateral strength (with allowance for over-strength) of the supporting columns, as noted for the nonliquefaction case. These factors provide an approximate allowance for the fact that inertia

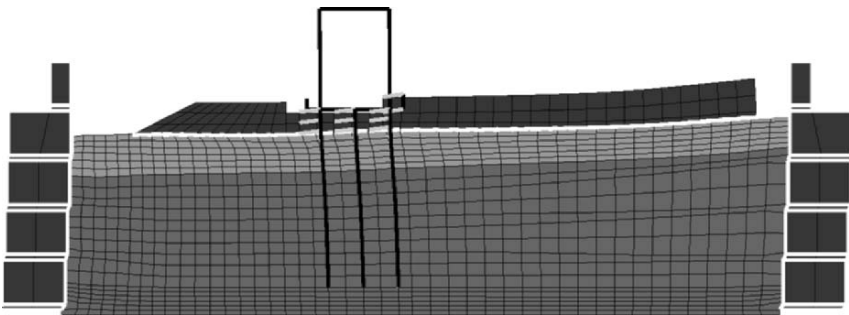


Fig. 12.8. Deformed finite element mesh with pore pressure contours

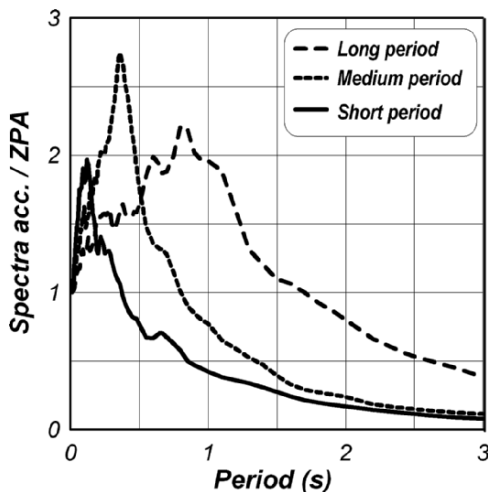
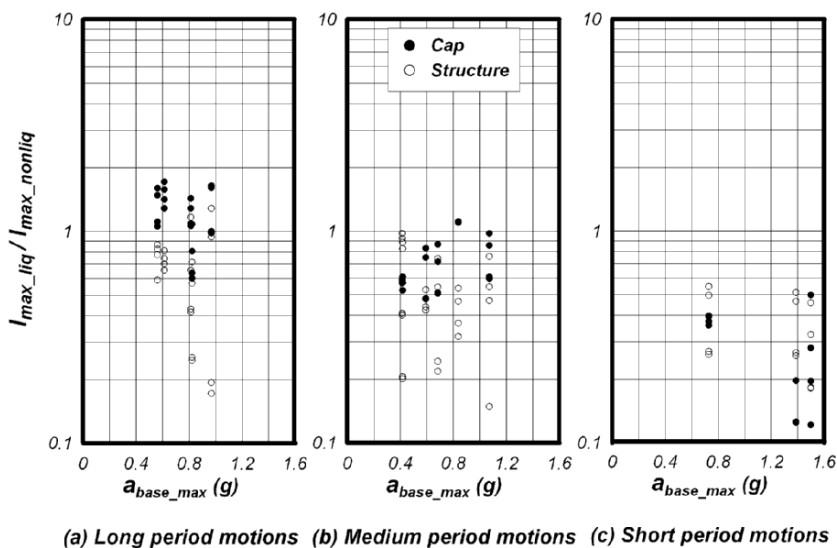


Fig. 12.9. Mean normalized acceleration response spectra (5% damped) for three bins of motions used in the dynamic FE analyses; ZPA = zero period acceleration



(a) Long period motions (b) Medium period motions (c) Short period motions
 Fig. 12.10. Ratios of the maximum inertia with liquefaction to the maximum inertia without liquefaction for the pile cap and superstructure from the dynamic FE parametric analyses

loads are expected to be smaller with liquefaction than without liquefaction. These factors are considered a reasonable starting point for design, although it is likely that they will be revised as additional parametric studies and experimental data become available.

Table 12.1. Inertial coefficients for BNWF.SD analyses of liquefaction cases

Motion* ($Sa_{T=1s}/ZPA$)	Pile cap		Superstructure	
	C_{liq}	C_{cc}	C_{liq}	C_{cc}
Long period (1.7–2.4)	1.4	0.85	0.75	0.65
Medium period (0.5–1.6)	0.75	0.85	0.55	0.65
Short period (≤ 0.4)	0.35	0.85	0.45	0.65

* See Figure 12.9 for examples of long-period, medium-period, and short-period input motions.

2.4.3. Perform the BNWF analysis

The BNWF analysis for the liquefaction case involves the simultaneous application of soil displacements to the free-field ends of the p–y springs and inertia loads to the pile cap and superstructure as illustrated in Figure 12.4(a). Guidance regarding appropriate combinations of these loads and soil displacements was developed from the results of dynamic centrifuge model tests, dynamic finite element analyses, and equivalent static BNWF analyses.

The dynamic FE analyses showed that the critical loading condition for the pile foundations corresponded most closely to the occurrence of peak or near-peak lateral ground displacements in conjunction with significant inertia loads for a wide variety of soil profile, pile foundation, superstructure, and ground motion characteristics. This observation is consistent with the experimental observations from: (1) centrifuge models of pile-group-supported structures in profiles of sloping ground, like that shown in Figure 12.2, wherein the critical loading cycle involved a local peak in the transient ground displacements plus a local peak in the inertia load (Brandenberg et al., 2005; Chang et al., 2005) and (2) large-scale shaking table tests of structures supported on pile groups in level soil profiles having a dry sand crust over saturated sand, wherein the peak bending moments occurred when the lateral ground displacements and inertia loads were both large and acted in the same direction (Tokimatsu et al., 2005). Both of these experimental studies involved structures with natural periods of 0.8 s or less and soil profiles whose equivalent natural periods after liquefaction were in the range of 1 to 2 s. Tokimatsu et al. (2005) suggested that the lateral soil displacements and inertia loads would be out-of-phase if the structure's natural period was larger than the liquefied ground's natural period, based on their observations from tests involving dry sand profiles with much smaller natural periods. The dynamic FE analyses by Chang (2007) did, in fact, show that the structure's inertia load became more out-of-phase with the lateral ground displacement when the superstructure period was 3 s and the liquefied ground's natural period was about 1 to 2 s. The superstructure inertia load was relatively small for this long-period structure, such that the pile-cap inertia (which was more in-phase with crust displacements) became a larger fraction of the total inertia load imposed on the pile foundation. Consequently, the critical loading condition for the pile foundation of this structure with a natural period of 3 s and subject to lateral spreading was still reasonably approximated by a near-peak lateral ground displacement with a significant fraction of the peak total inertia load.

The recorded responses in Figure 12.3 for a centrifuge model having the configuration shown in Figure 12.2 also show that the peak downslope lateral load from the crust often occurred during strong shaking, even though the lateral ground displacements (and relative displacements between the pile cap and surrounding ground) continued to increase after strong shaking had ended. In this situation, the static BNWF approximation of the critical loading cycle would involve a significant fraction (but not all) of the ultimate lateral ground displacement plus a fraction of the peak inertia loads. In other situations, it is feasible that the critical loading cycle would involve the peak inertia loads with some other fraction of the ultimate ground displacements. Methods for estimating lateral spreading displacements are, however, not refined enough to attempt partitioning the displacements into portions that occur during versus after shaking. Thus, it is believed to be sufficient for design purposes to analyze the liquefaction case using the ultimate lateral ground displacements with inertia loads determined according to the factors in Table 12.1.

The application of soil displacements in-phase with inertia loads does not mean that the resulting lateral spreading loads will be in-phase. For example, Figure 12.11 shows the results of dynamic FE analyses for the model geometry shown in Figure 12.2 with four different values of pile bending stiffness (EI). Time series for the lateral loads imposed by the spreading crust against the pile cap are shown along with the inertia loads from the pile cap and superstructure. The lateral spreading loads and the inertia loads are largely out-of-phase (nonadditive) at the critical loading cycles for the two more flexible pile cases, while they are largely in-phase (additive) at the critical loading cycles for the two stiffer pile cases. In all four cases, the lateral soil displacements (not loads) and the inertia loads were largely in-phase at the critical loading cycles regardless of the foundation stiffness.

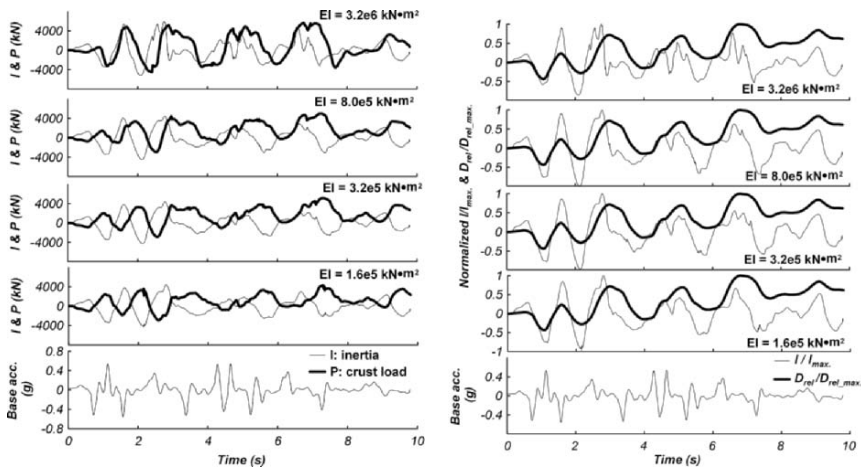


Fig. 12.11. Influence of pile bending stiffness (EI) on the phasing of (a) lateral crust load P and total structural inertia I acting on the pile cap and (b) normalized lateral crust displacements and structural inertia acting on the pile cap in dynamic FE analyses

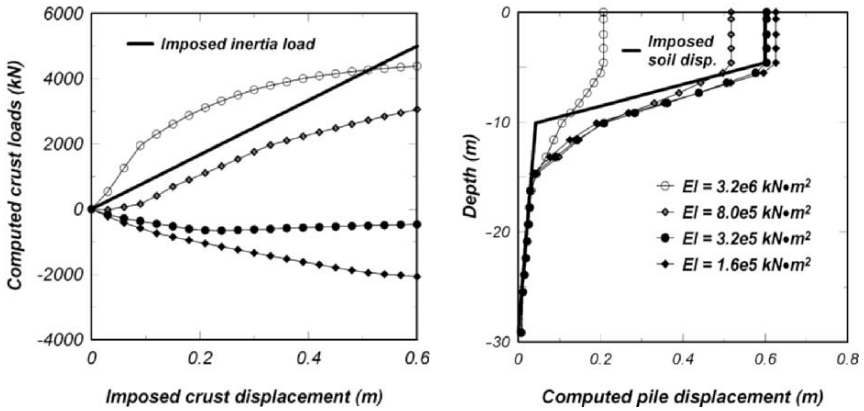


Fig. 12.12. Influence of pile bending stiffness (EI) on the results of static BNWF_SD pushover analyses: (a) computed crust load versus imposed crust displacement, (b) computed pile displacement profiles and imposed soil displacement profile

Equivalent static BNWF analyses were performed for the same four cases analyzed in the above dynamic FE analyses. The lateral soil displacements and inertia loads were applied simultaneously as linearly increasing with time to their final values. The lateral soil load, which is a computed response, and the imposed inertia load are plotted versus the imposed soil displacement in Figure 12.12. For the two stiffer pile cases, these equivalent static analyses predict that the pile cap will move less than the free-field soil and thus the lateral spreading soil load will act in the same direction as the inertia loads (i.e., in-phase loads). For the two more flexible pile cases, these equivalent static analyses predict that the pile cap will move more than the free-field soil and thus the lateral load from the crust will actually be resisting the inertia loads (i.e., out-of-phase loads). Thus, the equivalent static BNWF analyses were able to predict the effect that pile bending stiffness had on the dynamic phasing of lateral spreading and inertia loads (Figures 12.11 and 12.12).

The results of parametric analyses showed that the equivalent static BNWF analyses with the simultaneous application of ultimate lateral ground displacements and appropriate fractions of peak inertia loads were consistently able to predict the dynamic phasing of the lateral spreading and inertia loads, and that this phasing depends primarily on:

- Pile foundation stiffness
- Crust strength and stiffness
- Inertia load magnitude
- Ground displacement magnitude

The ground motion characteristics and the superstructure period affected the phasing of crust and inertia loads primarily through their influence on the ground displacement and inertia load magnitudes.

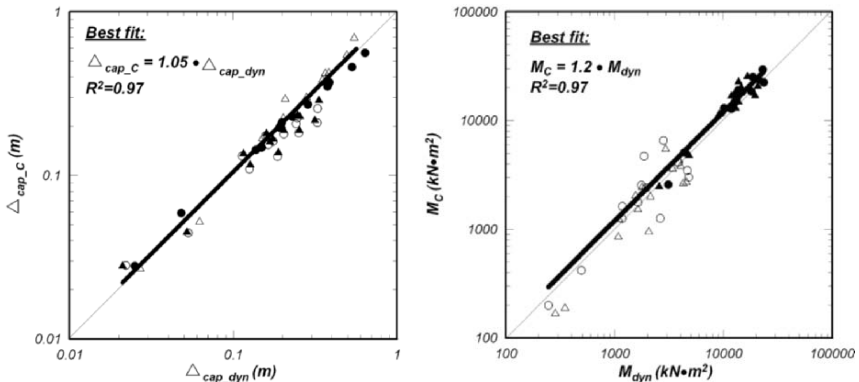


Fig. 12.13. Comparison of results from equivalent static BNWF_SD analyses (identified by subscript c) and dynamic FE analyses (identified by subscript dyn): (a) maximum pile-cap displacements and (b) maximum pile bending moments

Equivalent static BNWF analyses using the above guidelines were able to reasonably approximate the peak responses from the dynamic FE analyses (Chang, 2007). This is illustrated in Figure 12.13 showing the peak pile bending moments and peak pile-cap displacements from the equivalent static BNWF analyses versus those from the dynamic FE analyses. These results include a wide range of ground motion characteristics, pile foundation stiffness, and superstructure periods. The agreement is quite reasonable given the approximations involved in the equivalent static analyses.

In certain cases, a pile foundation's response to lateral spreading is relatively uncoupled (physically) from its response to inertia loading. For example, the lateral spreading of a strong thick crust may cause bending of the piles at large depths, while the superstructure's inertial loads may be transferred to the soil at shallower depths, such that the two loading mechanisms have little overlapping influence and could have been analyzed as separate load cases. In other situations, the two loading mechanisms may have overlapping influence such that they cannot reasonably be analyzed as separate load cases. In practice, it is often difficult to predict whether the effects of lateral spreading and inertia loading can be analyzed as separate load cases or not, without actually performing an equivalent static BNWF analysis to determine how strongly they interact. Thus, it is both simpler and more reliable, and therefore recommended, to perform the equivalent static BNWF analysis with soil displacements and inertia loads applied simultaneously.

2.5. ADDITIONAL COMMENTS FOR PILE GROUPS IN LATERAL SPREADS

The sensitivity of the computed foundation response to variations in the major input parameters should always be evaluated. Shear force and bending moments at the pile-cap connection as well as the permanent displacements of a pile cap were found to be most sensitive to inertial loads, lateral spreading displacements, crust properties, and pile

foundation characteristics (structural and geotechnical capacities). Other parameter variations can investigate factors such as the shape of the soil displacement profile and the p -multipliers for liquefied layers, although these factors were generally of lesser importance in determining pile-cap displacements and loads at the pile-cap connection. If the bending moment distribution beneath the ground surface is important, then the soil displacement profile and p -multipliers for liquefied layers can be of greater importance. For most parameter variations, it is important to consider best estimates with high and low ranges because it is not always evident which will result in a conservative estimate of foundation response. For example, a conservative estimate of pile response for the nonliquefaction case might correspond to a softer load transfer relationship between the pile cap and surrounding crust (e.g., weaker crust strengths, assumption of zero shear on the base and sides of the pile cap, larger relative displacements to mobilize the crust loads) whereas a conservative estimate of pile response for the liquefaction case might instead correspond to a stiffer estimate of the same load transfer relationship (e.g., stronger crust strengths, inclusion of base shear on the pile cap, etc.).

The equivalent static BNWF analysis method that uses imposed limit pressures in the lateral spreading soils (BNWF_LP in Figure 12.4b) has serious limitations relative to the BNWF method that uses imposed soil displacements (BNWF_SD in Figure 12.4a). The use of limit pressures may be reasonable for cases where the lateral spreading ground displacements are large, the displacements of the underlying nonliquefied soils are very small, and the pile foundation is stiff enough that the limit pressures are truly mobilized. If the lateral spreading displacements are insufficient to mobilize passive pressures from the crust, the use of limit pressures can be overly conservative. If significant shear strains develop in the underlying nonliquefied layers, the limit pressures approach may still need to include free-field soil displacements for the underlying nonliquefied layers to avoid significantly under-predicting pile and pile-cap displacements. Conditions that affect the lateral soil pressures, when they are below their limit values, are sufficiently complicated that it is impractical to develop simple guidelines for their estimation. For this reason, the BNWF_SD approach is preferable to the BNWF_LP approach for general design purposes.

3. Pinning effects for approach embankments

3.1. DEFINITION AND BACKGROUND

This section considers the local analysis of a bridge abutment in an approach embankment (Figure 12.1) for the case where liquefaction has been triggered in the underlying soils. As the embankment soils spread longitudinally, the piles and bridge superstructure can develop reaction forces that are significant relative to the mass of a finite-width embankment. These “pinning” forces reduce the embankment displacements relative to those that would occur in the absence of any pinning force. The result is a coupled system wherein demands imposed on the bridge depend on embankment displacements, which in turn depend on the degree to which the piles and bridge superstructure pin the embankment.

The beneficial effect of this coupling diminishes as the mass of the spreading embankment soil increases relative to the available pinning forces.

The effect of pinning is illustrated by the results of a dynamic centrifuge model test comprised of two identical 8.5-m-tall (prototype) embankments facing each other across an open channel, as shown by the cross-section in Figure 12.14 and the photograph of the dissected model in Figure 12.15. The embankments were made of coarse dry sand, and were underlain by a layer of loose sand, which was in turn underlain by dense sand. The water table was just above the top of the loose sand. One embankment had a group of eight 1.1-m-diameter piles at the crest (two rows of four piles), while the other embankment had no piles. Earthquake shaking with a peak base acceleration of 0.7 g caused the

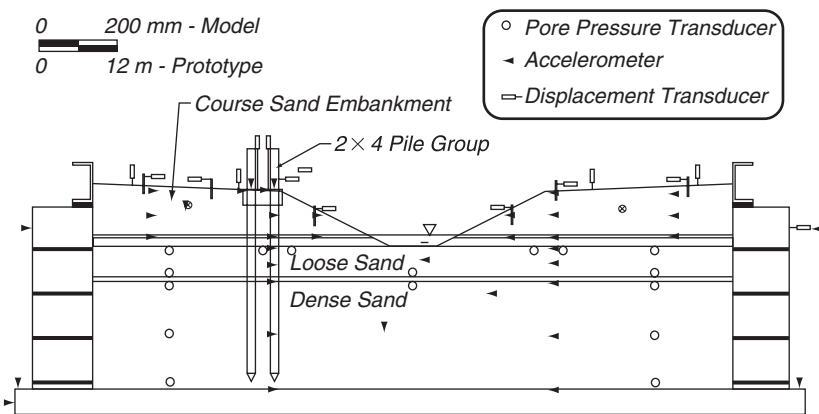


Fig. 12.14. Cross-section of centrifuge model with two opposing embankments that are about 8.5-m tall in prototype; one with a pile group and one without



Fig. 12.15. Photograph of the centrifuge model during dissection; note that the pile cap displaced 0.75 m (prototype) toward the channel while the opposing embankment crest displaced 1.7 m (prototype) toward the channel

loose sand layer to liquefy and the embankment crests to displace longitudinally toward the channel by about 0.75 and 1.7 m for the embankments with and without piles, respectively. Thus, the pile pinning effect reduced longitudinal embankment displacements by 50% to 60% for this model. The embankments also developed substantial transverse spreading and surface settlements, which are important considerations for evaluating the post-earthquake accessibility or serviceability of a bridge.

The design procedures for estimating pile pinning effects on embankments are described in the next section, after which they are illustrated by application to the dynamic centrifuge model test shown in Figures 12.14 and 12.15.

3.2. PROCEDURES FOR ESTIMATING PILE PINNING EFFECTS

Procedures for estimating pile pinning effects on longitudinal embankment displacements have been used in practice and incorporated in recommended specifications for seismic design of bridges (e.g., Martin et al., 2002). The first evaluation of these types of procedures against physical data was based on centrifuge data (Boulanger et al., 2006), from which a number of modifications to the details of the procedures described in Martin et al. (2002) were recommended. These procedures can be represented by three primary parts:

- Estimate the longitudinal displacement of the embankment soil mass for a range of restraining forces from the piles and bridge superstructure.
- Estimate the longitudinal restraining force exerted on the embankment mass by the piles and bridge superstructure for a range of imposed embankment displacements.
- Determine the compatible displacement and interaction force between the embankment mass and the piles and bridge superstructure.

Each of these three parts is discussed in more detail in the following sections.

3.2.1. *Estimating embankment displacements for a range of restraining forces*

The estimation of embankment displacements due to liquefaction is complicated by the need to account for a range of possible restraining forces from the piles and bridge superstructure. Of the four methods that were previously described for estimating free-field lateral spreading displacements, only two provide a means to account for the effect of restraining forces: (1) Newmark sliding block methods and (2) nonlinear dynamic numerical analyses. The method of integrating potential liquefaction-induced shear strains can only be used for the case of zero restraining force, and the available empirical models for lateral spreading are not applicable to bridge abutments. For this reason, designers have turned to Newmark (1965) sliding block methods as the first step in the design process, after which the potential benefits of more complicated dynamic numerical analyses can be considered.

The first step is to perform slope stability analyses of the embankment, such as illustrated in Figure 12.16 for the centrifuge model from Figure 12.14. Residual shear strengths (S_r) of the liquefied layers may be estimated using case history based correlations between

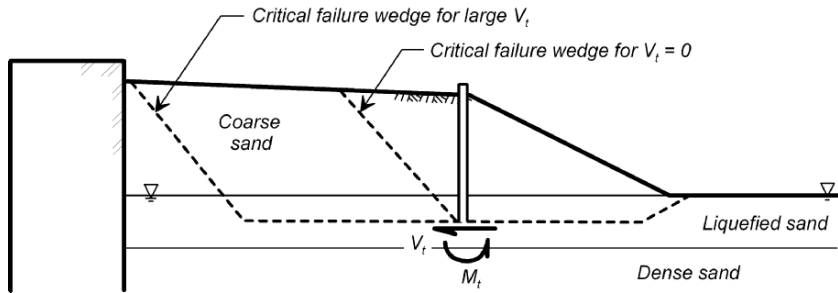


Fig. 12.16. Critical slope stability failure surfaces for different values of pile restraining force

S_r/σ_{vc}' ratios and SPT or CPT penetration resistances. The total shear force (V_t) and bending moment (M_t) in the piles at the slope stability failure surface can be represented by an equivalent force-couple, such as having the pile shear force act alone at a distance equal to M_t/V_t above the slope stability failure surface. Large point forces can produce numerical errors in the limit equilibrium analyses, such that V_t is often represented as a distributed force or an equivalent increase in soil shear strength along some portion of the failure surface. The slope stability analyses are used to determine yield accelerations (k_y) for a range of possible restraining forces. For each restraining force, the yield acceleration is the value of the horizontal seismic coefficient that produces a factor of safety of unity against slope instability. These slope stability analyses must consider a range of possible failure surfaces because the most critical failure surface can increase substantially in size with increasing restraining force (e.g., Figure 12.16).

Embankment displacements for each of the possible restraining forces are then computed based on the yield acceleration and the design ground motion parameters. This step could be performed by either: (1) performing Newmark sliding block calculations using a specified set of acceleration time series or (2) using a regression model for Newmark sliding block displacements, such as the one developed by Bray and Travararou (2007). The results of these analyses are a plot of embankment displacement versus restraining force per unit thickness of the analyzed section.

The tributary (transverse) width for the embankment mass is used to establish a common dimension between the force–displacement relationships for the embankment and for the pile foundation/bridge superstructure. Consider the embankment transverse cross-section shown in Figure 12.17. The piles and bridge superstructure will be restraining movement of an embankment mass that includes the soil defined by the embankment crest width, plus a portion of the side slope masses. This is accounted for by adopting an equivalent tributary width whose mass includes a portion of the side slope masses, with one-half of the side slope mass recommended as a reasonable value for design.

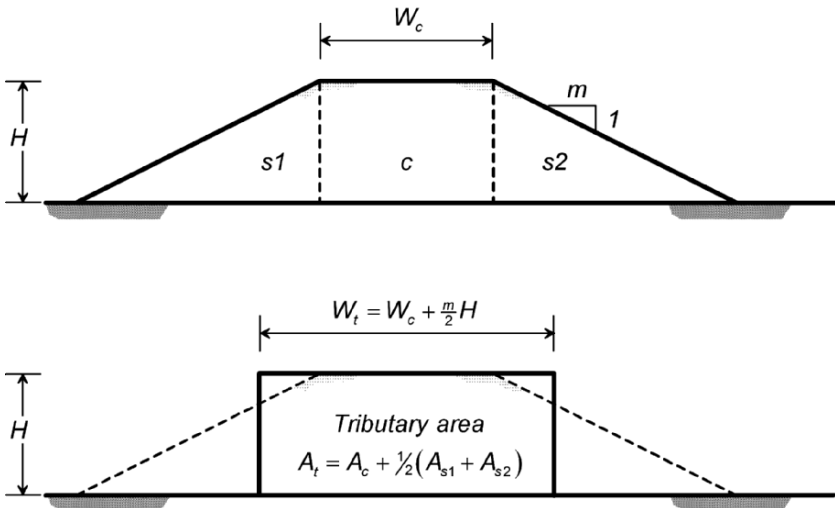


Fig. 12.17. Transverse section of an abutment showing the equivalent tributary width that is assumed to interact with the restraining forces from the pile foundation and bridge superstructure

3.2.2. Estimating pile/bridge restraining forces for a range of displacements

The restraining forces from the pile foundation and bridge superstructure are estimated for a range of possible embankment displacements. Inertia from the bridge structure will alternate between causing an increase and decrease in the restraining force on the embankment. The equivalent static representation of restraining forces from the pile foundation and bridge superstructure neglects the transient influence of bridge inertia forces.

The restraining force from the pile foundation is determined using an equivalent static BNWF.SD pushover analysis. In this analysis, the imposed soil displacements are progressively increased and the shear forces and bending moments in the piles at the location of the slope stability failure surface are determined. The ultimate shear force that can develop will be limited by plastic hinging in the piles. The moment capacity of the piles, and hence their shear resistance, may be further reduced by geometric effects (i.e., $P-\Delta$ or buckling) as the abutment displacements become significant (Martin et al., 2002).

The development of restraining forces from the bridge superstructure with increasing embankment displacement depends on the structural configuration and details (e.g., bearings, expansion joints, shear capacity of seat abutment back wall) and the characteristics of the embankment soils (e.g., passive resistance against an abutment back wall that is designed to break away during design loading). The restraining force that develops at the abutment must be transferred to either the intermediate bents or to the opposite abutment.

Pushover analyses of the global bridge structure can be used to estimate this load transfer behavior.

The combined restraining forces from the pile foundation and bridge superstructure will progressively increase as the embankment displacement increases during earthquake shaking. Newmark sliding block analyses for the embankment are, however, most commonly based on the assumption that the restraining forces are constant throughout shaking. To provide consistency between these two uncoupled analyses, the “equivalent constant restraining force” from the piles and bridge superstructure can be taken as the average resistance that develops between the start of shaking (zero embankment displacement and hence zero resistance) and the end of shaking (the resistance for the final embankment displacement).

3.2.3. *Compatibility of embankment and pile displacements*

A compatible displacement and interaction force between the embankment slide mass and the pile foundation/bridge superstructure can be determined from the relationships developed in the previous steps. Graphically, the solution is the intersection of the force–displacement relationships determined separately for the embankment slide mass and the pile foundation/bridge superstructure.

3.3. EVALUATION AGAINST CENTRIFUGE MODEL TESTS

The recommended procedures for pinning analyses are illustrated for the dynamic centrifuge model test shown in Figures 12.14 and 12.15 and described previously. Analysis results for the embankment slide mass are presented in Figure 12.18, including (a) the relationship between yield acceleration and pile restraining force as determined by slope stability analyses and (b) the relationship between embankment slide mass displacement and pile restraining force as determined by Newmark sliding block calculations using the accelerations recorded in the dense sand beneath the slide mass. These analysis results are particularly sensitive to the residual shear strength of the liquefied soil, as illustrated in Figure 12.18 by the different results for S_r/σ_{vc} ratios of 0.22 and 0.26.

The computed pushover force–displacement response for the piles and the corresponding equivalent constant restraining force are shown in Figure 12.19. The imposed soil displacement profile was trilinear with depth, and corresponded to shear strains of 1%, 6%, and 3% in the dense sand, loose sand, and embankment sand, respectively, when the embankment crest displacement was equal to 0.75 m. The p–y spring capacities for the nonliquefied sands immediately above and below the liquefied layer were reduced to account for the influence of the nearby weak liquefied soils; the p–y capacities were assumed to be unaffected at a distance of two diameters from the liquefied layer, and to vary linearly to a value equal to that for the liquefied soil at the actual liquefied soil interface (based on 3D FE analysis results for layered soils by Yang and Jeremic, 2002).

The solution for compatible abutment displacements can be obtained from Figure 12.19 as the intersection of: (1) the pile foundation’s equivalent constant restraining force versus displacement curve and (2) the embankment slide mass displacement versus constant

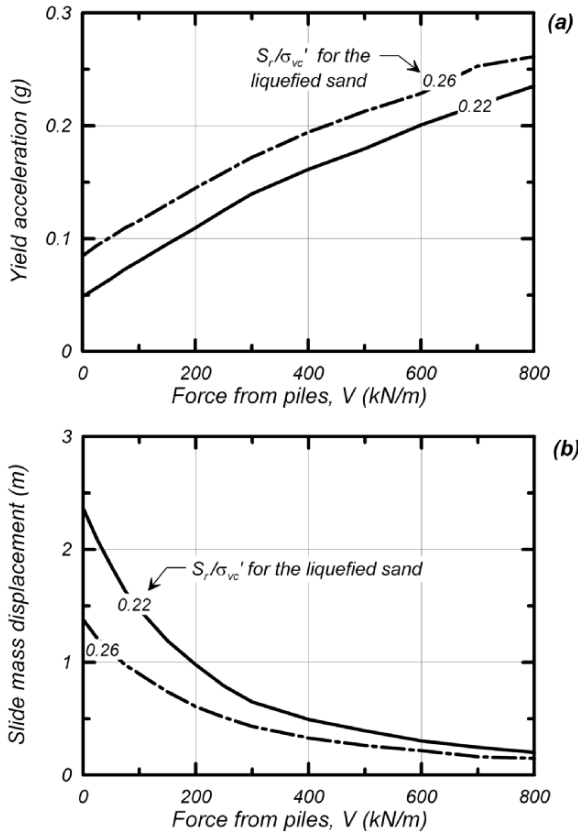


Fig. 12.18. Results of embankment displacement analyses for different restraining forces from the piles: (a) yield acceleration from slope stability analyses and (b) embankment slide mass displacements from Newmark sliding block calculations

restraining force curve. Embankment slide mass displacement curves are shown for S_r/σ_{vc}' ratios of 0.22 and 0.26 because this range of S_r/σ_{vc}' ratios produced estimated displacements for zero restraining force that bracket the observed displacement of about 1.7 m at the crest of the nonpiled embankment in the centrifuge tests. The corresponding solutions for compatible abutment (or crest) displacements on the piled embankment range from 0.55 to 0.70 m, with the larger value being close to the observed crest displacement of about 0.75 m. Computed bending moments in the piles for this range of compatible displacements were also in reasonable agreement with the values measured in the centrifuge test. Good agreement between computed and observed responses for the piled embankment was, however, only obtained after the methodology for computing embankment displacements was calibrated to the observed crest displacement for the nonpiled embankment.

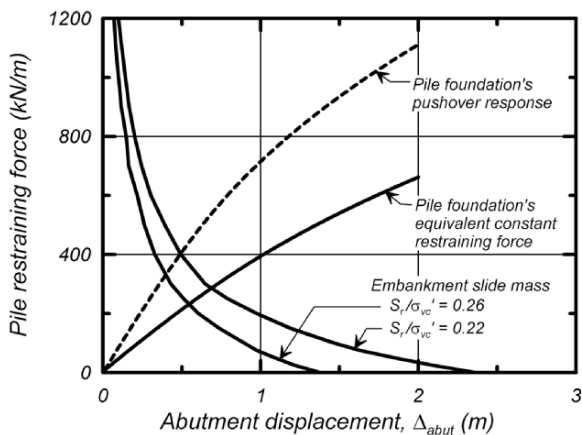


Fig. 12.19. Compatibility between the computed embankment slide mass displacements and the equivalent constant restraining force from the pile foundation

These and other results suggest that the recommended pinning analysis procedures provide a reasonable design approach for estimating the relative effect that pinning forces can have on embankment displacements. Despite the approximations and uncertainties involved, the methodology can be used to bracket the range of likely pinning effects with sufficient accuracy for decision making in many situations. In other situations, dynamic numerical analyses may provide insights into the system response characteristics that are valuable enough to warrant the additional engineering costs. For either analysis method, the final design must account for the significant uncertainties involved in predicting liquefaction-induced ground displacements, as previously discussed for lateral spreads.

4. Other issues and considerations

The response of the global bridge system for the liquefaction case needs to be evaluated after the individual bents and abutments have been evaluated as local systems. A dynamic analysis of the global bridge system is often performed for the nonliquefaction case (e.g., Caltrans, 2006), in which the soil is often represented by spring elements attached to the structure model. A dynamic analysis of the global bridge system for the liquefaction case is far more complicated because the inclusion of dynamic ground displacements requires some type of continuum modeling for the soil profile. Alternatively, an equivalent static analysis of the global bridge system for the liquefaction case may be performed wherein a number of different possible loading combinations would need to be considered; for example, liquefaction effects at one or more locations in combination with inertia demands in different directions. The development of improved guidelines for analyses of global bridge systems for the liquefaction case is an area of ongoing research.

Another loading case that needs to be considered is down-drag on the piles due to earthquake-induced settlements. Rollins and Strand (2006) presented measurements of down-drag forces on a pile during reconsolidation of surrounding soils that had been liquefied by in situ blasting. Down-drag in liquefied soils can be analyzed using neutral-plane methods with appropriate modifications for the liquefaction case (Boulanger and Brandenburg, 2004).

Performance-based design or evaluation of bridges for liquefaction effects requires further discussion of performance objectives and related considerations. Procedures for conducting performance-based design analyses with a formal accounting of uncertainties have been developed for pinning analyses at bridge abutments (Ledezma and Bray, 2006) and for global bridge systems using nonlinear dynamic finite element analyses (Kramer et al., 2006, unpublished PEER report).

5. Summary remarks

Recommendations were presented herein for the seismic design of pile foundations for liquefaction effects using equivalent static BNWF analysis methods. Discussions were focused on two local subsystems for bridges: (1) pile groups in laterally spreading ground away from any approach embankments and (2) pile groups for approach embankment abutments where the restraining or “pinning” effects of the piles and bridge superstructure can be advantageous.

For pile groups embedded in large lateral spreads, equivalent static BNWF analyses with imposed free-field soil displacements and structural inertia forces reasonably matched results from centrifuge model tests and results from a suite of dynamic FE analyses. Guidelines for estimating and combining lateral spreading demands and inertia loads were derived from the suite of FE analyses.

For pile groups in approach embankment abutments, pinning forces from the piles and bridge superstructure can restrain the embankment against lateral spreading in the longitudinal direction. Coupling Newmark sliding block analyses with equivalent static BNWF pushover analyses provided reasonable estimates of the reductions in embankment displacements that were observed in centrifuge model tests of embankments with and without piles. Guidelines for performing these types of pinning analyses were presented.

Acknowledgments

Funding was provided by Caltrans under Contracts No. 59A0162 and 59A0392 and by the Pacific Earthquake Engineering Research (PEER) Center, through the Lifelines Program and the Earthquake Engineering Research Centers Program of the National Science Foundation, under Contract No. 2312001. Recent upgrades to the centrifuge were funded by NSF Award No. CMS-0086588 through the George E. Brown, Jr. Network for Earthquake Engineering Simulation (NEES). The contents of this paper do not necessarily represent a policy of either agency or endorsement by the state or federal government. The authors

appreciate the contributions of U. Gulerce and the Center for Geotechnical Modeling staff in performing the centrifuge tests, the valuable comments and discussions provided by I. M. Idriss, D. W. Wilson, A. Abghari, A. Perez-cobo, and T. Shantz over the duration of these studies, and the technical discussions with other PEER researchers studying liquefaction effects on bridges, including P. Arduino, S. Ashford, J. Bray, A. Elgamal, C. Ledezma, S. Kramer, G. Martin, and Z. Yang.

REFERENCES

- American Petroleum Institute (1993) Recommended practice for planning, design and constructing fixed offshore platforms. API RP 2A–WSD, 20th ed, American Petroleum Institute
- Boulanger RW, Kutter BL, Brandenburg SJ, Singh P, Chang D (2003) Pile foundations in liquefied and laterally spreading ground: Centrifuge experiments and analyses. Report UCD/CGM-03/01, Center for Geotechnical Modeling, University of California, Davis, 205 pp, <http://cgm.engineering.ucdavis.edu/>
- Boulanger RW, Brandenburg SJ (2004) Neutral plane solution for liquefaction-induced down-drag on vertical piles. Proc, Geotechnical Engineering for Transportation Projects, GSP 126, MK Yegian and E Kavazanjian, eds, ASCE, pp 403–410
- Boulanger RW, Tokimatsu K (2006) Geotechnical Special Publication No 145: Seismic Performance and Simulation of Pile Foundations in Liquefied and Laterally Spreading Ground. ASCE Press, Reston, VA, 321 pp
- Boulanger RW, Chang D, Gulerce U, Brandenburg SJ, Kutter BL (2006) Evaluating pile pinning effects on abutments over liquefied ground. Seismic Performance and Simulation of Pile Foundations in Liquefied and Laterally Spreading Ground, GSP 145, ASCE, pp 306–318
- Brandenburg SJ, Boulanger RW, Kutter BL, Chang D (2005) Behavior of pile foundations in laterally spreading ground during centrifuge tests. J. Geotech. Geoenviron. Eng. 131(11): 1378–1391
- Brandenburg SJ, Boulanger RW, Kutter BL, Chang D (2007a) Static pushover analyses of pile groups in liquefied and laterally spreading ground in centrifuge tests. J. Geotech. Geoenviron. Eng., ASCE, 133, in press
- Brandenburg SJ, Boulanger RW, Kutter BL, Chang D (2007b) Liquefaction-induced softening of load transfer between pile groups and laterally spreading crusts. J. Geotech. Geoenviron. Eng., ASCE 133(1): 91–103
- Bray JD, Travasarou T (2007) Simplified procedure for estimating earthquake-induced deviatoric slope displacements. J. Geotech. Geoenviron. Eng., ASCE 133(4): 381–392
- Caltrans (2006) Seismic Design Criteria, Version 1.4, June
- Chang D, Boulanger RW, Kutter BL, Brandenburg SJ (2005) Experimental observations of inertial and lateral spreading loads on pile groups during earthquakes. Earthquake Engineering and Soil Dynamics, GSP 133, ASCE
- Chang D, Boulanger RW, Brandenburg SJ, Kutter BL (2006) Dynamic analyses of soil–pile–structure interaction in laterally spreading ground during earthquake shaking. Seismic Performance and Simulation of Pile Foundations in Liquefied and Laterally Spreading Ground, GSP 145, ASCE, pp 218–229
- Chang D (2007) Inertial and lateral spreading demands on soil–pile–structure systems in liquefied and laterally spreading ground during earthquakes. PhD dissertation, University of California, Davis
- Cubrinovski M, Ishihara K (2006) Assessment of pile group response to lateral spreading by single pile analysis. Seismic Performance and Simulation of Pile Foundations in Liquefied and

- Laterally Spreading Ground, GSP 145, ASCE, pp 242–254
- Dobry R, Taboada V, Liu L (1995) Centrifuge modeling of liquefaction effects during earthquakes. Proc 1st Intl Conf on Earthquake Geotechnical Engineering, K Ishihara, ed, Tokyo, Japan, vol 3, pp 1291–1324
- Dobry R, Abdoun T, O'Rourke TD, Goh SH (2003) Single piles in lateral spreads: Field bending moment evaluation. *J. Geotech. Geoenviron. Eng.*, ASCE 129(10): 879–889
- Ledezma C, Bray JD (2006) A probabilistic design procedure that incorporates the pile-pinning effect in bridge foundations undergoing liquefaction-induced lateral spreading Fifth National Seismic Conf on Bridges and Highways, MCEER-06-SP09, Paper B22
- Liyanapathirana DS, Poulos HG (2005) Pseudostatic approach for seismic analysis of piles in liquefying soil. *J. Geotech. Geoenviron. Eng.*, ASCE 131(12): 1480–1487
- Malvick EJ, Kutter BL, Boulanger RW, Kulasingam, R (2006) Shear localization due to liquefaction-induced void redistribution in a layered infinite slope. *J. Geotech. Geoenviron. Eng.*, ASCE 132(10): 1293–1303
- Martin GR, March ML, Anderson DG, Mayes RL, Power MS (2002) Recommended design approach for liquefaction induced lateral spreads. Proc 3rd National Seismic Conf and Workshop on Bridges and highways, MCEER-02-SP04, Buffalo, NY
- Matlock H (1970) Correlations of design of laterally loaded piles in soft clay. Proc Offshore Technology Conf, Houston, vol 1, pp 577–594
- Newmark NM (1965) Effects of earthquakes on dams and embankments. *Geotechnique*, London, 15(2): 139–160
- Rollins KM, Gerber TM, Lane JD, Ashford SA (2005) Lateral resistance of a full-scale pile group in liquefied sand. *J. Geotech. Geoenviron. Eng.*, ASCE 131(1): 115–125
- Rollins KM, Strand SR (2006) Downdrag forces due to liquefaction surrounding a pile. Proc, 8th US National Conf on Earthquake Eng, San Francisco, CA, paper 1646
- Tokimatsu K, Asaka Y (1998) Effects of liquefaction-induced ground displacements on pile performance in the 1995 Hyogoken-Nambu earthquake. Special Issue of Soils and Foundations, Japanese Geotechnical Society, pp 163–177
- Tokimatsu K (2003) Behavior and design of pile foundations subjected to earthquakes. Proc, 12th Asian Regional Conf on Soil Mechanics and Geotechnical Engineering, Singapore, August 4th–8th
- Tokimatsu K, Suzuki H, Sato M (2005) Effects of inertial and kinematic interaction on seismic behavior of pile with embedded foundation. *Soil Dyn. Earthquake Eng.*, 25: 753–762
- Wilson DW, Boulanger RW, Kutter BL (2000) Observed seismic lateral resistance of liquefying sand. *J. Geotech. Geoenviron. Eng.* 126(10): 898–906
- Yang Z, Jeremic B (2002) Numerical analysis of pile behavior under lateral loads in layered elastic-plastic soils. *Intl. J. Numer. Anal. Meth. Geomech.*, 26: 1385–1406
- Yang Z, Elgamal A, Parra E (2003) Computational model for cyclic mobility and associated shear deformation. *J. Geotech. Geoenviron. Eng.*, ASCE 129(12): 1119–1127

CHAPTER 13

SEISMIC ANALYSIS AND DESIGN OF GEOTECHNICAL STRUCTURES

Susumu Iai and Tetsuo Tobita

Disaster Prevention Research Institute, Kyoto University, Japan

iai@geotech.dpri.kyoto-u.ac.jp; tobita@geotech.dpri.kyoto-u.ac.jp

Abstract. The paper discusses the emerging trends in seismic analysis and design of geotechnical structures. Soil consists of soil particles. The fundamental study on this aspect of soil has come to the stage where the results of the study can be readily incorporated as an essential part of seismic analysis of soil–structure systems. Geotechnical earthquake engineers and researchers are encouraged to look into this fundamental study. By expanding the concept of performance-based design, a paradigm shift can be achieved from construction-oriented to service-oriented approach. The service-oriented approach will open a new horizon for design and promote the holistic approach for providing better designed built-environment. Designing a large urban area against combined hazards, such as those caused by the Sumatra earthquake of 2004, poses a new challenge in seismic design. The approach that is most appropriate for a large urban area may be different from those used for the current practice design used for individual structure and should be newly developed. These emerging trends in seismic design have to be extensively studied and carefully applied in practice, especially for designing new and large geotechnical structures that have to meet the rapidly growing social and economic demands in Asia and those for redevelopment of urban areas around the world.

1. Introduction

Geotechnical structures typically consist of soil and structural parts such as buried structures (e.g. buried tunnels, box culverts, pipelines, and underground storage facilities), foundations (e.g. shallow and deep foundations and underground diaphragm walls), retaining walls (e.g. soil retaining and quay walls), pile-supported wharves and piers, earth structures (e.g. earth and rockfill dams and embankments), gravity dams, landfill and waste sites. Seismic performance of geotechnical structures is significantly affected by ground displacement. In particular, soil–structure interaction and effects of liquefaction play major roles and pose difficult problems for engineers.

Objective of this paper is to review how these problems have been dealt with in the recent development of seismic analysis and design. In the previous review (Iai, 1998), when the effective stress analysis began to be applied to seismic design in practice, it was decided best to begin by discussing the essential stress–strain behavior of soil under cyclic loading rather than going into the details in the mechanics of assemblage of soil particles. Almost a decade has passed since then. Extensive developments have been made in

seismic analysis of geotechnical works both in research and practice. It is about the time to explore the next level of knowledge in the discipline of geotechnical engineering. The time is ripe to discuss the fundamental aspect of mechanics of assemblage of soil particles as related to the soil behavior under cyclic loading among the geotechnical earthquake engineers and researchers. Thus, the paper begins by discussing this fundamental aspect of analysis. Some of the findings useful in practice of seismic analysis are also reviewed with respect to the seismic analyses of embankments, embedded structures and soil-pile systems.

The paper then discusses the emerging trends in the fundamental conceptual framework for seismic design of geotechnical structures. One trend is centered round the concept of performance. There is an important paradigm shift from structure-oriented to service-oriented approach. The other trend demands a new approach readily applicable for designing large urban area against combined hazards such as those due to tsunamis and earthquake motions. The paper concludes with a proposal that will be useful for designing new and large geotechnical works that have to meet the rapidly growing social and economic demands in Asia and those for redevelopment of urban areas around the world.

2. Assemblage of soil particles

A granular material consists of an assemblage of particles with contacts newly formed or disappeared, changing the micromechanical structures during macroscopic deformation. Among various constitutive models proposed for granular materials, a model that characterizes a structure of the assemblage of particles has capability to reproduce the distinctive behavior of granular materials due to that structure (Iai and Ozutsumi, 2005).

Stress in granular materials as defined for continuum is given by a certain average of contact forces between the particles. In assemblage of spherical particles, the contact force P_k can be partitioned into the direction of contact normal n_k and tangential direction t_k as (see Figure 13.1, left)

$$P_k = F n_k + S t_k \quad (13.1)$$

Macroscopic stress is given by taking an average over the contact forces within the representative volume element R having volume V as (e.g. Thornton, 1989)

$$\sigma_{kl} = \frac{2}{V} \sum_R r (F n_k n_l + S t_k n_l) \quad (13.2)$$

where r denotes radius of spheres.

Before taking the average over all the contacts of random orientation, a structure can be identified by systematically grouping the contacts according to the orientation. The first level of structures is identified by choosing those pairs of a contact force and a contact

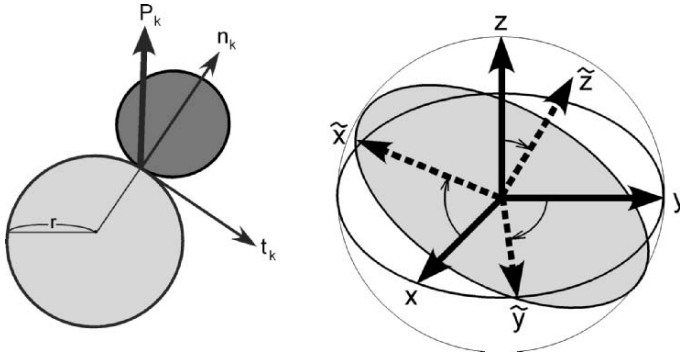


Fig. 13.1. Contact normal n_k , tangential direction t_k and contact force P_k defined at particle contact (left) and virtual plane of two dimensional shear mechanism defined by local coordinate indicated by the broken line vectors (right) (Iai and Ozutsumi, 2005)

normal that are parallel to a plane (Iai, 1993). Assemblage of those pairs constitutes a two dimensional mechanism and hereafter called “virtual two dimensional mechanism.” In order to identify the structure of the virtual two dimensional mechanism, the local coordinates \tilde{x} , \tilde{y} , \tilde{z} are introduced by taking \tilde{z} axis normal to the plane and \tilde{y} axis parallel to the x - y plane of the reference frame that is defined by the coordinates x , y , z (see Figure 13.1, right).

The second level of structures is identified within the virtual two dimensional mechanism by systematically grouping the contacts according to the orientation relative to \tilde{x} axis. For convenience, the orientation ranging from 0 to $\pi/2$ relative to \tilde{x} axis is divided into I sets of zones, each ranging from $(\omega_i - \Delta\omega/2)/2$ to $(\omega_i + \Delta\omega/2)/2$ for $i = 1, \dots, I$, where

$$\omega_i = (i - 1)\Delta\omega \tag{13.3}$$

$$\Delta\omega = \pi/I \tag{13.4}$$

Contact normal $\tilde{n}_k^{(i)}$ is taken in the plane as a representative direction with an angle $\omega_i/2$ relative to \tilde{x} axis. By systematically identifying and combining the couples of contacts that have the contact normals perpendicular to each other, the structure of the stress contribution $\tilde{\sigma}_{kl}$ from the virtual two dimensional mechanism is identified as follows (Iai, 1993):

$$\tilde{\sigma}_{kl} = \tilde{p}\delta_{kl} + \sum_{i=1}^I \left(\tilde{q}_F^{(i)} \left\langle \tilde{n}_k^{(i)}, \tilde{n}_l^{(i)} \right\rangle + \tilde{q}_S^{(i)} \left\langle \tilde{t}_k^{(i)}, \tilde{n}_l^{(i)} \right\rangle \right) \Delta\omega \tag{13.5}$$

where δ_{ij} denotes Kronecker delta and

$$\left\langle \tilde{n}_k^{(i)}, \tilde{n}_l^{(i)} \right\rangle = \tilde{n}_k^{(i)}\tilde{n}_l^{(i)} - \tilde{n}_k^{(i+I)}\tilde{n}_l^{(i+I)} \tag{13.6}$$

$$\left\langle \tilde{t}_k^{(i)}, \tilde{n}_l^{(i)} \right\rangle = \tilde{t}_k^{(i)}\tilde{n}_l^{(i)} - \tilde{t}_k^{(i+I)}\tilde{n}_l^{(i+I)} = \tilde{t}_k^{(i)}\tilde{n}_l^{(i)} + \tilde{n}_k^{(i)}\tilde{t}_l^{(i)} \tag{13.7}$$

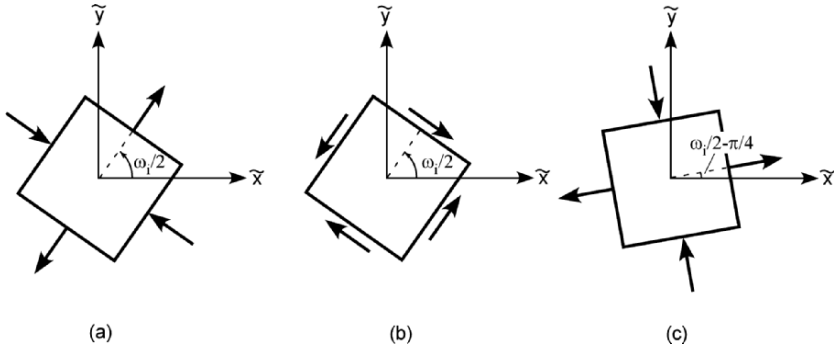


Fig. 13.2. Stress component in the direction of $\omega_i/2$ relative to \tilde{x} axis; (a) biaxial shear $\langle \tilde{n}_k^{(i)}, \tilde{n}_l^{(i)} \rangle$, (b) simple shear $\langle \tilde{t}_k^{(i)}, \tilde{n}_l^{(i)} \rangle$, (c) biaxial shear with additional rotation of $-\pi/4 \langle \tilde{n}_k^{(i-1/2)}, \tilde{n}_l^{(i-1/2)} \rangle$

The scalars \tilde{p} , $\tilde{q}_F^{(i)}$, $\tilde{q}_S^{(i)}$ in Eq. (13.5) represent the stress contributions obtained by an average of contact forces with respect to the isotropic, biaxial shear and simple shear mechanisms, where $\tilde{q}_F^{(i)}$ and $\tilde{q}_S^{(i)}$ are defined per unit ω . In particular, the biaxial shear due to the normal component of contact forces F is given by Eq. (13.6), the simple shear due to the tangential component of contact forces S given by Eq. (13.7) as shown in Figure 13.2(a) and (b). Since biaxial shear and simple shear are indistinguishable in the tensor representation except for the difference in the orientation of $\pi/4$ as shown in Figure 13.3(b) and (c), the stress contribution of a virtual two dimensional mechanism in Eq. (13.5) is written as

$$\tilde{\sigma}_{kl} = \tilde{p}\delta_{kl} + \sum_{i=1}^I \tilde{q}^{(i)} \langle \tilde{t}_k^{(i)}, \tilde{n}_l^{(i)} \rangle \Delta\omega \quad (13.8)$$

where

$$\tilde{q}^{(i)} = \tilde{q}_F^{(i-1/2)} + \tilde{q}_S^{(i)} \quad (13.9)$$

Although the tensor $\langle \tilde{t}_k^{(i)}, \tilde{n}_l^{(i)} \rangle$ represents simple shear and called “virtual simple shear mechanism,” formation of columnar structure in the assemblage of particles (e.g. Oda, 1974; Oda et al., 1985) indicates that the contributions from the couples due to normal components of contact forces $\tilde{q}_F^{(i-1/2)}$ is predominant in the shear stress contributions $\tilde{q}^{(i)}$. In fact, Eq. (13.8) can be rewritten in terms of “virtual biaxial shear mechanisms” as

$$\tilde{\sigma}_{kl} = \tilde{p}\delta_{kl} + \sum_{i=1}^I \tilde{q}^{(i)} \langle \tilde{n}_k^{(i-1/2)}, \tilde{n}_l^{(i-1/2)} \rangle \Delta\omega \quad (13.10)$$

In this paper, Eq. (13.8) with a term “virtual simple shear mechanism” will be used in order to maintain the consistency with those used in the previous papers (Towhata and Ishihara, 1985b; Iai et al., 1992a). The concept of the model, however, is better described by Eq. (13.5), where the couples of normal components of contact forces are explicitly written.

In order to describe the macroscopic stress–strain relationship of a granular material, the stress contributions in Eq. (13.8) should be defined as a function of macroscopic strain field ε_{kl} . As an assumption of the simplest in its kind, the isotropic stress contribution \tilde{p} is defined as a function of

$$\varepsilon = \delta_{mn}(\varepsilon_{mn} - \varepsilon_0\delta_{mn}) \tag{13.11}$$

and each virtual simple shear stress contribution $\tilde{q}^{(i)}$ is defined as a function of

$$\tilde{\gamma}^{(i)} = \left\langle \tilde{t}_m^{(i)}, \tilde{n}_n^{(i)} \right\rangle (\varepsilon_{mn} - \varepsilon_0\delta_{mn}) = \left\langle \tilde{t}_m^{(i)}, \tilde{n}_n^{(i)} \right\rangle \varepsilon_{mn} \tag{13.12}$$

where the term $\varepsilon^{0\delta_{mn}}$ in the right hand side of Eqs. (13.11) and (13.12) represents the volumetric strain tensor due to dilatancy. The scalar $\tilde{\gamma}^{(i)}$ defined in Eq. (13.12) is the projection of macroscopic strain field into the direction of virtual simple shear mechanism $\left\langle \tilde{t}_k^{(i)}, \tilde{n}_l^{(i)} \right\rangle$ and called “virtual simple shear strain.”

The incremental stress–strain relation is obtained in the similar manner as described above and is given by

$$d\tilde{\sigma}_{kl} = d\tilde{p}\delta_{kl} + \sum_{i=1}^I d\tilde{q}^{(i)} \left\langle \tilde{t}_k^{(i)}, \tilde{n}_l^{(i)} \right\rangle \Delta\omega \tag{13.13}$$

The incremental stress contributions are given by

$$d\tilde{p} = \tilde{K}_{L/U}d\varepsilon \tag{13.14}$$

$$d\tilde{q}^{(i)} = \tilde{G}_{L/U}^{(i)}d\tilde{\gamma}^{(i)} \tag{13.15}$$

where the loading (L) and unloading (U) for the isotropic and virtual simple shear mechanisms are defined by the signs of $d\varepsilon$ and $d\tilde{\gamma}^{(i)}$, respectively. From Eqs. (13.11) through (13.15), the incremental constitutive equation is given by

$$d\tilde{\sigma}_{kl} = \tilde{D}_{klmn} d(\varepsilon_{mn} - \varepsilon_0\delta_{mn}) \tag{13.16}$$

$$\tilde{D}_{klmn} = \tilde{K}_{L/U}\delta_{kl}\delta_{mn} + \sum_{i=1}^I \tilde{G}_{L/U}^{(i)} \left\langle \tilde{t}_k^{(i)}, \tilde{n}_l^{(i)} \right\rangle \left\langle \tilde{t}_m^{(i)}, \tilde{n}_n^{(i)} \right\rangle \Delta\omega. \tag{13.17}$$

By superposing these two dimensional mechanisms over J sets of planes, each with a solid angle of $\Delta\Omega^{(j)}$, covering a unit sphere, the macroscopic stress–strain relationship

in the three dimensional space is obtained as follows:

$$\sigma_{kl} = p\delta_{kl} + \frac{1}{4\pi} \sum_{j=1}^J \sum_{i=1}^I q^{(ij)} \left\langle t_k^{(ij)}, n_l^{(ij)} \right\rangle \Delta\omega \Delta\Omega^{(j)} \tag{13.18}$$

$$d\sigma_{kl} = D_{klmn} d(\varepsilon_{mn} - \varepsilon_0 \delta_{mn}) \tag{13.19}$$

$$D_{klmn} = K_{L/U} \delta_{kl} \delta_{mn} + \frac{1}{4\pi} \sum_{j=1}^J \sum_{i=1}^I G_{L/U}^{(ij)} \left\langle t_k^{(ij)}, n_l^{(ij)} \right\rangle \left\langle t_m^{(ij)}, n_n^{(ij)} \right\rangle \Delta\omega \Delta\Omega^{(j)} \tag{13.20}$$

$$dp = K_{L/U} d\varepsilon \tag{13.21}$$

$$dq^{(ij)} = G_{L/U}^{(ij)} d\gamma^{(ij)} \tag{13.22}$$

where $n_k^{(ij)}$ and $t_k^{(ij)}$ denote the contact normal $\tilde{n}_k^{(i)}$ and tangential direction $\tilde{t}_k^{(i)}$ defined in the j -th plane and the loading (L) and unloading (U) for the isotropic and virtual simple shear mechanisms are defined by the signs of $d\varepsilon$ and $d\gamma^{(ij)} = \left\langle t_m^{(ij)}, n_n^{(ij)} \right\rangle \varepsilon_{mn}$, respectively.

When the inherent soil fabric is assumed to be isotropic, the virtual simple shear mechanism is defined by a hyperbolic relation under a constant confining stress as follows:

$$q^{(ij)} = \frac{\gamma^{(ij)} / \gamma_v}{1 + |\gamma^{(ij)} / \gamma_v|} q_v \tag{13.23}$$

where q_v and γ_v are the parameters for defining the hyperbolic relationship and called the virtual shear strength and virtual reference strain. Substitution of Eq. (13.23) into Eq. (13.22) yields

$$G_L^{(ij)} = \frac{1}{(1 + |\gamma^{(ij)} / \gamma_v|)^2} \frac{q_v}{\gamma_v} \tag{13.24}$$

Hysteresis characteristics are assigned by appropriately specifying the tangential stiffness for unloading and reloading by using an extended Masing rule (Iai et al., 1990, 1992a, b) for representing realistic behavior of sands such as those given by Hardin and Drnevich (1972). If no memory is given to the set of $q^{(ij)}$ and other Masing variables, the material becomes isotropic again once the applied stress is removed. The anisotropy in inherent soil fabric can be introduced by specifying the virtual shear strength and virtual reference strain as $q_v^{(ij)}, \gamma_v^{(ij)}$ that are specific to i -th mechanism in j -th plane.

The parameters q_v and γ_v can be determined by the shear modulus at small strain level and failure criterion of soil (Iai et al., 1992a; Iai and Ozutsumi, 2005). In particular, the shear modulus at small strain level is given by

$$G_m = G_{ma} |p'/p'_a|^{m_G} \quad (13.25)$$

where G_{ma} are the shear modulus measured at laboratory with an effective mean stress p'_a . The power index m_G typically takes the value of 0.5 for sand. The failure criterion for sand is often approximated by Mohr–Coulomb criterion given by

$$\frac{\sigma'_1 - \sigma'_3}{2} = \left(c \cot \phi_f - \frac{\sigma'_1 + \sigma'_3}{2} \right) \sin \phi_f \equiv \tau_{\max} \quad (13.26)$$

where σ'_1 and σ'_3 denote major and minor principal stresses, c and ϕ_f denote cohesion and internal friction angle, and τ_{\max} denotes shear strength. Other failure criteria such as Tresca, von Mises, extended Tresca and Drucker-Prager can also be introduced. Any of these failure criteria can be used to identify the virtual shear mechanism parameter q_v and γ_v . The results take the following general form:

$$\begin{aligned} q_v &\propto \tau_{\max} \\ \gamma_v &\propto \tau_{\max}/G_m \end{aligned} \quad (13.27)$$

The coefficients are given as an integral of direction components of multiple mechanism. See Iai and Ozutsumi (2005) for details.

With the dilatancy $d\varepsilon_0$ in Eq. (13.19) specified as a function of cumulative plastic shear work (Towhata and Ishihara, 1985a; Iai et al., 1992a), the strain space multiple mechanism model has ten primary parameters as shown in Table 13.1; two specify elastic properties of soil, two specify plastic shear behavior, and the rest control dilatancy.

As summarized in Eqs. (13.18) through (13.22) the strain space multiple mechanism model characterizes a twofold structure of an assemblage of particles in granular materials. The first structure is represented by J sets of virtual two dimensional mechanisms, the second by I sets of virtual simple shear mechanisms of one dimensional nature. Second order fabric tensors are naturally incorporated in the direct stress–strain relationship

Table 13.1. Model parameters of strain space multiple mechanism model (Iai et al., 1992a)

Symbol	Type of mechanism	Parameter designation
K_{ma}	Elastic Volumetric	Rebound modulus
G_{ma}	Elastic Shear	Shear modulus
ϕ_f	Plastic Shear	Internal friction angle
h_{\max}	Plastic Shear	Upper bound for hysteretic damping factor
ϕ_p	Plastic Dilatancy	Phase transformation angle
p_1	Plastic Dilatancy	Parameter controlling initial phase of cumulative dilatancy
p_2	Plastic Dilatancy	Parameter controlling final phase of cumulative dilatancy
w_1	Plastic Dilatancy	Parameter controlling overall cumulative dilatancy
S_1	Plastic Dilatancy	Parameter controlling ultimate limit of dilatancy
c_1	Plastic Dilatancy	Parameter controlling threshold limit for dilatancy

in Eq. (13.18), fourth order fabric tensors in the incremental constitutive equations in Eqs. (13.19) and (13.20) (Iai, 1993). Evolution of these fabric tensors is governed by the collective effects of the multiple mechanisms specified by Eqs. (13.21) and (13.22). An example of evolution of fabric tensors during rotation of principal stress axes can be found in Iai et al. (1994).

3. Some findings on seismic analysis

Some of the findings useful in practice of seismic analysis are reviewed with respect to the seismic analyses of soil under initial deviator stress, embankments, embedded structures and retaining walls as follows. These findings can be recognized as the priority areas for further study in seismic analysis.

3.1. CYCLIC DEFORMATION OF SOIL UNDER INITIAL DEVIATOR STRESS

The effect of dilatancy, especially induced by the stress path in the vicinity of failure line, governs the gradual or rapid increase in strain amplitude during cyclic loading. For undrained cyclic loading tests of soil with lateral normal strain constrained, usually called liquefaction tests, primary focus of the strain components is directed on shear strain amplitude. Typical results of measured (Matsuo et al., 2000) and computed stress–strain and stress path are shown in Figure 13.3 (Ozutsumi, 2003). In this figure, conventional model is based on the algorithm that dilatancy is defined as a function of cumulative shear strain energy as mentioned earlier. The modified model is based on the algorithm that dilatancy is defined as a function of partial components of cumulative shear strain energy, in which the contributions from the shear strain energy from the stress path beyond the phase transformation line (i.e. dilatative regime) is intentionally not taken into account. This minor modification in the algorithm for computing dilatancy does not affect the computed stress–strain and stress path for conventional liquefaction tests as shown in Figure 13.3.

For stress–strain and stress path for lateral normal strain unconstrained but with keeping the axial stress difference constant, that is often the case with two or three dimensional deformation of soil–structure systems, the effect of dilatancy on the strains becomes significant as shown in Figure 13.4. In fact, the difference in the computed normal strain component from the conventional and modified algorithms are almost in two order in magnitude. Further parameter study suggests that the algorithm best describes the existing laboratory data when the algorithm does not take into account the shear strain energy for stress path beyond the line between the phase transformation line and the failure line. Although these findings are tied down to the specific form of constitutive equations, these findings can be generalized into a statement that dilatancy in the vicinity of failure line should be carefully studied in the development of soil model.

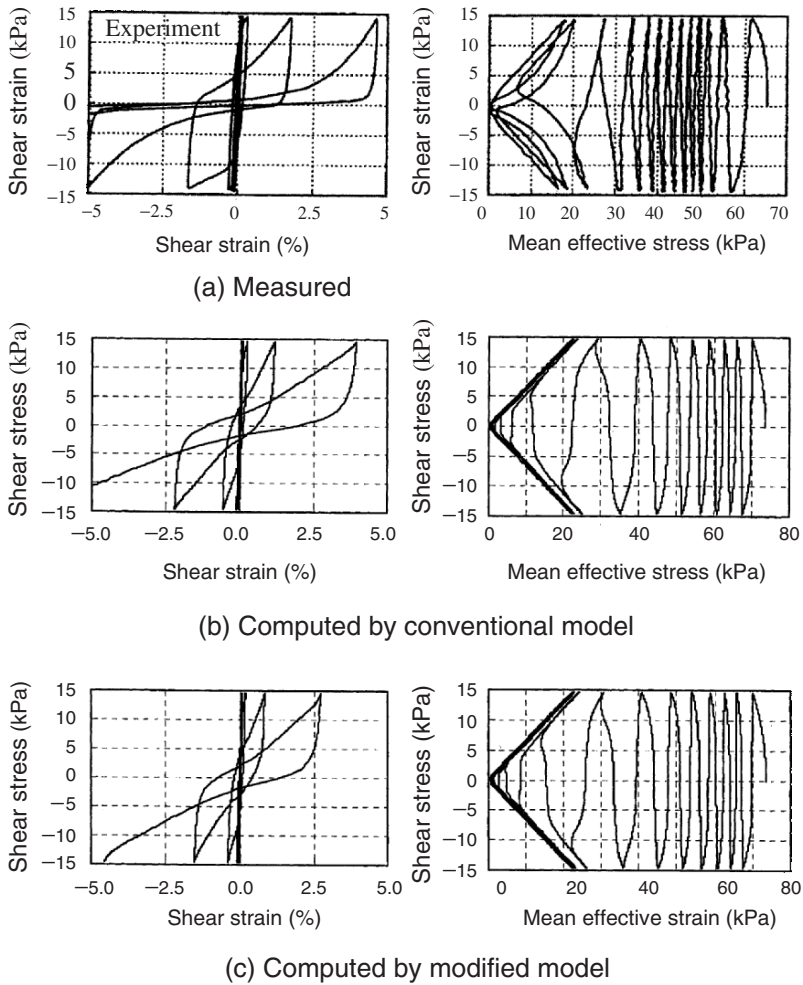


Fig. 13.3. Stress–strain and stress path for lateral normal strain constrained (Ozutsumi, 2003)

3.2. EFFECT OF RESIDUAL STRENGTH OF SOIL ON SEISMIC SETTLEMENTS OF EMBANKMENTS

Many types of river dikes and embankments have been analyzed through the strain space multiple shear mechanism model and mostly successful in reproducing the varying degree of crest settlements depending on the geotechnical condition of foundation (Ozutsumi et al., 2002; Tobita et al., 2006a). However, recent experience in analysis of one particular type of river dike, the dike No.1 of the Shiribeshi-Toshibeshi river, Hokkaido,

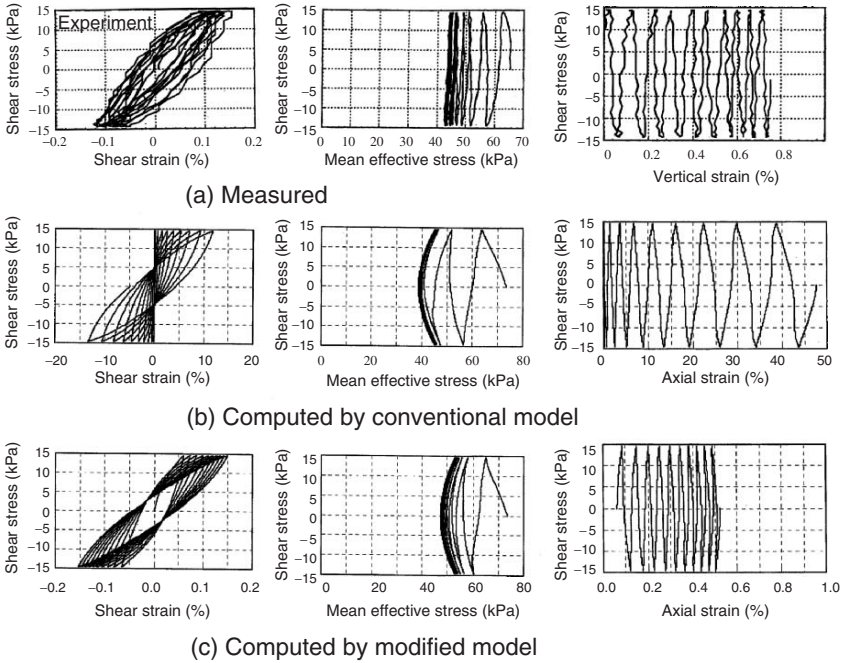


Fig. 13.4. Stress–strain and stress path for lateral normal strain unconstrained with constant axial stress difference (Ozutsumi, 2003)

Japan, during 1993 Hokkaido-Nanseioki earthquake of Richter magnitude 7.8, poses a new challenge. This dike was heavily damaged during the earthquake as shown in Figure 13.5. The dike was constructed on loosely deposited sandy deposit with a thickness of about 5 m as shown in Figure 13.6.

The results of the analysis typically show a pattern of deformation such as shown in Figure 13.7. However, the degree of deformation is found to be excessively sensitive to the type of algorithm and the details in the computation scheme for time integration. When the modification in the algorithm for computing dilatancy discussed earlier is adopted with improved integration scheme, the result shows very small settlements as shown in Case A in Figure 13.8.

Since the shear strains induced in the foundation soil are in the order of several tens of percent, effect of residual strength S_{uS} are studied in addition to the effect of cyclic mobility. The results are shown in Table 13.2 and Figure 13.8. The best fit to the measured crest settlement is given for Case D2 but the residual strength S_{uS} is apparently very low. Cases C1 through C4 are more or less in the range of those reported in the literature based on the laboratory tests. Further study in this aspect of soil may be necessary.



Fig. 13.5. Damage to a river dike at the Shiribeshi-toshibetsu river, Hokkaido, Japan, during Hokkaido-Nansei-oki earthquake of 1993

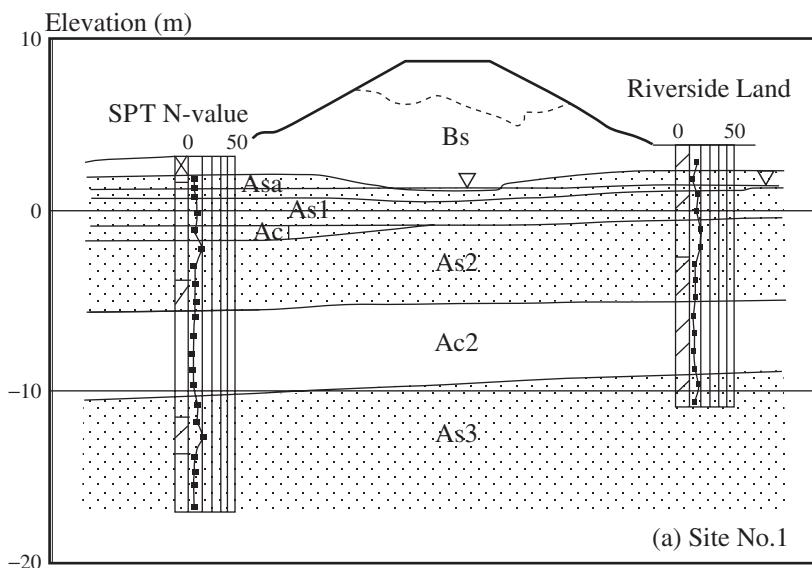


Fig. 13.6. Cross section of the river dike

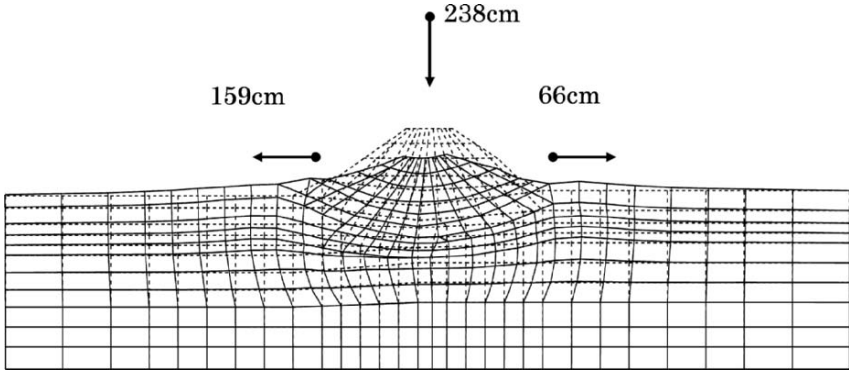


Fig. 13.7. Computed deformation of river dike (Ozutsumi et al., 2002)

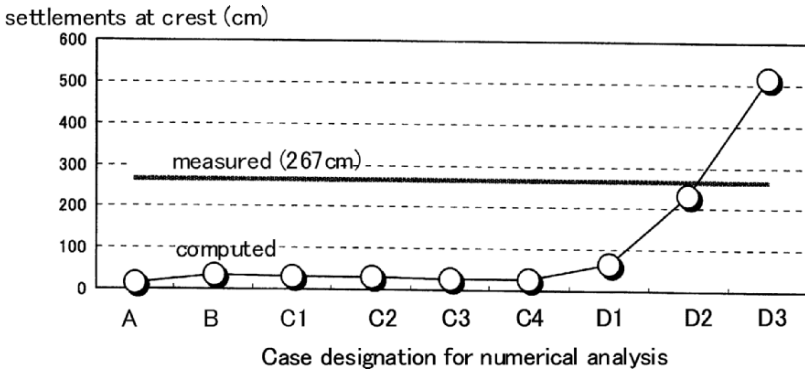


Fig. 13.8. Computed settlements at crest

Table 13.2. Case designation for numerical analysis

Case no.	S_{us} (kPa) for $A_{sa}-A_{ca}$	S_{us} (kPa) for A_{s1}	S_{us} (kPa) for A_{s2}
A	∞	∞	∞
B	0.1	180	50
C1	25	180	50
C2	50	180	50
C3	75	180	50
C4	100	180	50
D1	0.1	100	25
D2	0.1	25	7
D3	0.1	15	5

3.3. EFFECT OF INCREASE IN EARTH PRESSURES ON BURIED STRUCTURES

Analysis of a buried RC structure was also performed (Wang et al., 2006). The cross section of a model RC structure for centrifuge tests is shown Figure 13.9. The effective stress analysis using the finite element mesh shown in Figure 13.10 resulted in the good agreement with the measured response of soil–structure system as shown in Figure 13.11.

The computed results, in particular, showed gradual increase in the lateral earth pressures in association with the increase in excess pore water pressure, and finally reached to the average level that coincides with the initial vertical total stress. The resulting deformation of RC structure, as shown in Figure 13.12, indicates the important failure mechanism, in that the plastic hinges first appear in the corners of the RC cross section, and gradually induces the plastic region towards the center of the side walls due to the cyclic effects as well as the gradual increase in lateral earth pressure mentioned earlier. This gradual increase in the lateral earth pressure should never be ignored in design of underground structures.

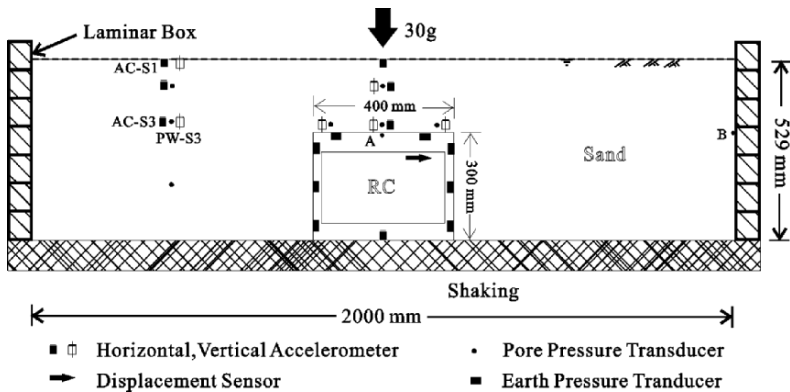


Fig. 13.9. Cross section of buried structure model for centrifuge test

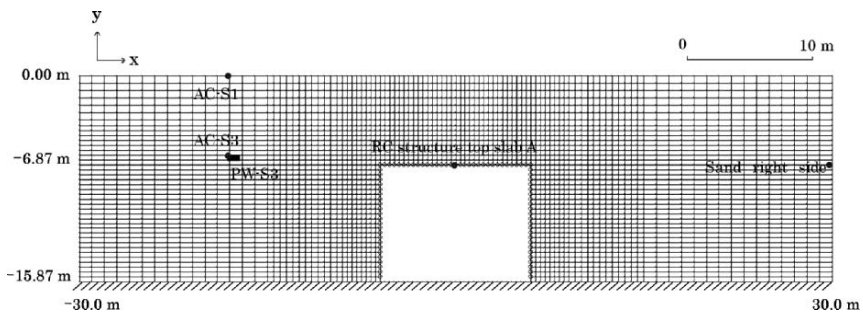


Fig. 13.10. Finite element mesh for analysis

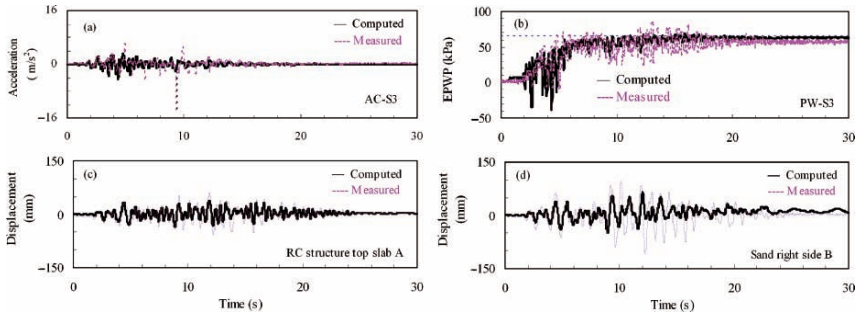


Fig. 13.11. Computed and measured responses of buried RC structure (Wang et al., 2006)

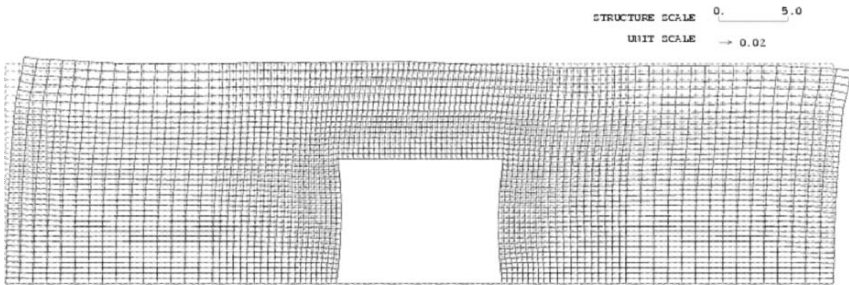


Fig. 13.12. Computed residual deformation of buried RC structure (Wang et al. 2006)

3.4. EFFECT OF INITIAL STRESS IN THE BACKFILL SOIL ON RETAINING WALLS

Initial stress conditions for seismic analysis play a significant role. An example is shown on a sheet pile quay wall (Kameoka and Iai, 1993). In this study, initial earth pressures before the earthquake were varied by applying forced displacements between anchor and sheet pile wall as shown in Figure 13.13. The results of the seismic analysis, shown in Figure 13.14, indicate that higher initial earth pressure applied on the wall results in smaller seismic bending moments and displacements. Based on these findings, it is recommended that the initial conditions for sheet pile quay walls be computed by step-by-step gravity analysis, closely following the actually construction sequence (Miwa et al., 2003).

4. Performance-based design

The 1995 Hyogoken-Nambu earthquake drastically changed the affirmative recognition of the seismic design practice in Japan. The peak accelerations during this earthquake ranged from 0.5 to 0.8 g, causing catastrophic damage to highly developed and mod-

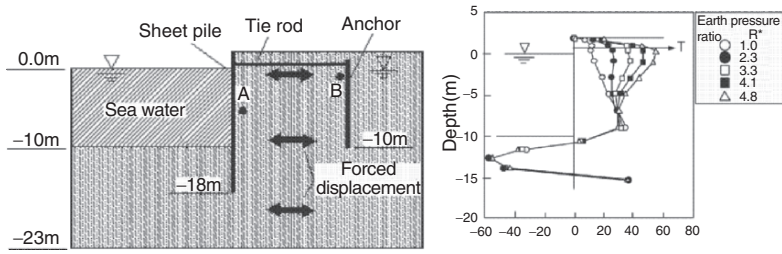


Fig. 13.13. Cross section of quay walls (left) and earth pressure distribution given as initial condition (right)

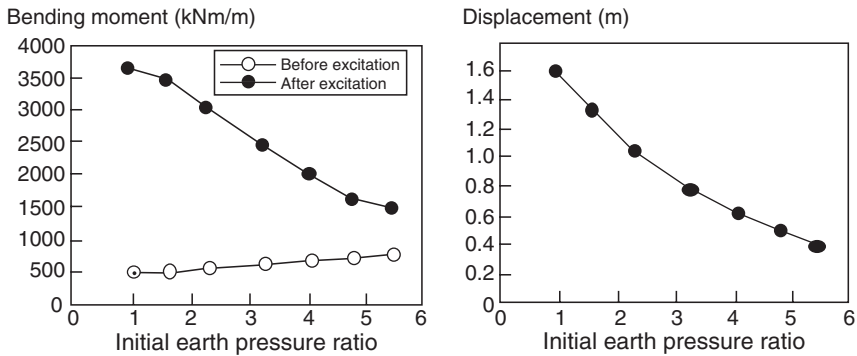


Fig. 13.14. Computed earthquake-induced bending moment and displacement (Kameoka and Iai, 1993)

ernized urban areas as shown in Figures 13.15 and 13.16. This event posed a challenge in earthquake engineering and motivated the adoption of performance-based design in practice.

The goal is to overcome the limitations present in conventional seismic design. Conventional building code seismic design is based on providing capacity to resist a design seismic force, but it does not provide information on the performance of a structure when the limit of the force-balance is exceeded. If we demand that limit equilibrium not be exceeded in conventional design for the relatively high intensity ground motions associated with a very rare seismic event, the construction/retrofitting cost will most likely be too high. If force-balance design is based on a more frequent seismic event, then it is difficult to estimate the seismic performance of the structure when subjected to ground motions that are greater than those used in design.

In performance-based design, appropriate levels of design earthquake motions must be defined based on its variability and acceptable levels of structural damage must be clearly identified. Two levels of earthquake motions are typically used as design reference motions.



Fig. 13.15. Damage to steel piles for pile-supported-wharf in Kobe Port during 1995 Hyogoken-Nambu earthquake



Fig. 13.16. Damage to an access to a bridge at Kobe-Nishinomiya during 1995 Hyogoken-Nambu earthquake

Table 13.3. Acceptable level of damage in performance-based design*

Acceptable level of damage	Structural	Operational
Degree I: Serviceable	Minor or no damage	Little or no loss of serviceability
Degree II: Repairable	Controlled damage**	Short-term loss of serviceability***
Degree III: Near collapse	Extensive damage in near collapse	Long-term or complete loss of serviceability
Degree IV: Collapse****	Complete loss of structure	Complete loss of serviceability

* Considerations: Protection of human life and property, functions as an emergency base for transportation, and protection from spilling hazardous materials, if applicable, should be considered in defining the damage criteria in addition to those shown in this table.

** With limited inelastic response and/or residual deformation.

*** Structure out of service for short to moderate time for repairs.

**** Without significant effects on surroundings.

Table 13.4. Performance grades S, A, B and C

Performance grade	Design earthquake	
	Level 1 (L1)	Level 2 (L2)
Grade S	Degree I: Serviceable	Degree I: Serviceable
Grade A	Degree I: Serviceable	Degree II: Repairable
Grade B	Degree I: Serviceable	Degree III: Near collapse
Grade C	Degree II: Repairable	Degree IV: Collapse

The acceptable level of damage is specified according to the specific needs of the users/owners of the facilities and may be defined on the basis of the acceptable level of structural and operational damage given in Table 13.3. The structural damage category in this table is directly related to the amount of work needed to restore the full functional capacity of the structure and is often referred to as direct loss due to earthquakes. The operational damage category is related to the amount of work needed to restore full or partial serviceability. Economic losses associated with the loss of serviceability are often referred to as indirect losses.

Once the design earthquake levels and acceptable damage levels have been properly defined, the required performance of a structure may be specified by the appropriate performance grade S, A, B or C defined in Table 13.4. In performance-based design, a structure is designed to meet these performance grades.

5. Emerging trends in design

Emerging trends in design further developed along the line of performance-based design may be summarized as follows.

5.1. FROM DESIGN-FOR-CONSTRUCTION TO DESIGN-FOR-PERFORMANCE

The concept of operational damage introduced in the performance-based design plays a significant role in emerging trends in design. In conventional design, construction of a good geotechnical work was the sole objective of design. In the emerging trends in design, providing appropriate function and service rather than a physical construction becomes the final objective of design. There is an important paradigm shift from structure-oriented to performance-oriented approach.

5.2. FROM STANDARDIZED-DESIGN TO SITE-SPECIFIC-DESIGN

Conventional design relied on the standardized earthquake loads such as those specified by design spectra and seismic coefficient. If needed, variability of these loads was considered in a framework such as reliability design methodology but the loads were standardized. In the emerging trends in design, site-specific earthquake motions are used for achieving the optimum design best suited for the construction site.

5.3. FROM ANALYSIS-OF-STRUCTURAL/FOUNDATION PARTS TO ANALYSIS-OF-SOIL-STRUCTURE SYSTEM

Conventional design was based on the analysis of structural or soil part idealized to fit to the simplified methodologies. In the emerging trends in design, analysis of whole soil-structure system and identification of failure modes are the bases.

In fact, these emerging trends in design are incorporated in the International Standard (ISO) on seismic actions for designing geotechnical works (Iai, 2005).

5.4. FURTHER EMERGING TRENDS: PRODUCING SERVICE

The discussions on these emerging trends in design can be extended further. By expanding the concept of performance-oriented approach, a new horizon of design will become apparent. Instead of trying to reduce the cost for construction, the new objective of design will be to increase the service produced by the designing process. Instead of constructing buildings and producing goods and works based on the concept of production efficiency through mass production process and ending up producing unnecessary products and infrastructures, the new objective of design will be to offer performance and service required by the society.

The concept of offering performance and service further triggers us to have a new look at civil engineering structures. Instead of trying to optimize individual structures for

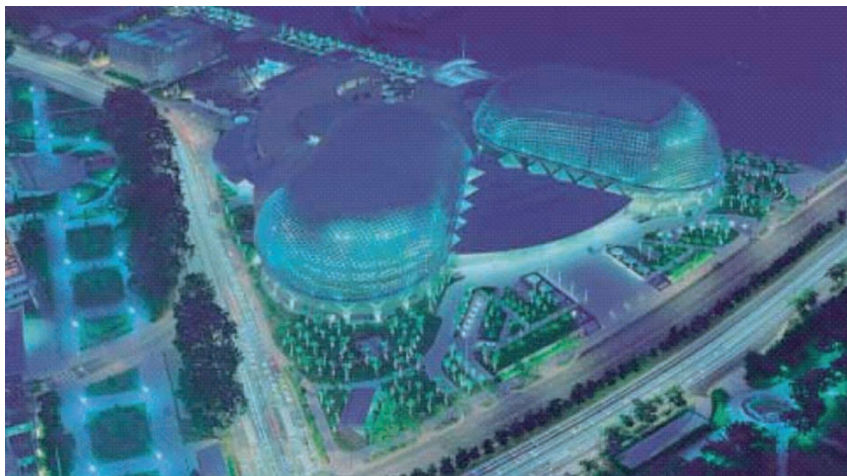


Fig. 13.17. Large waterfront development, Singapore (Penta Ocean)

construction, we can define a system consisting of a group of structures and try to optimize it. The structural system can be as large as an entire urban system. In this case, we can look at this system as built environment rather than social infrastructure. Once we establish the function and objective of the built environment, then we can further expand our design approach for natural environment and the interaction between the built and natural environments. Instead of using conventional materials such as steel and concrete, new materials and intelligent technologies may offer a completely new performance and service. Instead of trying to maintain the old infrastructure based on life-cycle management, we can renovate and redevelop those infrastructures to achieve required and enhanced performance and service. Based on these emerging trends, objective of the seismic design may be transformed into the new objective to create a space of safety and security in the decade to come (see Figure 13.17).

The approaches and new concepts in design discussed above will be useful for designing new and large geotechnical works that have to meet the rapidly growing social and economic demands in Asia and those for redevelopment of urban areas around the world.

6. Designing large urban areas against combined hazards

The extreme event of tsunamis, such as those caused by the Sumatra earthquake of 2004 to the Sumatra area (Tobita et al., 2006b) might not be easy to cope with the design strategy discussed in the previous chapter. The height of the tsunamis ranged from 5 to 30 m. Over a 3 km inland from the coast line was affected by the tsunami. The coastal area, as shown in Figure 13.18, was washed away due to the combined effects of liquefaction during the earthquake and erosion by the tsunami. Long distance such as tens of kilometers should be covered for appropriate vulnerability assessment.



Fig. 13.18. Coastal area of Banda Aceh, Indonesia, before (above) and after (below) the Indian Ocean-Sumatra earthquake of 2004 (after Quickbird)

One way to cope with this is to use a simplified design charts. In fact, sets of design charts were developed based on a series of parametric studies on embankments and gravity structures (Higashijima et al., 2006). These design charts are incorporated in a spread sheet format. Input data required are: (1) basic parameters defining the cross section of structures, (2) geotechnical conditions as represented by SPT N-values and (3) earthquake data, as represented by wave form, peak ground acceleration, or distance. Alternative way to cope with this extreme event is to set up a reasonable strategy to evacuate and

recovery. In order to enhance the quality of evacuation, education, early warning system and better city planning can be beneficial. Constructing a reasonable set of evacuation lands with enough height may be also useful. These evacuation lands may be utilized for either community facilities, parks or religious purpose facilities for daily use of residents. In this way of combining the multiple objectives of the facilities instead of pursuing the sole objective, better planning for mitigating disasters may be achieved.

Securing the robust evacuation route is also important. In the example of the district shown in Figure 13.18, at least one bridge should be robust enough to allow evacuation immediately after the earthquake. In the highly developed urban area, fires, collapse of buildings and other associated events that close the evacuation route must be evaluated for better planning of evacuation.

Early recovery of the damaged urban areas should also be well planned. Emergency base for recovery, hospitals, and other important facilities should be robust enough to be functional in the extreme event.

7. Conclusions

The review of recent developments in seismic analysis and discussions on the emerging trends in design may be summarized as follows:

- (1) Soil consists of soil particles. The fundamental study on this aspect of soil has come to the stage where the results of the study can be readily incorporated as an essential part of seismic analysis of soil–structure systems. Geotechnical earthquake engineers and researchers are encouraged to look into this fundamental study because new knowledge is always learned by going back to the fundamentals.
- (2) Recent seismic analysis indicates that (i) dilatancy induced by the stress path in the vicinity of failure line should be carefully studied and incorporated into the soil model, (ii) residual strength of soil may play significant role in inducing crest settlements of river dikes, (iii) earth pressure increase induced by the excess pore water pressure rise should be considered for designing buried structures and (iv) initial stress conditions plays significant role in seismic behavior of sheet pile walls.
- (3) In conventional design, construction of a good geotechnical work was the sole objective of design. In the emerging trends in design, providing appropriate function and service rather than a physical construction becomes the final objective of design. There is an important paradigm shift from structure-oriented to performance-oriented approach. Conventional design relied on the standardized approach. If needed, variability in these standardized values was considered in a framework such as reliability design methodology in a standardized manner. In the emerging trends in design, site-specific approach is adopted for achieving the optimum design best suited for the construction site. Conventional design was based on the analysis of structural or soil part idealized to fit to the simplified methodologies.

In the emerging trends in design, analysis of whole soil–structure system and identification of failure modes are the bases.

- (4) The discussions on these emerging trends in design can be extended further. By expanding the concept of performance-oriented approach, a new horizon of design will become apparent. Instead of trying to reduce the cost for construction, the new objective of design will be to increase the service produced by the designing process. Instead of constructing buildings and producing things based on the concept of production efficiency through mass production process and ending up producing unnecessary products and infrastructures, the new objective of design will be to offer performance and service required by the society and human.
- (5) Designing large urban area against combined hazards such as those caused by the Sumatra earthquake of 2004 poses new challenge in design. One way to cope with this is to use a simplified design charts. In fact, sets of design charts were developed based on a series of parametric studies on embankments and gravity structures. Alternative way to cope with this extreme event is set up a reasonable strategy to evacuate and recovery. In order to enhance the quality of evacuation, education, early warning system and better city planning could be beneficial. Combining the multiple objectives of the facilities such as an emergency purpose and community or religious gathering purpose instead of pursuing the sole objective may be beneficial to better planning for mitigating disasters.

These reviews on the emerging trends in analysis and design will be useful for designing new and large geotechnical works that have to meet the rapidly growing social and economic demands in Asia and those for redevelopment of urban areas around the world.

REFERENCES

- Hardin BO, Drnevich VP (1972) Shear modulus and damping in soils: design equation and curves. *Journal of Soil Mechanics and Foundations Division, ASCE* 98, SM7: 667–692
- Higashijima M, Fujita I, Ichii K, Iai S, Sugano T, Kitamura M (2006) Development of a simple seismic performance evaluation technic for coastal structures. 2006 Ocean Development Symposium
- Iai S, Matsunaga Y, Kameoka T (1990) Parameter identification for a cyclic mobility model. Report of the Port and Harbour Research Institute, vol 29, 4, pp 57–83
- Iai S, Matsunaga Y, Kameoka T (1992a) Strain space plasticity model for cyclic mobility. *Soils and Foundations* 32(2): 1–15
- Iai S, Matsunaga Y, Kameoka T (1992b) Analysis of undrained cyclic behavior of sand under anisotropic consolidation. *Soils and Foundations* 32(2): 16–20
- Iai S (1993) Micromechanical background to a strain space multiple mechanism model for sand. *Soils and Foundations* 33(1): 102–117
- Iai S, Kameoka T, Towhata I (1994) Analysis of non-coaxiality by multi-mechanism model. Proc. 8th Int. Conf. Computer Methods and Advances in Geomechanics, Morgantown, pp 599–604
- Iai S (1998) Seismic analysis and performance of retaining structures, *Geotechnical Earthquake Engineering and Soil Dynamics III: Geotechnical Special Publication No.75, ASCE*, pp 1020–1044

- Iai S (2005) International standard (ISO) on seismic actions for designing geotechnical works—An overview. *Soil Dynamics and Earthquake Engineering* 25: 605–615
- Iai S, Ozutsumi O (2005) Yield and cyclic behaviour of a strain space multiple mechanism model for granular materials. *International Journal for Numerical and Analytical Methods in Geomechanics* 29(4): 417–442
- Kameoka T, Iai S (1993) Numerical analyses on the effects of initial stress conditions on seismic performance of sheet pile quay walls, Technical Note of Port and Harbour Research Institute, No.751, pp 1–29 (in Japanese)
- Matsuo O, Shimazu T, Uzuoka R, Mihara M, Nishi K (2000) Numerical analysis of seismic behavior of embankments founded on liquefiable soils. *Soils and Foundations* 40(2): 21–40
- Miwa S, Ozutsumi O, Ikeda T, Oka Y, Iai S (2003) Evaluation of earthquake damage to sheet pile type quay walls by effective stress analysis considering initial stress condition. *Proceedings of Structural Engineering* 49A: 369–380
- Oda M (1974) A mechanical and statistical model of granular material. *Soils and Foundations* 14(1): 13–27
- Oda M, Nemat-Nasser S, Konishi J (1985) Stress-induced anisotropy in granular masses. *Soils and Foundations*, 25(3): 85–97
- Ozutsumi O, Sawada S, Iai S, Takeshima Y, Sugiyama W, Shimazu T (2002) Effective stress analyses of liquefaction-induced deformation in river dikes. *Soil Dynamics and Earthquake Engineering* 22: 1075–1082
- Ozutsumi O (2003) Research on Numerical Analysis for Evaluation of Seismic Damage to Soil–Structure Systems on Liquefiable Ground. Doctors Dissertation, Kyoto University (in Japanese)
- Thornton C (1989) A direct approach to micromechanically based continuum models for granular material. *Mechanics of Granular Materials*, XII ICSMFE, Special Volume, pp 145–150
- Tobita T, Iai S, Ueda K (2006a) Dynamic behavior of a sand levee on saturated sand deposits. Proc. 8th U.S. National Conf Earthquake Engineering, San Francisco, Paper No. 1114
- Tobita T, Iai S, Chairullah B, Asper W (2006b) Reconnaissance report of the 2004 Sumatra-Andaman, Indonesia, Earthquake—Damage to geotechnical works in Band Aceh and Meulaboh. *Journal of Natural Disaster Science* 28(1) (in print)
- Towhata I, Ishihara K (1985a) Shear work and pore water pressure in undrained shear. *Soils and Foundations*, 25(3): 73–85
- Towhata I, Ishihara K (1985b) Modelling soil behaviour under principal stress axes rotation. Proc. 5th Int. Conf. Numerical Methods in Geomechanics, Nagoya, vol 1, pp 523–530
- Wang MW, Iai S, Tobita T (2006) Seismic simulation of underground RC structures. Proc. 6th Japan–Taiwan Seminar on Natural Hazard Mitigation, Kyoto, CD-ROM

CHAPTER 14

SIMPLIFIED SEISMIC SLOPE DISPLACEMENT PROCEDURES

Jonathan D. Bray¹

Dept. Civil & Environ. Engineering, Univ. of California, Berkeley, USA

Abstract. Simplified seismic slope displacement procedures are useful tools in the evaluation of the likely seismic performance of earth dams, natural slopes, and solid-waste landfills. Seismically induced permanent displacements resulting from earthquake-induced deviatoric deformations in earth and waste structures are typically calculated using the Newmark sliding block analogy. Some commonly used procedures are critiqued, and a recently proposed simplified procedure is recommended for use in engineering practice. The primary source of uncertainty in assessing the likely performance of an earth/waste structure during an earthquake is the input ground motion, so the proposed method is based on the response of several realistic nonlinear fully coupled stick-slip sliding block models undergoing hundreds of recorded ground motions. The calculated seismic displacement depends primarily on the ground motion's spectral acceleration at the degraded period of the structure and the structure's yield coefficient and fundamental period. Predictive equations are provided for estimating potential seismic displacements for earth and waste structures.

1. Introduction

The failure of an earth dam, solid-waste landfill, or natural slope during an earthquake can produce significant losses. Additionally, major damage without failure can have severe economic consequences. Hence, the potential seismic performance of earth and waste structures requires sound evaluation during design. Seismic evaluations of slope stability range from using relatively simple pseudostatic procedures to advanced nonlinear finite element analyses. Performance is best evaluated through an assessment of the potential for seismically induced permanent displacements. Following largely from the landmark paper of Newmark (1965) sliding block analyses are utilized as part of the seismic evaluation of the likely performance of earth and waste structures. Simplified Newmark-type procedures such as Makdisi and Seed (1978) are routinely used to provide a rough assessment of a system's seismic stability. Some of these procedures are critiqued in this paper, and a recently proposed simplified method for estimating earthquake-induced deviatoric deformations in earth and waste structures is summarized and recommended for use in practice.

2. Seismic displacement analysis

2.1. CRITICAL DESIGN ISSUES

Two critical design issues must be addressed when evaluating the seismic performance of an earth structure. First, are there materials in the structure or its foundation that will lose significant strength as a result of cyclic loading (e.g., soil liquefaction)? If so, this should be the primary focus of the evaluation, because large displacement flow slides could result. The soil liquefaction evaluation procedures in Youd et al. (2001) are largely used in practice; however, recent studies have identified deficiencies in some of these procedures. For example, the Chinese criteria should not be used to assess the liquefaction susceptibility of fine-grained soils. Instead, the recommendations of recent studies such as Bray and Sancio (2006) based on soil plasticity ($PI < 12$) and sensitivity ($w_c/LL > 0.85$) should be followed. Flow slides resulting from severe strength loss due to liquefaction of sands and silts or post-peak strength reduction in sensitive clays are not discussed in this paper.

Second, if materials within or below the earth structure will not lose significant strength as a result of cyclic loading, will the structure undergo significant deformations that may jeopardize satisfactory performance? The estimation of seismically induced permanent displacements allows an engineer to address this issue. This is the design issue addressed in this paper.

2.2. DEVIATORIC-INDUCED SEISMIC DISPLACEMENTS

The Newmark sliding block model captures that part of the seismically induced permanent displacement attributed to deviatoric shear deformation (i.e., either rigid body slippage along a distinct failure surface or distributed deviatoric shearing within the deformable sliding mass). Ground movement due to volumetric compression is not explicitly captured by Newmark-type models. The top of a slope can displace downward due to deviatoric deformation or volumetric compression of the slope-forming materials. However, top of slope movements resulting from distributed deviatoric straining within the sliding mass or stick-slip sliding along a failure surface are mechanistically different than top of slope movements that result from seismically induced volumetric compression of the materials forming the slope.

Although a Newmark-type procedure may appear to capture the overall top of slope displacement for cases where seismic compression due to volumetric contraction of soil or waste is the dominant mechanism, this is merely because the seismic forces that produce large volumetric compression strains also often produce large calculated displacements in a Newmark method. This apparent correspondence should not imply that a sliding block model should be used to estimate seismic compression displacements due to volumetric straining. There are cases where the Newmark method does not capture the overall top of slope displacement, such as the seismic compression of large compacted earth fills (e.g., Stewart et al., 2001). Deviatoric-induced deformation and volumetric-induced

deformation should be analyzed separately by using procedures based on the sliding block model to estimate deviatoric-induced displacements and using other procedures (e.g., Tokimatsu and Seed, 1987) to estimate volumetric-induced seismic displacements.

The calculated seismic displacement from Newmark-type procedures, whether the procedure is simplified or advanced, is viewed appropriately as an index of seismic performance. Seismic displacement estimates will always be approximate in nature due to the complexities of the dynamic response of the earth/waste materials involved and the variability of the earthquake ground motion. However, when viewed as an index of potential seismic performance, the calculated seismic displacement can and has been used effectively in practice to evaluate earth/waste structure designs.

3. Components of a seismic displacement analysis

3.1. GENERAL

The critical components of a seismic displacement analysis are: (1) earthquake ground motion, (2) dynamic resistance of the structure, and (3) dynamic response of the potential sliding mass. The earthquake ground motion is the most important of these components in terms of its contribution to the calculation of the amount of seismic displacement. The variability in calculated seismic displacement is primarily controlled by the significant variability in the earthquake ground motion, and it is relatively less affected by the variability in the earth slope properties (e.g., Yegian et al., 1991b; Kim and Sitar, 2003). The dynamic resistance of the earth/waste structure is the next key component, and the dynamic response of the potential sliding mass is generally third in importance. Other factors, such as the method of analysis, topographic effects, etc., can be important for some cases. However, these three components are most important for a majority of cases. In critiquing various simplified seismic displacement procedures it is useful to compare how each method characterizes the earthquake ground motion and the earth/waste structure's dynamic resistance and dynamic response.

3.2. EARTHQUAKE GROUND MOTION

An acceleration-time history provides a complete definition of one of the many possible earthquake ground motions at a site. Simplified parameters such as the peak ground acceleration (*PGA*), mean period (T_m), and significant duration (D_{5-95}) may be used in simplified procedures to characterize the intensity, frequency content, and duration, respectively, of an acceleration-time history. Preferably, all three, and at least two, of these simplified ground motion parameters should be used. It is overly simplistic to characterize an earthquake ground motion by just its *PGA*, because ground motions with identical *PGA* values can vary significantly in terms of frequency content and duration, and most importantly in terms of its effects on slope instability. Hence, *PGA* is typically supplemented by additional parameters characterizing the frequency content and duration of the ground motion. For example, Makdisi and Seed (1978) use earthquake

magnitude as a proxy for duration in combination with the estimated *PGA* at the crest of the embankment; Yegian et al. (1991b) use predominant period and equivalent number of cycles of loading in combination with *PGA*; and Bray et al. (1998) use the mean period and significant duration of the design rock motion in combination with its *PGA*.

Spectral acceleration has been commonly employed in earthquake engineering to characterize an equivalent seismic loading on a structure from the earthquake ground motion. Similarly, Travarasou and Bray (2003a) found that the 5% damped elastic spectral acceleration at the degraded fundamental period of the potential sliding mass was the optimal ground motion intensity measure in terms of efficiency and sufficiency (i.e., it minimizes the variability in its correlation with seismic displacement, and it renders the relationship independent of other variables, respectively, Cornell and Luco, 2001). The efficiency and sufficiency of estimating seismic displacement given a ground motion intensity measure were investigated for dozens of intensity measures. Other promising ground motion parameters included *PGA*, spectral acceleration (S_a), root mean square acceleration (a_{rms}), peak ground velocity (*PGV*), Arias intensity (I_a), effective peak velocity (*EPV*), Housner's response spectrum intensity (*SI*), and Ang's characteristic intensity (I_c). For period-independent parameters (i.e., no knowledge of the fundamental period of the potential sliding mass is required), Arias intensity was found to be the most efficient intensity measure for a stiff, weak slope, and response spectrum intensity was found to be the most efficient for a flexible slope.

No one period-independent ground motion parameter, however, was found to be adequately efficient for slopes of all dynamic stiffnesses and strengths. Spectral acceleration at a degraded period equal to 1.5 times the initial fundamental period of the slope (i.e., $S_a(1.5T_s)$) was found to be the most efficient ground motion parameter for all slopes (Travarasou and Bray, 2003a). An estimate of the initial fundamental period of the potential sliding mass (T_s) is required when using spectral acceleration, but an estimate of T_s is useful in characterizing the dynamic response aspects of the sliding mass (e.g., Bray and Rathje, 1998). Spectral acceleration does directly capture the important ground motion characteristics of intensity and frequency content in relation to the degraded natural period of the potential sliding mass, and it indirectly partially captures the influence of duration in that it tends to increase as earthquake magnitude (i.e., duration) increases. An additional benefit of selecting spectral acceleration to represent the ground motion is that spectral acceleration can be computed relatively easily due to the existence of several attenuation relationships and it is available at various return periods in ground motion hazard maps (e.g., <http://earthquake.usgs.gov/research/hazmaps/>).

3.3. DYNAMIC RESISTANCE

The earth/waste structure's yield coefficient (k_y) represents its overall dynamic resistance, which depends primarily on the dynamic strength of the material along the critical sliding surface and the structure's geometry and weight. The yield coefficient parameter has always been used in simplified sliding block procedures due to its important effect on seismic displacement.

The primary issue in calculating k_y is estimating the dynamic strength of the critical strata within the slope. Several publications include extensive discussions of the dynamic strength of soil (e.g., Blake et al., 2002; Duncan and Wright, 2005; Chen et al., 2006), and a satisfactory discussion of this important topic is beyond the scope of this paper. Needless to say, the engineer should devote considerable resources and attention to developing realistic estimates of the dynamic strengths of key slope materials. In this paper, it is assumed that k_y is constant, so consequently, the earth materials do not undergo severe strength loss as a result of earthquake shaking (e.g., no liquefaction).

Duncan (1996) found that consistent (and assumed to be reasonable) estimates of a slope's static factor of safety (FS) are calculated if a slope stability procedure that satisfies all three conditions of equilibrium is employed. Computer programs that utilize such methods as Spencer, Generalized Janbu, and Morgenstern and Price may be used to develop sound estimates of the static FS . Most programs also allow the horizontal seismic coefficient that results in a $FS = 1.0$ in a pseudostatic slope stability analysis to be calculated, and if a method that satisfied full equilibrium is used, the estimates of k_y are fairly consistent. With the wide availability of these computer programs and their ease of use, there is no reason to use a computer program that incorporates a method that does not satisfy full equilibrium. Simplified equations for calculating k_y as a function of slope geometry, weight, and strength are found in Bray et al. (1998) among several other works. The equations provided in Figure 14.1 may be used to estimate k_y for the simplified procedures presented in this paper.

The potential sliding mass that has the lowest static FS may not be the most critical for dynamic analysis. A search should be made to find sliding surfaces that produce low k_y values as well. The most important parameter for identifying critical potential sliding masses for dynamic problems is k_y/k_{max} , where k_{max} is the maximum seismic coefficient, which represents the maximum seismic loading considering the dynamic response of the potential sliding mass as described next.

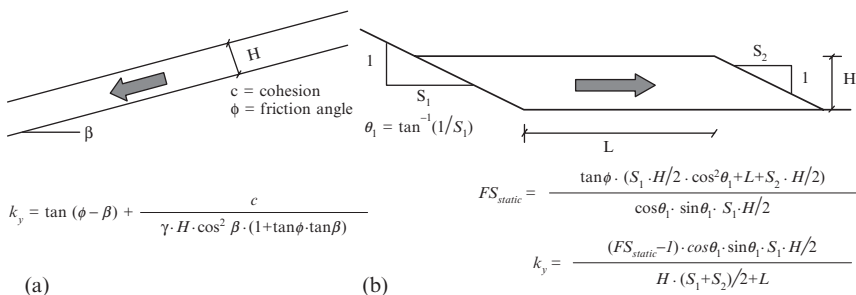


Fig. 14.1. Simplified estimates of the yield coefficient: (a) shallow sliding and (b) deep sliding

3.4. DYNAMIC RESPONSE

Research by investigators (e.g., Bray and Rathje, 1998) has found that seismic displacement also depends on the dynamic response characteristics of the potential sliding mass. With all other factors held constant, seismic displacements increase when the sliding mass is near resonance compared to that calculated for very stiff or very flexible slopes (e.g., Kramer and Smith, 1997; Rathje and Bray, 2000; Wartman et al., 2003). Many of the available simplified slope displacement procedures employ the original Newmark rigid sliding block assumption (e.g., Lin and Whitman, 1986; Ambraseys and Menu, 1988; Yegian et al., 1991b), which does not capture the dynamic response of the deformable earth/waste potential sliding mass during earthquake shaking.

As opposed to the original Newmark (1965) rigid sliding block model, which ignores the dynamic response of a deformable sliding mass, Makdisi and Seed (1978) introduced the concept of an equivalent acceleration to represent the seismic loading of a potential sliding mass (Figure 14.2) based on the work of Seed and Martin (1966). The horizontal equivalent acceleration (*HEA*)-time history when applied to a rigid potential sliding mass produces the same dynamic shear stresses along the potential sliding surface that is produced when a dynamic analysis of the deformable earth/waste structure is performed. The decoupled approximation results from the separate dynamic analysis that is performed assuming that no relative displacement occurs along the failure plane and the rigid sliding block calculation that is performed using the equivalent acceleration-time history from the dynamic response analysis to calculate seismic displacement.

Although the decoupled approximation of Makdisi and Seed (1978) inconsistently assumes no relative displacement in the seismic response analysis and then calculates a seismically induced permanent displacement, it has been judged by many engineers to provide a reasonable estimate of seismic displacement for many cases (e.g., Lin and Whitman, 1983; Rathje and Bray, 2000). However, it is not always reasonable, and it can lead to significant overestimation near resonance and some level of underestimation for cases where the structure has a large fundamental period or the ground motion is an intense near-fault motion. A nonlinear coupled stick-slip deformable sliding block model offers a more realistic representation of the dynamic response of an earth/waste structure by accounting for the deformability of the sliding mass and by considering the simultaneous occurrence of its nonlinear dynamic response and periodic sliding episodes

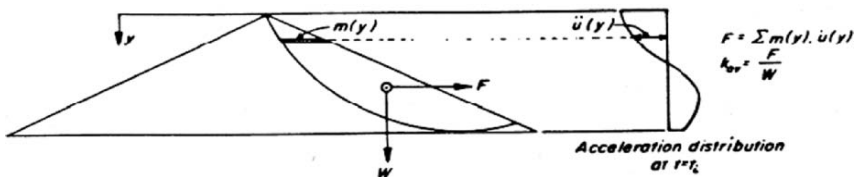


Fig. 14.2. Equivalent acceleration concept for deformable sliding mass (Seed and Martin, 1966)

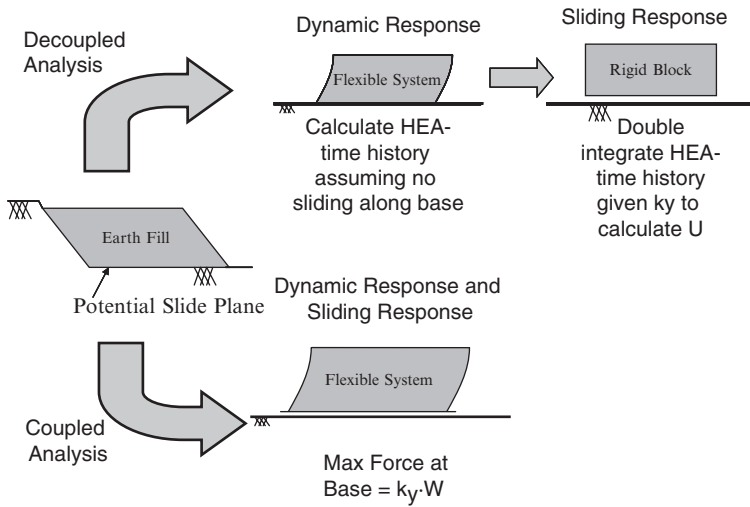


Fig. 14.3. Decoupled dynamic response/rigid sliding block analysis and fully coupled analysis

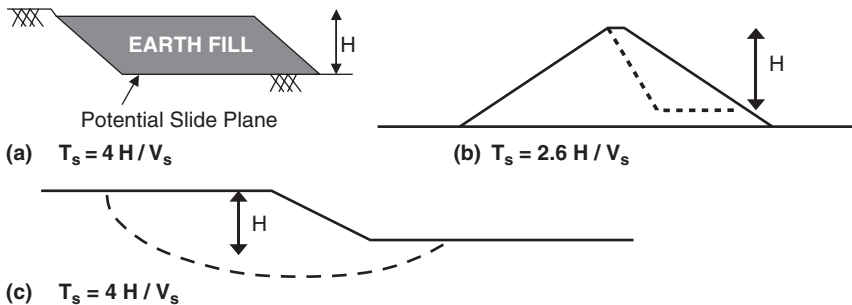


Fig. 14.4. Estimating the initial fundamental period of potential sliding blocks

(Figure 14.3). In addition, its validation against shaking table experiments provides confidence in its use (Wartman et al., 2003).

For seismic displacement methods that incorporate the seismic response of a deformable sliding block, the initial fundamental period of the sliding mass (T_s) can normally be estimated using the expression: $T_s = 4H/V_s$ for the case of a relatively wide potential sliding mass that is either shaped like a trapezoid or segment of a circle where its response is largely 1D (e.g., Rathje and Bray, 2001), where H = the average height of the potential sliding mass, and V_s is the average shear wave velocity of the sliding mass. For the special case of a triangular-shaped sliding mass that largely has a 2D response, the expression: $T_s = 2.6H/V_s$ should be used. Examples of the manner in which T_s should be estimated are shown in Figure 14.4.

4. Critique of some simplified seismic displacement methods

4.1. GENERAL

Comprehensive discussions of seismic displacement procedures for evaluating the seismic performance of earth/waste structures have been presented previously by several investigators (e.g., Makdisi and Seed, 1978; Seed, 1979; Lin and Whitman, 1983; Ambraseys and Menu, 1988; Yegian et al., 1991a, b; Marcuson et al., 1992; Jibson, 1993; Ambraseys and Srbulov, 1994; Bray et al., 1995; Ghahraman and Yegian, 1996; Kramer and Smith, 1997; Bray and Rathje, 1998; Finn, 1998; Jibson et al., 1998; Rathje and Bray, 2000; Stewart et al., 2003; Rathje and Saygili, 2006). There is not sufficient space in this paper to summarize and critique all pertinent studies. In this paper, some of the most commonly used simplified procedures for evaluating seismic displacement of earth and waste fills will be discussed with a focus on methods that do not assume that potential sliding mass is rigid.

4.2. SEED (1979) PSEUDOSTATIC SLOPE STABILITY PROCEDURE

First, several simplified pseudostatic slope stability procedures are commonly used in practice. They include Seed (1979) and the Hynes-Griffin and Franklin (1984). Both methods involve a number of simplifying assumptions and are both calibrated for evaluating earth dams wherein they assumed that <1 m of seismic displacement constituted acceptable performance. They should not be applied to cases where seismically induced permanent displacements of up to 1 m are not acceptable, which is most cases for evaluating base sliding of lined solid-waste landfills or houses built atop compacted earth fill slopes. Additionally, they provide a limited capability to assess seismic performance, because they do not directly address the key performance index of calculated seismic displacement.

The Seed (1979) pseudostatic slope stability method was developed for earth dams with materials that do not undergo severe strength loss that have crest accelerations less than $0.75 g$. Using a seismic coefficient of 0.15 with appropriate dynamic strengths for the critical earth materials, performance is judged to be acceptable if $FS > 1.15$. The characteristics of the earthquake ground motion and the dynamic response of the potential slide mass to the earthquake shaking are represented by the seismic coefficient of 0.15 for all cases. Use of $FS > 1.15$ ensures that the yield coefficient (i.e., dynamic resistance of the earth dam) will be greater than 0.15 by an unknown amount. Thus, the earthquake ground motion and dynamic resistance and dynamic response of the earth dam are very simply captured in this approach, and the amount of conservatism involved in the estimate and the expected seismic performance is uncertain. An earth structure that satisfies the Seed (1979) recommended combination of seismic coefficient, FS , and dynamic strengths may displace up to 1 m, so satisfaction of this criteria does not mean the system is "safe" for all levels of performance.

4.3. MAKDISI AND SEED (1978) SIMPLIFIED SEISMIC DISPLACEMENT METHOD

The first step in the widely used Makdisi and Seed (1978) approach is the evaluation of the material's strength loss potential. They recommend not using their procedure if the loss of material strength could be significant. If only a minor amount of strength loss is likely, a slightly reduced shear strength, which often incorporates a 10% to 20% strength reduction from peak undrained shear strength, is recommended. The strength reduction is applied because of the use of a rigid, perfectly plastic sliding block model, wherein if peak strength was used the accumulation of nonlinear elasto-plastic strains for cyclic loads below peak would be significantly underestimated (i.e., zero vs. some nominal amount). Based on these slightly reduced best estimates of calibrated dynamic strengths and slope geometry and weight, k_y is then calculated in the second step.

In step three, the PGA that occurs at the crest of the earth structure is estimated. This is one of the greatest limitations of this method. As shown in Figure 14.5, which presents results of 1D SHAKE analyses of columns of waste placed atop a firm foundation for a number of ground motions, the PGA (or maximum horizontal acceleration, MHA) at the top of the landfill varies significantly. There is great uncertainty regarding what value of PGA to use. This is critical, because in the next step, the maximum seismic coefficient (k_{max}) is estimated as a function of the PGA at the crest and the depth of sliding below the crest. Thus, the uncertainty in the estimate of k_{max} is high, because the uncertainty

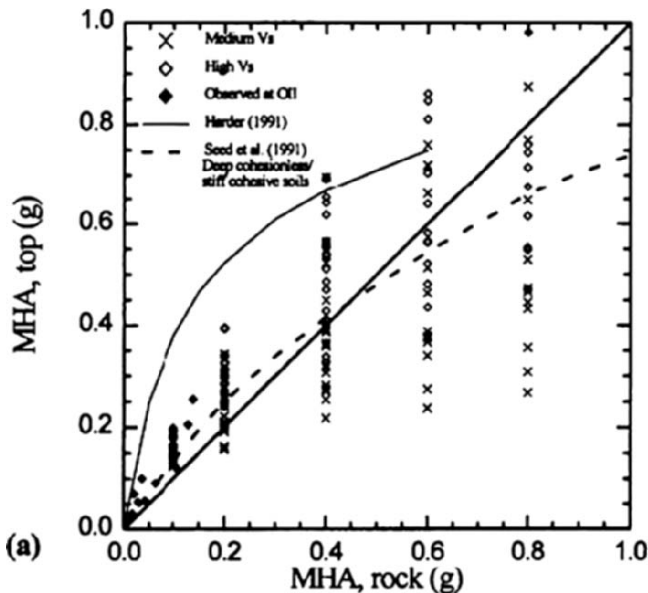


Fig. 14.5. Maximum horizontal acceleration at top of waste fill vs. MHA of rock base (Bray and Rathje, 1998)

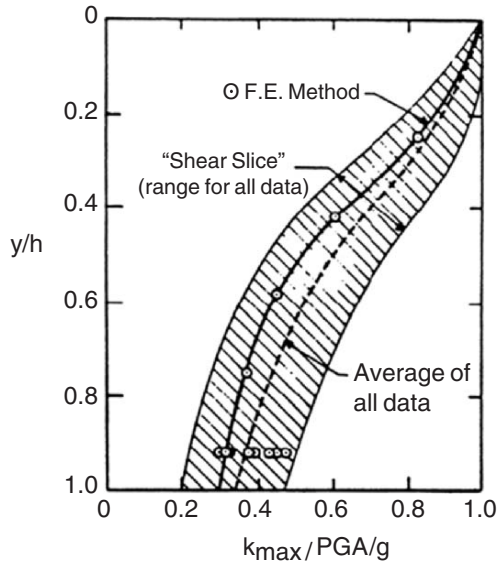


Fig. 14.6. Estimating seismic coefficient as a function of the peak acceleration at the crest and the depth of sliding (Makdisi and Seed, 1978)

in estimating the crest PGA is high. Even with advanced analyses, estimating the crest PGA is difficult, and the need to perform any level of dynamic analysis to estimate the crest PGA conflicts with the intent of a simplified method that should not require more advanced analysis.

Moreover, the bounds shown on the Makdisi and Seed (1978) plot of k_{max}/PGA vs. y/h (Figure 14.6) are not true upper or lower bounds. Stiff earth structures undergoing ground motions with mean periods near the degraded period of the earth structure can have k_{max} values exceeding 50% of the crest PGA for the base sliding case (i.e., $y/h = 1.0$), and flexible earth structures undergoing ground motions with low mean periods can have k_{max} values less than 20% of the crest PGA for base sliding.

When typically used in practice, the final step is to estimate seismic displacement as a function of the ratio of k_y/k_{max} and earthquake magnitude. Again the range shown in Figure 14.7 does not constitute the true upper and lower bounds of the possible seismic displacement, as only a limited number of earth structures were analyzed with a very limited number of input ground motions. As recommended by Makdisi and Seed (1978): “It must be noted that the design curves presented are based on averages of a range of results that exhibit some degree of scatter and are derived from a limited number of cases. These curves should be updated and refined as analytical results for more embankments are obtained.” Similar to how the Seed and Idriss (1971) simplified liquefaction triggering procedure was updated through Seed et al. (1985) and then Youd et al. (2001), it is time to update and move beyond the Makdisi and Seed (1978) design curves.

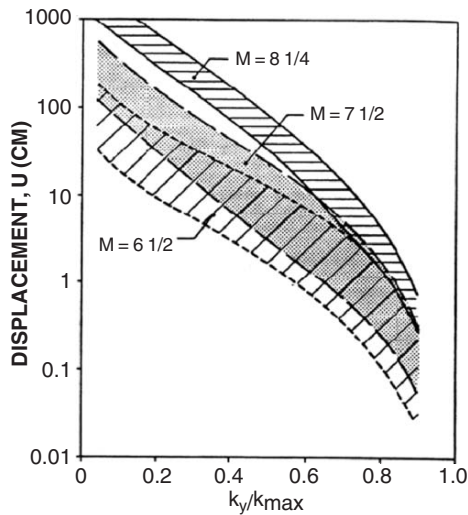


Fig. 14.7. Seismic displacement vs. k_y/k_{max} and magnitude (Makdisi and Seed, 1978)

The Makdisi and Seed (1978) simplified seismic displacement method is one of the most significant contributions to geotechnical earthquake engineering over the past few decades. But as they recommended, their design curves should be updated as the profession advances. Since 1989, the number of recorded ground motions has increased dramatically. Thousands of well recorded ground motions are now available. The Makdisi and Seed (1978) work is based on a limited number of recorded and modified ground motions. Moreover, the important earthquake ground motion at a site is characterized by the *PGA* at the crest of the slope and earthquake magnitude. The *PGA* at the crest of the slope is highly variable and important frequency content aspects of the ground motion are not captured. The analytical method employed was relatively simple (e.g., primarily the shear slice method and a few equivalent-linear 2D finite element analyses). The decoupled approximation was employed, there is no estimate of uncertainty, and the bounds shown in the design curves are not true upper and lower bounds.

4.4. BRAY ET AL. (1998) SIMPLIFIED SEISMIC DISPLACEMENT APPROACH

The Bray et al. (1998) method is largely based on the work of Bray and Rathje (1998) which in turn follows on the works of Seed and Martin (1966), Makdisi and Seed (1978), and Bray et al. (1995). The methodology is based on the results of fully nonlinear decoupled one-dimensional D-MOD (Matasovic and Vucetic, 1995) dynamic analyses combined with the Newmark rigid sliding block procedure. To address the importance of the dynamic response characteristics of the sliding mass, six fill heights with three shear wave velocity profiles each with multiple unit weight profiles and two sets of strain-dependent shear modulus reduction and material damping relationships were used.

More importantly, taking advantage of the greater number of recorded earthquake ground motions available at the time, dozens of dissimilar scaled and unmodified recorded earthquake rock input motions were used with *PGAs* ranging from 0.2 *g* to 0.8 *g*. Their method was calibrated against several case histories of waste fill performance during the 1989 Loma Prieta and 1994 Northridge earthquakes, and later validated against observed earth fill performance.

The Bray et al. (1998) procedure provides a more comprehensive assessment of the earthquake ground motions, seismic loading, and seismic displacement calculations, but it requires more effort than the Makdisi and Seed (1978) procedure. In the first step, the ground motion is characterized by estimating the *MHA*, T_m , and D_{5-95} for outcropping rock at the site given the assigned design moment magnitude and distances for the identified key potential seismic sources. The intensity, frequency content, and duration for the median earthquake ground motion level for deterministic events are estimated using several available ground motion parameter empirical relationships (e.g., Figure 14.8). The rock site condition is used, which is also consistent with the site condition used in the development of probabilistic ground motion hazard maps. Additionally, a seismic site response analysis is not required to estimate the *PGA* at the top of slope.

For the deep sliding case, the initial fundamental period of the potential sliding mass (T_s) is estimated as discussed previously (i.e., $T_s \approx 4H/V_s$). With the ratio of T_s/T_m , the normalized maximum seismic loading (i.e., $(MHEA)/((MHA_{rock})(NRF))$, where *MHEA* is the maximum horizontal equivalent acceleration and *NRF* is the nonlinear response factor) can be estimated with the graph shown in Figure 14.9, or the equation provided below, when $T_s/T_m > 0.5$

$$\ln(MHEA/(MHA_{rock}NRF)) = -0.624 - 0.7831 \ln(T_s/T_m) \pm \epsilon \quad (14.1)$$

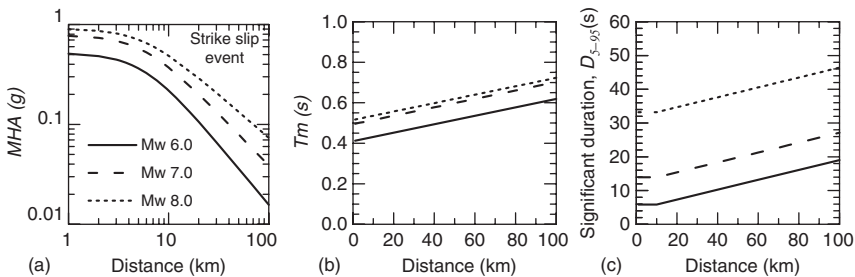


Fig. 14.8. Simplified characterization of earthquake rock motions: (a) intensity—*MHA* for strike-slip faults (for reverse faults, use $1.3 * MHA$ for $M_w \geq 6.4$ and $1.64 * MHA$ for $M_w = 6.0$, with linear interpolation for $6.0 < M_w < 6.4$) (Abrahamson and Silva, 1997), (b) frequency content— T_m (Rathje et al., 2004), and (c) duration— D_{5-95} (Abrahamson and Silva, 1996)

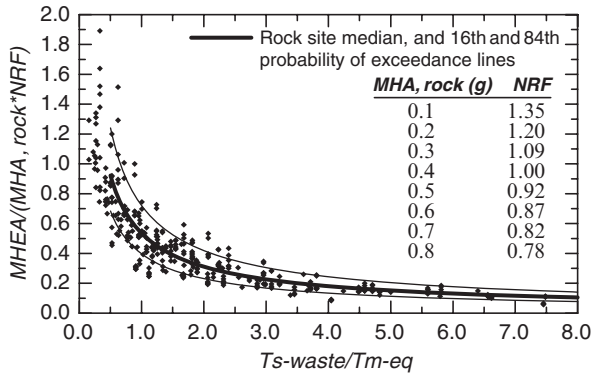


Fig. 14.9. Normalized maximum horizontal equivalent acceleration vs. normalized fundamental Period of sliding mass (Bray and Rathje, 1998)

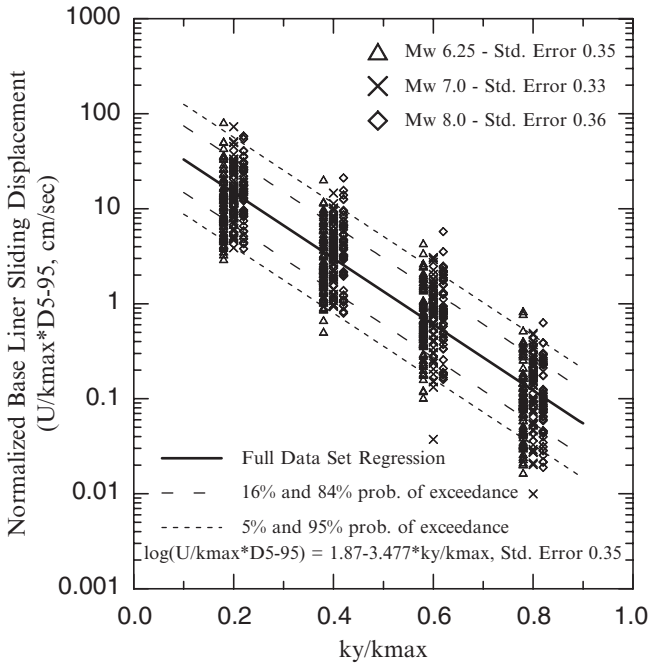


Fig. 14.10. Normalized base liner sliding displacements (from Bray and Rathje, 1998)

where $\sigma = 0.298$. The seismic coefficient $k_{max} = MHEA/g$. With an estimate of k_y , the normalized seismic displacement can be estimated as a function of k_y/k_{max} using Figure 14.10, or this equation

$$\log_{10}(U/(k_{max}D_{5-95})) = 1.87 - 3.477(k_y/k_{max}) \pm \varepsilon \tag{14.2}$$

where $\sigma = 0.35$. The seismic displacement (U in cm) can then be estimated by multiplying the normalized seismic displacement value by the median estimates of k_{max} and D_{5-95} . The normalized seismic loading and displacement values are estimated at the median and 16% exceedance levels to develop a range of estimated seismic displacements.

The Bray et al. (1998) seismic slope displacement procedure provides median and standard deviation estimates of the seismic demand and normalized seismic displacement, but does so only in an approximate manner to develop a sense of the variability of the estimated displacement. It is limited in that it was not developed in a rigorous probabilistic manner. However, Stewart et al. (2003) were able to use this procedure to develop a probabilistic screening analysis for deciding if detailed project-specific seismic slope stability investigations are required by the 1990 California Seismic Hazards Mapping Act. Additionally, the Bray and Rathje (1998) simplified seismic displacement procedure was adopted in the guidance document by Blake et al. (2002) for evaluating seismic slope stability in conformance with the "Guidelines for Evaluating and Mitigating Seismic Hazards in California" (CDMG, 1997).

As noted previously, the Bray et al. (1998) method is also limited by the decoupled approximation employed in the seismic response and Newark sliding block calculations. Although many more ground motions were used than were used by Makdisi and Seed (1978), with the large number of well-recorded events since 1998, significantly more ground motions are now available. These shortcomings motivated a more recent study, which is summarized in the next section of this paper.

5. Bray and Travararou (2007) simplified seismic displacement procedure

5.1. EARTHQUAKE GROUND MOTIONS

Currently available simplified slope displacement estimation procedures were largely developed based on a relatively modest number of earthquake recordings or simulations. This study took advantage of the recently augmented database of earthquake recordings, which provides the opportunity to characterize better the important influence of ground motions on the seismic performance of an earth/waste slope. As discussed previously, the uncertainty in the ground motion characterization is the greatest source of uncertainty in calculating seismic displacements.

The ground motion database used by Bray and Travararou (2007) to generate the seismic displacement data comprises available records from shallow crustal earthquakes that occurred in active plate margins (PEER strong motion database (<http://peer.berkeley.edu/smcat/index.html>)). These records conform to the following criteria: (1) $5.5 \leq M_w \leq 7.6$, (2) $R \leq 100$ km, (3) Simplified Geotechnical Sites B, C, or D (i.e., rock, soft rock/shallow stiff soil, or deep stiff soil, respectively, Rodriguez-Marek et al., 2001), and (4) frequencies in the range of 0.25 to 10 Hz have not been filtered out. Earthquake records totaling 688 from 41 earthquakes comprise the ground motion

database for this study (see Travararou, 2003 for a list of records used). The two horizontal components of each record were used to calculate an average seismic displacement for each side of the records, and the maximum of these values was assigned to that record.

5.2. DYNAMIC RESISTANCE OF THE EARTH/WASTE STRUCTURE

The seismic coefficient is calculated as described before using a computer program that has a slope stability method that satisfies all three conditions of equilibrium, or for preliminary analyses, a simplified estimate of k_y can be calculated using the equations provided previously in Figure 14.1.

5.3. DYNAMIC RESPONSE OF THE POTENTIAL SLIDING MASS

The nonlinear coupled stick-slip deformable sliding model proposed by Rathje and Bray (2000) for one-directional sliding was used by Bray and Travararou (2007). The seismic response of the sliding mass is captured by an equivalent-linear viscoelastic modal analysis that uses strain-dependent material properties to capture the nonlinear response of earth and waste materials. It considers a single mode shape, but the effects of including three modes were shown to be small. The results from this model have been shown to compare favorably with those from a fully nonlinear D-MOD-type stick-slip analysis (Rathje and Bray, 2000), but this model can be utilized in a more straightforward and transparent manner. The model used is one-dimensional (i.e., a relatively wide vertical column of deformable soil) to allow for the use of a large number of ground motions with wide range of properties of the potential sliding mass in this study. One-dimensional (1D) analysis has been found to provide a reasonably conservative estimate of the dynamic stresses at the base of two-dimensional (2D) sliding systems (e.g., Vrymoed and Calzascia, 1978; Elton et al., 1991) and the calculated seismic displacements (Rathje and Bray, 2001). However, 1D analysis can underestimate the seismic demand for shallow sliding at the top of 2D systems where topographic amplification is significant. For this case, the seismic loading (which can be approximated by PGA for the shallow sliding case) can be amplified as recommended by Rathje and Bray (2001) for moderately steep slopes (i.e., $\sim 1.25 PGA$) and as recommended by Ashford and Sitar (2002) for steep ($> 60^\circ$) slopes (i.e., $\sim 1.5 PGA$).

The nonlinear coupled stick-slip deformable sliding model of Rathje and Bray (2000) can be characterized by: (1) its strength as represented by its yield coefficient, k_y , (2) its dynamic stiffness as represented by its initial fundamental period, T_s , (3) its unit weight, and (4) its strain-dependent shear modulus and damping curves. Seismic displacement values were generated by computing the response of the idealized sliding mass model with 10 values of its yield coefficient from 0.02 to 0.4 and with 8 values of its initial fundamental period from 0 to 2 s to the entire set of recorded earthquake motions described previously. Unit weight was set to 18 kN/m^3 , and the Vucetic and Dobry (1991) shear modulus reduction and damping curves for a $PI = 30$ material were used. For the baseline case, the overburden-stress corrected shear wave velocity (V_{s1}) was set to 250 m/s,

and the shear wave velocity profile of the sliding block was developed using the relationship that shear wave velocity (V_s) is proportional to the fourth-root of the vertical effective stress. The sliding block height (H) was increased until the specified value of T_s was obtained. For common T_s values from 0.2 to 0.7 s, another reasonable combination of H and average V_s were used to confirm that the results were not significantly sensitive to these parameters individually. For nonzero T_s values, H varied between 12 and 100 m, and the average V_s was between 200 and 425 m/s. Hence, realistic values of the initial fundamental period and yield coefficient for a wide range of earth/waste fills were used.

5.4. FUNCTIONAL FORMS OF MODEL EQUATIONS

Situations commonly arise where a combination of earthquake loading and slope properties will result in no significant deformation of an earth/waste system. Consequently, the finite probability of obtaining negligible (“zero”) displacement should be modeled as a function of the independent random variables. Thus, during an earthquake, an earth slope may experience “zero” or finite permanent displacements depending on the characteristics of the strong ground motion and the slope’s dynamic properties and geometry. As discussed in Travararou and Bray (2003b), seismically induced permanent displacements can be modeled as a mixed random variable, which has a certain probability mass at zero displacement and a probability density for finite displacement values. Displacements smaller than 1 cm are not of engineering significance and can for practical purposes be considered as negligible or “zero.” Additionally, the regression of displacement as a function of a ground motion intensity measure should not be dictated by data at negligible levels of seismic displacement.

Contrary to a continuous random variable, the mixed random variable can take on discrete outcomes with finite probabilities at certain points on the line as well as outcomes over one or more continuous intervals with specified probability densities. The values of seismic displacement that are smaller than 1 cm are lumped to $d_0 = 1$ cm. The probability density function of seismic displacement is then

$$f_D(d) = \tilde{p}\delta(d - d_0) + (1 - \tilde{p})\tilde{f}_D(d) \quad (14.3)$$

where $f_D(d)$ is the displacement probability density function; \tilde{p} is the probability mass at $D = d_0$; $\delta(d - d_0)$ is the Dirac delta function; and $\tilde{f}_D(d)$ is the displacement probability density function for $D > d_0$.

The predictive model for seismic displacement consists of two discrete steps. First, the probability of occurrence of “zero” displacement (i.e., $D \leq 1$ cm) is computed as a function of the primary independent variables k_y , T_s , and $S_a(1.5T_s)$. The dependence of the probability of “zero” displacement on the three independent variables is illustrated in Figure 14.11. The probability of “zero” displacement increases significantly as the yield coefficient increases, and decreases significantly as the ground motion’s spectral acceleration at the degraded period of the slope increases. The probability of “zero” displacement decreases initially as the fundamental period increases from zero, because the slope is

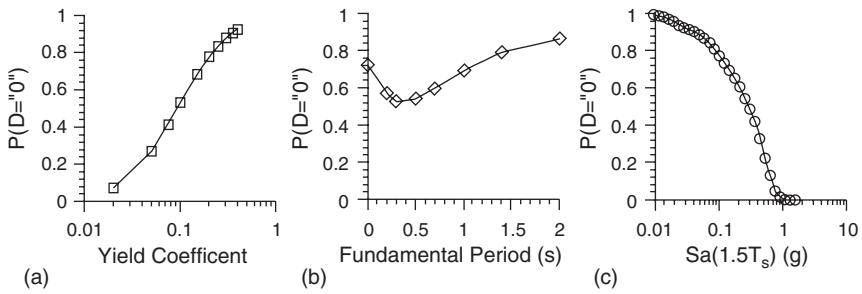


Fig. 14.11. Dependence of the probability of negligible displacement ($D < 1$ cm) on the (a) yield coefficient, (b) initial fundamental period, and (c) spectral acceleration at 1.5 times the initial fundamental period (Bray and Travarasou, 2007)

being brought near to the mean period of most ground motions. However, this probability increases sharply as the slope's period continues to increase as it is now moving away from the resonance condition. A probit regression model was used for this analysis (Green, 2003), and the selection of the functional form for modeling the probability of occurrence of “zero” displacement was guided by the trends shown in Figure 14.11.

In the case where a non-negligible probability of “nonzero” displacement is calculated, the amount of “nonzero” displacement needs to be estimated. A truncated regression model was used as described in Green (2003) to capture the distribution of seismic displacement, given that “nonzero” displacement has occurred. The estimation of the values of the model coefficients was performed using the principle of maximum likelihood.

5.5. EQUATIONS FOR ESTIMATING SEISMIC DEVIATORIC DISPLACEMENTS

As mentioned, the model for estimating seismic displacement consists of two discrete computations of: (1) the probability of negligible (“zero”) displacement and (2) the likely amount of “nonzero” displacement. The model for computing the probability of “zero” displacement is

$$P(D = \text{“0”}) = 1 - \Phi \left(-1.76 - 3.22 \ln(k_y) - 0.484(T_s) \ln(k_y) + 3.52 \ln(S_a(1.5T_s)) \right) \quad (14.4)$$

where $P(D = \text{“0”})$ is the probability (as a decimal number) of occurrence of “zero” displacements, D is the seismic displacement in the units of cm, Φ is the standard normal cumulative distribution function (i.e., NORMSDIST in Excel), k_y is the yield coefficient, T_s is the initial fundamental period of the sliding mass in seconds, and $S_a(1.5T_s)$ is the spectral acceleration of the input ground motion at a period of $1.5T_s$ in the units of g .

This first step can be thought of as a screening analysis. If there is a high probability of “zero” displacements, the system performance can be assessed to be satisfactory for

the ground motion hazard level and slope conditions specified. If not, the engineer must calculate the amount of “nonzero” displacement (D) in centimeters using

$$\begin{aligned} \ln(D) = & -1.10 - 2.83 \ln(k_y) - 0.333 (\ln(k_y))^2 + 0.566 \ln(k_y) \ln(S_a(1.5T_s)) \\ & + 3.04 \ln(S_a(1.5T_s)) - 0.244 (\ln(S_a(1.5T_s)))^2 \\ & + 1.5T_s + 0.278(M - 7) \pm \varepsilon \end{aligned} \tag{14.5}$$

where: k_y , T_s , and $S_a(1.5T_s)$ are as defined previously for Eq. (14.4), and ε is a normally-distributed random variable with zero mean and standard deviation $\sigma = 0.66$. To eliminate the bias in the model when $T_s \approx 0$ s, the first term of Eq. (14.5) should be replaced with -0.22 when $T_s < 0.05$ s. Because the standard deviation of Eq. (14.5) is 0.66 and $\exp(0.66) \approx 2$, the median minus one standard deviation to median plus one standard deviation range of seismic displacement can be approximately estimated as half the median estimate to twice the median estimate of seismic displacement. Hence, the median seismic displacement calculated using Eq. (14.5) with $\varepsilon = 0$ can be halved and doubled to develop approximately the 16% to 84% exceedance seismic displacement range estimate.

The residuals of Eq. (14.5) are plotted in Figure 14.12 vs. some key independent variables. The residuals of displacement vs. magnitude, distance, and yield coefficient show no significant bias. There is only a moderate bias in the estimate at $T_s = 0$ and 2 s. The overestimation at 2 s is not critical, because it is rare to have earth/waste sliding masses with periods greater than 1.5 s, and Eq. (14.5) is conservative. However, the rigid body case (i.e., $T_s = 0$) can be important for very shallow slides, and Eq. (14.5) is unconservative for this case. The estimation at $T_s = 0$ s can be corrected by replacing the first term (i.e., -1.10) in Eq. (14.5) with -0.22 . Hence, it is reasonable to use Eq. (14.5) for cases where T_s ranges from 0.05 to 2 s, and the first term of these equations should be replaced with -0.22 if $T_s < 0.05$ s.

It is often useful to establish a threshold displacement for acceptable seismic performance and then estimate the probability of this threshold displacement being exceeded.

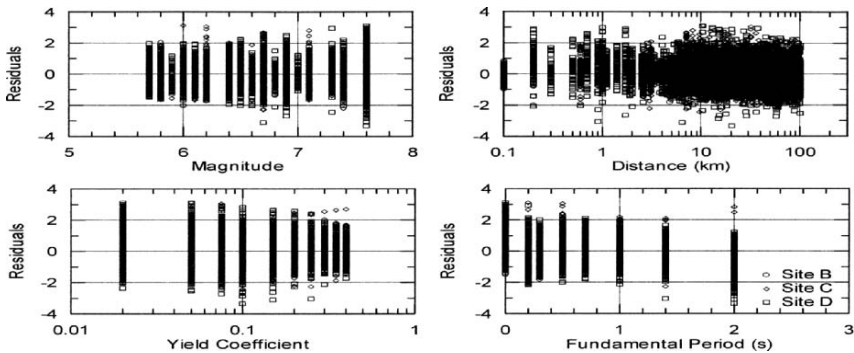


Fig. 14.12. Residuals ($\ln D_{\text{data}} - \ln D_{\text{predicted}}$) of Eq. (14.5) plotted vs. magnitude, rupture distance, the yield coefficient, and the initial fundamental period (Bray and Travararou, 2007)

Additionally, often a range of expected seismic displacements is desired. The proposed methodology can be used to calculate the probability of the seismic displacement exceeding a selected threshold of displacement (d) for a specified earthquake scenario and slope properties. For example, consider a potential sliding mass with an initial fundamental period T_s , yield coefficient k_y , and an earthquake scenario that produces a spectral acceleration of $S_a(1.5T_s)$. The probability of the seismic displacement (D) exceeding a specified displacement threshold (d) is

$$P(D > d) = [1 - P(D = "0")] \cdot P(D > d | D > "0") \tag{14.6}$$

The term $P(D = "0")$ is computed using Eq. (14.4). The term $P(D > d | D > "0")$ may be computed assuming that the estimated displacements are lognormally distributed as

$$P(D > d | D > "0") = 1 - P(D \leq d | D > "0") = 1 - \Phi\left(\frac{\ln d - \ln \hat{d}}{\sigma}\right) \tag{14.7}$$

where $\ln(\hat{d})$ is computed using Eq. (14.5) and $\sigma = 0.66$.

The trends in the Bray and Travararou (2007) seismic displacement model are shown in Figures 14.13 and 14.14. For the $M_w = 7$ earthquake at a distance of 10 km scenario (i.e., Figures 14.13a,b), the importance of yield coefficient is clear. As yield coefficient increases, the probability of "zero" seismic displacement increases and the median estimate of nonzero displacement decreases sharply. The fundamental period of the potential sliding mass is also important, with values of T_s from 0.2 to 0.4 s leading to a higher likelihood of seismic displacement. For a $M_w = 7.5$ earthquake at different levels of

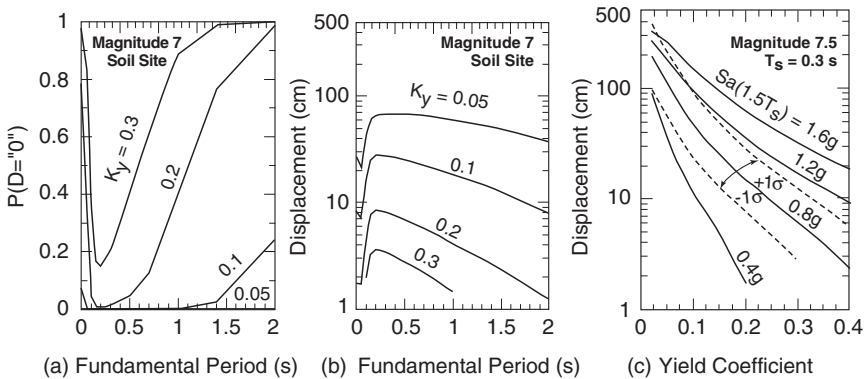


Fig. 14.13. Trends from the Bray and Travararou (2007) model: (a) probability of negligible displacements and (b) median displacement estimate for a $M_w = 7$ strike-slip earthquake at a distance of 10 km, and (c) seismic displacement as a function of yield coefficient for several intensities of ground motion ($M_w = 7.5$) for a sliding block with $T_s = 0.3$ s

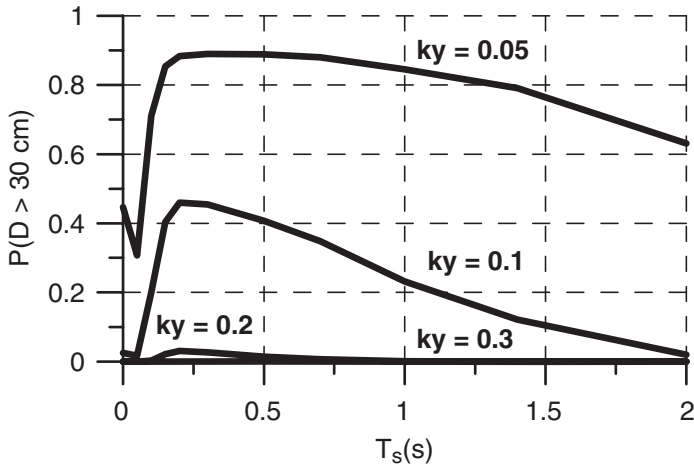


Fig. 14.14. Probability of exceeding 30 cm of seismic displacement for a $M_w = 7$ strike-slip earthquake at a distance of 10 km using Eq. (14.6) for selected k_y and T_s values

ground motion intensity at the degraded period of the sliding mass (Figure 14.13c), yield coefficient is again shown to be a critical factor, with large displacements occurring only for lower k_y values. Of course, the level of ground motion at a selected k_y value is also a dominant factor. The uncertainty involved in the estimation of seismic displacement for $S_a(0.45s) = 0.8g$ is shown to be approximately half to double the median estimate. Lastly, Eq. (14.6) was used with the results for the case presented in Figures 14.13a, b to calculate the probability of exceeding a selected threshold seismic displacement of 30 cm as shown in Figure 14.14.

5.6. MODEL VALIDATION AND COMPARISON

The Bray and Travararou (2007) model was shown to predict reliably the seismic performance observed at 16 earth dams and solid-waste landfills that underwent strong earthquake shaking. Some of the case histories used in the model validation are presented in Table 14.1. In all cases, the maximum observed displacement (D_{max}) is that portion of the permanent displacement attributed to stick-slip type movement and distributed deviatoric shear within the deformable mass, and crest movement due to volumetric compression was subtracted from the total observed permanent displacement when appropriate to be consistent with the mechanism implied by the Newmark method. The observed seismic performance and best estimates of yield coefficient and initial fundamental period are based on the information provided in Bray and Rathje (1998), Harder et al. (1998), and Elgamal et al. (1990). Complete details regarding these parameters and pertinent seismological characteristics of the corresponding earthquakes can be found in Travararou (2003).

Table 14.1. Comparison of the maximum observed displacement with three simplified methods

Earth Dam/Waste Fill	EQ	Obs. D_{max} (cm)	k_y	T_s (s)	$Sa(1.5T_s)$ (g)	Bray and		Makdisi and	Bray et al.
						Travasrou, 2007 $P(D = "0")$	D (cm)	Seed, 1978 D (cm)	1998 D (cm)
(1)	(2)	(3)	(4)	(5)	(6)	(7)	(8)	(9)	(10)
Pacheco Pass LF	LP	None	0.30	0.76	0.12	1.0	"0"	0	0
Marina LF	LP	None	0.26	0.59	0.30	0.9	"0"	0	0
Austrian Dam	LP	50	0.14	0.33	0.94	0.0	20–70	1–30	20–100
Lexington Dam	LP	15	0.11	0.31	0.78	0.0	15–65	0–10	30–110
Lopez Canyon C-B LF	NR	None	0.35	0.45	0.43	0.85	"0"	0	0
Chiquita Canyon C LF	NR	24	0.09	0.64	0.35	0.0	10–30	1–40	3–20
Sunshine Canyon LF	NR	30	0.31	0.77	1.40	0.0	20–70	0	0
OII Section HH LF	NR	15	0.08	0.00	0.24	0.1	4–15	3–30	2–25
La Villita Dam	S3	1	0.20	0.60	0.20	0.95	"0"	0	0
La Villita Dam	S5	4	0.20	0.60	0.41	0.25	"0"–10	0–1	0

LP: 1989 Loma Prieta; NR: 1994 Northridge; S3 and S5 from Elgamal et al. (1990)

The comparison of the simplified methods' estimates of seismic displacement (columns 8–10) with the maximum observed seismic permanent displacement (column 3) is shown in Table 14.1. For this comparison, only the best estimate of the slope's yield coefficient, its initial fundamental period, and the spectral acceleration at 1.5 times the initial fundamental period of the slope are considered. Hence, the computed displacement range is due to the variability in the seismic displacement given the values of the slope properties and the seismic load.

There are four cases shown in Table 14.1 in which the observed seismic displacement was noted as being "None," or ≤ 1 cm. For these cases, all of the simplified methods indicate that negligible displacements are expected (i.e., $D \leq 1$ cm), which is consistent with the good seismic performance observed of these earth/waste structures. Only the Bray and Travararou (2007) method provides sufficient resolution to indicate the correct amount of observed displacement for La Villita Dam for Event S5 and that moderately more displacement should be expected for Event S5 instead of S3.

There are three cases of observed moderate seismic displacement for solid-waste landfills during the 1994 Northridge earthquake (i.e., $D_{max} = 15\text{--}30$ cm). For these cases, the Bray and Travararou (2007) method indicates a very low chance of "zero" displacement occurring. Moreover, the observed seismic displacements are all within the ranges of the seismic displacement estimated by this method. The Makdisi and Seed (1978) and Bray et al. (1998) simplified methods provide reasonable, albeit less precise, estimates of the observed displacements for two of the cases, and both significantly underestimate the level of seismic displacement observed at the Sunshine Canyon landfill (i.e., both estimate 0 cm when 30 cm was observed).

Lastly, there are two cases of moderate seismic displacement of earth dams shaken by the 1989 Loma Prieta Earthquake. The Bray and Travararou (2007) method provides refined and more accurate estimates of the observed seismic displacement due to deviatoric straining at these two dams than the other two simplified methods. The Bray and Travararou (2007) screening equation clearly indicates that the likelihood of negligible (i.e., "zero") displacements is very low, and the 16% to 84% exceedance range for the nonzero displacement captures the observed seismic performance.

In judging these simplified methods, it is important to note that they provide predominantly consistent assessments of the expected seismic performance. However, the Bray and Travararou (2007) method captures the observed performance better than existing procedures. Moreover, it is superior to the prevalent simplified seismic displacement methods, because it characterizes the uncertainty involved in the seismic displacement estimate and can be used in a probabilistic seismic hazard assessment.

5.7. ILLUSTRATIVE SEISMIC EVALUATION EXAMPLE

The anticipated performance of a representative earth embankment in terms of seismically induced permanent displacements is evaluated to illustrate the use of the Bray and

Travasrou (2007) simplified seismic displacement method. The earth fill is 30 m high and has a side slope of 2H:1V with a shape similar to that shown in Figure 14.4a. The embankment is located on a rock site at a rupture-distance of 12 km from a $M_w = 7.2$ strike-slip fault. A simplified deterministic analysis is performed to evaluate the potential movement of a deep slide through the base of the earth embankment.

The average shear wave velocity of the earth fill was estimated to be 300 m/s. For the case of base sliding at the maximum height of this trapezoidal-shaped potential sliding mass, the best estimate of its initial fundamental period is $T_s = 4H/V_s = (4)(30\text{ m})/(300\text{ m/s}) \approx 0.4\text{ s}$. The degraded period of the sliding mass is estimated to be 0.6 s (i.e., $1.5T_s = 1.5(0.4\text{ s}) = 0.6\text{ s}$). The yield coefficient for a deep failure surface was estimated to be 0.14 from a pseudostatic slope stability analyses performed with total stress undrained shear strength properties of $c = 10\text{ kPa}$ and $\phi = 20^\circ$ for the compacted earth fill.

The best estimate of the spectral acceleration at the degraded period of the sliding mass can be computed as the mean of the median predictions from multiple attenuation relationships. Using Abrahamson and Silva (1997) and Sadigh et al. (1997) for the rock site condition for a strike-slip fault with $M_w = 7.2$ and $R = 12\text{ km}$, $S_a(0.6\text{ s}) = 0.44\text{ g}$ and 0.52 g , respectively. Thus, the design value of S_a at the degraded period of sliding mass is 0.48 g, its initial fundamental period is 0.4 s, and k_y is 0.14.

The probability of “zero” displacement occurring is computed using Eq. (14.4) as

$$P(D = “0”) = 1 - \Phi(-1.76 - 3.22 \ln(0.14) - 0.484(0.4) \ln(0.14) + 3.52 \ln(0.48)) = 0.01 \quad (14.8)$$

There is only a 1% probability of negligible displacements (i.e., $< 1\text{ cm}$) occurring for this event. Hence, it is likely that non-negligible displacements will occur. The 16% and 84% exceedance values of seismic displacement can be estimated using Eq. (14.5) assuming that these values are approximately half and double the median estimate, respectively. The median seismic displacement is calculated using

$$\begin{aligned} \ln(D) = & -1.10 - 2.83 \ln(0.14) - 0.333 (\ln(0.14))^2 \\ & + 0.566 \ln(0.14) \ln(0.48) + 3.04 \ln(0.48) - 0.244 (\ln(0.48))^2 \\ & + 1.50(0.4) + 0.278(7.2 - 7) = 2.29. \end{aligned} \quad (14.9)$$

The median estimated displacement is $D = \exp(\ln(D)) = \exp(2.29) \approx 10\text{ cm}$, and the 16% to 84% exceedance displacement range is 5 to 20 cm. Thus, the seismic displacement due to deviatoric deformation is estimated to be between 5 and 20 cm for the design earthquake scenario. The direction of this displacement should be oriented parallel to the direction of slope movement, which will be largely horizontal for this case. For the total crest displacement of the embankment, a procedure such as Tokimatsu and Seed (1987) would be required to estimate the vertical settlement due to cyclic volumetric compression of the compacted earth fill.

6. Conclusions

A new simplified semi-empirical predictive model for estimating seismic deviatoric-induced slope displacements has been presented after critiquing a few other simplified seismic displacement methods for earth and waste structures. The Bray and Travararou (2007) method is based on the results of nonlinear fully coupled stick-slip sliding block analyses using a comprehensive database of hundreds of recorded ground motions. The primary source of uncertainty in assessing the likely performance of an earth/waste system during an earthquake is the input ground motion, so this model takes advantage of the wealth of strong motion records that have recently become available. The spectral acceleration at a degraded period of the potential sliding mass ($S_a(1.5T_s)$) was shown to be the optimal ground motion intensity measure. The system's seismic resistance is best captured by its yield coefficient (k_y), but the dynamic response characteristics of the potential sliding mass is also an important influence, which can be captured by its initial fundamental period (T_s). This model captures the mechanisms that are consistent with the Newmark method, i.e., deviatoric-induced displacement due to sliding on a distinct plane and distributed deviatoric shearing within the slide mass.

The Bray and Travararou (2007) method separates the probability of "zero" displacement (i.e., ≤ 1 cm) occurring from the distribution of "nonzero" displacement, so that very low values of calculated displacement that are not of engineering interest do not bias the results. The calculation of the probability of negligible displacement occurring using Eq. (14.4) provides a screening assessment of the likely seismic performance. If the likelihood of negligible displacements occurring is not high, then the amount of "nonzero" displacement is estimated using Eq. (14.5). The 16% to 84% exceedance seismic displacement range can be estimated approximately as half to twice the median seismic displacement estimate or this range can be calculated accurately using Eqs. (14.6) and (14.7). The first term of Eq. (14.5) is different for the special case of a nearly rigid Newmark sliding block.

The Bray and Travararou (2007) seismic displacement model provides estimates of seismic displacements that are generally consistent with documented cases of earth dam and solid-waste landfill performance. It also provides assessments that are not inconsistent with other simplified methods, but does so with an improved characterization of the uncertainty involved in the estimate of seismic displacement. The proposed model can be implemented rigorously within a fully probabilistic framework for the evaluation of the seismic displacement hazard, or it may be used in a deterministic analysis. In all cases, however, the estimated range of seismic displacement should be considered merely an index of the expected seismic performance of the earth/waste structure.

Acknowledgments

Support for this work was provided by the Earthquake Engineering Research Centers Program of the National Science Foundation under award number EEC-2162000 through the Pacific Earthquake Engineering Research Center (PEER) under award numbers NC5216 and NC7236. Additional support was provided by the David and Lucile

Packard Foundation. Much of the work presented in this paper is based on the Ph.D. research performed by Dr. Thaleia Travasarou of Fugro-West, Inc while she was at the University of California at Berkeley. Her intellectual contributions to developing the Bray and Travasarou (2007) simplified method is gratefully acknowledged. Discussions with Professor Armen Der Kiureghian of the Univ. of California at Berkeley, Professor Ellen Rathje of the Univ. of Texas at Austin, and Professor Ross Boulanger of the Univ. of California at Davis were also of great value.

REFERENCES

- Abrahamson NA, Silva WJ (1996) Empirical Ground Motion Models., Report Prepared for Brookhaven National Laboratory, USA
- Abrahamson NA, Silva WJ (1997) Empirical response spectral attenuation relations for shallow crustal earthquakes. *Seismological Research Letters* 68(1): 94–127
- Ambraseys NN, Menu JM (1988) Earthquake-induced ground displacements. *Journal of Earthquake Engineering and Structural Dynamics* 16: 985–1006
- Ambraseys NN, Srbulov M (1994) Attenuation of earthquake-induced displacements. *Journal of Earthquake Engineering and Structural Dynamics* 23: 467–487
- Ashford SA, Sitar N (2002) Simplified method for evaluating seismic stability of Steep Slopes. *Journal of Geotechnical and Geoenvironmental Engineering* 128(2): 119–128
- Blake TF, Hollingsworth RA, Stewart JP (eds) (2002) Recommended procedures for implementation of DMG Spec. Pub. 117 guidelines for analyzing and mitigating landslide hazards in California., Southern California Earthquake Center, Los Angeles, June
- Bray JD, Augello AJ, Leonards GA, Repetto PC, Byrne RJ (1995) “Seismic stability procedures for solid waste landfill. *Journal of Geotechnical Engineering, ASCE* 121(2): 139–151
- Bray JD, Rathje ER (1998) Earthquake-induced displacements of solid-waste landfills. *Journal of Geotechnical and Geoenvironmental Engineering, ACE* 124(3): 242–253
- Bray JD, Rathje EM, Augello AJ, Merry SM (1998) Simplified seismic design procedures for geosynthetic-lined, solid waste landfills. *Geosynthetics International* 5(1–2): 203–235
- Bray JD, Sancio RB (2006) Assessment of the liquefaction susceptibility of fine-grained Soils. *Journal of Geotechnical and Geoenvironmental Engineering, ASCE* 132(9): 1165–1177
- Bray JD, Travasarou T (2007) Simplified procedure for estimating earthquake-induced deviatoric slope displacements. *Journal of Geotechnical and Geoenvironmental Engineering, ASCE* 133(4): 381–392
- Chen WY, Bray JD, Seed R.B (2006) Shaking table model experiments to assess seismic slope deformation analysis procedures. *Proc. 8th US Nat. Conf. EQ Engrg., 100th Ann. Earthquake Conf. Commemorating the 1906 San Francisco Earthquake, EERI, April, Paper 1322*
- Cornell C, Luco N (2001). Ground motion intensity measures for structural performance assessment at near-fault sites. *Proc. U.S.–Japan joint workshop and third grantees meeting, U.S.–Japan Coop. Res. on Urban EQ. Disaster Mitigation, Seattle, Washington*
- Duncan JM (1996) State of the art: limit equilibrium and finite element analysis of slopes. *ASCE, Journal of Geotechnical Engineering* 122(7): 577–596
- Duncan JM, Wright SG (2005) *Soil Strength and Slope Stability*. John Wiley & Sons, Inc., New Jersey
- Elgamal A-W, Scott R, Succarieh M, Yan L (1990) La Villita dam response during five earthquakes including permanent deformations. *Journal of Geotechnical Engineering* 10(116): 1443–1462

- Elton DJ, Shie C-F, Hadj-Hamou T (1991) One- and two-dimensional analysis of earth Dams". Proc. 2nd Int. Conf. Recent Advancements in Geotechnical Earthquake Engineering and Soil Dynamics, St. Louis, MO, pp 1043–1049
- Finn WD (1998) Seismic safety of embankments dams: developments in research and practice 1988–1998. Proc. Geotech. Earthquake Engrg. Soil Dynamics III, ASCE, Geotechnical Spec. Pub. No. 75, Dakoulas, Yegian and Holtz (eds), Seattle, WA, pp 812–853
- Ghahraman V, Yegian MK (1996) Risk analysis for earthquake-induced permanent deformation of earth dams. Proc. 11th World Conf. on Earthquake Engineering, Acapulco, Mexico. Paper No. 688. Oxford: Pergamon
- Green W (2003) *Econometric Analysis*. 5th Edition. Prentice Hall
- Harder LF, Bray JD, Volpe RL, Rodda KV (1998) Performance of Earth Dams During the Loma Prieta Earthquake. Professional Paper 1552-D, The Loma Prieta, California Earthquake of October 17, 1989 Earth Structures and Engineering Characterization of Ground Motion
- Hynes-Griffin ME, Franklin AG (1984) Rationalizing the seismic coefficient method. Misc. Paper No. GL-84-13, U.S. Army Engr. WES, Vicksburg, MS
- Jibson RW (1993). Predicting earthquake induced landslide displacements using Newmark's sliding block analysis. Trans. Res. Rec, Nat. Acad. Press, 1411, pp 9–17
- Jibson RW, Harp EL, Michael JA (1998) A method for producing digital probabilistic seismic landslide hazard maps: an example from the Los Angeles, California, Area. USGS Open-File Report, pp 98–113
- Kim J, Sitar N (2003) Importance of spatial and temporal variability in the analysis of seismically-induced slope deformation. Proc. 9th Int. Conf. Applications of Statistics and Probability in Civil Engineering, San Fran., Calif. Millpress Science Publishers
- Kramer SL, Smith MW (1997) Modified Newmark model for seismic displacements of compliant slopes. J. Geotechnical Geoenvironmental Engineering, ASCE 123(7): 635–644
- Lin J-S, Whitman RV (1983) Decoupling approximation to the evaluation of earthquake-induced plastic slip in earth dams., Earthquake Engineering and Structural Dynamics 11: 667–678
- Lin J-S, Whitman R (1986) Earthquake induced displacements of sliding blocks. Journal of Geotechnical Engineering 112(1): 44–59
- Makdisi F, Seed H (1978) Simplified procedure for estimating dam and embankment earthquake-induced deformations. Journal of Geotechnical Engineering 104(7): 849–867
- Marcuson WF, Hynes ME, Franklin AG (1992) Seismic stability and permanent deformation analysis: the last 25 years. Stability and Performance of Slopes and Embankments—II, Berkeley, California, pp 552–592
- Matasovic N, Vucetic M (1995) Seismic Response of Soil Deposits Composed of Fully-Saturated Clay and Sand Layers. Proc. 1st Int. Conf. Earthquake Geotech. Engrg., Tokyo, Japan, Nov. 14–16, V. 1, pp 611–616
- Newmark NM (1965) Effects of earthquakes on dams and embankments. Geotechnique, London 15(2): 139–160
- Rathje EM, Bray JD (2000) Nonlinear coupled seismic sliding analysis of earth structures. Journal of Geotechnical and Geoenvironmental Engineering 126(11): 1002–1014
- Rathje EM, Bray J.D (2001) One- and two-dimensional seismic analysis of solid-waste landfills. Canadian Geotechnical Journal 38(4): 850–862
- Rathje EM, Faraj F, Russell S, Bray JD (2004) Empirical relationships for frequency content parameters of earthquake ground motions. Earthquake Spectra, Earthquake Engineering Research Institute 20(1): 119–144

- Rathje EM, Saygili G (2006) A vector hazard approach for Newmark sliding block analysis. Proc. Earthquake Geotech. Engrg. Workshop, University of Canterbury, Christchurch, New Zealand, Nov. 20–23
- Rodriguez-Marek A, Bray JD, Abrahamson N (2001) An empirical geotechnical seismic site response procedure. *Earthquake Spectra* 17(1): 65–87
- Sadigh K, Chang C-Y, Egan JA, Makdisi F, Youngs RR (1997) Attenuation relationships for shallow crustal earthquakes based on California strong motion data. *Seismological Research Letters* 68(1): 180–189
- Seed HB (1979) Considerations in the earthquake-resistant design of earth and rockfill dams. *Geotechnique* 29(3): 215–263
- Seed HB, Martin GR (1966) The seismic coefficient in earth dam design. *Journal of the Soil Mechanical and Foundation Division, ASCE* 92 No. SM 3: pp 25–58
- Seed HB, Idriss IM (1971) Simplified procedure for evaluating soil liquefaction potential. *Journal of SMFE, ASCE* 97(9): 1249–1273
- Seed HB, Tokimatsu K, Harder LF, Chung RM (1985) Influence of SPT procedures in soil liquefaction resistance evaluation. *Journal of Geotechnical Engineering* 111(12): 1425–1445
- Stewart JP, Bray JD, McMahon DJ, Smith PM, Kropp AL (2001) Seismic performance of hillside fills. *Journal of Geotechnical and Geoenvironmental Engineering ASCE* 127(11): 905–919
- Stewart JP, Blake TF, Hollingsworth, RA (2003) A screen analysis procedure for seismic slope stability. *Earthquake Spectra* 19(3): 697–712
- Tokimatsu K, Seed HB (1987) Evaluation of settlements in sands due to earthquake shaking. *Journal of Geotechnical Engineering, ASCE* 113(8): 861–878
- Travasarou T (2003) Optimal ground motion intensity measures for probabilistic assessment of seismic slope displacements. Ph.D. Dissertation, U.C. Berkeley
- Travasarou T, Bray JD (2003a) Optimal ground motion intensity measures for assessment of seismic slope displacements. 2003 Pacific Conference on Earthquake Engineering, Christchurch, New Zealand, Feb
- Travasarou T, Bray JD (2003b) Probabilistically-based estimates of seismic slope displacements. Proc. 9th Int. Conf. Applications of Statistics and Probability in Civil Engineering, San Fran., Calif. Paper No. 318. Millpress Science Publishers
- Vrymoed JL, Calzascia ER (1978) Simplified determination of dynamic stresses in earth dams. Proc., EQ Engrg. Soil Dyn. Conf., ASCE, New York, NY, pp 991–1006
- Vucetic M, Dobry R (1991) Effect of soil plasticity on cyclic response. *Journal of Geotechnical Engineering* 17(1): 89–107
- Wartman J, Bray JD, Seed RB (2003) Inclined plane studies of the Newmark sliding block procedure. *Journal of Geotechnical and Geoenvironmental Engineering, ASCE* 129(8): 673–684
- Yegian M, Marciano E, Ghahraman V (1991a) Earthquake-induced permanent deformations: probabilistic approach. *Journal of Geotechnical Engineering* 117(1): 18–34
- Yegian M, Marciano E, Ghahraman V (1991b) Seismic risk analysis for earth dams. *Journal of Geotechnical Engineering* 117(1): 35–50
- Youd, TL, Idriss, IM, Andrus, RD, Arango, I, Castro, G, Christian, JT, Dobry, R, Finn, WD, Liam, Harder, Jr., LF, Hynes, ME, Ishihara, K, Koester, JP, Liao, SSC, Marcuson, III, WF, Martin, GR, Mitchell, JK, Moriwaki, Y, Power, MS, Robertson, PK, Seed, RB, and Stokoe, II, KH (2001) Liquefaction resistance of soils: summary report from the 1996 NCEER and 1998 NCEER/NSF workshops on evaluation of liquefaction resistance of soils. *Journal of Geotechnical and Geoenvironmental Engineering ASCE* 127(10): 817–833

CHAPTER 15

DEVELOPMENTS OF SOIL IMPROVEMENT TECHNOLOGIES FOR MITIGATION OF LIQUEFACTION RISK

Ikuo Towhata

Department of Civil Engineering, University of Tokyo, Japan
towhata@geot.t.u-tokyo.ac.jp

Abstract. Studies on liquefaction have a history of more than 40 years since Niigata and Anchorage were attacked by disastrous earthquakes. The topics of interest have changed with time and recent interest is focused on advanced mitigation which can achieve cost-effectiveness and/or is useful for existing structures. The present text describes recent experimental studies in both laboratory and field. The concerned mitigation technologies consist of blasting for low cost, grouting of colloidal silica for existing and sensitive structures, and drain pipes which are feasible in a small space under an existing structure. The conducted tests showed how they have advantages over other methods if they are used in appropriate conditions.

1. Introduction

The aim of technological developments for mitigation of liquefaction risk has been changing in the past in the following manners. Until 1970, the major interest lay in the identification of the causative mechanism of liquefaction. Example of this type may be found in Yoshimi (1967). Studies in those days helped development of mitigation technologies such as densification and drainage. At the same time, Koizumi (1966) compared SPT-N in Niigata City before and after the 1964 quake, showing that liquefaction potential is closely related with density of sand. This study resulted thereafter in design formula for evaluation of liquefaction potential based on penetration resistance in soils.

While the above studies continued in 1980s in a more detailed and precise manner, a different viewpoint emerged. The new point was twofold, consisting of interests in mechanism of permanent displacement of ground and performance-based mitigation. The latter implies that inexpensive mitigation should be allowed if the extent of ground deformation is sufficiently small. This idea is considered important nowadays in design of lifelines and other structures for which costly mitigation measures are not appropriate. Hence, prediction of the performance of subsoil with and without mitigation against liquefaction attracts engineering concern. In other words, there is a strong trend towards performance-based design.

Technological development is also focused on existing structures. Being overlain by a structure in use, the subsoil cannot be easily improved. In particular, powerful tamping by a big machine with ground vibration and/or noise is extremely difficult. Another issue

is the cost which is needed for soil improvement. It is going to be more difficult to spend expenditures that exceed benefits gained from the mitigation. With these recent situations, the present paper addresses topics and achievements in mitigation measures against liquefaction.

2. Sand densification

2.1. GENERAL REMARKS

Densification of sand has been one of the most important mitigation measures for liquefaction problems. Sand compaction pile in particular has been studied and constructed intensely. In practice, pressurized air of, for example, 500 kPa, is frequently used to help formation of sand columns in ground. Okamura et al. (2005, 2006) suggested that the pressurized air remains for a long time in subsoil and reduces the degree of saturation. Reduced saturation thus achieved improves liquefaction resistance of soil. Since the conventional design principle of sand compaction pile assumes soil to be fully saturated, this new point implies additional safety margin. Another safety margin may be the long-term increase of SPT-N; see Figure 15.1. Otherwise called ageing, this feature further increases the liquefaction resistance. The mechanism behind this ageing is not known yet. Moreover, the SAVE Technology (Ohbayashi et al., 2006) achieved static installation of sand compaction piles and drastically reduced noise as well as ground vibration (Figures 15.2 and 15.3). This has made it possible to execute sand compaction piles within a few meters from existing structures.

2.2. BLASTING

From the viewpoint of cost, blasting is a very promising technology. Port and Airport Research Institute conducted blasting study in Tokachi Harbor in 2001 and a young

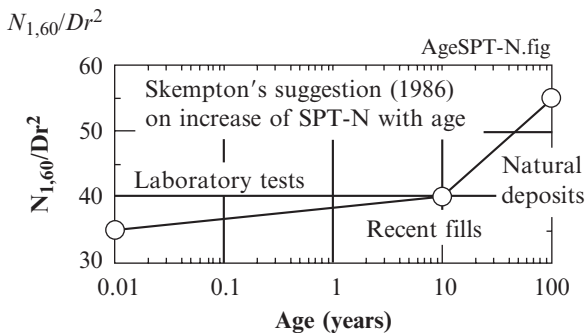


Fig. 15.1. Skempton's suggestion on increase in SPT-N with age (relative density, Dr , in decimal)

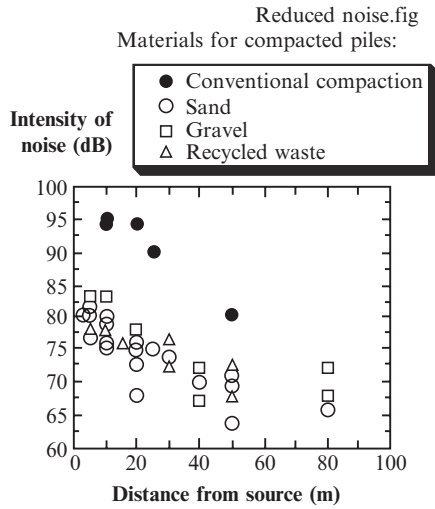


Fig. 15.2. Intensity of noise during static construction of sand compaction piles (by Fudo-Tetra Corporation)

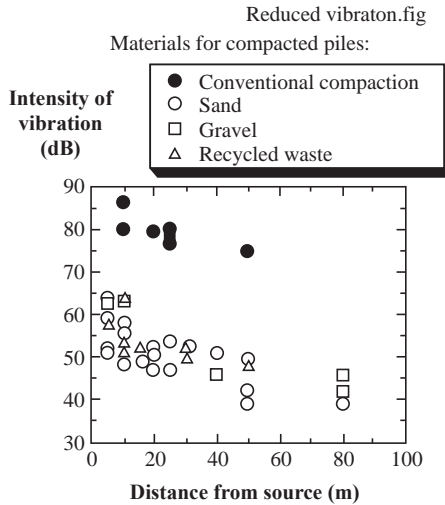


Fig. 15.3. Intensity of ground vibration during static construction of sand compaction piles (by Fudo-Tetra Corporation)

reclaimed land liquefied (Figure 15.4). It is already known that blasting is able to increase SPT-N of sandy ground significantly (Figure 15.5). It seems to the author, however, that more efforts have to be made to improve its efficiency so that sand density may be sufficient to survive a very strong design earthquake. The very strong design earthquake



Fig. 15.4. Liquefaction induced by subsoil blasting in Tokachi Harbor

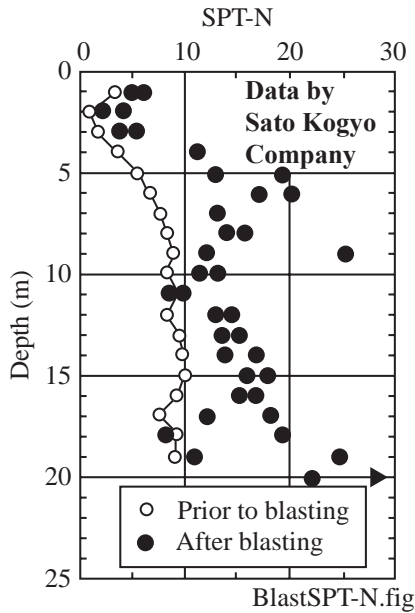


Fig. 15.5. Increase of SPT-N by blasting (data by Sato Kogyo Inc.)

means the one which may occur once every hundreds of years. A key to improve the efficiency of blasting seems to lie in the stress-induced anisotropy of sand fabric.

Arthur et al. (1977) conducted repeated loading of principal stress, while changing its orientation. It was thereby shown that the greater volume change (dilatancy) is produced

when the orientation of principal stress is varied more profoundly from the previous loading. Being called stress-induced anisotropy, the effects of previous loading direction on deformation during a subsequent loading were demonstrated experimentally by Oda (1972). His microscopic observation showed that the direction of grain-to-grain contact plane governs the overall behavior of sand and that the statistic nature of the contact directions is changed by the stress history. One cycle of loading and unloading of principal stress, σ_1 , in a selected direction to a large deformation generates many contact planes perpendicular to this stress orientation, thus increasing soil rigidity against further loading in the same direction. What is important in Oda's study is that the number of contact planes in other directions decreases and accordingly the sand rigidity in other directions decreases as well. Yamada and Ishihara (1981) made the same finding in undrained shear tests on cubic soil samples.

The effects of varying σ_1 orientation is further indicated in what follows. Figure 15.6 shows the stress state in a torsion shear device in which stress difference of $(\sigma_v - \sigma_h) / 2$ and τ_{vh} are loaded independently. Consequently, the orientation of the major principal stress, σ_1 , is denoted by β . A cyclic loading test was carried out on loose Toyoura sand in an undrained manner, where the two components of shear stress, $(\sigma_v - \sigma_h) / 2$ and τ_{vh} , were applied to a sample alternately and the β angle changed by 90° . Figure 15.7 illustrates the stress-path diagram where the decrease of the effective mean principal stress, $P' \equiv (\sigma'_1 + \sigma'_2 + \sigma'_3) / 3$, which is equal to the development of excess pore water pressure, is plotted against shear stress components. It is therein shown that the first loading of τ_{vh} developed a substantial excess pore water pressure, the second and the third loadings of the same stress component did not reduce P' so much because the orientation of the principal stress did not change ($\beta = \text{constant at } 45^\circ$), in contrast the fourth loading cycle was associated with $(\sigma_v - \sigma_h) / 2$ and $\beta = 0^\circ$, resulting in more significant excess pore water pressure, and the fifth loading came back to τ_{vh} and $\beta = 45^\circ$ again; causing substantial excess pore water pressure.

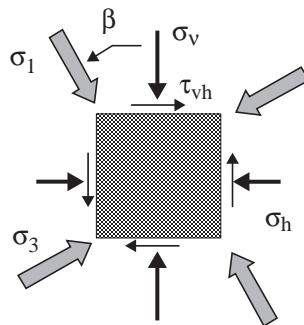


Fig. 15.6. Two independent shear stress components and orientation of principal stress axis

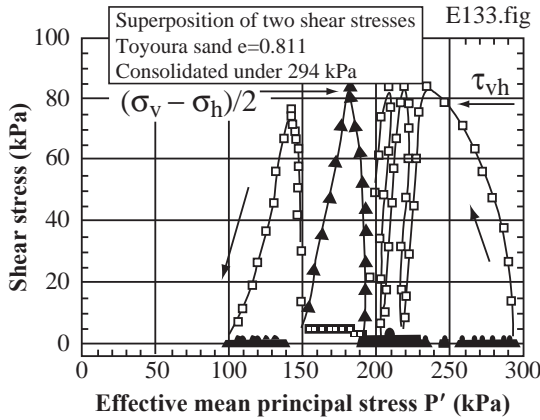


Fig. 15.7. Effects of stress axis rotation on efficient development of pore water pressure

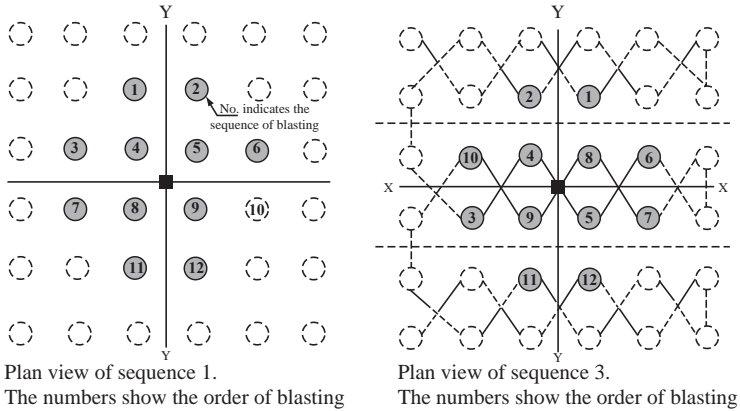


Fig. 15.8. Plan view of blasting sequences for soil densification

The present blasting is planned and carried out with a blasting sequence which starts from one end of a site towards the other. Typically, this sequence is similar to sequence 1 in Figure 15.8. This figure attempts to simplify the blasting effects as a stress history in the horizontal plane. When a point amid blasting points is concerned, the stress history is represented by the magnitude of principal stresses and their orientation. For example, the impact by a blasting is represented by the arrival of compressional wave (P wave) in the radial direction (Figure 15.9) followed by extension. In other words, the major principal stress, σ_1 , occurs first in the radial direction, and, in the second half of one shaking cycle, σ_3 follows in the same direction. It is hence supposed that more efficient sequence of blasting may be found by making some blasting sequence which produces more significant rotation of principal stress orientations.

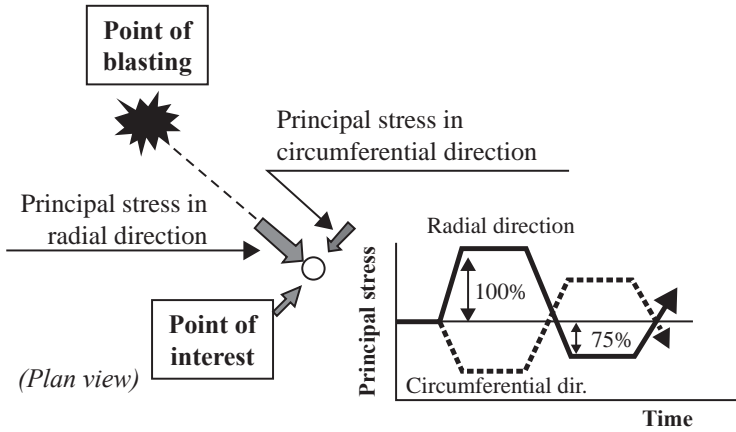


Fig. 15.9. Schematic diagram of stress variation induced by single shot of blasting

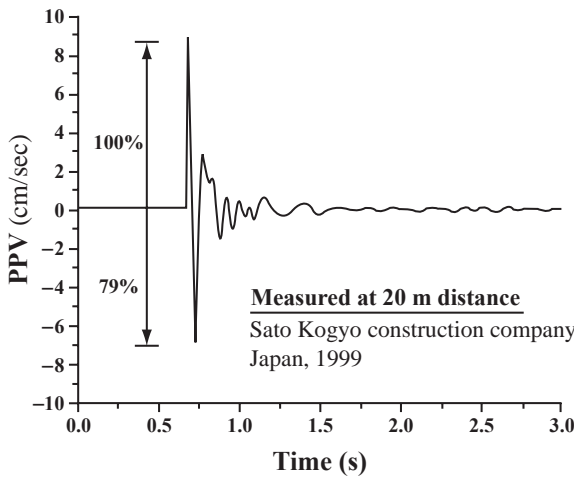


Fig. 15.10. Example of soil particle velocity in radial direction as induced by single blasting

The impact produced by a single cycle of P wave can be understood by Figure 15.10 which illustrates the soil particle velocity in the radial direction induced by a blasting. It is seen there that the first compressional impact is significant and the following extension is of less magnitude, while the following stress variation is negligible for practical purposes. When the P wave velocity in soil is designated by V_p , the radial displacement, u , due to blasting is expressed as

$$u(r, t) = U(t - r/V_p) \tag{1}$$

where r stands for the distance measured from the wave source along the wave path and t is the elapsed time. Note that this equation stands for wave propagation in the positive direction of r . Accordingly, the soil velocity, compressional strain, and the compressional stress, σ , in the r direction are derived as

$$\text{Velocity} = \partial u / \partial t = U' \tag{2}$$

$$\text{Normal strain} = -\partial u / \partial r = U' / Vp \tag{3}$$

$$\sigma = E \times (\text{normal strain}) = \frac{E}{Vp} U' = \frac{E}{Vp} \times \text{velocity} \tag{4}$$

Thus, the velocity history in Figure 15.8 also implies that the stress history is reasonably represented by one cycle of loading (Figure 15.9), and, moreover, the unloading in the second half of the cycle is less significant than the first half. Hence, the present study supposes that the intensity of stress increments during first compression and the following extension have the ratio of 100:75 (Figure 15.9). The magnitude of stress is determined by an empirical formula on

$$\text{maximum velocity : } PPV = 1.73 \left[\frac{R}{\sqrt{W}} \right]^{-1.25} \tag{5}$$

in which PPV designates the maximum soil velocity (m/s), R the distance from the point of blasting, and W the weight of the employed explosive (kgf). For experimental reproduction of stress–strain history caused by blasting, the maximum velocity given by Eq. (5) was converted to strain by Eq. (3), firstly, and the strain was further converted to stress history by using such an experimental data as the monotonic undrained triaxial compression in Figure 15.11.

With these points in mind, two sequences of blasting around the point of interest are discussed. The first and the second sequence employ order of blasting which starts from one end towards the other. By ignoring blasting at far distances, the P wave propagation from two consecutive blastings is found to induce principal stress in similar directions;

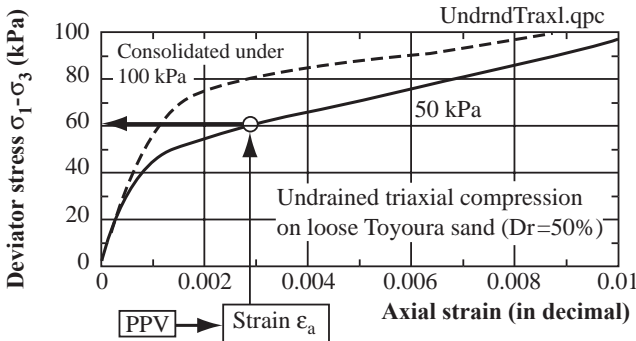


Fig. 15.11. Monotonic undrained loading of triaxial compressional stress

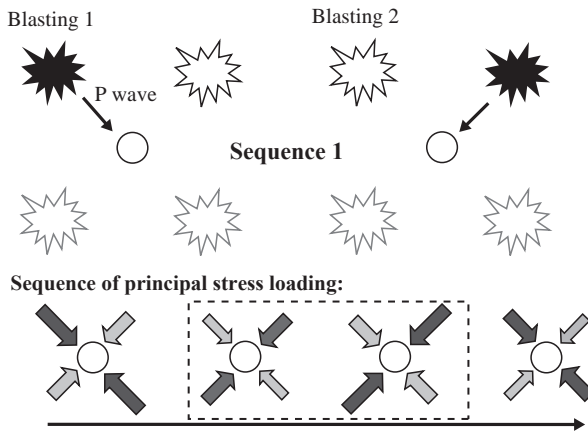


Fig. 15.12. Orientation of principal stresses produced by sequence 1

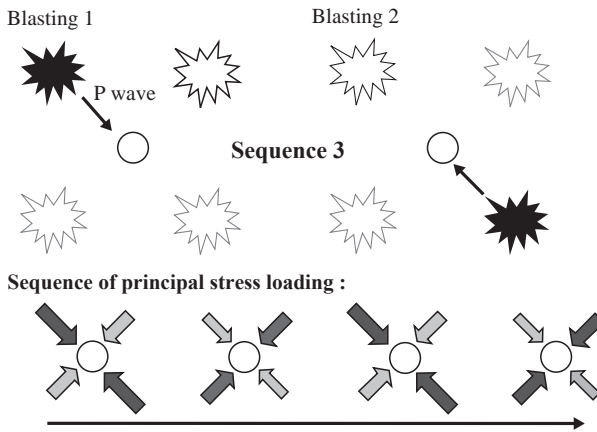
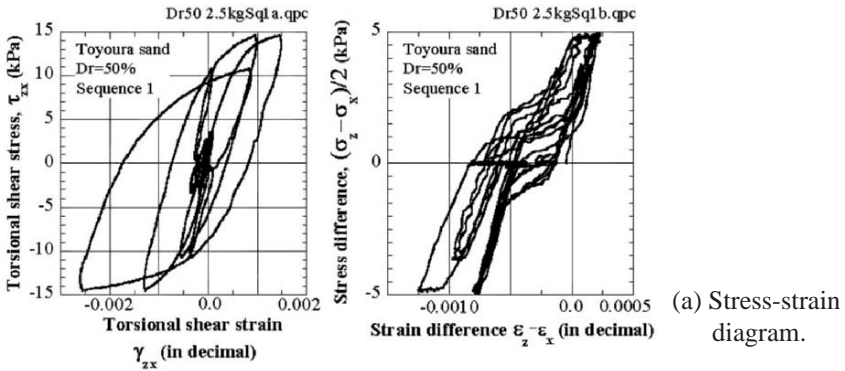


Fig. 15.13. Orientation of principal stresses produced by sequence 3

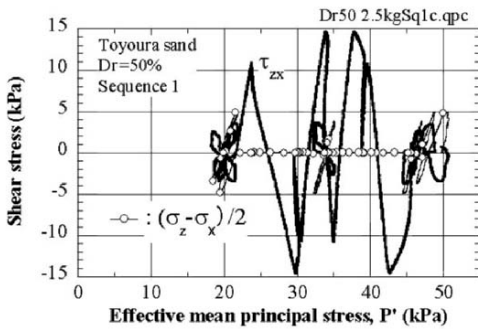
see Figure 15.12; the second half of the first blasting and the first half of the second blasting produce the same direction of major principal stress. This situation is not favorable for efficient densification of sand. In contrast, the sequence 3 in Figure 15.13 periodically changes the orientation of principal stresses and is expected to densify soil more efficiently.

2.3. EXPERIMENTAL REPRODUCTION OF BLASTING STRESS

Undrained torsion shear tests were conducted to reproduce the stress history induced by different blasting sequences. Test results obtained by stress sequences 1 and 3



(a) Stress-strain diagram.



(b) Stress-path diagram.

Fig. 15.14. Loading of sequence 1 on isotropically consolidated sand specimen. (a) Stress-strain diagram. (b) Stress-path diagram.

(Sendir et al., 2006; Wassan et al., 2006) are compared in Figures 15.14 and 15.15. For these tests, specimens of Toyoura sand were consolidated isotropically under 50 kPa and were sheared in a torsion shear device. The sample size was 10 cm in outer diameter, 6 cm in inner diameter, and 20 cm in height. It is evident that sequence 3 produced more profound effects on sand such as greater shear strain and higher excess pore water pressure.

The densification effects of different sequences of blasting are examined in Figure 15.16. It is shown herein that sequence 3 produces the greatest volumetric strain upon dissipation of generated excess pore water pressure. Therefore, it may be stated that the efficiency of soil improvement can be improved by considering the sequence of blasting and without increasing the amount of explosive resources. Note further that the present study is limited to a two-dimensional consideration of blasting sequences (Figure 15.8). However, a similar approach to the problem is possible.

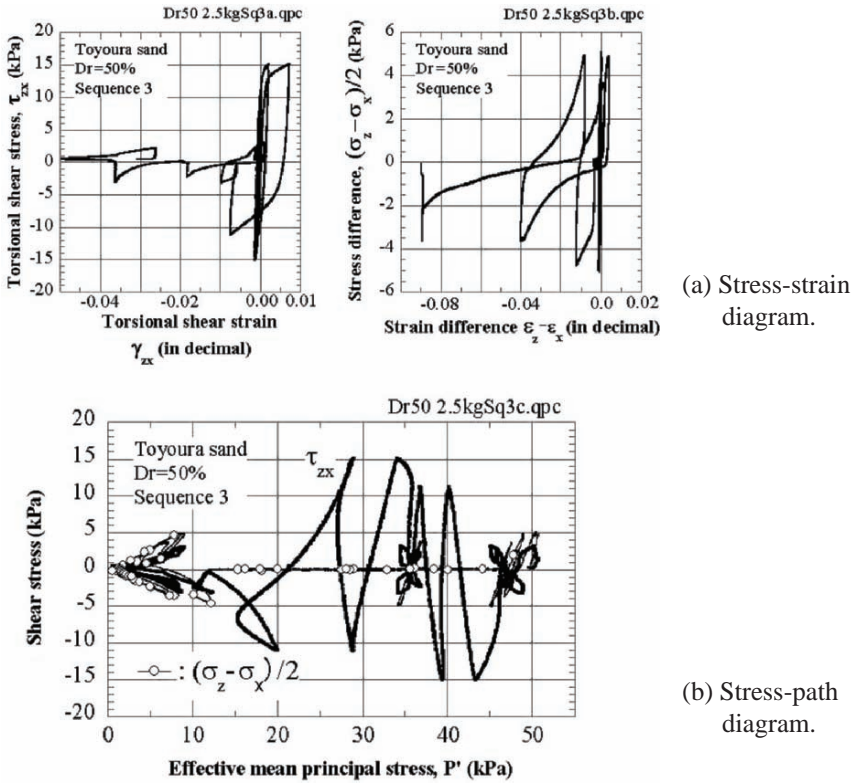


Fig. 15.15. Loading of sequence 3 on isotropically consolidated sand specimen (a) Stress-strain diagram. (b) Stress-path diagram.

3. Soil improvement by grouting

3.1. GENERAL REMARKS

Grouting and solidification of liquefiable sand has an advantage that it does not produce harmful ground vibration and noise. Its shortcoming may be that it is more costly than aforementioned densification. Thus, it is important to find a situation in which the advantage of grouting is particularly useful. One of such advantageous situations lies in soil improvement under existing structures. Figure 15.17 shows an example of the effects of subsoil liquefaction on liquid storage tanks. Since such a storage site has many pipelines among tanks, it is difficult for big soil improvement machines to come in. It is evidently unacceptable to cause subsidence of foundation of tanks as a consequence of densification. With these in mind, this part of the paper addresses solidification of soil by means of injection of colloidal silica.

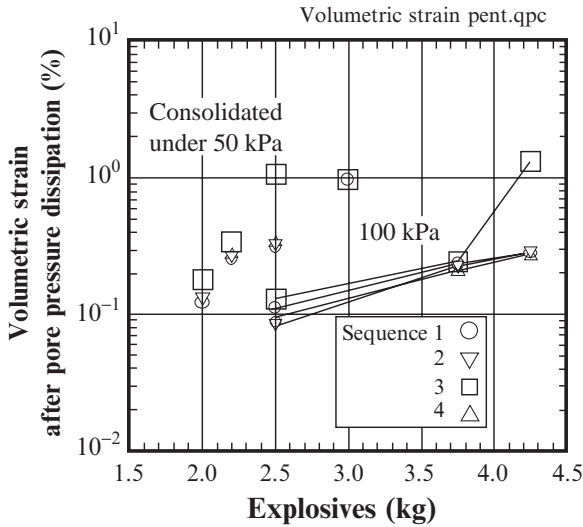


Fig. 15.16. Comparison of volumetric strain after undrained cyclic loading and dissipation of excess pore water pressure



Fig. 15.17. Distortion of liquid storage tanks due to subsoil liquefaction (Kobe, 1995)

Being different from cement mixing, the use of grouting for soil improvement has been limited to short-term improvement. The reasons why its permanent use was difficult were weathering and deterioration of the properties of improved soil, accidents in the past that injected liquid contaminated well water and affected human health, and difficulty in uniform seeping.

Among these, the third issue means that concerned soil has to be improved uniformly (Figure 15.18); improvement only in cracks is not accepted. After 1990s, a new kind of colloidal silica emerged in the market and overcame the abovementioned problems. For example, Figure 15.19 illustrates the long-term stability of the mechanical properties of grouted sand.

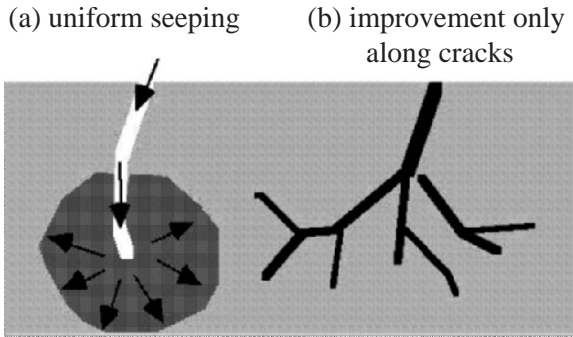


Fig. 15.18. Configuration of ground improvement by injection of liquid grout

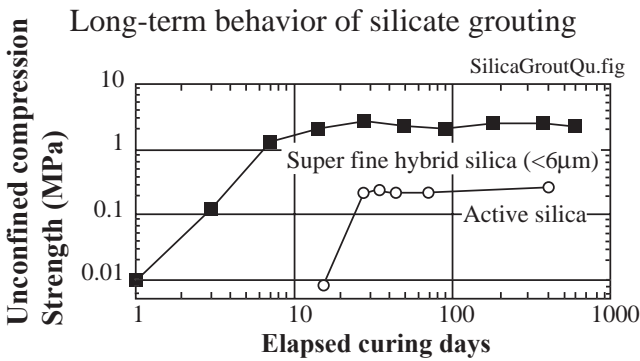


Fig. 15.19. Unconfined compression strength of sand improved by colloidal silica (data by Miwa et al., 2001; Yonekura et al., 2001)

Liquid of colloidal silica is injected into ground through tubes or piles under relatively low pressure. Figure 15.20 shows the ongoing injection through multiple tubes, and a good size of solidified mass of soil is formed. The very small size of colloidal silica particles (typically 10 nm) makes it possible for the silicate grout to seep into fine sand and silty sand. Figure 15.21 manifests an excavated mass of sand which is an evidence of uniform seeping due to very low viscosity and very fine size of silica grains in the liquid.

One of the advantages of the injection of colloidal silica liquid is its capability to improve soils under existing structures (Figure 15.22). This aim is achieved by drilling a hole in an oblique direction (Figure 15.23) and installing an injection nozzle (Figure 15.24).

The extent of uniform seeping was examined by reproducing the process in a laboratory model ground (C. Conlee of Drexel University during her internship at University of Tokyo). Liquid of colloidal silica was injected under low pressure into sandy ground, and



Fig. 15.20. Injection of colloidal silica liquid through multiple tubes into sandy ground



Fig. 15.21. Excavation of soil mass as solidified by silica grouting

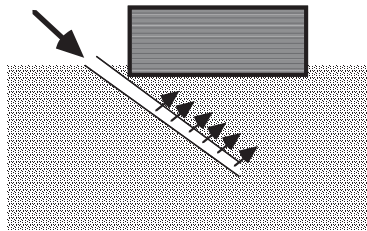


Fig. 15.22. Soil improvement under existing structure

the visual observation of seeping was made easy by dyeing the liquid with green color. Figure 15.25 verifies the idea of uniform seeping. This extent of uniform seeping is equivalent with that of water which is demonstrated by red color in Figure 15.26. Moreover, Figure 15.27 indicates that the colloidal silica liquid can seep uniformly even into sandy ground with gravel layer in spite of the permeability contrast.



Fig. 15.23. Inclined drilling of borehole for grouting under existing structure



Fig. 15.24. Example of nozzle for injection of liquid (at site of Penta-Ocean Inc.)

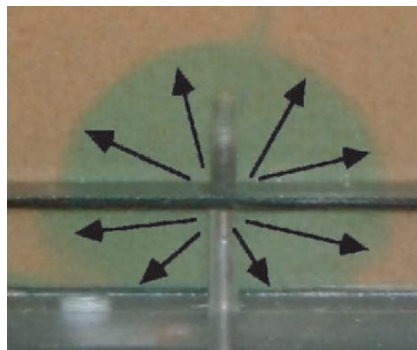


Fig. 15.25. Uniform seeping in sand of colloidal silica liquid which is colored green

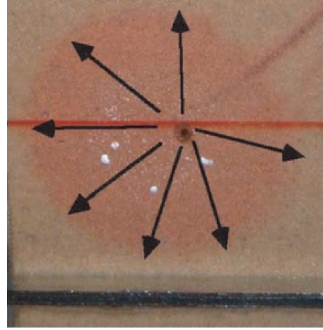


Fig. 15.26. Seeping of dyed water into clean sand

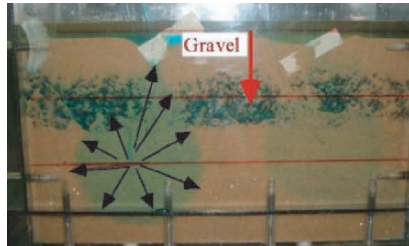


Fig. 15.27. Uniform seeping of colloidal silica liquid into sand with gravel layer

3.2. UNDRAINED TRIAXIAL TESTS ON SAND IMPROVED BY COLLOIDAL SILICA

Laboratory shear tests were carried out on the effects of colloidal silica on improvement of liquefaction resistance of loose sand (Kabashima and Towhata, 2000; Towhata and Kabashima, 2001). Tested specimens were prepared by reproducing the in-situ stress history as much as possible; loose water-saturated sand was consolidated in a container in a Ko manner under realistic stress levels (Figure 15.28), silicate liquid seeped into sand under the anisotropic consolidation pressure, and then the sand was cured for 5 weeks under sustained stress. Curing under stress was considered important because of the possibility that consolidation and deformation of sand after solidification of grout might destroy bonding which was made by solidified silica (Figure 15.29). Specimens thus prepared were firstly tested by undrained triaxial monotonic shear; both compression and extension tests. In Figure 15.30, sand which was improved by silicate liquid shows better behavior than untreated sand. Furthermore, liquefaction resistance was improved by colloidal silica as well (Figure 15.31).

One of the study interests lay in the possible breakage of bonding and grouting effects due to cyclic loading. It was feared that the first strong earthquake may be well resisted by bonding but cyclic stress during future earthquake would not be. This issue was

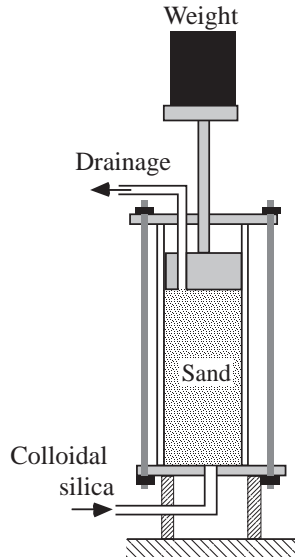


Fig. 15.28. Curing under sustained stress of sand treated by colloidal silica liquid

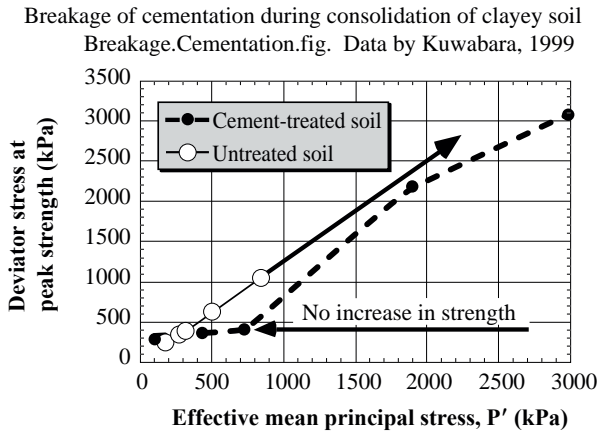


Fig. 15.29. Example of broken cementation in clay due to consolidation volume change

investigated in Figure 15.32 where sand improved by colloidal silica was subjected to cyclic loading until a certain magnitude of strain occurred and then was sheared in a monotonic undrained manner. It is found in this figure that stiffness of the improved sand (tangent of stress–strain curve) after cyclic loading is still better than that of unimproved sand. Thus, no fear is needed of breach of grouting effects.

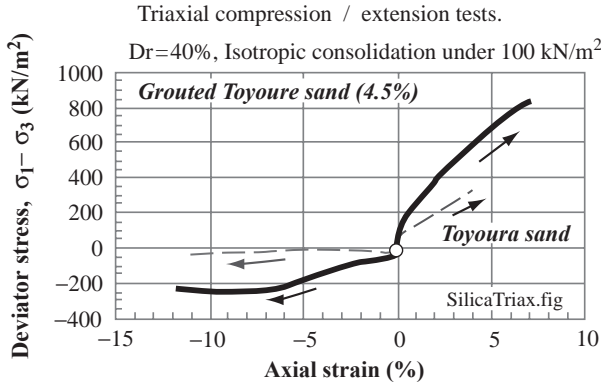


Fig. 15.30. Comparison of sand improved by colloidal silica and untreated sand by means of undrained triaxial tests

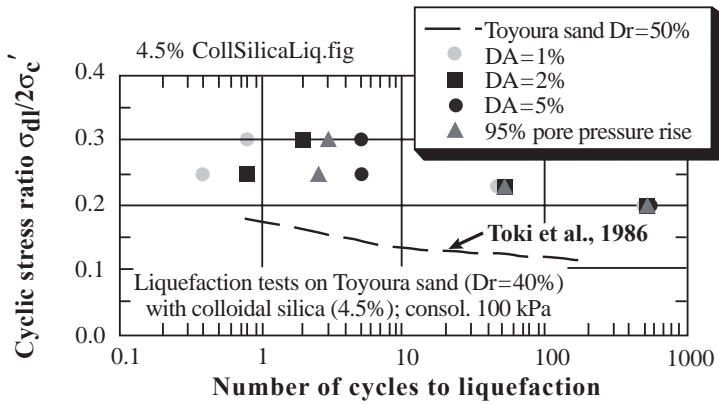


Fig. 15.31. Resistance of sand against liquefaction increased by colloidal silica

In Figure 15.33, sand of 40% relative density was improved and was compared with densified sand without grouting. This comparison was made in terms of the residual deformation after 30 cycles of triaxial compression as well as the monotonic behavior after this cyclic loading. It may be found that the behavior of grouted sand is equivalent with densification to 80% relative density.

Figure 15.34 shows the appearance of solidified colloidal silica. It is substantially soft and, hence, it is difficult to understand why such a soft material improves the undrained shear behavior of sand. One possible answer to this question may be the volume compressibility of this material (di Benedetto, 2001). Being soft, this material decreases its volume upon compression and allows less excess pore water pressure to develop than

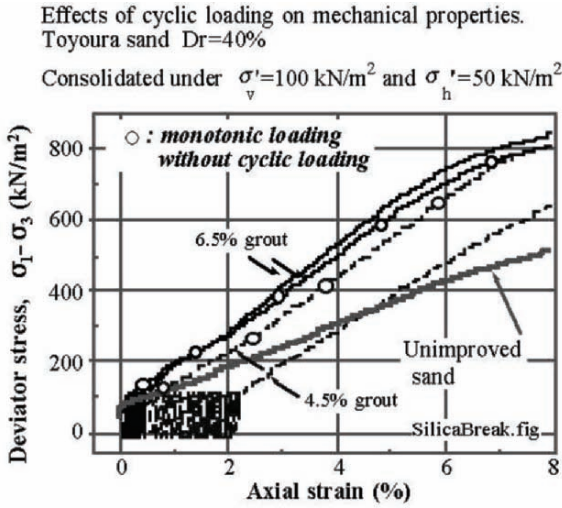


Fig. 15.32. Triaxial compression of grouted sand after cyclically induced deformation

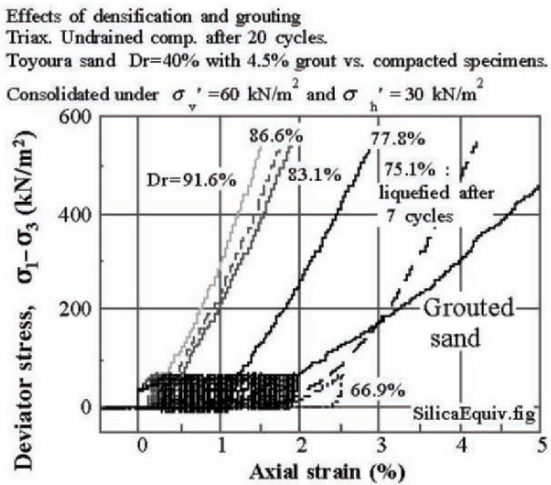


Fig. 15.33. Densification of sand equivalent to grouting

pore water which is practically incompressible. Note that excess pore water pressure is generated in consequence of incompressibility of pore water upon negative dilatancy of sand.

To understand the mechanical behavior of solidified colloidal silica, a series of unconfined compression tests were carried out. Figure 15.35 shows a specimen prior to test; the sample measured 7 cm in height, 4.7 cm in diameter, and 129 g in weight. The tested

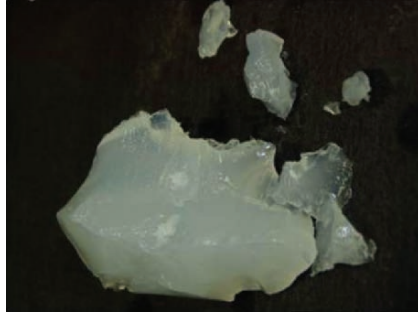


Fig. 15.34. Appearance of solidified colloidal silica

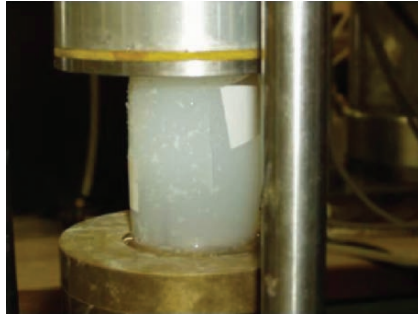


Fig. 15.35. Unconfined compression test on solidified colloidal silica material

material was cured for 30 days in water so that drying might be avoided. Figure 15.36 illustrates the shape of the sample after failure. Due probably to some heterogeneity, the central part remained after large deformation.

The test results are presented in Figures 15.37 and 15.38. The special interest lay in the measurement of lateral strain. Hence, two sets of laser displacement transducers were placed at $1/3$ and $2/3$ of the sample height in order to monitor the lateral displacement at the sample surface. As seen in Figure 15.35, sheets of white paper were attached to the surface so that reflection of laser beam was facilitated. The test results in Figure 15.38 indicates that the ratio of axial and lateral strains, which is namely the Poisson ratio ν , is around 0.3. Thus, the material has a volume compressibility; if $\nu = 0.5$, volume does not change during shear. It is therefore possible that the liquefaction resistance of sand is improved by volume compressibility of solidified silica. It should be recalled that constant volume of pore water is the important cause of high excess pore water pressure during undrained shear.

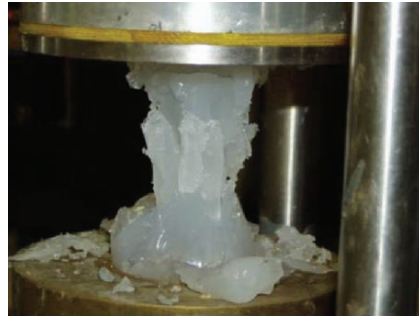


Fig. 15.36. Ultimate shape of colloidal silica sample after failure in unconfined compression test

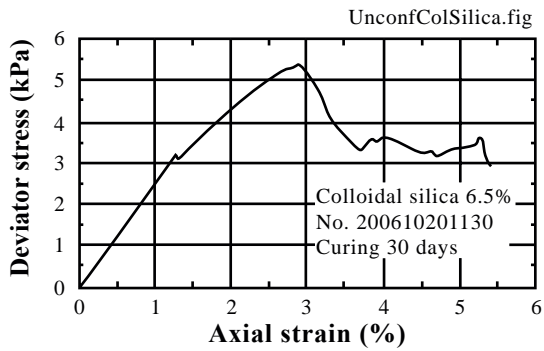


Fig. 15.37. Stress–strain behavior of solidified colloidal silica in unconfined compression test

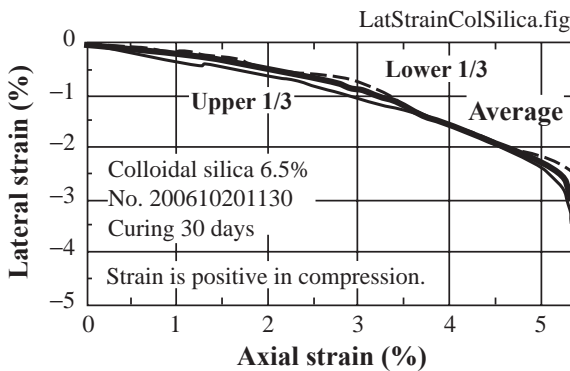


Fig. 15.38. Lateral deformation of colloidal silica plotted against axial strain in unconfined compression test

4. Dissipation of excess pore water pressure

Quick dissipation of pore pressure by means of gravel drain has been one of the useful measures to mitigate liquefaction problems. One of the good points of this method is that gravel drain does not make noise, ground vibration, or ground deformation upon installation. Hence, it is possible to employ this method near existing structures (Figure 15.39). There are, however, situations in which a tall installation machine (Figure 15.39) cannot be employed. One of them is the liquefaction problem of pile foundation of elevated railways and flyovers (Figure 15.40).

Harada et al. (2004, 2006) developed metal pipe drains which can be installed in loose sand by mechanical blows. Since the size of a required blow machine is limited, it is possible to execute it under elevated structures. This drain pipe is called a screen pipe (Figure 15.41) which is made of metal rods in the axial direction with metal rings surrounding them. Very small spacing between rings allows pore water to flow into the pipe, thereby dissipating the excess pore water pressure, while the field shaking tests showed that clogging is negligible after liquefaction. Since the pipe is hollow, its permeability is significantly higher than that of gravel drain.

Verification of the effects of a screen pipe was conducted in a laminar box of a 1-G model scale (Figure 15.42) as well as in the field. In a laminar box, a model ground (Figure 15.43) measured 99 cm in depth and therein a group pile of 2×2 in size was installed. The pile heads were connected to each other by a pile cap and screen pipes were placed both inside and outside the group pile. The horizontal size of the group pile was $26 \text{ cm} \times 26 \text{ cm}$. Pore fluid was a solution of cellulose which made the viscosity of pore



Fig. 15.39. Construction of gravel drain (Fudo-Tetra Inc.)

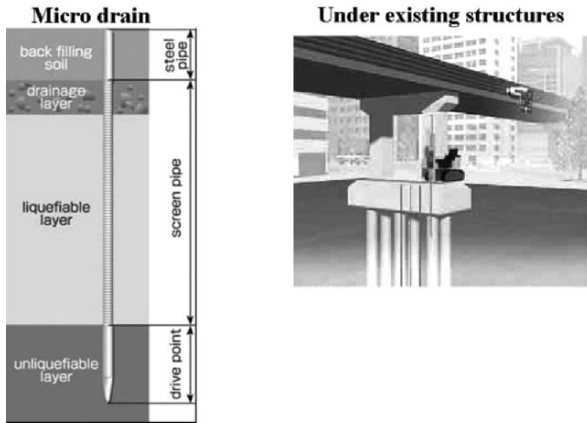


Fig. 15.40. Need for soil improvement under bridges and flyovers (Zenitaka Corp.)

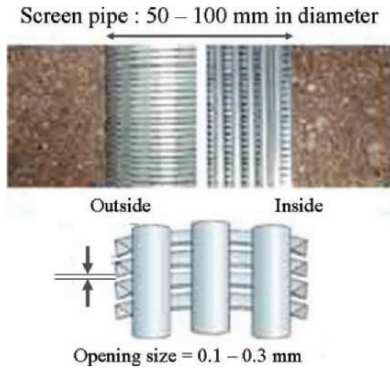


Fig. 15.41. Details of screen pipe for dissipation of excess pore water pressure (Zenitaka Corp.)

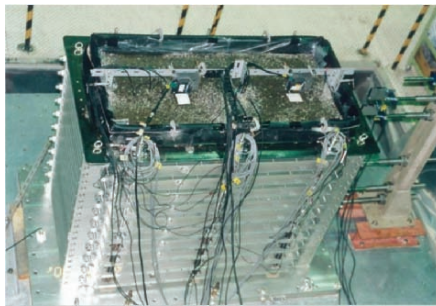


Fig. 15.42. Laminar box for 1-G model test on screen pipe (Harada et al., 2006)

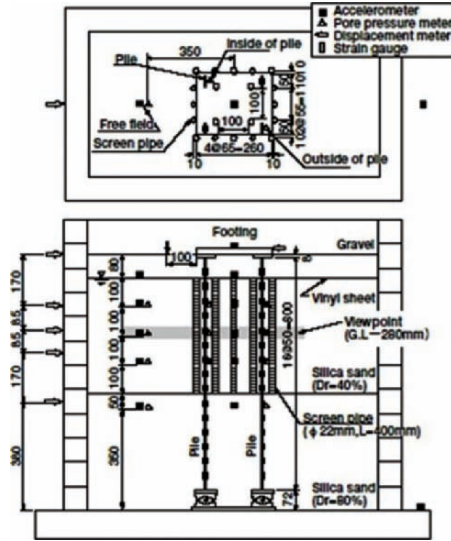


Fig. 15.43. Configuration of 1-G model for screen-pipe test (Harada et al., 2006)

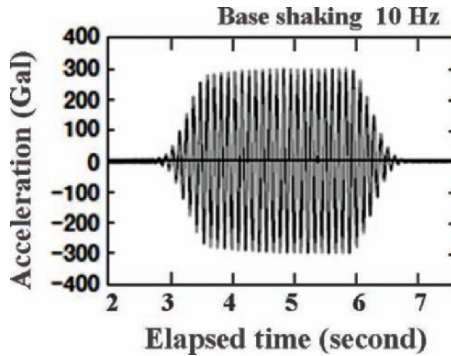


Fig. 15.44. Time history of base shaking with 300 Gal in amplitude (Harada et al., 2006)

fluid 11 times greater than water in order to consider the similitude to some extent. Base shaking was produced in a harmonic manner in the longitudinal direction of the laminar box with a frequency of 10 Hz (Figure 15.44), while varying the intensity of acceleration.

Figure 15.45 compares time histories of excess pore water pressures in two cases; one with and the other without screen pipes. In the former case, the pipes surrounded the group pile with a spacing of 60 mm. It is supposed that the installation of drains around an existing foundation is feasible in practice of protection from liquefaction problems. Figure 15.45 clearly indicates that excess pore water pressures inside and outside the

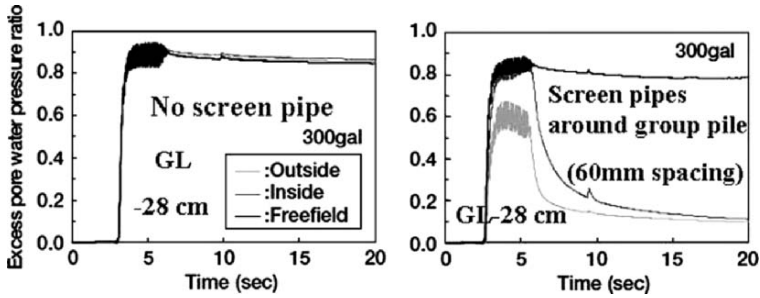


Fig. 15.45. Time history of excess pore water pressure with and without mitigation of screen pipes (Harada et al., 2006)

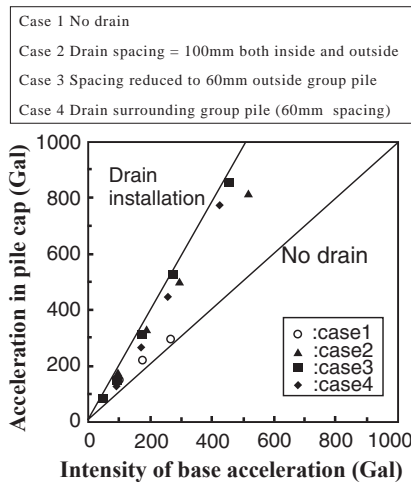


Fig. 15.46. Amplification of acceleration with and without screen pipes (Harada et al., 2006)

group pile dissipated quickly when screen pipes were installed, while those without pipes lasted for a long time. It is also shown that pore pressure in the free field (far from screen pipes) did not dissipate quickly.

It should be recalled, however, that the use of drains increases the response acceleration at ground surface and the pile cap. Figure 15.46 compares the acceleration in the pile cap in four cases: (1) without screen pipe drain, (2) screen pipes with spacing of 100 mm both inside and surrounding the group pile, (3) spacing was maintained at 100 mm inside the group pile, while reduced to 60 mm outside, and (4) pipes were installed only outside with spacing of 60 mm as already illustrated in Figure 15.43. Case 1 without drainage indicates reduced acceleration in pile cap due to subsoil liquefaction and its insulation

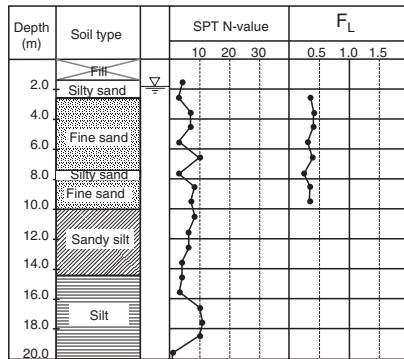


Fig. 15.47. Soil profile at site of in-site screen-pipe tests (Harada et al., 2006)

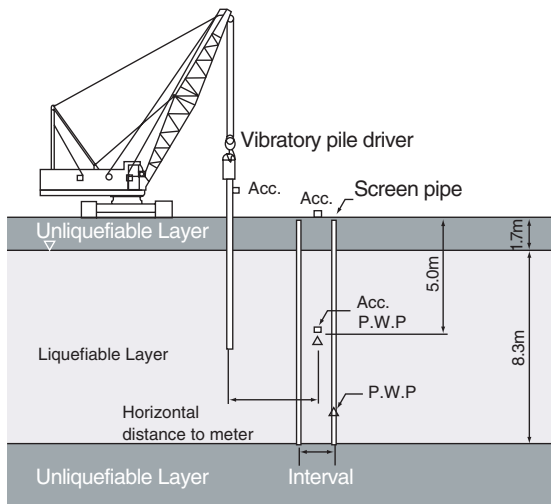


Fig. 15.48. Configuration of screen pipes and shaker (Harada et al., 2006)

effects. However, other cases developed much greater response. It is therefore important that mitigation of liquefaction may cause another problem of inertia force which has to be treated by structural reinforcement.

The following part describes in-situ tests on screen pipes. The soil condition of the testing site is illustrated in Figure 15.47. Four screen pipes were installed in a square configuration as illustrated in Figure 15.48. Figure 15.49 demonstrates a portable equipment for installation of pipes. The spacing between pipes was 1.5 m (case 2), 1.0 m (case 3), or 0.5 m (case 4). Case 1 had no screen pipe. The diameter and the opening of the pipe were 48.6 and 0.3 mm, respectively. Ground shaking was produced by a pile vibration at 18.3 Hz.



Fig. 15.49. Portable equipment for percussive penetration of screen pipe

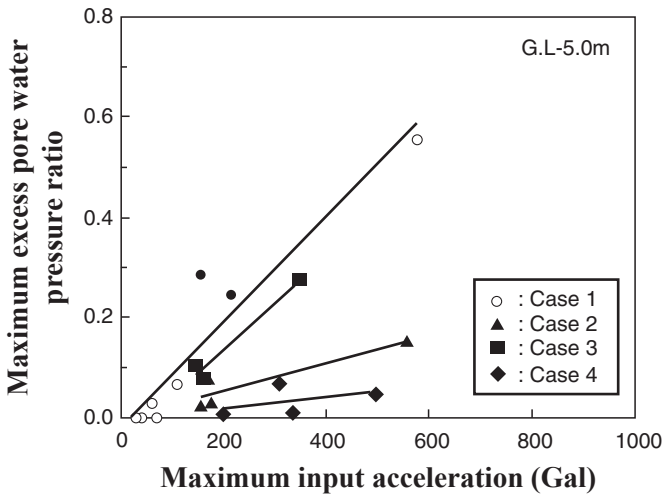


Fig. 15.50. Excess porewater pressure which was mitigated by screen pipes (Harada et al., 2006)

Figure 15.50 indicates the development of excess pore water pressure. The shorter the pipe spacing, the lower the excess pore water pressure. Moreover, the temperature of ground water which was ejected due to liquefaction was measured to be 16°C. This temperature was identical with the ground water temperature prior to shaking. Hence, there seems to be no heating effects in subsoil liquefaction. After testing, the screen pipes were excavated (Figure 15.51) to make sure that significant clogging did not occur in the screen of pipes and that the drainage effects would be efficient during future earthquakes.



Fig. 15.51. Appearance of excavated screen pipe after liquefaction tests (Harada et al., 2006)

5. Conclusion

One of the most important topics in liquefaction problem is the mitigation for existing structures. It is certainly essential to achieve reasonably low cost for this. In this regard, the present text reviewed three kinds of possibilities which were namely densification, grouting, and drainage. It was shown that there are promising technical developments in this field. It should be borne in mind that detailed soil-mechanic knowledge would help technical development efficiently.

Acknowledgements

The experiments described in this text were conducted by the following people: Mr. N. Harada of Zenitaka Corporation, Mr. Y. Kabashima who was an undergraduate student at University of Tokyo, Mr. T. Wassan, a former master student, Miss Seda Sendir, a graduate student, and Miss C. Conlee, a graduate student of Drexel University on NSF Summer Internship in Tokyo. Collaboration with Toa Corporation, Dr. S. Tsujino of Sato Kogyo Corporation, and Dr. S. Shimada of Kyokado Engineering Co., LTD. is deeply acknowledged by the author.

REFERENCES

- Arthur JRF, Chua KS, Dunstan T (1977) Induced anisotropy in a sand. *Geotechnique* 27(1): 13–30
di Benedetto H (2001) Personal communication
Harada N, Towhata I, Takatsu T, Tsunoda S, Sesov V (2004) Development of new drain method for protection of existing pile foundation from liquefaction effects. *Proc. the 11th International*

- Conference on Soil Dynamics and Earthquake Engineering and the 3rd International Conference on Earthquake Geotechnical Engineering, Berkeley, Vol. 2, pp 498–505
- Harada N, Towhata I, Takatsu T, Tsunoda S, Sesov V (2006) Development of new drain method for protection of existing pile foundations from liquefaction effects. *Soil Dynamics and Earthquake Engineering Journal* 26(4): 297–312
- Kabashima Y, Towhata I (2000) Improvement of dynamic strength of sand by means of infiltration grouting. Proc. 3rd International Conference on Ground Improvement Techniques – 2000, Singapore, pp 203–208
- Koizumi Y (1966) Changes in density of sand subsoil caused by the Niigata earthquake. *Soils and Foundations* 6(2): 38–44
- Miwa M, Yonekura R, Nagoshi T, Shimada S (2001) Characteristics of active silica grout produced ion-exchange process (2), Proc. 36th Japan National Conference on Geotechnical Engineering, Tokushima, pp 1121–1122 (in Japanese)
- Oda M (1972) The mechanism of fabric changes during compressional deformation of sand. *Soils and Foundations* 12(2): 1–18
- Ohbayashi J, Harada K, Fukada H, Tsuboi H (2006) Trends and developments of countermeasure against liquefaction in Japan. Proc 8th US National Conference on Earthquake Engineering, CD ROM Paper No.1936, San Francisco
- Okamura M, Teraoka T (2005) Shaking table tests to investigate soil desaturation as a liquefaction countermeasure. *Geotechnical Special Publication, ASCE* 145: 282–293
- Okamura M, Ishihara M, Tamura K (2006) Degree of saturation and liquefaction resistance of sand improved with sand compaction pile. *Journal of Geotechnical and Geoenvironmental Engineering, ASCE* 132(2): 258–264
- Sendir S, Wassan TH, Towhata I, Tsujino S (2006) Increasing effectiveness of explosive compaction by changing the order of blasts. CD-ROM Proc. 12th Japan Earthquake Engineering Symposium, Tokyo
- Skempton AW (1986) Standard penetration test procedures and the effects in sands of overburden pressure, relative density, particle size, ageing and overconsolidation. *Geotechnique* 36(3): 425–447
- Toki S, Tatsuoka F, Miura S, Yoshimi Y, Yasuda S, Makihara Y (1986) Cyclic undrained triaxial strength of sand by a cooperative test program. *Soils and Foundations* 26(3): 117–128
- Towhata I, Kabashima Y (2001) Mitigation of seismically-induced deformation of loose sandy foundation by uniform permeation grouting, Proc. Earthquake Geotechnical Engineering Satellite Conference, 15th International Conference on Soil Mechanics and Geotechnical Engineering, Istanbul, Turkey, pp 313–318
- Wassan TH, Towhata I, Tsujino S (2006) The effect of different firing sequences on plastic volumetric strains during blast-induced ground compaction, Proc. 7th International Congress on Advances in Civil Engineering, Istanbul
- Yamada Y, Ishihara K (1981) Undrained deformation characteristics of loose sand under three-dimensional stress conditions. *Soils and Foundations* 21(1): 97–107
- Yonekura R, Nagoshi T, Shimada S, Mori M (2001) A durability experiment of suspension type hybrid silicas grout. Proc. 36th Japan National Conference on Geotechnical Engineering, Tokushima, pp 1117–1118 (in Japanese)
- Yoshimi Y (1967) An experimental study of liquefaction of saturated sands. *Soils and Foundation*, 7(2): 20–32

CHAPTER 16

REMEDICATION METHODS AGAINST LIQUEFACTION WHICH CAN BE APPLIED TO EXISTING STRUCTURES

Susumu Yasuda

*Department of Civil and Environmental Engineering, Tokyo Denki University, Japan
yasuda@g.dendai.ac.jp*

Abstract. Many kinds of remediation methods against liquefaction have been developed and applied to structures since the 1964 Niigata earthquake. However, only a few remediation methods which can be applied to existing structures have been developed. A huge number of old structures in the world have not been treated to resist liquefaction. Recently, several new techniques to treat existing structures have been developed. In this paper, restrictions to be considered in remediation techniques for existing structures are discussed first. Then recent remediation methods for existing raft foundations, pile foundations, embankments, sea walls, and buried structures are introduced together with the principle of remediation. Remediation methods for liquefaction-induced flow are also introduced.

1. Introduction

During the 1964 Niigata earthquake, many oil tanks settled due to liquefaction in Japan. However, some tanks had no damage because their foundation ground had been compacted by vibro-floatation (Watanabe, 1966). This was the first time that the effectiveness of compaction of the ground against liquefaction was recognized. Based on this experience, the ground under several new tanks was improved at a factory in Hachinohe City. Shortly after the improvement work, the 1968 Tokachi-oki earthquake hit the site and demonstrated the effectiveness of the compaction method again (Ohsaki, 1970). After these events, many kinds of remediation methods were developed. However, almost all the methods developed applied to new structures. The Japanese Geotechnical Society published a book on remediation measures against liquefaction in 1993 in Japanese, and translated it into English in 1998 (JGS, 1998). Almost all the methods introduced in the book were remediation methods for new structures. The main principle was soil improvement to prevent liquefaction by densification methods, such as the sand compaction pile method, the vibro-floatation method, etc. The soil improvement techniques were not easy to apply to existing structures.

Though many kinds of remediation methods against liquefaction were developed and applied to new structures, a huge number of old structures have not been treated to resist liquefaction. Remediation of the old structures is quite important. For example, many oil storage tanks, river dikes, and timber houses which are not treated exist in large cities. Liquefaction-induced damage to the not-treated structures is a serious concern. Recently, several unique soil improvement techniques which can be applied to the ground under existing structures have been developed. Moreover, several techniques to strengthen structures to prevent their collapse if the ground should be liquefied have been

developed. These techniques can be applied to existing structures. In this paper, these recent treatment methods against liquefaction which can be applied to existing structures, are introduced.

2. Remediation methods against liquefaction compiled in 1993 (partially quoted from Yasuda, 2005a)

As mentioned above, in 1993, the Japanese Geotechnical Society compiled remediation methods against liquefaction (JGS, 1998). Table 16.1 illustrates the compiled methods. These methods are classified into two categories: (i) those that improve the liquefiable soil to prevent liquefaction, and (ii) those that strengthen structures to prevent their collapse if the ground should be liquefied. In the first category, ground is improved to increase liquefaction strength by the following factors: (1) high density, (2) not-liquefiable grain size, (3) stable skeleton or (4) low saturation. Other methods to prevent liquefaction are: (5) immediate dissipation of increased excess pore pressure, (6) reduction of shear stress by increasing confining pressure, (7) reduction of shear stress by building an underground wall.

Appropriate countermeasures in the second category differ by the type of structure. In the countermeasures shown in Table 16.1, the additional pile method has been applied to bridge foundations, but other methods have been applied to only a few structures.

Among the measures, the sand compaction method has been most widely used because of its high reliability. In the original method, a casing was pushed down and pulled up by a vibrating hammer. Therefore, the method could not be applied at sites with neighboring structures because of the strong vibration. However, a new method to push down and pull up the casings by static rotating force was developed recently. This “non-vibratory sand compaction pile method” has been applied near existing structures. Of solidification methods, the deep mixing method has been applied in many cases, recently. Of dissipation and control of pore water pressure methods, the gravel drain method has been applied for many sites. These solidification and gravel drain methods can be applied at sites with neighboring structures because of their low noise and vibration.

Recently, several new remediation techniques, which are not listed in Table 16.1, have been developed in Japan. In the first category, the compaction grouting method and seepage grouting method have been applied to several structures. In the second category, the ringed type sheet-pile wall method has been developed. Details of these techniques are described in the revised version of “Remedial Measures against Soil Liquefaction (JGS, 2004, in Japanese).”

3. Restrictions to be considered in remediation techniques for existing structures

Though many remediation techniques against liquefaction have been developed, as shown in Table 16.1, several restrictions apply to these techniques when used for existing structures. Restrictions to be considered are as follows:

- (1) Unique techniques are necessary to improve the ground under existing structures.
- (2) Special machines without noise and vibration must be used.

Table 16.1(1). Countermeasures against liquefaction (modified from JGS, 1998)

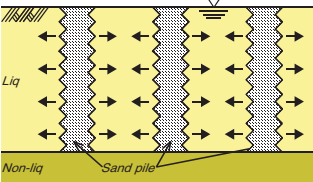
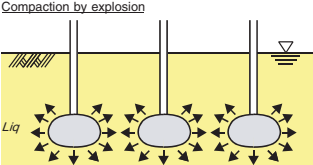

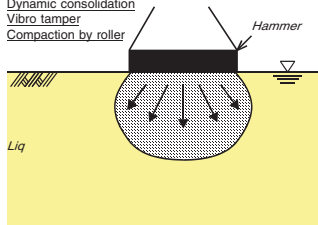
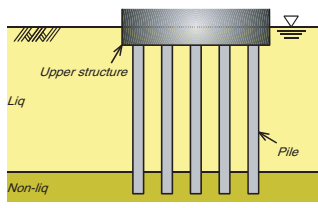
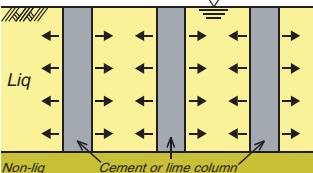
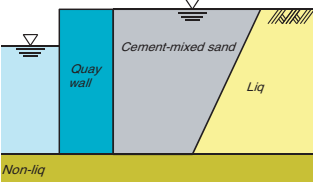
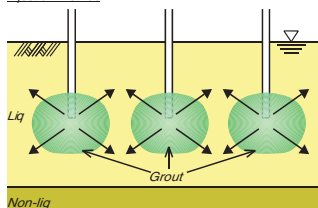
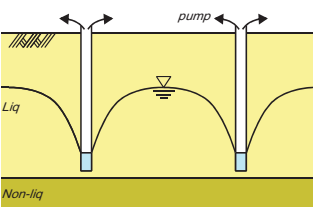
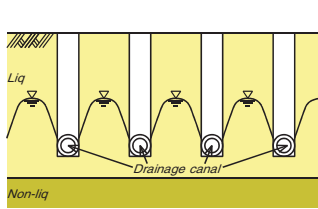
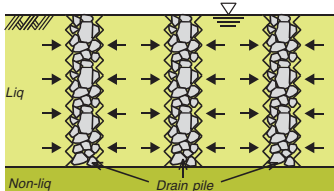
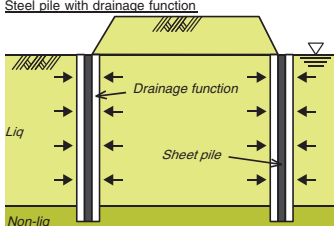
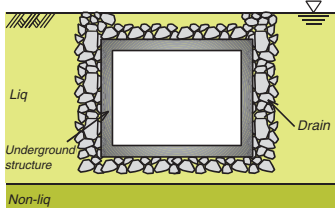
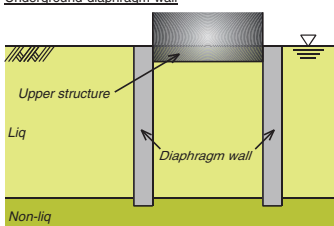
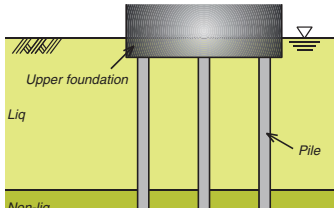
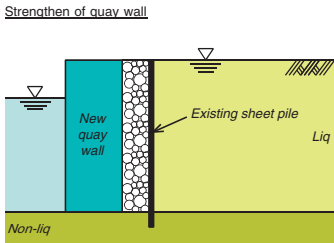
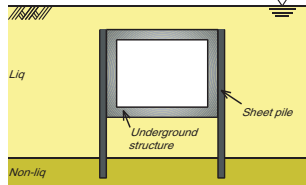
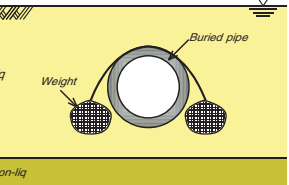
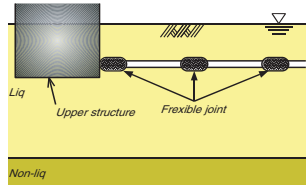
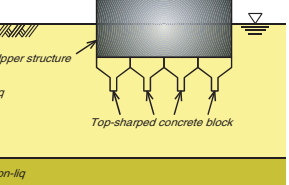
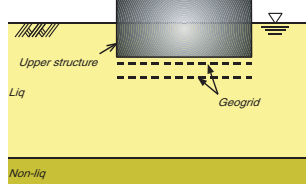
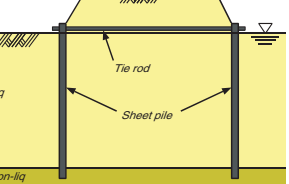
Principle of improvement	Description	
Increase of density	<p>Sand compaction pile Vibro rod method Vibro flotation</p>  <p>Stone column</p>  <p>Compaction by explosion</p> 	<p>Dynamic consolidation Vibro tamper Compaction by roller</p>  <p>Group pile method</p> 
Soildification	<p>Deep mixing method Quick lime pile method</p>  <p>Pre-mixing method</p> 	<p>Injection method</p> 
Reduction of degree of saturation and increase of effective stress	<p>Deep well</p> 	<p>Dewatering by trenches</p>  <p>Liq : Liquefiable layer Non-liq : Non liquefiable layer</p>

Table 16.1(2). Countermeasures against liquefaction (modified from JGS, 1998)

Principle of improvement	Description	
Dissipation and control of pore water pressure	<p><u>Drain pile</u></p>  <p><u>Steel pile with drainage function</u></p> 	<p><u>Drain installation for surrounding area</u></p> 
	Control of shear deformation and interception of excess pore water pressure	<p><u>Underground diaphragm wall</u></p> 
Counter-measure from structural aspect		<p><u>Pile foundation</u></p>  <p><u>Strengthen of quay wall</u></p> 

Liq : Liquefiable layer
 Non-liq : Non liquefiable layer

Table 16.1(3). Countermeasures against liquefaction (modified from JGS, 1998)

Principle of improvement	Description	
Structural counter-measure	<p><u>Lift prevention pile or sheet pile</u></p>  <p>Liq</p> <p>Non-liq</p> <p>Underground structure</p> <p>Sheet pile</p>	<p><u>Constraint of surroundings</u></p>  <p>Liq</p> <p>Non-liq</p> <p>Buried pipe</p> <p>Weight</p>
	<p><u>Absorption of ground deformation by flexible joint</u></p>  <p>Liq</p> <p>Non-liq</p> <p>Upper structure</p> <p>Flexible joint</p>	<p><u>Provision of supplemental foundation for mat foundation</u></p>  <p>Liq</p> <p>Non-liq</p> <p>Upper structure</p> <p>Top-sharped concrete block</p>
	<p><u>Reinforcement of mat foundation by geogrid</u></p>  <p>Liq</p> <p>Non-liq</p> <p>Upper structure</p> <p>Geogrid</p>	<p><u>Sheet piling for embankment</u></p>  <p>Liq</p> <p>Non-liq</p> <p>Tie rod</p> <p>Sheet pile</p>
	<p>Liq : Liquefiable layer Non-liq : Non liquefiable layer</p>	

- (3) In tank yards or housing complexes, small machines must be used because many structures stand close each other.
- (4) Soil investigation in the ground under existing structures is difficult. Geotechnical data is needed to estimate liquefaction potential and appropriate countermeasures.

Of the two categories of remediation methods shown in Table 16.1, generally speaking techniques to prevent liquefaction are difficult to apply to existing structures. However, special techniques which can be applied to existing structures, such as the compaction grouting method and seepage grouting method, have been developed recently.

On the contrary, the remediation techniques in the second category, which strengthen structures to prevent their collapse if the ground should be liquefied, can be applied to existing structures easily. Several new techniques have been developed and applied recently. In the design to strengthen structures, the allowable deformation of the structures must be defined because the strengthening effect must be judged based on the deformation of the structures. This means that performance-based design must be introduced. However, not enough studies on performance-based design have been undertaken. Only a few allowable deformations have been proposed (e.g., Yasuda, 2005b). Future studies on

performance-based design are necessary to develop remediation methods to strengthen existing structures.

To overcome the restrictions mentioned above, several remedial measures which can be applied to existing structures have recently been developed and applied. Examples of treated existing structures are briefly explained below.

4. Remediation methods for existing raft foundations

4.1. PRINCIPLE OF REMEDIATION

The best remediation method for existing structures is to improve the ground under the structures to prevent liquefaction. Some techniques to improve the ground are available, if bore holes can be drilled through the floor of a structure. Soil improvement under a structure is also possible from outside the structure by using special techniques.

The second-best choice is to decrease the settlement of a structure by some method, such as installing underground walls around the structure. Liquefaction of the ground under structures occurs for two reasons: (i) densification of the ground due to the eruption of underground water, and (ii) movement of the ground horizontally, as schematically shown in Figure 16.1. As the settlement due to the first reason occurs not only under a structure but also in surrounding ground, relative settlement between the structure and surrounding ground may be negligible. In contrast, the horizontal movement of the ground under a structure induces large relative settlement. Therefore, it is important to reduce the horizontal movement to decrease the relative settlement of a structure. By installing underground walls, horizontal movement can be reduced.

4.2. EXAMPLE OF TREATED STRUCTURES

4.2.1. A tank yard in Kawasaki (partially quoted from Ohmori, 1979; JGS, 1998)

As schematically shown in Figure 16.2(1), a tank yard was treated by the dewatering method. Cut-off walls with low permeability were installed around the yard. Then 26 wells were installed and the water level was lowered. The water level is still about 3 m lower than it had been.

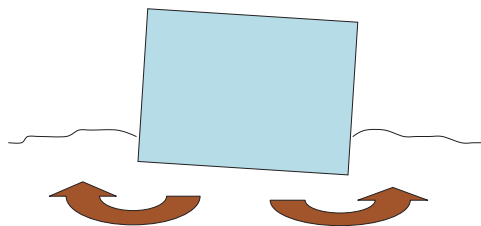


Fig. 16.1. Mechanism of liquefaction-induced settlement of building due to the movement of the ground under it

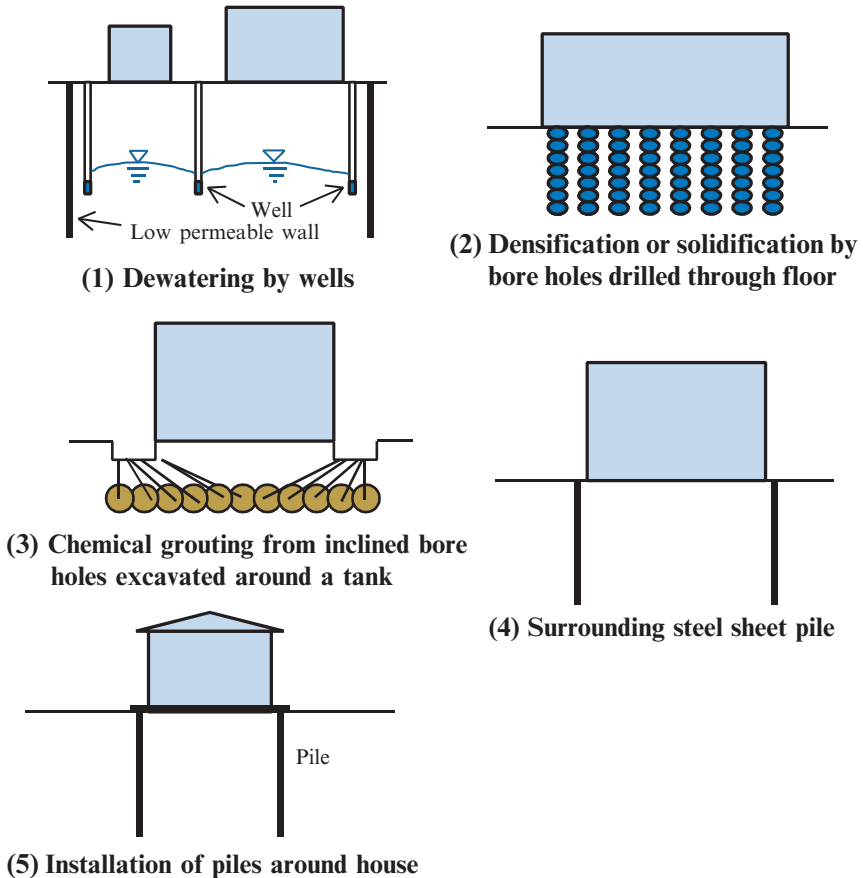


Fig. 16.2. Remediation methods for existing raft foundations

4.2.2. Fisherman's Wharf (partially quoted from TC4, 2001)

Compaction grouting was performed at the Fisherman's Wharf Pier 45 after it was damaged by liquefaction-related ground deformations during the 1989 Loma Prieta earthquake. The remediation options that were considered includes installing pile foundations where the shed were founded on fill, vibro-compaction or deep densification of the fill if the sheds were to be removed, and compaction grouting of the fill if the shed were to be maintained. Compaction grouting had the advantage of being least disruptive to this popular tourist attraction and being workable within the confines of the sheds. The design objective was to mitigate the potential for catastrophic failure of the structure and seawall due to liquefaction of the fill during the design earthquake.

4.2.3. The Yokohama Customs Building (partially quoted from Kaneko et al., 2003)

The Yokohama Customs Building was constructed in 1923 and was repaired in 2001. A thick soil layer estimated to be liquefiable layer underlaid the building and its bottom was

inclined towards the bay. This layer was compacted by the compaction grouting method, which can be applied inside a room as shown in Figure 16.2(2). Bore holes were drilled and cement mortar was pushed into the holes to densify the liquefiable layer.

4.2.4. *An oil tank in Kawasaki (partially quoted from Nikkei Construction, 2005)*

In Japan, liquefaction was taken into consideration in the design code for oil tanks in 1978. Old tanks constructed before then were not treated against liquefaction. In 1994, the design code was revised to treat the existing old tanks against liquefaction. About 8000 old tanks had to be treated against liquefaction. In Kawasaki City, an old tank was treated by the injection method. The capacity of the tank was 4843 kl. The depth of the liquefiable layer was about 10 m. As shown in Figure 16.2(3), the ground just outside the tank was excavated 1.3 m deep. Then inclined bore holes were drilled from the dig into the ground under the tank. Then, multi-permeation grouting was injected through the drilled holes. Silica type grouting material with durability and high permeability was injected to make improvement balls with diameters of 2 m. In total 139 improvement balls were constructed under the tank.

4.2.5. *An oil tank (partially quoted from Sawauchi et al., 1992)*

Another old tank was treated by the sheet-pile-ring method. A steel sheet pile was installed around the tank, and the top of the wall was connected to foundation gravel with a concrete ring as shown in Figure 16.2(4).

4.2.6. *A timber house*

A timber house settled and tilted due to liquefaction during the 2004 Tokachi-oki earthquake (Yasuda et al., 2004). After the earthquake, piles were installed just outside the house and the pile heads were connected with concrete beams extended from the footing, as shown in Figure 16.2(5).

4.3. OTHER RELATED STUDIES

The effectiveness of several kinds of countermeasures for existing power transmission towers with four footings was studied by centrifuge tests and analyses (Yasuda et al., 2001). In the analyses, a computer program “ALID (Yasuda et al., 1999)” was used. Five cases with and without countermeasures were tested and analyzed:

Case 1: without countermeasure,

Case 2: connecting tops of four footings with a concrete slab,

Case 3: connecting tops of four footings with a concrete slab, and replacing the ground under the slab with gravel,

Case 4: connecting tops of four footings with a concrete slab, and surrounding them with sheet piles, and

Case 5: connecting tops of four footings with a concrete slab, and improving the ground under the footings by densification method.

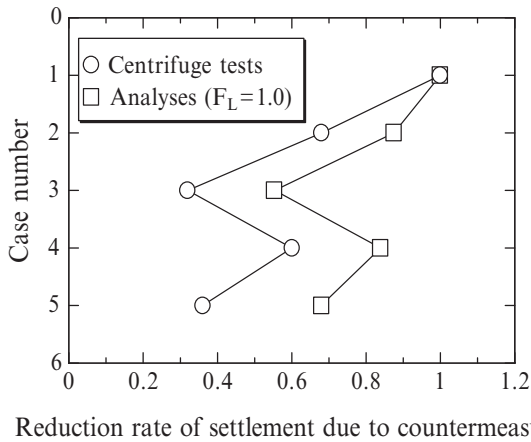


Fig. 16.3. Reduction rate of settlement of footings due to countermeasures (Yasuda et al., 2001)

Figure 16.3 compares the rates of settlement reduction due to these countermeasures. The order of effectiveness of countermeasures in tests and analyses was the same. Once the tops of the footings were connected with a concrete slab and the soil under the slab was replaced with gravel, the movement of the liquefied soil in the inner direction and tilting of footings were prevented, reducing the settlement of the footings. Surrounding the footings with sheet piles prevented the movement of liquefied soil in the outer direction. Densification of the ground under the footings also reduced the settlement in Case 5.

5. Remediation methods for existing pile foundations

5.1. PRINCIPLE OF REMEDIATION

In a pile foundation, if the tips of the piles are shallower than the bottom of the liquefiable layer, additional long piles must be installed. If the tips are supported by a non-liquefiable layer, horizontal displacement at the top of the piles and bending moment induced in the piles should be smaller than the allowable displacement and bending moment, respectively. Installation of additional piles or improvement of the ground around existing piles can decrease the displacement and the bending moment.

5.2. EXAMPLE OF TREATED STRUCTURES

5.2.1. A bridge (partially quoted from JGS, 1998)

As illustrated in Figure 16.4(1), the columns supporting an old bridge were reinforced. These columns were underlaid by wooden piles of 7 m in length. Following enlargement work on the superstructure, prestressed concrete piles with a diameter of 300 mm and a length of 7 m were added, and the footings were enclosed by steel sheet piles of 10 m in

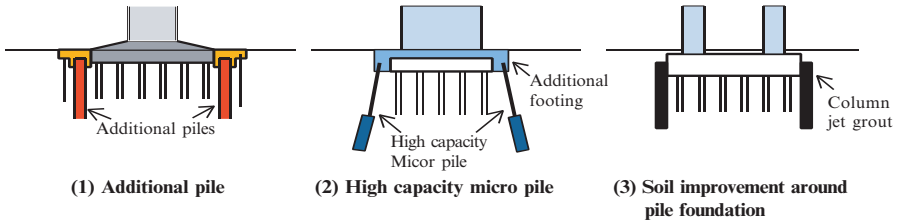


Fig. 16.4. Remediation methods for existing pile foundations

length to prevent erosion. By conducting detailed analyses, it was confirmed that forces acting on the piles were within the ultimate bearing capacity.

5.2.2. A bridge (partially quoted from JGS, 2004)

The columns supporting another bridge were strengthened against liquefaction with additional piles. High capacity micropiles, as shown in Figure 16.4(2), were selected, because the bridge girders were not high enough to drive piles of normal length. Micropiles of 177.8 mm in diameter were driven in a slightly inclined direction to bear some of the horizontal force.

5.2.3. Elevated bridges in Kobe (partially quoted from Hanshin Express Way, 1997; TC4, 2001)

Many elevated bridges with pile foundations were damaged due to liquefaction caused by the 1995 Hyogoken-nambu (Kobe) earthquake. Some of the damaged piles were strengthened by methods to improve the surrounding ground. The column jet grout method was applied to a pile foundation of the Hanshin Expressway, as shown in Figure 16.4(3). For the elevated bridge of the Rokko Liner, the deep mixing method was selected to improve the ground surrounding damaged caisson foundations.

6. Remediation methods for existing embankments

6.1. PRINCIPLE OF REMEDIATION

If the soil of an embankment liquefies, it is necessary to prevent the flow of the liquefied soil. Lowering the water level in the embankment by installing horizontal drain pipes may prevent liquefaction. On the contrary, if the soil under an embankment liquefies, large settlement of the embankment occurs due to horizontal movement of the ground under the embankment, as schematically shown in Figure 16.5. In this case, restricting the movement by some technique, such as the installation of underground walls at the toes of the embankment, can reduce the settlement, just as it prevents the settlement of raft foundations.

6.2. EXAMPLE OF TREATED STRUCTURES

6.2.1. The Tokaido Shinkansen (partially quoted from Nasu, 1984; JGS, 1998)

The Tokaido Shinkansen Railway (Japanese Bullet Train) started business in 1964, the same year of the 1964 Niigata earthquake. Some sections run over areas where

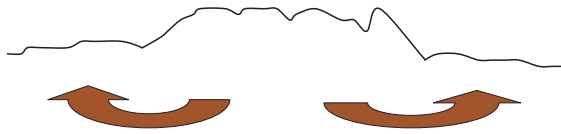


Fig. 16.5. Mechanism of deformation of an embankment due to liquefaction of the soil under the embankment

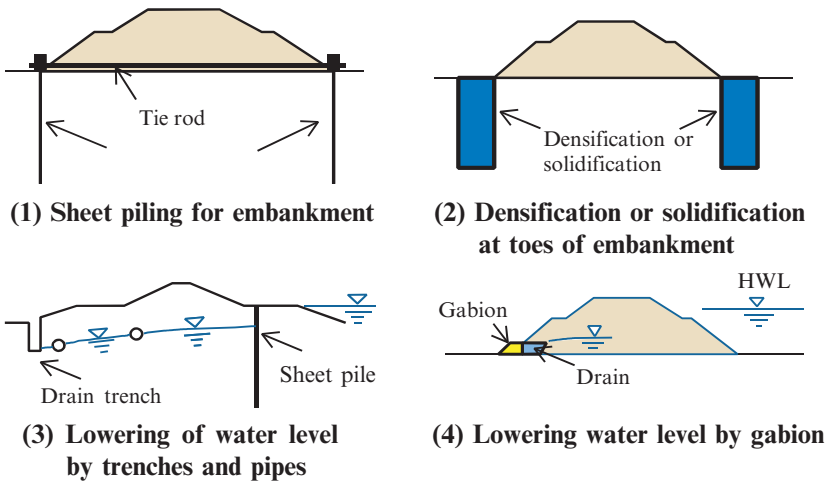


Fig. 16.6. Remediation methods for existing embankments

liquefaction is possible during future earthquakes. As liquefaction may damage railway embankments, a sheet-pile enclosed method has been developed to protect them as illustrated in Figure 16.6(1). The design method of the remedial measure was based on several shaking table tests and analyses. This method has been applied at several sites. The dimensions of the sheet piles and tie-rods differ according to conditions of the ground and embankments. At an embankment with a height of 8 m and a width of 32 m, liquefiable layers were deposited to a depth of about 14 m. For this embankment, sheet piles with lengths of 18.5 and 16.5 m were installed at both toes and connected with tie-rods.

6.2.2. *Yodogawa River dike (partially quoted from TC4, 2001)*

The 1995 Kobe earthquake caused extensive damage to the Yodogawa dike. During the restoration work, a countermeasure against liquefaction-induced settlement was applied (TC4, 2001). At the Nishijima dike section, the outer part of the dike was not damaged. Only the inner was rebuilt. The stability of this part was improved by installing double rows of steel sheet piles at the toe and placing gravel between the rows.

6.2.3. *Arakawa River dike (partially quoted from JGS, 1998)*

The deep mixing method was applied to the embankment of the Arakawa River embankment in Tokyo, as shown in Figure 16.6(2). A loose sand layer where liquefaction was anticipated was 3 to 6 m thick. It was planned to use the deep mixing method for a width

of 10 m and a depth of 24 m to stabilize the foundation ground against external seismic force. Using external forces, a stability analysis was conducted that included sliding, overturning, bearing capacity of the stratum, and circular slip failure.

6.2.4. Hachirogata Polder dike (partially quoted from Civil Eng. Dept. Akita Prefecture, 1990)

Polder dikes in Hachirogata in Japan have been damaged by several earthquakes since their construction. During the restoration work after the 1983 Nihonkai-chube earthquake, an investigation was conducted to make the dikes resist earthquakes because they had been damaged repeatedly, as shown in Figure 16.6(3). Counterweight fills, foundation improvement, dewatering, etc. were investigated as possible liquefaction countermeasures. Improving the foundation of the loose sand layer widely covering this area would have cost an enormous amount. Therefore, the basic idea for the design of countermeasures was to increase the overburden pressure by dewatering. Sheet piles were driven into the riverside toes, drains were installed and drainage trenches were dug.

6.2.5. Tokachi River dike (partially quoted from Hokkaido Development, 1994)

The Tokachi River dike suffered severe damage during the 1993 Kushiro-oki earthquake. During the restoration work, gabions and drains were applied at the toe of a dike. The water level inside the dike was measured after the restoration work. It was confirmed that the water level was lowered with the treatments.

7. Remediation methods for existing sea walls

7.1. PRINCIPLE OF REMEDIATION

Liquefaction of the ground behind a sea wall increases the earth pressure on the sea wall. Liquefaction of the ground under a sea wall decreases the bearing strength of the ground. These two triggers cause large movement, tilting, and settlement of the sea wall. Therefore, the best measure is to prevent liquefaction of the ground behind a sea wall and/or the foundation ground under a sea wall. The other measure is to increase the resistance to movement of a sea wall by some restraining work.

7.2. EXAMPLE OF TREATED STRUCTURES

7.2.1. Kushiro Port (partially quoted from TC4, 2001)

Kushiro Port is located on the island of Hokkaido, Japan's northern most island. At this port, the seabed deposit, on which quay walls were constructed and backfilled with dredged sand, is relatively dense. The only liquefiable soils are the loosely deposited backfill sand. Following the lessons learned from the damage to Akita Port during the 1983 Nihonkai-chubu earthquake, remediation measures were applied to some quay walls. At the No. 1 wharf, in the east district, backfill sand just behind the wall was treated with gravel drains, and the ground behind the gravel drains was treated with sand compaction piles. After these treatments, the 1993 Kushiro-oki earthquake hit Kushiro Port. The treated quay wall suffered no damage though not-treated quay walls suffered severe damage. The damaged quay walls were treated during the restoration work.

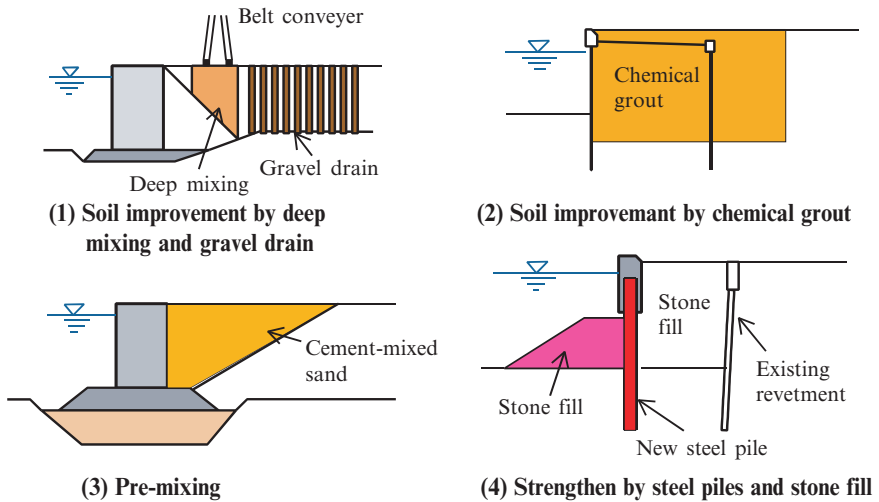


Fig. 16.7. Remediation methods for existing sea walls

Figure 16.7(1) shows one of the quay walls, which was treated by the deep mixing method and the gravel drain method.

7.2.2. Port of Oakland (partially quoted from TC4, 2001)

Stone columns were installed at the Seventh St. Marina Terminal, Port of Oakland, California, after it was damaged in the 1989 Loma Prieta earthquake, to mitigate liquefaction risk during future earthquake. A 12 m wide zone of stone columns was constructed along the rear of the wharf. The stone column extended mostly through 4 to 7 m thick existing perimeter rock fill dike used to retain hydraulic filling of the terminal area. The dike rests on a 4.3 to 8.2 m thick hydraulically-placed sand base. These sands are predominantly clean and liquefiable. Underneath the dike and sand base, there is an 11 to 25 m thick layer of native silty and clayey sand. The upper 1.5 m of this layer was considered potentially liquefiable.

7.2.3. Ishikari Port (partially quoted from Kawamura et al., 2001)

At a quay wall in Ishikari Port, the ground behind the quay wall was improved with permeation grouting as illustrated in Figure 16.7(2). The quay wall is a steel sheet-pile wall with tie wires. Though many tie wires intersect at a corner of the quay wall, the permeation method could be applied.

7.2.4. Kobe Port (partially quoted from TC4, 2001)

Many port-related facilities in Kobe Port were severely damaged during the 1995 Kobe earthquake. At the time of the earthquake, the port had 186 quay walls, about 90% of which were caisson walls. Most of these caisson walls moved toward the sea by a maximum about 5 m and an average of 3 m, and inclined about four degrees toward the sea. Several restoration methods were applied after the earthquake. One was the pre-mix method, as shown in Figure 16.7(3). A temporary sheet pile was installed in the ground

behind the sea wall, and the space between the sea wall and the temporary sheet pile was excavated. Then, sand mixed with cement was filled in the ditch.

7.2.5. A quay wall in Tokyo (partially quoted from JGS, 1998)

A quay wall was constructed in 1969 as a revetment of a canal facing Tokyo Bay. Seismic inspection revealed a loose silty sand layer of 4 m in thickness that was susceptible to liquefaction. A countermeasure against liquefaction, the quay wall was strengthened with self-supporting steel pipe piles, as shown in Figure 16.7(4). New steel pipe piles with a length of 28.5 m were installed, sandstone fill was placed in front of the pipe piles as foot protection and the space between the existing and newly driven piles was filled with gravel.

8. Remediation methods for existing buried structures

8.1. PRINCIPLE OF REMEDIATION

Yasuda et al. (1995) conducted several shaking table tests to demonstrate the mechanism of uplift and factors which affect the uplift of buried pipes. In their tests, the movement of soil grains during the uplift of a model pipe was observed in detail. The movement was estimated by measuring the displacement of chips of noodles which were installed between the soil and the front glass of the model container. The excess pore water pressure increased gradually due to shaking. Then, when the excess pore water pressure at the bottom of the pipe reached the initial overburden pressure, i.e., when liquefaction occurred, the pipe started to rise gradually. Simultaneously, liquefied soils on both sides of the pipe moved toward the bottom of the pipe as shown in Figure 16.8. It was hypothesized that liquefaction and the movement of the liquefied soil toward the bottom of the pipe must continue for a long time to induce large uplift. Therefore, the installation of a pair of underground walls at both sides of a buried structure must reduce the uplift of the structure.

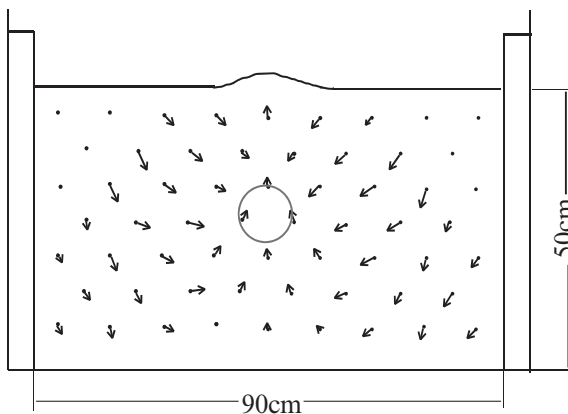


Fig. 16.8. Movement of soil particles during uplift of a pipe (Yasuda et al., 1995)

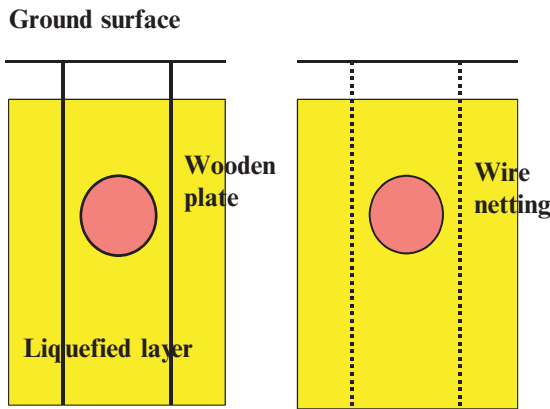
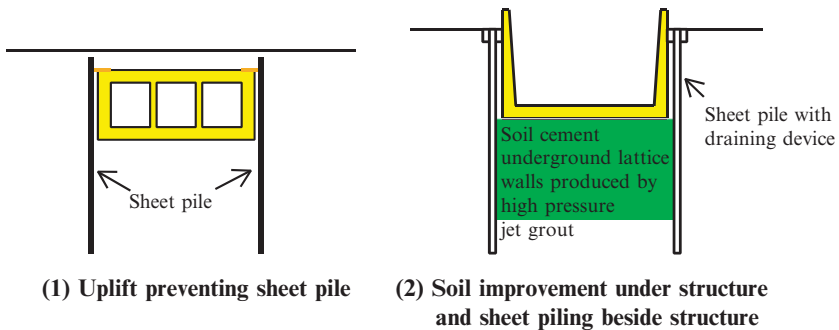


Fig. 16.9. Previous study on the effect of two types of countermeasures for a pipe



(1) Uplift preventing sheet pile (2) Soil improvement under structure and sheet piling beside structure

Fig. 16.10. Remediation methods for existing underground structures

Yasuda et al. also conducted shaking table tests to study the effectiveness of the two types of countermeasures shown in Figure 16.9 in preventing the movement of liquefied soil. A pair of wooden plates or wire nettings was installed beside the model pipe. These wooden plates prevented uplift. Moreover, the wire nettings also prevented the uplift of the pipe even though the excess pore water pressure ratio at the bottom of the pipe increased up to 1.0, because the netting prevent the movement of liquefied soil grains under the pipe.

8.2. EXAMPLE OF TREATED STRUCTURES

8.2.1. A multi-service tunnel (partially quoted from JGS, 1998)

A countermeasure of driving sheet piles was applied to a multi-service tunnel, as shown in Figure 16.10(1). The sheet piles were driven besides the tunnel to the depth of 22.6 m to reach the lower non-liquefiable layer. In the design of thickness of the sheet piles, earth pressure, hydrostatic pressure, and dynamic water pressure were considered. The vertical stability of the structure was also designed by considering the uplift force due to excess pore pressure.

8.2.2. *A subway station in Tokyo (partially quoted from Yokota et al., 2001)*

Near Kitasenjyu Station of the Chiyoda subway line in Tokyo, the uplift of an underground tunnel due to liquefaction was a concern. Thus, high pressure jet grouting was applied through the floor of the tunnel to make soil cement underground lattice walls, as illustrated in Figure 16.10(2). Two effects on liquefaction-induced uplift were expected: (i) prevention of the movement of liquefied soil from surrounding ground to the bottom of the tunnel, and (ii) a decrease of shear deformation of the soil in the lattice.

9. Remediation methods for existing structures affected by ground flow

9.1. PRINCIPLE OF REMEDIATION

In the Japanese Geotechnical Society, the probabilities of several kinds of countermeasures against liquefaction-induced flow were discussed by the “Technical Committee on Liquefaction-induced Flow and Permanent Deformation of the Grounds and Earth Structures during Earthquakes” from 1995 to 1998. Table 16.2 shows the ideas of the countermeasures summarized by the committee (JGS, 1998; Kanatani et al., 2000). There are three categories of countermeasures against the damage to structures due to liquefaction-associated ground flow. The most reliable measure is to improve the ground in the entire area to prevent the occurrence of liquefaction. However this measure is uneconomical and cannot be applied under or near existing structures.

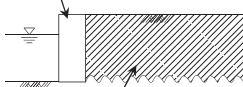
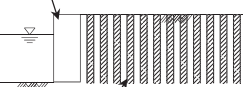
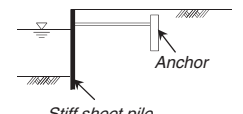
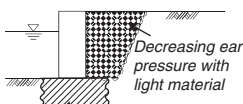
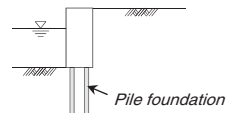
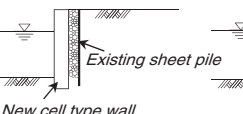
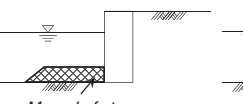
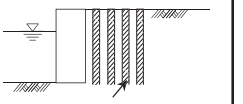
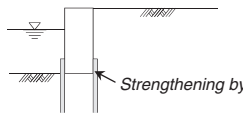


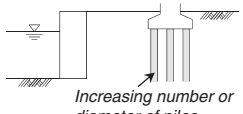
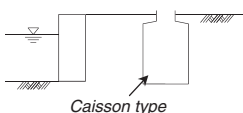
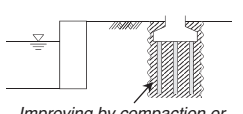
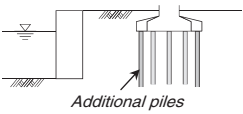
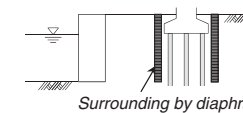
The second measure is to strengthen a sea wall to prevent ground flow, if the ground behind the sea wall is liquefied. Strengthening the ground with a wall, sand piles or densification of a small area of the ground also prevents or decreases ground flow even though liquefaction occurs in the ground. The third measure is to strengthen structures, for example, strengthening a pile foundation with additional piles, to prevent damage even though liquefaction and associated flow of the ground occurs. Among these countermeasures, several methods have been applied to quay walls and express highways in Tokyo, Kobe, and Osaka.

9.2. EXAMPLE OF TREATED STRUCTURES

9.2.1. *Metropolitan Expressway in Tokyo (partially quoted from Yasuda and Ogasawara, 2004; Yasuda, 2005a)*

On the Metropolitan Expressway in Tokyo, the Bay Shore Route and several other routes run along or cross coasts, canals, and rivers. There was concern that the foundations of bridges on these roads might be damaged by liquefaction-induced flow. Thus, a technical committee was organized to study the possibility of damage, appropriate countermeasures and design of the measures, from 1995 to 1997, after the Kobe earthquake. In the study, several kinds of countermeasures against liquefaction-induced flow were listed and compared by focusing on their effectiveness, adaptability, and cost. The installation of steel pipes to make a preventing wall between bridge foundations and sea walls was selected because this method is economic. The effectiveness of this method was confirmed by

Table 16.2. Countermeasures against liquefaction-induced flow behind quay

Concept of countermeasure	New structure	Existing structure
Prevention of the occurrence of liquefaction	<p><New quay wall></p> <p><i>New quay wall</i></p>  <p><i>Improving by compaction or cementation</i></p>	<p><Existing quay wall></p> <p><i>Existing quay wall</i></p>  <p><i>Improving by compaction or cementation</i></p>
Prevention of the occurrence of flow though liquefaction occurs	<p><New quay wall></p> <p>(1)Construction of stable quay wall</p>  <p><i>Anchor</i></p> <p><i>Stiff sheet pile</i></p>  <p><i>Decreasing earth pressure with light material</i></p> <p><i>Improving by compaction or cementation</i></p>  <p><i>Pile foundation</i></p>	<p><Existing quay wall></p> <p>(1)Strengthening quay wall</p>  <p><i>Existing sheet pile</i></p> <p><i>New cell type wall</i></p> <p><i>Decreasing earth pressure with light material</i></p>  <p><i>Mound of stones</i></p>  <p><i>Partial improvement by compaction or cementation</i></p>  <p><i>Strengthening by pile foundation</i></p> <p>(2)Decreasing of displacement of the ground behind quay wall</p>  <p><i>Steel piles or diaphragm wall</i></p>  <p><i>Improving by compaction or cementation</i></p>
Keeping of service ability though liquefaction-induced flow occurs	<p><New pile foundation></p>  <p><i>Increasing number or diameter of piles</i></p>  <p><i>Caisson type foundation</i></p>  <p><i>Improving by compaction or cementation</i></p>	<p><Existing pile foundation></p>  <p><i>Additional piles</i></p>  <p><i>Surrounding by diaphragm or cement mixing wall</i></p>

conducting several analyses and centrifuge tests. Then, this method was applied to Akebono, Ariake, Katsushima, and Ayasegawa sites. In the design procedure decided by the technical committee, the deformation of pile foundations is estimated by the seismic deformation method, in which ground displacement is estimated first, and then horizontal force is applied to piles through soil springs. The ground displacement is estimated by residual deformation analysis in which the reduction of shear modulus due to liquefaction is considered. The reduction of the soil springs due to liquefaction is also considered. Allowable displacement of the top of the pile foundation was defined as twice the displacement which causes the pile to yield. At the Akebono site, a liquefiable sandy layer is deposited from the ground surface to a depth of about 10 m. Two bridge foundations founded on 18 cast-in place concrete piles are located about 20 m behind a sea wall, as shown in Figure 16.11. The sea wall is a sheet-pile wall and is estimated to be unstable during future earthquakes. Figure 16.12 shows the analyzed deformation of the ground due to liquefaction. The estimated displacement of the surface of the ground surrounding the bridge foundations was 1.2 m. If the surrounding ground moves 1.2 m,

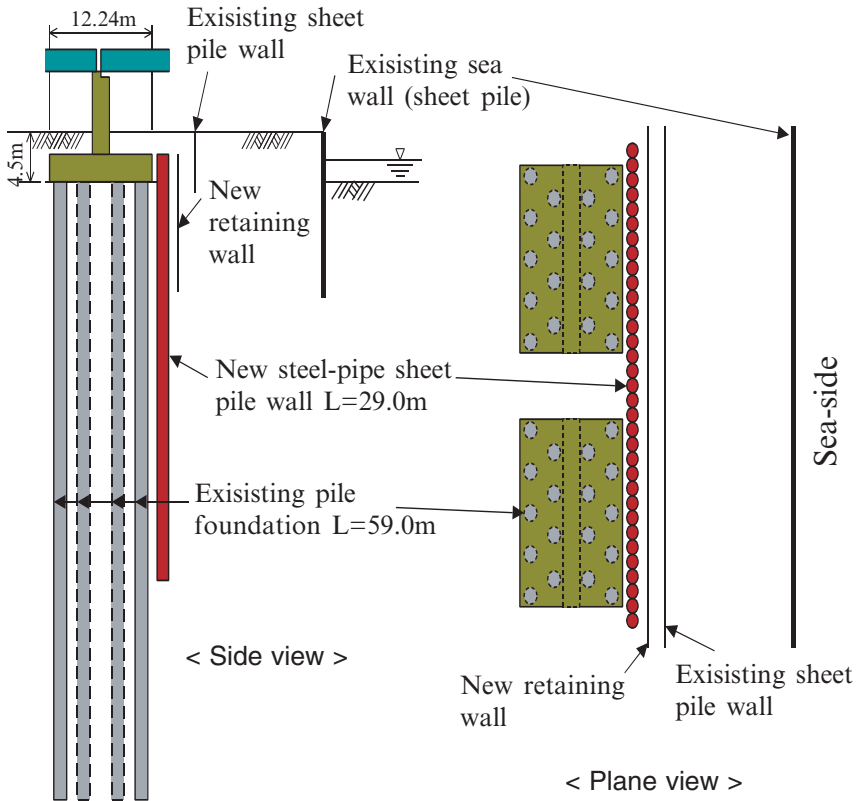


Fig. 16.11. Countermeasure method applied to the Tokyo Metropolitan Express Highway in the Akebono district

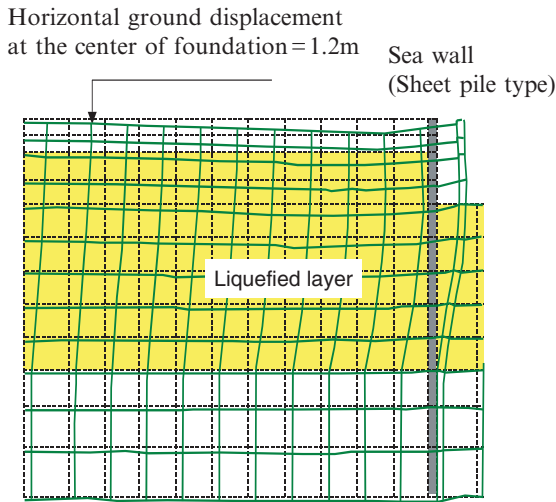


Fig. 16.12. Analyzed liquefaction-induced deformation of the ground at Akebono district Ogasawara et al. 1999

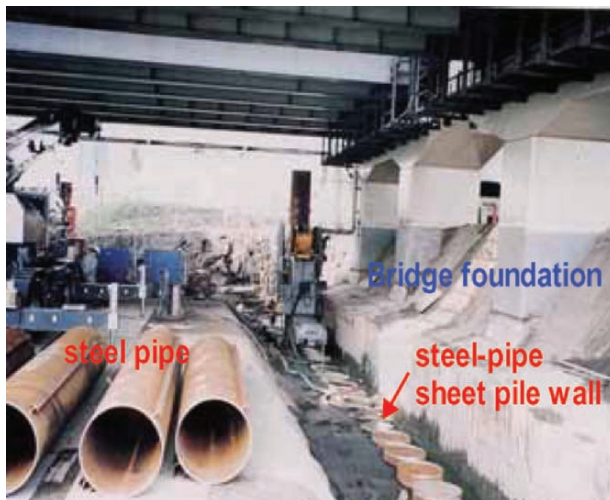


Photo 16.1. Installation work of steel pipes in the Akebono district

the displacement of the top of the piles becomes about 4.5 times the allowable displacement. But if the ground displacement can be reduced to less than 50 cm, the displacement of the top of piles can be limited within the allowable displacement. Therefore, the size of the steel pipes was designed to reduce the ground displacement to less than 50 cm. The steel pipes selected were 1200 mm in diameter, 22 mm in thickness and 29 m in depth, as shown in Figure 16.11. These steel pipes were installed continuously to make a preventative wall, as shown in Photo 16.1.

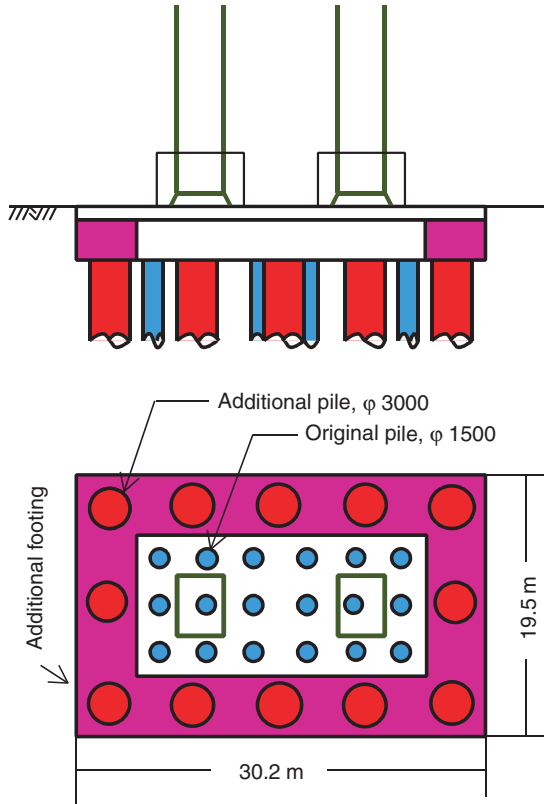


Fig. 16.13. Restoration method applied to the Hanshin Express Highway

9.2.2. Hanshin Expressway (partially quoted from JGS, 2004; Yasuda, 2005b)

On the Hanshin Expressway, many pile foundations of elevated bridges were damaged due to liquefaction-induced flow during the 1995 Kobe earthquake. The damaged foundations were restored by adding piles and improving the soil. Cast-in place concrete-steel composite piles with a diameter of 3 m were constructed around the existing footings, as shown in Figure 16.13. Then additional footings were constructed.

10. Concluding remarks

Remediation methods against liquefaction which can be applied to existing structures are introduced in this paper. The remediation of old structures is very important because a huge number of these structures have not been treated against liquefaction. More remediation methods for existing structures must be developed. In the design of remediation methods for existing structures, it is desired to introduce performance-based design methods.

REFERENCES

- Civil Eng. Dept. Akita Prefecture (1990) Construction history volume of disaster restoration work in Hachirogata dykes (in Japanese)
- Hanshin Express Way (1997) Report on restoration work (in Japanese)
- Hokkaido Development (1994) Report on restoration work of Tokachi River dike (in Japanese)
- Kanatani M, Okada S, Yasuda S (2000) Countermeasures against liquefaction-induced flow. *Tsuchi-to-Kiso*, JSSMFE 48(3): 43–48 (in Japanese)
- Kaneko O et al. (2003) Countermeasure against liquefaction to strengthen foundation of historical buildings. 2003 Annual Conference, Architectural Institute of Japan, B-1: 431–432 (in Japanese)
- Kawamura K et al. (2001) Soil improvement by permeation grouting method of existing quay wall. *Kisoko* 29(5): 33–36 (in Japanese)
- Nasu M (1984) Countermeasures on fill embankment of New Tokaido Line. *The Foundation Engineering and Equipment* 12(7): 64–68 (in Japanese)
- Nikkei Construction, 10(4), 2005 (in Japanese)
- Ogasawara M, Tani K, Matuo T., Sakamoto S. (1999) A study on measures against ground flow using the finite element method. Proceedings of the 2nd International Conference on Earthquake Geotechnical Engineering, pp 335–339
- Ohmori K (1979) Design and construction example in soft ground-tank foundation (reinforcement by pore pressure decrease). *Kisoko* 18(12): 122–129 (in Japanese)
- Ohsakai Y. (1970) Effects of sand compaction on liquefaction during the Tokachioki earthquake. *Soils and Foundations* 10(2): 112–128
- Sawauchi I, Suzuki T, Hamada T, Aoyagi T, Ando N (1992) A study on countermeasure against liquefaction. 47th Annual Conference of Japan Society of Civil Engineering 3: 280–281 (in Japanese)
- TC4, ISSMGE (2001) Case histories of post-liquefaction remediation, JGS
- The Japanese Geotechnical Society (1998) Remedial measures against soil liquefaction. Balkema
- The Japanese Geotechnical Society (2004) Remedial measures against soil liquefaction (Revised version). JGS (in Japanese)
- Yasuda S, Nagase H, Itafuji S, Sawada H., Mine K (1995) A study on the mechanism of the floatation of buried pipes due to liquefaction. Proceedings of the 7th International Conference on Soil Dynamics and Earthquake Engineering, SDEE 95, pp 125–132
- Yasuda S, Yoshida N, Adachi K, Kiku H., Gose S (1999) A simplified analysis of liquefaction-induced residual deformation. 2nd International Conference on Earthquake Geotechnical Engineering, pp 555–560
- Yasuda S, Abo H, Yoshida N, Kiku H, Uda M (2001) Analyses of liquefaction-induced deformation of grounds and structures by a simple method. 4th International Conference on Recent Advances in Geotechnical Earthquake Engineering and Soil Dynamics, Paper No. 4.34.
- Yasuda S, Morimoto I, Kiku H, Tanaka T (2004) Reconnaissance report on the damage caused by three Japanese earthquakes in 2003. Proceedings of the 3rd International Conference on Earthquake Geotechnical Engineering and 11th International Conference on Soil Dynamics & Earthquake Engineering, Keynote Lecture, 1, pp 14–21
- Yasuda S, Ogasawara M (2004) Studies on several countermeasures against liquefaction-induced flow and an application of a measure to existing bridges in Tokyo. *Journal of Japan Association for Earthquake Engineering*, 4(3) (Special Issue)
- Yasuda S (2005a) Survey of recent remediation techniques in Japan, and future applications. *Journal of Earthquake Engineering* 9(Special Issue 1): 151–186

- Yasuda S (2005b) Recent several studies and codes on performance-based design for liquefaction in Japan. Proceedings of Geotechnical Earthquake Engineering Satellite Conference, pp 46–53
- Yokota M, Yoshimura T, Hirano T (2001) Study on the analyses and countermeasure for liquefaction at the tunnel near Kitasenju Subway Station. 36th Annual Conference of Japan Society of Civil Engineering 3: 256–257 (in Japanese)
- Watanabe T. (1966) Damage to oil tank refinery plants and a building on compacted ground by the Niigata earthquake and their restoration. *Soils and Foundations* 6(2): 86–99

CHAPTER 17

LIFELINE PERFORMANCE UNDER EXTREME LOADING DURING EARTHQUAKES

T.D. O'Rourke¹ and A.L. Bonneau²

¹ *Cornell University, Ithaca, USA*
tdo1@cornell.edu

² *Cornell University, Ithaca, USA*
alb66@cornell.edu

Abstract. Soil–structure interaction under extreme loading conditions includes performance during earthquakes, floods, landslides, large deformation induced by tunneling and deep excavations, and subsidence caused by severe dewatering or withdrawal of minerals and fluids during mining and oil production. Such loading conditions are becoming increasingly more important as technologies are developed to cope with natural hazards, human threats, and construction in congested urban environments. This paper examines extreme loading conditions with reference to earthquakes, which are used as an example of how extreme loading influences behavior locally and throughout geographically distributed systems. The paper covers performance from the component to the system-wide level to provide guidance in developing an integrated approach to the application of geotechnology over large, geographically distributed networks. The paper describes the effects of earthquake-induced ground deformation on underground facilities, and extends this treatment to the system-wide performance of the Los Angeles water supply during the 1994 Northridge earthquake. Large-scale experiments to evaluate soil–structure interaction under extreme loading conditions are described with reference to tests of abrupt ground rupture effects on underground pipelines. Large-scale tests and the development of design curves are described for the forces imposed on pipelines during ground failure.

1. Introduction

From a geotechnical perspective, extreme loading conditions are those that induce large plastic, irrecoverable deformation in soil. They are often associated with significant geometric changes in the soil mass, such as shear rupture, heave and void formation, and are accompanied by a peak, or maximum, interaction force imposed on embedded structures. Such loading takes soil well beyond the range of deformation related to the conventional design of civil structures. It applies to performance under unusual, extreme conditions. Such conditions include earthquakes, floods, landslides, large deformation induced by tunneling and deep excavations, and subsidence caused by severe dewatering or withdrawal of minerals and fluids during mining and oil production. Such loading conditions are becoming increasingly more important as technologies are developed to cope with natural hazards, human threats, and construction in congested urban environments.

Extreme loading conditions for soils are often accompanied by extreme loading conditions for structures. Examples include soil/structure interaction associated with pipelines

subjected to fault rupture, piles affected by landslides, and soil failure imposed on underground facilities by explosions, flooding, and the collapse of voids. Such conditions induce large plastic, irrecoverable structural deformation that involves both material and geometric nonlinear behavior. Hence, analytical and experimental modeling for soil–structure interaction under these conditions requires the coupled post-yield simulation of both soil and structural response. Such behavior generally poses significant challenges to our analytical capabilities, thus requiring large-scale experimental and case history data to improve the simulation process and validate the models.

Extreme loading conditions, especially those associated with natural hazards and severe human threats, may affect large systems of structures. Consider, for example, Figure 17.1, which is a photograph of the corner of Wall and Williams Streets in New York City in 1917. The congestion shown in this photograph has not improved in the last 90 years, and is indicative of the situation in a multitude of cities worldwide. The photo illustrates at least two important features of the built environment. First, much of critical infrastructure is located underground, and its fate is intimately related to that of the surrounding ground. Second, the crowded nature of urban and suburban developments increases risk due to proximity. Damage to one facility, such as a cast iron water main, can rapidly cascade into damage in surrounding facilities, such as electric and telecommunication cables and gas mains, with system-wide consequences. Soil surrounding critical underground infrastructure is frequently both the perpetrator and mediator of loading that can affect the systemic performance of an entire city.



Fig. 17.1. Underground infrastructure at Wall and Williams Streets in New York City, 1917

In this paper, soil–structure interaction under extreme loading conditions is examined with reference to earthquakes, which are used as an example of how extreme loading influences behavior at local and geographically distributed facilities. The paper begins with the effects of earthquake-induced ground deformation on underground facilities, and then expands this treatment to consider the system-wide performance of the Los Angeles water supply during the 1994 Northridge earthquake. Large-scale experiments to evaluate soil–structure interaction under extreme loading conditions are described with reference to tests of abrupt ground rupture effects on steel and high density polyethylene pipelines. Large-scale tests and the development of design curves are described for the forces imposed on pipelines during ground failure. The paper covers performance from the component to the system-wide level to provide guidance in developing an integrated approach to the application of geotechnology over large, geographically distributed networks.

2. Geotechnical earthquake loading

Earthquakes cause transient ground deformation (TGD) and permanent ground deformation (PGD), both of which affect underground pipelines. TGD is the dynamic response of the ground, and PGD is the irrecoverable movement that persists after shaking has stopped. PGD often involves large displacements, such as those associated with surface fault rupture and landslides. TGD can cause soil cracks and fissures triggered by pulses of strong motion that develop localized shear and tensile strains exceeding the strength of surficial soils. In these cases, crack widths and offsets are primarily a reflection of surficial ground distortion and gravity effects, such as local slumping. They should not be mistaken as an expression of PGD generated by ground failure mechanisms of larger scale.

The principal causes of PGD have been summarized and discussed by O'Rourke (1998). They are faulting, tectonic uplift and subsidence, and liquefaction, landslides, and densification of loose granular deposits. Liquefaction is the transformation of saturated cohesionless soil into a liquefied state or condition of substantially reduced shear strength (Youd, 1973). Liquefaction-induced pipeline deformation can be caused by lateral spread, flow failure, local subsidence, post-liquefaction consolidation, buoyancy effects, and loss of bearing (Youd, 1973; O'Rourke, 1998). It is widely accepted that the most serious pipeline damage during earthquakes is caused by PGD. Furthermore, it is well recognized that liquefaction-induced PGD, especially lateral spread, is one of the most pervasive causes of earthquake-induced lifeline damage (Hamada and O'Rourke, 1992; O'Rourke and Hamada, 1992).

Ground displacement patterns associated with earthquakes depend on PGD source, soil type, depth of ground water, slope, earthquake intensity at a given site, and duration of strong ground shaking (O'Rourke, 1998). It is not possible to model with accuracy the soil displacement patterns at all potentially vulnerable locations. Nevertheless, it is possible

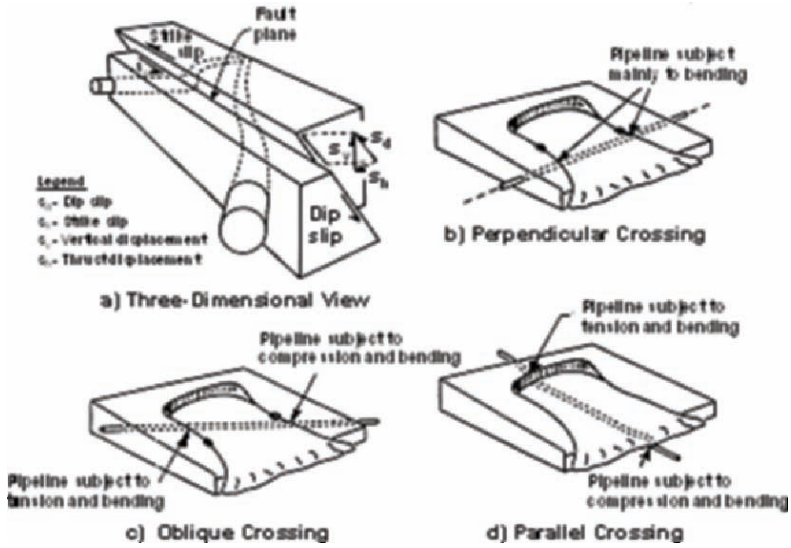


Fig. 17.2. Principal modes of soil–pipeline interaction triggered by earthquake-induced PGD (O’Rourke, 1998)

to set upper bound estimates of deformation effects on buried lifelines by simplifying spatially distributed PGD as movement concentrated along planes of soil failure.

Various modes of pipeline distortion caused by PGD are illustrated in Figure 17.2. Pipelines crossing a fault plane subjected to oblique slip are shown in Figure 17.2a. Reverse and normal faults promote compression and tension, respectively. Strike slip may induce compression or tension, depending on the angle of intersection between the pipeline and fault. Figure 17.2b shows a pipeline crossing a lateral spread or landslide perpendicular to the general direction of soil movement. In this orientation, the pipeline is subject to bending strains and extension. As shown in Figure 17.2c, the pipeline will undergo bending and either tension or compression at the margins of the slide when the crossing occurs at an oblique angle. Figure 17.2d shows a pipeline oriented parallel to the general direction of soil displacement. At the head of the zone of soil movement, the displacements resemble normal faulting; under these conditions, the pipeline will be subjected to both bending and tensile strains. At the toe of the slide, the displaced soil produces compressive strains in the pipeline.

Figure 17.3 shows a schematic of an underground pipeline deformed by mass movement of soil associated with a landslide or lateral spread. Two zones are identified for characterizing the soil–pipeline interaction. Near the center of the slide/lateral spread, two-dimensional (2-D) conditions control lateral forces mobilized against the pipe by relative horizontal displacement of the soil. Near the margins of the slide, where abrupt displacement of the ground occurs, the interaction between pipeline and soil is more

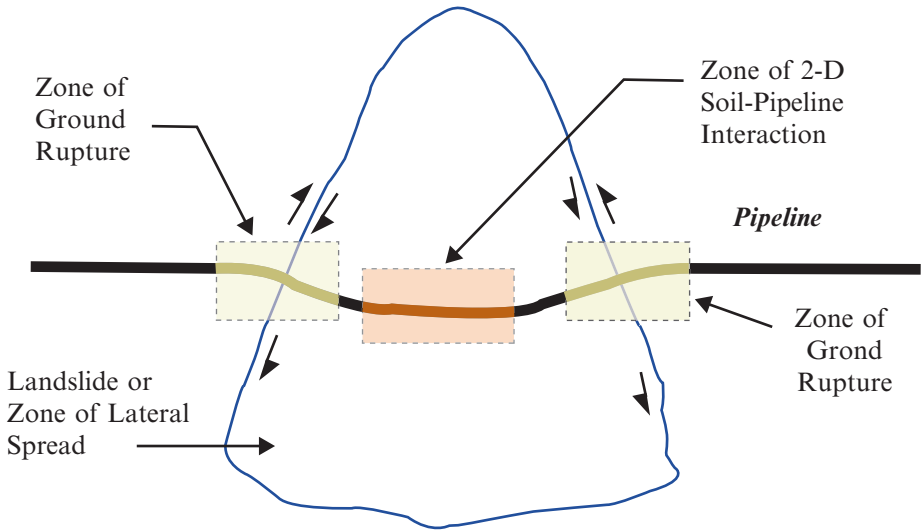


Fig. 17.3. Schematic of soil–pipeline interaction for landslides and/or lateral spread

complex. As will be discussed in a forthcoming section of the paper, the lateral forces mobilized against the pipe near the ground rupture plane involve three-dimensional (3-D) soil failure and interaction with the pipeline.

3. Lifeline system response to earthquakes

The 1994 Northridge earthquake caused the most extensive damage to a US water supply system since the 1906 San Francisco earthquake. Three major transmission systems, which provide over three-quarters of the water for the City of Los Angeles, were disrupted. Los Angeles Department of Water and Power (LADWP) and Metropolitan Water District (MWD) trunk lines (nominal pipe diameter ≥ 600 mm) were damaged at 74 locations, and the LADWP distribution pipeline (nominal pipe diameter < 600 mm) system was repaired at 1013 locations.

The earthquake-induced damage to water pipelines and the database developed to characterize this damage have been described elsewhere (O'Rourke et al., 1998, 2001; Jeon and O'Rourke, 2005), and only the salient features of this work are summarized herein. GIS databases for repair locations, characteristics of damaged pipe, and lengths of trunk lines according to pipe composition and size were assembled with ARCView software. Nearly 11,000 km of distribution lines and over 1,000 km of trunk lines were digitized.

Figure 17.4 shows the portion of the Los Angeles water supply system most seriously affected by the Northridge earthquake superimposed on the topography of Los Angeles. The figure was developed from the GIS database, and shows all water supply pipelines plotted with a geospatial precision of ± 10 m throughout the San Fernando

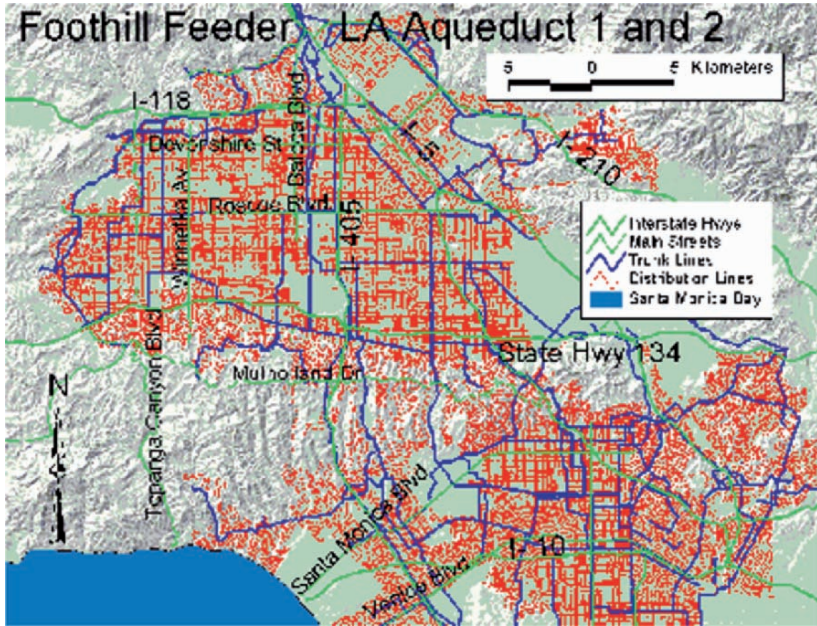


Fig. 17.4. Map of Los Angeles water supply system affected by Northridge earthquake (O'Rourke and Toprak, 1997; O'Rourke, 1998)

Valley, Santa Monica Mountains, and Los Angeles Basin. The rectilinear system of pipelines is equivalent to a giant strain gage. Seismic intensity in the form of pipeline damage can be measured and visualized by plotting pipeline repair rates and identifying the areas where the largest concentrations of damage rate occur. The resulting areas reflect the highest seismic intensities as expressed by the disruption to underground piping.

To develop a properly calibrated strain gage, it is necessary to select a measurement grid with material having reasonably consistent properties and a damage threshold sensitive to the externally imposed loads being measured. Figure 17.5 presents charts showing the relative lengths of LADWP and MWD trunk and distribution lines, according to pipe composition. As shown by the pie chart, the most pervasive material in the LA distribution system is CI. The 7,800 km of CI pipelines have the broadest geographic coverage with sufficient density in all areas to qualify as an appropriate measurement grid. Moreover, CI is a brittle material subject to increased rates of damage at tensile strains on the order 250 to 500 $\mu\epsilon$. It is therefore sufficiently sensitive for monitoring variations in seismic disturbance.

Figure 17.5 presents a map of distribution pipeline repair locations and repair rate contours for cast iron (CI) pipeline damage. The repair rate contours were developed by dividing the map into 2 km \times 2 km areas, determining the number of CI pipeline repairs in each area, and dividing the repairs by the distance of CI mains in that area. Contours

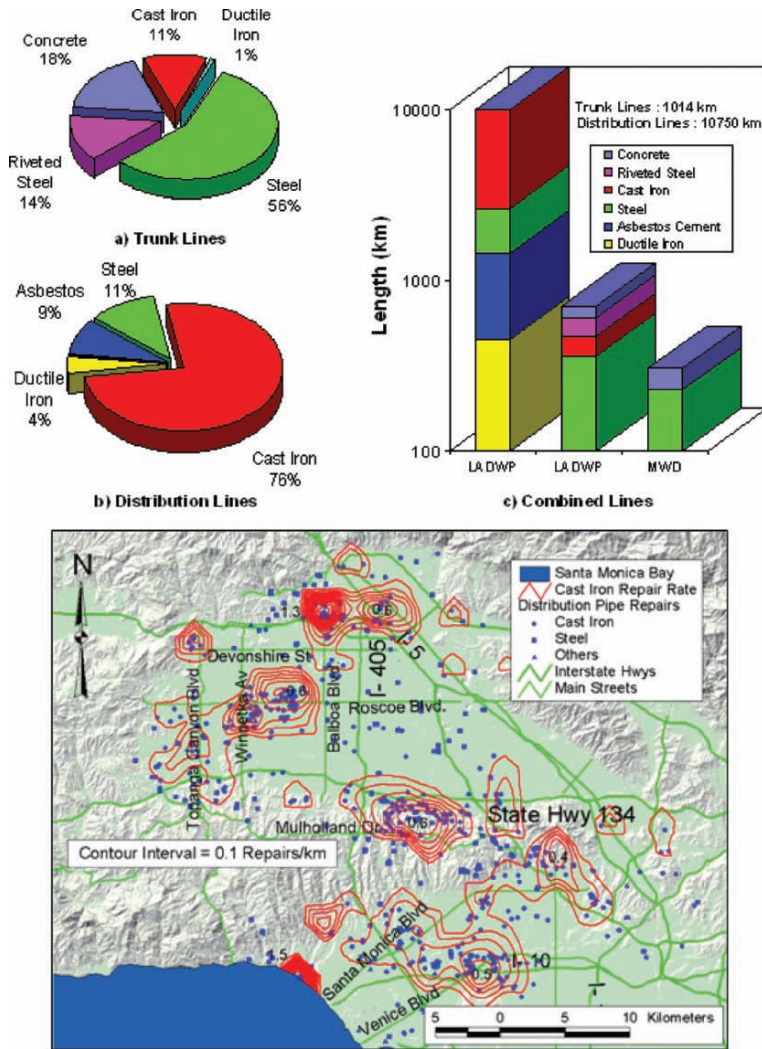


Fig. 17.5. Cast iron pipe repair rate contours for Northridge earthquake (O'Rourke and Toprak, 1997)

then were drawn from the spatial distribution of repair rates, each of which was centered on its tributary area. A variety of grids were evaluated, and the 2 km × 2 km grid was found to provide a good representation of damage patterns for the map scale of the figure (Toprak et al., 1999).

The zones of highest seismic intensity are shown by areas of concentrated contours. In each instance, areas of concentrated contours correspond to zones where the geotechnical

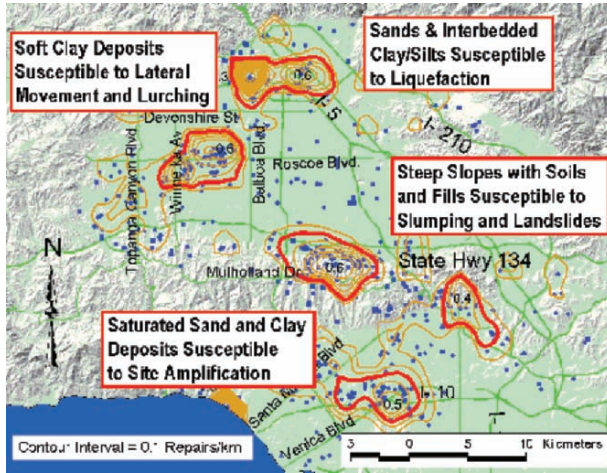


Fig. 17.6. Geotechnical characteristics of the areas of concentrated pipeline damage after the Northridge earthquake

conditions are prone either to ground failure or amplification of strong motion. Each zone of concentrated damage is labeled in Figure 17.6 according to its principal geotechnical characteristics. In effect, therefore, Figure 17.5 is a seismic hazard map for the Los Angeles region, calibrated according to pipeline damage during the Northridge earthquake.

Of special interest is the location of concentrated repair rate contours in the west central part of San Fernando Valley (designated in Figure 17.6 as the area of soft clay deposits). This area was investigated by USGS researchers, who found it to be underlain by local deposits of soft, normally consolidated clay. Field vane shear tests disclosed clay with uncorrected, vane shear undrained strength, $S_{uvst} = 20\text{--}25$ kPa, at a depth of 5 m, just below the water table. USGS investigators concluded that the saturated sands underlying this site were not subjected to liquefaction during the Northridge earthquake. Newmark sliding block analyses reported by O'Rourke (1998) provide strong evidence that near source pulses of high acceleration were responsible for sliding and lurching on the soft, normally consolidated clay deposit. The results of GIS analysis and site investigations have important ramifications because they show a clear relationship between PGD, concentrated pipeline damage, and the presence of previously unknown deposits of normally consolidated clay.

The records from approximately 240 free field rock and soil stations were used to evaluate the patterns of pipeline damage with the spatial distribution of various seismic parameters. Figure 17.7 shows the CI pipeline repair rate contours superimposed on peak ground velocity (PGV) zones, which were developed by interpolating the maximum horizontal velocities recorded at the strong motion stations. Using the GIS database, a pipeline repair rate was calculated for each PGV zone, and correlations were made between the repair rate and average PGV for each zone. As explained by O'Rourke (1998), similar

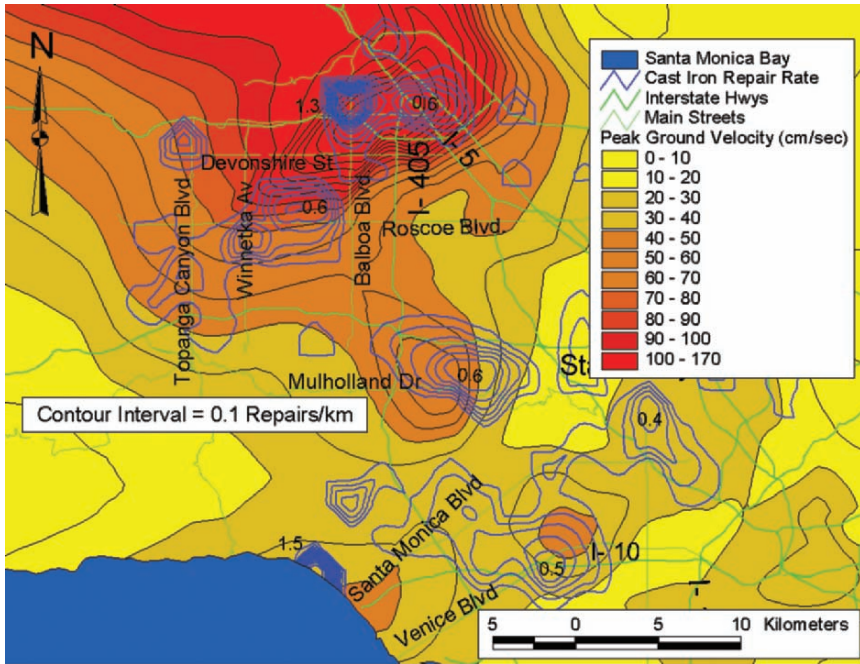


Fig. 17.7. Pipeline repair rate contours relative to Northridge earthquake peak ground velocity (O’Rourke and Toprak, 1997)

correlations were investigated for pipeline damage relative to spatially distributed peak ground acceleration, spectral acceleration and velocity, Arias Intensity, Modified Mercalli Intensity (MMI), and other indices of seismic response. By correlating damage with various seismic parameters, regressions were developed between repair rate and measures of seismic intensity.

The most statistically significant correlations for both distribution and trunk line repair rates were found for PGV. Such correlations are important for loss estimation analyses that are employed to assess the potential damage during future earthquake and develop corrective measures and emergency response procedures to reduce the projected losses (e.g., Whitman et al., 1997).

Figure 17.8a presents the linear regression that was developed between CI pipeline repair rates and PGV on the basis of data from the Northridge and other US earthquakes. Figure 17.8b shows repair rate correlations for steel, CI, ductile iron (DI), and asbestos cement (AC) distribution lines. The regressions indicate that the highest rate of damage for a given PGV was experienced by steel pipelines. This result at first seems surprising because steel pipelines are substantially more ductile than CI and AC pipelines. Steel distribution pipelines in Los Angeles, however, are used to carry the highest water pressures

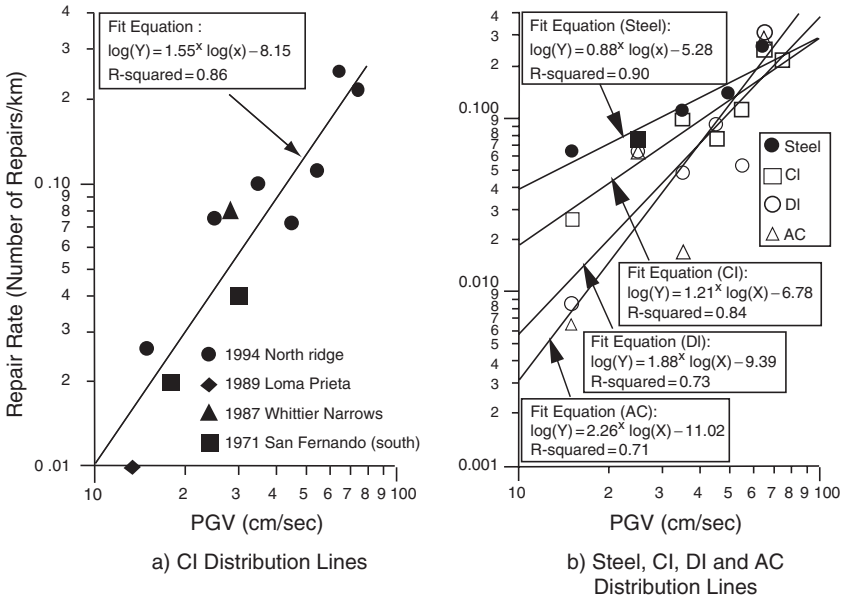


Fig. 17.8. Pipeline repair rate correlation with PGV for steel, CI, DI, and AC distribution lines

and are subject to corrosion that has been shown to intensify their damage rates in previous earthquakes (Isenberg, 1979).

The regressions in Figure 17.8 were developed after the data were screened for lengths of pipeline that represent approximately 1.5% to 2.5% of the total length or population for each type of pipe affected by the earthquake (O'Rourke and Jeon, 1999). This procedure reduces the influence of local erratic effects that bias the data derived from small lengths of pipeline. The use of this filtering procedure leads to statistically significant trends and regressions that are applicable for $PGV \leq 75 \text{ cm s}^{-1}$. For the Northridge earthquake, zones with PGV exceeding 75 cm s^{-1} generally correspond to locations where PGD, from sources such as liquefaction and landsliding, was observed. Hence, this screening technique tends to remove damage associated with PGD, resulting in correlations relevant for TGD.

4. Large-scale tests of ground rupture effects on steel pipelines with elbows

A key component of modern research involving geotechnical engineering for extreme loading conditions has been testing at very large scale. This paper refers to three programs involving large scale experiments that were performed to evaluate the effects of earthquake-induced ground rupture on welded steel and high density polyethylene (HDPE) pipelines.

The first of these experimental programs has been described in detail by Yoshisaki, et al. (2001), and only the salient features are presented here. The experiments were performed to evaluate the performance of steel gas distribution pipelines with 90° elbows. The response of pipeline elbows, deformed by adjacent ground rupture and subject to the constraining effects of surrounding soil, is a complex interaction problem. A comprehensive and reliable solution to this problem requires laboratory experiments to characterize the 3-D response of the elbow under axial and flexural loading, an analytical model that embodies soil–structure interaction combined with 3-D elbow response, and full-scale experimental calibration and validation of the analytical model.

Figure 17.9 illustrates the concept of the large-scale experiments. A steel pipeline with an elbow was installed under the actual soil, fabrication, and compaction procedures encountered in practice, and then subjected to lateral soil displacement (Yoshisaki et al., 2001). The scale of the experimental facility was chosen so that large soil movements are generated, inducing soil–pipeline interaction unaffected by the boundaries of the test facility. Figure 17.10 shows the ruptured experimental pipeline in two halves of the experimental basins that held a total of 60–65 metric tons of sand. The basins were displaced 1 m relative to each other, as shown in the figure, to simulate the type of abrupt displacement generated by liquefaction-induced lateral spread, landslides, and surface faulting. The sand was obtained from a glacio-fluvial deposit, containing approximately 2% by weight of fines (see Figure 17.13). It was placed and compacted in 150-mm lifts with strict controls on water content and in situ density. Experiments were performed with dry

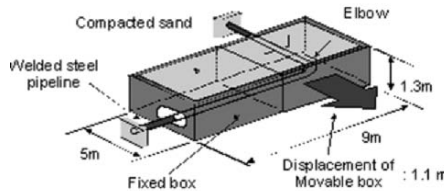


Fig. 17.9. Experimental concept for ground rupture–pipeline experiments

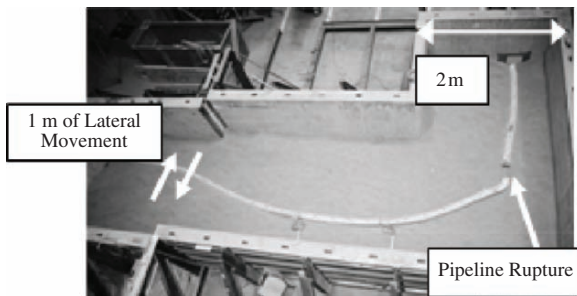


Fig. 17.10. Overhead view of soil deformation effects on experimental pipeline

sand (hygroscopic water content of 0.5%) and partially saturated sand (water contents of 3.1% and 3.4%).

A 100-mm-diameter pipeline with 4.1-mm wall thickness and a 0.9-m depth of cover was used in the tests. It was composed of two straight pipes welded to a 90° elbow. Both ends of the pipeline were bolted to reaction walls. The elbows were composed of STPT 370 steel (Japanese Industrial Standard, JIS-G3456) with a specified minimum yield stress of 215 MPa and a minimum ultimate tensile strength of 370 MPa. The straight pipe was composed of SGP steel (JIS-G3452) with a minimum ultimate tensile strength of 294 MPa. About 150 strain gages were installed on the pipe to measure strain during the tests. Extensometers, load cells, and soil pressure meters were also deployed throughout the test setup.

The large-scale experiments had three principal results. First, they were used to improve and validate a hybrid finite element model, which combines beam and shell elements for the pipeline with nonlinear p - y formulations to simulate soil-structure interaction (Yoshisaki et al., 2001). This model is now used by Tokyo Gas to plan and design pipelines for extreme loading conditions. Second, the analytical model was used to show that increasing the wall thickness of pipe, which is welded to the elbow, by 1.5 mm results in strain reduction of approximately 200% for abrupt ground rupture of 2 m. Simple, relatively inexpensive adjustments in pipeline fabrication, therefore, can lead to substantial improvements in performance. Third, the strains induced in the experimental pipeline were markedly higher for tests in partially saturated sand than for those in dry sand, even though most other variables were held constant.

5. Lateral soil-structure interaction during ground failure

To explore the effects of partially saturated sand on the lateral force conveyed to buried conduits due to relative soil-pipe displacement, a second series of tests were performed on pipe similar in size and composition as that investigated by Yoshisaki et al. (2001). The tests were designed to be similar to those performed by Trautmann and coworkers (Trautmann and O'Rourke, 1985; Trautmann et al., 1985), who established design charts from which p - y and q - z relationships can be developed for analyzing soil-structure interaction in response to lateral and vertical PGD. A detailed description of the tests and resulting data is provided by Turner (2004).

These design charts were developed on the basis of experiments in dry sand. However, the great majority of pipelines in the field are embedded in partially saturated soils. Shear deformation of partially saturated sand mobilizes surface tension, or negative pore water pressure, which increases shear resistance relative to that in dry sand under comparable conditions of soil composition, in situ density, and loading. Moreover, the geometry of the failed soil mass for partially saturated sand is significantly different than the flow and displacement pattern of dry sand around buried pipelines.

The experimental facility was constructed to model the effects of relative horizontal displacement between soil and pipe under conditions that duplicate the actual scale,

burial depth, and soil characteristics encountered in the field. Horizontal displacement was applied externally to a pipe section in a manner that allowed unrestricted vertical pipe movement as well as adjustments in pipe weight to replicate different contents such as gas, liquid fuel, and water.

The experimental facility was designed to induce maximum lateral displacement of 152 mm, with burial depths to 20 diameters. The experimental facility was composed of a test compartment, pipe loading system, instrumentation and data acquisition system, and soil handling equipment. Figures 17.11 and 17.12 show plan and profile photographs, respectively, of the test compartment.

The test apparatus consisted of a box with interior dimensions 2.4 m × 1.2 m × 1.5 m deep. A special collar was fabricated to fit on top of the testing apparatus (not shown in the figure) that extended the depth of pipe burial to 2.3 m. The apparatus was filled with a false wall that was removed when deep embedment depths (pipe depth exceeding

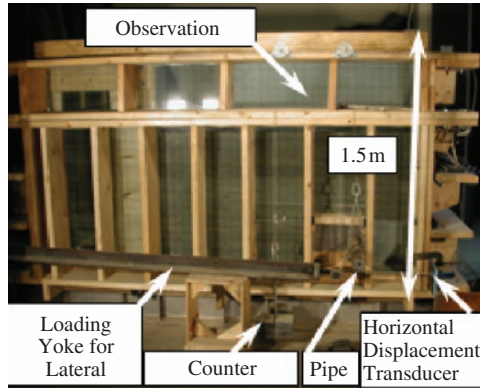


Fig. 17.11. Side view of experimental facility

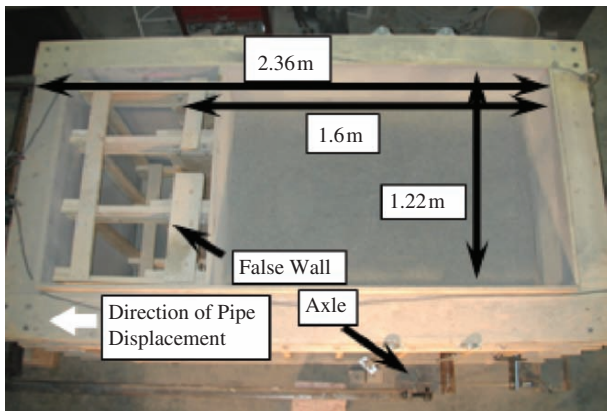


Fig. 17.12. Top view of experimental facility

10 times pipe diameter) were used. Lateral force and displacement were conveyed to the 152-mm-diameter steel pipe through a special yoke that allowed for vertical movement as the pipe was displaced forward. Loads were applied by means of a hydraulic cylinder, and were measured with a calibrated load cell. A counterweight system was used to adjust the experimental pipe weight to be consistent with pipe weight in the field. Lateral and vertical pipe movements were measured with extensometers, and soil movements were measured by means of wooden dowels, embedded in the soil mass, which were visible through the glass sidewalls.

Sand similar to that used in the large-scale experiments with the steel pipeline and 90° elbow was placed in 150-mm lifts and compacted. The grain size distribution of the experimental sand is presented in Figure 17.13. Frequent in situ density and moisture content tests were performed. Dry unit weight and moisture content in the sand mass were controlled to within $\pm 2\%$ and $\pm 0.5\%$, respectively. The sand was placed dry and at moisture contents of approximately 4% and 8%.

Figure 17.14 shows select plots of dimensionless force vs. dimensionless displacement for tests on partially saturated sand with dry unit weights between 16.3 and 16.6 kN m^{-3} at ratios of depth to pipe centerline to external pipe diameter (H/D) of 6 and 8.5, respectively. The dimensionless force is the maximum measured lateral force, F , divided by the

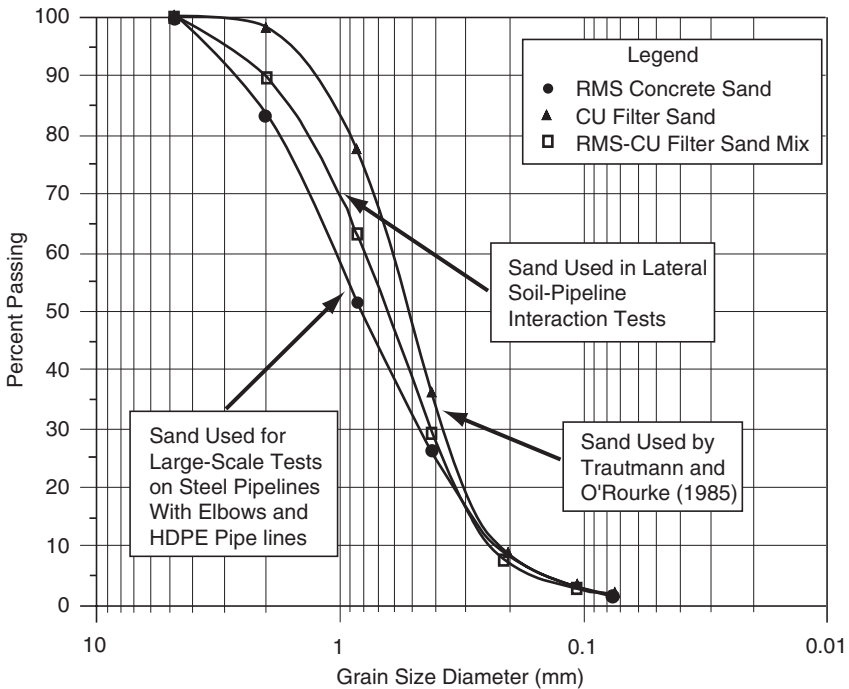


Fig. 17.13. Grain size distribution of the experimental sand

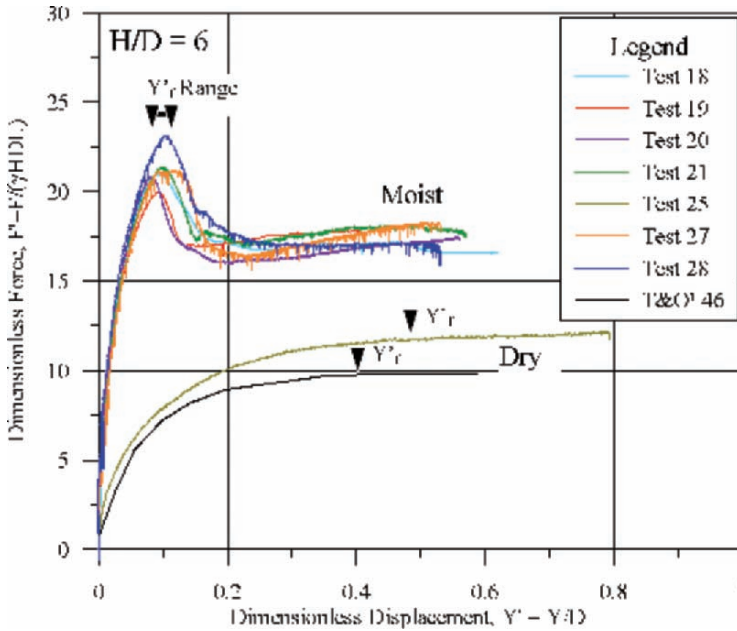


Fig. 17.14. Force-displacement curves for tests with dry unit weight of 16.3–16.7 kN m⁻³ and H/D = 6

Table 17.1. Summary information for tests with dry unit weight of 16.3–16.7 kN m⁻³ and H/D = 6

Line symbol	Water content (%)	Dry unit weight (kN m ⁻³)	Test no.	Friction angle ^{*2}	N _q
—	0	16.4	T&O ^{**1} 46	36	9.8
—	0	16.7	25	37.1–37.8	12.2
—	4.1	16.4	21	38.6–39.4	21.4
—	4.2	16.4	20	38.6–39.5	20.9
—	4.4	16.6	19	40.5–40.6	20.0
—	4.6	16.4	18	38.6–39.4	21.0
—	7.6	16.3	27	38.5–39.3	21.2
—	7.8	16.4	28	38.5–39.3	23.2

* Friction angle range, in degrees, determined from exponential and bi-linear fits to direct shear data.

** T&O = Test data from Trautmann and O'Rourke (1983).

product of soil unit weight, γ , H, D, and length of pipe, L. This term provides a value that can be scaled to various depths, diameters, and soil conditions of practical interest. Table 17.1 summarizes information for each moist sand test shown in Figure 17.14, including dry unit weight, water content, friction angle, and selected values of maximum

dimensionless force, N_q . The characteristic displacement, Y'_f , corresponding to maximum force is shown for each curve with an arrowhead. The term Y' is the ratio of the horizontal displacement, Y , to D .

For comparison with the moist sand test results, the figures also show force-displacement curves for dry sand obtained from this study and tests by Trautmann and O'Rourke (1983, 1985). The dry unit weight of the tests by Trautmann and O'Rourke (1983, 1985) was 16.4 kN m^{-3} . The dry unit weights obtained during the dry sand tests by Turner (2004) were 16.7 and 16.9 kN m^{-3} .

The force-displacement curves for moist sand tests reached a peak at relatively small displacement, typically at Y' between 0.1 and 0.2 , and then decreased to a lower constant value at larger displacements, typically at Y' of 0.2 to 0.3 . The maximum dimensionless force, N_q , for all moist sand tests and the corresponding dimensionless displacement, Y'_f , were selected at the initial peak in the curve. As shown in Figure 17.14, force-displacement curves for dry sand with similar dry unit weight as the moist sand tests did not exhibit peak behavior. Maximum force was selected for these tests using a horizontal asymptote to the force-displacement curve, and Y'_f was selected using Hansen's (1963) 90% criterion as described by Fellenius (1980). To compare moist and dry sand test results at a second dry unit weight for H/D of 6 , tests were also performed with dry unit weights of 15.7 and 15.8 kN m^{-3} , respectively, as described by Turner (2004).

The force-displacement curves shown in Figure 17.14 illustrate several important features of soil-pipe interaction. First, the test results for sand with 4% moisture are nearly identical to the results for sand with 8% moisture, including maximum force, displacement at maximum force, and curve shape. Second, for similar dry unit weight, tests in moist sand experienced about twice the maximum force associated with tests in dry sand. Third, displacement at maximum force, Y'_f , was smaller for the moist sand tests compared to dry sand tests at the same density. Moreover, the initial curve slope, or stiffness, is greater for the moist sand test results. Also, for the same dry unit weight, the moist sand force-displacement curves reach a peak value and decrease, typical of dense, dilative dry sand, whereas the dry force-displacement curves approach a horizontal asymptote, typical of loose or medium dense dry sand.

Figure 17.15 summarizes values of maximum force vs. dimensionless depth, as determined from the experimental data. Test results for dry, medium dense sand from Trautmann and O'Rourke (1983, 1985) are also shown, and an interpretive curve is drawn through the moist test results and extrapolated to other H/D ratios. For H/D less than 6 , this extrapolation was performed by multiplying the dry sand test results by the ratio of moist N_q to dry N_q determined at H/D of 6 . For H/D greater than 8.5 , the dry sand test data were multiplied by the ratio of moist N_q to dry N_q determined at H/D of 8.5 . The interpretive curve between H/D of 6 and 8.5 was drawn as a line connecting the moist sand data points.

The force associated with partially saturated sand is approximately twice that generated under dry sand conditions. Direct shear test results show that increased shear resistance

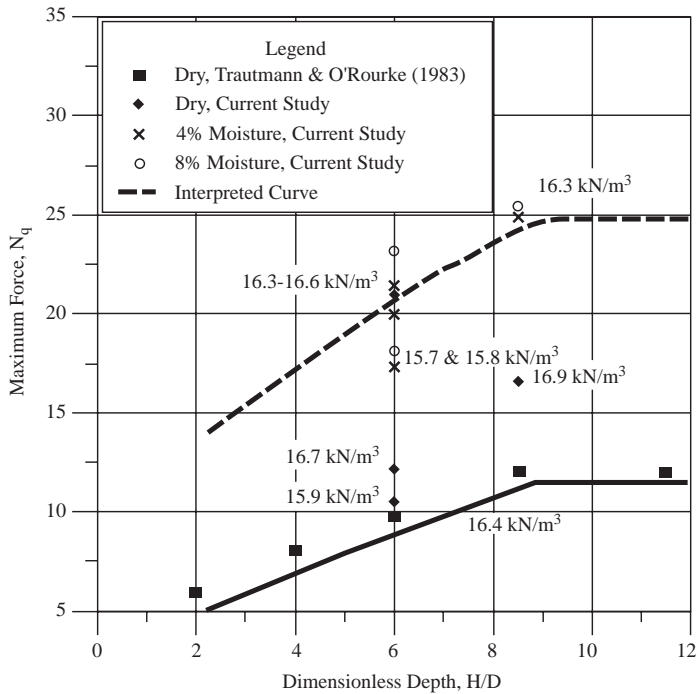


Fig. 17.15. Maximum dimensionless force vs. dimensionless depth for varying moisture content and dry unit weight

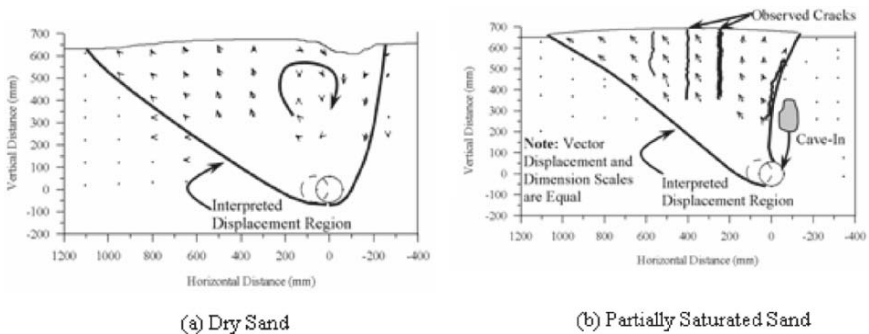


Fig. 17.16. Soil displacement patterns for dry and saturated sand

in partially saturated sand accounts only for about 30% of the increased lateral force relative to that for dry conditions. The principal cause of increased resistance can be explained with reference to Figure 17.16, which shows the soil deformation patterns in dry and partially saturated sands. Dry sand deformation shows distinct zones of heave and subsidence, with continuous rotational movement between well-developed passive and

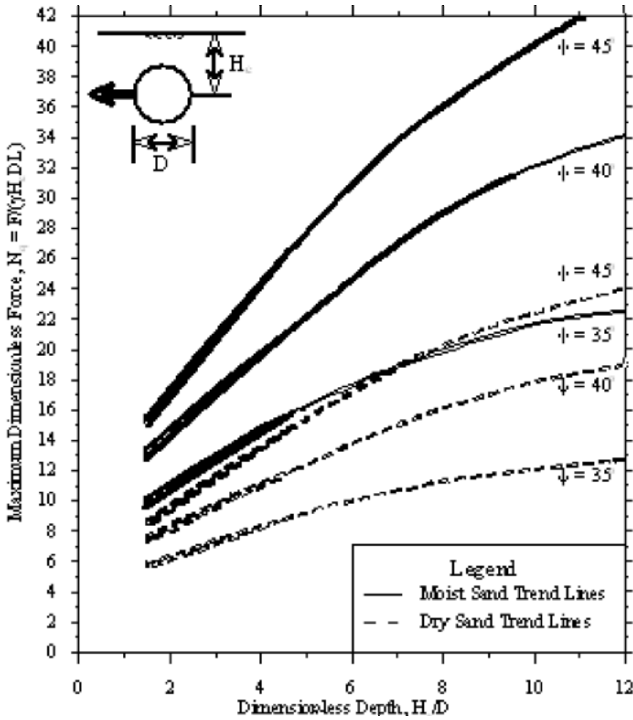


Fig. 17.17. N_q vs. H_c/D for horizontally loaded pipes in dry and moist sand

active zones in front of and behind the pipe, respectively. In contrast, partially saturated sand ruptures along distinct failure planes, creating a coherent mass of soil that is pushed forward and lifted in concert with the relative lateral movement of the pipe.

Figure 17.17 shows the maximum dimensionless force, N_q , vs. dimensionless depth, H_c/D , derived for partially saturated and dry sand tests with the experimental data of Turner (2004) and Trautmann and O'Rourke (1985). Note that predicted curves for a friction angle of 30° are not shown in Figure 17.17. Loose, dry sand consolidates during lateral loading, which, in effect, increases the friction angle and N_q values, and results in larger horizontal displacement to attain maximum load. Moist sand placed in the loose condition typically consists of a bulked, collapsible structure with inconsistent density, for which a uniform mass friction angle is not appropriate. Lateral loading of pipes in loose sand will result in collapse of the bulked structure and compaction of the sand, thereby increasing the dry unit weight and friction angle. With the available evidence from this and previous studies, a percent increase in N_q from dry to moist loose sand cannot be reliably predicted. Further experimental investigation is needed to confirm the force–displacement behavior of loose moist sand.

6. Large-scale tests of ground rupture effects on HDPE pipelines

A third series of experiments is being performed as part of joint research supported by the National Science Foundation (NSF) through the George E. Brown, Jr., Network for Earthquake Engineering Simulation (NEES), using the large-scale lifeline testing facility at Cornell University and the 150g-ton centrifuge at Rensselaer Polytechnic Institute (RPI). Information about the experimental program is provided by Cornell et al. (2006). Due to space limitations, only the salient features of the large-scale experiments are provided herein.

The soil for the large-scale experiments on HDPE is a glacio-fluvial, well graded sand similar to that used for full-scale experiments of soil–pipeline interaction on steel pipelines with elbows that were described previously (see Figure 17.13). The sand was placed and compacted in 200-mm-thick lifts. Moisture content was determined using a nuclear density gage as well as soil samples removed in standard tins for moisture content determination in the laboratory. Forty moisture content and 40 soil density measurements were taken per lift, for a total of 320 measurements over 8 lifts. The mean dry unit weight for all soil placed was 15.7 kN m^{-3} , with a standard deviation of 0.32 kN m^{-3} . There is 95% confidence that the mean dry unit weight of soil placed for testing is between 15.66 kN m^{-3} and 15.72 kN m^{-3} . Based on direct shear calibrations, the peak soil friction angle is between 39° and 40° . Mean moisture content was 4.1%, with a standard deviation of 0.77%. The 95% confidence interval for the mean moisture content is between 4.05% and 4.20%.

The experimental plastic pipelines were nominal 400-mm-diameter and nominal 250-mm-diameter, IPS, HDPE pipes, manufactured by the Chevron Phillips Chemical Company under the commercial name DRISCOPEX. The nominal 400-mm pipe has an outside diameter of 400.5 mm and wall thickness 24 mm. Electrofusion (EF) couplings were installed at each end of each specimen to provide anchor locations for connecting the experimental pipeline to the split-box test basin. The couplings use computer-controlled heating coils to fuse, or thermally bond, onto the HDPE pipe so that they are connected to the pipe at a strength comparable with that of the HDPE. The instrumentation layout for the test on the 400-mm-diameter pipeline included 148 strain gages, and was planned using results from finite element (FE) analyses. The experimental pipeline was buried at a depth of 0.9 m from ground surface to top of pipe.

Figure 17.18 shows an overhead view of the large-scale ground rupture test on the 400-mm-diameter HDPE pipeline. The split-box experimental chamber was approximately 10.7 m long, 3.2 m wide, and filled to a total depth of 1.5 m with partially saturated sand. The test involved approximately 91 metric tons of sand. A left lateral strike slip displacement of 1.2 m was imposed during testing over a period of 4 min. The angle of intersection between the rupture plane and pipeline was 65° , which induced tension and bending in the pipe.

Only the central 6 m of the experimental chamber are shown. The deformed shape of the pipeline is superimposed on the photo. The deformed shape was measured with

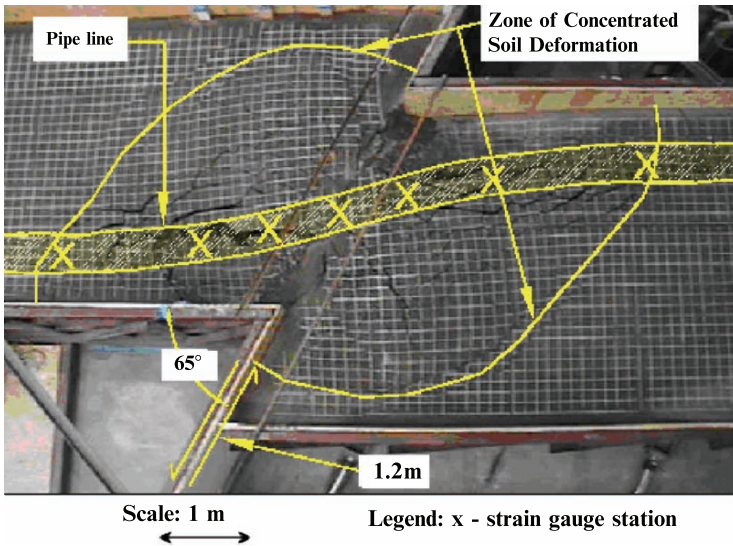


Fig. 17.18. Overhead view of the large-scale ground rupture test on the 400-mm-diameter HDPE pipeline

extensometer probes external to the pipe and lasers to measure successive chord lengths inside the pipeline.

The maximum axial strain measured was 8%, and the maximum circumferential strain measured was 6%. The end reactions were 520 kN. Figure 17.19 shows the axial strains measured directly along the east springline of the pipe for 0.3, 0.6, 0.9, and 1.2 m displacements. Figure 17.20 shows the strain along both the east and west springline at the maximum displacement of 1.2 m. As can be seen in the figure, the axial strains were symmetrically distributed with respect to the ground rupture location.

Figures 17.21 and 17.22 show the results of pre- and post-test laser profiling. A special robotic crawler, designed to inspect pipelines by ULC Robotics, Deer Park, NY, was used to transport a video camera and laser profiling device through the pipeline before and after the test. The laser generates an image of the pipe cross-section continuously as the crawler traverses the pipeline. The image is stored digitally, and provides a measurement of the shape. By subtracting the pre- and post-test images at the same location, the change in shape, or cross-sectional deformation, is determined. Figures 17.21 and 17.22 show pre- and post-test frames taken at 1 m south and north of the ground rupture, respectively. The racking and ovaling of the pipe is clearly evident at each location.

The laser profiling measurements showed maximum ovaling, or increase in pipe diameter, of 12% at the location of the ground rupture. The measurements also showed about 6% maximum loss of the internal cross-sectional area of the pipe. Most importantly, the laser profiling provided an accurate, continuous record of cross-sectional change in

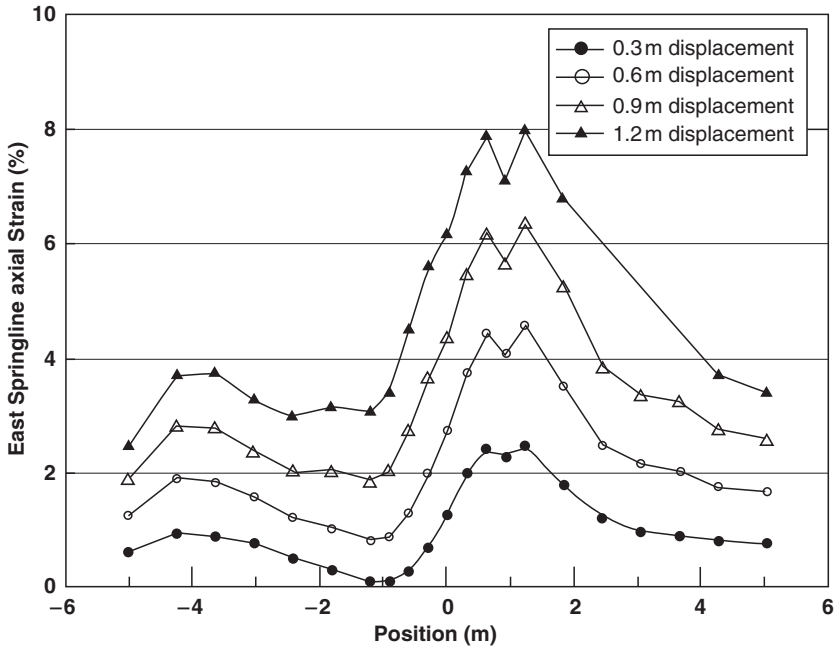


Fig. 17.19. East springline axial strains at ground displacement of 0.3, 0.6, 0.9, and 1.2 m

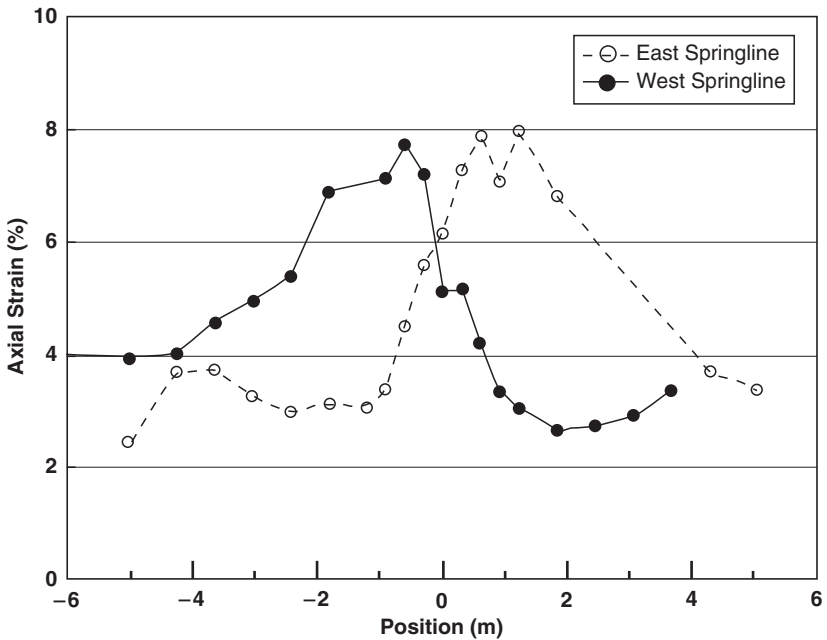


Fig. 17.20. East and west springline axial strain at 1.2 m displacement

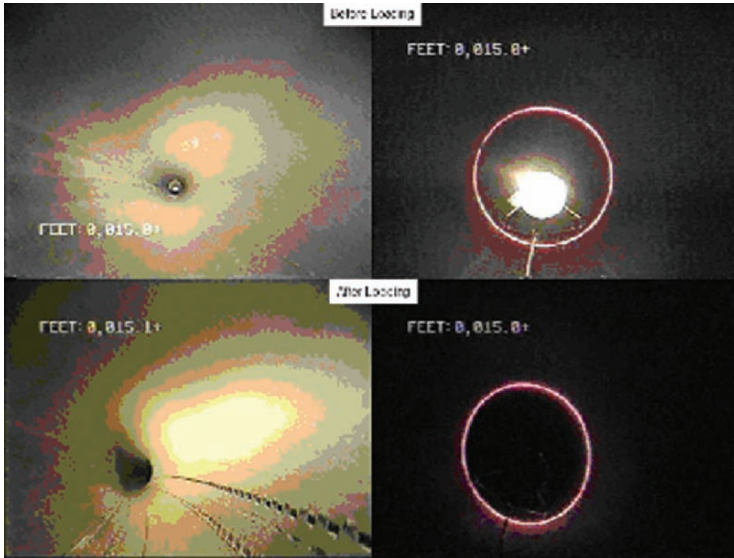


Fig. 17.21. Pre- and post-test photos 1 m south of ground rupture

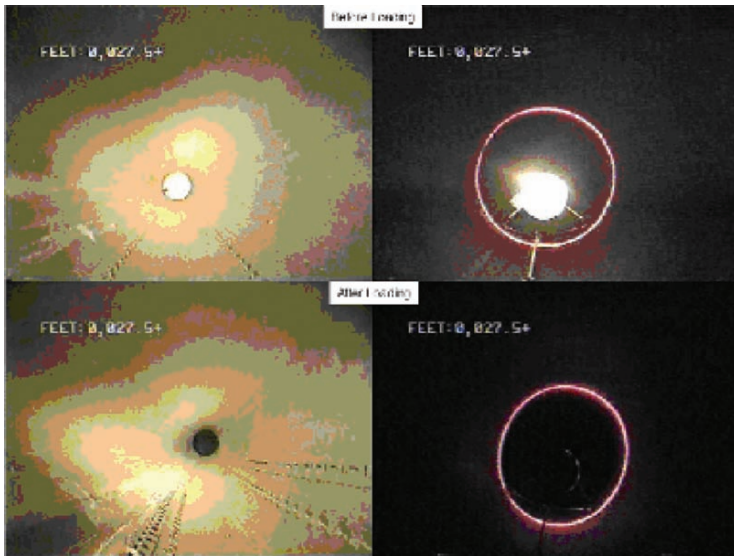


Fig. 17.22. Pre- and post-test photos 1 m north of ground rupture

shape, demonstrating that the full-scale pipeline deformed as a 3-D cylinder. Moreover, the change in orientation of the ovaling on either side of the ground rupture, as shown in the laser images, indicates that the pipeline was also subjected to a torsional, or twisting, deformation.

The HDPE experiments have three principal results. First, they demonstrate the flexibility and ductility of HDPE piping. Maximum measured tensile strains were only 8% at 1.2 m of offset, well below the ultimate strain capacity of the pipe. The axial load in the pipeline decreased by 40% within 2 h after ground rupture. Because HDPE is visco-elastic, it has the beneficial effect of reducing the load with time at anchorages outside the ground rupture zone. Second, the laser profiling shows significant ovaling and some torsion in the pipeline. The deformation of the pipeline therefore needs to be modeled as a cylindrical shell for an accurate representation of its behavior. Models based on beam-column deformation for this type of HDPE pipe will be approximate. Third, the soil deformation zone is 3-D, as illustrated in the figure. It develops during ground rupture progressively as a series of nonlinear soil rupture zones that increase in size longitudinally along the pipeline and are confined to a distance of approximately 9–10 pipe diameters on either side of the soil rupture plane.

This latter observation is significant. The 3-D soil-pipeline deformation differs substantially from the 2-D deformation in the central zone of landslide and lateral spread movement depicted in Figure 17.3, and generates *p*-*y* interaction with less lateral force and larger relative displacement than is applicable for the 2-D conditions. Measurements pertaining to these 3-D conditions are being performed with tactile force sensors manufactured by Tekscan, Inc. These devices consist of a matrix of pressure sensitive transducers, embedded in a fabric that covers all or part of the surface of the experimental pipeline. Preliminary results indicate that peak lateral forces per unit length of pipeline in partially saturated soil near the ground rupture plane are about 40%–50% of those measured for 2-D conditions.

7. Concluding remarks

Soil-structure interaction under extreme loading conditions includes performance during earthquakes, floods, landslides, large deformation induced by tunneling and deep excavations, and subsidence caused by severe dewatering or withdrawal of minerals and fluids during mining and oil production. Such loading conditions are becoming increasingly more important as technologies are developed to cope with natural hazards, human threats, and construction in congested urban environments.

This paper examines extreme loading conditions with reference to earthquakes, which are used as an example of how extreme loading influences behavior at local and geographically distributed facilities. The paper covers performance from the component to the system-wide level to provide guidance in developing an integrated approach to the application of geotechnology over large, geographically distributed networks. Specific topics covered include geotechnical earthquake loading, lifeline response to earthquakes, large-scale tests of ground rupture effects, and soil-structure interaction during ground failure.

Permanent ground deformation (PGD) is the most damaging consequence of an earthquake for underground facilities, including regional distribution networks for water and

natural gas. The sources of PGD involve landslides, soil liquefaction, and surface faulting. The generic patterns of displacement for earthquake-triggered ground failure are similar to those for landslides, subsidence, and ground deformation associated with deep excavation, tunneling, and mining activities.

The systematic analysis of pipeline repair records after the 1994 Northridge earthquake show the locations of important seismic and geotechnical hazards and are used to identify zones of potential ground failure not recognized in previous explorations and risk assessments. Moreover, the systematic assessment of pipeline repairs with GIS result in regressions that link damage rates to various levels of strong motion. Such relationships are important for loss estimation studies of future earthquake effects to plan for and reduce the potential for seismic disruption.

Large-scale tests of pipeline response to abrupt ground rupture have resulted in analytical models that can simulate such behavior at critical locations, such as pipeline elbows, where local soil restraint and the 3-D distribution of deformation leads to increased risk of failure. Large-scale tests of soil–pipeline interaction show that soil–structure interaction for partially saturated sand results in significantly greater concentration of pipeline strain than for dry sand. Full-scale tests of soil–structure interaction for buried pipelines subjected to large horizontal movements under 2-D conditions indicate that maximum lateral forces are approximately twice as high for large horizontal displacement in partially saturated sand as for dry sand. These conditions apply to pipeline locations near the center of a lateral spread or landslide. Design charts are developed on the basis of experimental results to predict maximum lateral load for different depths of burial, pipe diameters, and soil angle of shear resistance associated with partially saturated and dry sand.

Large-scale tests on HDPE pipelines show that such piping has the flexibility and ductility to withstand substantial amounts of abrupt ground deformation. Because of its viscoelastic characteristics, the axial load in HDPE relaxes after ground failure, thus having the beneficial effect of reducing loads on anchorages either side of the concentrated soil deformation.

A complex 3-D soil deformation and rupture pattern is observed either side of the strike slip rupture plane in large-scale tests. The progressive, 3-D characteristics of soil failure near the main ground rupture plane results in a p – y relationship significantly different than that for 2-D conditions in partially saturated sand. The large-scale tests show that 3-D conditions near the abrupt ground rupture result in peak lateral force per unit pipeline length that are approximately 40%–50% of the peak lateral force for pipe with similar geometry, depth, and soil under 2-D conditions of relative soil–pipe horizontal displacement.

Acknowledgments

Thanks are extended to the National Science Foundation, Multidisciplinary Center for Earthquake Engineering Research, Los Angeles Department of Water and Power, NEES

Inc., and Tokyo Gas Company, Ltd. for their generous support of the work presented in this paper. The large-scale experiments on HDPE pipelines were performed with the facilities of the George E. Brown, Jr., Network for Earthquake Engineering Simulation. Recognition is also extended to previous students and current members of the Cornell research team, for their contributions to portions of the work reported in the paper, including HE Stewart, MC Palmer, TK Bond, JE Turner, Y Wang, P Shi, NA Olsen, JM Jezerski, and JF Chipalowsky. Recognition is also extended to Cornell's research partners at PPI, including MJ O'Rourke, T Abdoun, and MD Symans.

REFERENCES

- Cornell University, Rensselaer Polytechnic Institute, and Sciencenter Discovery Center (2006) NEESR Annual Report, report submitted to National Science Foundation, nees@cornell.edu
- Fellenius BH, (1980) The analysis of results from routine pile load tests. *Ground Engineering*, 13(6): 19–31
- Hamada M, O'Rourke TD, eds (1992) *Case Studies of Liquefaction and Lifeline Performance during Past Earthquakes*. National Center for Earthquake Engineering Research, State University of New York at Buffalo, Buffalo, NY, February 1992, Technical Report NCEER-92-0001
- Hansen JB (1963) Discussion of "hyperbolic stress-strain response: cohesive soils," by R.L. Kondner. *Journal of the Soil Mechanics and Foundations Division, ASCE* 89(SM4): 241–242
- Isenberg J (1979) Role of corrosion in water pipeline performance in three US earthquakes. *Proc. of the 2nd US National Conference on Earthquake Engineering*, Stanford, CA, August 1979, pp 683–692
- Jeon S-S, O'Rourke TD (2005) Northridge earthquake effects on pipelines and residential buildings. *Bulletin of the Seismological Society of America*, BSSA 95-1:1–25
- O'Rourke TD, Hamada M, eds (1992) *Case Studies of Liquefaction and Lifeline Performance during Past Earthquakes*. National Center for Earthquake Engineering Research, State University of New York at Buffalo, Buffalo, NY, Technical Report NCEER-92-0002
- O'Rourke TD, Toprak S (1997) GIS assessment of water supply damage from the Northridge earthquake. *Spatial Analysis in Soil Dynamics and Earthquake Engineering*, ASCE, Frost D, ed
- O'Rourke TD (1998) An Overview of Geotechnical and Lifeline Earthquake Engineering. *Geotechnical Special Publication No. 75*, ASCE, Pakoulis P, Yegian M, Holtz D, eds, Reston, VA, 1998, II, 1392–1426
- O'Rourke TD, Toprak S, Sano Y (1998) Factors affecting water supply damage caused by the Northridge earthquake. *Proc. of the 6th US National Conference on Earthquake Engineering*, Seattle, WA, June 1998, pp 1–12
- O'Rourke TD, Jeon S-S (1999) Factors affecting the earthquake damage of water distribution systems. *Proc. of the 5th US Conference on Lifeline Earthquake Engineering*, Seattle, WA, ASCE, Reston, VA, August 1999, pp 379–388
- O'Rourke TD, Stewart HE, Jeon S-S (2001) Geotechnical aspects of lifeline engineering, *Proc. of Institution of Civil Engineers Geotechnical Engineering*, Vol 149, Issue 1, January 2001, pp 13–26
- Toprak S, O'Rourke TD, Tutuncu I (1999) Geographic information system (GIS) characterization of spatially-distributed lifeline damage. *Proc. of the 5th US Conference on Lifeline Earthquake Engineering*, Seattle, WA, ASCE, Reston, VA, August 1999, pp 110–119

- Trautmann CH, O'Rourke TD (1983) Behavior of Pipe in Dry Sand Under Lateral and Uplift Loading. Geotechnical Engineering Report 83-7, Cornell University, Ithaca, New York
- Trautmann CH, O'Rourke TD (1985) Lateral force-displacement response of buried pipe. *Journal of Geotechnical Engineering*, ASCE, Reston, VA 111(9):1068-1084
- Trautmann CH, O'Rourke TD, Kulhawy FH (1985) Uplift force-displacement response of buried pipe. *Journal of Geotechnical Engineering*, ASCE 111(9):1061-1067
- Turner JE (2004) Lateral Force-Displacement Behavior of Pipes in Partially Saturated Sand, Master of Science Thesis, Cornell University, Ithaca, New York
- Whitman RV, Anagnos T, Kircher CA, Lagorio HJ, Lawson RS, Schneider P (1997) Development of a national earthquake loss estimation methodology. *Earthquake Spectra* 13(4):643-661
- Yoshisaki K, O'Rourke TD, Hamada M (2001) Large deformation behavior of buried pipelines with low-angle elbows subjected to permanent ground deformation. *Journal of Structural Mechanics and Earthquake Engineering*, JSME 4(50):215-228
- Youd TL (1973) Liquefaction, Flow, and Associated Ground Failure. US Department of the Interior, Washington, D.C., Geologic Survey Circular 688

CHAPTER 18

SEISMIC RISK ASSESSMENT OF UNDERGROUND STRUCTURES UNDER TRANSIENT GROUND DEFORMATIONS

Roberto Paolucci¹ and Kyriazis Pitilakis²

¹ *Depart. of Structural Engineering, Politecnico di Milano, Milano, Italy*

² *Depart. of Civil Engineering, Aristotle University of Thessaloniki, Greece*

Abstract. Some relevant issues concerning the seismic risk assessment of underground structures under transient ground deformations are dealt with in this paper, mainly referring to: (i) the evaluation of earthquake-induced ground strains and the re-examination of the currently used formulas for design; (ii) the analysis of their spatial variability as a function of the lateral soil heterogeneities, including the role of surface waves; (iii) the ratio between shear and axial strains; and (iv) the main problems to be faced in the construction of hazard maps for seismic risk assessment of underground structures. A detailed example of application to the risk assessment of the water pipeline system in the town of Düzce, Turkey, is provided, including the numerical simulation of seismic wave propagation from the source of the Nov. 12, 1999, earthquake to the Düzce basin and the comparison of 1D and 2D results in terms of peak ground strains. The effect of different vulnerability functions on the risk assessment, either in terms of peak ground velocity or peak ground strain, is also addressed. Finally, a further example of risk assessment of the water transmission system in Thessaloniki is summarized.

1. Introduction

It is widely recognized that, unlike above-ground structures that act as a kind of “inertial” filter on the incident ground motion, the seismic response of underground structures is predominantly affected by the deformation of the surrounding soil, while soil–structure interaction effects are generally negligible (St John and Zarah, 1987). Therefore, one of the critical aspects behind the seismic design and assessment of underground structures is the proper definition of the input ground motion that cannot be directly deduced from the standard spectral representation of seismic actions.

Leaving aside the case of earthquake-induced ground failures, such as fault ruptures, liquefaction or landsliding, that will not be covered in this paper, the procedures for determination of seismic design actions on underground structures are generally based on a simplified evaluation of transient ground strains under the assumption of plane waves propagating in a homogeneous unbounded medium (Newmark, 1967; Yeh, 1974). Referring to the comprehensive state-of-art of Hashash et al. (2001) for the review of different formulas applicable to the various deformation modes, we limit ourselves here for simplicity to the case of longitudinal strains that are generally considered to be the main

deformation mechanism for buried pipelines. In this case, the peak ground strain PGS_a along the longitudinal axis a of the structure is calculated as

$$PGS_a = \frac{PGV_a}{\kappa C} \quad (18.1)$$

where PGV_a is the peak particle velocity along the a direction, C is a suitable measure of wave propagation velocity, and κ is a correction parameter to account for maximization of strain as a function of the angle ϕ formed by the direction of propagation of the plane wave with respect to the longitudinal axis of the structure. Simple theoretical derivations, first reported by Yeh (1974), show that for S-waves $C = V_s$, V_s being the S-waves propagation velocity, and $\kappa = 2$, corresponding to $\phi = 45^\circ$.

The appropriate selection of κ and C is not straightforward, since it depends on the wave type (P, S, or surface waves), on the incidence angle and on the local soil properties. Furthermore, the available technical guidelines provide some contradictory practical rules. For example, according to ALA (2001a,b), C should be taken as “the apparent propagation velocity for seismic waves (conservatively assumed to be 2 km/s)”, while $\kappa = 2$ for S-waves and $\kappa = 1$ otherwise. According to Eurocode 8 Part 4 for buried pipelines (CEN, 2006), C is the “apparent wave speed” and the selection of the wave type shall be made “based on geophysical considerations”, while it is implicitly assumed $\kappa = 1$. A more detailed definition of the above parameters is provided by the French guidelines AFPS/AFTES (2001), according to which C is the apparent wave propagation velocity that is suggested to be taken as $\min(1 \text{ km/s}, V_s)$, where V_s should be averaged over a depth equal to the fundamental wavelength, while $\kappa = 2$ to maximize the axial strains with respect to the incident angle.

Based on the previous indications, the seismic action in a buried pipeline deduced from the AFPS/AFTES guidelines would be at least two times larger than using the ALA ones, while a comparison with EC8-Part4 is not straightforward because it implies the arbitrary selection of the apparent wave propagation velocity, with values typically ranging between 2 and 4 km/s (see e.g. Abrahamson, 2003).

Therefore, the practical application of eq. (18.1) is subject to numerous, and partly arbitrary, assumptions, mainly due to the lack of sound methods for transient ground strain evaluation and to the lack of a comprehensive set of experimental validations. Referring to the thorough state-of-art of Zerva (2003), the proper identification of the wave type and the corresponding apparent velocity may account for one order of magnitude of variability in the ground strain estimation, while an additional factor of 2–3 may be due to spatial incoherence of ground motion (Zerva, 1992).

Besides the proper evaluation of the apparent velocity of wave propagation in eq. (18.1), a suitable correlation to estimate earthquake-induced transient ground strains should also account for the different frequency, and hence magnitude, dependence of peak ground motion parameters and of their possible non-simultaneous occurrence, as will be shown later in the application to the Düzce case, where PGS is carried by late surface

waves arrivals induced by the basin edge, while *PGV* by the first S-waves. Furthermore, although ground strains affecting buried pipelines are expected to be more pronounced for medium to long period waves, the surface geology and site effects may play a very important role as well, especially when they affect also the apparent velocity and the ground motion incoherence.

A further important remark should be made on the strain component, either axial or shear, to be adopted. It is well known that, while for shallow small-diameter buried pipelines seismic design is mainly governed by axial loads, for large-diameter pipelines or tunnels bending and cross-sectional distortions induced by shear strains may also be significant. Since the ratio of axial to shear strain at a certain location strongly depends on the wave type, incidence angle, earthquake magnitude and depth, as will be shown later in this paper by some preliminary numerical results, we have distinguished throughout the text peak axial strains, denoted as *PGSa* from the peak shear strains, denoted as *PGSs*, unless this distinction is not relevant for presentation of results.

In the first part of this paper some of the previous limitations in the use of eq. (18.1) will be discussed, addressing mainly (i) the experimental validations of the empirical relationships for peak ground strain evaluation, highlighting the role of spatial incoherency of ground motion, and (ii) the effect of strong lateral discontinuities in soil properties.

In the second part, we introduce some recent studies on the seismic risk assessment of buried lifeline systems, mainly related to the experience acquired in some recent projects in Europe and Turkey in order to highlight the practical implications of ground strains and *PGV* evaluation in the vulnerability assessment of complex lifeline networks.

2. Earthquake-induced transient ground strains

2.1. EXPERIMENTALLY BASED *PGS*–*PGV* RELATIONS FROM DENSE SEISMIC NETWORKS

Due to the lack of direct strain measurements during seismic ground motion, an experimental basis should be provided to the evaluation of earthquake-induced ground strains, typically in terms of a suitable measure of peak ground strain and its relationship with other more frequently used ground motion parameters, such as peak ground velocity (*PGV*) or acceleration (*PGA*). A possible solution is to make use of data collected within very dense seismic networks (Bodin et al., 1997; Gomberg et al., 1999). This approach has been recently used by Smerzini et al. (2006), who considered the weak motion records of a temporary network in Parkway Valley, New Zealand, in which the close spacing of the stations, of the order of few tens of meters, allowed them to reconstruct, through a suitable interpolation procedure, the three-component displacement field at ground surface, from which the components of the strain tensor at ground surface could be calculated. Subsequently, the same procedure has been applied by Paolucci and Smerzini (2007)

to the strong motion records obtained by the UPSAR dense array during the 2003 San Simeon M6.5 and the 2004 Parkfield M6.0 earthquakes (Fletcher et al., 2006; Wang et al., 2006). Ground conditions are quite different for the Parkway Valley and UPSAR arrays. Referring to Chávez-García et al. (1999) and to Wang et al. (2006), respectively, for more details, it is sufficient to recall here that Parkway Valley is a small basin, 30 to 40 m deep, filled with layers of mixed mud, gravels, and sands with V_s varying from ~ 150 to ~ 350 m/s, overlying a stiff conglomerate formation, while the UPSAR array is located on stiffer soils, possibly characterized by moderate topography effects (34 m elevation difference between the lowest and the highest station; geological structures fairly uniform and horizontally layered; $V_s \sim 400$ m/s at surface).

A summary of the earthquake records considered is provided in Table 18.1.

For the UPSAR array, the spacing between adjacent stations is less favorable than for Parkway Valley, as it ranges from few tens of meters up to few hundreds of meters. However, considering the rule of thumb of a 90% accuracy in the evaluation of strains if the separation distance Δ among adjacent stations is less than 1/4 of the dominant wavelength (Bodin et al., 1997), an apparent wave propagation velocity at the site $V_{app} = 2.5$ km/s (Fletcher et al., 2006) and a representative value $\Delta = 250$ m, it can be deduced that the displacement wavefield can be reconstructed with a sufficient degree of accuracy up to $f = V_{app}/4\Delta = 2.5$ Hz. A more accurate determination, not reported here for brevity, suggests that the average error in terms of *PGV* predicted by the interpolation procedure ranges between 18% and 34% for both arrays. A similar level of error can be indirectly inferred also for *PGS*, due to its strong correlation with *PGV*.

The spatial interpolation of the displacement wavefield at ground surface allows one to obtain some interesting features of the strain field, such as:

- the principal strains and principal directions and their possible correlation with the prevailing wave propagation direction;
- the variation with azimuth of the strain tensor components and of their correlation with the representative parameters of ground motion severity, such as *PGV*.

Table 18.1. List of earthquakes considered for experimental evaluation of ground strains. Peak values are calculated as the maximum absolute value of the horizontal components, among all stations

Earthquake	M_w	Epicentral distance (km)	No. of available records	<i>PGA</i> (cm/s ²)	<i>PGV</i> (cm/s)	<i>PGD</i> (cm)
Parkway 1	4.9	81	17	10.7	0.53	0.037
Parkway 2	4.2	81	17	0.8	0.04	0.003
Parkfield	6.0	11.6	11	487.1	25.40	4.27
San Simeon	6.5	55	11	238.0	16.55	5.71

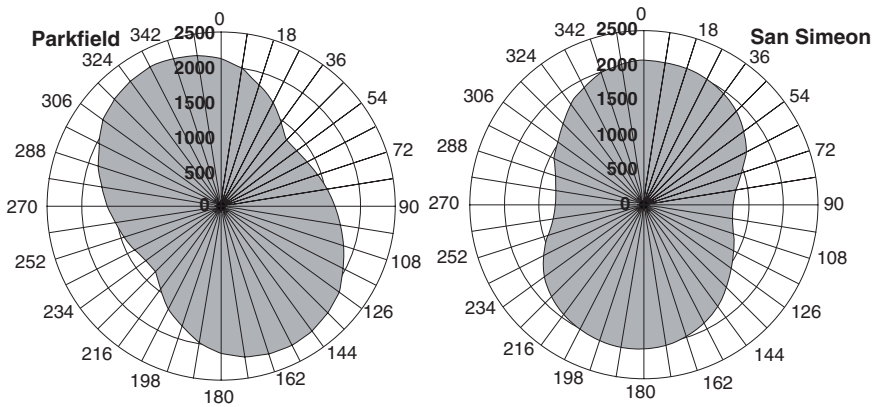


Fig. 18.1. Dependence on azimuth of the $PGV/PGSa$ ratio, as determined from the observed $PGSa$ – PGV least-squares best-fit lines along the directions defined in the radar plot. Adapted from Paolucci and Smerzini (2007)

Note that, since strains are calculated at the ground surface, the shear components in the vertical plane are supposed to be either vanishing or negligible, and attention will be focused only on the axial components of strain ($PGSa$).

Referring to Paolucci and Smerzini (2007) for more details, we introduce here a selection of some representative results useful for applications. First, in Figure 18.1 the variation with azimuth of the C values of the correlation (1) between $PGSa$ and PGV , considering $\kappa = 1$, is shown for two of the earthquakes in Table 18.1.

To obtain these plots, the strain and velocity components along a prescribed direction have been evaluated at each station of the array: C is then calculated as the inverse of the slope of the least-squares best-fit line connecting the $PGSa$ and PGV pairs along that direction. It is interesting to note that the variation with azimuth of C is moderate, ranging typically from about 1200 to 2300 m/s.

A further interesting result is illustrated in Figure 18.2, where the peak value of the largest principal strain as a function of the largest absolute value of ground velocity is shown for each earthquake and each station of the array. This selection of $PGSa$ and PGV has been chosen to make these parameters invariant with respect to the reference system, and, as a consequence, to the specific direction selected.

The notable feature of Figure 18.2 is that all data tend to be aligned, with a relatively small dispersion and irrespective of the earthquake magnitude, distance, site conditions or prevailing wave type, along a line with equation

$$\begin{aligned} \log_{10} PGSa &= \alpha \log_{10} PGV - \beta, \text{ i.e.} \\ PGSa &= PGV^\alpha / 10^\beta \end{aligned} \tag{18.2}$$

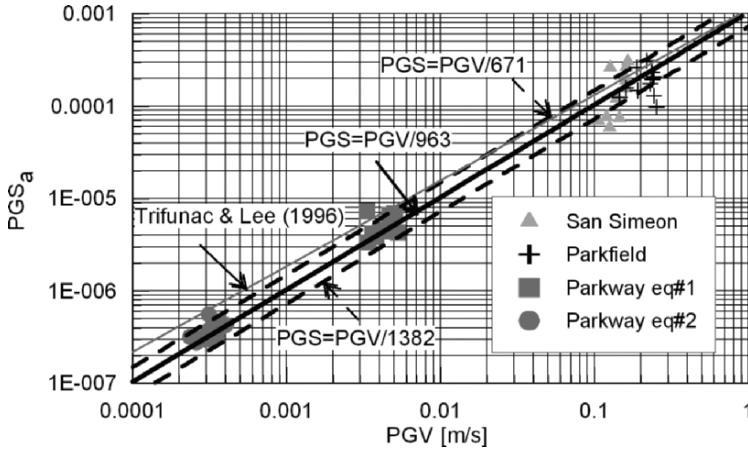


Fig. 18.2. Correlation of observed PGS_a - PGV pairs for the four earthquakes listed in Table 18.1. To make the selected parameters independent of the reference system, PGV is the peak absolute value of velocity, while PGS_a is the peak principal strain. Superimposed is the curve obtained by eq. (1a) of Trifunac and Lee (1996), considering $V_s = 400$ m/s and epicentral distance $D = 20$ km.

where $\alpha = 0.955$ and $\beta = 3.07$, and PGV is in m/s. If the parameter α is forced to be unity, the best fit line turns out to be

$$PGS_a = PGV / \psi \tag{18.3}$$

where $\psi = 963$ m/s is the median value, while 671 m/s and 1382 m/s correspond to the 16° and 84° percentile, respectively.

As shown in Figure 18.2, a good agreement is found with the relationship proposed by Trifunac and Lee (1996), based on a large set of artificially generated synthetic time histories for different soil conditions, who also found a weak dependence of the PGS - PGV relationship on earthquake magnitude, epicentral distance and local site conditions.

These results suggest that the interpretation of ψ in eq. (18.3) as the horizontal wave propagation velocity of the prevailing wave type (either apparent velocity of body waves or phase velocity of surface waves) may be misleading. For example, the value of ψ deduced for the Parkfield event is about 2.5 times smaller than the apparent wave propagation velocity estimated at the UPSAR site by spatial cross-correlation analyses (Fletcher et al., 2006). Similarly, Bodin et al. (1997) deduced a ψ value from a microarray in Mexico City three times smaller than the prevailing phase velocity of surface waves.

Indeed, wave passage is only one of the factors affecting the spatial variation of ground motion, the other ones being coherency and site effects. Abrahamson (2003) has recently proposed a model for transient ground strain evaluation, where the relative contributions of wave passage (*WP*), spatial incoherence (*SI*) and site effects (*SE*) are made explicit and summed in an empirical relationship between *PGS* and *PGD*:

$$PGS/PGD = WP + SI + SE \tag{18.4}$$

where $WP = \exp(5.8 - 0.69M)/C$, $SI = 3 \cdot 10^{-5}$, $SE = 3 \cdot 10^{-5}$ and *PGD* is measured in centimeters. Considering $C = 2 \text{ km/s} = 2 \cdot 10^5 \text{ cm/s}$, it turns out that the *SI* contribution to transient ground strains is more relevant than the *WP* one for $M > 5.8$. It is also interesting to note that there is a remarkable agreement of eq. (18.4) with the present data. In Figure 18.3, the *PGS*–*PGD* pairs for the four datasets considered are reported and compared with the corresponding predictions obtained using eq. (18.4), where $SE = 0$ for the UPSAR and $SE = 3 \cdot 10^{-5}$ for Parkway, due to different ground conditions. All predictions lie close to ground strains obtained by spatial interpolation.

Although both eqs. (18.3) and (18.4) deserve further investigations and improvements, they strongly highlight the need to corroborate by experimental observations the current, probably too simplistic and under conservative approach for transient ground strain evaluation, synthesized by eq. (18.1).

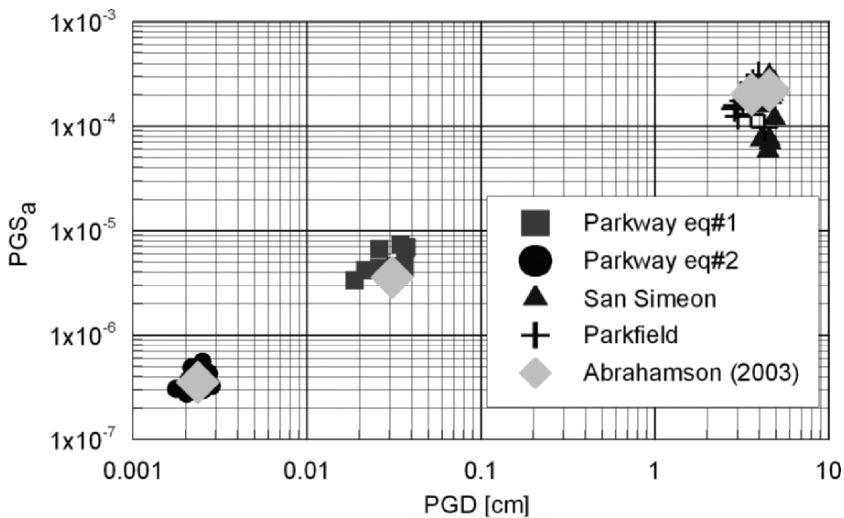


Fig. 18.3. *PGS*–*PGD* pairs for the four earthquakes listed in Table 18.1. The symbols corresponding to the Abrahamson (2003) relationship are plotted using the average *PGD* observed for each earthquake and the corresponding magnitude. From Paolucci and Smerzini (2007)

2.2. EVALUATION OF PGS IN THE PRESENCE OF STRONG LATERAL HETEROGENEITIES

Damage to buried structures is often concentrated in areas with variable subsurface conditions and non-uniform ground properties in horizontal direction. This was observed for instance after the 1994 Northridge (Trifunac and Todorovska, 1997) and the 1995 Kobe earthquakes (Takada et al., 2002) in regions characterized by strong lateral discontinuities, as an inclined ground surface or an inclined soil–bedrock interface. These situations, where the correlation between PGS and PGV is typically worse than in cases where the soil profile consists of horizontal layers, are not taken into account by the simple solutions for ground strain evaluation, such as eq. (18.1) or eq. (18.3).

The first studies of the PGS – PGV dependence in the presence of strong lateral variation of soil properties are reported by O’Rourke and Liu (1999). More recent investigations have been performed by Scandella and Paolucci (2006), through a set of parametric analyses by 2D in-plane numerical simulations of seismic wave propagation by a spectral element code (Faccioli et al., 1997; Stupazzini, 2004). Results shown in the following refer to the horizontal strain, calculated at ground surface ($PGSa$). A typical example of numerical results is shown in Figure 18.4, where it is clear that $PGSa$ and PGV occur at the same spatial location (x denotes distance from the basin edge) only for low values of the dipping angle ($\alpha < 10^\circ$), while the larger is the dip angle the larger is the spatial distance between points where the maximum value of either $PGSa$ or PGV occurs.

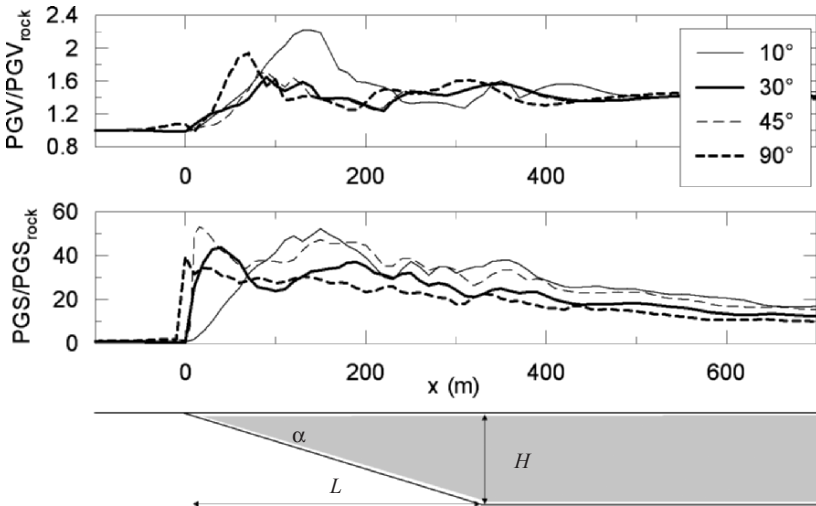


Fig. 18.4. A simplified open basin model, separated laterally by the bedrock by a dipping edge with angle α , for a parametric numerical study of the $PGSa$ – PGV relationship in the presence of strong lateral discontinuities. Adapted from Scandella and Paolucci (2006)

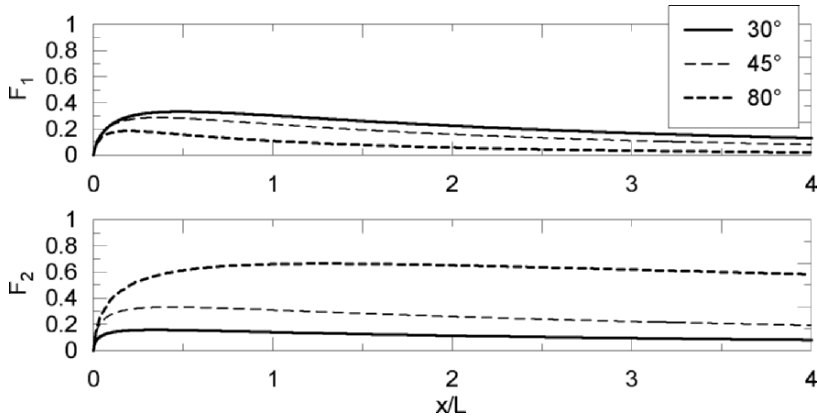


Fig. 18.5. Functions F_1 and F_2 in eq. (18.4) calibrated on 2D in-plane numerical analyses. From Scandella and Paolucci (2006)

Based on such parametric analyses, an empirical relationship fitting the numerical results was found, which takes the form

$$PGS_a = \frac{1 - \eta}{1 + \eta} \frac{PGV}{V_s} [F_1(x/L, \alpha) + F_2(x/\bar{H}, \alpha)] \quad (18.5)$$

where V_s is the shear wave velocity of the (homogeneous) basin, η is the soil–bedrock impedance ratio ($\eta < 1$) and the two functions F_1 and F_2 depend on the dip angle α , the normalized position x/L of the site with respect to the basin-edge contact; the geometrical meaning of L and $\bar{H} = L \tan \alpha$ is clear from Figure 18.4. The exact expressions of F_1 and F_2 are reported in Scandella and Paolucci (2006), while their variation as a function of the non-dimensional variable x/L is plotted in Figure 18.5. Note that in eq. (18.5) PGS_a and PGV are both measured at ground surface in the horizontal direction, so that the equation should in principle be applied to shallow buried pipelines. Furthermore, eq. (18.5) is based on vertically incident plane S-waves, while more general incidence angles or wave types are not included. However, the numerical analysis of seismic wave propagation in almost near field conditions shown in the sequel for the Düzce case suggests that a good approximation is also achieved by eq. (18.5) also in this case.

Numerous examples of independent validations of eq. (18.5) based on numerical simulations of the seismic response of real geological cross-sections can be found in Lessloss (2006). Here we will summarize the numerical work carried out for transient ground strain calculations in Düzce, Turkey, that was hit by two major earthquakes on August 17 (M_w 7.4) and Nov. 12, 1999 (M_w 7.1), the latter one originated by a fault rupture at about 10 km distance from the town. Leaving to the following sections the details on the damage survey and the risk assessment of the water pipeline system, we show here some of the results obtained by a numerical simulation of ground motion in Düzce, involving

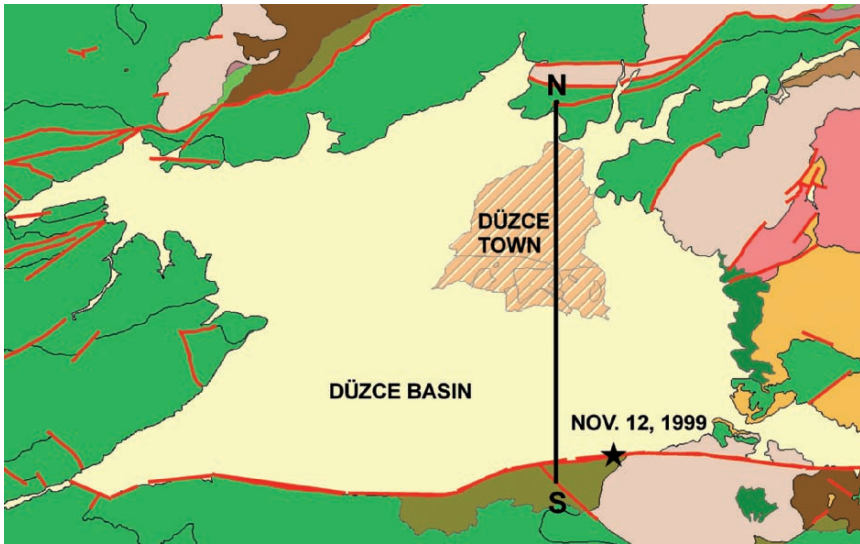


Fig. 18.6. Geological map of the Düzce basin and surrounding area, including the epicenter of the Nov. 12 1999 earthquake and the trace of the NS cross-section considered in this study

the coupled analysis of the effects induced by the seismic source, the propagation path, and the geological site conditions at ground surface. As shown in Figure 18.6, the Düzce basin extends north of the right-lateral strike-slip fault, a major northern strand of the North Anatolian Fault, which ruptured during the Nov. 12 earthquake.

The seismic response of a NS cross-section of the basin, passing through the center of the town, was analyzed. To reduce the computational effort required by accounting for the simultaneous effects of the seismic wave propagation from the Düzce fault rupture and of the sedimentary basin where the town is located, the Domain Reduction Method (DRM), devised by Bielak et al. (2003), was adopted. This is a rigorous method for subcontracting the analysis into two coupled steps, as shown in Figure 18.7. In the first step, a 3D analysis of the seismic wave propagation from the source into a layered half-space has been carried out using the approach by Hisada and Bielak (2003), while in the second step, the Spectral Element Method (SEM) developed by Faccioli et al. (1997) and implemented in the software GeoELSE (Stupazzini, 2004) has been used to simulate the 2D wave propagation in the region of interest. The DRM implementation in the spectral element code is illustrated by Faccioli et al. (2005) and Stupazzini et al. (2006).

A detailed presentation of the numerical procedure and results, together with a comparison with ground motion recorded at the accelerograph station inside town, can be found in Scandella et al. (2007). We show here only some relevant results for ground strain

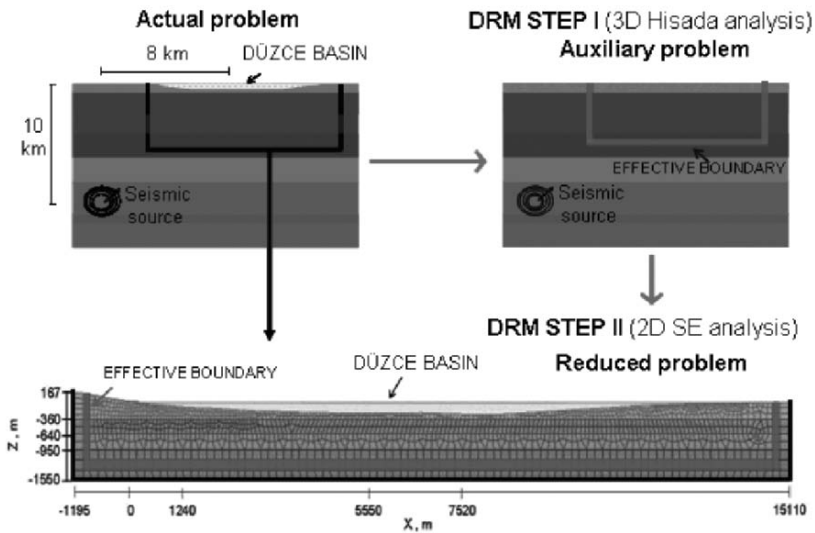


Fig. 18.7. Sketch of the two-step DRM procedure applied to the case of the Düzce. Step I: 3D analysis of the source and the wave propagation in the half-space. Step II: 2D wave propagation in the Düzce basin by means of the Spectral Element Method. From Scandella et al. (2007). S-wave propagation velocities inside the basin range from 300 to 450 m/s, and from 1350 to 2700 m/s inside the bedrock

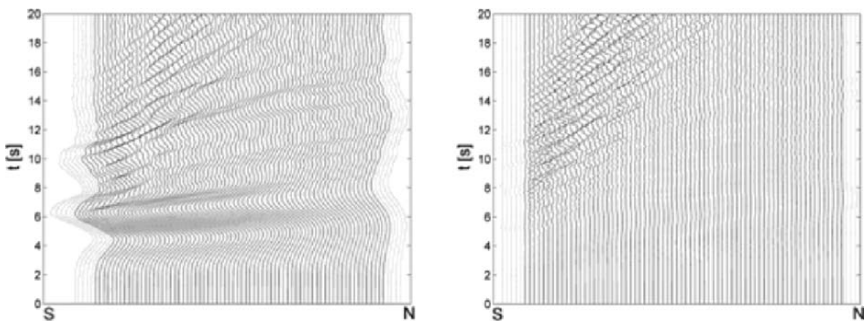


Fig. 18.8. Left: horizontal displacement time histories at the receivers located along the NS cross-section of the Düzce basin. Right: longitudinal strain time histories. Dotted lines refer to points outside the basin. Adapted from Scandella et al. (2007)

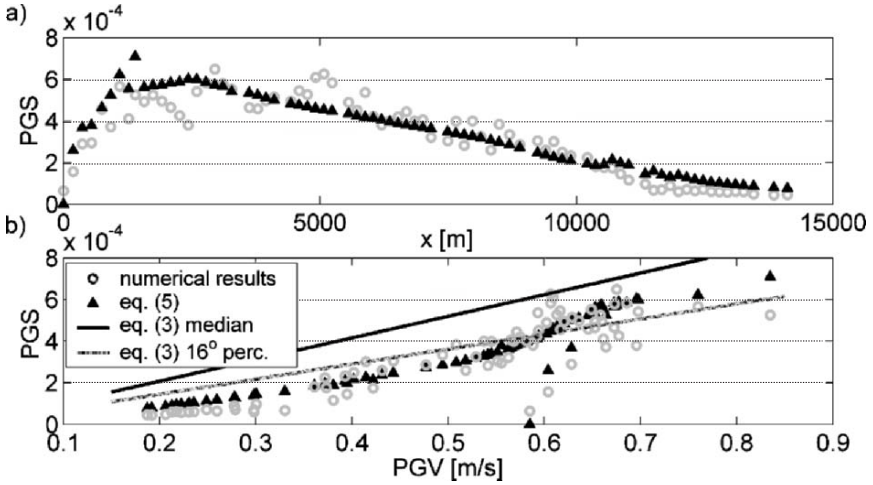


Fig. 18.9. From top to bottom: (a) comparison between the spatial variation of $PGSa$ obtained by numerical simulations (open circles) and by eq. (18.5) (solid triangles); (b) $PGSa$ vs. PGV pairs at ground surface simulated (open circles) and obtained by eq. (18.5) (solid triangles). The line corresponding to eq. (18.3) is also shown for comparison

evaluation. In Figure 18.8, the horizontal displacement time histories simulated at the surface of the Düzce basin are plotted, together with the corresponding horizontal (in-plane) components of ground strain. It is clear that, corresponding to the lateral (South) edge of the basin, surface waves are generated and that the largest horizontal (in-plane) strain components are carried by such waves, while the strains induced by the nearly in-phase S arrivals are much smaller. Furthermore, since PGS is carried in this case by Rayleigh waves, while PGV by S-waves, a straightforward correlation between PGS and PGV such as eqs. (18.1) or eq. (18.3) should be considered with care.

In Figure 18.9 the spatial variation of $PGSa$ along the cross-section is shown, together with the corresponding relationship with the horizontal PGV . Both numerical values and the ones obtained by eq. (18.5) are shown, demonstrating a reasonable agreement. It is worth noting that the values obtained by 2D analyses lie close to the 16th percentile of variability of the experimental results shown in the previous section (eq. 18.3). The underestimation of ground strains with respect to the median value of (3) can likely be attributed to an oversimplified soil model assumed in the numerical calculations, and a consequent excess of spatial coherency of the simulated ground motion with respect to reality. It should also be noticed that linear-elastic behavior of soil was considered in these analyses. Non-linearity should act as a “filter” of strains larger than a certain threshold, depending on soil strength: this effect should be considered in more detail in future studies.

3. Hazard maps and seismic risk assessment of underground pipeline systems

Seismic risk assessment for underground structures has generally been performed based on *PGV* hazard maps, since the corresponding vulnerability functions are usually defined in terms of *PGV* as well (NIBS, 2004). However, the large scatter of such relationships and the close link between earthquake ground deformations and seismic loads in underground structures has suggested replacing *PGV* with *PGS* as the parameter to quantify ground motion severity. In this perspective, O'Rourke and Deyoe (2004) have recently re-examined the available data on damage to pipeline systems and deduced a new relationship between repair rate on the pipeline network and *PGS*. The drawback of this approach is that its application for seismic risk assessment requires production of hazard maps in terms of *PGS*. In the absence of well established approaches to evaluate transient ground strains, or of sound formulas relating *PGS* to other peak parameters of ground motion, *PGS*-based hazard maps are typically obtained in two ways, the alternative approaches involving either a large set of 2D numerical simulations along various azimuths or a fully 3D one being presently too demanding:

- a) by constructing a *PGV* hazard map (either by probabilistic hazard studies or in terms of a scenario earthquake) and transposing it into *PGS* (either axial or shear, see comments in the sequel) through a straightforward division of *PGV* by a suitable measure of the apparent wave propagation velocity;
- b) by performing a large set of 1D wave propagation analyses with the best information available on the local ground properties and a selection of the input motion compatible with the target hazard; these analyses may lead either to a map with the spatial distribution of *PGV*, whence *PGS* can be deduced as at point (a), or they can provide the shear strain at a selected depth (the shear strain at surface being vanishing).

While the main drawback of approach (a) has been extensively discussed in the first part of this paper, approach (b) involving a direct calculation of *PGS* through 1D ground motion simulations, suffers of two major limitations.

Firstly, ground strains obtained by 1D analyses of S-wave propagation are purely of shear nature, with a relatively sharp variation with depth, and they cannot be translated straightforwardly in terms of longitudinal strains. While shear strains (γ) are mostly interesting for seismic design of tunnels in a transversal cross-section, seismic design of pipelines is mainly governed by longitudinal strains (ϵ). As shown in Figure 18.10, referring to the results of 2D numerical simulations of SV wave propagation along two geological cross-sections in Thessaloniki for a M6.5 earthquake, the relationship between peak ground values of γ (*PGSs*) and ϵ (*PGSa*) is very scattered: at around 3 m depth, where most pipelines are embedded, the ratio between *PGSs* and *PGSa* ranges between about 1 and 4, with a mean value around 1.75. At larger depths, as shown in Figure 18.10 for a representative depth of 15 m, this ratio is even higher, as expected for incidence of SV waves. Although further studies are recommended to assess a general relationship between *PGSs* and *PGSa* as a function of depth, earthquake magnitude and site characteristics, the results shown in Figure 18.10 support the use of calculated shear strains for both axial and transversal

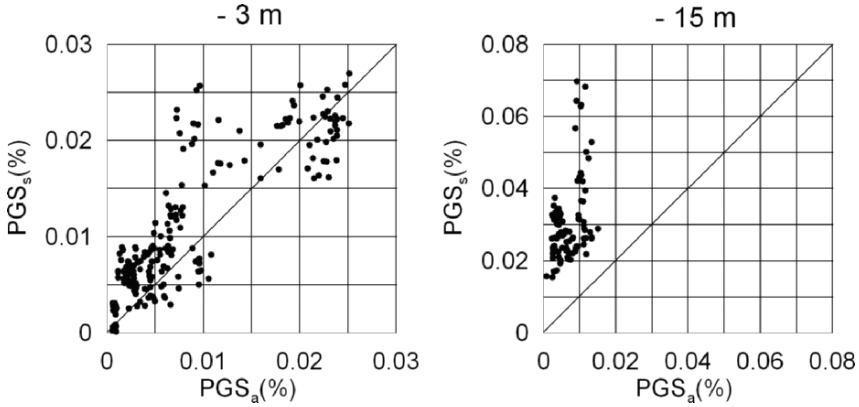


Fig. 18.10. Peak values of shear strain and the corresponding longitudinal (horizontal) strain at 3 m (left) and 15 m (right) depth obtained by 2D numerical simulations of two geological cross-sections in Thessaloniki, subject to in-plane vertical incidence of S-waves. A M6.5 earthquake scenario was considered

ground strain evaluation and pipeline response, at least as a first approximation at shallow depths (<5 m).

As a second drawback of the (b) approach, 1D numerical simulations neglect the effects of lateral variation of soil properties and the onset of surface waves. PGS_s close to the surface deduced from 1D analyses are typically smaller than the PGS_a provided by 2D simulations. An explanation of this result lies in the fact that the 2D results are mostly affected by laterally induced surface waves, since they generally refer to geological cross-sections with important lateral variations of soil properties.

When hazard maps in terms of PGA , PGV , or PGS are available, then the risk assessment of pipeline systems and networks is carried out using appropriate empirical and semi-empirical vulnerability or fragility expressions of expected damages (often in terms of Repair Ratio per kilometer RR/km) with the hazard parameters; usually with the peak ground velocities (eq. 18.6 after O'Rourke and Ayala, 1993) and more recently with the peak ground strains (eq. 18.7 after O'Rourke and Deyoe, 2004). Further information on the seismic risk assessment of lifelines may be found in ALA (2001a,b), NIBS (2004), O'Rourke and Liu (1999), and Pitilakis et al. (2004).

$$RR = 0.0001 \cdot (PGV)^{2.25} \quad (PGV \text{ in cm/s}) \quad (18.6)$$

$$RR = 513 \cdot (PGS)^{0.89} \quad (18.7)$$

The methodology applied herein is summarized in Pitilakis et al. (2004). It comprises two main branches; the evaluation of the spatial variability of ground motion for different seismic scenarios and the description of the lifeline network under consideration (geometry, materials, typology, classification). For each typology a specific fragility curve is proposed. Then, through the combination of the appropriate fragility curves for each

element of different typology and the estimated seismic actions (i.e. ground motion parameters like PGV and PGS), we evaluate the number, the type (i.e. leaks, breaks) and the location of the damages. There are three issues of great importance and equally large difficulty in the risk assessment of lifeline systems as described above. The first one, discussed already in previous paragraphs, is related to the accuracy of estimating the spatial variability, and the characteristics of ground motion (amplitudes, frequency content) in a specific site, for example a city. Local surface geology, 2D and 3D geometry of alluvial deposits and basins, soil characteristics, seismotectonic features, and methods of analysis are among the basic parameters which play a crucial role in the accuracy of estimated ground motions. The application which follows will attempt to illustrate further the difficulties and the complexity of the problem of the selection of the ground motion parameter when it is to be used for the seismic risk assessment of spatially extended systems.

The second problem is the inherent difficulty to know the exact geometry and typology of the lifeline systems, comprising often hundred of kilometers of pipes, constructed in different periods with different materials and procedures. The third major problem is the empirical nature of the fragility curves and the lack of many different well documented studies for different earthquakes and systems around the world. While in Japan and America there are some good data, in Europe there is a tremendous penury of information and usually the available data are not well documented. Among the few exceptions the recent Lefkas earthquake (M_w 6.5, 2003) in the Ionian islands in Greece, which affected seriously the water systems of the city (Alexoudi, 2005). This is the main reason of moderate credibility when using available fragility curves without proper validation and improvement. In this sense it is very important to develop theoretical fragility curves applying sophisticated numerical models.

4. Application examples

The first example presented and discussed herein concerns the seismic risk assessment of the main water system of Düzce (Turkey) seriously damaged during the devastating M_w 7.1 earthquake in 1999, already affected by the previous M_w 7.4 Kocaeli 1999 earthquake. As liquefaction phenomena have not been observed in Düzce, damages are due only to ground shaking. The reported damages, without any distinction between breaks and leaks, are summarized in Figure 18.11 (Tromans, 2004). The documentation is poor and the data are summed per district. Moreover there is no reference to the percentage and the intensity of damages during the previous (only three months before) earthquake of Kocaeli.

The full re-examination of the damage reports few years after the earthquake reveals at least 21 well documented cases, which are described in Figure 18.12 (Pitilakis et al., 2005).

Düzce is located in the center of a large plain (Figure 18.6). The geotechnical conditions are characterized by medium rigidity sands and clays with gravels ($V_s = 300\text{--}450$ m/s) of high thickness. In the center of the city, due to the river crossing, the surface soils (mainly silty sands) are looser with mean V_s of the order of 200–250 m/s. The seismic

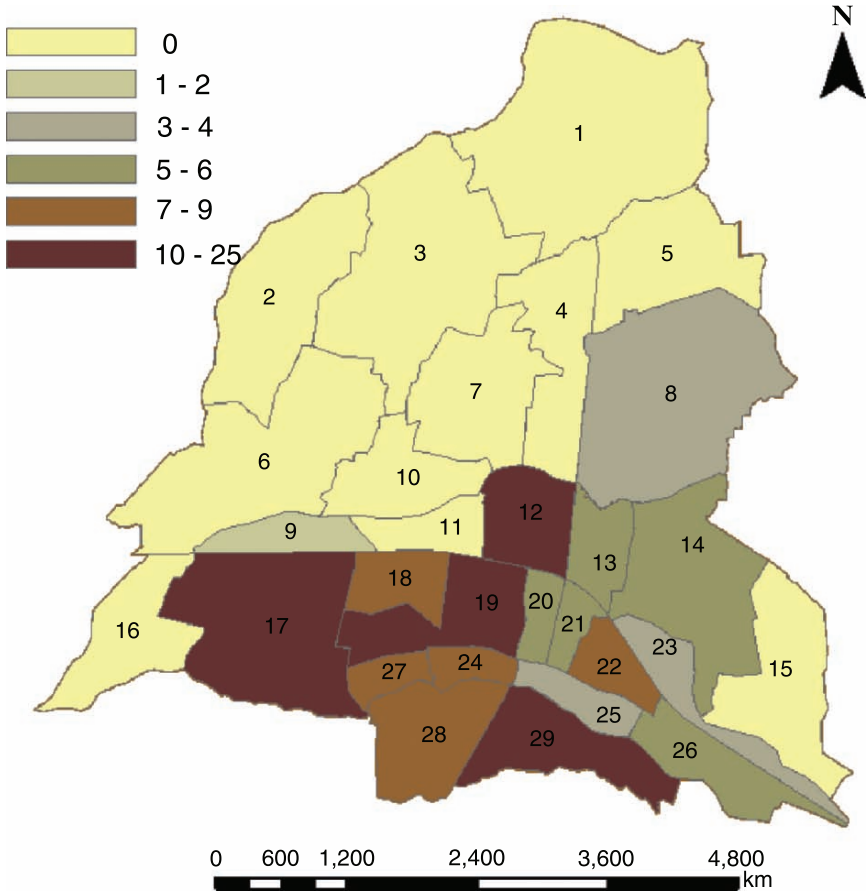


Fig. 18.11. Observed average failures per district of potable water system in Düzce following the Kocaeli–Düzce earthquake sequence: August–November 1999

bedrock is found at about 120–150 m depth. Figures 18.13 and 18.14 present the available geotechnical and geophysical surveys and two typical cross-sections of the city. (Pitilakis et al., 2006, Final report MERP project). The evaluation of the hazard maps of ground motion is carried out using a 1D equivalent linear approach. As input motion at the seismic bedrock, we used the deconvolution of the recorded motion at the Meteorological Station located in the town center.

The computed *PGV* values in Düzce (background in Figure 18.15) are varying from 0.6 to 0.85 m/s depending on local soil conditions. The computed shear strains (*PGSs*) at 2 m depth range from $7.0 \cdot 10^{-5}$ to $2.3 \cdot 10^{-4}$, while the peak values within the top 15 m from $5 \cdot 10^{-4}$ to $2.3 \cdot 10^{-3}$ (Figure 18.16). Accepting an average ratio $PGSs/PGSa \approx 1.75$, based on the results of Figure 18.10, and considering an average *PGSs* (shear strains) in

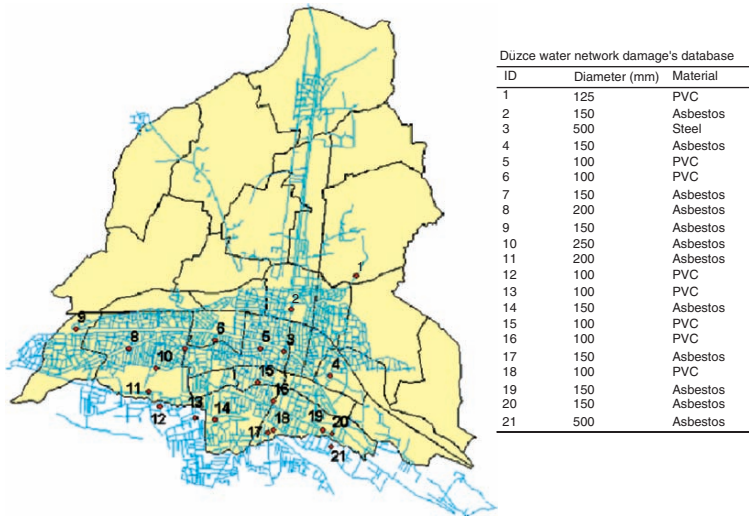


Fig. 18.12. Water mains system of Düzce and documented damages after the Kocaeli and Düzce, 1999 earthquakes (Alexoudi et al., 2007)

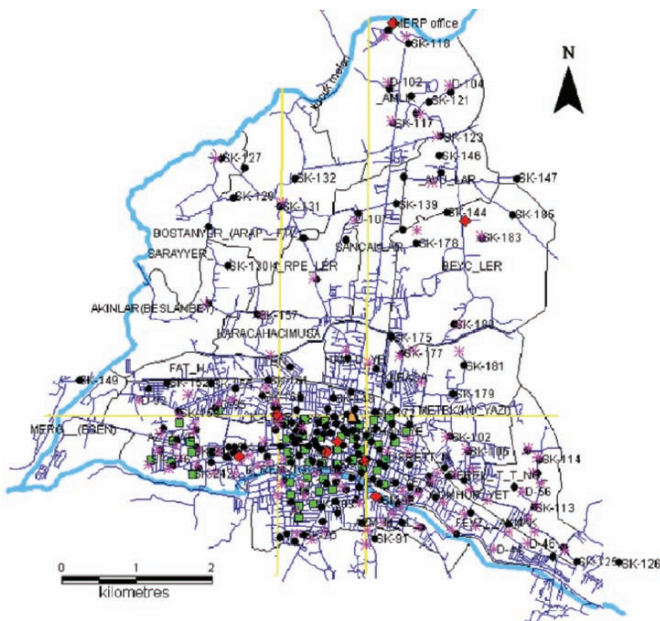


Fig. 18.13. Map of Düzce (Turkey) showing the main water system network, the location of the shallow (circles) and deep (rhombs) geotechnical, geophysical (rhombs), and microtremor (rectangles) surveys and the typical cross-sections NS and EW

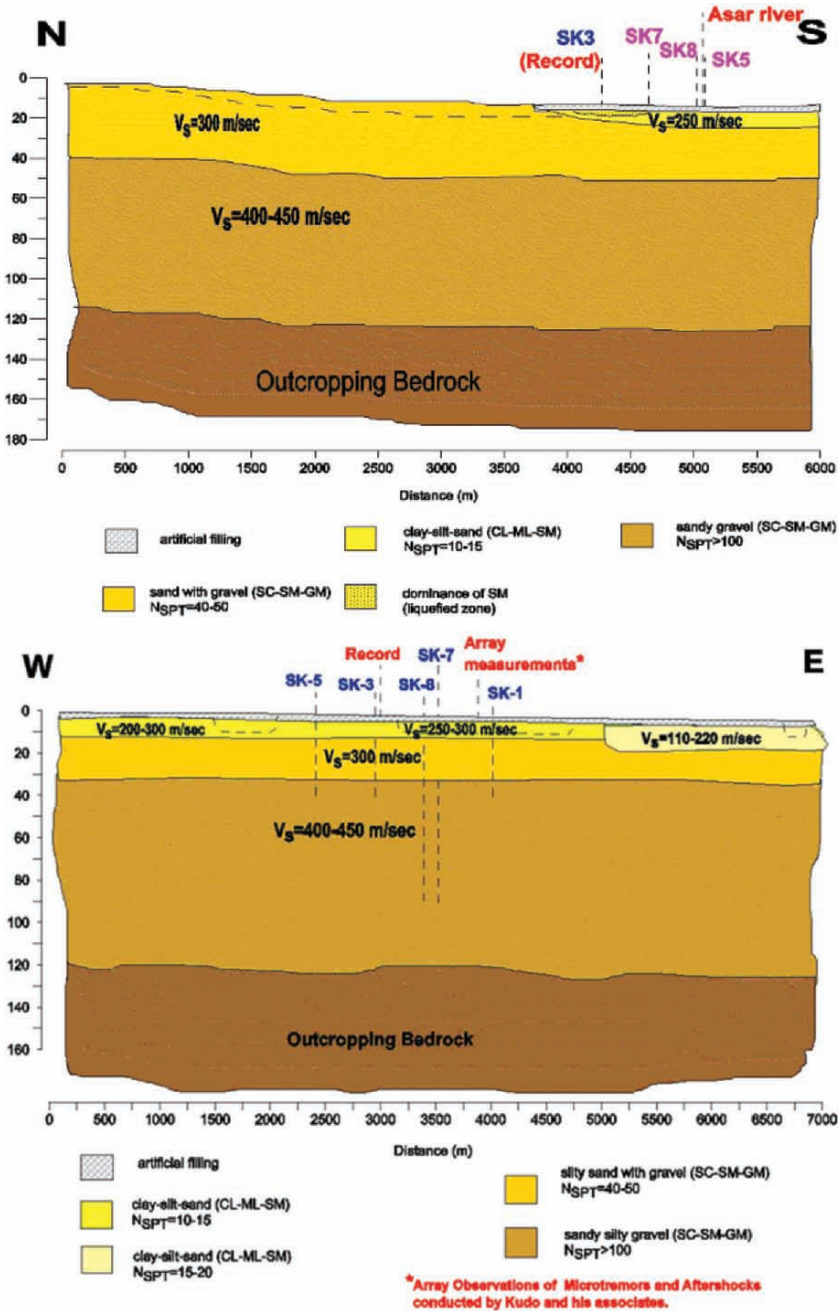


Fig. 18.14. Typical geotechnical cross-sections in Düzce (a) NS and (b) EW

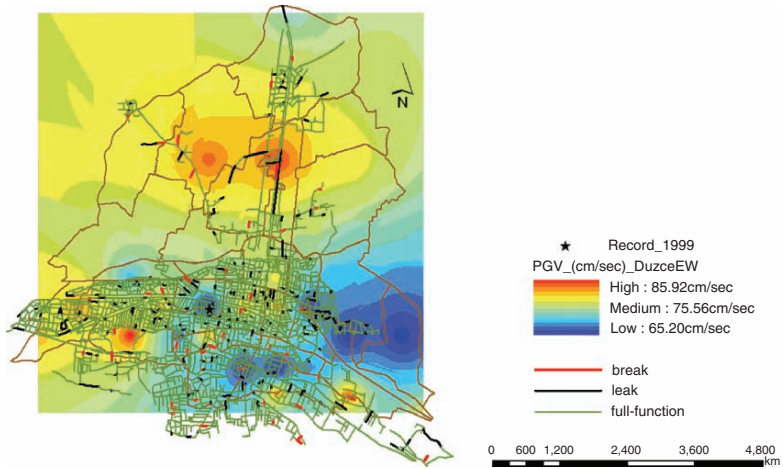


Fig. 18.15. (a) Computed PGV values in Düzce for the M_w 7.1, 1999 event based on 1D-EQL analysis of ground motion. (b) For the same event damage assessment of water mains system (breaks, leaks) applying the PGV approach (O'Rourke and Ayala, 1993)

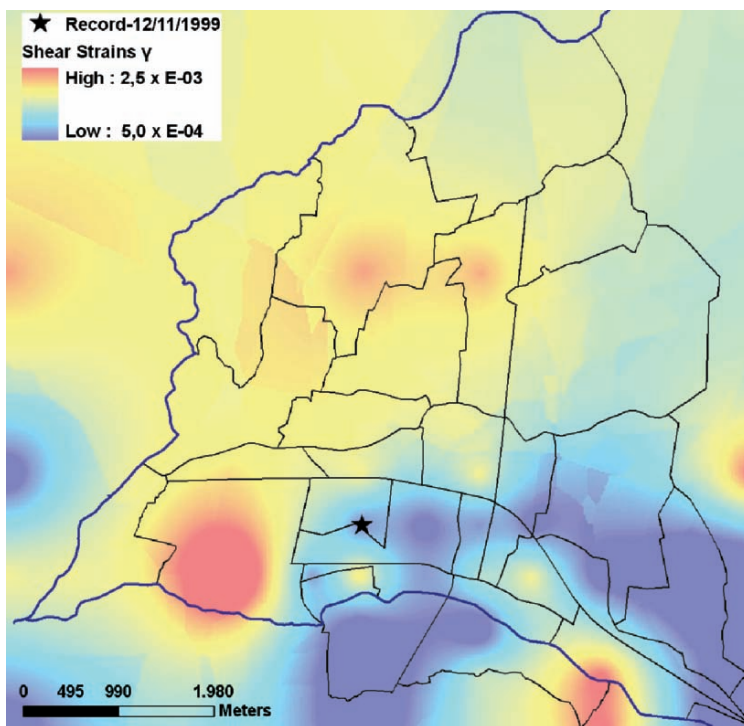


Fig. 18.16. Variation of maximum shear strains $PGSs$ in the top 15 m. Input motion: deconvolution of Düzce Nov. 12, 1999 record, at the Meteorological Station—EW component

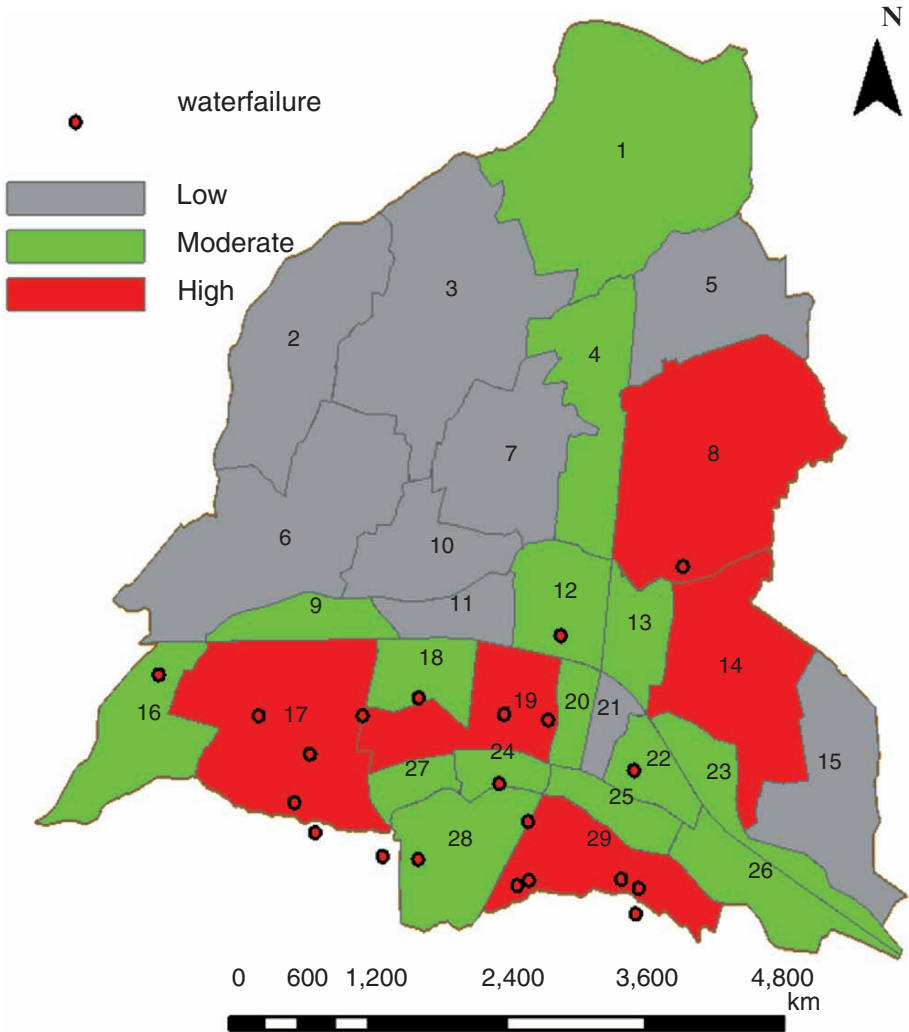


Fig. 18.17. Vulnerability assessment (damage states) of the water mains in Düzce for the M7.1, 1999 earthquake based on the PGV approach. With red dots the post earthquake fully documented pipeline damages

the top loose soil layers of the order of $1.4 \cdot 10^{-3}$, the estimated $PGSa$ (axial strains) are very close to the computed $PGSa$ values with a 2D model (Figure 18.9), as well as to the estimated values based on the $PGSa$ – PGV relationship shown in Figure 18.2, (i.e. $8 \cdot 10^{-4}$ against to $7 \cdot 10^{-4}$). Moreover considering the recorded and the computed values of PGV (Figure 18.15), both ranges of $PGSa$ values are close to the ones suggested by eq. (18.3).

In Figure 18.16 we present the vulnerability assessment of the water systems in Düzce for the strong earthquake that has damaged the city in 1999, using eq. (18.6) based on PGV values. The classification of the damages rate per district is presented in Figure 18.17. In the subsequent Figure 18.18 we present the same synthetic results based on the O'Rourke

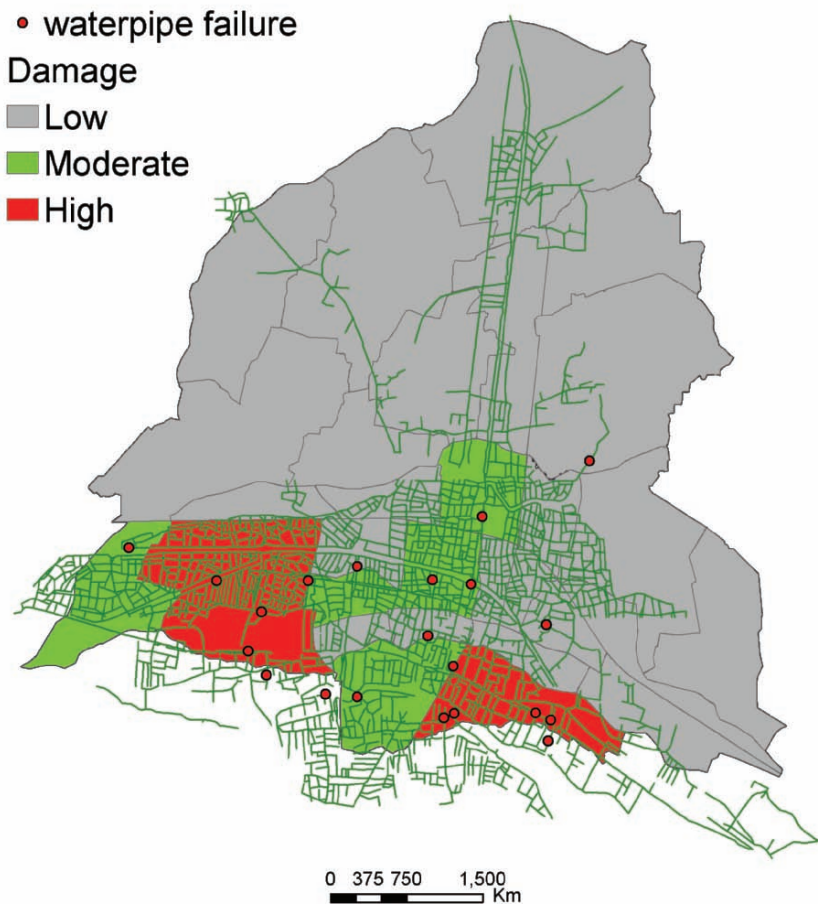


Fig. 18.18. Vulnerability assessment (damage states) of water mains in Düzce for the M7.1,1999 earthquake) based on the PGS approach

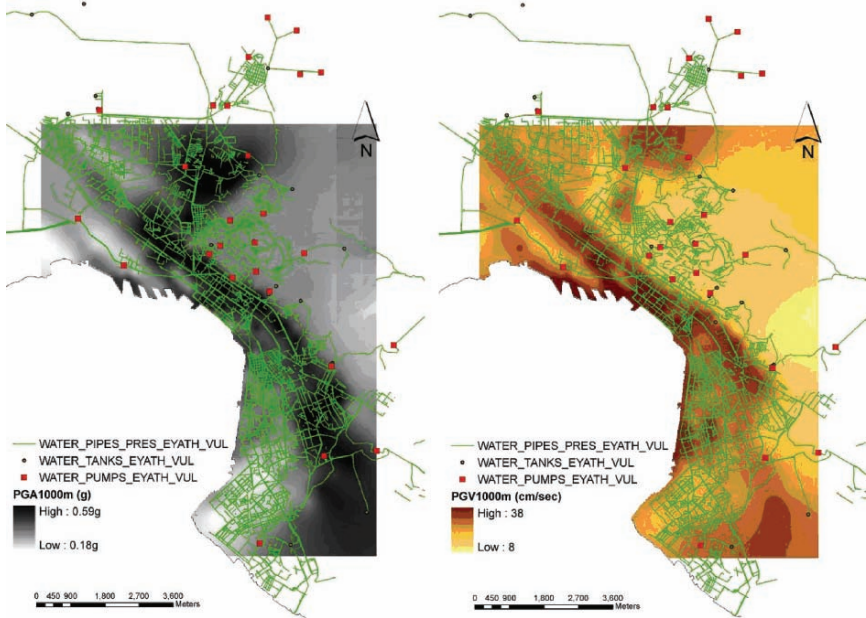


Fig. 18.19. Spatial distribution of *PGA* (left) and *PGV* (right) values in Thessaloniki for the seismic scenario of 1000 years

and Deyoe vulnerability curve (eq. 18.7) and the estimated *PGS* reported in Figure 18.16. The number of failures for the total length of the pipes in each district define the damage state as follows: low: $10 <$, moderate: 10–50, and high > 50 estimated damages per district. The agreement among the approaches is good in certain districts but not for the entire system. Based on the case of Düzce we may conclude that while the methods for specifying and calculating *PGS* are improving, vulnerability curves in terms of *RR/km-PGS* deserve further studies. In general the spatial distribution of damages of the potable water system is reasonably well correlated to the actual observed damages illustrated in Figures 18.11 and 18.12, with the exception of certain districts having limited length of pipes and hence lower probability of having many failures.

The second example of risk assessment of a complex water system comes from Thessaloniki. For the 1000 years scenario (SRMLIFE research project, 2003–2007), Figure 18.19 present the estimated hazard parameters in terms of *PGA* and *PGV* values. To assess the vulnerability and damage rates we applied again the empirical vulnerability relationship of eq. (18.6) for the pipes and appropriate fragility curves for reservoirs and pumping stations (NIBS, 2004). In Figure 18.20 we illustrate the expected damages in the potable water system, consisting of reservoirs, pumping stations, and few hundred of kilometers of pipes.

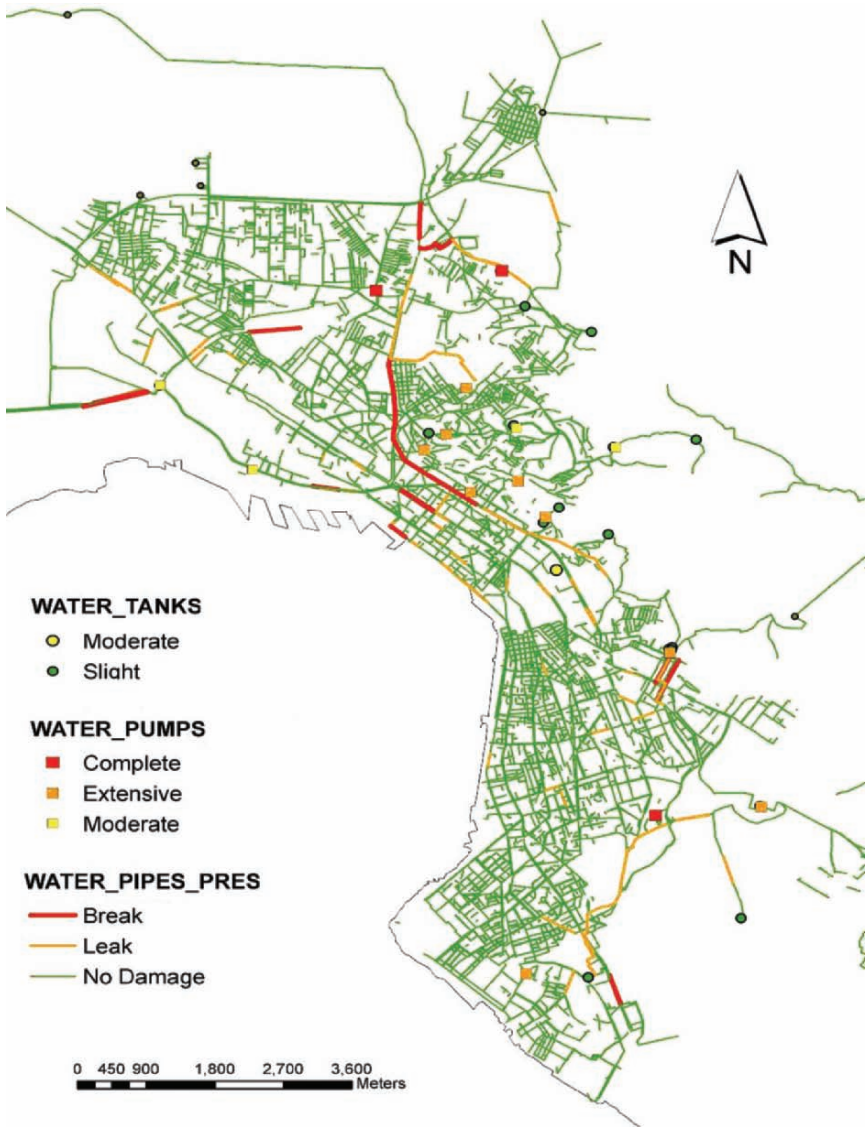


Fig. 18.20. Damages of the water system in Thessaloniki for the 1000 years scenario (Alexoudi et al., 2007)

5. Conclusions

The strategic role of underground structures and buried pipeline networks, and their critical response during strong earthquakes, require more adequate tools for the determination of design loads and to support seismic risk assessment analyses.

In the first part of this paper, we have addressed the recent developments made to derive sound and well established formulas for transient ground strain evaluation as a function of peak parameters of earthquake ground motion. For this purpose, recent transient ground strain evaluations have been introduced, obtained by a suitable spatial interpolation of the displacement wavefield recorded by dense seismic networks during earthquakes with different magnitude and epicentral distance. These data support recent research works on this subject, and highlight that transient ground strains are not only affected by wave passage effects, as generally assumed in formulas for design, but also site effects, especially in terms of lateral variations of soil properties, and spatial incoherency of ground motion. The latter effects play an important role, at least comparable to the wave passage. Further experimental studies on dense seismic arrays and numerical parametric investigations are recommended, especially with reference to: (i) the dependence on azimuth of the peak ground strains, that was found to affect results by at least a factor of two (see Figure 18.1); (ii) the quantification of the ratio between peak values of shear strain vs. axial strain, as a function of magnitude, depth, and ground conditions; (iii) the role of non-linearity in the *PGS*–*PGV* relationships, and that of the spatial incoherency of earthquake ground motion as well.

The previous studies will also provide material for production of more reliable hazard maps in terms of peak ground strains and their application to seismic risk assessment of underground structures: at present, these are affected by a significant degree of uncertainty and limitations, extensively discussed in this paper. In spite of such uncertainties, the seismic risk assessment studies presented in this paper, mainly based on 1D linear equivalent wave propagation analyses, seem to be robust and in good agreement with the results shown in the first part of this paper, at least for peak ground strain evaluations. *PGV* and/or *PGS* based vulnerability curves to estimate the expected damages for buried pipelines, besides their empirical nature, are reasonably accurate when extensive and well focused site effect studies are available and ground conditions and surface geology are also well known. Hazard and risk map resulting from the application of *PGV* and *PGS* values may be used for the risk management of lifeline systems. Vulnerability functions using *PGS* are very promising but they need advanced studies to reduce uncertainties, while the empirical data correlating strains with *RR/km* are still very limited and thus the reliability of the proposed function is rather low for the moment.

Acknowledgments

This work was partially funded by the European Commission within the Lessloss Project (GOCE-CT-2003-505488). The first author (RP) acknowledges funding from the DPC-RELUIS National Research Project No.6 Sub-Project “Costruzioni in sotterraneo—

Gallerie e caverne in roccia”. Authors are grateful to Ezio Faccioli for fruitful comments and discussions throughout the work. The material of figures from 18.1 to 18.10 has been taken from the PhD Thesis of Laura Scandella and the Master Thesis of Chiara Smerzini, whose enthusiastic help has been fundamental for the contribution of the first author of this paper. The contribution by W.R. Stephenson and G.Q. Wang, who kindly provided, respectively, the Parkway Valley and UPSAR data for the San Simeon earthquake, is also gratefully recognized. The second author is grateful to Anastasios Anastasiadis lecturer in AUTH, as well as to Dr Maria Alexoudi and PhD student Dimitra Manou for providing and elaborating data and their substantial help in preparing figures of the second part of the paper. Most of the work presented herein and especially in the second part comes from two research programs, MERP and SRMLIFE funded by EU and GSRT of Greece, respectively.

REFERENCES

- Abrahamson N (2003) Model for strain from transient ground motion. In: Proc. Workshop on the Effect of Earthquake-Induced Transient Ground Surface Deformations on At-Grade Improvements, CUREE. Publication No. EDA-04, curee.org/projects/EDA/docs/CUREE-EDA04.pdf Oakland, CA, USA
- AFPS/AFTES (2001) Guidelines on earthquake design and protection of underground structures, Working group of the French association for seismic engineering (AFPS) and French tunneling association (AFTES), Version 1, May 2001
- Alexoudi M (2005) Contribution to seismic assessment of lifelines in urban areas. Development of holistic methodology for seismic risk. PhD Thesis, Civil Engineer Department, Aristotle University of Thessaloniki, Greece (in Greek)
- Alexoudi M, Anastasiadis A, Pitilakis K (2007) Risk assessment of water systems in earthquake prone areas. In: Proc. 4th Int. Conf. Earthquake Geotechnical Engineering, June 25–28, 2007, Thessaloniki, Greece, Paper No. 1632
- American Lifelines Alliance (2001a) Seismic Fragility Formulations for Water Systems. Part 1—Guideline. Technical report prepared by a public–private partnership between FEMA and ASCE, 104 pp
- American Lifelines Alliance (2001b) Seismic Fragility Formulations for Water Systems. Part 2—Appendices. Technical report prepared by a public–private partnership between FEMA and ASCE, 239 pp
- Bielak J, Loukakis K, Hisada Y, Yoshimura C (2003) Domain reduction method for three-dimensional earthquake modeling in localized regions. Part I: Theory. Bulletin of the Seismological Society of America 93:817–824
- Bodin P, Gomberg J, Singh SK, Santoyo MA (1997) Dynamic deformations of shallow sediments in the Valley of Mexico, part I: Three-dimensional strains and rotations recorded on a seismic array. Bulletin of the Seismological Society of America 87:528–539
- CEN (2006) Eurocode 8—Design of structures for earthquake resistance. Part 4: Silos, tanks and pipelines. prEN 1998-4, Final draft, January 2006, Comité Européen de normalisation, Brussels
- Chávez-García FJ, Stephenson WR, Rodríguez M (1999) Lateral propagation effects observed at Parkway, New Zealand. A case of history to compare 1D versus 2D site effects. Bulletin of the Seismological Society of America 89:718–732
- Faccioli E, Maggio F, Paolucci R, Quarneroni A (1997) 2D and 3D elastic wave propagation by a pseudo-spectral domain decomposition method. Journal of Seismology 1:237–251

- Faccioli E, Vanini M, Paolucci R, Stupazzini M (2005) Comment on “Domain reduction method for three-dimensional earthquake modelling in localized regions, Part I: Theory. *Bulletin of the Seismological Society of America* 95:763–769
- Fletcher JB, Spudich P, Baker LM (2006) Rupture propagation of the 2004 Parkfield, California, earthquake from observations at the UPSAR. *Bulletin of the Seismological Society of America* 96:S129–S142
- Gomberg J, Pavlis G, Bodin P (1999) The Strain in the array is mainly in the plane (waves below 1 Hz). *Bulletin of the Seismological Society of America* 89:1428–1438
- Hashash YMA, Hook JJ, Schmidt B, Yao J (2001) Seismic design and analysis of underground structures. *Tunneling and Underground Space Technology* 16:247–293
- Hisada Y, Bielak J (2003) A theoretical method for computing near fault ground motion in a layered half-spaces considering static offset due to surface faulting, with a physical interpretation of fling step and rupture directivity. *Bulletin of the Seismological Society of America* 93:1154–1168
- Lessloss (2006) Technical report on the evaluation of earthquake ground deformations, with applications to representative geological configurations of selected cities, Lessloss Project Deliverable 87—Risk mitigation for earthquake and landslides integrated project
- National Institute of Building Sciences (NIBS) (2004) Earthquake loss estimation methodology. HAZUS. Technical manuals, FEMA, Washington, D.C.
- Newmark NM (1967) Problems in wave propagation in soil and rocks. In: *Proc. Int. Sym. Wave Propagation and Dynamic Properties of Earth Materials*, Univ. of New Mexico Press, pp 7–26
- O’Rourke MJ, Liu X (1999) Response of buried pipelines subjected to earthquake effects. *Monograph Series MCEER*
- O’Rourke MJ, Deyoe E (2004) Seismic damage to segmented buried pipe. *Earthquake Spectra* 20:1167–1183
- Paolucci R, Smerzini C (2007) Earthquake-induced ground strains from dense seismic networks. Submitted for publication to *Earthquake Spectra*
- Ptilakis K, Alexoudi A, Argyroudis S, Monge O, and Martin C (2004) Chapter 9: Vulnerability assessment of lifelines. C.S. Oliveira, A. Roca, and X. Goula ed. *Assessing and Managing Earthquake Risk. Geo-Scientific and Engineering Knowledge for Earthquake Risk mitigation: Developments, Tools and Techniques*, Springer Publ
- Ptilakis K, Alexoudi M, Kakderi K, Manou D, Batum E, Raptakis D (2005) Vulnerability analysis of water supply systems in strong earthquakes. The case of Lefkas (Greece) and Düzce (Turkey). In: *Int. Sym. Geodynamic of Easter Mediterranean: Active Tectonics of the Aegean*, June 15–18, Istanbul, Turkey
- Ptilakis K et al. (2006) Final Report Marmara Earthquake Rehabilitation Project—An Integrated Intervention for the Rehabilitation of Düzce
- Scandella L, Paolucci R (2006) Earthquake induced peak ground strains in the presence of strong lateral soil heterogeneities. In: *Proc. 1st Europ. Conf. Earthquake Engineering and Seismology*, Geneva, Switzerland, Paper No. 550
- Scandella L, Harmandar E, Faccioli E, Paolucci R, Durukal E, Erdik M (2007) Numerical evaluation of earthquake induced round strains: the case of Düzce. In: *Proc. 4th Int. Conf. Earthquake Geotechnical Engineering*, Thessaloniki, Greece, Paper No. 1214
- Smerzini C, Faccioli E, Paolucci R, Scandella L, Stephenson WR (2006) Surface ground strains evaluated from weak motion records of dense seismograph arrays: the case of Parkway Valley, New Zealand. In: *Proc. 1st Europ. Conf. Earthq. Eng. and Seism.*, Geneva, Paper No. 879
- SRMLIFE (2003–2007) Development of a global methodology for the vulnerability assessment and risk management of lifelines, infrastructures and critical facilities. Application to the

- metropolitan area of Thessaloniki. Research Project, General Secretariat for Research and Technology, Greece
- Stupazzini M (2004) A spectral element approach for 3D dynamic soil–structure interaction problems, Ph.D. Thesis, Politecnico di Milano, Italy
- Stupazzini M, Scandella L, Paolucci R, Vanini M (2006) From the seismic source to the structural response: advanced modelling by the spectral element method. In: Proc. 1st Europ. Conf. Earthq. Eng. and Seism., Geneva, Switzerland, Paper No. 770
- St John CM, Zarah TF (1987) Aseismic design of underground structures. *Tunneling and Underground Space Technology* 2:165–197
- Takada S, Hassani L, Fukuda K (2002) Damage directivity in buried pipelines of Kobe city during the 1995 earthquake. *Journal of Earthquake Engineering* 6:1–15
- Trifunac MD, Lee VW (1996) Peak surface strains during strong earthquake motion. *Soil Dynamics and Earthquake Engineering* 15:311–319
- Trifunac MD, Todorovska MI (1997) Damage distribution during the 1994 Northridge, California, earthquake of 1994: density of pipe breaks and surface strains. *Soil Dynamics and Earthquake Engineering* 16:193–207
- Tromans I (2004) Behavior of buried water supply pipelines in earthquake zones. Ph.D. Thesis, Imperial College, Dept. of Civil and Environmental Engineering, London
- Wang GQ, Tang GQ, Jackson CR, Zhou XY, Lin QL (2006) Strong ground motion observed at the UPSAR during the 2003 M6.5 San Simeon and 2004 M6.0 Parkfield, California, earthquakes. *Bulletin of Seismological Society of America* 96: S159–S182
- Yeh GCK (1974) Seismic analysis of slender buried beams. *Bulletin Seismological Society of America* 64:1551–1562
- Zerva A (1992) Spatial incoherence effects on seismic ground strains. *Probabilistic Engineering Mechanics* 7:217–226
- Zerva A (2003) Transient ground strains: estimation, modeling and simulation. In: Proc. Workshop on the Effect of Earthquake-Induced Transient Ground Surface Deformations on At-Grade Improvements, CUREE Publication No. EDA-04, curee.org/projects/EDA/docs/CUREE-EDA04.pdf Oakland, CA, USA

CHAPTER 19

ISSUES IN SEISMIC RISK ASSESSMENT OF TRANSPORTATION NETWORKS

Anne S. Kiremidjian, Evangelos Stergiou, and Renee Lee

Stanford University, Department of Civil and Environmental Engineering, Terman 238, Stanford, CA 94305-4020, USA

Tel: 650-723-4164

Fax: 650-723-7514

ask@stanford.edu

Abstract. Seismic risk assessment of transportation networks has been the subject of several studies over the past two decades. Many advances have been made during this time, however, numerous issues remain. Recent research addressing some of these issues has demonstrated their importance for rational decision making. In this paper an overview is presented of the most commonly used transportation network risk assessment methodology. Important issues that have received limited attention over the years are identified and recent developments to address these issues are presented. The paper draws on research conducted under the Pacific Earthquake Engineering Center with many contributors (Moore et al., 2005; Fan and Nie, 2006; Kiremidjian et al., 2003; Lee and Kiremidjian 2006; Stergiou and Kiremidjian, 2006).

Formulations for network functionality loss under a scenario event and for a suite of possible earthquakes that can affect the system are developed first. It is shown that functionality loss is not only an important part of the risk assessment, but is of the same order of magnitude and in some cases is greatly exceeded than the loss from direct physical damage to network components. Liquefaction appears to be the most important hazard in the loss computation for such systems; however, more robust models are needed to determine the degree to which liquefaction dominates the risk. Correlation of ground motion between bridge sites and correlation of damage between bridges with comparable designs are often ignored in transportation risk analysis. It is again demonstrated that these correlations are important contributors to the uncertainty of loss. When the risk from all earthquakes events is considered, network functionality analysis becomes computationally intractable. A simple method based on Monte Carlo simulation with importance sampling is presented for that purpose. The various conclusions are illustrated through an application to a sample network within the San Francisco Bay region.

1. Introduction

The 1989 Loma Prieta earthquake closed 142 roads in the San Francisco Bay Area, several of which remained closed for more than six months. Five years later, the 1994 Northridge earthquake caused approximately the same number of closures. More than a dozen remained closed for several months after that event as well. A study by ABAG (1997) reports that if the Peninsula segment of the San Andreas Fault ruptures an estimated 428 roads may be closed. In the same study a rupture on the northern segment of the Hayward Fault would result in nearly 900 roadway closures. In the worst case

scenario, a rupture along the entire length of the Hayward Fault would close almost 1500 streets and highways (ABAG 1997). While the ABAG study provides information on street and bridge closures, it falls short of estimating the economic consequences for these closures. Large number of closures that do not have a significant economic impact would not be as critical as fewer closures with a great economic impact.

In order to systematically evaluate the earthquake risk to transportation systems, it is necessary to develop a methodology that includes the direct loss from damage to network components and the loss from limited functionality of the network system. Several recent studies have investigated the losses from failures of transportation networks. For example, Basoz and Kiremidjian (1996) compute the risk of a transportation network after an earthquake event for emergency planning purposes. Shinozuka (2000) studied the performance of the highway network in the Los Angeles area after the 1994 Northridge earthquake and developed a probabilistic framework to predict the effect of bridge repairs after the event. In another study for the same area, Shinozuka et al. (2003) used Monte Carlo simulation to estimate the damage of bridges and its consequences to the performance of the transportation network. Kiremidjian et al. (2006) assessed the damage of the Bay Area transportation network bridges after four low probability but high consequence earthquake scenarios in the Bay Area and estimated the network delays for fixed and variable post-event trip demand. The same study addressed the problem of post-event emergency response planning and presented an example application for six hospitals located in the East Bay. Moore et al., (2005) explored the economic impact of electric power loss in the Los Angeles and Orange County area on the transportation network and the local economy. Cho et al. (2003) studied the transportation network post-event performance for variable demand and estimated the losses based on the total delays after the event.

The Federal Emergency Management Agency developed Hazards U.S. (HAZUS), a software for risk mitigation and planning. The methodologies in HAZUS (1999) estimate the structural and the downtime losses after natural disasters; however, these methodologies do not have capabilities for network analysis of lifeline systems including transportation systems. Until recently, very few software tools were available for the risk assessment of network systems. In an effort to overcome the lack of tools, the California Department of Transportation is developing software for Risks from Earthquake Damage to Roadway Systems (REDARS). REDARS is a seismic risk analysis software package that estimates the structural and operational losses of transportation network systems and is expected to enable the California Department of Transportation (Caltrans) to improve its ability to plan for and respond to earthquake emergencies.

In all previous studies, the risk to the transportation system is assessed under the assumption that the ground motion and damage to bridges in the network are uncorrelated. Similarly, the risk is computed either for specific scenario events or through Monte Carlo simulation with many of the uncertainties in model parameters ignored. Consideration of the correlation and other parameter uncertainties poses a significant computational challenge when the risk assessment includes network analysis.

In this paper, the general formulation for risk assessment of transportation system that considers the uncertainty of the various parameters is presented. A method for including the correlations of ground motion and bridge damage is described based on recent developments by Lee and Kiremidjian (2006) and efficient methods for computation of the risk function with the various uncertainties is discussed. The various methods are illustrated through applications to sub-networks of the transportation systems of the San Francisco Bay Area. Estimates of the direct losses and functionality losses are obtained for the study region and the contribution of each type of loss is quantified to determine its importance.

2. Overview of transportation risk assessment

The performance of transportation networks when subjected to earthquakes is highly dependent on the performance of their components. These components are subject to different ground motions and ground deformations that cause various levels of damage. It is the goal of this paper to present a formulation for seismic risk analysis not only due to structural loss, but also, due to post-event network disruption, both expressed in monetary units.

There are three main components in the risk formulation presented in this paper. The first part consists of the estimation of the structural damage and risk analysis at the component level (bridges). In the second part we compute network functionality loss. In the last part, we aggregate the losses due to structural damage and network disruption in order to define the total loss.

2.1. COMPONENT RISK ANALYSIS

Probabilistic methods are particularly suitable for risk assessment and have been used extensively for that purpose. The results presented in this paper draw on the methodology proposed by the Pacific Earthquake Engineering Research Center (PEER). The PEER equation is given as follows:

$$P [DV > dv] = \iiint dF_{DV|DM} dF_{DM|EDP} dF_{EDP|IM} dF_{IM} \quad (19.1)$$

where

DV is the decision variable

DM is the damage measure

EDP is the engineering demand parameter

IM is the intensity measure

F is the cumulative distribution of the random variable

In Equation 19.1 the Markovian assumption is made when evaluating the various components of the integral, i.e. the dependence among variables is carried only to the previous

variable. This assumption significantly simplifies the analysis. Nevertheless, eq. (19.1) can be computationally challenging especially if many structures need to be evaluated.

IM in eq. (19.1) can either be a single variable or a vector of variables. It can represent ground motion at the site of a network component or ground deformation measure. The most commonly used ground motion IM s are peak ground acceleration and spectral acceleration. Ground deformation IM s represent amount of lateral spreading and/or settlement at a site. IM s are obtained through conventional probabilistic seismic hazard analysis expressed as the annual probability of exceedence of the IM at a location. To account for ground motion and ground deformation, the following formulation is developed (Kiremidjian et al., 2006):

$$\begin{aligned}
 P[DV \geq dv] = & I_A \iiint\limits_A dF_{DV|DM} dF_{DM|EDP} dF_{EDP|IM} dF_{IM} \\
 & + I_L \iiint\limits_L dF_{DV|DM} dF_{DM|EDP} dF_{EDP|IM=S_H} dF_{IM=S_H} \\
 & + I_L \iiint\limits_L dF_{DV|DM} dF_{DM|EDP} dF_{EDP|IM=S_V} dF_{IM=S_V}
 \end{aligned} \tag{19.2}$$

where

$$I_A = \begin{cases} 1 & \text{if there is no liquefaction, or landslide, or fault rupture at a site} \\ 0 & \text{if there is liquefaction or landslide or fault rupture at a site} \end{cases} \tag{19.3}$$

$$I_L = \begin{cases} 1 & \text{if there is liquefaction or landslides or fault rupture at a site} \\ 0 & \text{if there is no liquefaction or landslide or fault rupture at a site} \end{cases} \tag{19.4}$$

A = ground motion severity

S_H = horizontal ground displacement due to either liquefaction or landslides or to differential fault displacement

S_V = vertical ground displacement due to either liquefaction or landslides or differential fault displacement.

It is assumed in this formulation that either liquefaction, or landslides, or differential fault displacement from fault rupture occur at a site but none simultaneously. Similarly, if there is either liquefaction or landslide or fault displacement, they govern the damage and any damage due to ground shaking alone is considered to be already included in the ground deformation analysis.

Given the IM , the engineering demand parameter (EDP) is evaluated in terms of structural response measures such as deformations, accelerations, induced forces, or other appropriate quantities. Relationships between EDP and IM are obtained through inelastic simulations, implementing structural, geotechnical, and non-structural damage models. The EDP s are then related to Damage Measures (DM), which describe the physical damage. The DM s include descriptions of damage to structural elements, non-structural elements, and contents, in order to quantify the necessary repairs along with functional or life safety

implications of the damage. Specifically for bridges, DM describes the damage to their structural elements or the structural system. The final step in the assessment is to calculate the decision variables (DV) in terms of mean annual probabilities of exceedance, $v(DV)$. In general, the DV s relate to one of the three decision metrics that include, direct dollar losses, downtime (or restoration time), and casualties. The DV s are determined by integrating the conditional probabilities of DV given DM , $p[DV=dv|DM]$, with the mean annual DM probability of exceedance, $v[DM]$.

2.2. TRANSPORTATION NETWORK RISK ASSESSMENT

The PEER methodology is limited to estimating the risk to components of the system. In this section we present the network risk estimation method. Damage to the components of the network often results in the closure of specific links until these components are repaired. This action increases the level of congestion and travel time or reduces the number of trips taken. Trip reduction is very difficult to predict, however, logical estimates can be made given the socio-economic profile of the area of study.

The increase in travel time can be found with respect to a baseline scenario. Travel time delay, however, is highly correlated to the number of trips which are lost. The problem of the risk assessment of a transportation network becomes more complex under this approach, since the indirect loss has two components, the cost of the delays and the cost of the lost trips.

In order to develop a network risk assessment model, it is necessary first to formulate a *traffic assignment model*. A *traffic assignment model* allocates the traffic within the components of the network based on the supply and the demand for trips. The results of such an analysis are the flow and the time needed to travel through each component.

There are several traffic assignment models, however, the most popular models are the fixed and the variable demand assignment. The formulation for these two models was developed by Moore and Fan (2003) and is summarized in the Highway Demonstration Project (Kiremidjian et al., 2006). The reader is referred to these reports for further detail. We briefly describe the two models.

The fixed demand model for the traffic assignment assumes that the demand between each origin and each destination is constant and does not change after earthquake events. The advantage of this model is that it is simple to use. The disadvantage is that it fails when the demand greatly exceeds the capacity of the network due to its assumption of fixed demand.

The variable demand model for the traffic assignment assumes that the trip rates are influenced by the level of service of the network. If traveling becomes too expensive in terms of time or distance, the users are expected to change their habits in order to avoid the discomfort. After a major earthquake travelers will either have to accept the new congestion levels or decide not to travel. It is difficult to estimate how many passengers

will not travel; yet, reasonable assumptions can be made for the trip rate function between an origin and a destination and travel times.

In this paper the measure used for the network performance is the total delay of the passengers of the network. This is defined as the increase in the total travel time caused by earthquake induced damages. Essentially, it is the difference between the total travel time of the damaged network and the total travel time of the undamaged network. The total travel time is computed by the following equation:

$$T = \sum_{\text{all links}} x_i t_i(x_i) \quad (19.5)$$

$$D = T_{\text{before}} - T_{\text{after}} = \sum_{\substack{\text{all links} \\ \text{before}}} x'_i t'_i(x'_i) - \sum_{\substack{\text{all links} \\ \text{after}}} x_i t_i(x_i) \quad (19.6)$$

where

x_i is the flow on link i

$t_i(x_i)$ is the travel time on link i

T_{before} is the total travel time before the event

T_{after} is the total travel time after the event

D is the time delay caused by the event

and the primes refer to the parameters before the event.

The travel time on a link is calculated by utilizing a link performance function developed by the United States Bureau of Public Roads given as follows:

$$t_c = t_f \left(1 + a \left(\frac{V}{C} \right)^\beta \right) \quad (19.7)$$

where

t_c is the congested link travel time

t_f is the free flow link travel time

V is the link volume

C is the link capacity

a, β are calibration parameters, specific to the study region

Link travel time adjustments are made after some users have chosen a specific link which becomes less attractive to the other users. The adjustments are based on empirical data that require calibration of the parameters a and β with location, time of day and road type.

Transportation network functionality losses are directly related to travel time delay D per unit time (e.g. average daily traffic) computed over the duration of component closure. Operational loss as functions of time, where the time is duration of repairs of damaged bridges, is used to determine the loss of the system.

2.3. ESTIMATION OF TOTAL RISK

The risk can be expressed as the expected loss or the probability of exceeding a loss level. For spatially distributed systems estimation of the probability of exceeding loss level can be particularly challenging, because components of the system are subjected to different ground motions with each earthquake event. Most frequently a simulation approach is used to estimate the loss to a system where component and functionality loss is evaluated for each event and then the contribution of loss from all events is combined for a total risk formulation. In the following subsections we first address the estimation of expected loss and the uncertainty of that loss, referred to as *point estimates of loss* and then discuss the total risk curve analysis.

2.3.1. General formulation of point estimates of loss

The total expected loss for a given event is given by the following equation:

$$E(L|Q) = \int l_s f_{L_s|Q}(l_s|Q) dl_s + \int l_n f_{L_n|Q}(l_n|Q) dl_n \quad (19.8)$$

where

L_s is the structural loss of the components

Q is the scenario event

L_n is the loss due to network disruption

f is the probability density function of the random variable

$E(L|Q)$ is the expected value of loss L given the event Q

In eq. (19.8) the decision variable DV has been expressed in terms of monetary loss L . The event Q is defined by its magnitude, rupture length and location, rupture depth, and dip angle of fault. With these specifications, the IM are estimated for events with rate v_i at all bridge sites. The structural loss is evaluated based on the PEER methodology discussed in the previous section. The operational loss in the same equation requires a network analysis model with traffic assignments for the region presented in the preceding section. It implies that traffic delays D on various links of the system are first computed and then the losses L_n are estimated as function of the operational losses due to that time delay D .

The annualized risk for the system from all possible events that occur with rate v_i is expressed in the following equation:

$$v(L) = \sum_{\text{allevents}} v_i * \left\{ \sum_{\text{all network components}} \int l_s f_{L_s|Q}(l_s|Q) dl_s + \int l_n f_{L_n|Q}(l_n|Q) dl_n \right\} \quad (19.9)$$

where

L_s is the structural loss of the components

Q is the scenario event

L_n is the loss due to network disruption

f is the probability density function of the random variable

v is the annual rate of occurrence of an event or the rate of $DV = \text{total loss } L$

Equation 19.9 cannot be expressed in closed form and is evaluated numerically or through simulation. For large networks, the analytical complexity can be challenging and computational run-time can be excessive. Several methods have been proposed for efficient computation of the multiple integrals implicitly contained in eq. (19.9) through eqs. (19.1) and (19.2). Also implicit in this equation is the aggregation of loss from all network components. This aggregation is further discussed in the next section.

2.3.2. Point estimates of the structural loss for multiple sites and single event

Transportation planners and bridge engineers are usually interested in risk estimates that are applicable to multiple bridges in order to make decisions for retrofitting strategies or planning new routs. In this section, we will generalize the two methods for the estimation of the loss at a single site and apply them to a set of bridges. In the development that follows the dependence on the event Q is dropped to simplify the notation.

The loss from n components in a network is the sum of random variables. According to probability theory, the sum of the expected values of the loss of all the components will be equal to the expected value of the total loss. The variance of the total loss is equal to the sum of the variances, under the assumption that the damage of the components is uncorrelated. The equations follow:

$$E(\text{total loss}) = \sum_{\text{all bridges}} \{E(l_i)\} \quad (19.10)$$

$$\sigma^2 = \sum_{\text{all bridges}} \sigma_i^2$$

where

$E(l_i)$ is the expected value of the loss at a single site

σ_i is the variance of the loss at a single site

If the losses, however, are correlated, the variance is given by

$$E [L_{total}] = \sum_{i=1}^n E [L_i] \tag{19.11a}$$

$$\sigma_{L_{total}}^2 = \left[\sum_{i=1}^n \sigma_{L_i}^2 + \sum_{i=1}^n \sum_{\substack{j=1 \\ j \neq i}}^n \rho_{L_i L_j} \sigma_{L_i} \sigma_{L_j} \right] \tag{19.11b}$$

where ρ_{ij} is the correlation between loss L_i at sites i and loss L_j at site j within the system.

The challenge in evaluating eq. (19.11) is in estimating the correlations ρ_{ij} . Recent research by Lee and Kiremidjian (2006) has demonstrated that the losses at pairs of bridge sites are correlated through ground motion and bridge damage. In the following subsections we briefly summarize their results.

2.4. GROUND MOTION CORRELATION

In their formulation, pairs of ground motion are modeled as jointly normally distributed random variables with unit median conditioned on the magnitude and distance for that earthquake, and covariance matrix $\{\Sigma_{L_i, L_j}\}$ defined in terms of the earthquake error ε_l^2 , distance dependent correlated site error ε_s^2 , and uncorrelated residual error ε_r^2 arising from the attenuation model for the study region. The error terms $\{\varepsilon_l, \varepsilon_s, \varepsilon_r\}$ are assumed to be mutually uncorrelated zero-mean normally distributed random variables. With these assumptions, Lee and Kiremidjian provide the following formulation for the ground motion correlation for all pairs of sites when $i = j$:

$$\rho_{\varepsilon_i, \varepsilon_j} = \frac{Cov(\varepsilon_i, \varepsilon_j)}{\sqrt{Var(\varepsilon_i)}\sqrt{Var(\varepsilon_j)}} \neq \frac{\sigma_e^2 + \sigma_s^2 e^{-(r_{ij}/r_0)^2}}{\sigma_e^2 + \sigma_r^2 + \sigma_s^2} \tag{19.12}$$

As can be seen from eq. (19.12), the correlation decays with distance where r_0 is the standardized distance. The standardized distance r_0 represents the distance below which the correlation becomes 1. As the distance r_{ij} between sites i and j increases above the value of r_0 , the exponential term in eq. (19.12) approaches to zero.

2.5. DAMAGE CORRELATION

Correlation of damage between bridges of similar designs, material properties, construction methods and site characteristics can be expected to be relatively high when these bridges are subjected to ground motions from the same earthquake. In most applications, bridges are grouped by engineering bridge classes (HAZUS, 2000). Correlation of

bridges within a bridge class can be clearly seen since these bridges are presumed to perform in a similar manner in an earthquake. Partial between bridge class correlation can be explained by the seismic design requirements of bridges built under the same design criteria. Data required for the estimation of damage correlation are difficult to find if at all available. Therefore an equi-correlated assumption is made where the correlation ρ_{Di} , ρ_{Dj} is equal to a constant ρ_D . When two sites are subjected to the same ground motions, i.e. $u_i = u_j$, and the bridges at the two sites are in the same engineering class, then the bridges are considered to be perfectly correlated and the correlation coefficient is $\rho_D = 1$. The damage to two bridges of the same engineering class is considered to be uncorrelated if the ground motions at the two sites are different, i.e. $\rho_D = 0$ for $u_i \neq u_j$. For these two special cases, Lee and Kiremidjian (2006) develop closed form solutions for the joint probability density function of damage of pairs of bridges in a system. For partially correlated bridges closed form equation does not exist and the joint probability of damage needs to be evaluated numerically. They propose a numerical method for estimating these probabilities. The reader is referred to their paper for further detail.

2.5.1. Probability distributions of the structural loss for multiple sites and single event

In general, the first terms in eqs. (19.8) and (19.9) can be expanded to explicitly show the damage measure DM , engineering demand parameter EDP and intensity measure IM conditional probability density functions. The real challenge is in evaluating the probability density function (PDF) of loss for all bridges in the network system for a given event. The challenge is further increased when all possible events are considered. In this section we develop the aggregated loss from structural damage for a single event.

For a given event Q_j , $j = 1, 2, \dots, N$, the total loss resulting from damage to components (bridges) of the network is the sum of all the losses. Since the loss of each component is a random variable with its own distribution, the sum of the losses is a convolution of the individual probability density functions. That is,

$$L_{total} = L_1 + L_2 + L_3 + \dots + L_n \quad (19.13)$$

$$f_{L_{total}} = f_{L_1} \otimes f_{L_2} \otimes f_{L_3} \otimes \dots \otimes f_{L_n} \quad (19.14)$$

where

L_{total} is the total loss for a set of n bridges

L_i is the loss for bridge i , $i = 1, 2, \dots, n$ for a given event Q_j

f is the PDF of a random variable

\otimes is the symbol for convolution

In the above equations the subscript referring to the event j is dropped for simplicity of notation. Using the well known property that the convolution in the time domain becomes multiplication in the frequency domain, we can compute the probability density of L_{total}

by transforming the network component PDFs of loss, f_L , into the frequency domain, multiplying them in the same domain, and then apply the inverse transformations to obtain the probability density in the time domain. In order to reduce the error in transformation, two PDFs are transformed successively until the variables are exhausted and the total loss PDF is estimated. It is recalled that eqs. (19.14) and (19.15) are for a given event and the distributions are conditional on that event.

2.6. EVALUATION OF THE NETWORK FUNCTIONALITY LOSS

Undoubtedly, the network performance drops after an earthquake event because of its decrease capacity or components closure. In order to quantify this reduction in functionality we first estimate the expected value of the operational loss of the network relative to a baseline performance, which is the performance prior the earthquake. Then the uncertainty on that loss can be computed considering various sources of variability in the system.

2.6.1. *Expected value of network functionality loss*

Damage to network components defines the reduction in flow capacity. For example, a bridge with 20% damage will have to reduce its traffic by the same percentage in order to meet its demand. When the damage exceeds 40%, we assume that the bridge is closed and passengers have to make a detour.

Travel time delays are estimated by subtracting baseline travel times from the travel times in the network with reduced capacity. It is possible to convert this delay to monetary units, if we know the value of time and the number of passengers.

Bridge repair duration will depend on the damage level of the bridge and will vary for each bridge type. In order to have a realistic assessment of the total operational loss, we have to account for its evolution over time. To this effort, we are using the HAZUS estimates for restoration times for the different damage states. Network performance analyses are conducted immediately after the event and again after 1, 3, 7, 14, 30, 180 and 365 days. The results of these analyses are a mapping of the decrease in operational loss over time as bridges in the system are successively brought to back to full functionality. The total indirect loss is then the integral of this curve and must be added to the structural loss in order to estimate the total loss of the scenario. This operation represents the expected value of functionality loss for the transportation network.

2.6.2. *Uncertainties in network functionality loss*

There are numerous sources of uncertainty in the network functionality. These include the traffic assignment model, the post-event bridge closure decisions, the restoration time for individual bridges given their damage state, the value of trips taken and the number and value of trips lost. Treatment of these uncertainties requires that the transportation system be modeled as a stochastic network. Such a development is beyond the scope of the current paper and will be addressed in subsequent research.

2.7. TRANSPORTATION NETWORK RISK CURVE FROM MONTE CARLO SIMULATION WITH IMPORTANCE SAMPLING

Evaluation of eq. (19.9) that leads to the total risk curve is computationally very expensive. In general, there are three methods to compute eq. (19.9): (a) numerical integration; (b) conventional Monte Carlo simulations, and (c) Monte Carlo simulation with importance sampling. Numerical integration considers the full assessment of the equations describing the risk model. Monte Carlo simulation is an approximate method that randomly selects scenarios over time and evaluates the loss rate curve. It must be repeated many times to obtain stable results or it needs to be run over long forecast periods to capture all possible events. Importance sampling is again a simulation based approach that selects a combination of scenario events in the region in such a way that the mean and higher order moment of the risk rate curve are preserved with the minimum number of scenarios.

Considering the nature of the transportation network problem, analytical methods cannot be used for the risk assessment. Thus we choose the importance sampling method because it minimizes the analyses while preserving important components of the risk curve such as the mean and at least the second order moment (variance) of the loss rate. Then the losses from each scenario are combined as follows.

Earthquake events are assumed independent and follow a Poisson process. It is recalled that an event is defined by its magnitude, rupture length, rupture location, rupture depth, dip angle and annual rate of occurrence. We denote the probability of a scenario event to be $P[Q_j]$, $j = 1, 2, \dots, N$, where Q_j is the j th event that is identified as being important for the risk curve computation and N is the total number of events. If the loss for each scenario Q_j is L_j , $j = 1, 2, 3, \dots, N$, we order the losses in decreasing order the probability of exceeding the loss rate in a year is obtained by

$$L_n > L_{n-1} > \dots > L_k > \dots > L_1 \quad (19.15)$$

Then the probability of exceeding the loss rate in a year is obtained by

$$P[L_k \geq l] = 1 - \prod_{j=k}^n (1 - P[Q_j]) \quad (19.16)$$

In Equation 19.16, the assumptions are made that (i) individual losses are independent, (ii) the system is fully restored after each event, and (iii) only one event occurs at a time. While this equation is a simplification, it is computationally tractable and provides additional information over expected value loss estimates as will be demonstrated in the application section of this paper.

3. Application to the San Francisco Bay Area Transportation Network

The methodology on network seismic risk assessment presented in this paper is applied to the transportation network in the San Francisco Bay Area. For that purpose, the data on 2921 state and local bridges were obtained from the California Department of

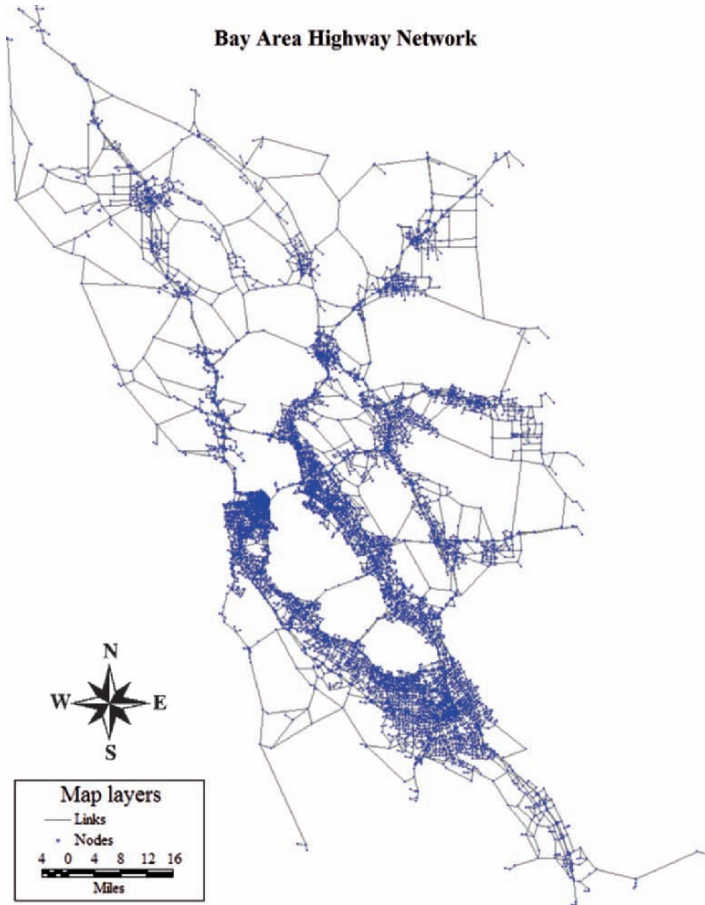


Fig. 19.1. Links and nodes of the MTC network

Transportation (Caltrans). Of these, structural information needed for the application is available for 1125 bridges. These bridges are classified into 28 engineering categories following the classification definitions in HAZUS (1999) and are used in the analysis presented herein. Furthermore, data on 29804 links and 10647 nodes comprising the San Francisco Bay Area highway network was provided by the Metropolitan Transportation Commission (MTC). Figure 19.1 shows the Bay Area highway network system with the nodes and links identified. For this system 1120 Transportation Analysis Zones (TAZ) are specified to determine trip origins and destinations (O-D). Daily traffic demand profile developed by Purvis (1999) is used to assign trips during various hours of the day with appropriate scaling factors. A vehicle car occupancy factor of 1.4 is recommended by MTC and is applied in the analysis (Caltrans, 2002). The value of time for users is assumed to be \$12.00/hr as recommended in the California Life Cycle Analysis Model

(Booz Allen & Hamilton Inc., 1999). Repair costs for bridges were provided by Caltrans (personal communications).

3.1. HAZARD ASSESSMENT

The seismicity in the San Francisco Bay Area is dominated by the San Andreas and Hayward faults. Magnitudes, their frequency of occurrence and rupture locations are well documented in a recent report by USGS (2003). For the purposes of our application, earthquakes of moment magnitude, $M_w = 6.75$ are considered to be appropriate lower threshold. The upper threshold values are 8.0 and 7.5 for the San Andreas and Hayward faults, respectively (USGS 2003). Considering various rupture locations along each fault, a total of 56 scenario events are identified and used in the risk assessment (see Stergiou and Kiremidjian, 2006 for further detail).

The Boore et al. (1997) ground motion attenuation model is used to predict site ground motions. For that purpose the local soil conditions are assessed according to the California Geological Survey (CGS). Ground motions are estimated at each bridge site in the network system with corresponding annual rate of occurrence (i.e. an IM value with a rate ν_{IM}).

Information on liquefaction susceptibility is obtained from the U.S. Geological Survey Open File Report 00-444 (USGS, 2000) and the methodology for liquefaction and landslide analysis provided in HAZUS (1999) is used to estimate liquefaction and landslide ground deformations at bridge locations.

3.2. DAMAGE ASSESSMENT

There is a significant ongoing effort to develop bridge fragility functions; however, none of these functions provide a comprehensive description of all bridge classes to enable complete application to a region. Thus, the damage functions provided in HAZUS are used in this paper for illustrative purposes. The conclusion will not change with different fragility functions, although the absolute values of loss may. In the HAZUS methodology, bridges can be in one of five damage states defined as: none, slight, moderate, extensive and complete. The probability of being or exceeding a damage level is characterized through a cumulative lognormal distribution conditional on the hazard level, IM . Such fragility functions are available for each of the 28 bridge classes in HAZUS.

3.3. STRUCTURAL LOSS

The loss from damage to bridges from each scenario event is estimated by multiplying the expected damage state of a bridge by its replacement value. Figure 19.2 shows the loss from damage to bridges due to ground shaking, liquefaction and landslides resulting from the potential occurrence of events on the San Andreas Fault. Similar results were also obtained for the scenario events on the Hayward fault and can be found in Stergiou

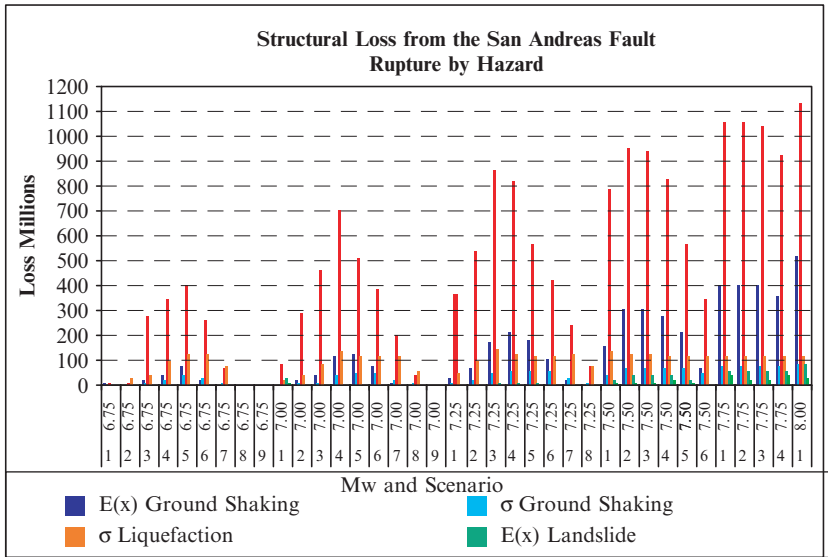


Fig. 19.2. Structural loss from the San Andreas fault rupture by hazard

and Kiremidjian, (2006). From that figure, the highest losses are from the magnitude 8.0 event on the San Andreas Fault, as expected. The contribution of losses due to liquefaction appears to be twice as large as those due to direct ground shaking. It is not clear, however, whether the large liquefaction losses are due to the crudeness of this component of the model. Investigations are currently underway to develop more theoretically sound models for liquefaction analysis that will enable more reliable estimation of these losses (Brandenberg personal communication). It is expected that the liquefaction losses will still be the largest contributors to direct structural loss, however, the predicted values may not be as large as reported herein. The loss from landslides is small in comparison to ground shaking and liquefaction.

The total replacement cost for the 1125 bridges considered in this study is estimated to \$2,891 Million. The total expected value of structural loss reaches a maximum of \$1.18 Billion for the San Andreas Fault scenarios and \$1.01 Billion for the Hayward Fault scenarios.

3.4. OPERATIONAL LOSS

Travel times to and from each TAZ in the San Francisco Bay Area were first evaluated before an event to develop the baseline results. For that purpose the transportation network analysis program Transcad GIS from Caliper Corporation (2004) was utilized. For each scenario event, the expected damage state for each bridge was determined and the restoration time from HAZUS were used to determine the duration of limited functionality. The network analysis was performed for 1, 3, 7, 14, 30, 180 and 265

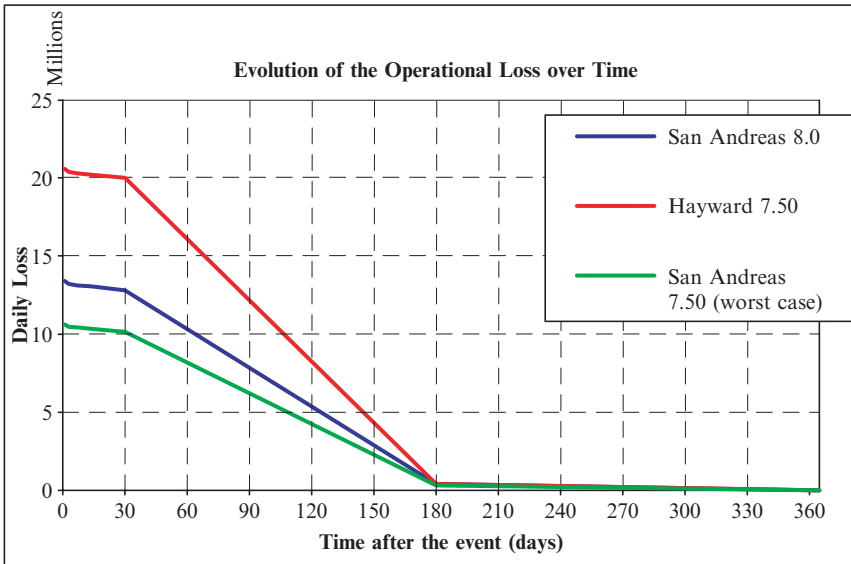


Fig. 19.3. Evolution of operational loss over time for three scenarios

days after the event has occurred to obtain the operational losses of the system. Example computation of daily losses due to reduced traffic on various links because of bridge closures is shown in Figure 19.3

The losses are integrated over the down time duration to obtain the total operational loss. Figure 19.4 shows the operational losses for each scenario earthquake on the San Andreas Fault. As can be seen from that figure, the operational losses reach a value of \$1.4 Billion significantly exceeding the direct structural losses of \$1.18B. Similar results are obtained also for the Hayward Fault scenario (see Stergiou and Kiremidjian, 2006); however, the operational losses reach \$2.12 Billion for the largest Hayward Fault scenario – almost twice the estimated direct structural loss value. The main reason for the large operational loss from the Hayward Fault scenarios is that there are more TAZs affected by these events and the traffic volume is larger on the links affected by these events. In these estimates *only commuter traffic was considered and it was assumed that the demand remains constant after an earthquake. If freight traffic has also been considered, the operational losses increase by a substantial amount since freight trips are five to six times more expensive than passenger trips.*

3.5. ANNUAL SEISMIC RISK ASSESSMENT

The structural and operational loss estimates for each scenario event are combined using eq. (19.16) to evaluate the annual risk for the transportation system. Figure 19.5 shows the annual risk curve and the corresponding best fitted equation. From the figure it can

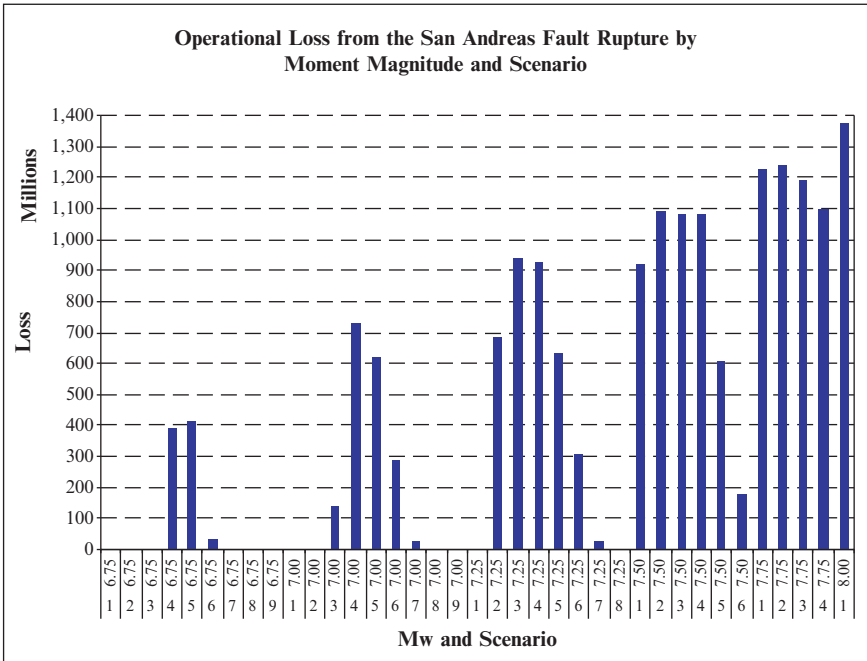


Fig. 19.4. Operational loss from the San Andreas fault rupture by moment magnitude and scenario

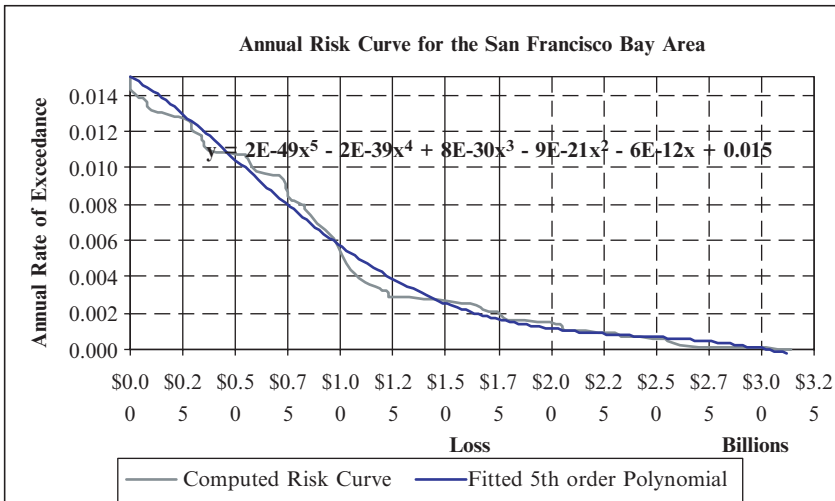


Fig. 19.5. Annual risk curve for transportation network

be seen that at the 500 year return period (or annual exceedence probability of 0.002) the loss is \$1.75 Billion. The loss level increases to \$2.25 Billion for the 1000 year return period and \$2.75 Billion at the 2000 year return period level. It is apparent from this curve and the values reported in Figures 19.2 and 19.4 that consideration of structural damage alone will greatly underestimate the system risk.

3.6. INFLUENCE OF GROUND MOTION AND DAMAGE CORRELATION ON LOSS COMPUTATIONS

Ground motion and damage correlation will have a direct influence on the estimation of loss uncertainty. In order to determine the importance of these correlations two small networks within the study area were selected and the loss coefficients of variation for direct structural damage were estimated. One of the networks has 16 bridges and the second consists of 9 bridges. Three levels of correlation were considered for ground motion that include perfect correlation, partial and no correlation (i.e. $\rho = 1, 0.5$ and 0). Damage correlation is conditional on ground motion, thus the effect of damage correlation is computed in relation to the ground motion correlation. Figure 19.6 shows the results of these analyses. From that figure it can be seen that the uncertainty in loss estimates increases significantly with increase in both ground motion and damage correlation. Furthermore, the contribution of ground motion correlation and damage correlation to the overall uncertainty appear to have equal weights. The size of the network does not appear to have an influence on the conclusions with similar results obtained for the 16 and nine component networks.

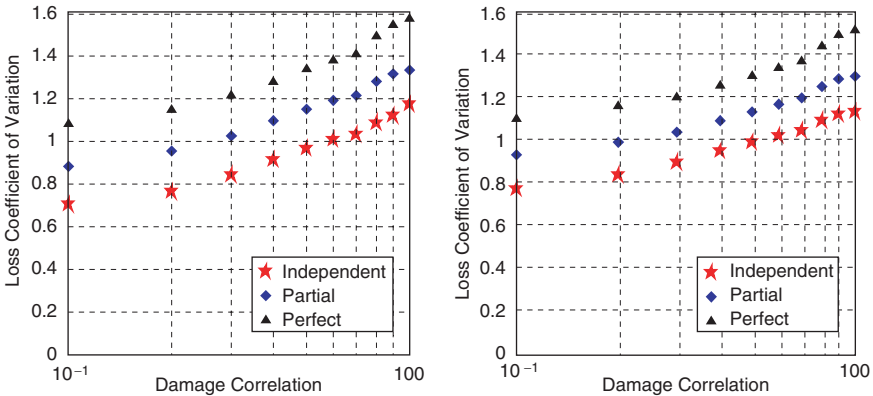


Fig. 19.6. Loss coefficient of variation for two networks, $N = 16$ (a) and $N = 9$ (b). Lowest marker points (★) result from independent ground motions. Highest marker points (▲) result from perfect ground motion correlation

4. Conclusions

A formulation for transportation network risk assessment is presented that considers ground motion, liquefaction and landslide hazards as well as the contribution of direct physical loss and operational loss. Application of the methodology to the San Francisco Bay Area shows that the operational loss is at least as large as the direct physical loss and can at times exceed that loss depending on the traffic conditions of the region, the network redundancy and the bridge resiliency in the system. It is found that liquefaction has the highest influence of all the hazards, but additional research to develop more robust methods of analysis is recommended. Consideration of ground motion and bridge damage correlation appears to be an important factor in the estimation of risk uncertainty and should be included. Finally, the contribution of each correlation appears to have an equal weight.

The risk assessment methodology and its application demonstrate the importance of consideration of uncertainty at various levels of the modeling. Decisions on the resilience of the system can be made rationally only if the overall risk is evaluated.

Acknowledgment

The partial support by the Earthquake Engineering Research Centers Program of the National Science Foundation, Award No. EEC-9701568 and the UPS Foundation Endowment is gratefully acknowledged.

REFERENCES

- Association of Bay Area Governments (ABAG) (1997) *Riding Out Future Quakes – Pre-earthquake Planning for Post-earthquake Transportation System Recovery in the San Francisco Bay Region*, ABAG Publications
- Basoz N, Kiremidjian AS (1996) *Risk Assessment for Highway Transportation Systems*. JA Blume Earthquake Engineering Research Center Technical Report No. 118, the Department of Civil Engineering, Stanford University, Stanford, CA
- Boore D, Joyner W, Fumal T (1997) Equations for estimating horizontal response spectra and peak acceleration from North American earthquakes: A summary of recent work. *Seismological Research Letters* 687(1):128–154
- Booz Allen & Hamilton Inc. (1999) *California Life Cycle Benefit/Cost Analysis Model*. California Department of Transportation, Sacramento, CA
- California Department of Transportation (2002) *2000–2002 California Statewide Household Travel Survey*
- Caliper Corporation (2004) *Transcad Software Technical Manual*
- Cho S, Fan YY, Moore J (2003) Modeling transportation network flows as a simultaneous function of travel demand, network damage, and network level of service. *Proceedings, Sixth U.S. Conference and Workshop on Lifeline Earthquake Engineering*, ASCE, August 10–13, 2003, Long Beach, CA, pp 868–877
- Fan Y, Nie Y (2006) Optimal routing for maximizing the travel time reliability. *Networks and Spatial Economics* 6(3):333–344

- HAZUS, (1999) Earthquake Loss Estimation Technical Manual. National Institute of Building Sciences, Washington, D.C
- Kiremidjian AS, Moore J, Fan YY, Basoz N, Yazali O, Williams M (2003) Pacific Earthquake Engineering Research Center Highway Demonstration Project. PEER 2006/04
- Lee R, Kiremidjian AS (2006) Uncertainty and Correlation for Loss Assessment of Spatially Distributed Systems, under review Earthquake Spectra
- Moore J, Fan Y (2003) Book review: New Analytical Advances in Transportation and Spatial Dynamics. In: Massimo Gastaldi and Aura Reggiani (eds), Ashgate Publishing Company, 2001, 318 pages. *Journal of Regional Science* 43(1):183–185
- Moore JE, Little RG, Cho S, Lee S (2005) Using Regional Economic Models to Estimate the Costs of Infrastructure Failures: The Cost of a Limited Interruption in Electric Power in the Los Angeles Region. Keston Institute for Infrastructure, University of Southern California
- Purvis C (1999) Peak spreading models: Promises and limitations. Proceedings, 7th TRB Conference on Application of Transportation Planning Methods, Boston, Massachusetts
- Shinozuka M (2000) Development of bridge fragility curves based on damage data. *Earthquake Engineering and Engineer Seismology: An International Journal* 2(2):35–45
- Shinozuka M, Murachi Y, Dong X, Zhou Y, Orlikowski MJ (2003) Effect of seismic retrofit of bridges on transportation networks. *Journal of Earthquake Engineering and Structural Dynamics* 2(2)
- Stergiou E and Kiremidjian AS (2006) Treatment of Uncertainties in Seismic Risk Analysis of Transportation Systems. The John A. Blume Earthquake Engineering Center, Report No. 156, Stanford University, Stanford, CA
- USGS (2000) Preliminary maps of quaternary deposits and liquefaction susceptibility, nine-county San Francisco Bay Region, California: A digital database – Open File Report 00-444, [<http://geopubs.wr.usgs.gov/open-file/of00-444/>]
- USGS (2003) Earthquake Probabilities in the San Francisco Bay Region: 2002–2031. Open File Report 03-214

Index

A

- Acceleration spectrum 35, 45, 75, 77, 78, 81, 86
- Accelerometer 38, 98, 100, 117, 293
- Active earth pressure (see Retaining walls)
- Active fault 37, 102, 186
- Amplification factor 32
- Angle of friction 140
- Arias intensity 74–76, 79, 80, 330, 415
- Axial strains
 - longitudinal strains 433, 443, 445

B

- Basin effects 37
- Bearing capacity 139, 201, 203, 204, 206, 209, 218, 219, 236, 237, 245–250, 252, 256–258, 260, 267, 270–272, 274, 394, 396
- Bedrock motion (see Ground motion)
- Bedrock outcropping motion (see Ground motion)
- Body waves 65, 438
- Borehole torsional shear test 363
- Building codes 53, 54, 67–69, 317

C

- Centrifuge test 93, 94, 111, 112, 119–121, 253, 254, 261–265, 271, 284, 298, 301, 315, 392, 393, 402
- Characteristic earthquake 44
- Characteristic site period 56

- Coherency 439, 444, 456
- Cohesion 309, 331
- Cone penetration test 107, 108
- Constitutive models 131, 132, 139, 143, 147, 148, 189, 195, 286, 304
- Countermeasure 386–389, 392, 393, 395, 396, 398–402
- Cross-hole test 98
- Cutoff frequency 28, 41
- Cyclic mobility 312
- Cyclic strength ratio 1, 8, 11, 15, 17, 20
- Cyclic stress ratio 82–84, 162, 172–174, 372
- Cyclic triaxial test 133, 159, 161

D

- Dam 3–5, 18, 19, 327, 334, 347, 348, 350
- Damping 23, 24, 29, 30, 43, 44, 69, 99, 138, 139, 185, 224–227, 236, 237, 309, 327, 341
- Damping ratio 30, 43, 45, 226
- Deaggregation 26, 45, 48
- Deconvolution 448, 451
- Deep foundations 185, 187, 194, 195, 303
- Degradation of shear modulus 253
- Design 3, 7, 8, 11, 12, 17, 20, 23–25, 34–37, 45, 68, 83, 86, 94, 95, 113, 123–125, 131, 137, 139, 151, 157, 169, 185, 186, 201–203, 209, 217–219, 221, 224, 225, 227, 228, 235, 237, 241, 245–247, 249, 252, 258, 260, 266, 267, 272, 273, 277–281, 283, 285–287, 289, 292–296, 299, 300, 303, 304, 315–317, 319–324,

327, 328, 330, 336–338, 349, 355–357,
389–392, 395, 396, 399–401, 404, 407,
409, 418, 430, 433, 435, 445, 456, 470
Design earthquakes 83, 317, 319, 349, 357, 391
Design ground motion 295
Deterministic seismic hazard analysis 350
Directivity 36, 207
Dispersion 38, 42, 64–66, 68, 134, 174, 437
Down-hole 98
Ductility 24, 201, 202, 207, 235, 236, 272,
429, 430
Duration 11, 69, 70, 119, 143, 146, 208, 209,
329, 330, 338, 409, 467, 471, 475, 476

E

Earth pressure (see Retaining walls)

Earthquake

epicenter 442
historical 26
intensity 143, 409
magnitude 36, 44, 78, 330, 336, 337, 435,
437, 438, 445

Earthquake resistant design 23, 123

Effective peak velocity 330

Epicenter 442

Epicentral distance 38, 438, 456

Equivalent linear model 74

Euroseistest 61, 62, 95, 98, 101, 138

Experiment 25, 63, 94, 98, 101, 104, 109,
113–116, 119, 127, 147, 185–187, 204,
253, 255, 257, 311, 312, 333, 407, 409,
416–418, 420, 425, 429

F

Fault 26, 37, 38, 40–42, 44, 56, 74, 75, 78, 81,
89, 103, 104, 113, 114, 185–201, 349,
408–410, 442, 462, 464, 467, 474–477

Fault rupture 114, 185–188, 191–195, 197,
200, 408, 409, 433, 441, 442, 461, 464,
475, 477

Finite difference method 62

Flow failure 5, 18, 19, 409

Focal depth 26, 45

Footing 102, 118, 139, 143, 144, 154, 156,
190, 201–203, 229–234, 236–241,

245–248, 250–252, 255–259, 263, 264,
266, 267, 272, 392–399, 404

Forced vibration 106, 138

Foundation 81, 96, 100, 102–104, 111,

115–117, 125, 131, 137–141, 243, 144,
146, 153, 155, 185–197, 199, 201–207,
209, 210, 217–237, 239–241, 245–273,
277–281, 283, 285–292, 295–297, 299,
300, 303, 311, 312, 320, 328, 335, 365,
376, 378, 385, 386, 388–394, 396,
400–404

Fourier amplitude spectrum 51, 55

Free-field motion 207

Frequency

fundamental 139

Fundamental mode of vibration 185

G

Geophone 155

G_{max} 155, 156, 226

Gravity walls 144, 202

Green's function 64, 65

Ground motion

coherency 435, 456

strong 23–51, 70, 96, 101, 143, 342

measurement

accelerogram 25, 27–29, 32, 45, 143

instrument arrays 99, 100

parameters

Arias intensity 74–76, 79, 80, 330, 415

characteristic intensity 330

peak acceleration 39, 73, 74, 79–81, 83,
95, 117, 316, 336

peak velocity 74

predominant period 267, 330

response spectrum intensity 330

rock outcropping motion 78, 81

Ground response analysis 74

equivalent linear 448

nonlinear 111

one-dimensional 117

two-dimensional 117

three-dimensional 117

transfer functions 62, 63, 68, 69, 99, 143

Ground velocity 74, 143, 330, 414, 415, 420, 437, 446
 Grouting 255, 365–373, 382, 386, 389, 391, 392, 397, 400

H

Historical seismicity 97
 Hypocenter 40, 41
 Hypocentral distance 41, 96

I

Impedance ratio 441
 Instrument arrays
 Euroseistest 61, 62, 95, 98, 101, 138
 Intensity 69, 73, 74, 81, 82

J

Jet grouting 400

L

Landslide (see Slope stability)
 Lateral spreading 4, 118, 185, 264, 277–283, 288–292, 294, 300, 464
 Lifelines 73, 81, 113, 115, 355, 407, 409–411, 425, 429, 435, 446, 447, 456, 462
 Liquefaction
 cyclic mobility 312
 effects 104, 105, 218, 245, 277, 278, 299, 300
 residual shear strength 1, 3, 4, 7, 8, 15, 17, 248, 249, 294, 297
 settlement 250, 252, 260, 263–265, 268, 269, 271, 272
 initiation
 cyclic strain approach 181
 cyclic stress approach 370
 energy dissipation approach 23
 factor of safety against liquefaction 82, 83, 253, 260, 262, 263, 270
 initial liquefaction 178
 liquefaction flow 1, 5, 18, 19
 resistance 84, 156, 356, 370, 374
 laboratory characterization 1, 3, 13, 17, 98, 162
 in situ test characterization 73, 79, 157, 279, 380

settlement
 saturated sand 2, 8, 120, 223, 288, 370, 414, 418, 420–425, 430
 susceptibility 73, 81–83, 85, 89, 101, 328, 474

Long period strong ground motion 23–51
 Longitudinal strains (see Axial strains)
 Love waves 102
 Low-rise structures 217, 235, 241

M

Magnitude 25–32, 34–36, 43–45, 47, 48, 53, 55, 56, 74, 78, 81, 83, 89, 96, 103, 143, 146, 186, 187, 199, 202, 219, 230, 233, 251, 284, 290, 310, 312, 330, 336–338, 344, 345, 360–362, 371, 434, 435, 437–439, 445, 456, 461, 467, 469, 472, 474, 475, 477
 modulus reduction curve 341
 moment 338, 474, 477
 Makdisi-Seed analysis 332, 335, 337, 338, 347, 348
 Masing behavior 308
 Material damping 337
 Microzonation 54, 67–69, 73, 76–83, 85–87, 89
 Mitigation 1, 124, 131, 137, 139–142, 256, 272, 355–357, 379, 380, 382, 462
 Model tests 131, 142, 277, 278, 285, 286, 288, 294, 297, 300, 377
 Modelling 53, 54, 56, 61, 62, 66, 99, 101, 118, 119, 122, 131–133, 135, 137, 139, 140, 143, 146–148, 186, 189, 201, 218, 228, 231–233, 235, 236, 238, 240
 Modified Mercalli intensity 415
 Modulus reduction curve (see Shear modulus)
 Moment magnitude (see Magnitude)
 Mononobe-Okabe method (see Retaining walls)

N

Natural frequency 139
 Natural hazards 407, 408, 429
 NEES 94, 102, 104, 107–109, 111, 113–116, 121–123, 125, 126, 153, 157, 425
 NEHRP Provisions 46, 74, 76, 86–89

Newmark sliding block analysis (see Slope stability)
 Nonlinear analysis
 of SDOF systems 24
 of soil deposits 141, 154, 169, 177, 186, 187
 Nonlinear models 236
 Normal fault 42, 187, 188, 410
 Normal stress 208, 251

P

Passive earth pressure 292
 Peak acceleration 39, 73, 81, 83, 95, 117, 316, 336
 Peak velocity 330
 Performance of surface foundations 217–243
 Period of vibration 23, 28, 33
 Permanent displacement 143, 146, 227, 279, 281, 291, 327, 328, 332, 334, 346, 348, 355, 435
 Phase velocity 64–66, 438
 Pile foundations 117, 268, 277–302, 376, 385, 388, 391, 393, 394, 400–402, 404
 Pipelines 113, 114, 185, 303, 365, 407, 409–412, 414–418, 420, 425, 426, 428–431, 433–435, 441, 445, 446, 452, 456
 Pore pressure ratio 248, 249, 254, 256–259, 282, 381, 399
 Power spectrum 142
 Predominant period 330
 Pressuremeter test 418
 Probabilistic seismic hazard analysis 26, 464
 Probability 77, 79, 80, 86, 87, 339, 342–346, 349, 350, 454, 462, 464, 465, 467, 468, 470–472, 474, 478

Q

Quality factor 96, 119, 131, 163, 228, 323, 324

R

Radiation damping 226
 Random variable 342, 344, 463, 467–470
 standard deviation 28, 32, 79, 153, 340, 344, 425
 variance 468, 469, 472
 Rayleigh damping 236

Rayleigh wave 38, 65, 151, 444
 Reflection 134, 135, 374, 409
 Refraction 64, 98
 Reinforced soil walls 143
 Remediation 385–387, 389–391, 393–400, 404
 Residual shear strength 1, 3, 4, 7, 8, 15, 17, 20, 248, 249, 294, 297
 Resonance 60, 141, 332, 343
 Resonant column test 98
 Response spectrum 23, 28, 34, 35, 37, 39, 43, 45, 68, 69, 73, 75, 76, 79, 81, 86, 88, 89, 227, 237, 279, 287, 330
 Retaining walls
 earth pressure 14, 116, 117, 144, 145, 284, 315–317, 323, 396, 399, 401
 dynamic response 111, 143, 154, 155, 185, 227, 279, 329–334, 337, 341, 350, 409
 failure 146, 327
 seismic displacements 327–329, 332, 340, 341, 345, 348, 350
 Richter magnitude 312
 Risk 53–55, 61, 68, 69, 124, 125, 137, 355, 397, 408, 430, 456, 461–463, 465, 467, 468, 472, 476–479
 Risk assessment 125, 430, 433, 435, 441, 445–447, 454, 456, 461–463, 465, 472, 474, 476, 479

S

Sampling 1, 6, 40, 72, 98, 99, 162, 461
 Saturation 104, 119, 172, 356, 386, 387
 Seismic hazard analysis 44, 73, 464
 deterministic 350
 probabilistic 464
 deaggregation 26, 45
 Seismic risk 53–55, 61, 69, 124, 137, 433, 435, 445–447, 456, 461–463, 472, 476
 Seismicity 46, 55, 58, 74, 95–97, 99, 103, 125, 474
 Seismograph 62, 64, 98
 Seismology 23, 54, 764, 95, 101
 Settlement (see Liquefaction)
 SH-wave 163
 Shaking table test 111, 112, 116, 138, 288, 395, 398, 399
 Shallow foundation 185, 187, 201–203, 205, 207, 217, 218, 221–225, 227–229, 231,

- 232, 234, 235, 237, 240, 241, 245–248, 251, 272
- Shape factor 219
- Shear modulus 99, 151, 155, 156, 226, 253, 308, 309, 337, 341, 402
- degradation 253
- Shear strain 9, 10, 99, 132, 141, 156, 189, 195, 197, 199, 225, 251, 280, 281, 292, 294, 297, 307, 310–312, 364, 435, 445, 446, 448, 451, 456
- Shear stress 9, 11, 73, 83, 132, 178, 250–253, 306, 307, 311, 312, 332, 359, 360, 386
- Single degree of freedom systems 116, 131, 138, 225
- Site effects 53–72, 87, 95, 96, 101, 137, 138, 435, 439, 456
- Slope stability 294–298, 327, 331, 334, 340, 341, 349
- Newmark sliding block analysis 264, 280, 294, 295, 297, 298, 300, 327, 332, 337, 350, 414
- landslides 113, 407–411, 417, 429, 430, 464, 474, 475, 479
- Soil improvement 272, 355, 356, 364–366, 368, 377, 385, 390, 394, 397, 399
- densification techniques 12, 250, 256, 272, 355, 356, 360, 363–366, 372, 373, 382, 385, 390–393, 395
- drainage techniques 178, 355, 371, 379, 381, 382, 387, 388, 396
- grouting and mixing techniques 355, 365–373, 382, 386, 389, 391, 392, 397, 400
- reinforcement techniques 174, 366, 386, 387, 394, 395, 397
- technologies 355–383, 385
- Soil mixing 397
- Soil-structure interaction 94, 95, 100–102, 120, 139, 141, 185, 227, 228, 232, 272, 303, 407–409, 417, 411, 429, 430, 433
- inertial interaction 224
- kinematic interaction 224
- Source and site factors 73–92
- Spatial variability 433, 446, 447
- Spectral analysis of surface waves 151
- Standard deviation 153
- Standard penetration (SPT) test 1, 3–8, 12–17, 82, 83, 98, 159–163, 167, 168, 174, 182, 266, 279, 280, 295, 313, 322, 355–358, 380
- State parameter 133
- Steady state 3, 7, 9, 155
- Stiffness 24, 83, 98, 99, 118, 131–134, 139, 140, 142, 151, 180, 185, 189, 190, 224–227, 229–232, 234, 236, 237, 278, 279, 286, 289–291, 308, 330, 341, 371, 422
- vertical 229–232, 234, 237
- rotational 204, 217, 229, 231, 232, 234, 237
- Stone columns 387, 397
- Strains
- axial (see Longitudinal) 178–180, 312, 362, 372, 375, 426, 427, 433–435, 453, 456
- transversal 445, 446
- shear 9, 10, 99, 132, 141, 156, 189, 195, 197, 199, 225, 251, 280, 291, 292, 294, 297, 307, 310–312, 364, 435, 445, 446, 448, 451, 456
- Stress drop 29, 45
- Stress path 133, 178, 310–312, 323, 359, 374, 365
- Stress-strain relationships 253, 307, 309
- Strong ground motion (see Ground motions)
- Surface wave magnitude (see Magnitude)
- Surface wave 43, 62–65, 98, 102, 151, 152, 157, 433, 434, 438, 444, 446
- SV-wave 445
- T**
- Time history 73–76, 78, 81, 86, 88, 89, 135, 140, 141, 143, 146, 147, 207, 209, 237, 332, 333, 378, 379, 438, 443, 444
- Topographic effects 329
- Torsional shear test 363
- Transfer function 62, 63, 68, 69, 99, 143
- Transportation 115, 319, 461–463, 465, 467, 468, 471–473, 475–477, 479
- Tsunami 304, 321
- U**
- Underground structures 185, 315, 388, 389, 433–439

V

Velocity

- Love waves 102
- p-waves 57, 135, 360–363
- particle 361, 434
- phase 64–66, 438
- Rayleigh waves 38, 65, 151, 444
- s-waves 66, 153, 154, 159, 160, 163–166, 169, 182, 434, 435, 441, 443–446

Viscous damping 34, 43, 236

W

Waste fills 334, 335, 338, 342, 347

Wave passage effect 49, 456

Wave propagation 37, 136, 155, 362, 433, 434, 436, 438–443, 445, 456

body waves 65, 438

one-dimensional 445

three-dimensional 37

two-dimensional 37, 442, 443

surface waves 43, 62–65, 98, 102, 151, 152, 157, 433, 434, 438, 446

Rayleigh waves 38, 65, 151, 444

Love waves 102

Wavelength 40, 55, 56, 65, 434, 436

Y

Yield acceleration 295, 297, 298

GEOTECHNICAL, GEOLOGICAL AND EARTHQUAKE ENGINEERING

1. A. Ansal (ed.): *Recent Advances in Earthquake Geotechnical Engineering and Microzonation*. 2004. ISBN: 1-4020-1827-4
2. C.S. Oliveira, A. Roca, X. Goula (eds.): *Assessing and Managing Earthquake Risk*. Geoscientific and Engineering Knowledge for Earthquake Risk Mitigation: developments, tools, techniques. 2006 ISBN: 1-4020-3524-1
3. To be published.
4. To be published.
5. To be published.
6. K.D. Pitilakis (ed.): *Earthquake Geotechnical Engineering*. 4th International Conference on Earthquake Geotechnical Engineering - Invited Lectures. 2007 ISBN: 978-1-4020-5892-9